FRACTURE MECHANICS
Twenty-Second Symposium

VOLUME II

Atluri/Newman/Raju/Epstein

EDITORS

ASTM STP 1131

STP 1131 (Volume II)

Fracture Mechanics: Twenty-Second Symposium (Volume II)

S. N. Atluri, J. C. Newman, Jr., I. S. Raju, and J. S. Epstein, editors

ASTM Publication Code Number (PCN)
04-011310-30

ASTM
1916 Race Street
Philadelphia, PA 19103

ASTM Publication Code No. (PCN): 04-011310-30
ISBN: 0-8031-1440-0
ISSN: 1040-3094

Peer Review Policy

Each paper published in this volume was evaluated by three peer reviewers. The authors addressed all of the reviewers' comments to the satisfaction of both the technical editor(s) and the ASTM Committee on Publications.

The quality of the papers in this publication reflects not only the obvious efforts of the authors and the technical editor(s), but also the work of these peer reviewers. The ASTM Committee on Publications acknowledges with appreciation their dedication and contribution to time and effort on behalf of ASTM.

Printed in Baltimore, MD
April 1992

Foreword

The Twenty-Second National Symposium on Fracture Mechanics was held on 26–28 June 1990 in Atlanta, Georgia. ASTM Committee E24 on Fracture Testing was the sponsor. The Executive Organizing Committee responsible for the organization of the meeting was composed of H. A. Ernst, Georgia Institute of Technology, who served as the symposium chairman, and the following vice-chairman: S. D. Antolovich, Georgia Institute of Technology; S. N. Atluri, Georgia Institute of Technology; J. S. Epstein, Idaho National Engineering Laboratory; D. L. McDowell, Georgia Institute of Technology; J. C. Newman, Jr., NASA Langley Research Center; I. S. Raju, North Carolina State A&T University; and A. Saxena, Georgia Institute of Technology. The proceedings have been divided into two volumes. H. A. Ernst, A. Saxena, and D. L. McDowell served as editors of Volume I and S. N. Atluri, J. C. Newman, Jr., I. S. Raju, and J. S. Epstein served as editors of Volume II.

Contents

SUMMARY

Introduction

The ASTM National Symposium on Fracture Mechanics (NSFM) is sponsored by ASTM Committee E24 on Fracture Testing. The objective of these symposia is to promote technical interchange between researchers in the field of fracture, not only within the United States but international, as evidence by participation in these proceedings. The meeting attracted about 165 researchers in the field of fracture with presentations covering a broad range of issues in materials, computational, theoretical, and experimental fracture.

The National Symposium on Fracture Mechanics is often the occasion at which ASTM awards are presented to recognize the achievements of current researchers. At the Twenty-Second Symposium several awards were presented. The ASTM Committee E24 Fracture Mechanics Medal was presented to Mr. Edward T. Wessel, Consultant and formerly with the Westinghouse Research and Development Center, Pittsburgh, for his outstanding leadership in guiding the Subcommittee on Elastic-Plastic and Fully-Plastic Fracture and the development of various elastic-plastic fracture mechanics standards. The ASTM Committee E24 George R. Irwin Medal was presented to Dr. John H. Underwood, U.S. Army Armament Research and Development Center, for his pioneering efforts in developing methods and standards in linear and nonlinear fracture mechanics. The ASTM Award of Merit and honorary title of Fellow were given to Dr. John P. Gudas, National Institute of Standards and Technology, for his distinguished service and leadership in Committee E24. Dr. Jun Ming Hu, University of Maryland, received the ASTM Committee E24 Best Student Paper award for his paper "Deformation Behavior During Plastic Fracture of C(T) Specimens." Dr. C. Michael Hudson, Chairman of Committee E24, made the presentations.

In 1989, ASTM Committee E24 lost one of its exceptional members and colleague, Professor Jerry L. Swedlow. For many years until his death, Dr. Swedlow was responsible to Committee E24 for the organizational oversight of all National Symposia on Fracture Mechanics. He played a crucial role, along with several others, in assuring the very high quality and vigor that we have come to associate with these Symposia. In the fall of 1989, the Executive Subcommittee of E24 passed the resolution initiating "The Jerry L. Swedlow Memorial Lecture" to be given at each National Symposium. The First Annual Jerry L. Swedlow Lecture was presented by Professor M. L. Williams, University of Pittsburgh. Dr. Williams presented a most interesting lecture which provided a "technical biography" of Professor Swedlow as well as suggesting various topics for future research (see ASTM STP 1131, Volume I).

We take this opportunity to express our appreciation to the late Jerry L. Swedlow, Chairman of the National Symposium on Fracture Mechanics Executive Subcommittee, for his support and guidance in initiating this symposium.

Executive Organizing Committee of the Twenty-Second National Symposium on Fracture Mechanics

Elastic Fracture Mechanics and Applications

C. Wm. Smith[1]

Experimental Determination of Fracture Parameters in Three-Dimensional Problems

REFERENCE: Smith, C. W., "**Experimental Determination of Fracture Parameters in Three-Dimensional Problems,**" *Fracture Mechanics: Twenty-Second Symposium (Volume II), ASTM STP 1131*, S. N. Atluri, J. C. Newman, Jr., I. S. Raju, and J. S. Epstein, Eds., American Society for Testing and Materials, Philadelphia, 1992, pp. 5–18.

ABSTRACT: Two established optical methods are described briefly with refinements to allow accurate near-tip measurements for three-dimensional cracked body problems. Several illustrations of their use are presented and compared with numerical results.

KEY WORDS: stress-intensity factors, three-dimensional photoelasticity, moiré interferometry, dominant eigenvalues, fracture mechanics, fatigue (materials)

Despite the early contributions of Sneddon [*1*] and Green [*2*], the field of analytical fracture mechanics was based largely on two-dimensional concepts until Irwin [*3*] recognized the technological importance of the surface flaw. Shortly thereafter, improvements in the speed and storage capacity of digital computers, together with the parallel development of numerical methods of analysis, opened the way to a study of three-dimensional fracture problems [*4–7*]. Many numerical analyses were then carried out rapidly, out-pacing the rather expensive and cumbersome parallel experiments for three-dimensional cracked body problems. In order to partially narrow this gap between analysis and experimental code validation, the author and his colleagues undertook an effort, beginning some two decades ago to develop relatively inexpensive optical modeling approaches to three-dimensional cracked body problems.

Beginning with the frozen stress photoelastic method [*8*], it was first refined for near-tip measurements and then applied to Mode I problems [*9*]. Later, it was extended to include all three local modes of analysis [*10*]. However, as the problems became more complex, it was deemed desirable to use two independent experimental methods of analysis of the same model in order to verify the experimental results independently of the numerical models. For this purpose, a refined high-density moiré method was developed for use in tandem with the frozen stress method [*11*].

In the present paper, after presenting a brief review of the methods themselves, the results from their application to several three-dimensional cracked body problems will be presented. The methods will be then used together to obtain fracture parameters outside the realm of linear elastic fracture mechanics (LEFM). Results will be compared with various analytical and numerical solutions.

[1]Alumni professor, Department of Engineering Science and Mechanics, Virginia Polytechnic Institute and State University, Blacksburg, VA 24061.

Optical Methods and Their Refinements for Near-Tip Measurement

When optical methods are applied to cracked body problems, some equipment modifications may be anticipated in order to enhance near-tip measurement. They will now be described briefly.

The method of frozen stress analysis was introduced by Oppel [*8*] in 1936. It involves the use of a transparent plastic that exhibits, in simplest concept, diphase mechanical and optical properties. That is, at room temperature, its mechanical response is viscoelastic. However, above its "critical" temperature, its viscous coefficient vanishes, and its behavior becomes purely elastic, exhibiting a modulus of elasticity of about 0.2% of its room temperature value and a stress fringe sensitivity of 20 times its room temperature value. Thus, by loading the photoelastic models above critical temperature, cooling under load, and then removing the load, negligible elastic recovery occurs at room temperature and the stress fringes and deformations produced mechanically above critical temperature are retained. Moreover, the "frozen" model may be sliced without altering its condition.

In order to determine useful optical data from frozen stress analysis, one needs to suppress deformations near the crack tip in the photoelastic material in its rubbery state above critical temperature and to be able to produce the same crack shape and size produced in the prototype. In order to accomplish the first objective, applied loads are kept very small, and a polariscope modified to accommodate the tandem application of Post-partial mirror fringe multiplication [*12*] and Tardy compensation [*13*] is employed. Such a polariscope developed by Epstein [*14*] is pictured in Fig. 1, which is self explanatory. Normally, fifth multiples of fringe patterns are read to a tenth of a fringe thus providing adequate data within about 1 mm of the crack tip to two hundredths of a fringe order.

Natural crack shapes are obtained by introducing a starter crack at the desired location in the photoelastic model of the structure before stress freezing by striking a sharp blade held normal to the crack surface with a hammer. The starter crack will emanate from the blade tip and propagate dynamically a short distance into the model and then arrest. Further growth to the desired size is produced when loaded monotonically above critical temperature. Loads are then reduced to stop growth and cooling is accomplished under reduced load. The shape of the crack is controlled by the body geometry and loads. By comparing crack shapes grown in photoelastic models by this process to those grown under tension-tension fatigue loads in steel, excellent correlation has been obtained [*15*] even when some crack closure was present at the free surface of the latter. It appears that the cracked body geometry and loads control the crack shape in thick, reinforced bodies and that the stress ratio, R (as long as it is positive), and plasticity or closure effects are of secondary importance.

Artificial cracks are made by machining into the body a desired shape, maintaining a vee-notch tip with an included angle not exceeding 30°. With this angle, near-tip stress fields are essentially the same as for branch cuts.

By removing thin slices of material that are oriented mutually orthogonal to the crack front and the crack plane locally, photoelastic analysis of these slices will yield the distribution of the maximum shear stress in the slice plane. Then, by expressing this stress in terms of the near-tip Mode I singular stress field equations including the contribution of the regular stresses in the near-tip zone as constants, one can arrive at an algorithm for extracting the stress-intensity factor (SIF) for each slice. The Mode I algorithm for stress is summarized in Appendix I based upon LEFM.

Moiré interferometry was introduced by Weller et al. [*16*] in 1948. As with the case for the frozen stress method, some modification of the usual approach is desirable in order to obtain accurate near-tip data. In the present case, a "virtual" grating was constructed

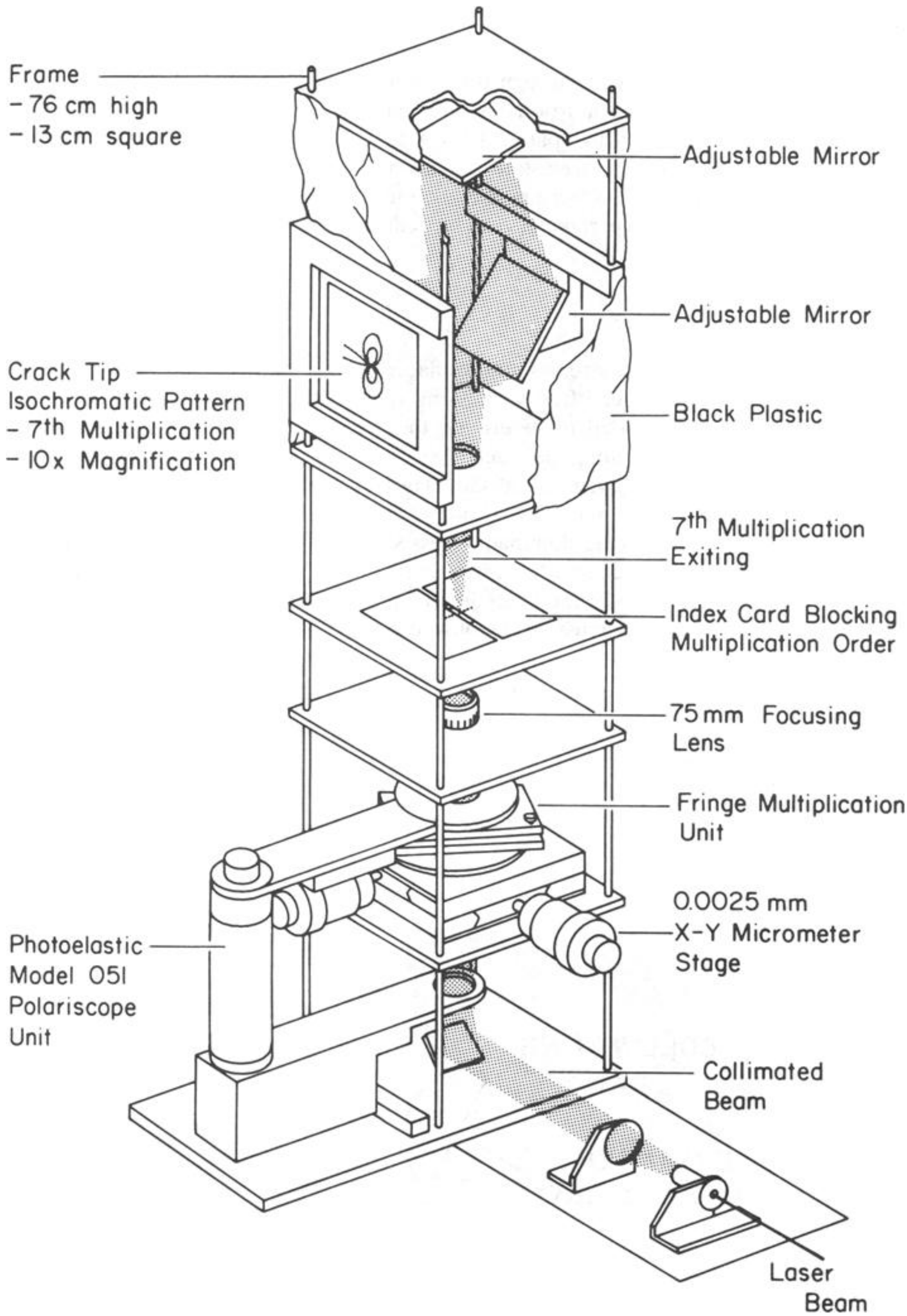

FIG. 1—*Precision polariscope.*

optically by reflecting part of an expanded laser beam from a mirror so as to intersect the unreflected part of the beam, forming walls of constructive and destructive interference which serve as the master grating (Fig. 2). The grating pitch is controlled by the wave length of light, Γ, and the angle, β. The specimen grating, a reflective phase grating, is transferred to the frozen slice and is viewed through the virtual grating as it (the former) deforms in order to see the moiré fringes proportional to the inplane displacement normal to the grating. By photographing the moiré fringe patterns produced on the surface of a frozen slice after it has been annealed to its stress-free state, the inverse of the displacement fields produced in the plane of the slice by stress freezing may be measured. Algorithms for converting this data into appropriate fracture parameters can be deduced from LEFM near-tip displacement field equations [*11*].

Three-Dimensional Effects

As implied in the foregoing, stresses and displacements in planes mutually orthogonal to the crack plane and its border often vary along the crack front. When this occurs, the foregoing methods may be used to determine the corresponding variation in the stress-intensity factor as one moves along the crack front. The vast majority of cracks that develop in structural components in service are surface flaws, whose borders intersect free surfaces of the body, usually at right angles. In such cases, not only does the SIF vary along the crack front, but the order of the dominant stress singularity is reduced locally where the crack intersects the free surface and this effect may be significant in nearly incompressible materials [*17*]. Optical data from the preceding methods may be also used to evaluate this effect, but special algorithms must be employed for that purpose. Such algorithms are recorded in Appendix II. The results from applying the preceding methods to determine the three-dimensional effects are illustrated by the following examples.

Example I—Stress-Intensity Factor Distribution Around the Border of a Nozzle Corner Crack in an Intermediate Test Vessel Model

Figure 3 is a photograph of the photoelastic test model that is about one eighth the size of the prototype. The shapes of natural cracks grown under internal pressure above critical

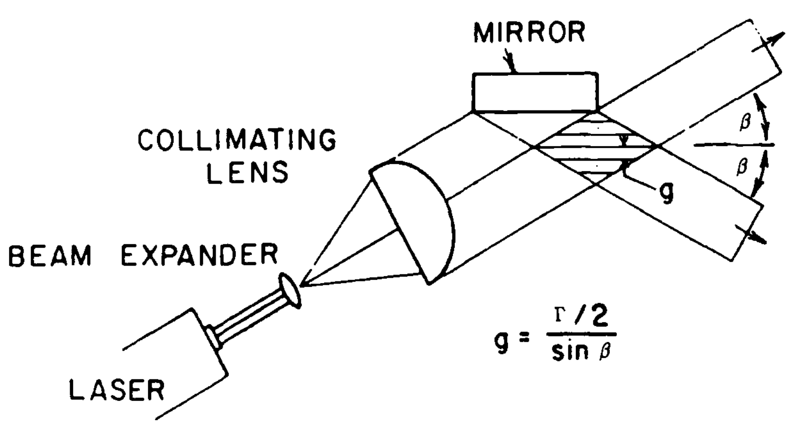

FIG. 2—*Virtual grating.*

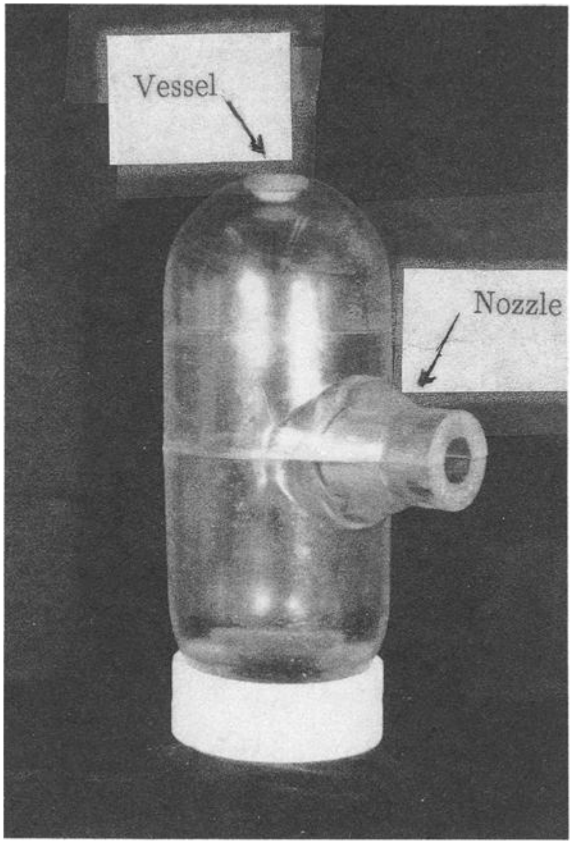

FIG. 3—*Model of intermediate test vessel (ITV).*

temperature are shown in Fig. 4 for increasing crack depths. By removing thin slices mutually orthogonal to the crack border and crack surface at intervals along each crack front after cooling under pressure and analyzing them photoelastically using the approach described in Appendix I, the stress-intensity factor (SIF) distributions shown in Fig. 5 were obtained showing how the SIF distribution changed as the crack shape changed. We note that the SIF increases near the middle of the crack front where growth is the slowest. That is, for stable crack growth, regions along the crack front where growth is slowest, or absent, will be regions where the K level builds up. When an increment of growth occurs in such a region, local stress is relieved and apparently transferred to adjacent regions. Kathiresan and Atluri [*18*] inserted the shape of the deepest crack (a/T = 0.71) into a three-dimensional finite element model that used special hybrid crack front elements along the crack border and isoparametric elements elsewhere and obtained the SIF distributions pictured in Fig. 5 for two values of Poisson's ratio. These results indicate approximately the influence of the high value of Poisson's ratio ($\nu \approx 0.48$) of the photoelastic material above critical temperature. Details of this study are found in Ref *19*.

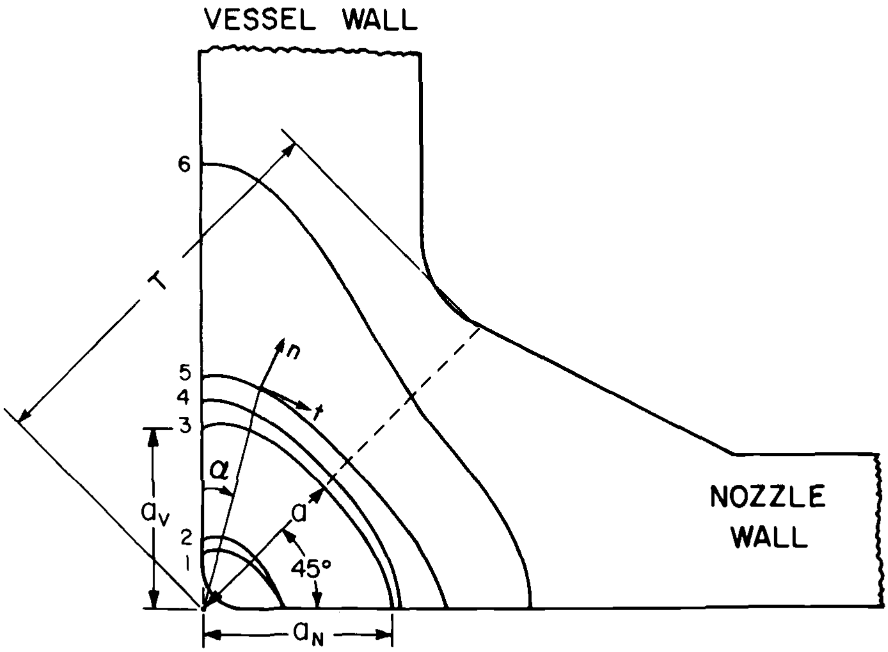

TEST	1	2	3	4	5	6
a_V (mm)	5.1	5.6	14.0	16.0	18.3	36.3
a_N (mm)	5.6	5.6	14.0	15.0	18.5	26.6
a (mm)	3.9	4.8	11.9	12.4	15.5	22.4
a/T	0.12	0.15	0.37	0.39	0.49	0.71

T = 31.8 mm for all tests

FIG. 4—*Crack shapes in ITV nozzle corner.*

Example II—Stress-Intensity Distribution Around the Border of a Semielliptical Surface Flaw in a Rocket Motor Model

Figure 6 shows the configuration of a photoelastic model that was capped on the ends and pressurized above critical temperature to grow a semielliptical natural crack from a small starter crack to one of moderate depth. After stress freezing and slicing as indicated, the slices were analyzed photoelastically and SIF values computed for each slice as described in Appendix I. The results from an average of three approximate test replications are shown in Fig. 7. The uniformity in the SIF level around the crack front at these depths suggests an absence of the effects of the star-shaped inner boundary. To emphasize this effect, a comparison was made between these experimental results and the Newman-Raju finite element model (FEM) for a surface flaw in a pressurized cylinder [*20*]. This was done by finding the "equivalent" inner radius that matched the FEM results with the experimental results at the inner or outer boundaries or both of the equivalent cylinder. Results are shown on Fig. 7. Details of this study are found in Ref *21*.

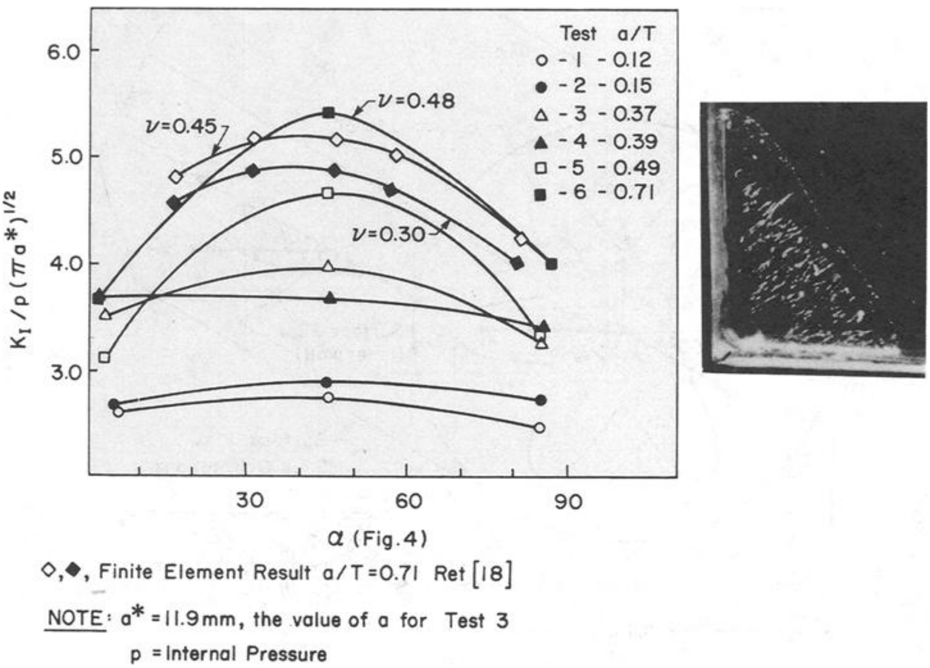

FIG. 5—*SIF distributions for nozzle corner cracks and FEM results* [18].

Example III—Determination of the Order of the Dominant Singularity when a Crack Intersects a Free Surface at Right Angles

The photoelastic model pictured in Fig. 8 contained an artificial (machined) straight front crack. After loading, stress freezing, slicing, and analyzing the slices photoelastically as before, linear gratings with a line of density equivalent to 2400 ℓ/mm were glued to one side of each slice and the slices were annealed, producing the inverse of the near-tip displacement field generated by stress freezing. A typical near-tip moiré pattern for the u_z displacement component is shown in Fig. 9. Using the algorithm of Appendix II (Eq 2), a distribution of $\lambda_\sigma(\lambda_\sigma = |\lambda_u - 1|)$ was obtained and is shown in Fig. 10. The solid curve tracks the moiré data. The value of λ_σ at the free surface of 0.35 compares favorably to Benthem's value of 0.33 [*17*]. Details of this study are found in Ref *22*.

Summary

Two refined optical methods, frozen stress photoelasticity and moiré interferometry, were described briefly and results from their use in examining near-tip three-dimensional effects in cracked body problems were presented and compared with analytical results. It is suggested that these experimental methods are useful in providing both input and validation information for three-dimensional cracked body problems.

Acknowledgments

The author wishes to acknowledge the contributions of his former students to parts of this work, especially W. H. Peters, J. S. Epstein, and J. C. Newman and that of his colleagues,

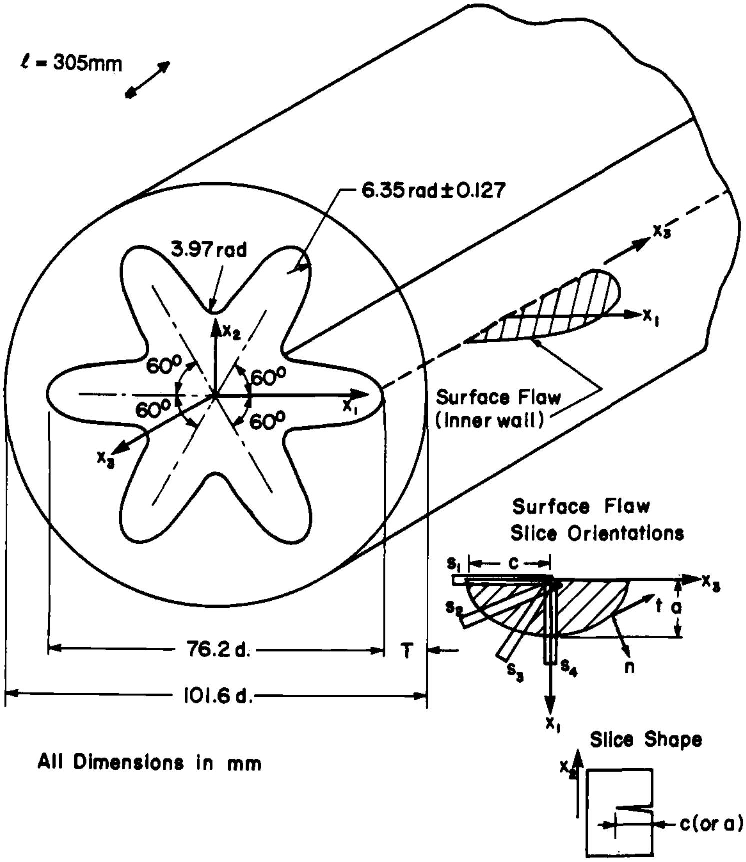

FIG. 6—*Rocket motor model configuration.*

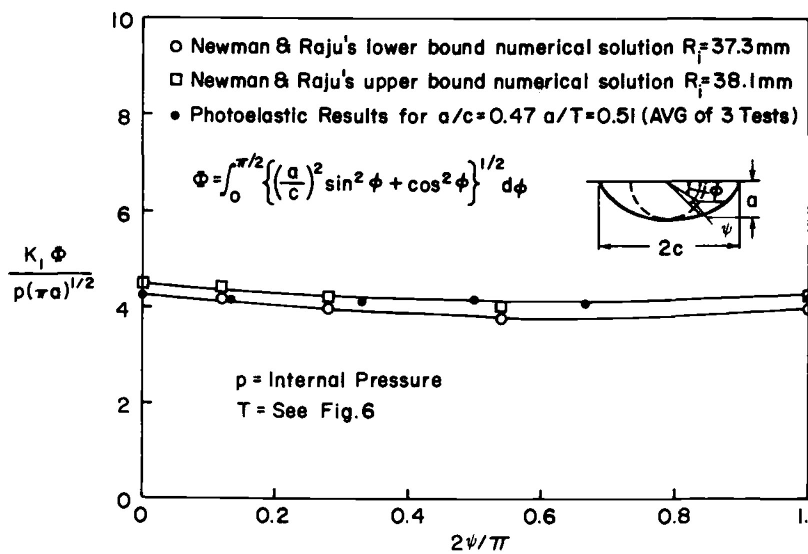

FIG. 7—*Comparison of SIF distribution along surface flaws in rocket motor models with Ref* 20 (R_i *are equivalent radii computed from Ref* 20 *so as to match the experimental data at inner* (lower) *and outer* (upper) *boundaries of the models).*

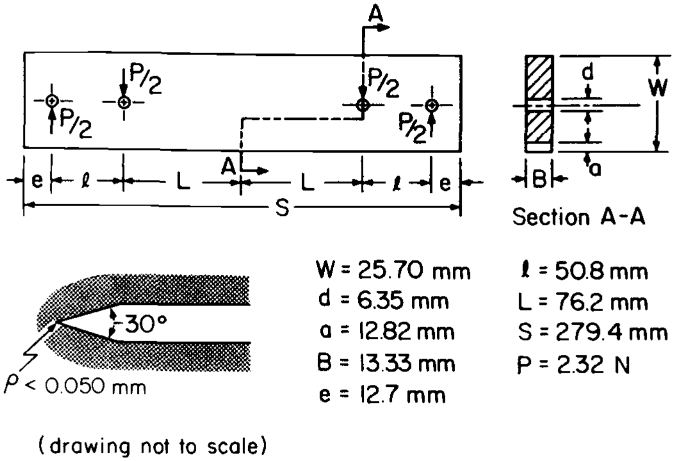

FIG. 8—*Four-point bending test specimen (FPBS).*

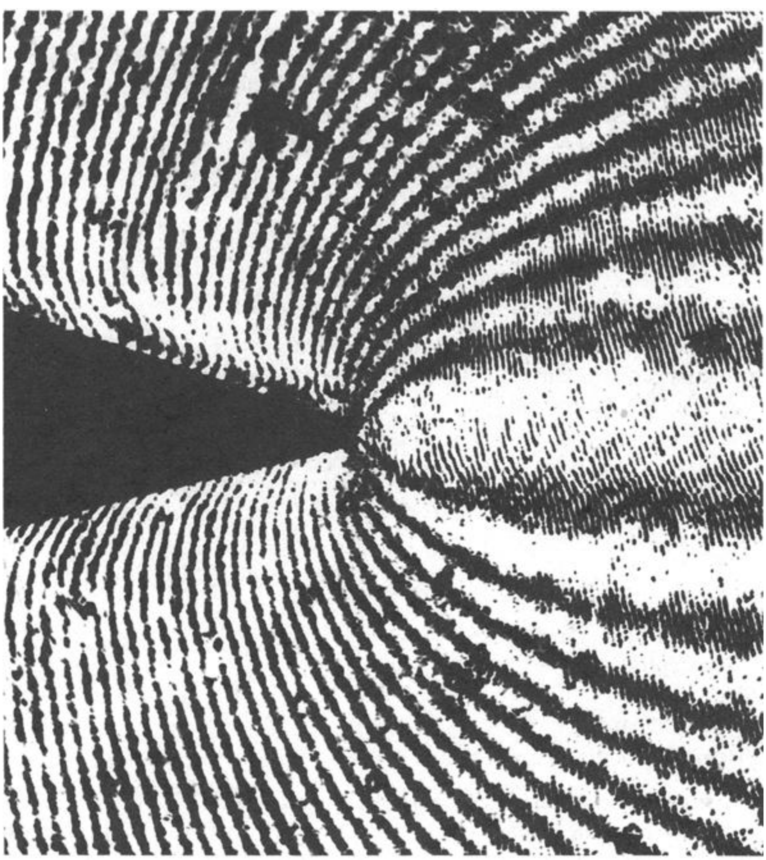

FIG. 9—*Moiré pattern for* u_z *for (FPBS).*

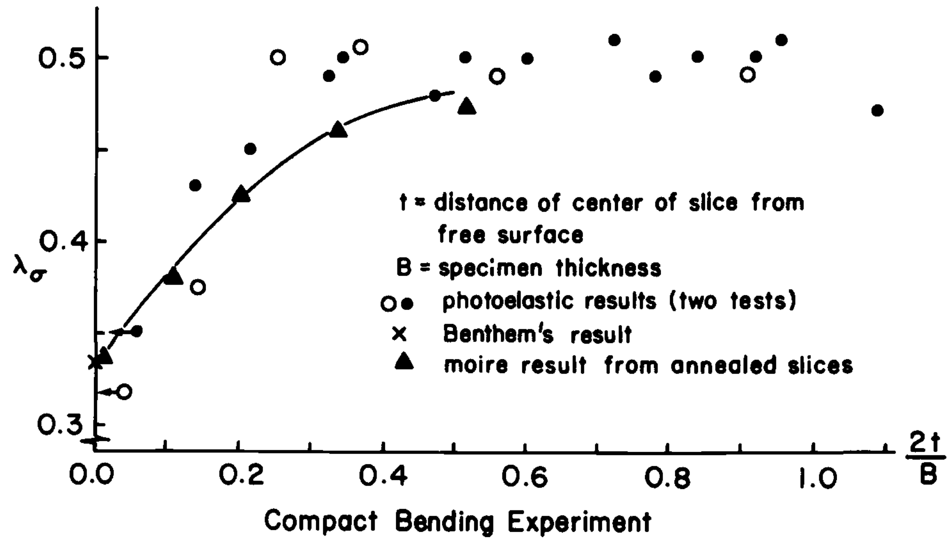

FIG. 10—λ_σ *distribution from FPBS using both moiré and photoelastic data.*

D. Post, S. N. Atluri, I. S. Raju, T. C. Cruse, A. F. Blom, and J. P. Benthem. He is also grateful to the Oak Ridge National Laboratory, National Science Foundation, and the U.S. Air Force Astronautics Laboratory, the latter under Contract No. F04611-88-K-0025 for support for parts of this work.

APPENDIX I

LEFM Frozen Stress Algorithm—Two-Parameter Approach

By choosing a data zone sufficiently close to the crack tip that a Taylor Series Expansion of the nonsingular stresses can be truncated to the leading terms, one may deduce, along $\theta = \pi/2$ (Fig. 11), the expression [*11*]

$$\frac{K_{AP}}{\bar{\sigma}(\pi a)^{1/2}} = \frac{K_1}{\bar{\sigma}(\pi a)^{1/2}} + \frac{\sqrt{8}\tau_0}{\bar{\sigma}}\left(\frac{r}{a}\right)^{1/2} \tag{1}$$

where

$K_{AP} = \tau_{\max}^{nz}\,(8\pi r)^{1/2}$,
$\bar{\sigma}$ = remote uniform stress,
a = crack depth,
K_1 = SIF,
τ_0 = nonsingular part of $\tau_{\max}^{nz}$, and
r = distance from crack tip in the nz plane.

Equation 1 suggests an elastic linear zone (ELZ) in a plot of $K_{AP}/\bar{\sigma}(\pi a)^{1/2}$ versus $(r/a)^{1/2}$. Experience shows this zone to lie usually between $(r/a)^{1/2}$ values of approximately 0.2 to 0.4. By extracting optical data from this zone and extrapolating across a near-tip nonlinear zone, an accurate estimate of $K_1/\bar{\sigma}(\pi a)^{1/2}$ can be obtained as illustrated in Fig. 12.

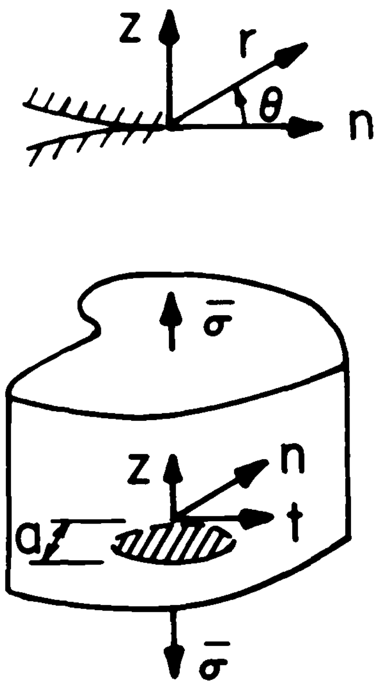

FIG. 11—*Near-tip coordinate system.*

APPENDIX II

Variable Eigenvalue Algorithms

When a crack border intersects a free surface at right angles, one has the intersection of three free surfaces that form a vertex singularity at the free surface. There is also a line-type LEFM singularity extending along the crack border inside the body. Excellent descriptions of this problem, based upon boundary integral and finite element analysis have been provided by Cruse [*23*] and Shivakumar and Raju [*24*]. Near the boundary, both singularities contribute to the local stress field. In the following discussion, an algorithm is developed using a pseudo-two-dimensional eigenvalue to estimate the projection of the vertex singularity effect into the plate thickness direction combined with the LEFM singularity.

Using Benthem's three-dimensional variables, separable eigenfunction expansion of the σ_{ij} and u_i near the crack tip at the free surface for a quarter infinite crack intersecting a half space at right angles [*17*] and the LEFM results as a guide, one can construct the following functional forms for the near tip $u_{z_{max}}$ and τ^{nz}_{max} [*22*] for extraction of λ_u and λ_σ from moiré and frozen stress data, respectively, along $\theta = \pi/2$ (Fig. 11). From Fig. 13, we have

$$\ln u_z = \ln D_z + \lambda_u \ln r \tag{2}$$

and from Fig. 14

$$\ln(\tau^{nz}_{max} - \tau_0) = \ln\left(\frac{\lambda_\sigma K_{\lambda_\sigma}}{\sqrt{2\pi}}\right) - \lambda_\sigma \ln r \tag{3}$$

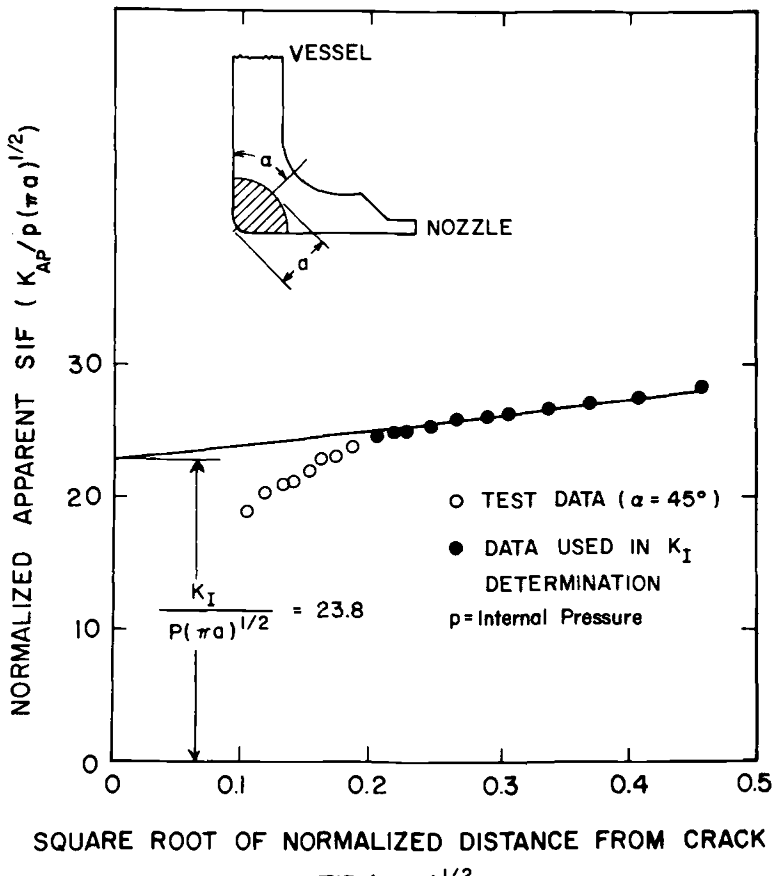

FIG. 12—*Determination of* K_I *from test data.*

where

u_z = displacement component in the z direction,
r = distance from the crack tip,
λ_u = dominant near-tip displacement eigenvalue,
τ_0 = nonsingular part of τ^{nz}_{max},
λ_σ = dominant stress eigenvalue, and
K_{λ_σ} = stress eigenfactor.

τ_0 is computed from LEFM (that is, assuming $\lambda_\sigma = 1/2$) at interior points and taken to be zero at the free surface to satisfy $|\lambda_\sigma| = 1 - \lambda_u$ there. Figures 13 and 14 present data from which Eqs 2 and 3 are used to determine λ_u and λ_σ, respectively.

This approach predicts a much thicker boundary layer effect than Refs *23* and *24* due to the vertex singularity. However, a full-field solution by Anders and Blom [*25*] yields comparable results.

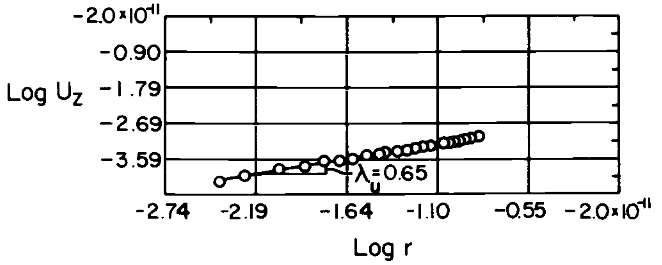

FIG. 13—*Determination of* λ_u *from moiré data.*

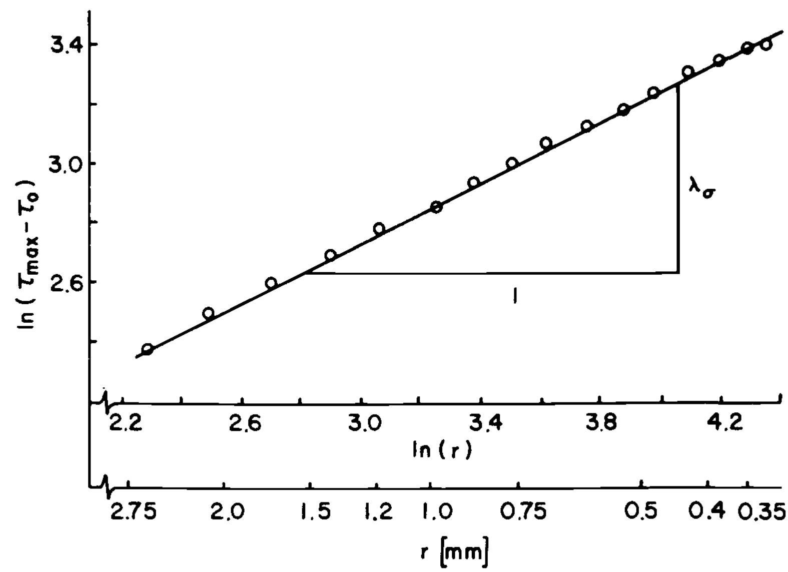

FIG. 14—*Determination of* λ_σ *from photoelastic data.*

References

[1] Sneddon, I. N., "The Distribution of Stress in the Neighborhood of a Crack in an Elastic Solid," *Proceedings*, Royal Society, Series A, Vol. 187, 1946, pp. 229–260.

[2] Green, A. E. and Sneddon, I. N., "The Distribution of Stress in the Neighborhood of a Flat Elliptical Crack in Elastic Solid," *Proceedings*, Cambridge Philosophical Society, Vol. 46, 1950, pp. 159–163.

[3] Irwin, G. R., "Crack Extension Force for a Part-Through Crack in a Plate," *Journal of Applied Mechanics*, Vol. 29, No. 4, Series E, Vol. 84, 1962, pp. 651–654.

[4] *The Surface Crack: Physical Problems and Computational Solutions*, J. L. Swedlow, Ed., Applied Mechanics Division, American Society of Mechanical Engineers, New York, 1972.

[5] "Computational Fracture Mechanics," E. F. Rybicki and S. E. Benzley, Eds., Computer Technology Committee of Pressure Vessels and Piping Division, American Society of Mechanical Engineers, New York, 1975.

[6] "Non-Linear and Dynamic Fracture Mechanics," N. Perrone and S. N. Atluri, Eds., Applied Mechanics Division, Vol. 35, American Society of Mechanical Engineers, New York, 1979.

[7] "Computational Fracture Mechanics—Nonlinear and 3-D Problems," P. D. Hilton and L. N. Gifford, Eds., PVP Vol. 85, AME Vol. 61, American Society of Mechanical Engineers, New York, 1984.

[8] Oppel, G., "Photoelastic Investigation of Three-Dimensional Stress and Strain Conditions," NACA TM 824, translated by J. Vanier, National Advisoring Committee on Aeronautics, 1937.
[9] Smith, C. W., "Use of Three Dimensional Photoelasticity and Progress in Related Areas," *Experimental Techniques in Fracture Mechanics 2*, A. S. Kobayashi, Ed., Society for Experimental Stress Analysis, Monograph No. 2, 1975, pp. 3–58.
[10] Smith, C. W., "Use of Photoelasticity in Fracture Mechanics," *Experimental Evaluation of Stress Concentration and Intensity Factors*, G. C. Sih, Ed., Martinus-Nijhoff, The Hague, The Netherlands, 1981, pp. 163–187.
[11] Smith, C. W. and Kobayashi, A. S., "Experimental Fracture Mechanics," *Handbook of Experimental Mechanics*, A. S. Kobayashi, Ed., Prentice Hall, 1987, pp. 891–956.
[12] Post, D., "Isochromatic Fringe Sharpening and Fringe Multiplication in Photoelasticity," *Proceedings*, Society for Experimental Stress Analysis, Vol. XII, No. 2, 1955, pp. 143–156.
[13] Tardy, M. L. H., "An Experimental Method for Measuring the Birefringence in Optical Materials," *Optics Review*, Vol. 8, 1929, pp. 59–69.
[14] Smith, C. W. and Epstein, J. S., "Measurement of Three Dimensional Effects in Cracked Bodies," *Proceedings*, Fifth International Congress on Experimental Mechanics, June 1984, pp. 102–110.
[15] Smith, C. W. and Peters, W. H., "Prediction of Flaw Shapes and Stress Intensity Factor Distributions in Three Dimensional Problems by the Frozen Stress Method," *Proceedings*, Sixth International Conference on Experimental Stress Analysis, Sept. 1978, pp. 861–864.
[16] Weller, R. and Shepard, B. M., *Proceedings*, Society for Experimental Stress Analysis, Vol. VI, No. 1, 1948, pp. 35–38.
[17] Benthem, J. P., "The Quarter Infinite Crack in a Half Space, Alternative and Additional Solutions," *International Journal of Solids and Structures*, Vol. 16, 1980, pp. 119–130.
[18] Kathireson, K. and Atluri, S. N., "Natural Shaped Flaws at Nozzle Corners from Pressure Loading and Thermal Shock," *Proceedings*, Fourth International Conference on Pressure Vessel Technologies, Vol. 1, 1980, pp. 163–168.
[19] Smith, C. W. and Peters, W. H., "Use of the Intermediate Test Vessel for Analyzing Nozzle Corner Cracks: A Photoelastic Analysis," *Proceedings*, Fourth International Conference on Pressure Vessel Technologies, Vol. 1, 1980, pp. 155–161.
[20] Newman, J. C. and Raju, I. S., "Stress Intensity Factors for Internal and External Cracks in Cylindrical Vessels," *Journal of Pressure Vessel Technology*, Vol. 104, Nov. 1982, pp. 293–298.
[21] Smith, C. W., "Fracture Parameter Measurements for Cracks Emanating from Curved Surfaces by the Frozen Stress Method," *Proceedings*, Ninth International Conference on Experimental Mechanics, Lyngby, Denmark, Vol. 5, Aug. 1990, pp. 1776–1785.
[22] Smith, C. W., Epstein, J. S., and Rezvani, M., "Measurement of Dominant Eigenvalues in Cracked Body Problems," *International Journal of Fracture*, Vol. 39, No. 1, 1989, pp. 15–24.
[23] Cruse, T. A., "Three Dimensional Elastic Surface Cracks," *Fracture Mechanics: Nineteenth Symposium, ASTM STP 969*, T. A. Cruse, Ed., American Society for Testing and Materials, Philadelphia, 1988, pp. 19–42.
[24] Shivakumar, K. N. and Raju, I. S., "Treatment of Singularities in Cracked Bodies," *International Journal of Fracture*, Vol. 45, No. 3, Oct. 1990, pp. 159–178.
[25] Blom, A. F. and Andersson, B., "On the Semi-Elliptic Surface Crack Problem: Detailed Numerical Solutions for Complete Elastic Stress Fields," *Surface Crack Growth: Models, Experiments, and Structures, ASTM STP 1060*, W. G. Reuter, J. H. Underwood, and J. C. Newman, Jr., Eds., American Society for Testing and Materials, Philadelphia, 1990, pp. 77–98.

Ivatury S. Raju,[1] James C. Newman, Jr.,[2] and Satya N. Atluri[3]

Crack-Mouth Displacements for Semielliptical Surface Cracks Subjected to Remote Tension and Bending Loads

REFERENCE: Raju, I. S., Newman, J. C., Jr., and Atluri, S. N., **"Crack-Mouth Displacements for Semielliptical Surface Cracks Subjected to Remote Tension and Bending Loads,"** *Fracture Mechanics: Twenty-Second Symposium (Volume II), ASTM STP 1131,* S. N. Atluri, J. C. Newman, Jr., I. S. Raju, and J. S. Epstein, Eds., American Society for Testing and Materials, Philadelphia, 1992, pp. 19–28.

ABSTRACT: The exact analytical solution for an embedded elliptical crack in an infinite body subjected to arbitrary loading was used in conjunction with the finite element alternating method to obtain crack-mouth-opening displacements (CMOD) for surface cracks in finite plates subjected to remote tension. Identical surface-crack configurations were also analyzed with the finite element method using 20-noded element for plates subjected to both remote tension and bending. The CMODs from these two methods generally agreed within a few percent of each other. Comparisons made with experimental results obtained from surface cracks in welded aluminum alloy specimens subjected to tension also showed good agreement.

Empirical equations were developed for CMOD for a wide range of surface-crack shapes and sizes subjected to tension and bending loads. These equations were obtained by modifying the Green-Sneddon exact solution for an elliptical crack in an infinite body to account for finite boundary effects. These equations should be useful in monitoring surface-crack growth in tests and in developing complete crack-face-displacement equations for use in three-dimensional weight-function methods.

KEY WORDS: cracks, elastic analysis, stress-intensity factor, crack-mouth-opening displacements, finite element method, finite element alternating method, surface crack, tension, bending loads, fracture mechanics, fatigue (materials)

Damage-tolerance analyses require accurate stress-intensity factors for two- and three-dimensional crack configurations. Experience with several crack configurations have shown that cracks in three-dimensional bodies tend to grow under fatigue loading with nearly elliptical crack fronts. Because these crack configurations occur frequently in aerospace structures, considerable attention has been devoted to analytical and experimental studies on these configurations. While considerable data exist in the literature on stress-intensity factors, very little information is available on crack-face displacements. Crack-face displacements are needed to develop more accurate three-dimensional weight-function methods. Crack-mouth displacements are also needed to develop compliance equations so that surface cracks can be monitored in fatigue-crack growth rate or fracture tests.

An approximate solution for the crack-face displacements for a surface crack in a plate under remote tension has been obtained by Fett [*1*] using the stress-intensity factor equations

[1]Senior scientist, North Carolina A&T State University, Greensboro, NC 27411.

[2]Senior scientist, Materials Division, NASA Langley Research Center, Hampton, VA 23665.

[3]Regents' professor and director, Center for Advancement of Computational Mechanics, Georgia Institute of Technology, Atlanta, GA 30332.

of Newman and Raju [2], the virtual crack extension method and conditions of self-consistency. In this paper, the exact analytical solution of Vijayakumar and Atluri [3], Nishioka and Atluri [4], and Raju [5] for an embedded elliptical crack in an infinite body subjected to arbitrary loading was used in conjunction with the finite element alternating method [6,7] to obtain crack-mouth-opening displacements (CMOD) for surface cracks in finite plates subjected to remote tension. Identical surface-crack configurations were also analyzed with the finite element method using 20-noded elements for plates subjected to both remote tension and bending. The CMODs from these two methods are compared with each other. The numerical CMODs are also compared with experimental results from McCabe et al. [8,9] on welded 2219-T87 aluminum alloy specimens with a surface crack in a plate subjected to tension.

Empirical equations were developed for CMOD for a wide range of surface-crack shapes and sizes subjected to tension and bending loads. These equations are obtained by modifying the Green and Sneddon [10] exact solution for an elliptical crack in an infinite body to account for finite boundary effects.

Analysis

A surface crack in a finite plate, as shown in Fig. 1, was analyzed. The three-dimensional finite element and finite element alternating methods were used to obtain the CMODs. In these analyses, Poisson's ratio (ν) was assumed to be 0.3. A comparison of stress-intensity factors from these two methods are given in Ref *11* for both surface and corner cracks in plates.

Two types of loading were applied to the surface-crack configuration: remote uniform tension and remote out-of-plane bending (bending about the X-axis). The remote uniform

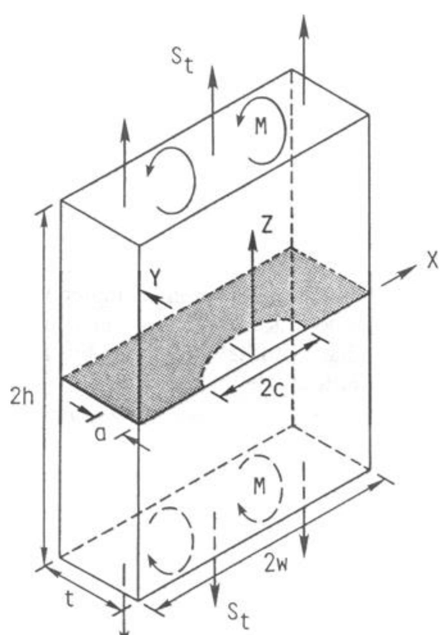

FIG. 1—*Surface crack in a plate.*

tensile stress is S_t acting in the Z-direction and the remote bending moment is M. The bending stress, S_b, is the outer fiber stress calculated at the origin ($X = Y = Z = 0$ in Fig. 1) without the crack present.

Three-Dimensional Finite Element Method

Figure 2 shows a typical finite element model for a surface crack in a rectangular plate. The finite element models employed 20-noded isoparametric parabolic elements throughout the body. Singularity elements were not used along the crack front. Typical models had about 800 elements and 5000 nodes. Symmetric boundary conditions were imposed on the $Z = 0$ and $X = 0$ planes. Models were subjected to either remote uniform stress or a linear bending stress on the $Z = h$ plane.

Finite Element Alternating Method

This method is based on the Schwartz-Neumann alternating method [*12*]. The alternating method uses two basic solutions of elasticity and alternates between these two solutions to satisfy the required boundary conditions of the cracked body [*13–15*]. One of the solutions is for the stresses in an uncracked finite solid, and the other is for the stresses in an infinite solid with a crack subjected to arbitrary normal and shear tractions. The solution for an uncracked body may be obtained in several ways, such as the finite element or boundary element method. In this paper, the three-dimensional finite element method was used.

The procedure is explained here briefly for Mode I problems. First, obtain the solution for the uncracked solid subjected to the given external loading using the finite element method. The finite element solution gives the stresses everywhere in the solid including the region over which the crack is present. The normal stresses acting on the region of the crack surfaces need to be erased to satisfy the crack-boundary conditions. The opposite of the stresses calculated on all boundaries are fit to n^{th} degree polynomials in terms of X- and Y-coordinates. From the polynomial stress distributions obtained, calculate the stress-intensity factor [*4*] for the current iteration. Use the analytical solution of an embedded

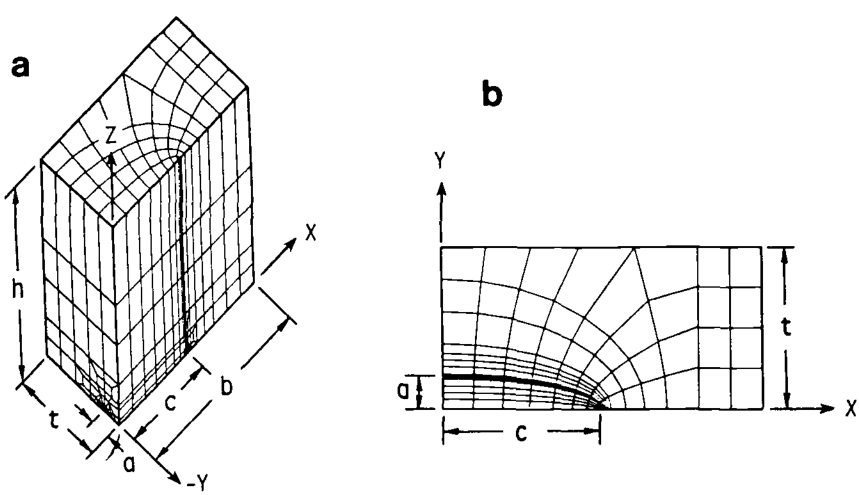

FIG. 2—*Finite element model of surface-cracked plate:* (a) *specimen model and* (b) *element pattern on Z = 0 plane.*

elliptic crack in an infinite solid subjected to the polynomial normal traction [*4*] to obtain the normal and tangential stresses on all of the external boundaries of the solid. The opposite of these stresses are then considered as the externally prescribed stresses on the uncracked solid. Again, solve the uncracked solid problem due to these prescribed surface tractions. This is the start of the next iteration. Continue this iteration process until the normal stresses in the region of the crack are negligibly small or lower than a prescribed tolerance level. The stress-intensity factors in the converged solution are simply the sum of the stress-intensity factors from all iterations.

The key element in the alternating method is, obviously, the analytical solution for an infinite solid with an embedded elliptical crack subjected to arbitrary normal and shear tractions. Such a solution was first obtained by Shah and Kobayashi [*16*] for tractions normal to the crack surface. However, this solution was limited to a third-degree polynomial function in each of the Cartesian coordinates describing the ellipse. Vijayakumar and Atluri [*3*] overcame this limitation and obtained a general solution of arbitrary polynomial order. Nishioka and Atluri [*4,6*] improved and implemented this general solution in a finite element alternating method and analyzed surface- and corner-cracked plates. The details of the finite element alternating method are well documented [*4–6*], and they are not repeated here.

In the three-dimensional finite element solution, 20-noded isoparametric parabolic elements were used to model the uncracked solid. Two types of idealizations have been used to analyze surface- and corner-crack configurations [*11*]. In the first type, the idealization was such that the elements on the $Z = 0$ plane conform to the shape of the crack in the cracked solid (see Fig. 3*a*). Although the finite element solution is for the uncracked body, such an idealization is convenient to perform the polynomial fit using the finite element stresses from the elements that are contained in the region of the crack. The mesh is then generated by simply translating in the Z-direction the mesh on the $Z = 0$ plane. This model will be referred to as the mapped model. A typical mapped model is shown in Fig. 3*a*. In the second type, simple rectangular idealizations were used to model the solid. This model

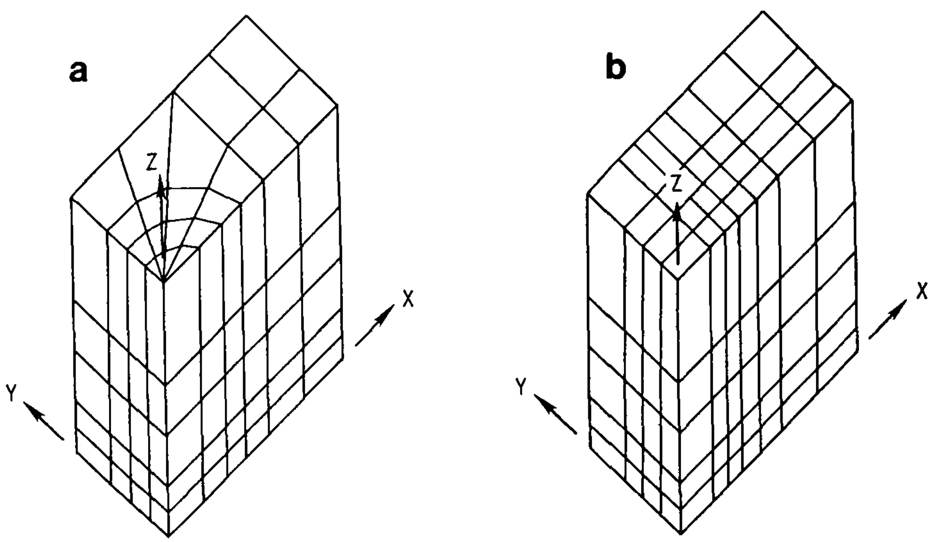

FIG. 3—*Finite element alternating models for surface-crack analysis:* (a) *mapped model and* (b) *rectangular model.*

is referred to as the rectangular model. A typical rectangular model is shown in Fig. 3*b*. Reference *11* showed that mapped and rectangular models give nearly identical results if sufficient degrees of freedom are used. However, the mapped models tend to converge faster than the rectangular models. Herein, mapped models will be used to obtain crack-surface displacements. Typical mapped models had about 250 elements and 1500 nodes; and the models used four elements to approximate the crack front. For all models, the solution converged to within 1% accuracy in five iterations (see Ref *11*).

Results and Discussion

In this section, CMOD equations for a surface crack in a finite thickness plate subjected to remote tension and bending loads are developed. The CMOD values calculated from the two numerical methods are compared with each other and with the proposed equations. CMOD values from the proposed equations are also compared with experimental results over a wide range in crack shapes and crack sizes for remote tension.

Crack-Mouth-Opening Displacements

The CMOD was expressed in the form of the Green-Sneddon solution for an embedded elliptical crack in an infinite body multiplied by a boundary-correction factor, G_i, as

$$EV/(S_i a) = 4(1 - \nu^2)/\Phi G_i(a/c,\ a/t,\ c/w) \tag{1}$$

where the subscript i denotes tension load ($i = t$) or bending load ($i = b$), V is the total displacement across the crack mouth ($X = Y = Z = 0$), a is the crack depth, c is the crack half-length, t is the thickness of the plate, w is half-width, and Φ is the shape factor of the ellipse (which is equal to the complete elliptic integral of the second kind). The shape factor, Φ, can be approximated by

$$\Phi^2 = 1 + 1.464(a/c)^{1.65} \quad \text{for} \quad a/c \leq 1 \tag{2a}$$

and

$$\Phi^2 = 1 + 1.464(c/a)^{1.65} \quad \text{for} \quad a/c > 1 \tag{2b}$$

The half-length of the bar, h, and the half-width, w, (see Fig. 1) were chosen large enough ($h/w = 2$ and $w/a = 25$) to have negligible free-boundary effects on crack-surface displacements. Values of normalized displacements ($EV/S_i a$) were calculated for various crack shapes ($a/c = 0.2$ to 1) with a/t values of 0.2, 0.5, and 0.8. The normalized displacements from the finite element and finite element alternating methods are given in Table 1. The current alternating method could not be used to analyze the semicircular ($a/c = 1$) crack configuration. The alternating method was also not used to analyze surface cracks under the remote bending loads. Experimental results from Ref *8* for an a/c ratio of 2 were also used to extend the equations to a/c ratios greater than 1.

Tension Loads—The boundary correction factor for surface cracks subjected to remote tension loading is

$$G_t = G_s G_w \tag{3}$$

TABLE 1—*Nondimensional CMOD* ($EV/S_t a$) *from finite element (and finite element alternating) method* ($\nu = 0.3$).

	a/t		
a/c	0.2	0.5	0.8
	TENSION		
1.0	3.040	3.284	3.758
0.8	3.440 (3.366)	3.816 (3.824)	4.562 (4.656)
0.6	3.914 (3.816)	4.554 (4.464)	5.826 (5.636)
0.4	4.486 (4.380)	5.696 (5.620)	8.178 (7.960)
1/3	4.702 (4.590)	6.254 (6.140)	9.500 (9.188)
0.2	5.198 (5.072)	7.958 (7.748)	14.30 (13.63)
	BENDING		
1.0	2.770	2.518	2.330
0.8	3.108	2.866	2.712
0.6	3.512	3.344	3.310
0.4	3.996	4.078	4.410
1/3	4.178	4.434	5.028
0.2	4.592	5.516	7.258

where

$$G_s = [1.18 + 0.08(c/a)^{0.5} + 0.65(c/a)^{1.15}(a/t)^2]g,$$
$$g = 1 \text{ for } a/c \leq 1,$$
$$g = c/a \quad \text{for} \quad a/c > 1, \text{ and}$$
$$G_w = \{\sec[\pi c(a/t)^{0.5}/(2w)]\}^{0.5}.$$

for $0.2 \leq a/c \leq 2$ and $a/t < 1$. These equations were found by using engineering judgment, appropriate limits, and trial and error.

Bending Loads—The boundary-correction factor for surface cracks subjected to remote bending loads is

$$G_b = G_s G_w H \tag{4}$$

where G_s and G_w are the same as in Eq 3, and H is the bending correction. The functional form of H was found by comparing the exact displacements for an embedded circular crack in an infinite solid subjected to remote tension and remote bending. The coefficients were found by trial and error, and H was given by

$$H = 1 - [0.7 - 0.2(a/c)^{0.5}](a/t)$$

for $0.2 \leq a/c \leq 2$ and $a/t < 1$.

Comparison of Crack-Mouth-Opening Displacements

The normalized CMODs calculated from the finite element method (FEM) and finite element alternating method (FEAM) are given in Table 1 (*top*). A comparison between the two methods and the proposed equation (Eqs 1 and 3) for remote tension is shown in Fig. 4. The results from the two methods agreed within a few percent of each other. The largest difference between the two methods occurred at deep cracks ($a/t = 0.8$) and for low aspect (a/c) ratios. The maximum difference was about 5%. The FEM tended to give higher CMOD values than the FEAM for all crack configurations analyzed. The equation, obtained by fitting to these results, gave CMOD values that were within about 3% of the FEM calculations.

Fett [1] has obtained an approximate solution for crack-opening displacements of semi-elliptical surface cracks in finite thickness plates under remote tensile loading. He used the Newman-Raju stress-intensity factor equations for local crack-front displacements and conditions of self-consistency to obtain full field crack-opening displacement equations. The equation for the boundary-correction factor on Eq 1 was

$$(G_t)_{\text{Fett}} = 1.13[M_1 + M_2(a/t)^2 + M_3(a/t)^4][1.1 + 0.35(a/t)^2] \quad (5)$$

where M_i are functions of a/c and a/t and are given in Ref *2*. The product of the terms in brackets give the stress-intensity boundary-correction factor at the free-surface location. A comparison among CMOD values from Fett's equation, finite element, finite element alternating, and the proposed equation are shown in Fig. 5. For low values of a/t, all results were within about 3% of each other. Results for $a/c = 0.6$ and 1 also agreed well for a/t ratios less than 0.8. However, for low a/c ratios and large a/t values, Fett's equation was substantially lower than both analyses and Eq 1 with G_t from Eq 3. The reason for this discrepancy is not known but, for deep cracks, the local stress-intensity factors may not be

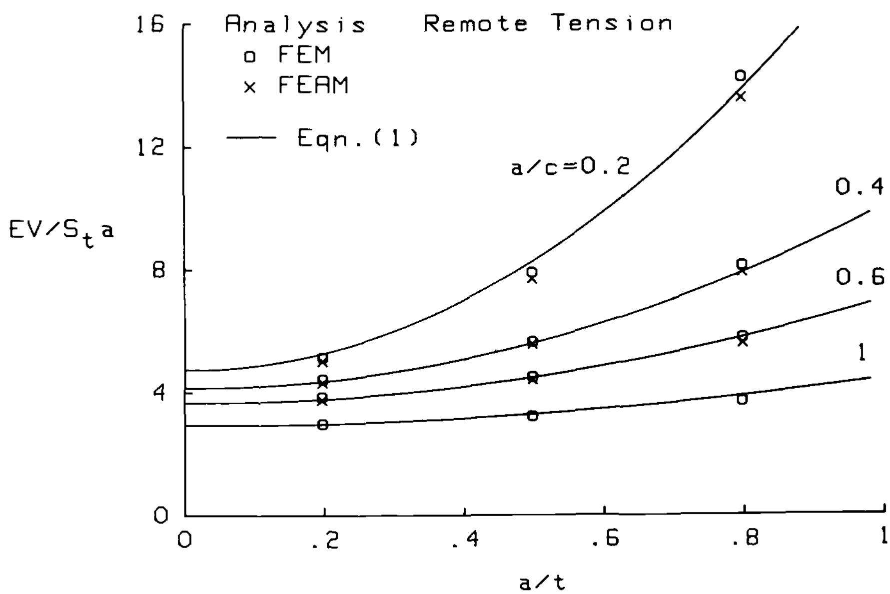

FIG. 4—*Comparison of normalized CMODs from finite element method, finite element alternating method, and proposed equation for surface crack under remote tension.*

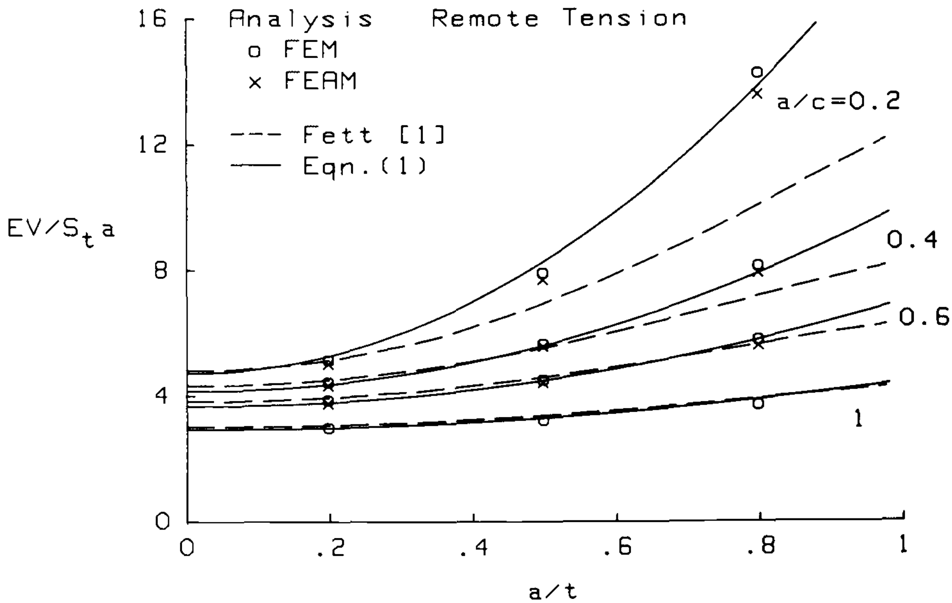

FIG. 5—*Comparison of normalized CMODs from Fett's equation, proposed equation, and analyses for surface crack under remote tension.*

sufficient to describe the CMOD due to the induced bending that develops in the surface-crack specimen.

McCabe et al. [*8,9*] conducted tests on welded 2219-T87 aluminum alloy surface-crack specimens subjected to remote tension. These tests covered a wide range in *a/t* and *a/c* ratios for several plate thicknesses. Semielliptical surface notches were electrical discharged machined (EDM) into each specimen to a specified *a/t* and *a/c* value. The EDM electrode had a thickness of 0.5 mm. The CMOD values were measured with a displacement gage mounted across the notch mouth with a total gage length of about 1 mm. A comparison between the CMOD values measured from tests and those calculated from the proposed equation for remote tension are shown in Fig. 6. The tests results agreed well (within about 6%) with the equation.

The normalized CMODs calculated from the FEM for remote bending are given in Table 1(*bottom*). A comparison between the FEM results and the proposed equation (Eqs 1 and 4) is shown in Fig. 7. The equation, obtained by fitting to these results, gave CMOD values that were within about 3% of the FEM calculations.

Concluding Remarks

Crack-mouth-opening displacements (CMODs) for surface cracks in rectangular plates were obtained using three-dimensional finite element and finite element alternating methods. The plates were subjected to remote tension and remote out-of-plane bending loads. A wide range of crack shapes were considered (a/c = 0.2 to 1). The crack-depth-to-plate-thickness (a/t) ratios ranged from 0.2 to 0.8. The CMODs from these two methods generally agreed within a few percent of each other (maximum difference was about 5%).

Empirical equations were developed for CMOD for a wide range in surface-crack shapes and sizes subjected to tension and bending loads. These equations were obtained by modifying the Green-Sneddon exact solution for an elliptical crack in an infinite body to account

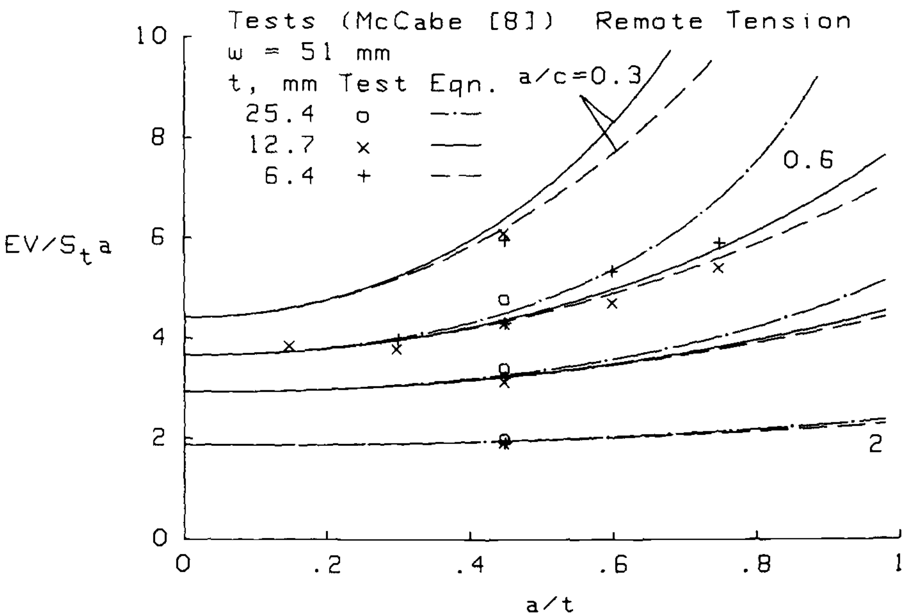

FIG. 6—*Comparison of normalized CMODs from tests and proposed equation for surface crack under remote tension.*

for finite boundary effects and loading. Comparisons made with Fett's crack-opening displacement equations at the crack mouth showed good agreement except for deep, low aspect (a/c) ratio surface cracks. Comparisons made between the proposed equation and experimental results obtained on surface cracks in welded aluminum alloy specimens under tension

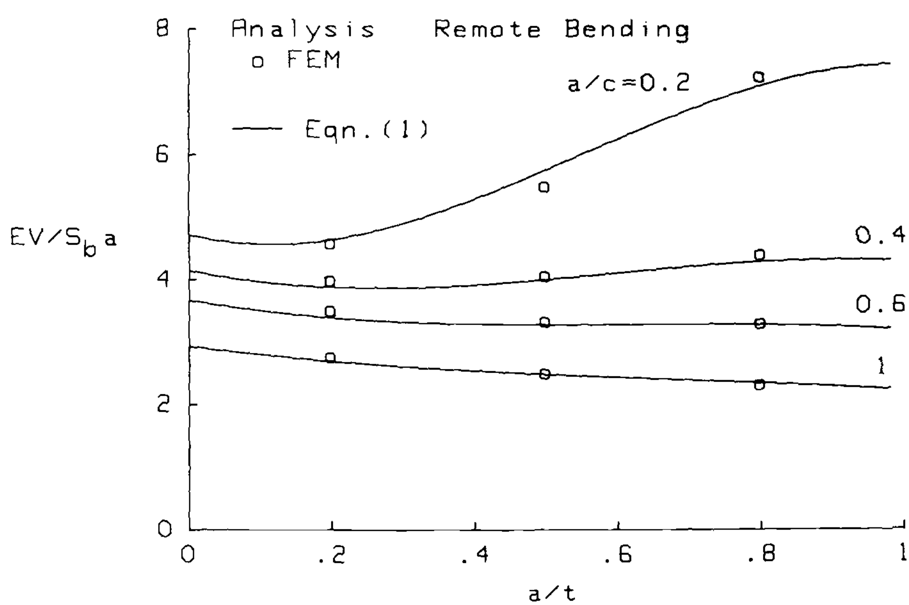

FIG. 7—*Comparison of normalized CMODs from finite element method and proposed equation for surface crack under remote bending.*

also showed good agreement. These equations should be useful in monitoring surface-crack growth in tests and in developing complete crack-face-displacement equations for use in three-dimensional weight-function methods.

Acknowledgment

Mr. Raju's contribution to this work was supported by the Center for Composite Materials Research at the North Carolina A&T State University, Greensboro, North Carolina, and under NASA Contract NAS1-18256 at the NASA Langley Research Center, Hampton, Virginia. Most of the computations presented in this paper were carried out on the supercomputer at the North Carolina Supercomputing Center (NCSC), Research Triangle Park, North Carolina.

References

[*1*] Fett, T., "The Crack Opening Displacement Field of Semi-Elliptical Surface Cracks in Tension for Weight Functions Applications," *International Journal of Fracture*, Vol. 36, 1988, pp. 55–69.

[*2*] Newman, J. C., Jr., and Raju, I. S., "An Empirical Stress-Intensity Factor Equation for the Surface Crack," *Engineering Fracture Mechanics Journal*, Vol. 15, 1981, pp. 185–192.

[*3*] Vijayakumar, K. and Atluri, S. N., "An Embedded Elliptical Flaw in an Infinite Solid, Subject to Arbitrary Crack-Face Tractions," *Transactions*, American Society of Mechanical Engineers, Series E, *Journal of Applied Mechanics*, Vol. 48, 1981, pp. 88–96.

[*4*] Nishioka, T. and Atluri, S. N., "Analytical Solution for Embedded Elliptical Cracks, and Finite Element Alternating Method for Elliptical Surface Cracks, Subjected to Arbitrary Loadings," *Engineering Fracture Mechanics*, Vol. 17, 1983, pp. 247–268.

[*5*] Raju, I. S., "Crack-Face Displacements for Embedded Elliptic and Semielliptical Surface Cracks," NASA CR-181822, National Aeronautics and Space Administration, Washington, DC, May 1989.

[*6*] Nishioka, T. and Atluri, S. N., "An Alternating Method for Analysis of Surface Flawed Aircraft Structural Components," *AIAA Journal*, American Institute of Aeronautics and Astronautics, Vol. 21, 1983, pp. 749–757.

[*7*] Nishioka, T. and Atluri, S. N., "The First-Order Variation of the Displacement Field Due to Geometrical Changes in an Elliptical Crack," presented at the American Society of Mechanical Engineers' Winter Annual Meeting, Dallas, 25–30 Nov. 1990.

[*8*] McCabe, D. E., Ernst, H. A., and Newman, J. C., Jr., "Application of Elastic and Elastic-Plastic Fracture Mechanics Methods to Surface Flaws," in Volume I of this publication.

[*9*] "Fracture Analysis and Supporting Data for Existing External Tank Fleet," Final Report, TD 812, MMC-ET-SE05-292, Contract No. NASA-30300, National Aeronautic and Space Administration, Washington, DC, Dec. 1988.

[*10*] Green, A. E. and Sneddon, I. N., "The Distribution of Stress in the Neighborhood of a Flat Elliptical Crack in an Elastic Solid," *Proceedings*, Cambridge Philosophical Society, Vol. 46, 1950, p. 159.

[*11*] Raju, I. S., Atluri, S. N., and Newman, J. C., Jr., "Stress-Intensity Factors for Small Surface and Corner Cracks in Plates," *Fracture Mechanics: Perspectives and Directions, ASTM STP 1020*, R. P. Wei and R. P. Gangloff, Eds., American Society for Testing and Materials, Philadelphia, 1989, pp. 297–316.

[*12*] Kantorovich, L. V. and Krylov, V. I., *Approximate Methods of Higher Analysis*, Interscience, New York, 1964.

[*13*] Shah, R. C. and Kobayashi, A. S., "On the Surface Flaw Problem," *In the Surface Crack: Physical Problems and Computational Solutions*, J. L. Swedlow, Ed., American Society of Mechanical Engineers, New York, 1972, pp. 79–142.

[*14*] Smith, F. W., "The Elastic Analysis of the Part-circular Surface Flaw Problem by the Alternating Method," *In the Surface Crack: Physical Problems and Computational Solutions*, J. L. Swedlow, Ed., American Society of Mechanical Engineers, New York, 1972, pp. 125–152.

[*15*] Smith, F. W. and Kullgren, T. E., "Theoretical and Experimental Analysis of Surface Cracks Emanating from Fastener Holes," AFFDL-TR-76-104, Air Force Flight Dynamics Laboratory, Dayton, OH, 1977.

[*16*] Shah, R. C. and Kobayashi, A. S., "Stress-Intensity Factors for an Elliptic Crack under Arbitrary Loading," *Engineering Fracture Mechanics*, Vol. 3, 1971, pp. 71–96.

Randall B. Stonesifer,[1] *Frederick W. Brust,*[2] *and Brian N. Leis*[2]

Stress-Intensity Factors for Long Axial Outer Surface Cracks in Large *R/t* Pipes

REFERENCE: Stonesifer, R. B., Brust, F. W., and Leis, B. N., "**Stress-Intensity Factors for Long Axial Outer Surface Cracks in Large *R/t* Pipes,**" *Fracture Mechanics: Twenty-Second Symposium (Volume II), ASTM STP 1131,* S. N. Atluri, J. C. Newman, Jr., I. S. Raju, and J. S. Epstein, Eds., American Society for Testing and Materials, Philadelphia, 1992, pp. 29–45.

ABSTRACT: Stress-intensity factors for axial surface flaws in pipes can be sensitive to the radius to thickness ratio (R/t) of the pipe depending on the depth to thickness (a/t) and the depth to length (a/c) ratios of the crack. This study combines solutions from the literature for plates and smaller R/t pipes with several new solutions for axial outer surface (OD) cracks in $R/t = 40$ pipes to obtain stress-intensity factors for $a/t = 0.25$, 0.50, and 0.75, and a/c in the range 0 to 1. The new solutions are obtained using the finite element alternating method.

KEY WORDS: cracks, surface cracks, stress-intensity factors, finite element method, finite element alternating method

Despite current concerns regarding its limitations when applied to highly loaded components made from tough materials [*1*], proof testing remains a popular method for certifying safety critical structural components. For example, proof testing is mandated under certain conditions for commercial aircraft, the space shuttle, and natural gas transmission line pipes. For gas transmission line pipe, proof tests are administered by over-pressurizing a section of pipe with water; thus the name "hydrotest" is given for line pipe proof tests. Concern in line pipe is for external axial surface cracks developed via a corrosion mechanism.

During hydrotesting of gas transmission line pipe, water pressures from 1.25 to 1.5 times the maximum operating (service) pressures are introduced. At these pressures, inelastic behavior can be significant for all but the smallest cracks. In addition, the pressures are held for a period of time so that primary creep crack growth occurs along with the ductile growth. An elastic-plastic-primary creep surface crack model was developed to aid in developing optimum proof test strategies and is reported elsewhere [*2*]. This model represents an extension of J-tearing theory to the time domain, and consists of a time-dependent plastic zone correction to the elastic surface crack solution. The purpose of this paper is to report stress-intensity factor solutions for axial external surface cracks in pipe that were developed for the preceding referenced model.

Figure 1 defines the geometric parameters of this study and illustrates the semielliptical surface flaw of interest. The inner pipe radius is denoted R. The elliptic angle, ϕ, is equal to 90° at the deepest point on the crack front and is equal to 0 and 180° at the points where the crack front intersects the surface.

[1]President, Computational Mechanics, Inc., Julian, PA 16844.
[2]Senior research scientist and research leader, respectively, Battelle Memorial Institute, Columbus, OH 43201.

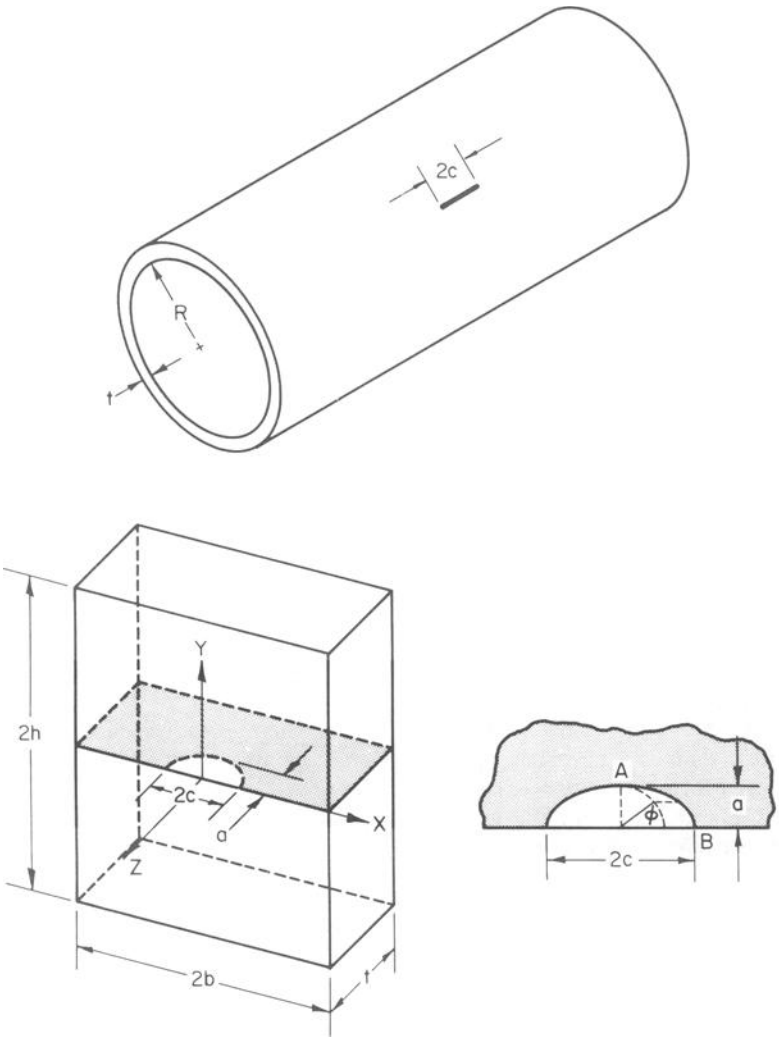

FIG. 1—*Definition of geometric parameters for pipes and plates with semielliptical surface flaws.*

The line pipe of concern is thin wall, large diameter pipe. A typical pipe might have a diameter of 900 mm and an R/t ratio of 40. While stress-intensity factors have been compiled in the literature for axial surface flaws in pipe, these are generally for R/t ratios of 20 and smaller. Solutions for surface flaws in plates can be applied to flaws in large R/t pipe, provided the depth of the flaw (a/t) is small enough for the given flaw aspect ratio (a/c) as to not induce significant bulging. The purpose of this work was to develop stress-intensity factor solutions for $R/t = 40$ pipe for situations where plate solutions are inadequate.

Background

Much has been written over the last 30 years on the subject of evaluating K_I for finite surface flaws in flat plates subjected to tensile loading. Newman [3] reviewed the methods and compared the resulting K_I solutions that were available up to 1979. The reviewed methods included analytical methods, experimental methods, and engineering estimates. Newman evaluated the performance of the methods by comparing predicted and experimental crack initiation data for a brittle material. Finite element methods with adequate grid refinement appeared to give the best estimates of K_I.

Using the finite element method and several levels of grid refinement to establish convergence, Raju and Newman [4] tabulated K_I solutions for semielliptical surface cracks in plates under tension for a wide range of geometric parameters. Later, Raju and Newman [5] fit a parametric equation to these results that made their results more convenient to use.

The review of Newman [3] included a number of solutions that were obtained using the finite element alternating method. Newman, however, favored the singular finite element approach over the alternating method. At the time of that review, however, existing alternating method programs were hampered by the lack of a sufficiently general analytical solution for the embedded elliptical crack of the alternating method models. Until Vijayakumar and Atluri [6] found a general solution to the embedded crack problem, all alternating method programs were plagued by the inability to represent high order traction variations on the crack surfaces. In addition, the extremely tedious nature of deriving and programming the analytical solutions make it likely that some reported solutions were not error free. Having the general solution to the embedded crack problem, Nishioka and Atluri [7] developed a relatively convenient method of implementing the solution within the framework of the finite element alternating method. The solution and equations resulting from Refs 6 and 7, referred to as the VNA solution, are used as the basis for the alternating method program used for the present study.

With the improved accuracy afforded by the VNA solution, the finite element alternating method is seeing increased usage for the solution of three-dimensional crack problems. Nishioka and Atluri used the method to obtain solutions for surface flaws in pressure vessels [8]. O'Donoghue, Nishioka, and Atluri [9] applied the method to interacting cracks under Mode I conditions. Simon, O'Donoghue, and Atluri [10] applied the method to mixed-mode problems. Raju, Atluri, and Newman [11] used the method to obtain solutions for small ($a/t \rightarrow 0$) surface and corner cracks in plates. Most recently, Raju, Newman, and Atluri have applied the method to the calculation of crack mouth displacements for semielliptical surface cracks subjected to remote tensile loading [12].

Numerical Method

The finite element alternating method program known as ALT3D [13] was used to generate the two- and three-dimensional solutions in this study. ALT3D combines the VNA solution [6,7] with three-dimensional finite element modeling to obtain stress-intensity factors for embedded or surface flaws in finite bodies subjected to arbitrary loading. The solutions are obtained through an iterative process whereby residual tractions on the crack surfaces and on the external surfaces are alternately corrected until the magnitudes of the residuals become negligible.

The alternating method has the following attractive features for obtaining stress-intensity factor solutions.

1. The finite element grid does not include the crack geometry, thus greatly simplifying grid generation and at the same time allowing one grid to be used for a variety of crack sizes and orientations.
2. For any given grid, the finite element stiffness matrix needs to be decomposed only one time (even if the crack geometry changes), thus making the method computationally efficient.

3. Although the VNA solution is for an embedded crack, the method can also handle partelliptical surface cracks.
4. A convenient result of using the VNA solution is that stress-intensity factors (Modes I, II, and III) are computed directly (no need for contour or surface integrals such as J or other means for indirectly computing stress-intensity factors from energy release rates).
5. Multiple cracks can be defined, and thus problems with interacting cracks can be solved.

ALT3D uses standard 8-noded isoparametric elements but then, at the user's option, adds incompatible displacement modes to provide improved bending response [*14*]. The VNA solution that is programmed into ALT3D allows crack surface tractions to be fit with polynomials of arbitrarily high order. Experience has shown that for practical refinement of finite element grids, fifth order polynomials are generally adequate. This corresponds to $m = 2$ ($M = 2$ in the notation of Refs *6* and *7*). ALT3D currently allows the user to specify m as 0 (zero and first order terms), 1 (zero through cubic terms), or 2 (zero through fifth order terms).

The iteration associated with the alternating method is stopped when the solution is considered to be sufficiently well converged. ALT3D can monitor convergence and halt the iteration process when the following is satisfied at each K calculation point specified by the user

$$\frac{|K_{\mathrm{I}}\Delta K_{\mathrm{I}}| + |K_{\mathrm{II}}\Delta K_{\mathrm{II}}| + |K_{\mathrm{III}}\Delta K_{\mathrm{III}}|}{K_{\mathrm{I}}^2 + K_{\mathrm{II}}^2 + K_{\mathrm{III}}^2} < \text{tolerance} \tag{1}$$

where K and ΔK are the cumulative and incremental stress-intensity factors associated with the current iteration and the tolerance is supplied by the user. The tolerance used in the current work was 0.001 with Ks being calculated at five equally spaced points along the half crack front.

Approach

While it would have been possible to generate all of the required solutions using the alternating method finite element program in this study, it was decided to rely as much as possible on solutions already in the literature. The available solutions were not for the $R/t = 40$ pipe size of interest, but it was known that R/t dependence of the solutions becomes large only for long, deep cracks. That is, for shallow or relatively short cracks, the stress-intensity factor solution is nearly identical to that for a plate ($R/t \rightarrow \infty$). Not only did this approach reduce the required number of solutions, it brought the subject of curvature and bulging effects into the study in a natural way.

For very long cracks ($a/c \rightarrow 0$) it is clear that the stress-intensity factor at the deepest point of the semielliptical surface crack must approach the value that would be obtained from a two-dimensional solution for an infinitely long crack. Having this two-dimensional solution is, therefore, very useful since it provides an upper bound on the solutions for finite aspect ratio cracks. Since the two-dimensional solution for an $R/t = 40$ pipe was not found in the literature, it was generated in this study. Rather than use a separate two-dimensional program, the same three-dimensional program was used to solve the two-dimensional problem by using a single layer of three-dimensional elements with appropriate boundary conditions to simulate plane strain conditions.

Rather than directly applying an internal pressure loading to the finite element models of this study, the loading was specified in terms of initial stress. This allowed the exact elasticity solution for hoop stresses in a cylinder to be used as the "applied loading" and thus eliminated the small errors in hoop stress that would have resulted if the pressure-induced hoop stresses for the uncracked pipe were computed with the finite element model.

The stress-intensity factor solutions of this study are normalized in the following way

$$F = \frac{K_I}{\frac{pR}{t}\left(\frac{\pi a}{Q}\right)^{1/2}} \tag{2}$$

where

t = pipe wall thickness,
R = inner pipe radius,
p = internal pressure,
a = crack depth,
c = half crack length, and
Q = shape factor approximated by
$Q = 1 + 1.464(a/c)^{1.65}$ for $a/c \leqq 1$
$Q = 1 + 1.464(c/a)^{1.65}$ for $a/c > 1$

When applying plate solutions to the cylindrical problem, the applied stress is assumed to be uniform and equal to pR/t.

Verification

To establish the accuracy that could be expected from the ALT3D solutions for surface cracks in piping, several solutions were first obtained for $R/t = 10$ pipe. Raju and Newman [*15*] have obtained solutions for this problem using three-dimensional finite elements with singular crack tip elements and a nodal force method for inferring stress-intensity factors. The Raju and Newman solutions have been verified by numerous investigators and are believed to be accurate to within a few percent. Generally, it is expected that the Raju and Newman solutions tend to fall below the exact solution.[3]

Figures 2*a* and *b* show the two finite element grids used for the $R/t = 10$ verification calculations. Figure 2*a* shows the coarser of the two grids and is referred to in the discussion as the 8-element grid since it has 8 elements through the thickness in the most refined portion of the grid. This 8-element grid has 2516 nodes and 1790 8-noded elements. The 16-element grid has 5056 nodes and 3951 elements. Both grids model a quarter of the pipe by taking advantage of the two orthogonal planes of symmetry. The length of the modeled pipe segment is twice the inner radius of the pipe, and the end of the modeled segment was modeled as being traction free.

The grids of Fig. 2 do not explicitly represent the crack, and therefore they can be used to model a variety of crack shapes. Figures 3 through 7 compare the current solutions with those of Ref *15*. Figures 3 and 4 compare results for two crack lengths with $a/t = 0.5$ and contain results from both the 8- and 16-element grids. It can be seen that current solutions are in good agreement with the reference solutions with solutions from the 16-element grid tending to give the largest stress-intensity factors of the three solutions. The point where the crack intersects the surface ($\phi = 0$) tends to be the location with the least favorable agreement. This may be related to the fact that K_I, the amplitude of the $r^{-1/2}$ stress field singularity, is possibly zero or undefined at this point as a result of the stress field singularity

[3]This expectation results from discussions between J. C. Newman, Jr., and R. B. Stonesifer.

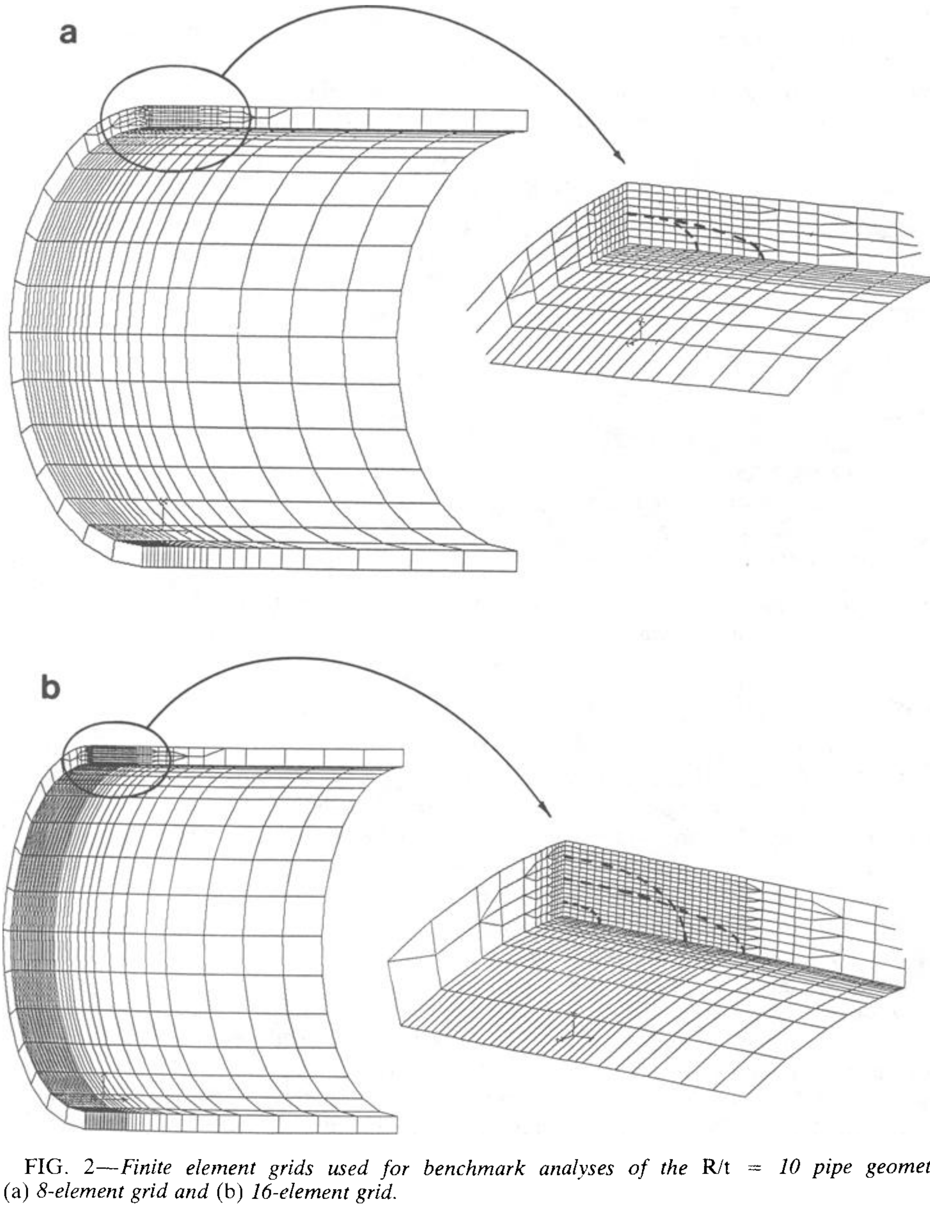

FIG. 2—*Finite element grids used for benchmark analyses of the* R/t = *10 pipe geometry:* (a) *8-element grid and* (b) *16-element grid.*

no longer being of the type $r^{-1/2}$. Benthem has found that the singularity at the surface point is $r^{-1/2}$ only if Poisson's ratio is zero [*16,17*]. For the present calculations, Poisson's ratio is assumed to be 0.3. The nonzero K_I values that are provided by the current solution and the reference solution can perhaps best be rationalized in terms of the fact that the energy release rate is not zero at the surface, and that the depth of influence of the surface effect is so small that the computed K_Is are representative of points very near the surface.

Figures 3 and 4 include a curve labeled "iteration 0." These curves represent the stress-intensity factor distributions that result when the initial hoop stresses are first applied to

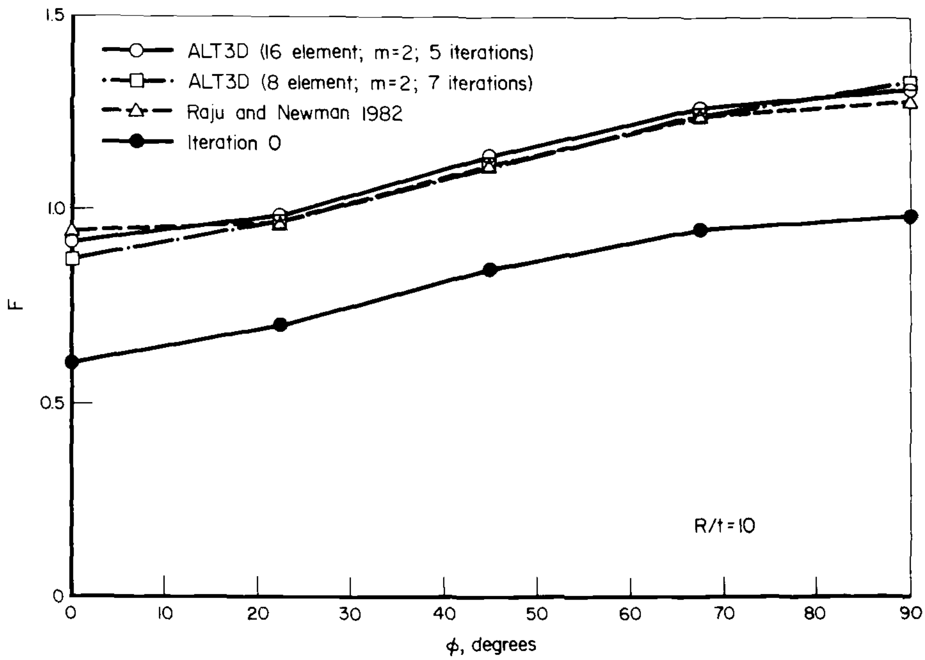

FIG. 3—*Comparison of current and reference solutions for an axial OD semielliptical surface flaw in an* R/t = *10 pipe (*a/t = *0.5;* a/c = *0.4).*

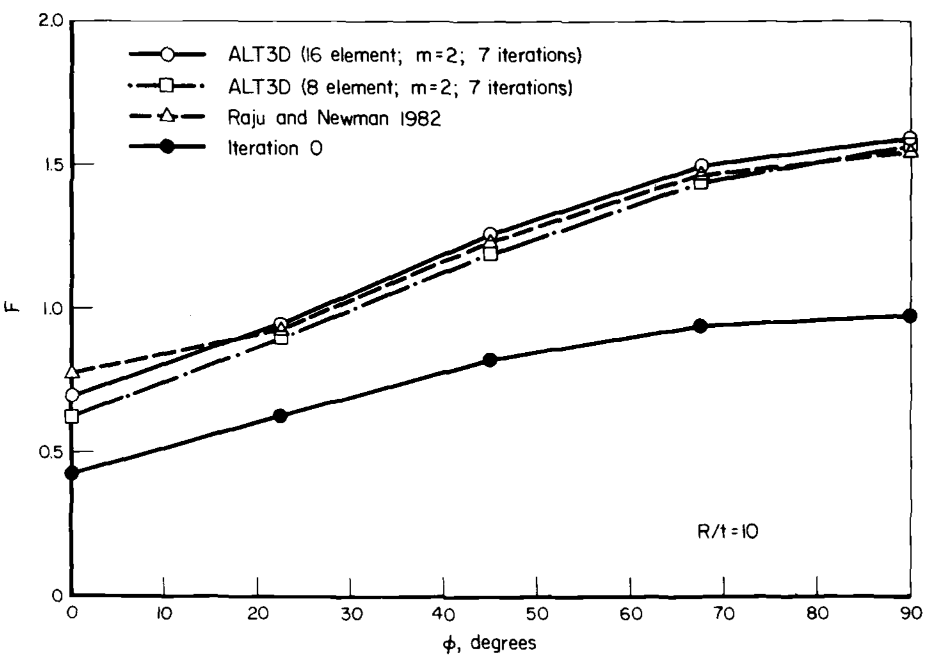

FIG. 4—*Comparison of normalized stress-intensity factors for an axial OD semielliptical surface flaw in an* R/t = *10 pipe (*a/t = *0.5;* a/c = *0.2).*

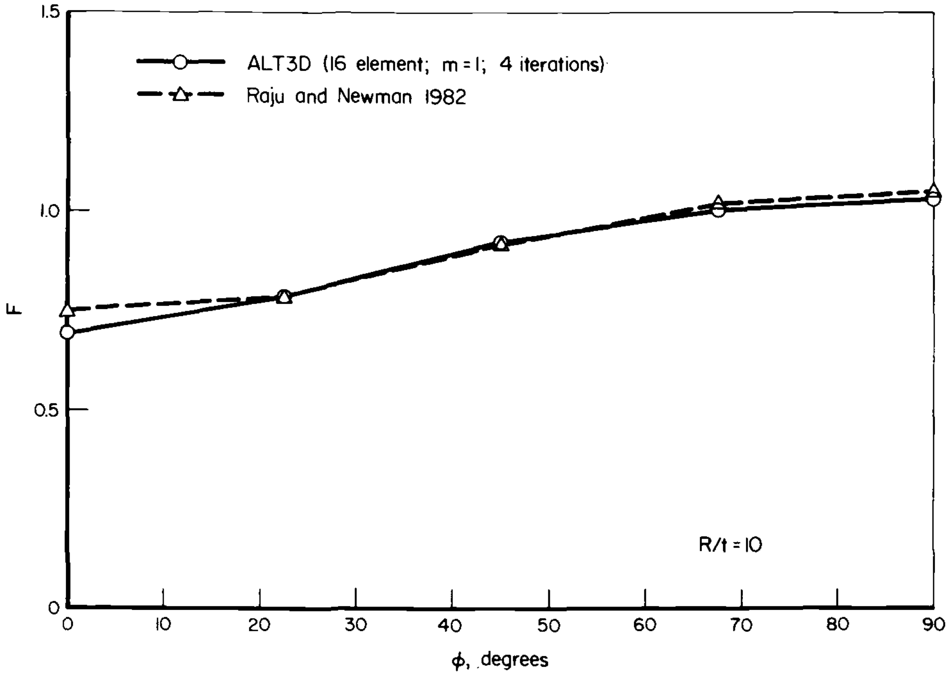

FIG. 5—*Comparison of current and reference solutions for an axial OD semielliptical surface flaw in an* R/t = *10 pipe (*a/t = *0.2;* a/c = *0.4).*

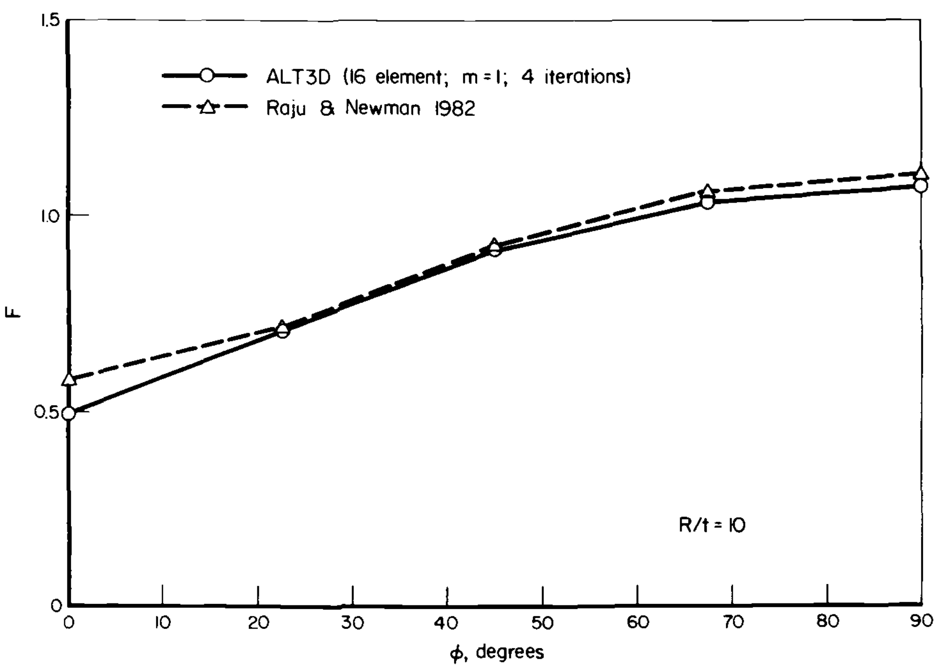

FIG. 6—*Comparison of normalized stress-intensity factors for an axial OD semielliptical surface flaw in an* R/t = *10 pipe (*a/t = *0.2;* a/c = *0.2).*

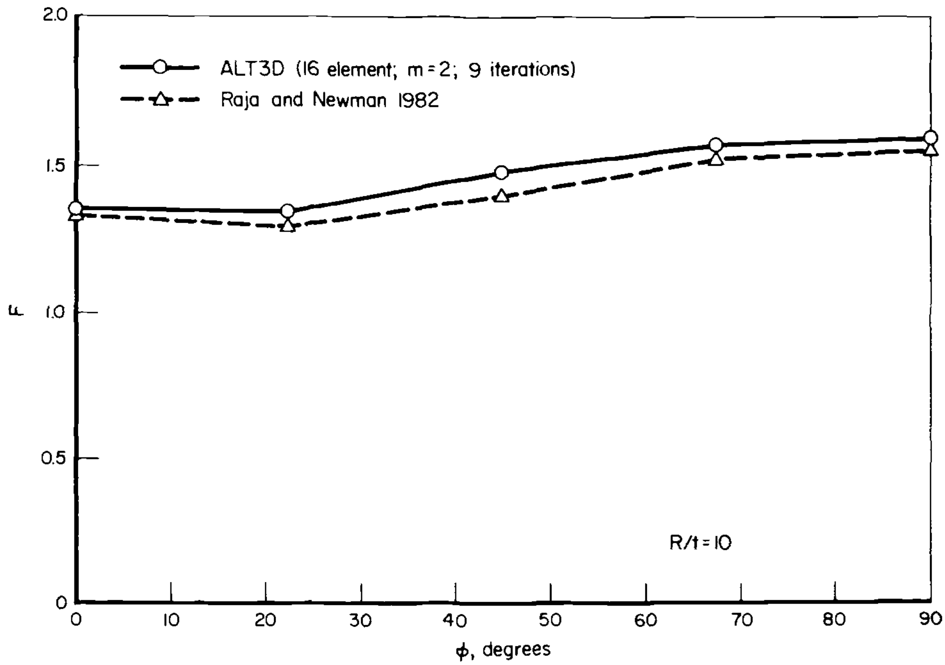

FIG. 7—*Comparison of current and reference solutions for an axial OD semielliptical surface flaws in an* R/t = *10 pipe (*a/t = *0.8;* a/c = *0.4).*

the analytical crack portion of the model. The difference between this curve and the final converged curve is due to interior and exterior pipe surface effects.

Figures 5, 6, and 7 compare ALT3D solutions to the Raju and Newman solutions for a/t = 0.2 and 0.8, and a/c = 0.2 and 0.4. The case of a/t = 0.8, a/c = 0.2 was not run because the refined region of the grid (see Fig. 2) did not extend far enough in the axial direction to accommodate this crack size. The solutions for a/t = 0.2 are in good agreement with the Raju and Newman solution except perhaps at the surface point. While the 16-element ALT3D solutions at a/t = 0.5 are above the reference solutions, this is not the case at a/t = 0.2. At a/t = 0.8, the ALT3D solution is further above the reference solution than at a/t = 0.5. The maximum difference for the a/t = 0.8 case is less than 6% and occurs at a point other than the surface point.

By the nature of the alternating method, the farther the problem is from that of an embedded crack far from external boundaries, the more iterations the solution will take to converge, and the more opportunity there will be for errors to accumulate.[4] Therefore, the two-dimensional problem of a deep single-edge crack in a plate is about as challenging a problem as can be devised for the three-dimensional alternating method. Since the constraint in the pipe geometry will be always greater than that for the plate, it is reasonable to expect that the errors for the two-dimensional single-edge crack solution should represent the upper bound on errors for an axial crack in a pipe with the same a/t. Therefore, as a final check on the ability of the program to provide accurate solutions for the R/t = 40 pipe problem, ALT3D was used to simulate a two-dimensional plane strain single-edge crack specimen. The a/t that was modeled was 0.75; the largest to be considered in this study. The grid was

[4]The errors are due to the finite element approximation and the finite order of the polynomials used by the analytical portion of the model.

similar to the most refined portion of the 16-element grid of Fig. 2 except that it was one-element-layer thick, was unwrapped to represent a plate cross section, and was cut off at a position that would correspond to a 30° segment of the $R/t = 40$ pipe. The calculated stress-intensity factor for a uniform applied stress was 4% below the value obtained from Ref *18*. This is expected to be a reasonable estimate of the accuracy of the stress-intensity factors at the deepest point of the three-dimensional solutions that follow.

Based on these results, it was concluded that the ALT3D program could be expected to provide reasonably accurate solutions to the problem of interest. A grid for the $R/t = 40$ analyses was generated using 16 elements through wall at the crack plane. Since long and deep cracks were of most interest, the grid was generated to accommodate these types of cracks. Figure 8 shows the form of this three-dimensional $R/t = 40$ pipe grid. A two-dimensional grid was also generated for the infinite length ($a/c = 0$) crack geometry. This grid had the same form as the most refined portion of the three-dimensional grid and had only a single layer of elements in the axial direction.

Results

After verifying the accuracy of the alternating method program and the adequacy of the grid refinement, the next step was to find a way to use the available solutions from the literature. While solutions were not found for $R/t = 40$ pipes, solutions were found for $R/t = 4$, 10, and 20 and for plates ($R/t \rightarrow \infty$). Figures 9 through 12 illustrate how these available solutions [*5,15,18,19*] were used to obtain useful information for the $R/t = 40$ geometry. The normalized stress-intensity factor (F) at the deepest point on the crack front is plotted versus t/R. Figure 9 shows the dependence of F on t/R for the limiting case of $a/c = 0$. Numerous solutions were available from the literature for this two-dimensional case; however, no solutions were found for the $R/t = 40$ case of interest. For $a/c = 0.2$

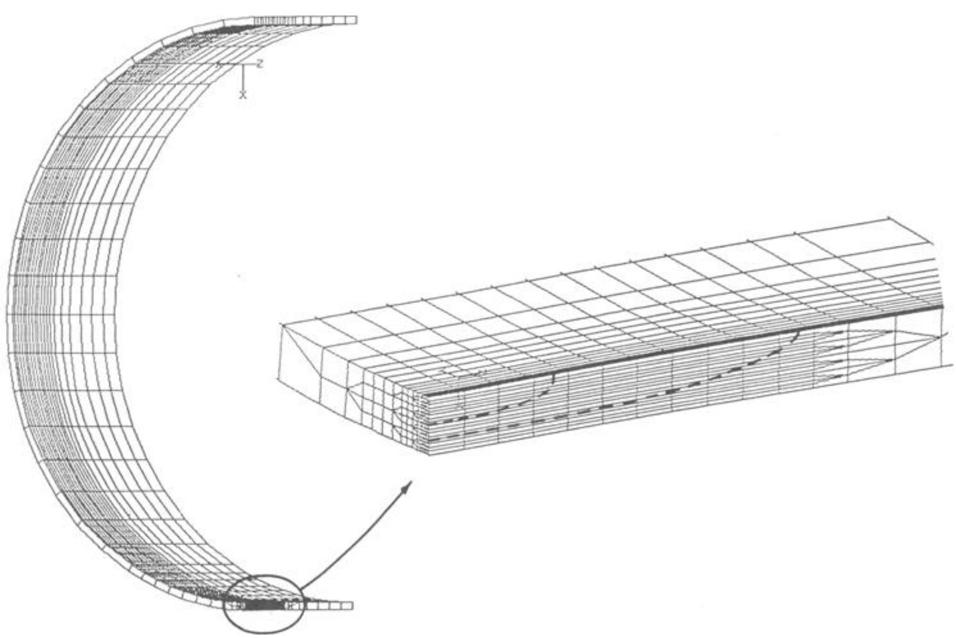

FIG. 8—*Finite element grid used for analyses of the* R/t = *40 pipe geometry.*

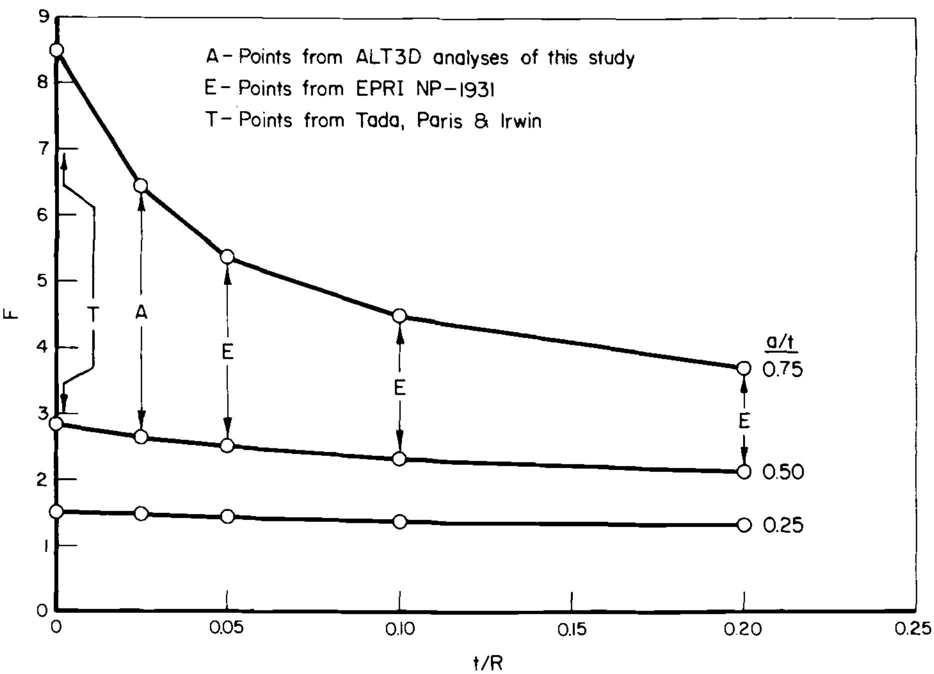

FIG. 9—*Normalized stress-intensity factors for infinitely long (*a/c = *0) cracks on the OD of various* R/t *pipes.*

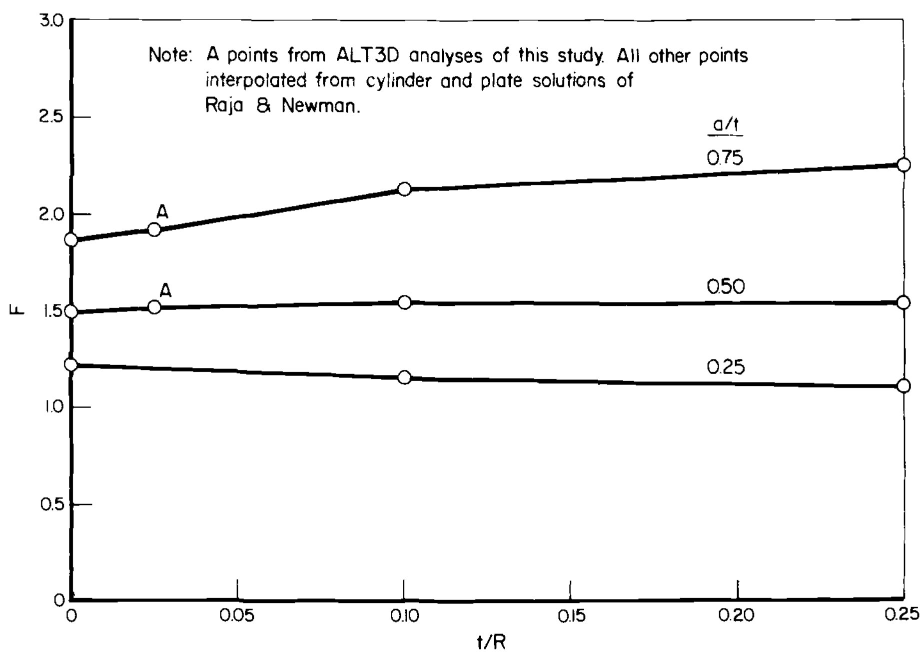

FIG. 10—R/t *dependence of the normalized stress-intensity factor at the deepest point of OD axial surface cracks with* a/c = *0.2.*

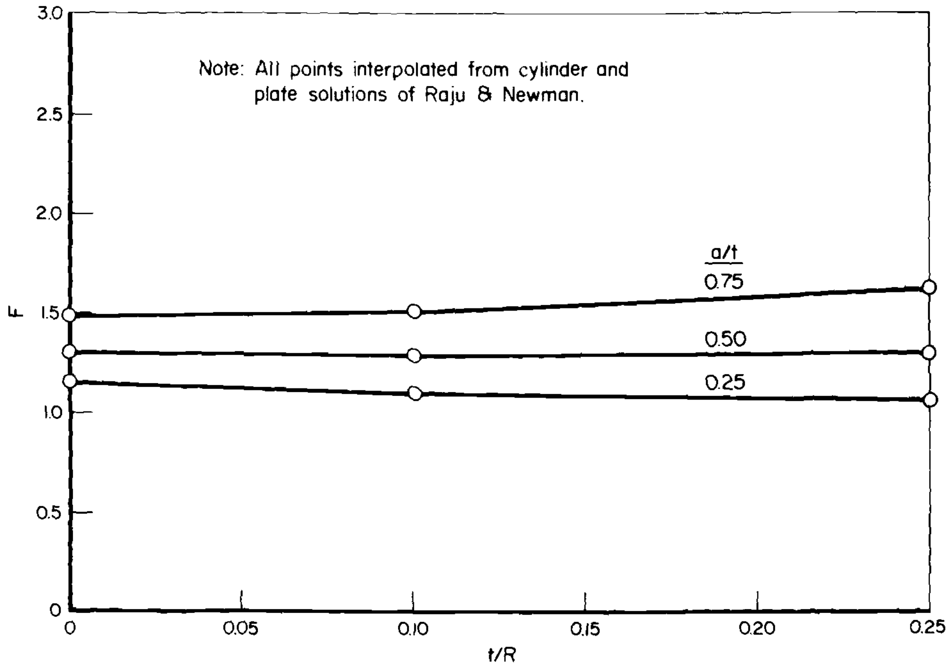

FIG. 11—*Solutions from the literature for the normalized stress-intensity factor at the deepest point of OD axial surface cracks with* a/c = *0.4.*

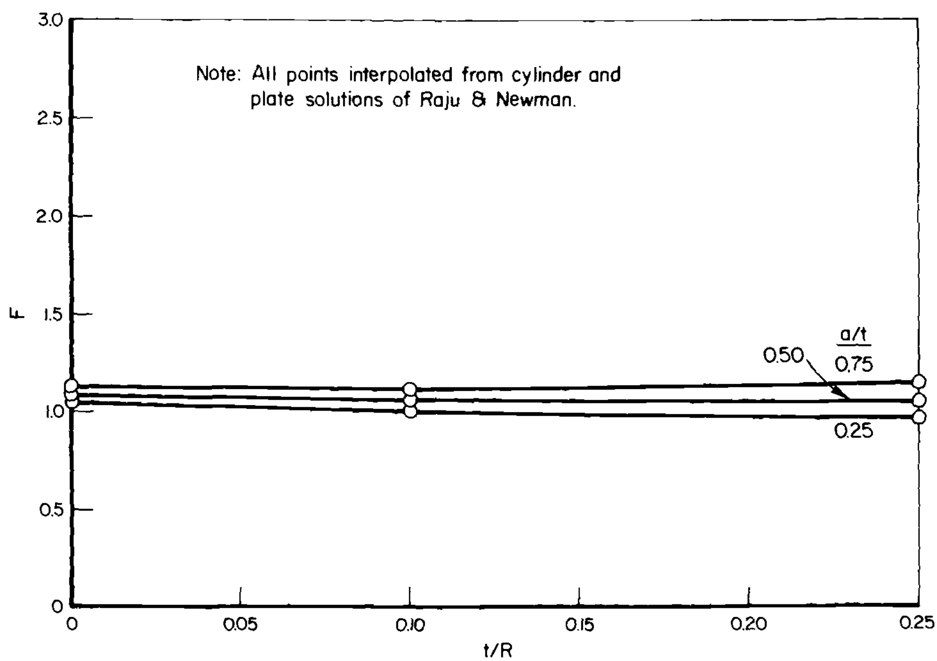

FIG. 12—*Solutions from the literature for the normalized stress-intensity factor at the deepest point of OD axial surface cracks with* a/c = *1.*

(Fig. 10), F was relatively independent of t/R for $a/t = 0.25$ and 0.50, but showed moderate dependence for $a/t = 0.75$. For $a/c = 0.4$ and 1.0 (Figs. 11 and 12), F was found to be relatively independent of t/R and linear interpolation for $R/t = 40$ was reasonable.

In Fig. 10, the shape of the curve for $a/t = 0.75$ between t/R of 0 and 0.1 was not clear from the available solutions, therefore a new solution was generated at $R/t = 40$ ($t/R = 0.025$). As a further check on the accuracy of the ALT3D calculations, an additional point was calculated at $R/t = 40$ for $a/t = 0.50$. Both points are seen to be in good agreement with the trends of the Raju and Newman results.

The original Raju and Newman solutions of Figs. 10, 11, and 12 were for $a/t = 0.2$, 0.5, and 0.8 while the EPRI solutions of Fig. 10 were for $a/t = 0.25$, 0.5, and 0.75. Interpolation of the Raju and Newman results [*15*] to $a/t = 0.25$ and 0.75 was considered preferable to extrapolation of the EPRI results [*19*], and therefore $a/t = 0.25$ and 0.75 were used throughout this study. The interpolations of the Raju and Newman solutions were performed using a quadratic interpolating polynomial.

It can be seen from Figs. 9 through 12 that the solutions have a significant dependence on the crack aspect ratio (a/c). The next step was therefore to determine the nature of this dependence. Basically, what was desired was the ability to determine the stress-intensity factor for any a/c between zero and unity. Taking points from the curves of Figs. 9 through 12 at $R/t = 40$, and plotting them versus a/c, it became clear that more solutions were needed between $a/c = 0$ and 0.2 if a reasonably accurate interpolation was to be possible for the a/t ratios of 0.5 and 0.75. Therefore, new solutions were generated for $a/c = 0.1$ and these two a/t ratios.

Figure 13 combines the $R/t = 40$ results from Figs. 9 through 12 with the newly generated solutions. The normalized stress-intensity factor, F, is plotted as a function of a/c for $a/t =$

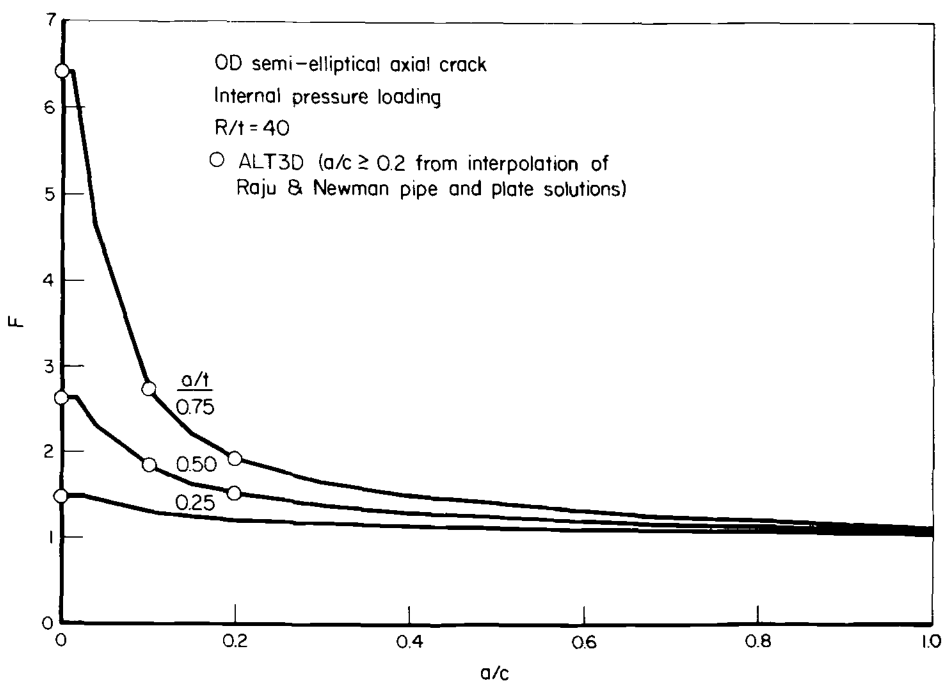

FIG. 13—*Normalized stress-intensity factors at the deepest point ($\phi = 90°$) for OD axial semielliptical surface cracks in* R/t $= 40$ *pipe.*

0.25, 0.50, and 0.75. While the new solutions at $a/c = 0.1$ significantly reduced the uncertainty concerning the $a/t = 0.5$ behavior, and also provided a significant improvement in the $a/t = 0.75$ trend for $a/c > 0.1$, there still remains a relatively large uncertainty in the shape of the $a/t = 0.75$ trend for $a/c < 0.1$. While it seems likely that the alternating method could be used to obtain a point at $a/c = 0.05$, this was not done in this study. The additional points between $a/c = 0$ and 0.1, used to define the piecewise linear curves of Fig. 13 and that are not identified with the plot symbol "A," are estimated values.

The plateaus that appear in Fig. 13 near $a/c = 0$ were included for two reasons. First, as can be seen from Fig. 14, computations using a line spring model [*20*] for very large aspect ratio cracks (a/c as small as 0.02) in $R/t = 10$ pipe suggest that the slope of the F versus a/c curves approach zero as a/c goes to zero. Second, by introducing a plateau, stress-intensity factor predictions are less likely to be nonconservative. In estimating the size of the plateaus from the $R/t = 10$ solutions, use was made of the observation that the plateaus decrease in size for larger values of a/t. Also, since the plateaus are believed to be a feature of the cylindrical geometry, it was assumed that the plateau size is inversely proportional to $\sqrt{R/t}$.

Table 1 summarizes the results of Fig. 13 in tabular form. The plateau values for a/c are seen to be 0.025, 0.017, and 0.013 for $a/t = 0.25$, 0.5, and 0.75, respectively.

Figure 15 compares the results of this study with predictions from equations proposed by Newman and Raju [*21*] and currently implemented in the NASA FLAGRO fatigue crack growth computer program [*22*]. It is seen that the Newman and Raju equation tends to be conservative. The largest degree of conservatism is, surprisingly, for $a/c > 0.2$ where the equation tends to be about 10% above the currently developed curves. There also appears to be significant conservatism for a/c approaching zero.

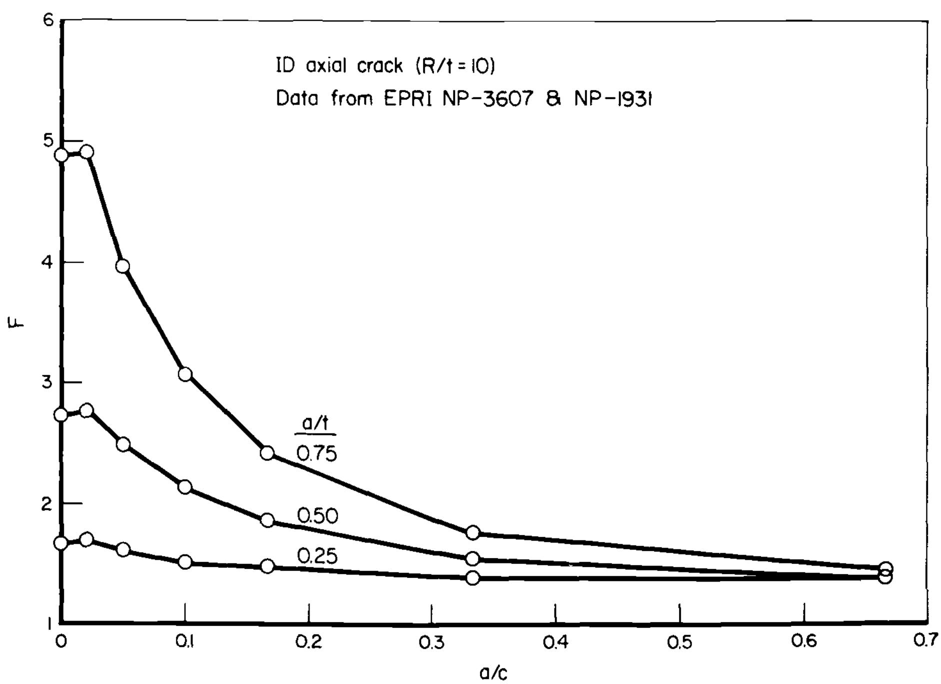

FIG. 14—*Line spring model results showing small* a/c *behavior for ID axial surface cracks in* R/t = *10 pipe.*

TABLE 1—*Normalized stress-intensity factors at the deepest point of OD axial semielliptical surface cracks in* R/T = *40 pipe.*

	F		
a/t	0.25	0.50	0.75
	A/C		
0.000	1.48[a]	2.64[a]	6.42[a]
0.013	...	...	6.42[b]
0.017	...	2.64[b]	...
0.025	1.48[b]	...	...
0.040	1.44[b]	2.29[b]	4.62[b]
0.100	1.30[b]	1.84[a]	2.74[a]
0.150	1.24[b]	1.62[b]	2.20[b]
0.200	1.20	1.52[a]	1.92[a]
0.300	1.17	1.38	1.65
0.400	1.14	1.30	1.49
0.667	1.09	1.17	1.27
1.000	1.04	1.08	1.12

[a]Computed in this study with the finite element alternating method.
[b]Estimated values.

Discussion

The finite element alternating method has been found to yield solutions that are in good agreement with those obtained using pure finite element approaches wherein the crack is directly represented in the finite element mesh and the crack tip singularity is incorporated

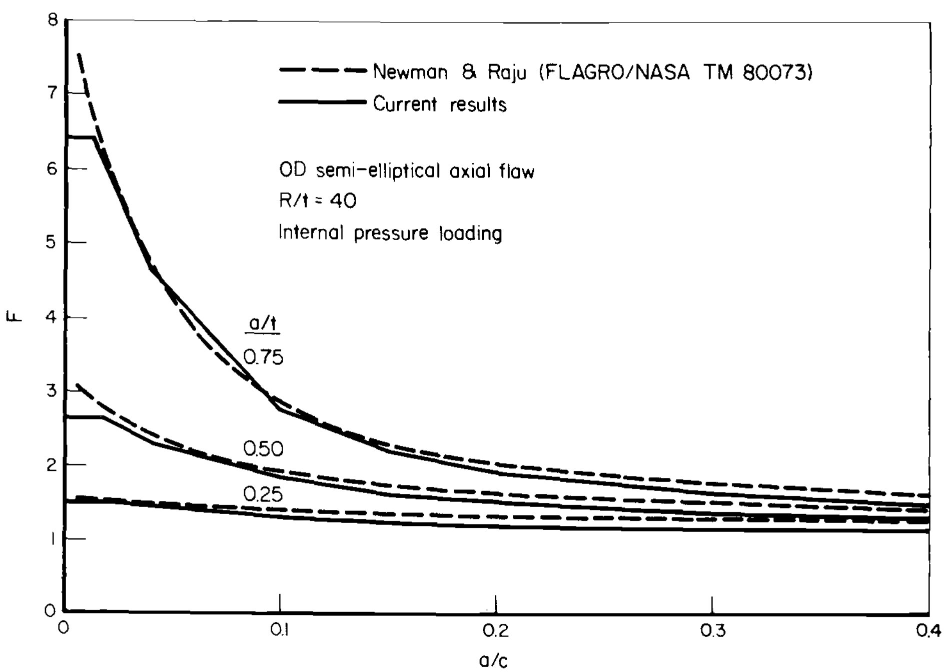

FIG. 15—*Comparison of current results with predictions from an equation proposed by Newman and Raju.*

into the model via special crack tip elements. This is consistent with the findings of Raju, Atluri, and Newman [*11*].

The alternating method has some advantages over the pure finite element approach in terms of computational efficiency but its primary advantage is ease of use. For a given crack geometry and a given level of accuracy, fewer finite element degrees of freedom are needed with the finite element alternating method. However, the cost savings associated with this reduction is often offset by the calculations for the analytical portion of the solution and by the need for several iterations. If only a single crack geometry is of interest, the alternating method may actually require more computational effort. The alternating method's biggest computational advantage comes from the fact that more than one crack geometry can be analyzed without having to again assemble and decompose the stiffness matrix. Each additional analysis requires only about 10% of the computation of the first analysis.

With the ever more powerful computers that are becoming available, the most significant advantage of the alternating method is not computational savings, but the reduced effort (man-hours) needed to generate the finite element mesh, run the analysis, and get the stress-intensity factors. Whereas the pure finite element approach requires a completely new analysis for each change in crack position or size, such changes with the alternating method involve changing only a few geometric parameters in the input file of the initial analysis. The other time saving aspect of the method is that mixed-mode stress-intensity factors are output at arbitrarily selected points on the crack front without any of the inconvenience of the usual post-processing steps associated with contour or domain integrals, energy release rates, or nodal force methods for obtaining stress-intensity factors from finite element solutions.

Conclusions

The alternating method finite element program, ALT3D, can be used to compute accurate stress-intensity factor solutions for semielliptical surface crack problems. Based on verification calculations, it is believed that the solutions obtained for the $R/t = 40$ pipe in this study are within 4% of the exact solutions.

Stress-intensity factor solutions for outer surface (OD) axial surface cracks are dependent strongly on R/t and a/c for long ($a/c < 0.2$), deep ($a/t > 0.5$) cracks in pipes with R/t greater than 10.

While it is believed that the current results are probably more accurate than the equations of Newman and Raju for $R/t = 40$ pipes, the equations appear to be conservative and eliminate the inconvenience of interpolating from a table. For example, estimating stress-intensity factors for an a/t other than those considered in this study would be inconvenient and prone to large interpolation error if done using Table 1. It would seem that with some relatively minor fine tuning, the Newman and Raju equation could be made to more closely fit the available solutions. The largest part of the conservatism of the equations for larger a/c appears to be the result of developing the equations for inner surface (ID) cracks and then somewhat arbitrarily assuming that stress-intensity factors for OD cracks are 1.1 times those for ID cracks.

The behavior of the normalized stress-intensity factor for a/c less than 0.05, in particular the slope of the curve as a/c approaches zero, is probably of little practical importance since cracks with such large aspect ratios would probably deviate significantly from the assumed semielliptical shape. For such cracks, use of the two-dimensional limiting value at $a/c = 0$ would seem to be most appropriate.

Acknowledgment

Financial support for this work was provided by the American Gas Association.

References

[1] McClung, R. C., Hudak, S. J., and Russell, D. A., "Towards an Analysis of Multiple Cycle Proof Testing Based on J Resistance Curves," *Fatigue Degradation and Fracture 1990*, W. H. Bamford et al., Eds., American Society of Mechanical Engineers, New York, June 1990.

[2] Brust, F. W. and Leis, B. N., "Primary Creep Crack Growth at Room Temperature in Surface Cracked Pipes," submitted for publication in *International Journal of Pressure Vessels and Piping*.

[3] Newman, J. C., "A Review and Assessment of the Stress-Intensity Factors for Surface Cracks," *Part Through Crack Fatigue Life Prediction, ASTM STP 687*, J. B. Chang, Ed., American Society for Testing and Materials, Philadelphia, 1979, pp. 16–42.

[4] Raju, I. S. and Newman, J. C., "Stress-Intensity Factors for a Wide Range of Semielliptical Surface Cracks in Finite-Thickness Plates," *Engineering Fracture Mechanics*, Vol. 11, 1979, pp. 817–829.

[5] Newman, J. C. and Raju, I. S., "Stress-Intensity Factor Equations for Cracks in Three-Dimensional Finite Bodies," *Fracture Mechanics: Fourteenth Symposium-Volume I: Theory and Analysis, ASTM STP 791*, J. C. Lewis and G. Sines, Eds., American Society for Testing and Materials, Philadelphia, 1983, pp. I-238–I-265.

[6] Vijayakumar, K. and Atluri, S. N., "An Embedded Elliptical Crack, in an Infinite Solid, Subject to Arbitrary Crack-Face Tractions," *Journal of Applied Mechanics*, Vol. 48, 1981, pp. 88–96.

[7] Nishioka, T. and Atluri, S. N., "Analytical Solution for Embedded Elliptical Cracks, and Finite Element Alternating Method for Elliptical Surface Crack, Subjected to Arbitrary Loadings," *Engineering Fracture Mechanics*, Vol. 17, No. 3, 1983, pp. 247–268.

[8] Nishioka, T. and Atluri, S. N., "Analysis of Surface Flaws in Pressure Vessels by a New 3-Dimensional Alternating Method," *Journal of Pressure Vessel Technology*, Vol. 104, No. 4, 1982, pp. 299–307.

[9] O'Donoghue, P. E., Nishioka, T., and Atluri, S. N., "Multiple Surface Cracks in Pressure Vessels," *Engineering Fracture Mechanics*, Vol. 20, 1984, pp. 545–560.

[10] Simon, H. L., O'Donoghue, P. E., and Atluri, S. N., "A Finite-Element-Alternating Technique for Evaluating Mixed Mode Stress Intensity Factors for Part-Elliptical Surface Flaws," *International Journal for Numeric Methods in Engineering*, Vol. 24, 1987, pp. 689–709.

[11] Raju, I. S., Atluri, S. N., and Newman, J. C., Jr., "Stress-Intensity Factors for Small Surface and Corner Cracks in Plates," *Fracture Mechanics: Perspectives and Directions (Twentieth Symposium), ASTM STP 1020*, R. P. Wei and R. P. Gangloff, Eds., American Society for Testing and Materials, Philadelphia, 1989, pp. 297–316.

[12] Raju, I. S., Newman, J. C., Jr., and Atluri, S. N., "Crack-Mouth Displacements for Semielliptical Surface Cracks Subjected to Remote Tension and Bending Loads," this volume, pp. 19–28.

[13] ALT3D User Manual, Version 1.0, Computational Mechanics, Inc., Julian, Pa., 1989.

[14] Wilson, E. L., Taylor, R. L., Doherty, W. P., and Ghaboussi, J., "Incompatible Displacement Models," *Numerical and Computer Methods in Structural Mechanics*, S. J. Fenves, N. Perrone, J. Robinson, and W. C. Schnobrich, Eds., Academic Press, Inc., New York, 1973.

[15] Raju, I. S. and Newman, J. C., "Stress-Intensity Factors for Internal and External Surface Cracks in Cylindrical Vessels," *Journal of Pressure Vessel Technology*, Vol. 104, 1982, pp. 293–298.

[16] Benthem, J. P., "State of Stress at the Vertex of a Quarter-Infinite Crack in a Half-Space," *International Journal of Solids Structures*, Vol. 13, 1977, pp. 479–492.

[17] Benthem, J. P., "The Quarter-Infinite Crack in a Half Space; Alternative and Additional Solutions," *International Journal of Solids Structures*, Vol. 16, 1980, pp. 119–130.

[18] Tada, H., Paris, P. C., and Irwin, G. R., *The Stress Analysis of Crack Handbook*, Del Research Corporation, Hellertown, PA, 1973.

[19] Kumar, V., German, M. D., and Shih, C. F., "An Engineering Approach for Elastic-Plastic Fracture Analysis," EPRI Report No. NP-1931, Electric Power Research Institute, Palo Alto, CA, July 1981.

[20] Kumar, V. et al., "Advances in Elastic-Plastic Fracture Analysis," EPRI Report No. NP-3607, Electric Power Research Institute, Palo Alto, CA, Aug. 1984.

[21] Newman, J. C., Jr., and Raju, I. S., Stress-Intensity Factors for Internal Surface Cracks in Cylindrical Pressure Vessels, NASA TM 80073, National Aeronautic and Space Administration, Washington, DC, July 1979.

[22] Fatigue Crack Growth Computer Program, "NASA/FLAGRO," August 1986 Version, March 1989 Revision, Materials Branch, Structures and Mechanics Division, NASA, LBJ Space Center, Houston, TX.

D. S. Dawicke,[1] K. N. Shivakumar,[2] J. C. Newman, Jr.,[3] and A. F. Grandt, Jr.[4]

An Inverse Method for the Calculation of Through-Thickness Fatigue Crack Closure Behavior

REFERENCE: Dawicke, D. S., Shivakumar, K. N., Newman, J. C., Jr., and Grandt, A. F., Jr., "**An Inverse Method for the Calculation of Through-Thickness Fatigue Crack Closure Behavior,**" *Fracture Mechanics: Twenty-Second Symposium (Volume II), ASTM STP 1131*, S. N. Atluri, J. C. Newman, Jr., I. S. Raju, and J. S. Epstein, Eds., American Society for Testing and Materials, Philadelphia, 1992, pp. 46–57.

ABSTRACT: An inverse technique was used to calculate through-thickness fatigue crack closure behavior. The through-thickness variation in crack opening stress-intensity factor was calculated by considering the variation in the three-dimensional stress-intensity factor, the variation in crack growth rate along the crack front, and a relationship between the crack growth rate and effective stress-intensity factor range ($da/dN - \Delta K_{eff}$). The three-dimensional stress-intensity factor variation was obtained from an elastic finite element analysis of specific crack front profiles observed experimentally. The variation in crack growth rate along the crack front was obtained experimentally from comparison of observed crack front changes. The $da/dN - \Delta K_{eff}$ relationship was estimated from high stress ratio, constant load amplitude, fatigue crack growth tests. The through-thickness crack opening stress-intensity factor results agreed with crack opening measurements obtained from fatigue striations, near-tip strain gages, and remote strain and displacement gages.

KEY WORDS: fatigue (materials), crack closure, through-thickness, inverse calculation, fatigue striations, fracture mechanics

The concept of plasticity induced fatigue crack closure was first introduced by Elber [*1–2*], who observed that propagating fatigue cracks will close while still under a tensile load. The closure of the crack tip reduces the stress-intensity factor range over which damage may occur. Elber referred to the reduced range as the "effective" stress-intensity factor range.

Fatigue crack closure behavior has been determined experimentally through the measurement of the load or stress-intensity factor at which the crack opens. The "standard" methods of measuring the crack opening stress-intensity factor involve the use of strain or displacement measurements both near and remote from the crack tip, the location of which has been shown to influence the observed crack opening stress-intensity factors [*3,4*]. A recent ASTM round-robin test program to measure fatigue crack closure illustrated the large variability seen in these types of measurement techniques [*5*].

[1]Graduate student, School of Aeronautics and Astronautics, Purdue University, West Lafayette, IN 47907; currently with Analytical Services and Materials, Inc., Hampton, VA 23665–5225.
[2]Senior scientist, Analytical Services and Materials, Inc., Hampton, VA 23665–5225.
[3]Senior scientist, NASA Langley Research Center, Hampton, VA 23665–5225.
[4]Head, School of Aeronautics and Astronautics, Purdue University, West Lafayette, IN 47907.

The dependence on measurement location and large variability of the common crack opening stress-intensity factor measurement techniques are, in part, a result of the three-dimensional nature of fatigue crack closure behavior. With the exception of very thin sheets, where the constraint is nearly plane stress over the entire thickness of the sheet, the through-thickness variation is due to the change in constraint from the so-called plane stress at the surface to plane strain in the interior conditions. This variation in constraint may result in a higher crack opening stress-intensity factor at the surface than in the interior. Experimental evidence of a through-thickness variation in crack closure behavior was observed through the use of optical interferometry on transparent polymers [*6,7*]. Similar results were obtained in metals using ultrasonic transmission [*8*] and fatigue striations [*9–11*].

The techniques required to obtain the through-thickness description of the fatigue crack closure behavior are complex, time consuming, and require a considerable investment in equipment. The objective of this research was to develop a simpler means of describing the through-thickness fatigue crack closure behavior. The resulting inverse method can be applied to many crack problems. Inverse techniques have been used to determine stress-intensity factors for complex geometries [*12*] and average crack opening loads [*13*].

The following section provides a description of the inverse crack opening stress-intensity factor calculation. Then the procedure is used to calculate the variation in crack opening load through-thickness for middle crack tension (MT) and compact tension (CT) specimens subjected to constant stress-intensity factor range loading. Comparisons of the calculated and experimentally measured crack opening loads are also presented.

Experimental and Numerical Methods

The inverse calculation required a combination of experimental and numerical information. The experimental portion of the calculation required a description of the crack front profile, the rate of change of the crack front profile, and relationship for the crack growth rate-effective stress-intensity factor range ($da/dN - \Delta K_{eff}$), independent of any crack opening load measurement. An independent $da/dN - \Delta K_{eff}$ relationship could be approximated, for many materials, from constant load fatigue crack growth tests conducted at high stress ratios. At high stress ratios, the crack would be open for the entire loading-unloading cycle, thus the effective stress-intensity factor range would be nearly equal to the applied stress-intensity factor range (ΔK).

The numerical portion of the calculation involves determining the through-thickness stress-intensity factor variation for the specific curved crack profiles observed experimentally. Three-dimensional stress-intensity factor solutions exist for part through cracks such as an elliptical surface crack [*14*]. Solutions for other crack configurations, such as curved through cracks, have been presented in the literature [*15–17*]. However, fatigue crack front profiles are highly irregular, requiring separate three-dimensional finite element analysis for each specific crack front profile. The three-dimensional equivalent domain integral (EDI) method [*18,19*], in conjunction with a 20-node isoparametric finite element analysis, was used in the present analysis.

Experimental Crack Growth Measurements

Constant load amplitude and constant stress-intensity factor range fatigue crack growth tests were conducted on 9.5 mm (0.375 in.) thick, 76.2 mm (3.0 in.) wide middle crack tension (MT) and compact tension (CT) specimens. The material used was 2024-T351 aluminum alloy. The constant load amplitude tests were conducted at stress ratios of $R = 0.1$ and $R = 0.5$, and the relationship between crack growth rate and stress-intensity factor range was determined, as shown in Fig. 1. Power law curve fits were used to describe the crack growth rate behavior of only the upper portion, $9.9 \leq \Delta K \leq 16.4$ MPa $\sqrt{m}$ ($9.0 \leq \Delta K \leq 15.0$ ksi $\sqrt{in.}$), of the data for the two stress ratios (the range of interest for the crack opening load measurements). The resulting power law descriptions indicate that the slope exponent (n) is 2.8 for the two stress ratios examined ($R = 0.1$ and 0.5).

$$\frac{da}{dN} = c\Delta K^n \tag{1}$$

The crack growth rate-effective stress-intensity factor range relationship was approximated from the constant load amplitude fatigue crack growth tests conducted at a stress ratio of $R = 0.5$. The fatigue striation and near-tip strain gage measurements indicated that, for the $R = 0.5$ tests of the 2024-T351 aluminum alloy, a small amount of crack closure was present only at the surfaces, thus the effective stress-intensity factor range was approximately equal to the applied stress-intensity factor range. This approximation would slightly underestimate the value of the power law constant (c), which would in turn lower the calculated fatigue crack opening load. The value of 4.0×10^{-10} for c was obtained from the $R = 0.5$ tests.

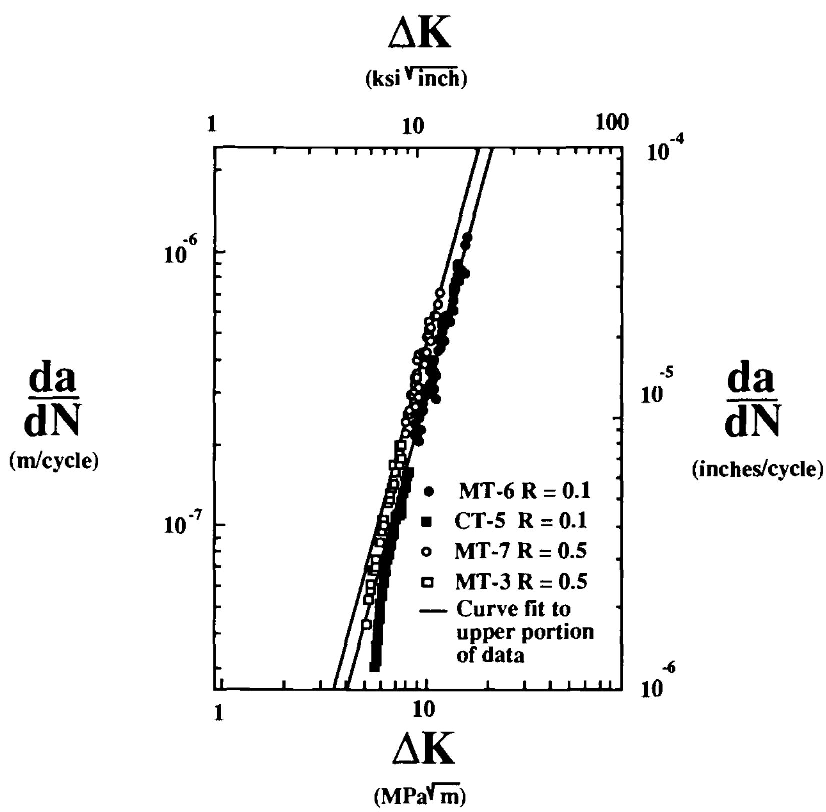

FIG. 1—*Constant load amplitude crack growth rate results and curve fit for 2024-T351 aluminum alloy.*

Constant stress-intensity factor range tests were conducted at $\Delta K = 13.8$ MPa $\sqrt{m}$ (12.6 ksi $\sqrt{in.}$) and a stress ratio of $R = 0.1$. The crack lengths were determined optically and the stress-intensity factor range was kept constant, within $\pm 2\%$, through load shedding. Crack opening load measurements were made at several crack lengths throughout each test, and after each measurement a series of high stress ratio ($R = 0.8$) cycles were applied. It was found that a crack advance of 0.12 mm (0.005 in.), under a stress ratio of $R = 0.8$, was sufficient to produce a visibly lighter region of crack growth, as shown in Fig. 2. The lighter regions, called marker bands, outline the crack front at the time of the application of the high stress ratio cycles. The inverse calculation could be made for each marker band.

The variation in crack growth rate along the crack front was obtained by comparison of consecutive marker bands. The crack growth rate along the crack front was constant for the

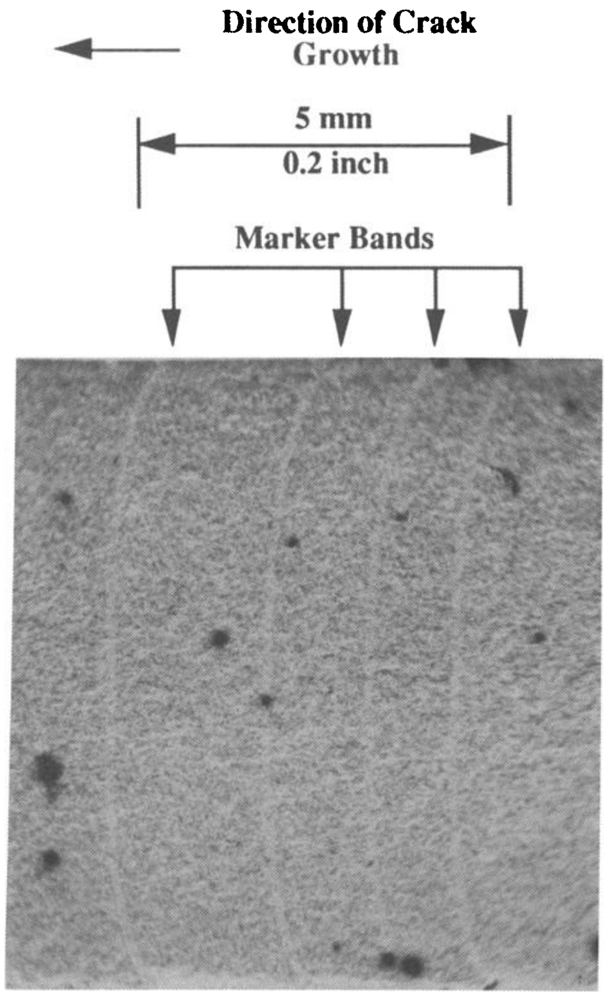

FIG. 2—*Photograph of marker bands indicating the crack front observed in MT-2 specimen, constant* $\Delta K = 13.8$ *MPa* $\sqrt{m}$ *(12.6 ksi* $\sqrt{in.}$*),* $R = 0.1$.

constant ΔK tests, as shown in Figs. 3 and 4. Figure 3 contains the digitized representations of two consecutive marker bands, and in Fig. 4 the two marker bands were superimposed by equating the crack lengths at one edge of the specimen. The superposition indicated that the crack front shape of the two consecutive marker bands was constant, thus the crack growth rate at each point along the crack front was constant. In general, the functional relationship describing the variation in crack growth rate along the crack front could be expressed as an experimentally determined function of position through-thickness (z).

$$\frac{da}{dN} = F_{cgr}(z) \tag{2}$$

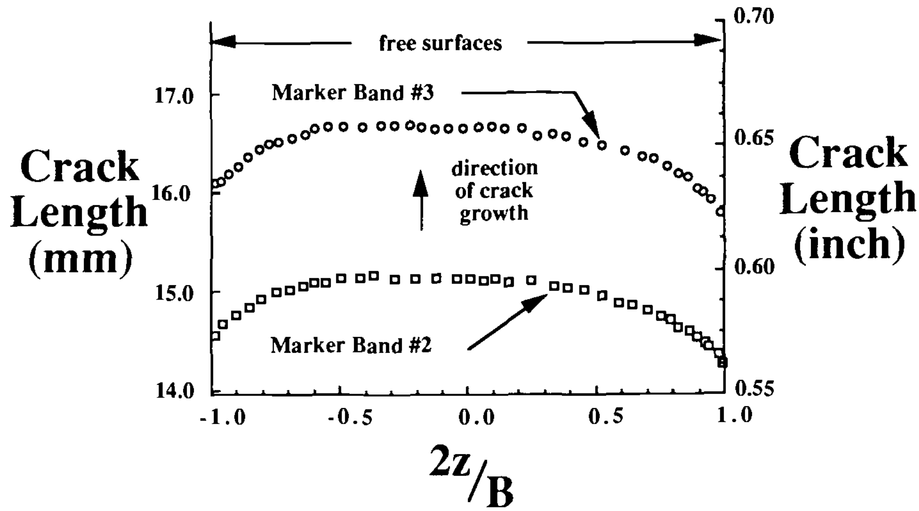

FIG. 3—*Digitized crack fronts for two consecutive marker bands of MT-2 test, constant* ΔK = *13.8 MPa* $\sqrt{m}$ *(12.6 ksi* $\sqrt{in.}$*),* R = *0.1.*

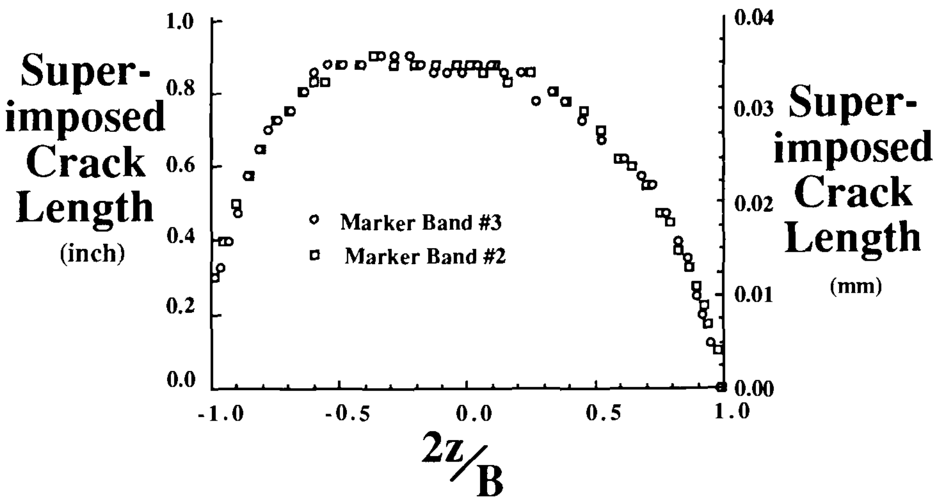

FIG. 4—*Superposition of the two consecutive crack fronts shown in Fig. 3 (note the abscissa scale change).*

Numerical Stress-Intensity Factor Calculations

The description of the variation of stress-intensity factor along the crack front required a knowledge of the specific shape of the crack front. In general, closed form solutions do not exist for three-dimensional stress-intensity factors, thus a numerical approach was required. In this study, the digitized crack fronts were incorporated into a three-dimensional finite element analysis model. Figures 5 and 6 show the three-dimensional finite element model of the specimen and the idealization of the crack front shown in Fig. 4, respectively. The model had 1024 twenty-node isoparametric elements and 5882 nodes, with three degrees of freedom per node. The stress-intensity factor was calculated at discrete points along the crack front using the EDI method. Details of this method are described in Ref *19*. The stress-intensity factor variation of the right half ($2z/B > 0$) of the crack front shape given in Fig. 3 was calculated using a plane strain approximation, as shown in Fig. 7. The functional relationship describing the variation in stress-intensity factor along the crack front could be expressed as a known numerically determined discrete function of position through-thickness ($K_{fe}(z)$).

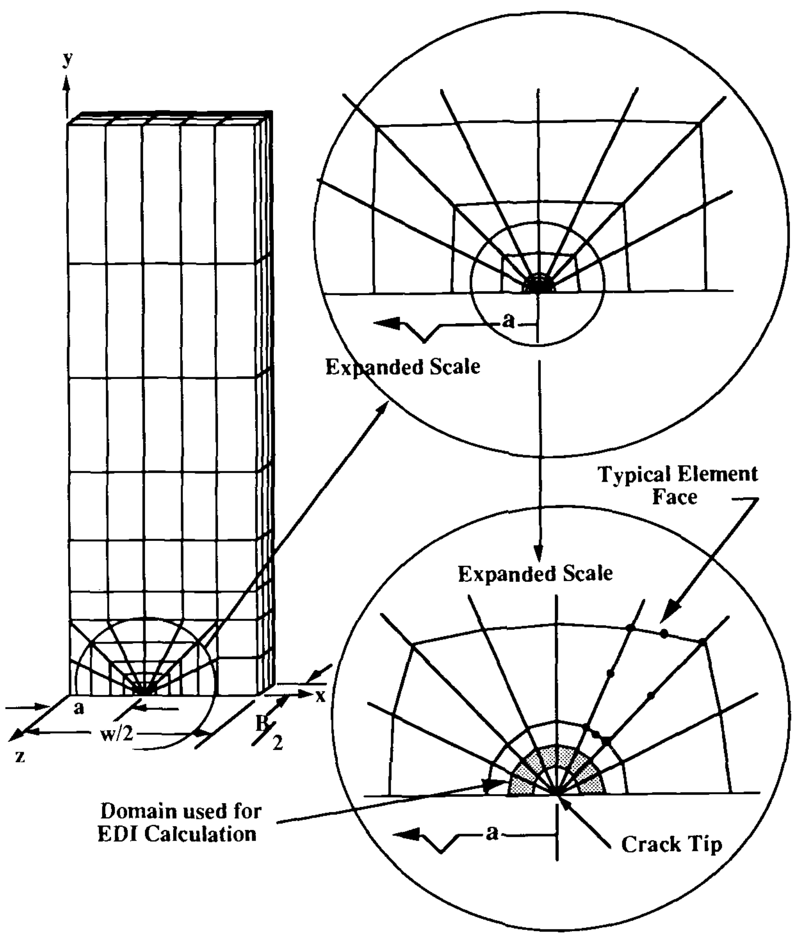

FIG. 5—*Finite element mesh used in the three-dimensional stress-intensity factor calculations*, a/w = *0.2*.

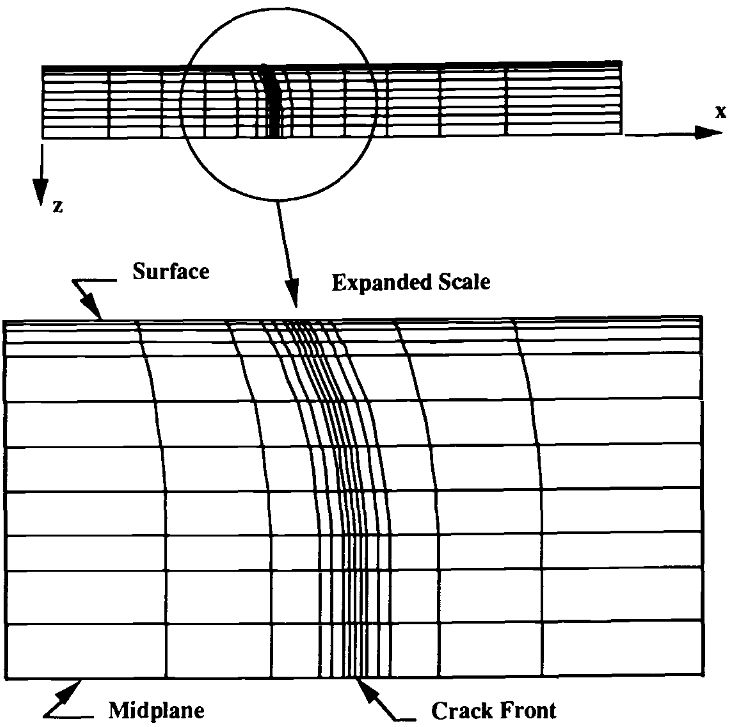

FIG. 6—*Crack plane view of the three-dimensional finite element mesh used in the stress-intensity factor calculation of the crack front given in Fig. 4 (symmetry assumed).*

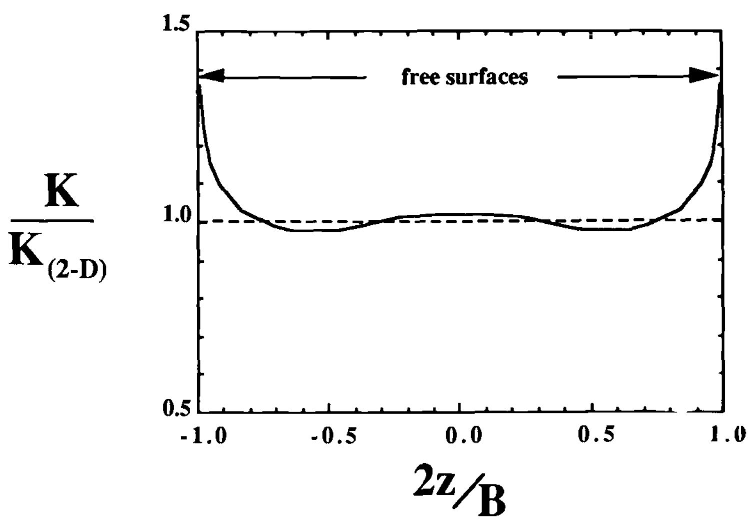

FIG. 7—*Three-dimensional stress intensity factor solution for the crack front shown in Fig. 4, symmetry about the midplane* (2z/B = *0.0) assumed.*

The effect of crack front shape (F_{cf}) could be obtained by normalizing the three-dimensional stress-intensity factor variation with respect to the two-dimensional stress-intensity factor (K_{2D}) for the same crack length and geometry.

$$F_{cf}(z) = K_{fe}(z)/K_{2D} \tag{3}$$

Inverse Method

The inverse method of determining the crack-opening stress-intensity factor requires three functional relationships:

1. A description of the crack growth rate along the crack front (for example, Fig. 3).
2. A description of the $da/dN - \Delta K_{eff}$ relationship (Eq 2).
3. A description of the variation of the stress-intensity factor along the crack front (Eq 3).

These three functional relationships (described in previous sections) allow the through-thickness variation in crack-opening stress-intensity factor to be determined from the point-wise application of Elber's [*1,2*] definition of the effective stress-intensity factor along the crack front,

$$\Delta K_{eff}(z) = K_{max}(z) - K_{open}(z) = K_{max}(z)\left(1 - \frac{K_{open}(z)}{K_{max}(z)}\right) \tag{4}$$

where $K_{open}(z)/K_{max}(z)$ is the normalized crack opening stress-intensity factor (equivalent to the normalized crack opening load) along the crack front. Allowing for a three-dimensional variation in stress-intensity factor and crack opening load and recognizing that the crack opening calculations were for tests conducted under constant ΔK (two-dimensional equivalent) conditions, Eq 4 may be expressed as

$$\Delta K_{eff}(z) = \frac{\Delta K_{2D}}{1 - R} F_{cf}(z)\left(1 - \frac{K_{open}}{K_{max}}(z)\right) \tag{5}$$

for the study reported herein.

The effective stress-intensity factor range was evaluated by measuring the crack growth rate at discrete points along the crack front and using the $da/dN - \Delta K_{eff}$ relationship, as illustrated in Fig. 8. The normalized crack opening load, ($F_{cf}(z)$) can easily be obtained from Eq 5.

Comparison with Experimental Measurements

The crack opening loads calculated using the inverse technique were compared with crack opening loads determined experimentally using fatigue striations, near-tip strain gages, backface strain gages, and remote displacement gages, as described in Ref *20*. The fatigue striations method was developed by Sunder et al. [*9–11*] and produced crack opening load measurements at discrete points through-thickness of the specimen. The near-tip strain gages provided an upper and lower bound on the through-thickness fatigue crack opening load behavior, detecting the high crack opening load at the surface and the lower crack opening loads in the interior. The backface strain gages and remote displacement gages produced

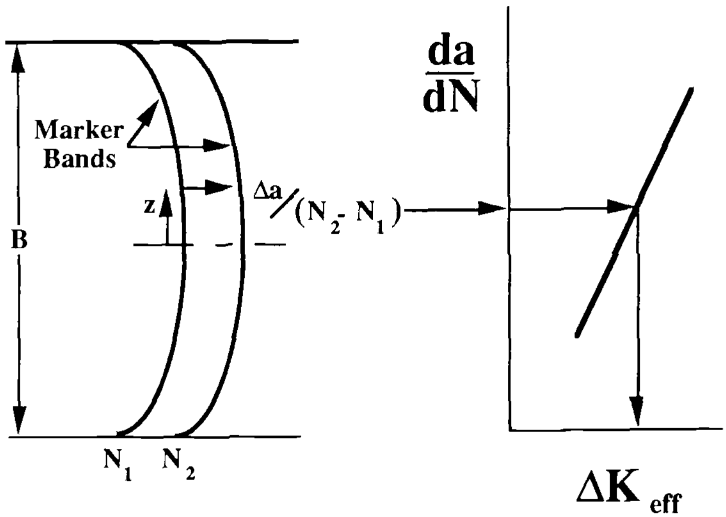

FIG. 8—*Schematic of technique used to determine the effective stress-intensity factor range from the crack growth rate along the crack front.*

an average crack opening load. The comparisons were made for MT and CT specimens subjected to constant stress-intensity factor range loading of ΔK = 13.8 MPa $\sqrt{m}$ (12.6 ksi $\sqrt{in.}$) at a stress ratio of R = 0.1.

Calculated crack opening loads, in terms of K_{open}/K_{max} along the crack front are compared with experimental measurements for MT and CT specimens [*20*] in Figs. 9 and 10, respectively. The calculated crack opening loads in the interior agreed with the results from the fatigue striations and with the lower bound of the near-tip strain gages. The calculated crack opening loads at the surface agreed with the upper bound of the near-tip strain gage and

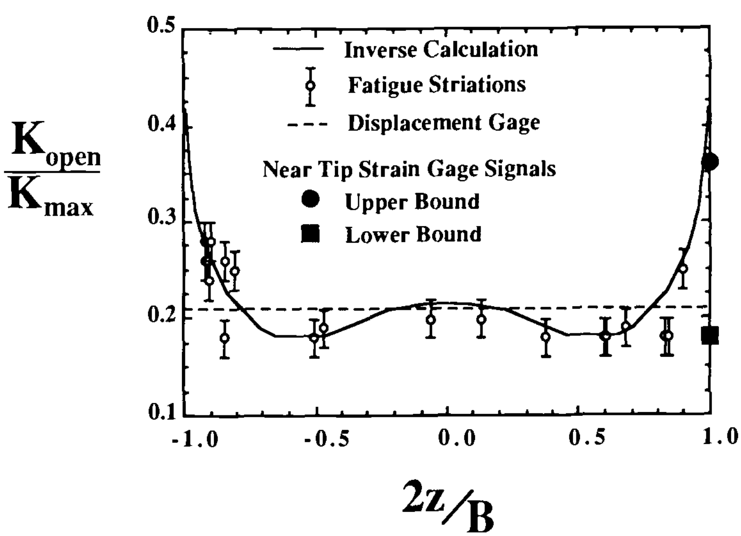

FIG. 9—*Comparison of the calculated and experimentally measured through-the-thickness fatigue crack opening loads for a middle crack tension specimen at a crack length of* 2a/w = *0.38,* R = *0.1.*

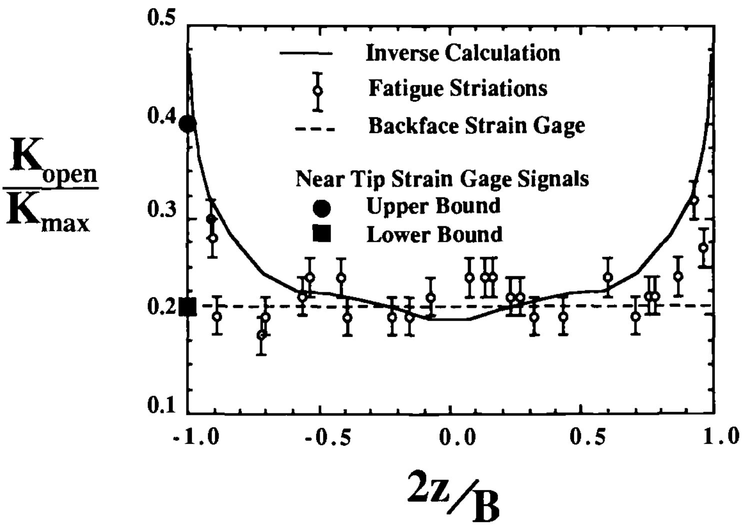

FIG. 10—*Comparison of the calculated and experimentally measured through-the-thickness fatigue crack opening loads for a compact tension specimen at a crack length of* 2a/W = *0.44*, R = *0.1*.

followed the trend of the near-surface fatigue striation crack opening loads. The calculated through-thickness crack opening loads also agreed with the results of a three-dimensional elastic-plastic finite element analysis reported in Ref *21*. Thus, the present inverse method provides an alternative method for calculating the crack opening load variation along the crack front. The measured through-thickness normalized crack opening loads (K_{open}/K_{max}) for the CT and MT specimens were similar, with values of 0.18 and 0.20 for the interiors of the MT and CT specimens, respectively. The calculated normalized crack opening load at the surface was 0.42 for the MT specimen and 0.47 for the CT specimen. The sharp increase in the crack opening load was confined to the region within 1.8 mm (0.07 in.) from the free surfaces (or 15% of the thickness) for both the CT and MT specimens.

The variation in shape of the calculated through-thickness crack opening loads of the CT and MT specimens are a result of the differences in the crack front profiles. The CT specimen exhibited more tunneling and had a slightly greater difference between the crack length at the surface and midthickness. The crack front profile differences may be due to subtle inherent variations in the state of stress in front of the crack in the CT and MT configurations.

Summary

This study introduced an inverse crack opening load calculation technique capable of describing through-thickness fatigue crack closure behavior. The calculation provided excellent agreement with experimentally measured through-thickness fatigue crack opening loads. The MT and CT specimens both exhibited a significant through-thickness variation in fatigue crack closure behavior, for constant ΔK, R = 0.1 conditions. The normalized crack opening load (K_{open}/K_{max}) of the MT specimen was 0.42 at the surface and 0.18 in the interior, while that of the CT specimen was 0.47 at the surface and 0.2 in the interior. The sharp increase in the crack opening load was confined to within 1.8 mm (0.07 in.) from the free surface (or 15% of the thickness) for both specimen configurations.

The through-thickness variation in crack opening load is an important consideration in the understanding of fatigue crack closure and its effect on crack growth. The large through-

thickness variation in measured and calculated crack opening load may explain the variability seen in the "standard" crack opening load measurement techniques. Measurement techniques that characterize the overall crack closure behavior with a single crack opening load will have considerable variability depending on which region of crack closure is emphasized. The measurement techniques that monitor near-tip quantities will produce higher values due to the close proximity to the higher crack opening load at the surface. Far field measurements will produce lower crack opening loads as the influence of the interior dominates the overall behavior.

The methods of experimentally measuring through-thickness fatigue crack closure behavior are very difficult and time consuming. The fatigue striation method requires extensive fractographic analysis, and other experimental techniques produce only a partial description of the through-thickness behavior. The inverse calculation provides a method of estimating the through-thickness fatigue crack closure behavior for many conditions and materials in which plasticity induced fatigue crack closure is the predominant mechanism. The method does require some experimental information, which is easily available through the application of marker bands and high stress ratio constant load amplitude tests. The numerical calculation of three-dimensional stress-intensity factors requires considerable computing resources, but the availability of high-speed computers makes the solutions within the grasp of many researchers.

References

[*1*] Elber, W., "Fatigue Crack Closure Under Cyclic Tension," *Engineering Fracture Mechanics*, Vol. 3, 1970, pp. 37–45.

[*2*] Elber, W., "The Significance of Fatigue Crack Closure," *Damage Tolerance in Aircraft Structures, ASTM STP 486*, American Society for Testing and Materials, Philadelphia, 1971, pp. 230–242.

[*3*] Sharpe, W. N., Jr., and Grandt, A. F., Jr., "A Preliminary Study of Fatigue Crack Retardation Using Laser Interferometry to Measure Crack Surface Displacements," *Mechanics of Crack Growth, ASTM STP 590*, American Society for Testing and Materials, Philadelphia, 1976, pp. 302–320.

[*4*] Macha, D. E., Corbly, D. M., and Jones, J. W., "On the Variation of Fatigue-Crack-Opening Load with Measurement Location," *Experimental Mechanics*, Vol. 19, 1979, pp. 207–213.

[*5*] Phillips, E. P., "Results of the Round Robin on Opening-Load Measurement," NASA Technical Memorandum 101601, NASA Langley Research Center, Hampton, VA, 1989.

[*6*] Pitoniak, F. J., Grandt, A. F., Jr., Montulli, L. T., and Packman, P. F., "Fatigue Crack Retardation and Closure in Polymethylmethacrylate,"*Engineering Fracture Mechanics*, Vol. 6, 1974, pp. 663–670.

[*7*] Ray, S. K., Grandt, A. F., Jr., and Andrew, S., "Three-Dimensional Measurement of Fatigue Crack Closure and Opening," *Basic Questions in Fatigue Volume II, ASTM STP 924*, R. P. Wei and R. P. Gangloff, Eds., American Society for Testing and Materials, Philadelphia, 1980, pp. 275–293.

[*8*] Sharpe, W. N., Jr., Corbly, D. M., and Grandt, A. F., Jr., "Effects of Rest Time on Fatigue Crack Retardation and Observations of Crack Closure," *Fatigue Crack Growth Under Spectrum Loads, ASTM STP 595*, American Society for Testing and Materials, Philadelphia, 1976, pp. 61–77.

[*9*] Sunder, R. and Dash, P. K., "Measurement of Fatigue Crack Closure Through Electron Microscopy," *International Journal of Fatigue*, Vol. 4, 1982, pp. 97–105.

[*10*] Anadan, K. and Sunder, R., "Closure of Part Through Cracks at the Notch Root," NAL PDMT 8625, National Aeronautical Laboratory, Bangalore, India, 1986.

[*11*] Anadan, K. and Sunder, R., "Closure of Part-Through Cracks at the Notch Root," *International Journal of Fatigue*, Vol. 9, No. 3, 1987, pp. 217–222.

[*12*] James, L. A. and Anderson, W. E., "A Simple Experimental Procedure for Stress-Intensity Factor Calibration," *Journal of Engineering Fracture Mechanics*, Vol. 1, 1963, pp. 565–568.

[*13*] Hillberry, B. M., Alzos, W. X., and Skat, A. C., Jr., "The Fatigue Crack Propagation Delay Behavior in 2024-T3 Aluminum Alloy Due to Single Overload/Underload Sequences," *Fatigue Crack Growth Under Spectrum Loads, ASTM STP 595*, American Society for Testing and Materials, Philadelphia, 1976, pp. 41–60.

[14] Newman, J. C., Jr., and Raju, I. S., "An Empirical Stress-Intensity Factor Equation for the Surface Cracks," *Engineering Fracture Mechanics*, Vol. 15, No. 1–2, 1981, pp. 185–192.
[15] Luchi, M. L. and Rizzuti, S., "Boundary Element Analysis of CT Specimens with Straight and Curved Crack Fronts," *International Journal of Fracture*, Vol. 34, 1987, pp. 23–40.
[16] Kuna, M., "Three-Dimensional Elastic Analysis of CT Specimen with Straight and Curved Crack Fronts," *International Journal of Fracture*, Vol. 19, 1982, pp. R63–R67.
[17] Fenner, D. N. and Abdul Mihsein, M. J., "Crack Front Elastic Stress State for Three-Dimensional Crack Problems," *International Journal of Fracture*, Vol. 25, 1984, pp. 121–131.
[18] Nikishkov, G. P. and Atluri, S. N., "Calculation of Fracture Mechanics Parameters for an Arbitrary Three-Dimensional Crack by the Equivalent Domain Integral Method," *International Journal for Numerical Methods in Engineering*, Vol. 24, 1987, pp. 1801–1821.
[19] Shivakumar, K. N. and Raju, I. S., "An Equivalent Domain Integral for Analyzing 3-D Crack Problems," NASA Contractors Report, NASA Langley Research Center, Hampton, VA, 1989.
[20] Dawicke, D. S., Grandt, A. F., Jr., and Newman, J. C., Jr., "Three-Dimensional Crack Closure Behavior," *Engineering Fracture Mechanics*, accepted for publication, 1989.
[21] Chermahini, R. G., Shivakumar, K. N., and Newman, J. C., Jr., "Three-Dimensional Finite-Element Simulation of Fatigue Crack Growth and Closure," *Mechanics of Fatigue Crack Closure, ASTM STP 982*, J. C. Newman, Jr., and W. Elber, Eds., American Society for Testing and Materials, Philadelphia, 1988, pp. 398–413.

Lynn M. Barker[1]

ASTM E 1304, The New Standard Test for Plane-Strain (Chevron-Notched) Fracture Toughness: Usage of Test Results

REFERENCE: Barker, L. M., "**ASTM E 1304, The New Standard Test for Plane-Strain (Chevron-Notched) Fracture Toughness: Usage of Test Results,**" *Fracture Mechanics: Twenty-Second Symposium (Volume II), ASTM STP 1131*, S. N. Atluri, J. C. Newman, Jr., I. S. Raju, and J. S. Epstein, Eds., American Society for Testing and Materials, Philadelphia, 1992, pp. 58–68.

ABSTRACT: The origins and rationale for the three plane-strain fracture toughnesses defined by the new ASTM Test Method for Plane-Strain (Chevron-Notch) Fracture Toughness of Metallic Materials (E 1304-89) are reviewed. K_{IvM} represents the toughness measured in a greatly simplified test, but it can be less accurate than K_{Iv} and K_{Ivj}. The test for K_{Iv} is complete with all the procedures and validity criteria necessary to assure accurate measurements of plane-strain critical stress-intensity factors. When a material exhibits a crack-jump behavior, the K_{Iv} procedure must be modified, and the toughness is called K_{Ivj}. This paper suggests that ASTM E 1304-89 toughness measurements can be used for the full range of applications appropriate to K_{Ic} values measured by the ASTM Test Method for Plane-Strain Fracture Toughness of Metallic Materials (E 399-83). However, a material-dependent constant, equal to about three times the crack-tip plastic zone radius, should be added to the preexisting flaw size in calculations of crack stability.

KEY WORDS: measurements, plane strain fracture toughness, chevron-notched specimens, metals, conservative calculations, fracture mechanics, standards

In late 1989, ASTM formally adopted ASTM Test Method for Plane-Strain (Chevron-Notch) Fracture Toughness of Metallic Materials (E 1304-89) [*1,2*]. Attributes of the new standard include simplified specimen preparation (no fatigue precracking), small specimen size, low cost per test, and the ability to measure the toughness at a more localized spot in the parent material. Figure 1 shows the chevron-notched specimen configuration, and Fig. 2 shows a schematic of a load-displacement test record.

To the new user, a puzzling aspect of ASTM E 1304-89 may be the introduction of three new symbols, K_{Iv}, K_{Ivj}, and K_{IvM}, for its quasistatically measured plane strain fracture toughnesses, none of which are claimed to be equivalent to the K_{Ic} measured by ASTM Test Method for Plane-Strain Fracture Toughness of Metallic Materials (E 399-83). This paper therefore discusses the origins, significance, and usage of the three toughness values that ASTM E 1304-89 measures.

Toughnesses Defined by ASTM E 1304

K_{IvM}

The original work on the chevron-notch test method envisioned using only the peak load in the test, P_M, plus a specimen size dimension and a calibrated dimensionless constant to

[1]President, Valyn International, Albuquerque, NM 87112.

(a)

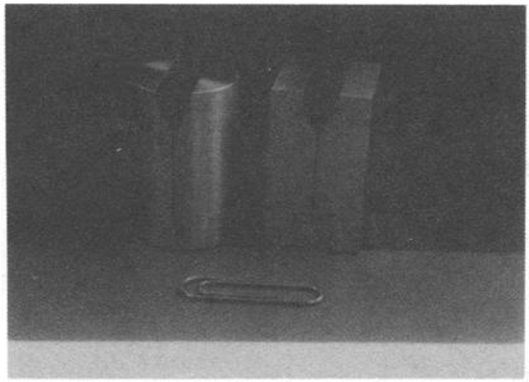

(b)

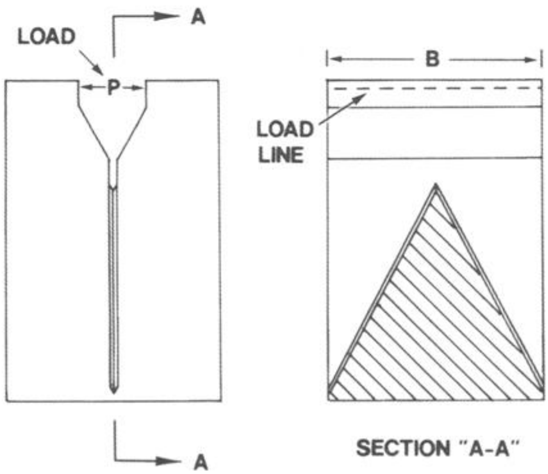

FIG. 1—(a) *Short rod and short bar chevron-notched specimens.* (b) *Side and plan views of the short rod. The load causes a crack to initiate at the point of the chevron and to advance downward through the shaded area, splitting the specimen in two. The toughness is measured when the crack front spans about one third of the specimen's* B*-dimension.*

calculate the toughness [*3,4*]. No fatigue precracking was required because a stable natural crack is created during the initial loading of the specimen well before the toughness measurement is taken. Also, no crack length measurement was required because it was shown analytically that the peak load should always occur at the same scaled crack length, called the critical crack length, regardless of the specimen material and the scaled specimen size. This resulted in an extremely simple fracture toughness test method that compared surprisingly well with K_{Ic}, especially for most brittle materials [*5,6*].

The original chevron-notched "short-rod" test method has been adopted with few changes in ASTM E 1304-89, and its result is given the symbol K_{IvM}, where the M stands for maximum load. The method is based on first principles of linear elastic fracture mechanics (LEFM), and it contains the minimum specimen size validity criterion, $B \geqslant 1.25(K_{IvM}/\sigma_y)^2$, to guard against too much plasticity in the specimen. Nevertheless, it lacks certain other validity checks to assure that LEFM conditions are sufficiently well satisfied for an accurate test

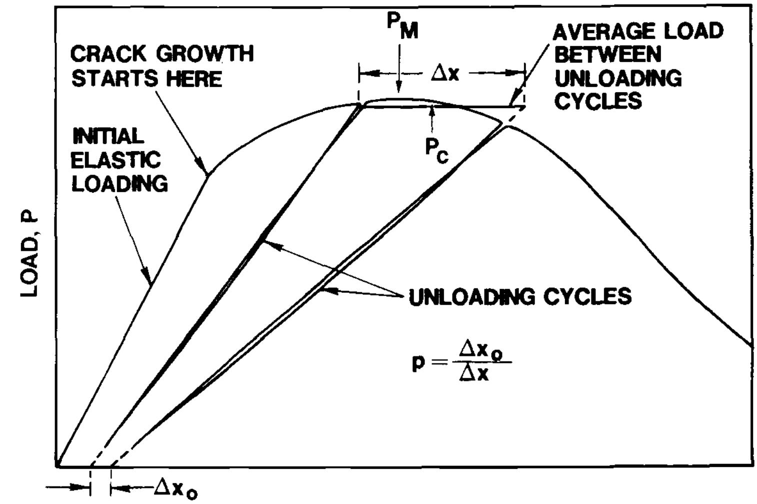

FIG. 2—*Schematic of a load-displacement test record for a chevron-notched specimen with smooth crack growth behavior. Some data analysis definitions and constructions are also shown.*

result. Therefore, the user must be aware that under certain circumstances, K_{IvM} can differ quite significantly from the inherently more accurate K_{Iv} and K_{Ivj} measurements of toughness.

K_{Iv}

The test for K_{Iv} was developed to improve test accuracy and to guard against sizable errors that can occur in the K_{IvM} method when LEFM conditions are not well satisfied. The assumption that the peak load occurs at the critical crack length is not used in the K_{Iv} test; rather, the load, P_c, corresponding to the critical crack length is obtained from two unloading compliance measurements of crack length during the test (note unloading cycles in Fig. 2). Having two fixes on the crack length allows the load at the critical crack length to be found by interpolation. Thus, the load (P_c) used in the toughness calculation may not be the peak load (P_M) in the test (Fig. 2), although it is usually close to P_M. One of the validity checks concerns the ratio of the peak load to the load at the critical crack length: If P_M/P_c exceeds 1.1, the test is invalid because the LEFM condition, $P_M = P_c$, is violated by too large a degree.

Another validity check in the K_{Iv} test concerns the behavior of the unloading slopes during the test. If the slopes deviate too much from ideal LEFM behavior, then instead of being close to zero, the p defined in the test (Fig. 2) will be outside of its prescribed range, $-0.05 \leq p \leq +0.10$, and the test is invalid. This criterion not only screens out specimens with too much plasticity, but also eliminates tests of specimens containing macroscopic residual stresses that are large enough to be detrimental to the test accuracy [7]. The minimum specimen size validity criterion, $B \geq 1.25(K_{Iv}/\sigma_y)^2$, must of course also be satisfied.

K_{Ivj}

Although the chevron-notch geometry promotes stable crack growth even in the most brittle materials, the crack speed is uncontrollable in certain materials; it is either zero or very high. A load-displacement test record of such a material is shown in Fig. 3. The crack

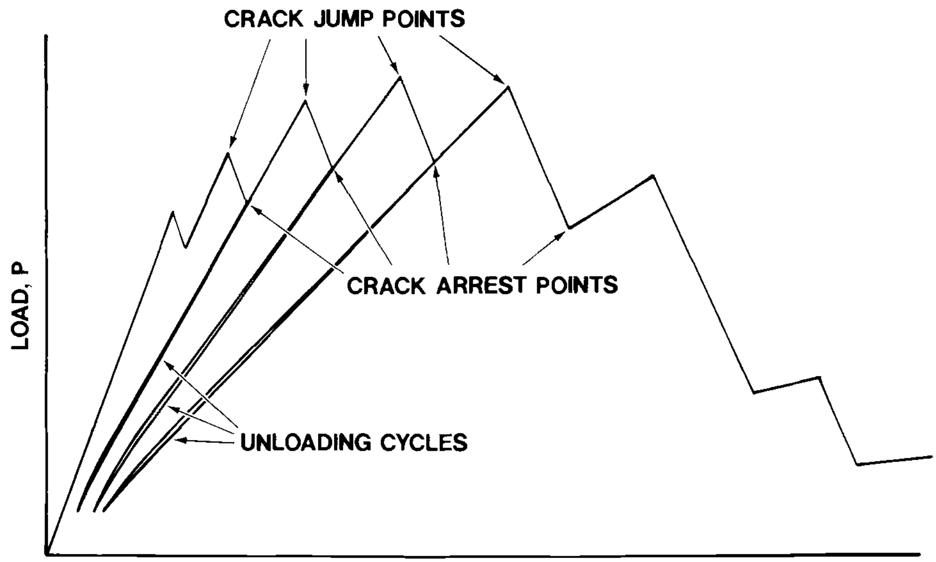

FIG. 3—*Load-displacement test record for a chevron-notched specimen with crack-jump behavior.*

jump behavior does not correlate with material brittleness. One way of explaining the crack jump behavior is to suppose that the critical stress-intensity factor for crack propagation in the material is a function of the crack speed, as was measured in Plexiglas, for example, by Johnson and Radon [8]. A decreasing critical stress intensity with increasing crack speed (Fig. 4) leads to crack jump behavior. The crack-jump behavior is a property of as many as 30% of all materials tested thus far by the chevron-notch method.

The primary reason for the K_{Ivj} distinction of crack-jump tests is that the crack jump behavior makes it impossible to follow the K_{Iv} test procedure. For example, the K_{Iv} method requires measurement of the crack-advancing load at the critical crack length, a_c. This is an easy task in smooth crack growth materials. In a crack-jump material, however, the critical stress-intensity factor must be calculated from the load required to initiate a crack jump from a crack-arrest point, and one cannot cause a prior crack jump to arrest precisely at a_c. Therefore, compliance measurements are made of the crack-arrest points that happen to occur within the central region of the specimen, and a calibration curve that is a function of crack length, rather than a calibration constant corresponding to a_c, is used to calculate K_{Ivj}.

Another major difference in the K_{Ivj} procedure is the omission of the p validity check (see preceding section on K_{Iv}). The value of p should be calculated from unloading slopes that start from a crack-advancing load, which is where the crack-tip plastic zone is at its maximum. In a crack-jump material, then, one would need to load the specimen up to the crack-jump load without initiating the jump, and then perform the unloading slope measurement. Because of scatter in the jump-initiating load, this is not possible. Performing unloadings from loads less than the jump-initiating loads would incur substantial errors, because the plastic zone size at the crack tip varies as the square of the applied load. Therefore, the value of p is not measured in the K_{Ivj} procedure, and the p validity check is omitted. This unavoidably makes the quality of the K_{Ivj} measurement somewhat less than that of K_{Iv}, and adds further justification for the use of a separate symbol for the measurement.

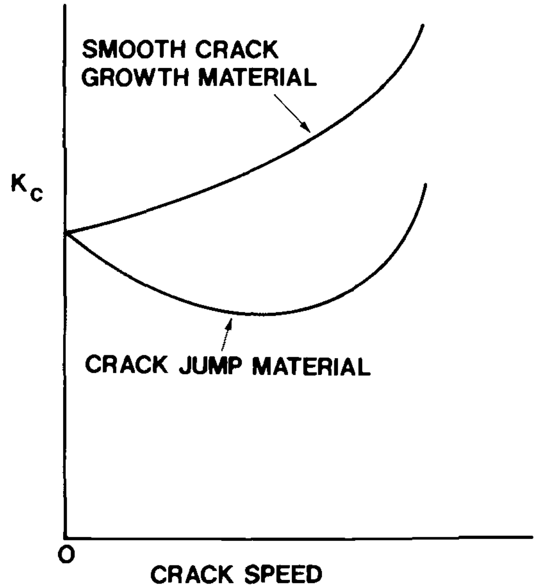

FIG. 4—*The critical stress-intensity factor can be a function of the crack speed. A decreasing* K_c *with increasing crack speed leads to the crack-jump behavior.*

Usage of ASTM E 1304 Test Results

Discussion

For the last two decades, ASTM E 399 has been the only recognized standard for measuring the plane-strain fracture toughness of metallic materials under quasi-static loading conditions. The E 399 test result, K_{Ic}, is recognized world-wide as "the" plane-strain fracture toughness. Now, however, the new E 1304 standard has introduced three additional symbols for plane-strain fracture toughness of metallic materials under quasi-static loading, none of which are necessarily equivalent to the ASTM E 399-83 K_{Ic}. What are the potential uses of these new values of fracture toughness?

One use is for the ranking of materials according to their plane-strain fracture toughness. This allows one to evaluate the effects of metallurgical variables or fabricating operations on the fracture toughness of new or existing materials. As far as is known, rankings of materials for these purposes by E 399 and E 1304 tests have always been the same. Another use might be for predicting the values of K_{Ic} of various lots of a given alloy, for example. According to E 1304, this is recommended only after an experimental study has been made to establish the correlation between K_{Ic} and the E 1304 result for the alloy of interest. A further important use concerns the ability of the chevron-notch test to measure the toughness at a much more localized spot in a parent material than has been possible using the E 399 test. This capability results from the smaller minimum chevron-notch specimen size for a valid test, and from the fact that the crack-front length at the toughness measurement spans only about one third of the specimen's B-dimension (see Fig. 1). This allows one to measure the toughness variation through the thickness of tough plates of aluminum, for example, as was done in Refs *9* and *10*.

The question also arises as to whether the ASTM E 1304-89 measurements of plane-strain toughness can be used directly in calculations of crack stability in a structure, as the K_{Ic} of

ASTM E 399-83 is used. The answer is yes, but the calculation should be revised slightly. The following paragraphs discuss the basic differences between the E 399 and E 1304 test methods, and suggest a procedure for crack stability calculations using E 1304 test results.

The ASTM E 399-83 test philosophy is based on measuring the critical stress-intensity factor necessary to produce the first motion of a pre-existing fatigue crack in the test material. One of the problems has been the definition of "first motion," since the crack must undergo at least a microscopic advance even by the time the load is raised to the fatigue pre-cracking level; otherwise, the fatigue pre-crack would not have grown. The difficulty is treated in E 399 by using an operational definition wherein first motion is said to occur either at crack instability or at the 5% offset point, whichever comes first. In either case, the toughness is ideally measured at some point on the plane-strain *R*-curve of the material, rather than always at the plateau of the plane-strain *R*-curve.

The ASTM E 1304-89 test, on the other hand, measures the critical stress-intensity factor corresponding to the advance of a steady-state crack [*11*], that is, the stress intensity at the plateau of the plane-strain *R*-curve [*12*]. This is one reason why E 1304 toughnesses often tend to be somewhat larger than E 399 K_{Ic} values.

Most crack stability calculations that use K_{Ic} values involve situations in which an assumed flaw in a structure, usually a fatigue crack, is loaded until it becomes unstable, leading to catastrophic failure. The failure occurs at a stress-intensity factor somewhere on the *R*-curve of the material [*13*]. The similarities between the K_{Ic} test and the assumptions in the calculation generate some faith in the calculated results, although the *R*-curve stress intensities corresponding to K_{Ic} and to the catastrophic failure point may not be the same.

Given that ASTM E 1304-89 test results correspond to the plateau of the plane-strain *R*-curve, a simple substitution of K_{Iv} for K_{Ic} might give a nonconservative result in a crack stability calculation. Since E 1304 tests are less expensive than E 399 tests, it would be an advantage to have a calculation procedure in which E 1304 test results could be used in conservative crack stability calculations.

A Conservative Calculation Procedure

An easy way to make use of ASTM E 1304-89 test results in crack stability calculations is to follow exactly the same procedure that would be used in a calculation involving K_{Ic}, with the following changes: (1) use the E 1304 toughness (preferably K_{Iv}) in place of K_{Ic}, and (2) substitute $a_0' = a_0 + \Delta a_s$ for the size, a_0, of the preexisting flaw or fatigue crack in the structure. Here, Δa_s is the distance that a fatigue precrack must advance under monotonic loading before its *R*-curve reaches the plateau value corresponding to the E 1304 stress intensity (Fig. 5). The conservatism of this approach is shown next, after which the evaluation of Δa_s is discussed.

According to *R*-curve theory, the load that will cause a structure with a precrack to catastrophically fail can be estimated graphically from the *R*-curve for the material [*13–15*]. First, the *R*-curve is plotted starting at the precrack length, a_0, in the structure (Fig. 5). Then stress intensity (K) versus crack length (a) curves are plotted on the same graph, each curve assuming a different load on the structure containing the crack, until the curve is found that is tangent to the *R*-curve (Line OA in Fig. 5). The point of tangency defines the critical stress-intensity factor, and the load of the tangent K versus a curve is the failure load. The slopes of the K versus a curves increase with increasing loads, of course.

From Fig. 5, it can be seen that if K_{Iv} is used along with the original crack length, a_0, to define the failure load, one would arrive at the failure load corresponding to Line OB. Since Line OB has a steeper slope than Line OA, the estimation of the failure load would be too high, a nonconservative result. However, if the crack-advance distance to attain the steady-

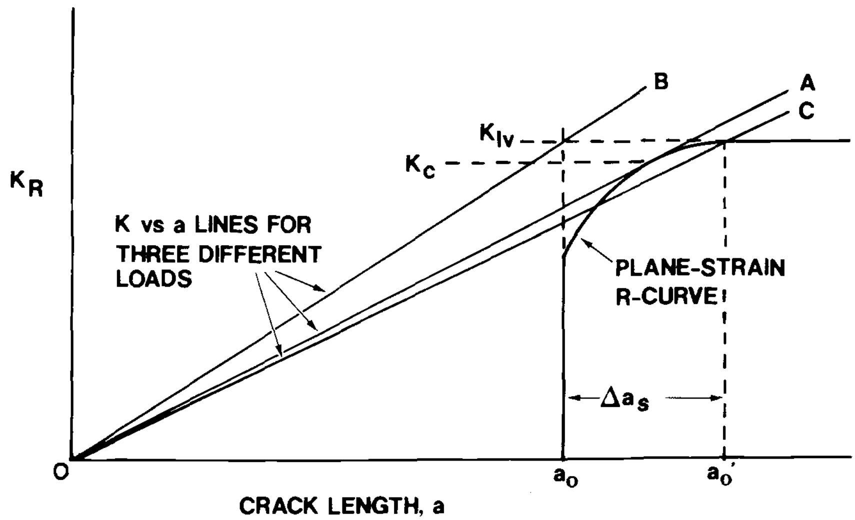

FIG. 5—*Schematic of a plane-strain* R-*curve with stress intensity versus crack length* (K *versus* a) *lines for three particular loads. Straight lines rather than the more usual curved* K *versus* a *relationships are used here for illustrative purposes.*

state stress intensity, Δa_s, is added to a_0 before making the calculation, one would arrive at the load corresponding to Line OC as the failure load. In this case, since Line OC has a smaller slope than Line OA, the estimation of the failure load would be smaller than the actual failure load, which would be a conservative result. It is apparent that using $a_0' = a_0 + \Delta a_s$ in place of a_0 will always give a conservative estimation of the failure load for any realistic shapes of the R-curve and the K versus a curves, and for any initial crack length, a_0.

Since E 1304 measures plane-strain fracture toughnesses, calculations using its test results are most accurate in cases involving only plane strain. However, as with the application of K_{Ic} to real-world problems, one can make use of the fact that the toughnesses of metals are probably always the least in plane strain. Therefore, in cases where the plane-strain constraint is imperfect, one should obtain conservative estimates of failure by using plane-strain toughness values.

Estimating Δa_s

The best way to obtain Δa_s would be to determine the plane-strain R-curve of the material and to measure Δa_s directly. Unfortunately, as pointed up by Irwin and Paris [*16*], a generally recognized method for measuring plane-strain R-curves has yet to be established, although one is certainly needed.

The author has made rough measurements of the plane-strain R-curve of a 4340 steel using fatigue precracked chevron-notched specimens. The steel was heat treated to a hardness of HRC 30, and had a yield strength of 862 MPa (125 ksi). The chevron-notched specimens had a diameter of 25.4 mm, and were machined from the center of a 50.8 mm diameter rod of the specimen material. The axis of the specimen was the same as the axis of the parent rod. The measured K_{Iv} was 122 MPa $\sqrt{m}$.

A schematic of the load versus specimen mouth-opening-displacement record of the tests is shown in Fig. 6. The upper-most envelope of the record, including the dashed-line portion

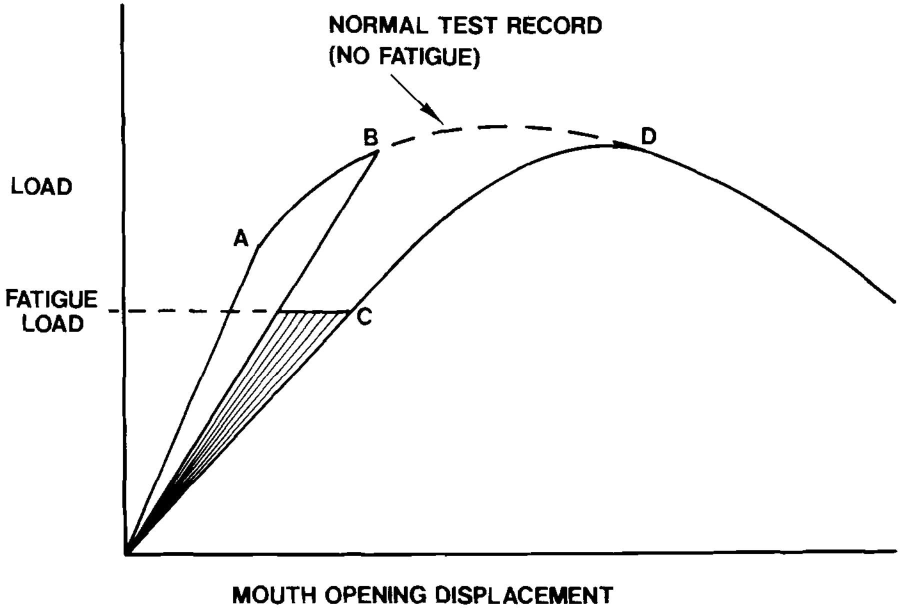

FIG. 6—*Schematic of the chevron-notched specimen test sequence used to measure the plane-strain* R-*curves of 4340 steel and 6061-T6 aluminum.*

of the smooth upper curve, denotes the load-displacement plot for a normal chevron-notch test in which steady-state crack conditions (constant K_{Iv}) prevail. To measure the R-curve, the specimen was loaded to crack initiation at the point of the chevron (Point A in Fig. 6), and further loaded to some Point B where the crack had already grown a short distance. From Point B, the specimen was fatigue cracked at a load that produced a stress-intensity factor of no more than 0.6 K_{Iv} at the crack tip, according to normal ASTM E 399-83 fatigue precracking procedure. The crack advance distance during fatigue cracking was determined by the compliance method. Following the fatigue cracking, the load was increased (Point C to Point D in Fig. 6) until it again matched the normal steady-state load-displacement envelope. Using the compliance method, a number of K_R versus Δa points were determined for the data trace from Point C to Point D and beyond. The average maximum of the K_R versus Δa curve was taken as K_{Iv}, and the resulting R-curve data for two specimens in terms of K_R/K_{Iv} versus Δa are shown in Fig. 7. It can be seen that Δa_s for this material is a little over 2 mm.

One would expect that Δa_s values should tend to vary with the size of the plastic zone that is present at the tip of the steady-state crack, because all effects of the fatigue precracking on the crack tip configuration and stress intensity should be lost after the crack advances by a distance equal to a very few plastic zone radii [*17*]. The Irwin plane-strain plastic zone radius [*18*], given by

$$r_y = (^1/_6\pi)\ (K_{Iv}/\sigma_y)^2 \text{ (plane strain)} \tag{1}$$

for the 4340 steel of Fig. 7 is about 1 mm. It can be seen that the R-curve reaches the plateau value after a crack advance of about $2r_y$.

Very recently, Johnson and McDermott [*19*] have made plane-strain R-curve measurements on 6061-T6 aluminum using the same procedure as just described. Their results

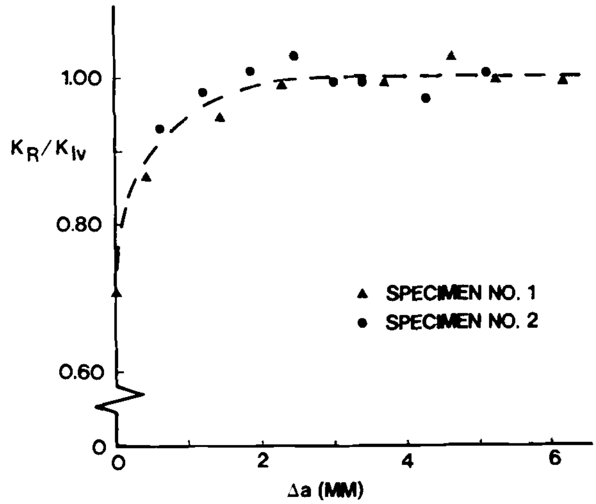

FIG. 7—*Plane-strain* R-*curve data for two 4340 steel specimens.*

indicate that the R-curve for this material approaches the plateau value at a crack advance distance of about $3r_y$ or less.

If plane-strain R-curve measurements were available on various other materials, it might be possible to make a generalized statement of the form

$$\Delta a_s \leqslant n r_y \tag{2}$$

where n is a number of the order of 3, for example. However, no other reasonably accurate plane-strain R-curve measurements of metals are known to the author. The literature does contain a number of R-curve measurements under conditions approaching plane stress. It is of interest to evaluate n for the case of plane stress, where the numerical constant in the Irwin r_y equation is three times as large

$$r_y = (1/2\pi)\,(K_c/\sigma_y)^2 \text{ (plane stress)} \tag{3}$$

From plane-stress data covering aluminum alloys [*20–23*], steels [*21,22,24*], and a titanium alloy [*25*], a good value of n appears to be 3. This is confirmed by Irwin and Paris [*16*], who noted that the plane-stress R-curve is generally within 5% of its plateau value after a crack growth of only about two plastic zone radii.

According to McCabe [*26*], plane-strain R-curves rise to the plateau value in a much shorter crack advance than their plane-stress counterparts. This would certainly be the case if n in Eq 2 is the same for both plane stress and plane strain, because the plastic zone size can be easily an order of magnitude smaller in plane strain than in plane stress.[2] Thus, McCabe's observation is consistent with a constant value of n between plane stress and plane strain.

To summarize, the plane-strain R-curve data on 4340 steel and 6061-T6 aluminum, the published plane-stress R-curve data on a number of materials, and McCabe's observation

[2]The plane-stress toughness, K_c, is larger than the plane-strain toughness, K_{Iv}, and the constant in the equation for the plane-stress r_y is $1/2\pi$, whereas it is $1/6\pi$ for plane-strain. Thus if K_c is twice as large as K_{Iv}, for example, the plane-stress r_y will be twelve times as large as the plane-strain r_y (see Eqs 1 and 3).

concerning the much smaller Δa_s in plane strain than in plane stress are all consistent with an upper limit of Δa_s of no more than about $3r_y$ in plane strain. Therefore, in crack stability calculations using chevron-notch test results, one might consider setting Δa_s equal to $3r_y$ if direct measures of Δa_s are not available.

For the sake of simplicity, the discussions here have glossed over some fine points, such as the distinction between physical crack length and effective crack length. Also, although it does not affect the analyses or conclusions of this paper, it should be mentioned that the crack extension, a, in a chevron-notched specimen is not constant along the crack front because of the triangular notch. Hopefully, this paper will stimulate further thinking and research that will refine the usage of ASTM E 1304-89 test results in crack stability calculations.

Conclusions

Although the introduction of three new symbols by ASTM E 1304-89 for plane-strain fracture toughness may at first seem unfortunate, the different symbols are necessary and beneficial in denoting the quality and the character of the different measurement procedures prescribed in the standard. Measurements of K_{IvM} are the simplest to make, but can contain hidden errors. Measurements of K_{Iv} should be done whenever careful, accurate determinations of plane-strain toughness are required. However, if a crack-jump behavior of the material prevents the usage of the K_{Iv} test procedure, the toughness can be well measured by the K_{Ivj} procedure.

In addition to using E 1304 toughness tests for quality control, material ranking, material screening, etc., it is suggested that chevron-notched specimen tests can be applied to any situation that would otherwise require measurements of E 399 K_{Ic} values, including engineering calculations of crack stability. However, in crack stability calculations, the assumed preexisting flaw size, a_0, should be enlarged by the crack advance distance, Δa_s, required for a fatigue precrack to evolve into the steady-state crack configuration. Various lines of evidence suggest that Δa_s is generally less than three times the crack-tip plastic zone radius, r_y. Plane-strain R-curve measurements on a number of different materials are recommended to further test and refine the relationship between Δa_s and r_y.

Acknowledgment

The author is very grateful to D. E. McCabe of Oak Ridge National Laboratory for consultations on R-curve phenomena, and to C. F. Johnson and S. M. McDermott of Terra Tek Systems for sharing their plane-strain R-curve data on 6061-T6 aluminum.

References

[1] ASTM Task Group E24.01.04, K. R. Brown, chairman, American Society for Testing and Materials, Philadelphia, 1989.

[2] Brown, K. R., "The Chevron Notched Fracture Toughness Test," *ASTM Standardization News*, Nov. 1988, pp. 66–69.

[3] Pook, L. P., "An Approach to a Quality Control K_{Ic} Testpiece," *International Journal of Fracture Mechanics*, Vol. 8, 1972, pp. 103–104.

[4] Barker, L. M., "A Simplified Method for Measuring Plane Strain Fracture Toughness," *Engineering Fracture Mechanics*, Vol. 9, 1977, pp. 361–369.

[5] Barker, L. M., "Evaluation of a Simple Method of Measuring Fracture Toughness in Both Brittle and Ductile Materials," *Proceedings*, ICM-II Conference, Boston, 1976, pp. 1547–1551.

[6] Barker, L. M., "Short Rod K_{Ic} Measurements of Al_2O_3," *Fracture Mechanics of Ceramics*, Vol. 3, R. C. Bradt, D. P. H. Hasselman, and F. F. Lange, Eds., Plenum Publishing Co., New York, 1978, pp. 483–494.

[7] Barker, L. M., "Residual Stress Effects on Fracture Toughness Measurements," *Advances in Fracture Research*, Vol. 5, D. Francois, Ed., ICF5, Cannes, France, 1981, pp. 2563–2570.
[8] Johnson, F. A. and Radon, J. C., "Molecular Kinetics and the Fracture of PMMA," *Engineering Fracture Mechanics*, Vol. 4, 1972, pp. 555–576.
[9] Brown, K. R., "The Use of the Chevron-Notched Short-Bar Specimen for Plane-Strain Toughness Determination in Aluminum Alloys," *Chevron-Notched Specimens: Testing and Stress Analysis, ASTM STP 855*, J. H. Underwood, S. W. Freiman, and F. I. Baratta, Eds., American Society for Testing and Materials, Philadelphia, 1984, pp. 237–254.
[10] Barker, L. M., "Specimen Size Effects in Short-Rod Fracture Toughness Measurements," *Chevron-Notched Specimens: Testing and Stress Analysis, ASTM STP 855*, J. H. Underwood, S. W. Freiman, and F. I. Baratta, Eds., American Society for Testing and Materials, Philadelphia, 1984, pp. 117–133.
[11] Rice, J. R., Drugan, W. J., and Sham, T-L., "Elastic-Plastic Analysis of Growing Cracks," *Fracture Mechanics (12th Conference), ASTM STP 700*, American Society for Testing and Materials, Philadelphia, 1980, pp. 189–221.
[12] Barker, L. M., "Chevron-Notched Specimens for Fracture Toughness Measurements Independent of *R*-Curve Effects," *Journal of Testing and Evaluation*, Vol. 17, No. 4, July 1989, pp. 218–223.
[13] Srawley, J. E. and Brown, W. F., "Fracture Toughness Testing," *Fracture Toughness Testing and Its Applications, ASTM STP 381*, American Society for Testing and Materials, Philadelphia, 1965, pp. 133–198.
[14] Krafft, J. M., Sullivan, A. M., and Boyle, R. W., "Effect of Dimensions on Fast Fracture Instability of Notched Sheets," *Proceedings*, Crack Propagation Symposium, College of Aeronautics, Cranfield, U.K., Vol. 1, 1961, pp. 8–26.
[15] McCabe, D. E. and Ernst, H. A., "A Perspective on *R*-Curves and Instability Theory," *Fracture Mechanics: Fourteenth Symposium, Volume I: Theory and Analysis, ASTM STP 791*, Lewis and Sines, Eds., American Society for Testing and Materials, Philadelphia, 1983, pp. I-561–I-584.
[16] Irwin, G. R. and Paris, P. C., "Elastic-Plastic Crack Tip Characterization in Relation to *R*-Curves," *Fracture 1977*, Vol. 1, ICF4, Waterloo, Canada, June 1977, pp. 93–100.
[17] Barker, L. M., "Theory for Determining K_{Ic} from Small, Non-LEFM Specimens, Supported by Experiments on Aluminum," *International Journal of Fracture*, Vol. 15, 1979, pp. 515–536.
[18] McClintock, F. A. and Irwin, G. R., "Plasticity Aspects of Fracture Mechanics," *Fracture Toughness Testing and Its Applications, ASTM STP 381*, American Society for Testing and Materials, Philadelphia, 1965, pp. 84–113.
[19] Johnson, C. F. and McDermott, S. M., Terra Tek Systems, private communication.
[20] Wang, D. Y. and McCabe, D. E., "Investigation of *R*-Curve Using Comparative Tests with Center-Cracked-Tension and Crack-Line-Wedge-Loaded Specimens," *Mechanics of Crack Growth, ASTM STP 590*, American Society for Testing and Materials, Philadelphia, 1976, pp. 169–193.
[21] Heyer, R. H. and McCabe, D. E., "Plane-Stress Fracture Toughness Testing Using a Crack-Line-Loaded Specimen," *Engineering Fracture Mechanics*, Vol. 4, 1972, pp. 393–412.
[22] Heyer, R. H. and McCabe, D. E., "Crack Growth Resistance in Plane-Stress Fracture Testing," *Engineering Fracture Mechanics*, Vol. 4, 1972, pp. 413–430.
[23] Pearson, H. S. and McCabe, D. E., "*R*-Curve Round-Robin Program for ASTM Recommended Practice for *R*-Curve Determination (E 561)," *Journal of Testing and Evaluation*, Vol. 14, 1986, pp. 191–199.
[24] Novak, S. R., "Resistance to Plane-Stress Fracture (*R*-Curve Behavior) of A572 Structural Steel," *Mechanics of Crack Growth, ASTM STP 590*, American Society for Testing and Materials, Philadelphia, 1976, pp. 235–242.
[25] Munz, D., Galda, K. H., and Link, F., "Effect of Specimen Size on Fracture Toughness of a Titanium Alloy," *Mechanics of Crack Growth, ASTM STP 590*, American Society for Testing and Materials, Philadelphia, 1976, pp. 219–234.
[26] McCabe, D. E., Oak Ridge National Laboratory, private communication.

Tulio N. Bittencourt,[1] Ahmabou Barry,[1] and Anthony R. Ingraffea[1]

Comparison of Mixed-Mode Stress-Intensity Factors Obtained Through Displacement Correlation, *J*-Integral Formulation, and Modified Crack-Closure Integral

REFERENCE: Bittencourt, T. N., Barry, A., and Ingraffea, A. R., "**Comparison of Mixed-Mode Stress-Intensity Factors Obtained Through Displacement Correlation, *J*-Integral Formulation, and Modified Crack-Closure Integral,**" *Fracture Mechanics: Twenty-Second Symposium (Volume II), ASTM STP 1131*, S. N. Atluri, J. C. Newman, Jr., I. S. Raju, and J. S. Epstein, Eds., American Society for Testing and Materials, Philadelphia, 1992, pp. 69–82.

ABSTRACT: This paper presents a comparison among stress-intensity factors for mixed-mode two-dimensional problems obtained through three different approaches: displacement correlation, *J*-integral, and modified crack-closure integral. All mentioned procedures involve only one analysis step and are incorporated in the post-processor page of a finite element computer code for fracture mechanics analysis (FRANC). Results are presented for a closed-form solution problem under mixed-mode conditions. The accuracy of these described methods then is discussed and analyzed in the framework of the their numerical results. The influence of the differences among the three methods on the predicted crack trajectory of general problems is also discussed.

KEY WORDS: stress-intensity factors, linear elastic fracture mechanics, displacement correlation, *J*-integral, modified crack closure, local mesh refinement, crack trajectory, history of stress-intensity factors, fracture mechanics, fatigue (materials)

The accurate numerical computation of stress-intensity factors is a key factor in the successful application of linear elastic fracture mechanics (LEFM) concepts. In the following sections, a brief introduction to three different approaches to stress-intensity factor (SIF) calculation is presented. The approaches are displacement correlation, *J*-integral, and modified crack-closure integral. These capabilities are incorporated into the program, FRANC [*1*], taking advantage of a sophisticated data structure organization and graphics visualization environment. Distinct values of stress-intensity factors obtained from each approach may be calculated easily and compared in an efficient and elegant way. Such a comparison provides a convenient quality-assurance check during the performance of crack growth simulations governed by LEFM.

Displacement Correlation Technique

The idea behind this procedure is to correlate obtained numerical solutions for displacements at specific locations with the analytic solutions that are expressed in terms of the

[1]Graduate students and professor of Structural Engineering, respectively, Department of Structural Engineering, School of Civil and Environmental Engineering and Program of Computer Graphics Fracture Group, Cornell University, Ithaca, NY 14850.

stress intensity factors. The type of element used to estimate the numerical values of the displacements is of particular interest. For quarter-point singular elements [2], the crack opening displacement (COD) profile at $x = r$ is given by

$$\mathrm{COD}(r) = (4u_{y,j-1} - u_{y,j-2})\sqrt{\frac{r}{L}} \tag{1}$$

Where $u_{y,j-1}$ and $u_{y,j-2}$ are the relative displacements in the X_2 direction at locations $j - 1$ and $j - 2$, and L is equal to Δa (Fig. 1).

The analytical expression for the COD at $x = r$, neglecting higher order terms, is the following

$$\mathrm{COD}(r) = K_{\mathrm{I}}\left(\frac{\kappa + 1}{G}\right)\sqrt{\frac{r}{2\pi}} \tag{2}$$

where κ is

$$\kappa = 3 - 4\nu \text{ inplane strain, and}$$

$$\kappa = \frac{3 - \nu}{1 + \nu} \text{ inplane stress}$$

and G is the shear modulus.

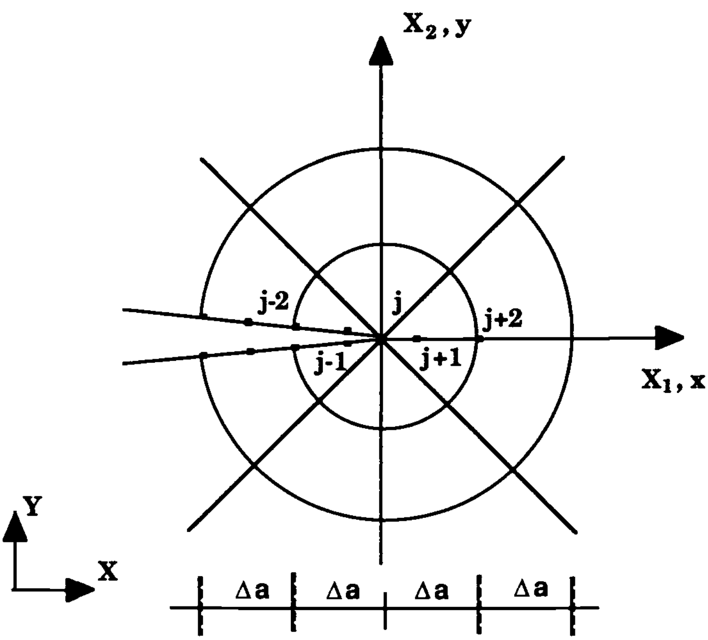

FIG. 1—*Crack-tip rosette of quarterpoint elements.*

By equating the numerical expression (Eq 1) to the analytical one (Eq 2), values of Mode I stress-intensity factor can be evaluated by

$$K_I = \left(\frac{G}{\kappa + 1}\right)\sqrt{\frac{2\pi}{L}}\,(4u_{y,j-1} - u_{y,j-2}) \tag{3}$$

Similarly for Mode II, the COD is replaced by the crack sliding displacement (CSD) and following the same steps just described

$$K_{II} = \left(\frac{G}{\kappa + 1}\right)\sqrt{\frac{2\pi}{L}}\,(4u_{x,j-1} - u_{x,j-2}) \tag{4}$$

Where $u_{x,j-1}$ and $u_{x,j-2}$ are the displacements in the X_1 direction at locations $j - 1$ and $j - 2$ (Fig. 1).

A more detailed discussion of the displacement correlation technique and types of singular elements can be found in Refs *2*, *3*, *4*, and *5*. The displacement correlation technique had been so far the only procedure available to compute stress-intensity factors in FRANC. This method has now been augmented with the two techniques described next.

J-Integral Formulation

As proposed by Rice [*6*], the components of the *J*-integral for two-dimensional problems are defined by the familiar expression

$$J_k = \lim_{\varepsilon \to 0} \int_{\Gamma\varepsilon} \left[W n_k - \sigma_{ij} \frac{\partial u_i}{\partial x_k} n_j \right] d\Gamma \tag{5}$$

where k varies from 1 to 2 and Γ_ε is a contour of a vanishing radius, ε, surrounding the crack tip. Usually, 1 and 2 correspond to the local crack-tip axes as displayed in Fig. 2.

The equivalent domain integral (EDI) representation [*7*] will be used here. The main advantage of this alternative is to replace the integration along the contour with another

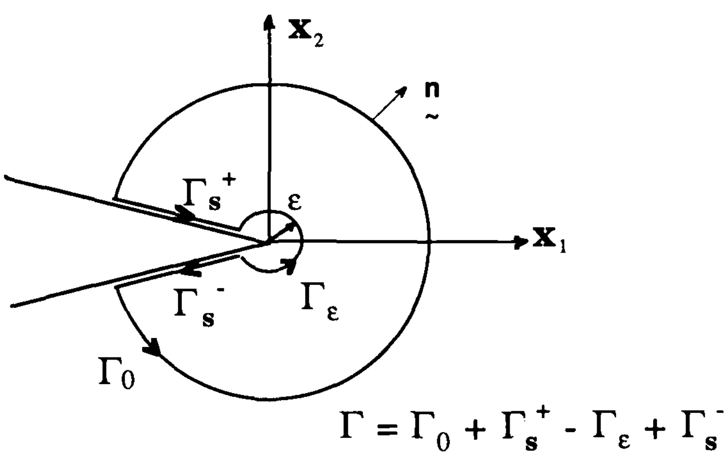

FIG. 2—*Crack-tip contours.*

over a finite size domain. This approach is very attractive in a finite element environment where routines to perform numerical integration over a domain of finite size are always available. The aim of the transformation of the integration domain is to express the integral over Γ_ε in terms of the closed contour, Γ. This objective is achieved when the integral over Γ_0 and Γ_s vanishes. A continuous function, $q(X_1,X_2)$, is employed to avoid the integrations along the mentioned contours. This function assumes unit value at the crack tip and zero along Γ_0 and Γ_s. The variation of $q(X_1,X_2)$ inside the domain is completely arbitrary. By introducing the weight function, q, the standard definition of the J-integral can be rewritten as

$$J_k = -\int_\Gamma \left[W\delta_{ij} - \sigma_{ij}\frac{\partial u_i}{\partial x_k}\right] qn_j d\Gamma \tag{6}$$

The preceding integral is performed along a closed contour and, therefore, can be written in terms of a domain integral by means of the divergence theorem. The final form of the J-integral in terms of the EDI representation is given by

$$J_k = -\int_A \left\{ W\frac{\partial q}{\partial x_k} - \sigma_{ij}\frac{\partial u_i}{\partial x_k}\frac{\partial q}{\partial x_j}\right\} dA - \int_A \left\{ \frac{\partial W}{\partial x_k} - \frac{\partial}{\partial x_j}\left[\sigma_{ij}\frac{\partial u_i}{\partial x_k}\right]\right\} qdA \tag{7}$$

It can be noticed that the second term of the preceding integral expression vanishes for elastic problems. Versions of Eqs 6 and 7 were first proposed by deLorenzi [*8*] and refined by Li et al. [*9*]. In the case of a homogeneous, isotropic, linear elastic material surrounding the crack tip, the relationship among the two components of the J-integral and the Modes I and II stress-intensity factors is established as [*10*]

$$J_1 = \frac{\kappa + 1}{8G}(K_I^2 + K_{II}^2) \tag{8}$$

$$J_2 = -\frac{2(\kappa + 1)}{8G} K_I K_{II} \tag{9}$$

The EDI J-integral was implemented in FRANC. An isoparametric displacement finite element formulation is used in this program. This makes the calculation of the gradients of displacements, strains, strain energy density, and the q function an easy task if the nodal values of these quantities are known. Of course, displacements are nodal values and the artificial weight function, q, may be provided by its nodal values. However, a problem arises when estimating the gradients of strains and of the strain energy density. An extrapolation from the Gauss point values to the nodal ones is employed to overcome this difficulty. This extrapolation may be performed by a least-square fit of the Gauss point values [*11*]. Once the nodal values of the mentioned quantities are obtained, the procedure to obtain their gradients at the Gauss points is straightforward, because the Jacobian of the isoparametric mapping has been computed already for the finite element analysis. After computing each term entering the integral expression (Eq 7), the final step is to perform a numerical integration using Gaussian quadrature (order 2 for the current implementation) over the elements belonging to the domain. It should be pointed up, however, that the second part of Eq 7 vanishes for elastic materials and that in this case the extrapolation has no effect on the values of the J components. Therefore, the second term in Eq (7) will be neglected in the calculations being presented later.

The user has complete control over the domain of integration, being able to change it interactively and reperform the calculations at his or her convenience. The internal values of the weight function, q, may be also controlled by the user. The default value for these values of q is one. Values of J_1 and J_2 per unit thickness with respect to the local crack-tip axes are provided. If the problem is linear elastic, Modes I and II stress-intensity factors are calculated from the J-integral components. It should be pointed up that the J-integral is commonly used to characterize the stress and strain fields around the crack for certain nonlinear material constitutive relationships. Obviously in these cases, values of stress-intensity factors have no meaning and, therefore, are not calculated.

Modified Crack-Closure Integral

The modified crack-closure integral method was first proposed by Rybicki and Kanninen [*12*]. By using this approach, it is possible to obtain the energy release rate values for Modes I and II, separately. The idea is to use Irwin's concept of crack-closure integral taking a virtual crack extension tending to zero in the limit and admitting that the displacement field ahead of the crack tip can be approximated by the one behind it. This simplification is very important because with only one analysis step the energy release rates can be estimated. Actually, in the computation of the crack-closure integral, two complete analyses are necessary: one to obtain the stress field ahead of the crack before propagation and another to compute the displacement field after a virtual crack extension is introduced. The crack-closure concept is very useful when dealing with cracks in heterogeneous materials. No assumption of isotropy or homogeneity around the crack is necessary. The energy release rate is estimated only in terms of the work done by the stresses (or equivalent nodal forces) over the displacements produced by the introduction of a virtual crack extension. As shown by Buchholz [*13*], the crack-closure concept may be applied in mixed-mode problems to estimate the direction of propagation. Buchholz et al. also have shown the applicability of the method for orthotropic materials and interface cracks [*14,15*].

The expressions for G_I (potential energy release rate in Mode I) and G_{II} (potential energy release rate in Mode II) may be obtained according to Irwin as

$$G_I = \lim_{\delta a \to 0} \frac{2}{\delta a} \int_{x=0}^{x=\delta a} \frac{1}{2} \sigma_{yy}(r = x, \phi = 0, a) u_y(r = \delta a - x, \phi = \pi, a + \delta a) dx \tag{10}$$

$$G_{II} = \lim_{\delta a \to 0} \frac{2}{\delta a} \int_{x=0}^{x=\delta a} \frac{1}{2} \sigma_{xy}(r = x, \phi = 0, a) u_x(r = \delta a - x, \phi = \pi, a + \delta a) dx \tag{11}$$

where σ_{xy} and σ_{yy} are shear and normal stresses ahead of the crack tip, and u_x and u_y are the displacements with respect to the local tip axes X_1 and X_2, respectively.

Self-similar virtual crack extension, δa, and the distribution of normal stress ahead of the crack tip is shown in Fig. 3.

Stress-intensity factors can be related to the values of the potential energy release rates through the following expressions in the case of plane strain and self-similar propagation

$$G_I = \frac{\kappa + 1}{8G} K_I^2 \tag{12}$$

$$G_{II} = \frac{\kappa + 1}{8G} K_{II}^2 \tag{13}$$

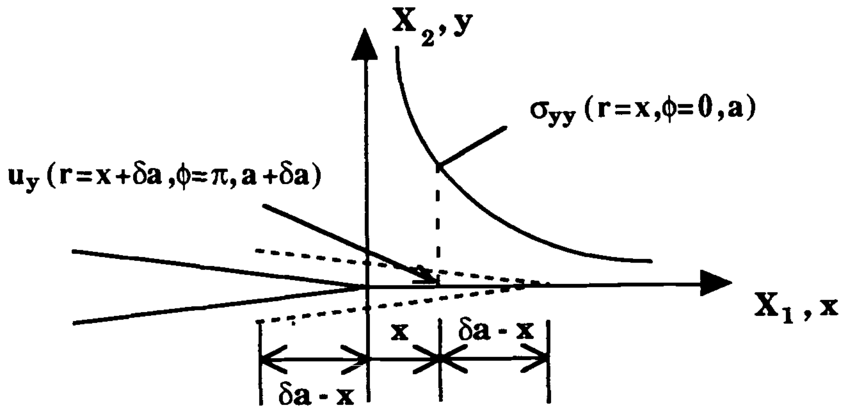

FIG. 3—*Analytical crack-closure integral method.*

In FRANC, a rosette of quarterpoint finite elements is placed around the crack tip (Fig. 1) to capture the singularity of the stress and strain fields. As shown by Ramamurthy et al. [16], the values of G_I and G_{II} through a modified crack-closure approach can be rewritten in terms of the equivalent nodal forces, F_y and F_x, and the relative nodal displacements, u_y and u_x (Fig. 1):

$$G_I = \left(\frac{1}{2\Delta a}\right)\begin{bmatrix} (C_{11}F_{y,j} + C_{12}F_{y,j+1} + C_{13}F_{y,j+2})u_{y,j-1} \\ +(C_{21}F_{y,j} + C_{22}F_{y,j+1} + C_{23}F_{y,j+2})u_{y,j-2} \end{bmatrix} \tag{14}$$

$$G_{II} = \left(\frac{1}{2\Delta a}\right)\begin{bmatrix} (C_{11}F_{x,j} + C_{12}F_{x,j+1} + C_{13}F_{x,j+2})u_{x,j-1} \\ +(C_{21}F_{x,j} + C_{22}F_{x,j+1} + C_{23}F_{x,j+2})u_{x,j-2} \end{bmatrix} \tag{15}$$

where

$$C_{11} = \frac{33\pi}{2} - 52 \qquad C_{12} = \frac{21\pi}{4} - 17 \qquad C_{13} = \frac{21\pi}{2} - 32$$

$$C_{21} = \frac{-33\pi}{8} + 14 \qquad C_{22} = \frac{21\pi}{16} - 3.5 \qquad C_{23} = \frac{-21\pi}{8} + 8$$

The results obtained by Ramamurthy et al. [16] for a Q8 quarterpoint element can be used for the T6 elements used in FRANC once the singularity, $1/\sqrt{r}$, is captured in both types of elements. The obtained formula should provide better results in the limit $\Delta a \to 0$, where Δa is the radius of the rosette of singular elements around the crack tip.

Examples

To compare the use of the presented techniques for stress-intensity factor computation, a closed-form example is performed. This example consists of a large plate with an inclined crack at its center (Fig. 4) for which stress-intensity factors are known in closed form (B is taken such that finite size effects can be neglected)

$$K_I = \sigma \sin^2\beta\sqrt{\pi a}$$

$$K_{II} = \sigma \sin\beta \cos\beta\sqrt{\pi a}$$

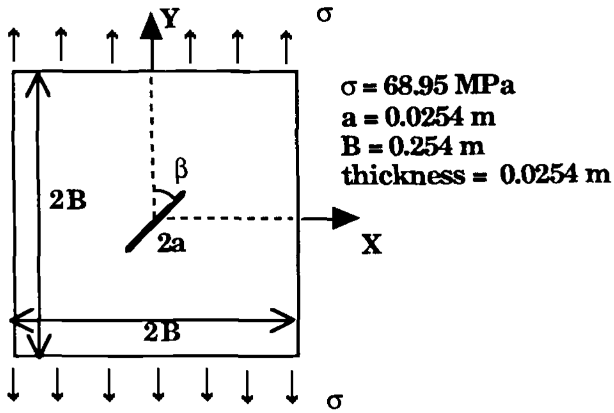

FIG. 4—*Example 1.*

By varying the angle β distinct levels of mixed-mode solutions are considered. For β = 90°, a pure Mode I problem is provided for example. Therefore, taking different values for β, it is possible not only to establish a comparison among the described techniques in terms of accuracy, but also to consider the effect of mixed-mode conditions on the numerical results.

Plane stress analyses are performed and results for β angles of 90, 60, 45, and 20° are presented (see Tables 1 through 4). Different levels of local mesh refinement around the crack tips are considered in order to verify convergence. Subdivisions of the initial rosette of singular elements with the ratio 0.5 are introduced in each mesh refinement step (Fig. 5). The basic noncracked model used is a 10 by 10 grid of Q8 finite elements. The cracks then are introduced using FRANC capabilities. The finite element meshes obtained for β = 90 and 60° are displayed in Figs. 6 and 7, respectively. For the remaining examples, the number of equations, nodal points, and elements are of the same order.

It can be observed that the results obtained through different methods are consistent, although distinct levels of accuracy are achieved depending on the mesh refinement introduced and on the amount of mixed-mode present. For pure Mode I, *J*-integral and modified crack-closure integral, both energy-based approaches, provided equivalent results in terms of accuracy versus mesh refinement. The values obtained with displacement correlation converged toward the theoretical ones, but much more slowly. The observed inaccuracies in Mode I stress-intensity factors through the displacement correlation technique are found to be consistent with the calculations by Banks-Sills and Bortman [*17*].

TABLE 1—*For β = 90° the theoretical values of the stress-intensity factors are:* K_I = *19.47 MPa* $\sqrt{m}$ *and* K_{II} = *0. MPa* $\sqrt{m}$.

Mesh Refinement	Displacement Correlation		*J*-Integral		Modified Crack Closure	
	K_I	K_{II}	K_I	K_{II}	K_I	K_{II}
1	21.54	−0.01	20.93[a]	−0.00[a]	19.27	−0.02
2	20.63	−0.00	19.68	−0.00	19.44	−0.03
3	20.11	−0.00	19.61	−0.00	19.51	−0.02
4	19.86	−0.00	19.58	−0.00	19.52	−0.02
5	19.74	−0.00	19.54	−0.00	19.52	−0.02

[a]Only singular elements in the integration domain.

TABLE 2—*For β = 60°, the theoretical values of the stress-intensity factors are:* K_I = *14.60 MPa* $\sqrt{m}$ *and* K_{II} = *8.43 MPa* $\sqrt{m}$.

Mesh Refinement	Displacement Correlation		J-Integral		Modified Crack Closure	
	K_I	K_{II}	K_I	K_{II}	K_I	K_{II}
1	16.08	8.77	16.45[a]	7.00[a]	14.51	8.28
2	15.41	8.40	15.29	6.81	14.64	8.45
3	15.01	8.21	15.15	6.98	14.67	8.46
4	14.84	8.10	15.04	7.10	14.67	8.46
5	14.74	8.03	14.99	7.15	14.67	8.45

[a]Only singular elements in the integration domain.

TABLE 3—*For β = 45°, the theoretical values of the stress-intensity factors are:* K_I = *9.74 MPa* $\sqrt{m}$ *and* K_{II} = *9.74 MPa* $\sqrt{m}$.

Mesh Refinement	Displacement Correlation		J-Integral		Modified Crack Closure	
	K_I	K_{II}	K_I	K_{II}	K_I	K_{II}
1	10.79	10.11	12.07[a]	8.00[a]	9.73	9.59
2	10.31	9.70	11.11	7.71	9.83	9.76
3	10.05	9.48	10.99	7.77	9.86	9.76
4	9.93	9.35	10.90	7.81	9.86	9.75
5	9.88	9.27	10.85	7.86	9.86	9.71

[a]Only singular elements in the integration domain.

TABLE 4—*For β = 20°, the theoretical values of the stress-intensity factors are:* K_I = *2.27 MPa* $\sqrt{m}$ *and* K_{II} = *6.26 MPa* $\sqrt{m}$.

Mesh Refinement	Displacement Correlation		J-Integral		Modified Crack Closure	
	K_I	K_{II}	K_I	K_{II}	K_I	K_{II}
1	2.49	6.52	3.97[a]	5.93[a]	2.31	6.29
2	2.41	6.24	4.34	4.69	2.33	6.29
3	2.34	6.10	3.32	5.42	2.33	6.33
4	2.32	6.01	2.91	5.62	2.33	6.31
5	2.31	5.97	2.67	5.71	2.33	6.29

[a]Only singular elements in the integration domain.

It was observed for this example that the *J*-integral approach loses accuracy for mixed-mode problems compared to the other two methods. This effect is more pronounced, the larger the relative value of Mode II stress-intensity factor is with respect to Mode I. It may be explained by the fact that in the *J*-integral derivation self-similar crack extension is assumed. The separation of the symmetrical and antisymmetrical fields as proposed by Bui [*18*] should improve the results. This approach has been applied by Atluri et al. [*19,20*] with highly accurate results for mixed-mode problems. In addition Eischen [*21*], and Kienzler and Kordisch [*22*] suggested improved methods for obtaining *J*-integrals for mixed-mode problems. These modifications and decomposition techniques permit the use of the *J*-integral and EDI approaches for a wide range of linear and nonlinear deformation crack problems. Another important feature that may be observed for the *J*-integral values is that, although

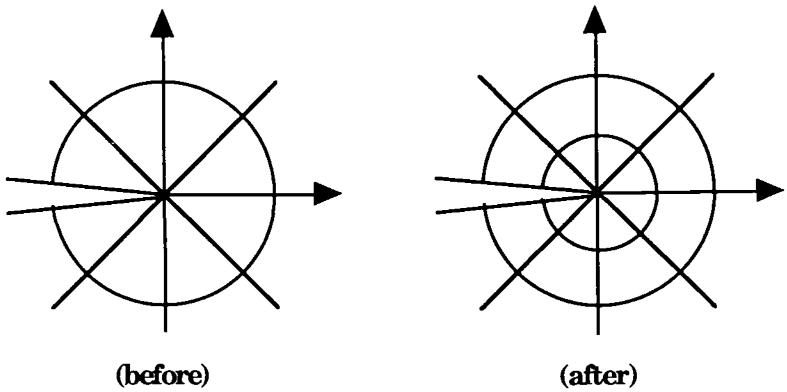

FIG. 5—*Local mesh refinement.*

not as accurate, they seem to indicate bounds to the theoretical values. When the mesh is refined, the new calculated values indicate the direction of convergence for both Modes I and II stress-intensity factors. It should be pointed up that this kind of behavior is not observed for Mode II values calculated through the displacement correlation technique. Actually, for all the β angles (different from 90°), the displacement correlation Mode II values started slowly diverging from the expected value when a local mesh refinement was introduced. Concerning the domain of integration for *J*-integral, it may be concluded that if only singular elements are used, the accuracy is compromised.

The modified crack-closure integral showed very good performance for all the applied mixed-mode conditions. Very accurate results were obtained for coarse meshes in all tested cases. Results oscillated around the theoretical values, however, without losing much ac-

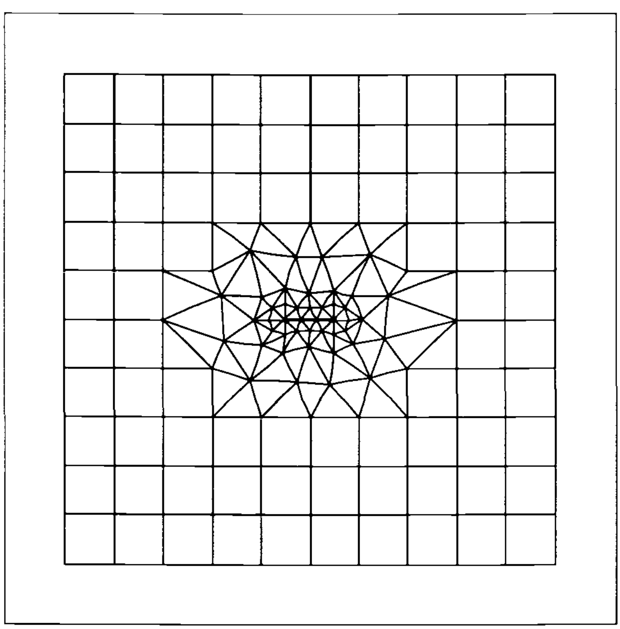

FIG. 6—*Finite element mesh (β = 90°) (992 equations, 498 nodes, and 186 elements).*

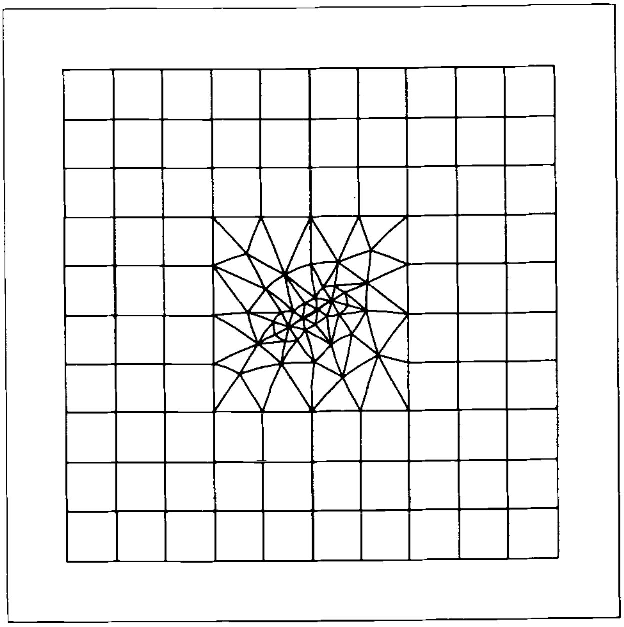

FIG. 7—*Finite element mesh (β = 60°) (944 equations, 474 nodes, and 172 elements)*

curacy when local mesh refinement was introduced. Theoretically, the more refined the local mesh ($\Delta a \rightarrow 0$), the more accurate the results should be.

As a second example of application of the methods described, the trajectories of crack extension are calculated for the structure in Fig. 8. The finite element mesh used is presented in Fig. 9. An initial crack is assumed. The evolution of the crack may be traced conveniently taking advantage of the underlying topology-based data structure in FRANC [23]. The propagation is performed in a stepwise way, driven by LEFM concepts. The crack increment at each step is the only arbitrary variable employed.

The direction of each crack increment and stability are determined using the maximum circumferential tensile stress criterion, σ_θ. This criterion takes into account the stress-intensity factors for the current state. Therefore, different approaches for stress-intensity

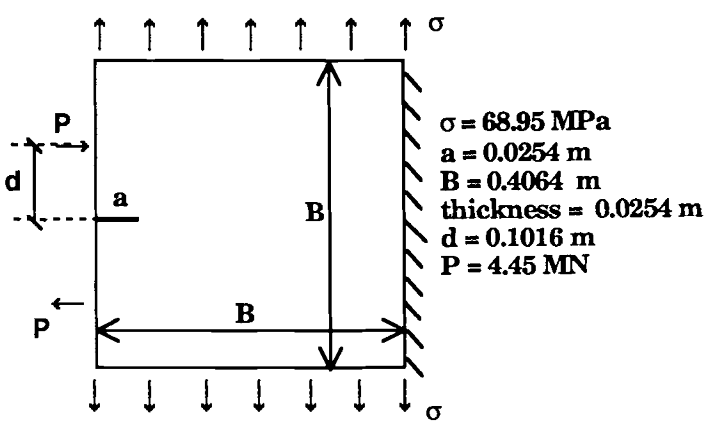

FIG. 8—*Edge-crack problem.*

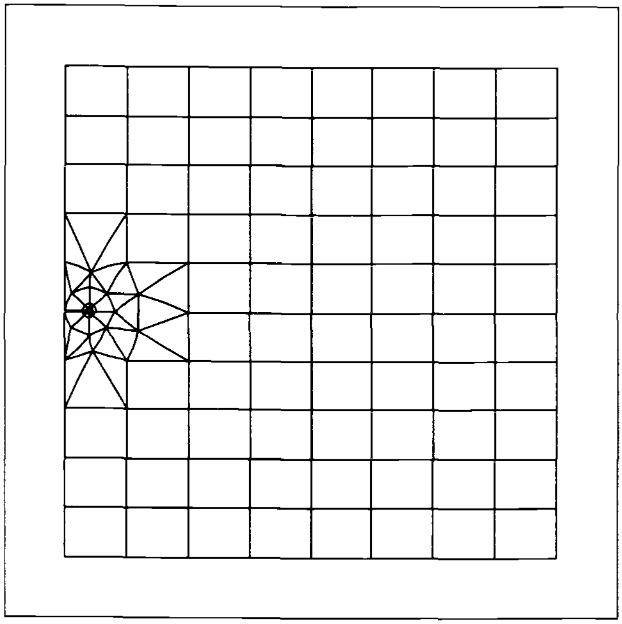

FIG. 9—*Edge-crack finite element model (720 equations, 381 nodes, and 124 elements).*

factor computation should not necessarily provide the same results in terms of trajectory. The crack increment at any step of propagation is kept constant. The same increment value, 0.0508 m, is used with each of the SIF methods under investigation. The trajectories obtained are shown in Fig. 10. The histories of Modes I and II stress-intensity factors with respect to the crack length are presented in Figs. 11 and 12, respectively. The results in both plots are presented in MPa $\sqrt{m}$ values.

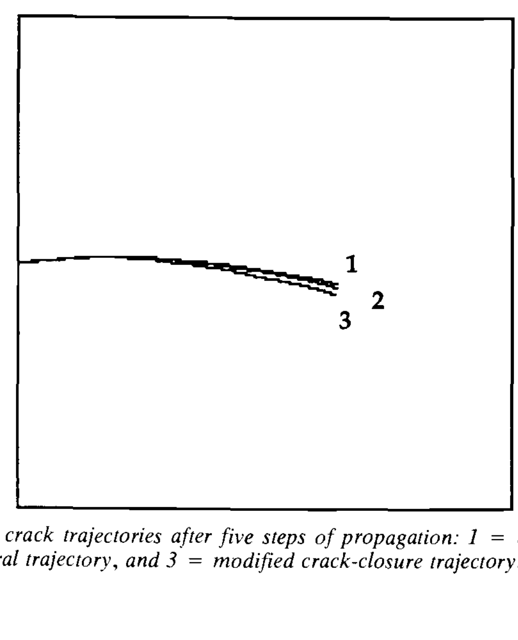

FIG. 10—*Predicted crack trajectories after five steps of propagation: 1 = displacement correlation trajectory, 2 = J-integral trajectory, and 3 = modified crack-closure trajectory.*

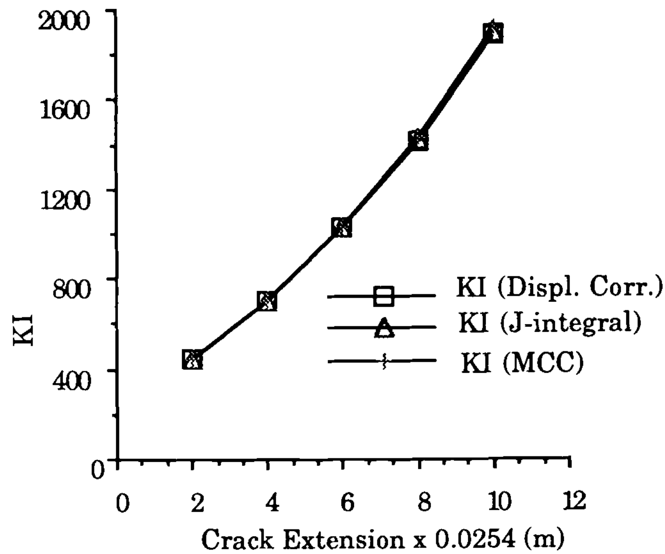

FIG. 11—*History of Mode I SIF.*

As can be seen from Fig. 10, the trajectories obtained are very close. The trajectories in this case are more sensitive to the crack increment chosen than to the SIF method used. This is a reasonable result since the direction of propagation provided by the σ_θ maximum theory depends on the ratio, K_I/K_{II}. From the histories of stress-intensity factors, it can be noticed that while Mode I values are almost the same, Mode II stress-intensity factors do not agree as well. Although distinct, these values are small compared to those for Mode I. Therefore, no substantial difference is noticed in the predicted crack paths in this example. However, considerably different crack trajectories are expected to be obtained if large differences in Mode II stress-intensity factors are computed from the three methods.

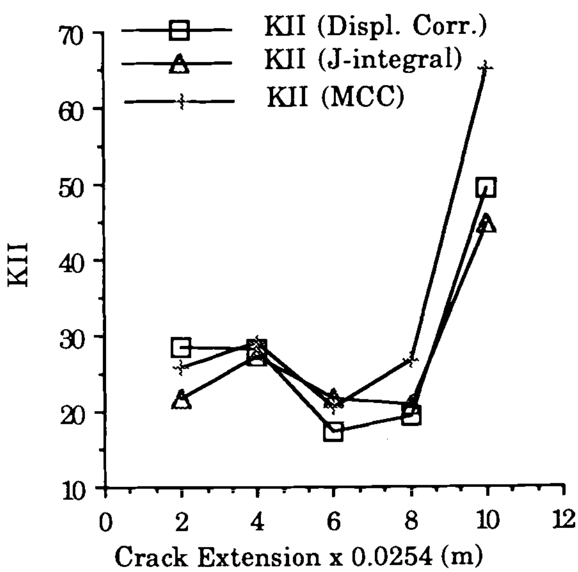

FIG. 12—*History of Mode II SIF.*

Conclusions

Three distinct approaches for stress-intensity factor computations have been compared: displacement correlation technique, J-integral, and modified crack-closure integral. Numerical results for different levels of mixed-mode conditions showed some interesting aspects of the numerical behavior of the described computational tools in terms of local mesh refinement.

The displacement correlation technique showed good convergence for Mode I stress-intensity factors (errors from 10 to 2%). However, for Mode II values, the technique presented a slight divergence from the theoretical result.

For the J-integral technique (EDI), poor accuracy was observed when only the quarter-point singular elements were considered in the domain of integration. Computed Mode II values were not accurate for all the investigated mixed-mode conditions, although a slow convergence was observed. The inaccuracy was more pronounced when Mode II became large relative to the Mode I value.

The modified crack-closure integral technique provided accurate results for all levels of local mesh refinement. The errors verified were within 3% for all the studied cases. Mode I stress-intensity factors converged quickly to an asymptotic result, while Mode II values showed a small oscillation around the analytical solution.

The observations presented so far were restricted to the analysis of the numerical results only. Although distinct levels of accuracy were obtained, the different approaches provided consistent results.

Some insight on the effects of the differences among the three SIF methods on the evolution of a initial crack is also provided. For the example presented, the crack trajectory is more sensitive to the crack increment than to the method used for computing stress intensity factors. The histories of the stress-intensity factors in terms of crack length may be stored along the evolution process. This is necessary information for a fatigue analysis, for example. The influence of the differences among the presented methods on the predicted fatigue life of a structure will be investigated in the future.

Acknowledgments

The authors would like to acknowledge the Cornell Program of Computer Graphics for continued support. The assistance and guidance provided by Wash Wawrzynek and Jose Luiz Sousa is deeply appreciated. This work was partially funded by CNPq (Brazilian Agency) and by the Digital Equipment and Grumman Aerospace Corporations.

References

[1] Wawrzynek, P. A. and Ingraffea, A. R., "An Edge-Based Data Structure for Two-dimensional Finite Element Analysis," *Engineering with Computers*, Vol. 3, 1987, pp. 13–20.

[2] Shih, C. F., de Lorenzi, H. G., and German, M. D., "Crack Extension Modelling with Singular Quadratic Isoparametric Elements," *International Journal of Fracture*, Vol. 12, 1976, pp. 647–651.

[3] Barsoum, R. S., "On the Use of Isoparametric Elements in Linear Fracture Mechanics," *International Journal of Numerical Methods in Engineering*, Vol. 10, 1976, pp. 25–37.

[4] Tracey, D. M., Discussion of "On the Use of Isoparametric Finite Elements in Linear Fracture Mechanics," by R. S. Barsoum, *International Journal of Numerical Methods in Engineering*, Vol. 11, 1977, pp. 401–402.

[5] Ingraffea, A. R. and Manu, C., "Stress Intensity Factor Computation in Three Dimensions with Quarter-Point Elements," *International Journal of Numerical Methods in Engineering*, Vol. 15, 1980, pp. 1427–1445.

[6] Rice, J. R. and Rosengren, G. F., "Plane-Strain Deformation Near a Crack for a Power-Law Hardening Material," *Journal of the Mechanics and Physics of Solids*, Vol. 16, 1968, pp. 1–12.
[7] Dodds, R. H., Jr., and Vargas, P. M., "Numerical Evaluation of Domain and Contour Integrals for Nonlinear Fracture Mechanics: Formulation and Implementation Aspects," University of Illinois at Urbana-Champaign, Department of Civil Engineering, 1988.
[8] deLorenzi, H. G., "3-D Elastic-Plastic Fracture Mechanics with ADINA," *International Journal of Computers and Structures*, Vol. 13, 1981, pp. 613–621.
[9] Li, F. Z., Shih, C. F., and Needleman, A., "A Comparison of Methods for Calculating Energy Release Rates," *Engineering Fracture Mechanics*, Vol. 21, 1985, pp. 405–421.
[10] Hellen, T. K. and Blackburn, W. S., "Nonlinear Fracture Mechanics and Finite Elements," *Engineering with Computers*, Vol. 4, 1987, pp. 2–14.
[11] Hinton, E. and Campbell, J. S., "Local and Global Smoothing of Discontinuous Finite Element Functions using Least Squares Method," *International Journal of Numerical Methods in Engineering*, Vol. 8, 1974, pp. 461–480.
[12] Rybicki, E. F. and Kanninen, M. F., "A Finite Element Calculation of Stress Intensity Factors by a Modified Crack Closure Integral," *Engineering Fracture Mechanics*, Vol. 9, 1977, pp. 931–938.
[13] Buchholz, F. G., "Finite Element Analysis of Crack-Propagation under Mixed-Mode Loading Conditions," *Proceedings, International Conference on Applied Mechanics*, Beijing, China, 1989.
[14] Buchholz, F. G., Kumosa, M., and Burger, M., "Finite Element Analysis of Mixed-Mode Fracture of Orthotropic Iosipescu-Specimens," *Conference Proceedings*, Reutlinger Arbeitstagung Finite Elemente in der Praxis, Federal Republic of Germany, 1989.
[15] Buchholz, F. G., Schulte-Frankenfeld, N., and Meiners, B., "Fracture Analysis of Mixed-Mode Failure Processes in a 3D-Fibre/Matrix Composite Cylinder," *Proceedings*, Sixth International Conference on Composite Materials, London, UK, 1987.
[16] Ramamurthy, T. S., Krishmamurthy, T., Badari Narayana, K., Vijayakumar, K., and Dataguru, B., "Modified Crack Closure Integral Method with Quarter Point Elements," *Mechanics Research Communications*, Vol. 13, No. 4, 1986.
[17] Banks-Sills, L. and Bortman, Y., "Reappraisal of the Quarter-Point Quadrilateral Element in Linear Elastic Fracture Mechanics," *International Journal of Fracture*, Vol. 25, 1984, pp. 169–180.
[18] Bui, H. D., "Associated Path Independent J-integrals for Separating Mixed Modes," *Journal of the Mechanics and Physics of Solids*, Vol. 31, No. 6, 1983, pp. 439–448.
[19] Chen, K. L. and Atluri, N., "Comparison of Different Methods of Evaluation of Weight Functions for 2D Mixed-Mode Fracture Analysis," *Engineering Fracture Mechanics*, Vol. 34, No. 4, 1989, pp. 935–956.
[20] Nikishkov, G. P. and Atluri, N., "Calculation of Fracture Mechanics Parameters for an Arbitrary Three-dimensional Crack, by the 'Equivalent Domain Integral' Method," *International Journal of Numerical Methods in Engineering*, Vol. 24, 1987, pp. 1801–1821.
[21] Eischen, J. W., "An Improved Method for Computing the J_2 Integral," *Engineering Fracture Mechanics*, Vol. 26, No. 5, 1987, pp. 691–700.
[22] Kienzler, R. and Kordisch, H., "Calculation of J_1 and J_2 Using the L and M Integrals," *International Journal of Fracture*, Vol. 43, 1990, pp. 213–225.
[23] Bittencourt, T. N., Wawrzynek, P. A., and Ingraffea, A. R., "Simplified Modeling of Failure in Unidirectional Composites," *Proceedings*, Fifth International Conference on Numerical Methods in Fracture Mechanics, Freiburg, Federal Republic of Germany, 1990.

Shah N. Malik[1]

Application of the Weight-Functions Method to Three-Dimensional Cracks Under General Stress Gradients

REFERENCE: Malik, S. N., "**Application of the Weight-Functions Method to Three-Dimensional Cracks Under General Stress Gradients,**" *Fracture Mechanics: Twenty-Second Symposium (Volume II), ASTM STP 1131*, S. N. Atluri, J. C. Newman, Jr., I. S. Raju, and J. S. Epstein, Eds., American Society for Testing and Materials, Philadelphia, 1992, pp. 83–112.

ABSTRACT: Recent advances in the weight-functions method have led to its application in determining stress-intensity factors (K) for corner and surface cracks. A major obstacle in accurately computing weight functions is that it not only requires the crack surface opening displacement (CSOD) fields, but also their rate of change with respect to the crack dimensions. In the present work, an approach similar to the two-dimensional Petroski and Achenbach method is developed and applied to determine the CSOD profiles as a function of three-dimensional crack dimensions. Near-crack-tip details as well as crack-mouth opening displacement (CMOD) were considered along with the Newman and Raju K-solutions for finite geometry three-dimensional problems of elliptical corner, surface, and subsurface (embedded) cracks. The weight functions determined from a uniform stress loading were then applied to compute K solutions for general stress gradients. Comparison of the obtained results with the Newman and Raju bending stress K solutions have shown excellent agreements even for quite deep corner and surface flaws. Corner cracks at circular holes were also used to verify the method.

KEY WORDS: weight functions, stress-intensity factors, elliptical corner, surface and subsurface cracks, general stress gradients, crack surface, crack mouth opening displacement fields, fracture mechanics, fatigue (materials)

Recent advances in the weight-functions method have led to its application in determining stress-intensity factors (K) for three-dimensional bodies containing planar cracks. The weight-functions method utilizes a known K solution distribution for a "reference" load, on a body with a given type of crack, to compute K values for any general loads acting on the same body. A major obstacle encountered in accurate computation of weight functions is the fact that the method requires not only the crack-surface opening displacement (CSOD) field, but also its rate of change (partial derivatives) with respect to the crack dimensions. Three-dimensional crack problems will consume excessive computational resources if one were to use either a finite element (FE) or a boundary integral equation (BIE) method to determine CSOD fields and their partial derivatives for each and every problem.

As an alternative approach, several methods have been applied recently with reasonable success for obtaining accurate estimates of the CSOD fields from known K solutions for any reference loading in two-dimensional through-the-thickness crack problems. A few

[1]Formerly: engineer, Life Methods Development, General Electric Company, Aircraft Engines, Cincinnati, OH 45215-6301. Presently: senior materials engineer, U.S. Nuclear Regulatory Commission, Washington, DC 20555

attempts have been reported, with limited success, for extending the two-dimensional approaches to three-dimensional crack problems. In the present work, a unique and a self-consistent method is developed to obtain CSOD fields accurately for three-dimensional crack problems, and applied to compute K solutions for any general stress gradients.

Background Review

A novel two-dimensional method developed by Petroski and Achenbach [*1*] has been found to be very accurate for determining crack-surface displacement fields in "edge crack" type problems. It utilizes a self-consistency condition for reference load K solutions and the elastic near-tip crack opening displacement behavior to obtain the entire CSOD field. Generalization of the Petroski-Achenbach (PA) method to three-dimensional semielliptical surface cracks in plates was done by Mattheck et al. [*2*]. They assumed the CSOD field for a semielliptical flaw to be similar to a set of two-dimensional edge cracks stacked, parallel to the minor axis of ellipse, along the curved crack-front; and to behave like a Griffith (center) crack at the free surface where mouths of all the edge cracks terminate.

Several applications of the equivalent two-dimensional "edge cracks set" approach to semielliptical surface flaws in pipes [*3*], flat plates [*4*], and to quarterelliptical corner cracks at circular holes in plates [*5,6*] have been reported with some success. There were a number of simplifying assumptions made in estimating the CSOD fields. For example, a drawback in Refs *5* and *6* is the use of the surface flaw type CSOD field to corner crack applications that will give considerable inaccuracies for larger cracks. Likewise, the reference K used to obtain CSOD fields for surface cracks in Refs *2* to *4* were not very accurate.

The K solution in any three-dimensional crack problem varies continuously along the crack front, and as such represents infinite degrees of freedom (DOF) for the local K values. Computational costs would be very prohibitive if the local K values were to be determined and used for predicting the growth of the crack front in three dimensional bodies. A simplifying general trend in the literature has been to assume that an initially elliptical-shaped crack will remain elliptical after any growth. It is then possible to define two "effective" K values [*7–9*], one along each of the major and minor axes of an elliptical flaw. The K values for these two independent DOF are shown [*8,9*] to represent strain-energy release rate obtained by creation of corresponding crack surface area, when one of the crack dimensions (major or minor axes) is kept fixed and the other is increased, while maintaining the crack front to be elliptical. The concept of the two DOF "effective" K values has been shown to have good correlation with experimental crack lengths and depths data [*10–13*] for a range of materials and loading conditions.

Another generalization of the Petroski-Achenbach (PA) method [*1*] was attempted recently [*14*] wherein the local K values were computed. However, a corner elliptical crack displacement field was used for both the surface and corner cracks. An additional assumption that the aspect-ratio, of the major to minor axes lengths, of the crack remains constant during growth was used to obtain the three-dimensional CSOD field. The resulting K solutions compared well with available results [*15*] only for very small surface cracks. This is expected since the larger surface cracks do not behave like corner cracks, and the elliptical aspect-ratios may remain constant [*11–13*] only during the initial part of crack propagation life. Also, the formulation for the surface crack in Ref *14* is applicable only to symmetric loadings, about the elliptical axes, resulting in equal growth of the two crack-tips at the free surface.

In other studies [*16,17*], a CSOD field was proposed but with a limitation of constant aspect-ratio crack growths. Results were obtained for embedded elliptical crack in an infinite body and for surface cracks in a semiinfinite body. Since any "finite width" correction factors, such as the ones considered in Refs *2,5,6,14–15*], were not used in developing the K solutions, the usefulness of the method for more practical applications in finite geometry specimens is yet to be evaluated.

Other recently developed methods of computing K solutions for three-dimensional cracks include the finite element alternating method (FEAM) [*18*], the line spring model (LSM) [*19*], the traction BIE [*20*] method, and the slice synthesis technique [*21*]. These methods are more suitable for generating the reference K solutions to a given crack geometry rather than to be used in a crack growth life prediction code. Weight-functions approaches that deal with the PA-type method to three-dimensional problems appear to be more cost effective in codes for predicting crack growth life.

Present Approach

From the review of the literature, it is clear that the methods for estimating CSOD fields in three-dimensional geometries are still not quite well established for weight-functions applications. One of the main objectives of the present work is to develop a systematic and self-consistent method of constructing CSOD fields from known reference K solutions for 3-dimensional elliptical crack geometries of major interest. The degree of accuracy of the computed CSOD fields is very strongly dependent on the degree of accuracy of the reference loading K solutions used in obtaining them. Towards this end, Newman and Raju [*15,22*] have presented a number of K solutions in the form of analytical expressions that are based on their finite element computations for uniform tension and bending loads on elliptical (quarter, semi, and full) cracks in various specimen geometries. These K solutions are accepted widely for their accuracy and have been found to correlate well with numerous experimental data [*12,13,23,24*] on crack growth residual lives, and with other computational results [*25,26*].

In the present work, the Newman and Raju K solutions [*15,22*] have been used to compute the reference CSOD fields in finite geometry fracture specimens under load-controlled loadings (far-field uniform tensile stresses). The elliptical crack geometries considered are the corner cracks in plates and at circular holes and surface and embedded (subsurface) cracks in plates of finite dimensions. To model the K variation along the crack front, the approach of two DOF "effective" K [*7–9*] values along the major and minor axes of the elliptical flaw was utilized. The second major objective of the present work was to determine K solutions for any general stress distribution acting on elliptical cracks of interest. For any subsurface or surface cracks, the loading could be nonsymmetrical about the axes of ellipse that may give rise to different K values at the two opposite crack-front locations along major or minor axes or both; and thereby leading to unequal growths at those opposite locations. The computed K solutions were then compared with results available for specific stress gradients published in the literature.

Crack-Surface Opening Displacement Field

The two-dimensional method [*1*] is more suited for estimating CSOD fields in edge crack type problems. For other two-dimensional crack geometries, such as center-cracked plates (CCP), a general method [*27,28*] has been proposed wherein the "total" crack opening displacement (COD) field is a multiplication of two terms. The first term represents a maximum crack-mouth opening displacement (CMOD) that is a function of crack size and applied loads. The second term is an assumed CSOD profile, and is dependent on the type of crack. That is, whether a center, or, edge type of crack geometry exists in the two-dimensional specimen. In essence the first term controls the amplitude of the maximum crack opening, and the second term describes the shape of opened crack. In the present work, this concept of COD estimation is extended to three-dimensional crack problems. In this regard the findings of Green and Snedden [29], that a uniform tension applied normal to an elliptical crack in an infinite elastic body creates an ellipsoidal crack opening shape, was utilized in constructing the second term in the COD fields.

For an elliptical crack geometry shown in Fig. 1, the total COD field for a "reference" Mode I loading on a three-dimensional finite geometry specimen is represented as

$$U_{ref}(a,c,x,y) \simeq [U_0(a,c) \cdot U_*(x/c,\ y/a)] \tag{1}$$

where $U_0(a,c)$ is the CMOD value at the origin, $x = y = 0$, of the elliptical crack and $U_*(x/c,\ y/a)$ is the assumed CSOD profile for an embedded, corner, or surface crack. The a is crack depth along the minor axis parallel to the y coordinate, and c is the crack length along the major axis parallel to the x coordinate in Fig. 1.

Green and Sneddon [29] have developed an exact solution for the CSOD profile of an embedded elliptical crack subjected to a uniform tensile stress in an infinite body. This CSOD profile in a finite geometry specimen is given as

$$U_*(x/c,\ y/a) \simeq \sqrt{[1 - (x/c)^2 - (y/a)^2]} \tag{2}$$

where $-c \leq x \leq c$ and $-a \leq y \leq a$.

In Eq 2, the U_* field represents two-dimensional center crack type behavior along the x and y axes that coincide with major and minor axes of the elliptical crack, respectively. It also satisfies the boundary condition of zero U_{ref} displacement along the elliptical crack front.

For a quarterelliptical corner crack, the U_* field should be such that it satisfies the two-dimensional edge crack behavior along x and y axes in Fig. 1. As such, the U_* field for a

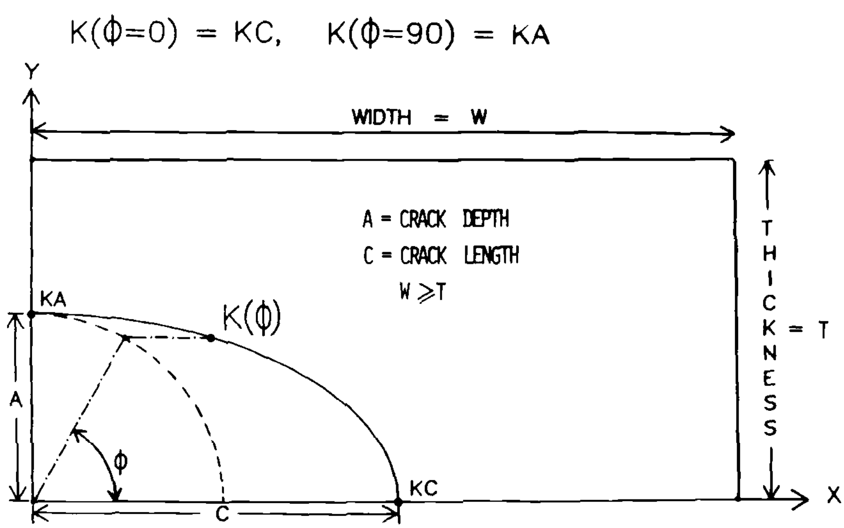

FIG. 1—*Quarterelliptical corner crack geometry in a plate specimen.*

corner crack could be represented as

$$U_*(x/c, y/a) \simeq \sqrt{[1 - \sqrt{\{(x/c)^2 + (y/a)^2\}}]} \tag{3}$$

where $x \leq c$ and $y \leq a$.

A representation similar to Eq 3 was used by Banks-Sills [*14*] for corner as well as surface cracks. It could be seen, however, that for surface cracks Eq 3 does not yield a two-dimensional center crack type response along the free surface (that is, at $y = a$ and $x = c$).

For semielliptical surface cracks, it is proposed that the U_* field should be such that it represents an edge crack type response along the crack depth directional axis, normal to the free surface, and behaves like a center crack along the free surface. The U_* field for a surface crack in Fig. 1 could be given as

$$U_*(x/c, y/a) \simeq \sqrt{[1 - (x/c)^2 - (y/a) \cdot \sqrt{\{1 - (x/c)^2\}}]} \tag{4}$$

with $-c \leq x \leq c$ and $y \leq a$.

To compute the CMOD field, $U_0(a,c)$ in Eq 1, the three-dimensional K solution for a reference load on a given specimen geometry is needed. As discussed earlier, the two DOF "effective" K approaches are selected to represent the three-dimensional reference K solution. Using Fig. 2, the "effective" reference K solutions, K_{ra} and K_{rc}, due to incremental (shaded) crack area growths dS_a and dS_c, respectively, for a quarterelliptical crack are given as

$$\begin{aligned}(K_{ra})^2 &= (1/dS_a) \cdot \int_{dS_a} [\{K_r(\phi)\}^2 \cdot d(\Delta S_a)] \\ &= \left(\frac{4}{\pi}\right) \int_{\phi=0}^{\pi/2} [K_r(\phi) \cdot \sin(\phi)]^2 \cdot d\phi\end{aligned} \tag{5}$$

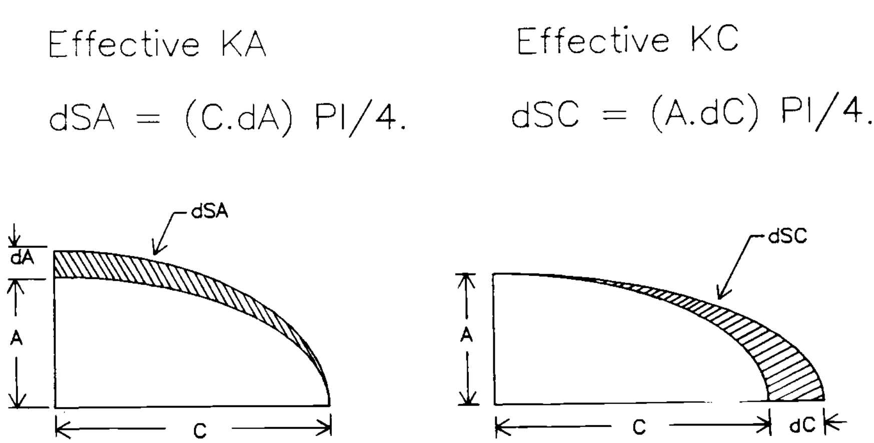

FIG. 2—*Two degrees of freedom model with effective KA and KC stress-intensity factors for a quarterelliptical corner crack.*

and

$$(K_{rc})^2 = (1/dS_c) \cdot \int_{dS_c} [\{K_r(\phi)\}^2 \cdot d(\Delta S_c)]$$

$$= \left(\frac{4}{\pi}\right) \int_{\phi=0}^{\pi/2} [K_r(\phi) \cdot \cos(\phi)]^2 \cdot d\phi \tag{6}$$

where, $dS_a = \pi c(da)/4$, and, $dS_c = \pi a(dc)/4$; with da and dc being the growth in crack depth (along minor axis) and crack length (along major axis), respectively.

The reference K along the elliptical crack front, $K_r(\phi)$, is taken from the Newman and Raju solution [15,22] for uniform tension loading. If the applied "new" load is the same as the reference load, $\sigma_r(x,y)$, the weight-function method satisfies a self-consistency condition [1,28] which in terms of the effective K along crack depth, K_{ra}, for a quarterelliptical crack is given as

$$(K_{ra})^2 = (4E'/\pi c) \cdot \int_{x=0}^{c} \int_{y=0}^{y(x)} [\{\sigma_r(x,y) \cdot (\partial U_{\text{ref}}/\partial a)\} \cdot dx\, dy] \tag{7}$$

where E' is the appropriate elastic modulus of the material. For the plane-strain condition, E' is replaced by $E/(1 - \nu^2)$. Upon application of Leibnitz theorem, the partial derivative sign, $(\partial/\partial a)$, can be taken outside the area integral in Eq 7. If then the decomposition of $U_{\text{ref}}(a,c,x,y)$ from Eq 1 is substituted into Eq 7, it can be shown that the CMOD expression for a quarterelliptical crack is

$$U_0(a,c) = \frac{\int_0^a [(K_{ra})^2 \cdot da]}{\left(\frac{4E'}{\pi c}\right) \int_x \int_y [\{\sigma_r(x,y) \cdot U_*(x/c,\, y/a)\} \cdot dx\, dy]} \tag{8}$$

where K_{ra} and U_* are known quantities are per Eqs 5 and 4. As such, the entire CSOD field for the reference loading can be estimated on the basis of the known K solution field as a function of a, c, and the crack-front angle, ϕ. It is to be noted that in deriving Eq 8, the effective K_{rc}, Eq 6, could be also used along with the incremental crack growth area, dS_c, to determine the expression for $U_0(a,c)$. If the reference load, $\sigma_r(x,y)$, is constant on the crack plane, it could be taken outside the crack surface area integral in the denominator of Eq 8 to further simplify the computation.

To quantify the general differences between the three crack surface opening displacement shapes, U_*, given by Eqs 2 to 4, the CSOD volume per unit CMOD value over a quarter-elliptical crack area can be defined as

$$\left[\int_x \int_y U_*(x/c,\, y/a) \cdot dx\, dy\right] \Big/ \left[\int_x \int_y dx\, dy\right] \tag{9}$$

The values of this "normalized" CSOD for any aspect-ratio, a/c, are computed to be 0.6667, 0.5658, and 0.5333 for an embedded (subsurface), surface, and corner crack, respectively. This implies that for a unit CMOD value, $U_0(a,c)$, among the three elliptical crack opening shapes, the embedded crack has the largest opening volume and is followed by the surface and then the corner cracks. This is true, based on physical grounds, since the embedded crack opens up as an ellipsoidal cavity at the crack mouth [29] with zero slopes along x and y axes, and the surface crack is assumed to open with a zero value of x-axis slope along the free surface. It would have been of significant interest if other investigators [2,5,6,14,17,30] had reported some convenient parameter, such as Eq 9, to compare their estimated displacement profiles, at least qualitatively.

Weight-Functions Computation

The K solutions for a new loading on the crack plane require computation of partial derivatives of the reference CSOD field U_{ref}, Eq 1, with respect to the two DOF crack-front extensions. The required displacement gradients for the elliptical crack are determined by using

$$(\partial U_{ref}/\partial a) = [(\partial U_0/\partial a) \cdot U_* + U_0 \cdot (\partial U_*/\partial a)]$$

and

$$(\partial U_{ref}/\partial c) = [(\partial U_0/\partial c) \cdot U_* + U_0 \cdot (\partial U_*/\partial c)] \tag{10}$$

Here, the partial derivatives of $U_*(x/c, y/a)$ are obtained in closed forms by using Eqs 2 to 4 for the embedded, corner, and surface cracks, respectively. Partial derivatives of the $U_0(a,c)$ field could be determined numerically by fitting bicubic splines to the discrete CMOD values obtained through 8. If a sufficient number of sets of crack lengths, c (major axis), and crack depths, a (minor axis), are considered, the bicubic splines fit would lead to accurate partial derivative values. The computed derivatives of the reference displacement field maintain their near-crack-tip behavior due to the presence of closed-form expressions for $U_*(x/c, y/a)$.

The two DOF "effective" K values for any new loading, $\sigma_{new}(x,y)$, are given as

$$K_a(a,c) = \left(\frac{E'}{K_{ra}}\right) \int_x \int_y [\sigma_{new}(x,y) \cdot (\partial U_{ref}/\partial S_a) \cdot dx\, dy] \tag{11}$$

and

$$K_c(a,c) = \left(\frac{E'}{K_{rc}}\right) \int_x \int_y [\sigma_{new}(x,y) \cdot (\partial U_{ref}/\partial S_c) \cdot dx\, dy] \tag{12}$$

where the incremental areas, dS_a and dS_c, of the elliptical crack front, shown in Fig. 1, involve major and minor axes increments, da and dc, in an appropriate manner for the embedded, corner, and surface cracks. The K_{ra} and K_{rc} are reference effective K values, Eqs 5 and 6, for the required a and c dimensions. Integrands in Eqs 11 and 12 are the weight functions.

In the following sections, formulations and discussions of the results obtained will be presented for quarterelliptical corner cracks in plates and at circular holes, semielliptical surface cracks, and elliptical embedded (subsurface) cracks in finite geometry specimens. Verifications of the computed three-dimensional K solutions for some specific stress gradients are carried out for which numerical or analytical results or both are available in the literature.

Corner Crack Specimen

A reference K solution along the quarterelliptical corner crack front, $K_r(\phi)$, under a uniform tensile stress, σ, in a finite cross-section plate, shown in Fig. 1, is taken from Newman and Raju's work [*15,22*]. In the present work, it is proposed that the parameter, λ, $= [\pi ac/(4TW)]$, which is found by equating the elliptical crack area with a through-thickness "single edge crack" area. This is quite different from the expression given in Ref *22*; where λ, defined as $[(c/W)\sqrt{(a/T)}]$, is not suitable for use in square cross-section ($T = W$) plates containing corner cracks. In square cross sections, the c/W and a/T dependencies should be interchangeable as used here.

The K expressions in Ref *22* are valid for $a/T \leq 1$, $c/W \leq 0.5$, and $0.2 \leq a/c \leq 2$. It is expected that there would not be significant errors if the a and c values exceed somewhat beyond the specified limits. Upon substituting the expressions for reference $K_r(\phi)$ from Ref *22* into Eq 5, the "effective" reference K_{ra} values are obtained for a set of values of a (from 0 to T) and c (from 0 to W). The K_{ra} values and the U_*, crack opening shape in Eq 3, are then used in Eq 8 to obtain discrete values of CMOD, $U_0(a,c)$. Here, σ_r is equal to a constant tensile stress, σ, on the crack plane. The line and area integrals in Eq 8 are computed numerically. For this purpose, the discrete values of $K_{ra}(a,c)$ were fit to one-dimensional cubic splines along the variable a (crack depth) for fixed values of c (crack length) for which $U_0(a,c)$ are to be determined.

Corner Crack Surface Opening Displacement

The total CSOD field, $U_r(a,c,x,y)$, for the reference loading is obtained by multiplying the CMOD values $[U_0(a,c)]$, computed from Eq 8, with the $U_*(x/c,y/a)$ field approximation, given in Eq 3. The elastic CMOD values, $U_0(a,c)$, obtained here can be used for comparison and calibration of experimental data. As an example, Fig. 3 shows the computed CMOD values for circular, $a/c = 1$, corner cracks ranging in size from 4% to full thickness of the plate specimen, and subjected to uniform tensile stress on the crack plane. There are no theoretical solutions available for CMOD values except that of embedded circular crack in an infinite body that is also shown in Fig. 3. The effect of the aspect ratio, a/c, on CMOD is shown in Fig. 4.

As discussed in the previous section, Eqs 10 through 12, partial derivatives of the reference CSOD field are required to obtain K solutions for the new loads. These partial derivatives, computed by using bicubic splines fit to the CMOD values, have singular behavior in the vicinity of the crack front. Since these displacement gradients are used as a part of the integrands in Eqs 11 and 12, the singular integrand needs a sufficiently refined mesh for computing the area integrals over the crack surface. The Gauss-Legendre method, such as in finite element analyses, is used in the present work to compute the area integrals. A rectangular mesh is laid over the crack surface area. The remaining triangular areas adjacent to, but within, the elliptical crack-front boundary are included in the numerical integration scheme to improve accuracy.

Corner Crack Effective K *Solutions*

The accuracy of the computed values of the effective K_a and K_c can be checked by taking the $\sigma_{new}(x,y)$ stress, in Eqs 11 and 12, to be the same as the reference stress, $\sigma_r(x,y)$, as shown in Eq 7. The resulting values of effective K_{ra} and K_{rc} can be compared with the Newman and Raju [*15,22,31*] solutions (when it is converted into effective K values as per Eqs 5 and 6). For a uniform tensile applied stress, the effective K_a and K_c values obtained

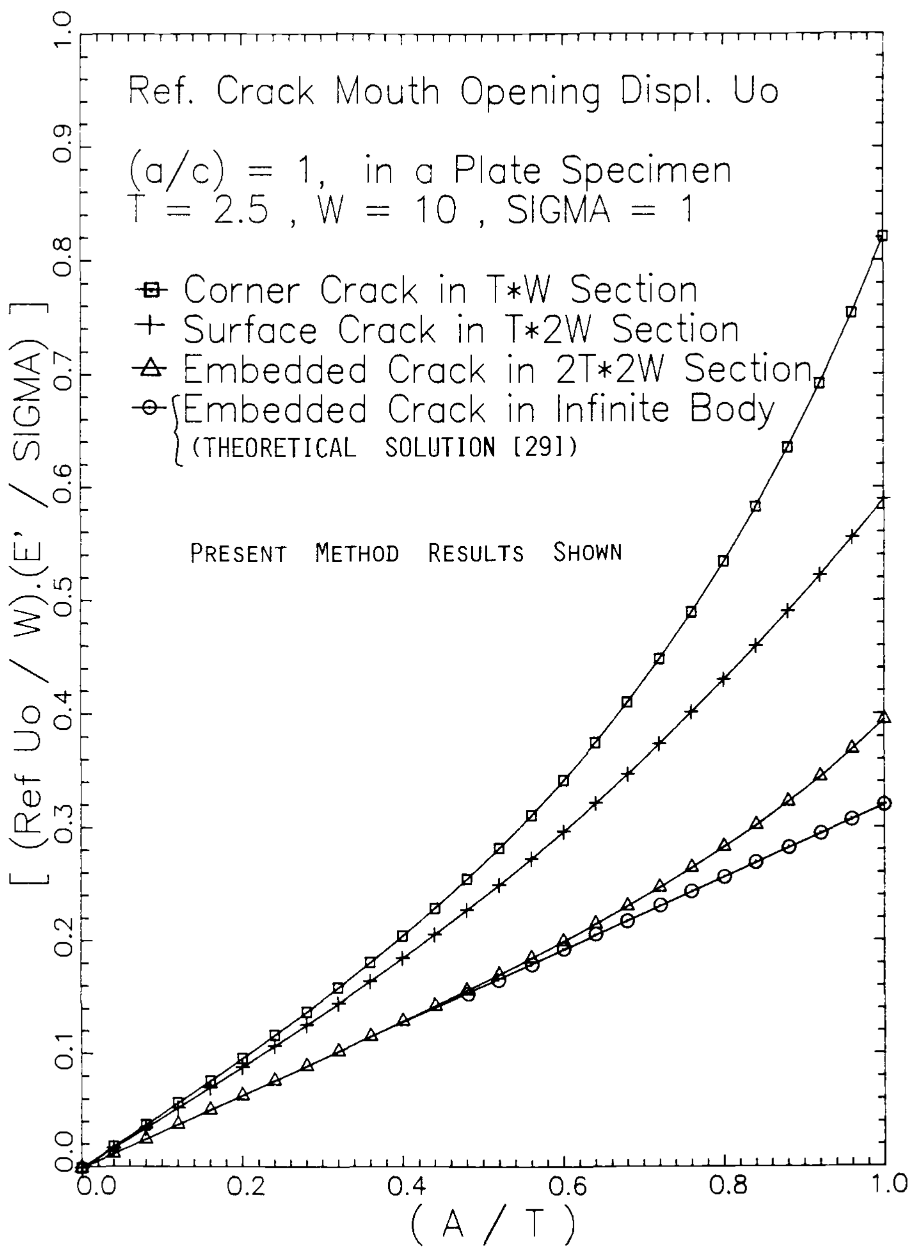

FIG. 3—*Reference crack-mouth opening displacement (CMOD) in circular corner, surface, and sub-surface (embedded) cracks under a uniform tensile stress.*

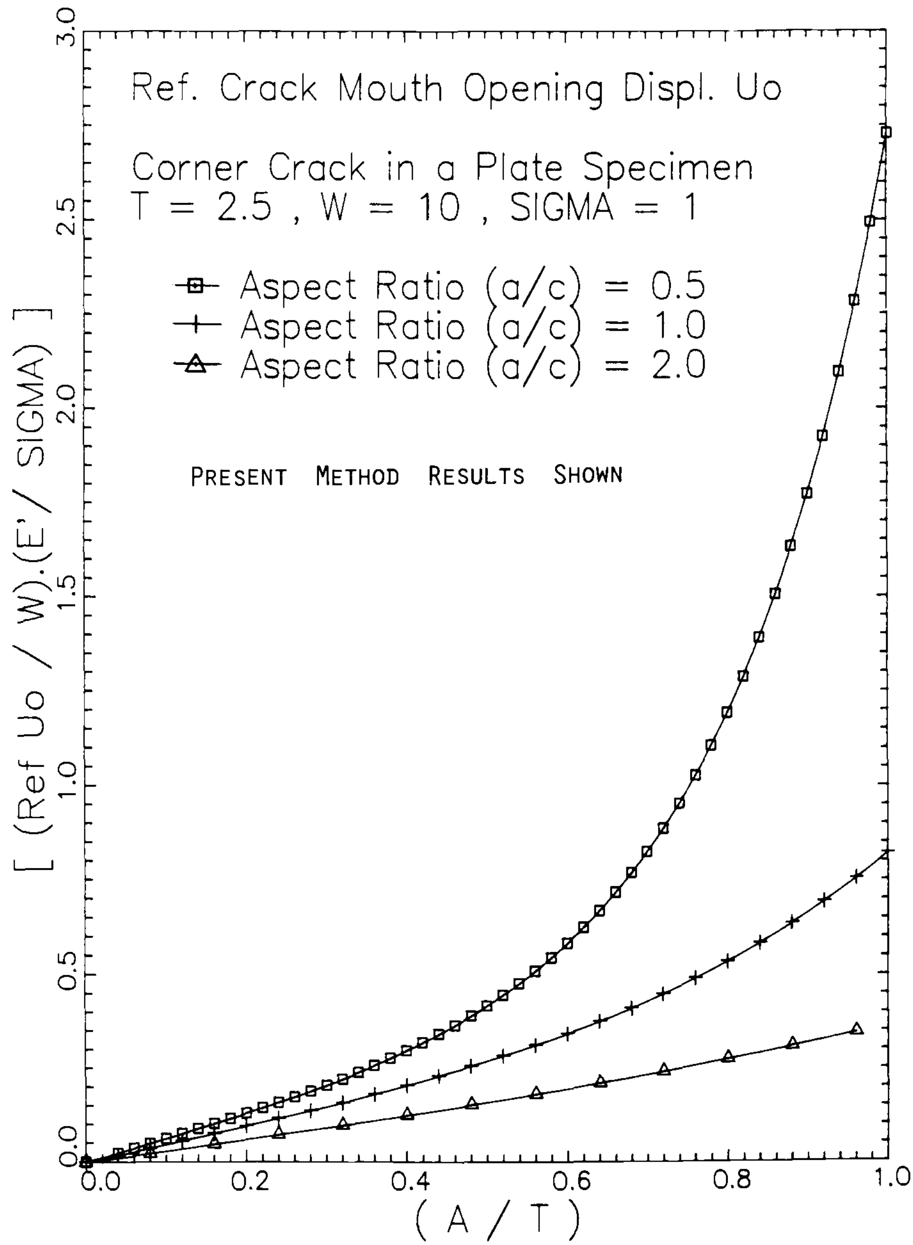

FIG. 4—*Reference crack-mouth opening displacement (CMOD) in various aspect ratio, quarter-elliptical, corner cracks under a uniform tensile stress.*

by the present method are within 5% of the Newman and Raju (NR) solutions for various a/c ratios (0.5, 1, 2, and 0.2) and for a/T ratios ranging from very small to very large (≤ 1). This excellent comparison gives the confidence that the numerical computations strategy is working satisfactorily.

Newman and Raju [22,31] have also provided corner crack K solutions for the "out-of-plane bending" moment on plates resulting in linearly decreasing stress on the crack plane. The present method was then applied to determine effective K values for a bending stress acting on elliptical corner cracks of various aspect ratios. The $U_0(a,c)$ field in Eq 8 was computed by using the NR "uniform" tensile stress K solution [15,22]. The new effective K solutions computed using Eqs 11 and 12 included an out-of-plane bending stress for $\sigma_{new}(x,y)$. The resulting K values are compared with the NR bending stress K solutions [22]. These comparisons are presented in Figs. 5 through 7. It could be seen that the effective K values by the present method and the NR solution compare extremely well. The differences are only of the order of 5% in most cases, and up to 10% in some cases, for the a/c ratios of 0.5, 1, and 2; and for various a/T ratios extending well into compressive bending stress regions. The accuracy of the bending K results obtained by using the present method is much more superior than by the solutions from a recently developed three-dimensional weight-functions method [14] where the differences, as compared to NR solutions, were as large as 25 to 30% for a/T ratios going only up to 0.4.

The verification of corner crack "effective" K_a and K_c solutions just described for the bending stress field demonstrates the validity of the concepts and accuracy of implementation of the proposed new weight-function method for three-dimensional crack problems. It is expected that a similar degree of accuracy can be maintained for K solutions under any general stress gradients on corner cracks, as demonstrated by the results for corner cracks at holes that are presented in a separate section of this paper. For corner cracks under general stress gradients, there are no well-accepted solutions available in the literature, except for those located at holes in plates.

Surface Crack Specimens

Reference K solution along a semielliptical surface crack-front, $K_r(a,c,\phi)$, under a uniform tensile stress in a finite cross-section rectangular plate is taken from Newman and Raju [15,22]. The "effective" reference K_{ra} values are then computed using Eq 5 for various a and c values. The $K_{ra}(a,c)$ and $U_*(x/c, y/a)$, the crack opening shape from Eq 4, were then used in Eq 8 to obtain discrete values of the CMOD for semielliptical surface cracks. The computed reference CSOD fields were compared with an analytical power series approximation by Fett [30]. Figure 8 shows this comparison for a circular surface crack at the free surface, X/c, and at the maximum depth locations, Y/a. It is to be noted that a parabolic crack opening shape at maximum depth and an elliptical profile at the free surface was also obtained by Cruse [32,33] using a boundary element method. The comparison of the CSOD fields in Fig. 5 is very good. In weight-functions computations, the CSOD field is not used directly, but it is the rate of change of CSOD field with respect to the crack length and depth that is needed. Therefore, the accuracy with which these partial derivatives are computed is of prime importance.

The computed CMOD values for surface cracks under uniform tensile stress are shown in Figs. 3 and 9 for three aspect ratio, a/c, values (0.5, 1, and 2). It could be seen in Fig. 3 that at lower a/T ratios the surface crack CMOD values are somewhat smaller than the values for corner cracks. But for much deeper cracks, this difference becomes significant. As discussed earlier, there are no published works in the literature on computed elastic CMOD values for surface cracks with which to compare the present results. Raju, Newman,

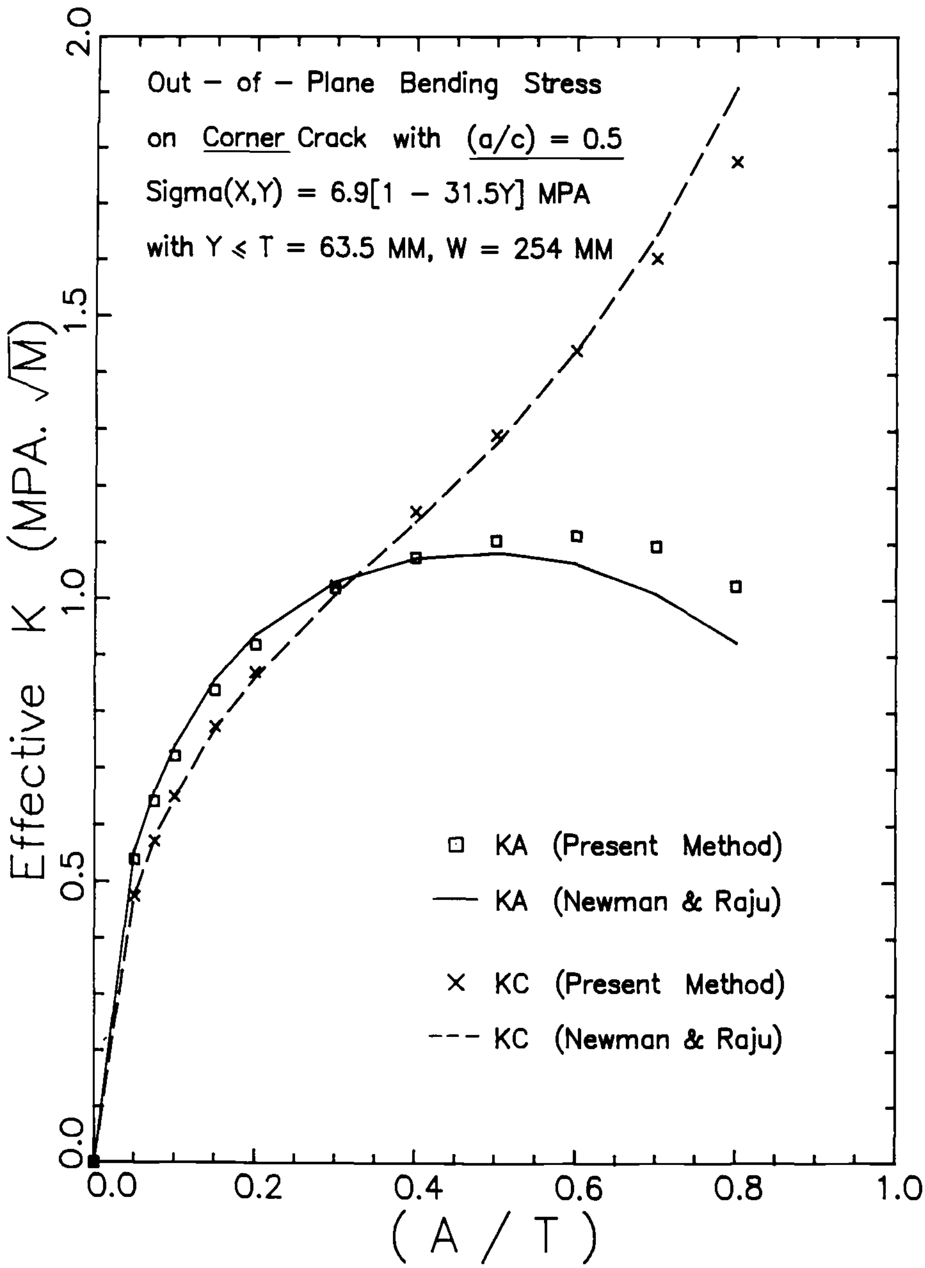

FIG. 5—*Comparison of effective* K *values for an out-of-plane bending stress on corner cracks with an aspect ratio,* a/c, *of* ½.

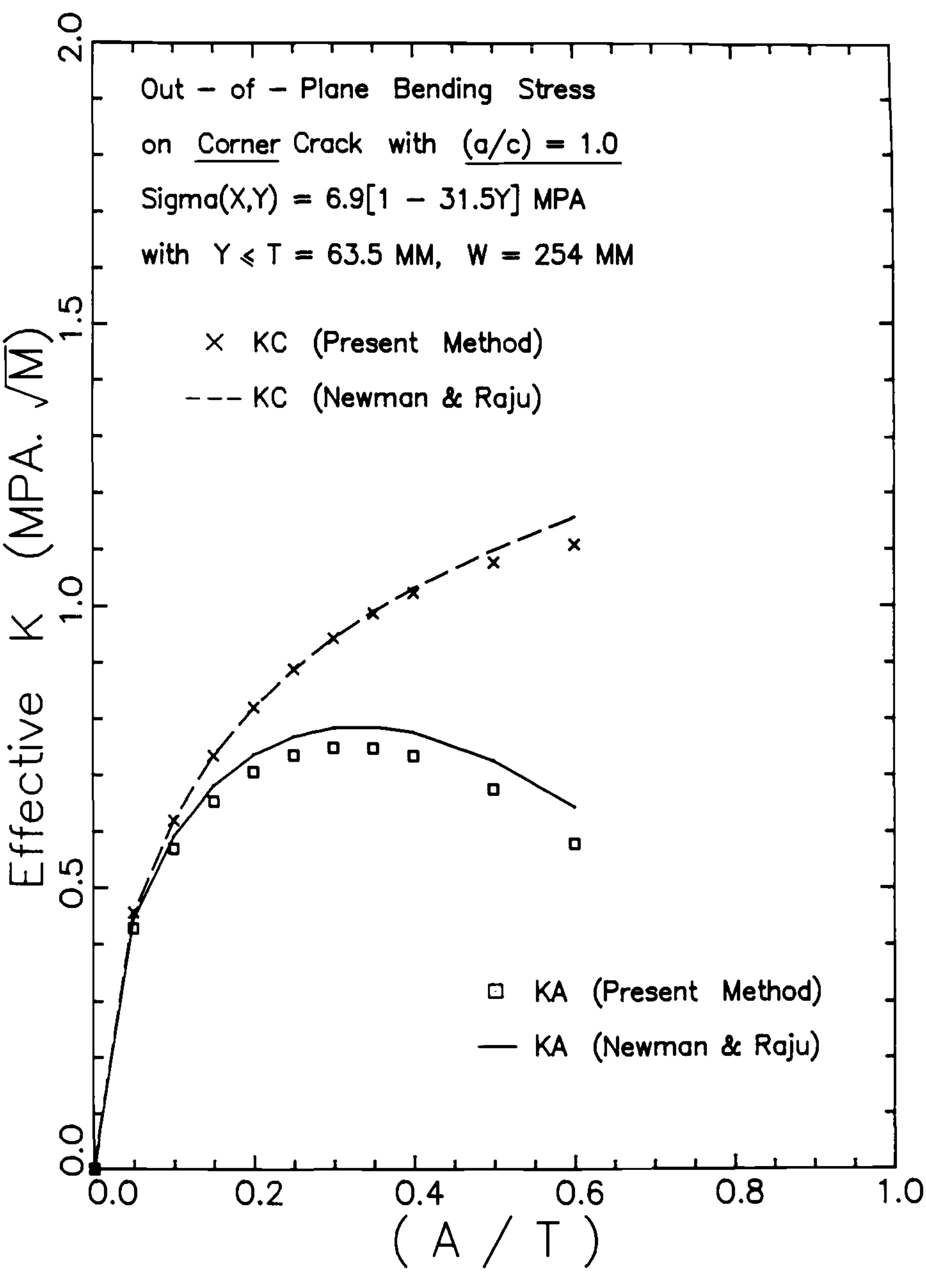

FIG. 6—*Comparison of effective* K *values for an out-of-plane bending stress on corner cracks with an aspect ratio,* a/c, *of 1.*

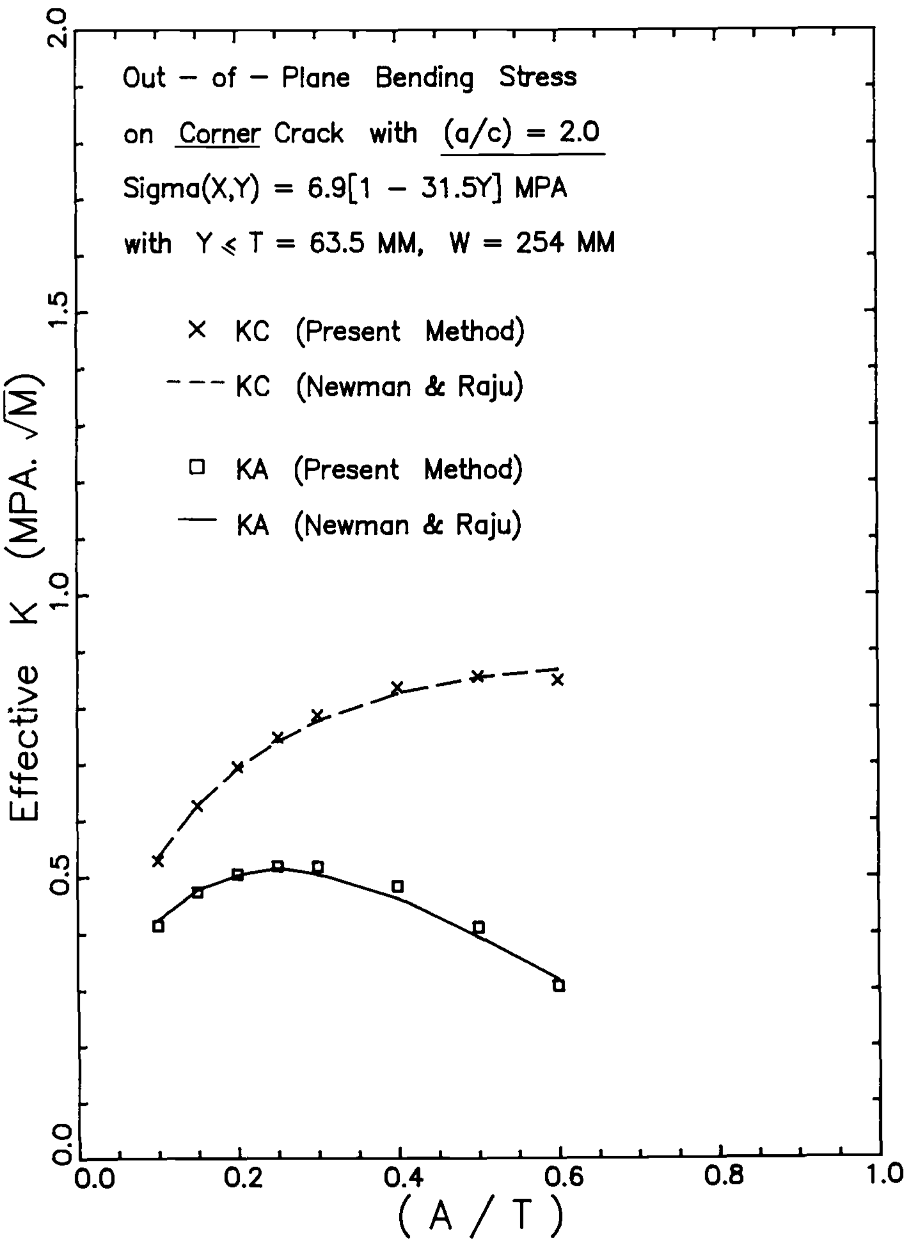

FIG. 7—*Comparison of effective* K *values for an out-of-plane bending stress on corner cracks with an aspect ratio,* a/c, *of 2.*

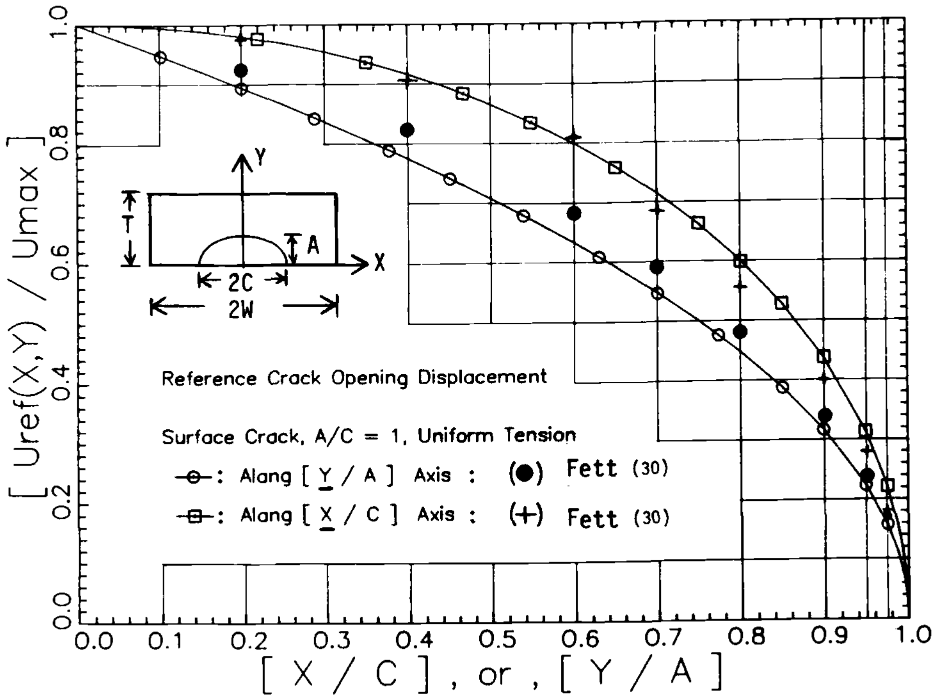

FIG. 8—*Reference crack surface opening displacement (CSOD) for semielliptical surface cracks in a plate under a uniform tensile stress field.*

and Atluri [*34*] have just recently presented CMOD values for surface cracks under uniform tension and bending stresses. A brief comparison of the present results with a "draft" version of Ref *34* reveals very good agreement. For example, the CMOD values using the equations proposed in Ref *34* for uniform tensile load are within 6% of the present results for a/c = 1 (a/T values ranging from 0.2 to 0.8), within 9% for a/c = 0.5, and within 1% for a/c = 2. The percentage difference between the CMOD values by the two methods decreased substantially for larger a/T values.

The computed effective K values by the present method, for surface cracks under uniform tensile stress, are within 5% of the Newman and Raju solutions [*15*,*22*] for a/c ratios of 0.5, 1, and 2; and for a/T values ranging from 0 to 1. This again confirms that the present computational strategy for surface cracks is working very well. The method was then applied to the case of out-of-plane bending stress acting on surface cracks. The reference COD field was obtained from NR "uniform" tensile stress K values [*15*,*22*]. Figures 10 through 12 show the results obtained for a/c ratios of 0.5, 1, and 2, respectively. For most of the computed effective K values, the maximum percentage difference relative to NR solutions [*15*,*22*] were under 5%; and for a few cases at larger a/T ratios, the differences became as high as 10%. This level of K solution matching for bending stresses gives good verification of the developed method for surface cracks.

A nonsymmetric loading, leading to two different values of K_c at the free surface (K_{c1} and K_{c2}), was applied. A linearly varying inplane stress of the type $\sigma_{new}(x,y) = 6.9[1 - 7.874x]$ MPA, with -0.127 m $< x <$ 0.127 m, was considered. Here, total width, W is 0.254 m; and the thickness, T, is 0.0635 m. It was assumed that the surface crack is located at one half of the width, W, where the value of coordinate, x, is equal to zero. Figure 13 shows

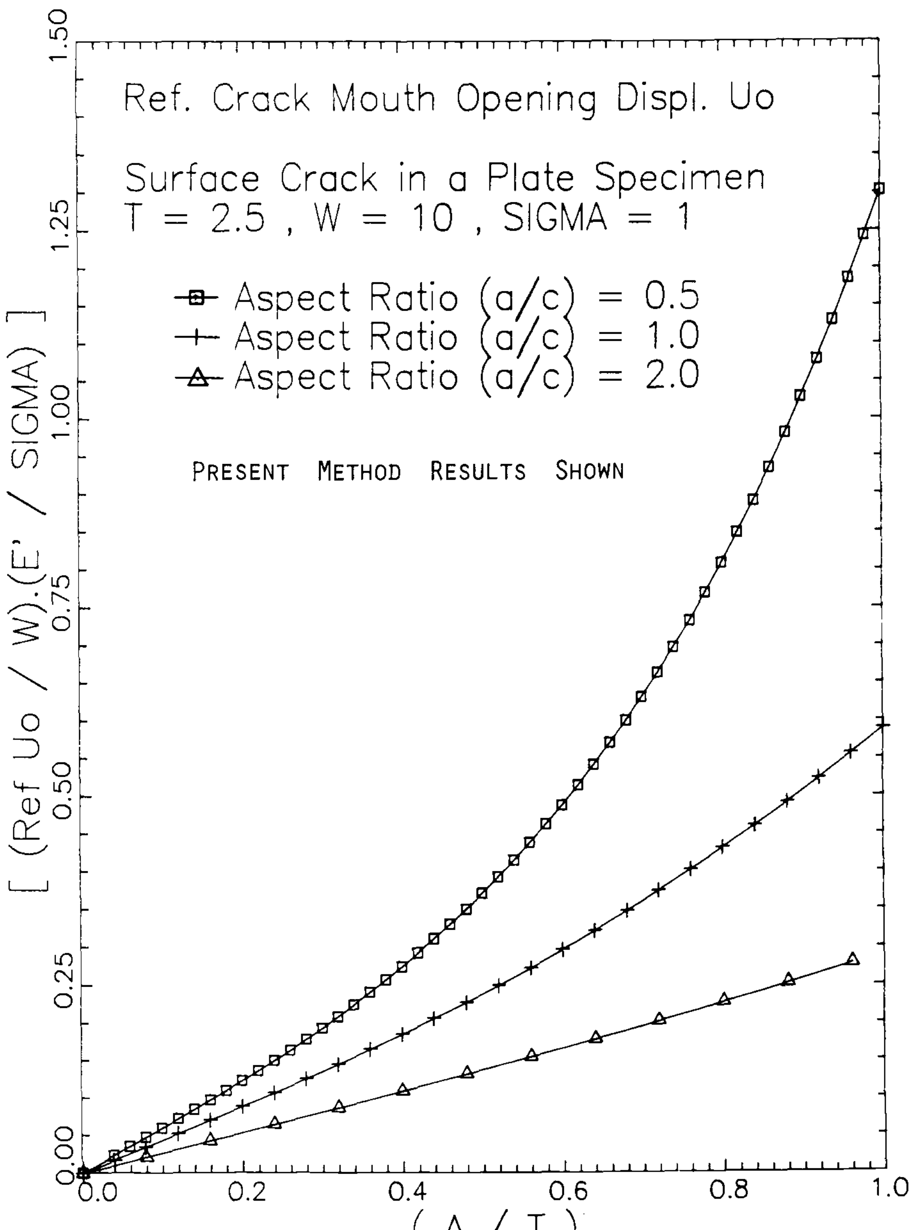

FIG. 9—*Reference crack-mouth opening displacement (CMOD) in various aspect ratio, semielliptical, surface cracks under a uniform tensile stress.*

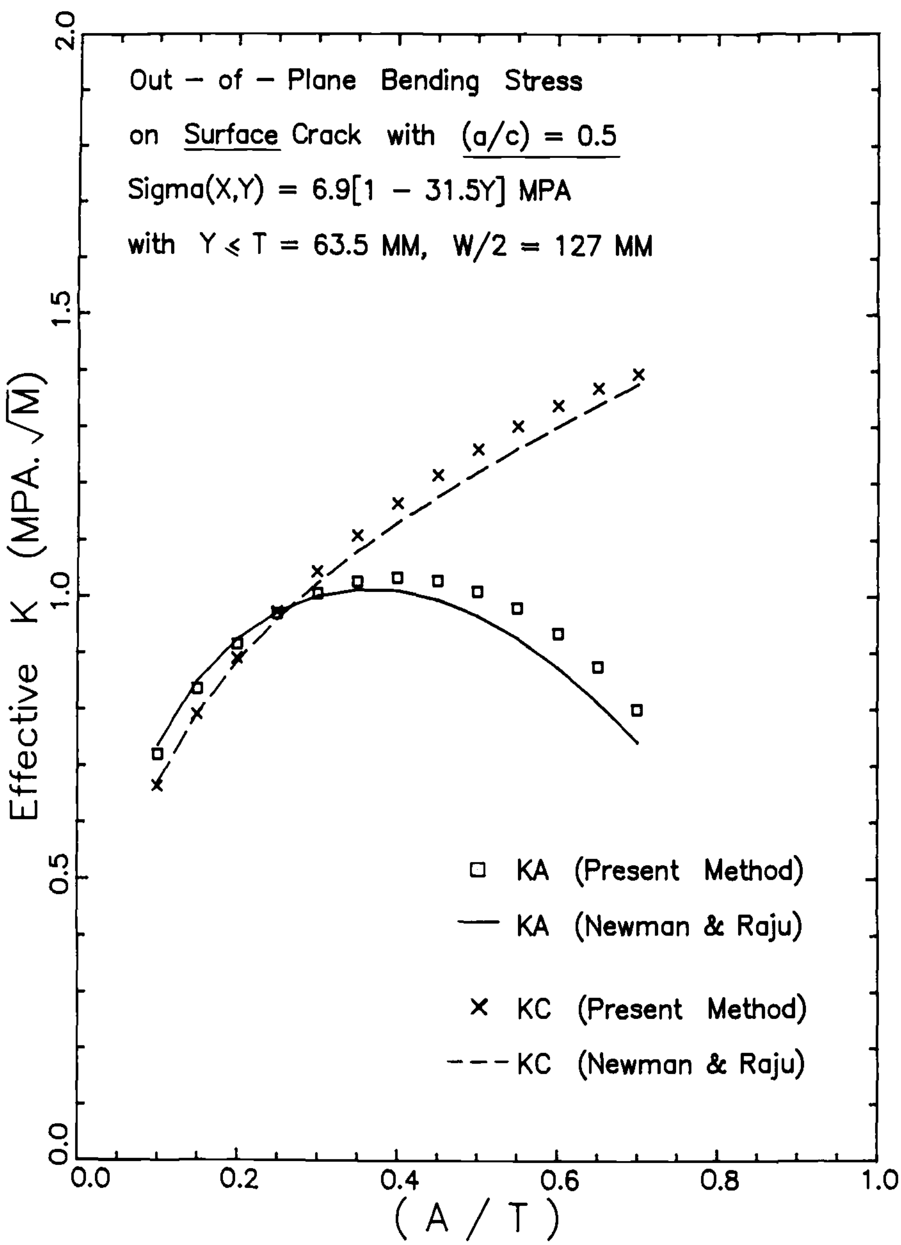

FIG. 10—*Comparison of effective* K *values for an out-of-plane bending stress on surface cracks with an aspect ratio,* a/c, *of* ½.

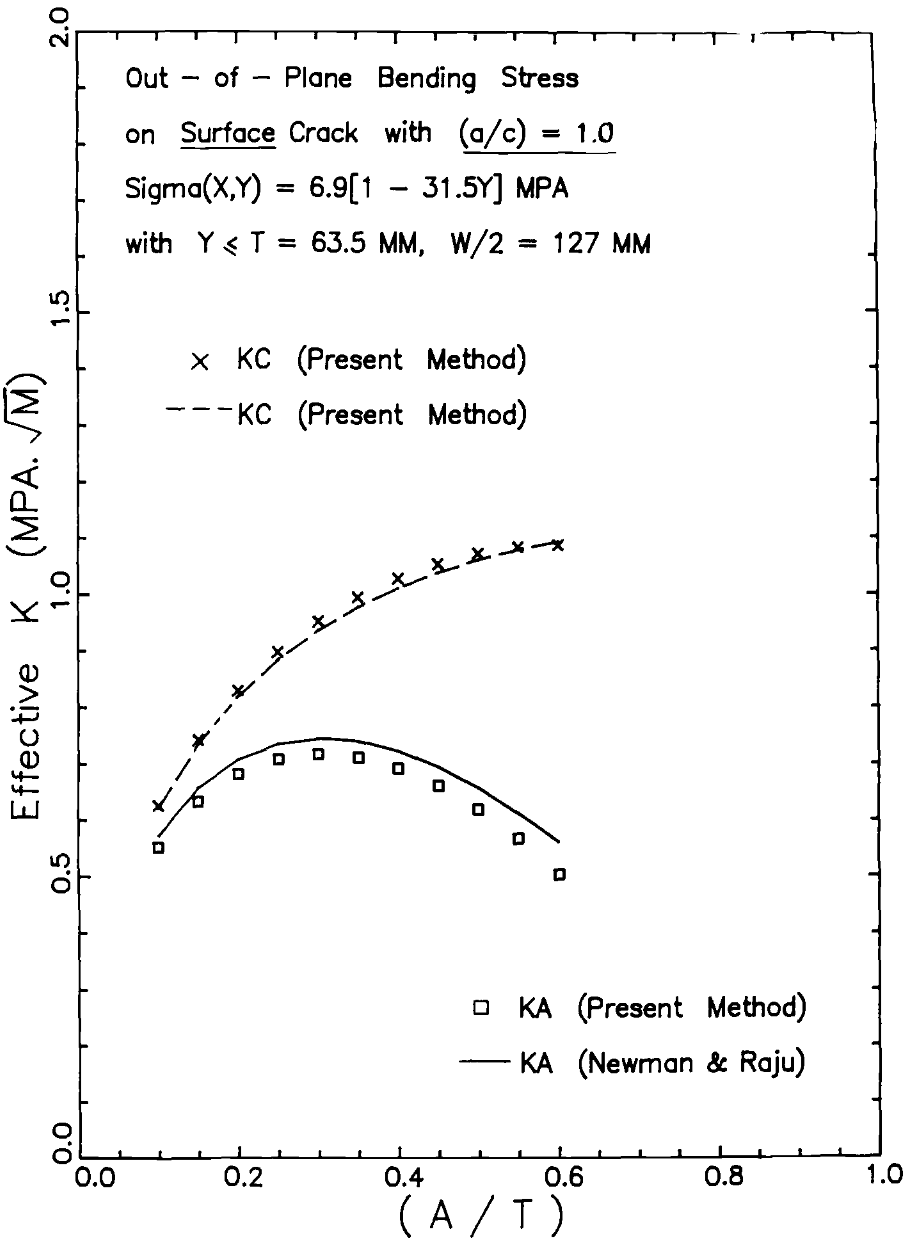

FIG. 11—*Comparison of effective* K *values for an out-of-plane bending stress on surface cracks with an aspect ratio,* a/c, *of 1.*

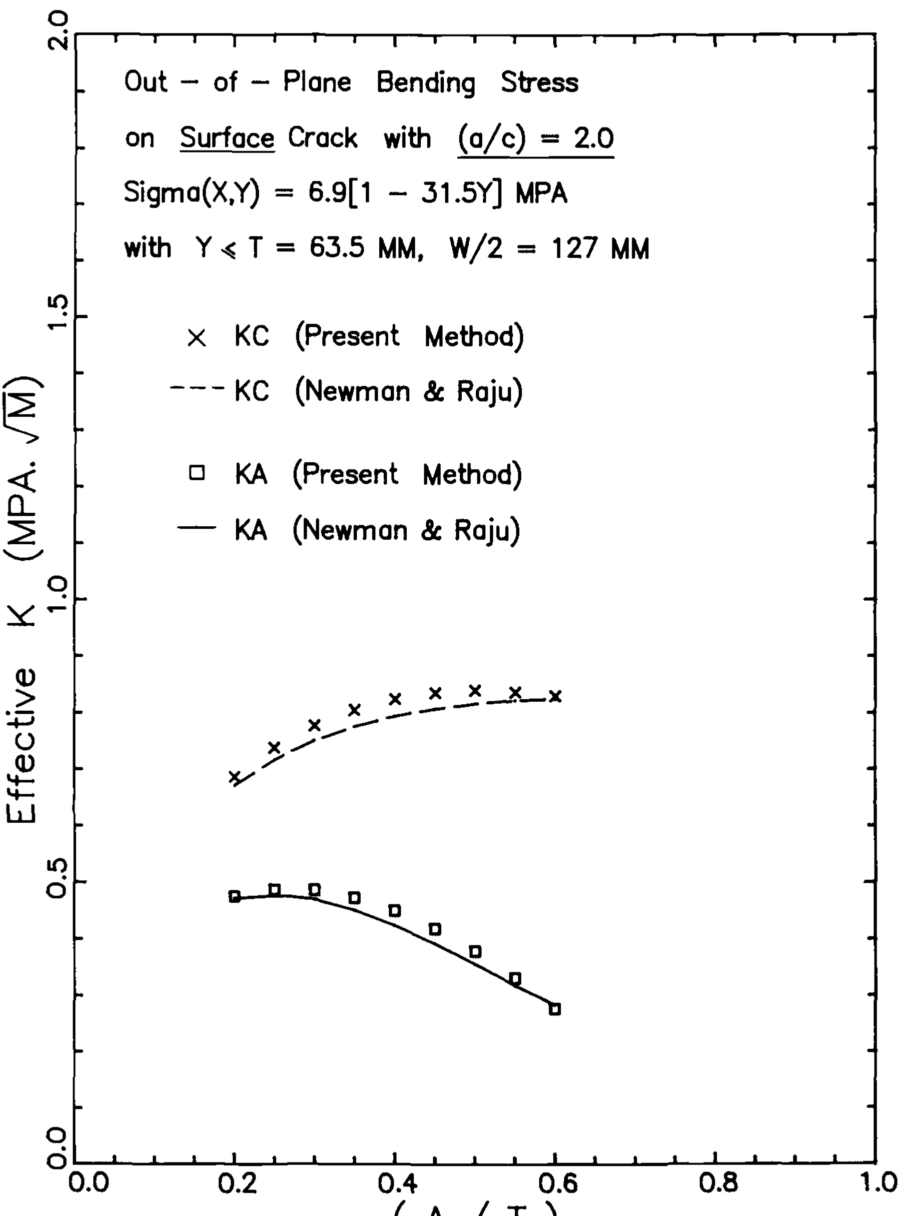

FIG. 12—*Comparison of effective* K *values for an out-of-plane bending stress on surface cracks with an aspect ratio,* a/c, *of 2.*

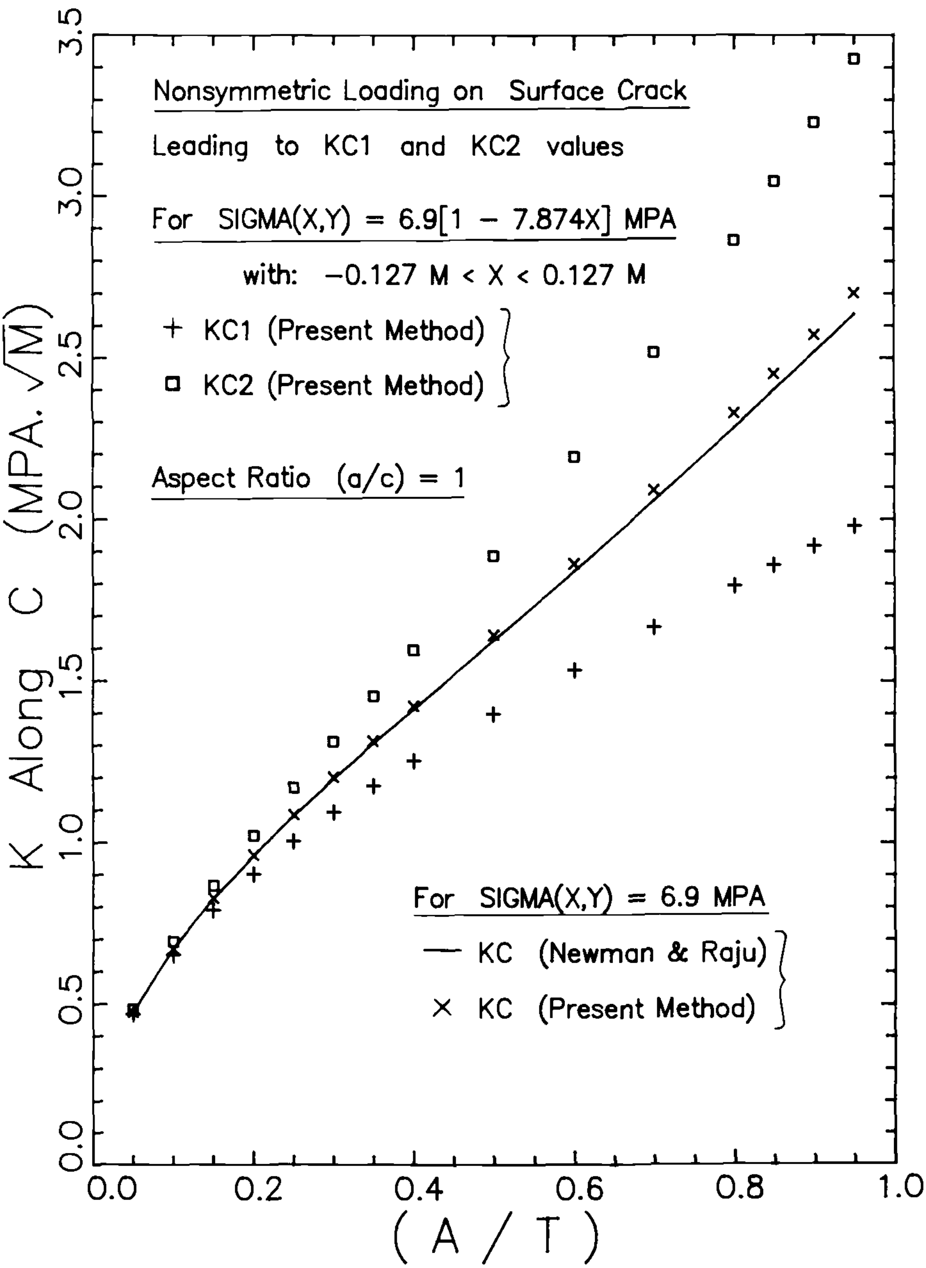

FIG. 13—*Effective* K_c *values for a nonsymmetric loading on surface cracks with an aspect ratio,* a/c *of 1.*

the K_{c1} and K_{c2} values as a function of a/T for an aspect ratio, a/c, of 1. Since the stress is dropping down linearly across the width, from 13.8 MPA to zero, the K_{c1} values are smaller than K_{c2} values. The average of the K_{c1} and K_{c2} values at a given a/T ratio is found to be equal to the corresponding K_c value for a "constant" applied stress of 6.9 MPA. This fact is also shown in Fig. 13, where the K_c values by the present method as well as from Newman and Raju are plotted. Therefore, the amount of decrease in K_{c1} value from K_c is the same as the amount of increase in the K_{c2} value from the K_c. This provides a partial verification for the unequal K values at the free surface crack tips, K_{c1} and K_{c2}, due to nonsymmetric loading on surface cracks. Similar conclusions could be drawn from Fig. 14, where the crack aspect ratio, a/c, is ½. At present, there are no K solutions available in the literature, for nonsymmetric loadings, with which to directly compare the present results.

Subsurface Cracks

For embedded (subsurface) elliptical cracks, the Green and Sneddon [*29*] expression for CSOD profile, as given in Eq 2, was used. To obtain the CMOD values, Eq 8 was used along with the NR K solutions [*15,22*] for finite geometry specimens containing subsurface cracks. Figures 3 and 15 show the resulting CMOD values for subsurface cracks in finite geometry specimens as well as in an infinite body. It could be seen that, for the T/W ratio considered, the CMOD values for finite geometry subsurface cracks are very close to the exact solution in an infinite body with smaller a/T ratios. This gives further confidence and verification of the developed method for computing COD fields in subsurface cracks for weight-functions applications. Also, it could be seen from Fig. 3 that the CMOD values, at any a/T ratio, for subsurface cracks are the smallest, followed by the surface and then the corner crack values.

Table 1 shows the computed effective K values for uniform tensile stress on finite geometry specimens containing subsurface elliptical cracks for several aspect ratios, a/c, as well as for a number of a/T values ranging from very small to very large (0.1 to 0.8). It could be seen that both K_a and K_c values are within 5% of the Newman and Raju solution for all the cases considered. Pure bending loads on subsurface elliptical cracks were not considered due to possible crack-surface closures that may cause K values to become negative for the closed portion of the crack front.

The present formulation for subsurface flaws is general enough to handle any stress gradients including those that are unsymmetric about the elliptical crack axes that may lead to unequal K values (for example, K_{a1} and K_{a2}; K_{c1}, and K_{c2}) at two opposite locations along the crack front. Unsymmetric stresses were applied to subsurface cracks; and Eqs 11 and 12 resulted in unequal K values at crack depths and lengths. However, at present there are no solutions available in the literature for unsymmetric stress gradients with which to compare the obtained results. It seems that either gathering experimental data on unsymmetric crack growths, or, using a finite element method would be a reasonable way to verify these K values.

Corner Crack at Circular Hole

The K values for corner cracks emanating from a circular hole in a plate are somewhat smaller than the K values for the same crack located at a plate corner and subjected to the same "ahead of circular hole" stress gradients. This is due to the presence of a finite circumference of the hole that results in constrained boundary conditions at the crack mouth [*35,36*]. To determine the effect of a bolt hole on corner crack K solutions, Newman and Raju [*15,22*] have developed empirical equations for $K(\phi)$ along the crack fronts that are based on their finite element analyses [*37*]. These K equations were obtained for "two

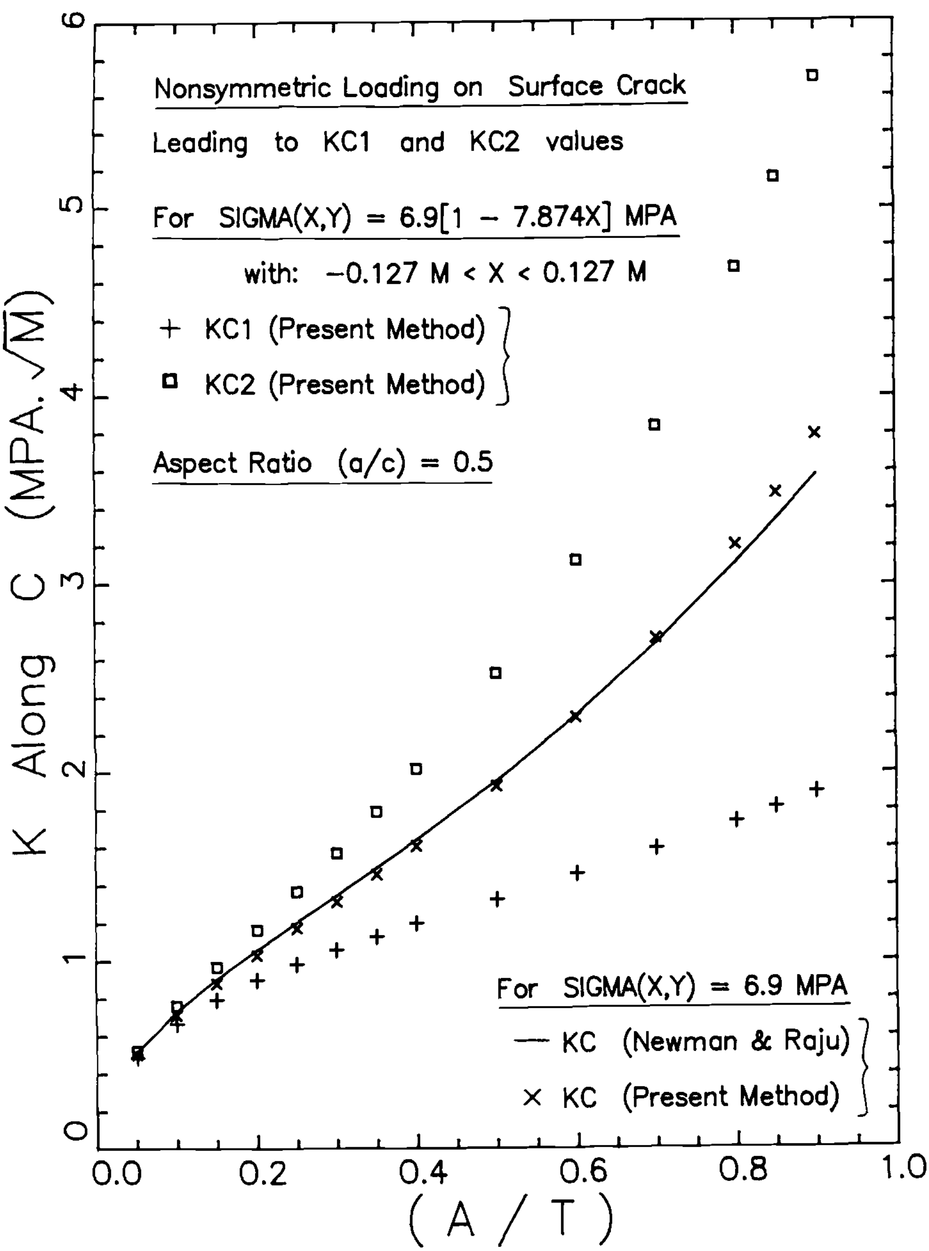

FIG. 14—*Effective* K_c *values for a nonsymmetric loading on surface cracks with an aspect ratio,* a/c, *of* 1/2.

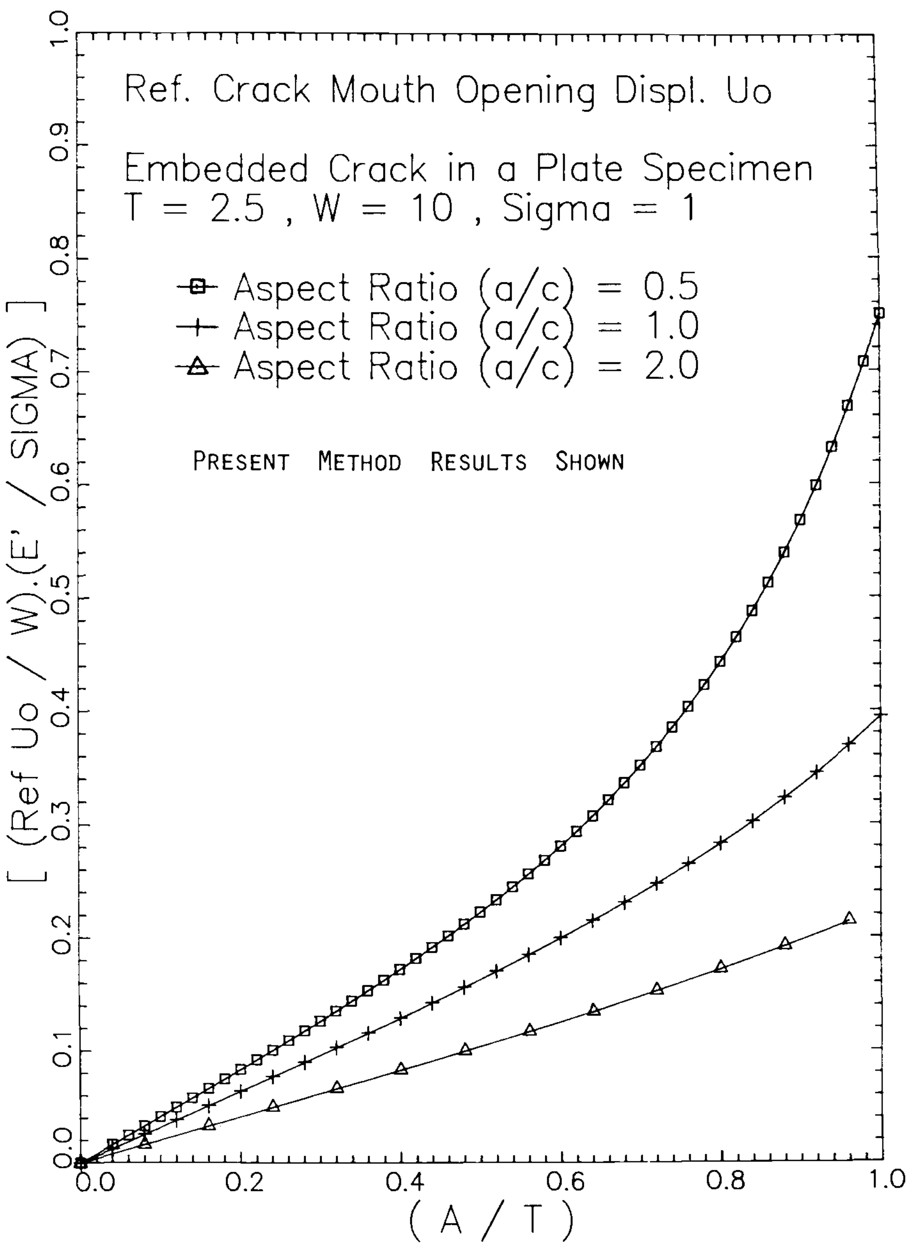

FIG. 15—*Reference crack-mouth opening displacement (CMOD) in various aspect ratio, elliptical subsurface (embedded) cracks under a uniform tensile stress.*

TABLE 1—*Comparison of effective* K *values for embedded (subsurface) cracks under uniform tension stress* σ(x,y) = *1 ksi: half thickness,* T = *2.5 in.; half width,* W = *10 in.; and scale: 1 ksi = 6.895 MPa (1 in. = 25.4 mm).*

a along *T*, *c* along *W*	K_a (*K* along Crack Depth *a*)			K_c (*K* along Crack Length *c*)		
Crack Size Ratios (*a*/*T*, *a*/*c*)	Newman and Raju [*15*, *22*] Effective *K* ksi$\sqrt{\text{in.}}$	New Weight Function Effective *K*, ksi$\sqrt{\text{in.}}$	Percentage Difference, %	Newman and Raju [*15*, *22*] Effective *K*, ksi$\sqrt{\text{in.}}$	New Weight Function Effective *K* ksi$\sqrt{\text{in.}}$	Percentage Difference, %
0.1, 1.0	0.5649	0.5515	2.4	0.5649	0.5439	3.7
0.1, 1.5	0.6448	0.6156	4.5	0.5841	0.5563	4.7
0.1, 2.0	0.6929	0.6650	4.0	0.5897	0.5691	3.5
0.15, 1.0	0.69231	0.6687	3.4	0.69228	0.6560	5.2
0.2, 1.0	0.8003	0.7659	4.3	0.8002	0.7641	4.5
0.2, 2.0	0.9847	0.9452	4.0	0.8379	0.8072	3.7
0.2, 3.0	1.0612	1.0212	3.7	0.8417	0.8075	4.1
0.3, 1.0	0.9841	0.9476	3.7	0.9834	0.9487	3.5
0.4, 1.0	1.1445	1.0937	4.4	1.1420	1.1004	3.6
0.5, 1.0	1.2946	1.2430	4.0	1.2877	1.2527	2.7
0.6, 1.0	1.4438	1.3808	4.3	1.4277	1.3947	2.3
0.7, 1.0	1.5998	1.5367	3.9	1.5664	1.5523	0.9
0.8, 1.0	1.7701	1.6971	4.1	1.7061	1.7152	−0.5

symmetric" corner cracks at the opposite sides of a central hole in a finite plate under remote, uniform tension, and linear bending stresses.

Specimen geometry and size details of a corner crack at a circular hole in a plate are shown in Fig. 16. If the radius, R, of the hole is very small in comparison with the specimen half width, W, then the concentrated elastic stress distribution, $\sigma_{ref}(x,y,z = 0)$, ahead of the hole for an applied uniform tensile far-field stress, σ, is given [38] in closed form as

$$\sigma_{ref}(x,y,z = 0) = \sigma[1 + 0.5\{R/(x + R)\}^2 + 1.5\{R/(x + R)\}^4] \tag{13}$$

where $0 \leq x \leq (W - R)$. The present weight-function method was applied to determine the K values for corner cracks at holes. The NR K solutions for two symmetric cracks at a hole and the reference stress given in Eq 13 were used in Eqs 8, 11, and 12 to obtain the effective K values. The NR K values [15] for two symmetric corner cracks at a hole are used as a reference solution in the present weight function method to obtain a new set of reference displacement field, its partial derivatives, and the effective K values. These K values are presented in Tables 2 through 4 for crack aspect ratios, a/c, of 0.5, 1, and 2. It could be seen that the effective K values by the present weight-function method are in

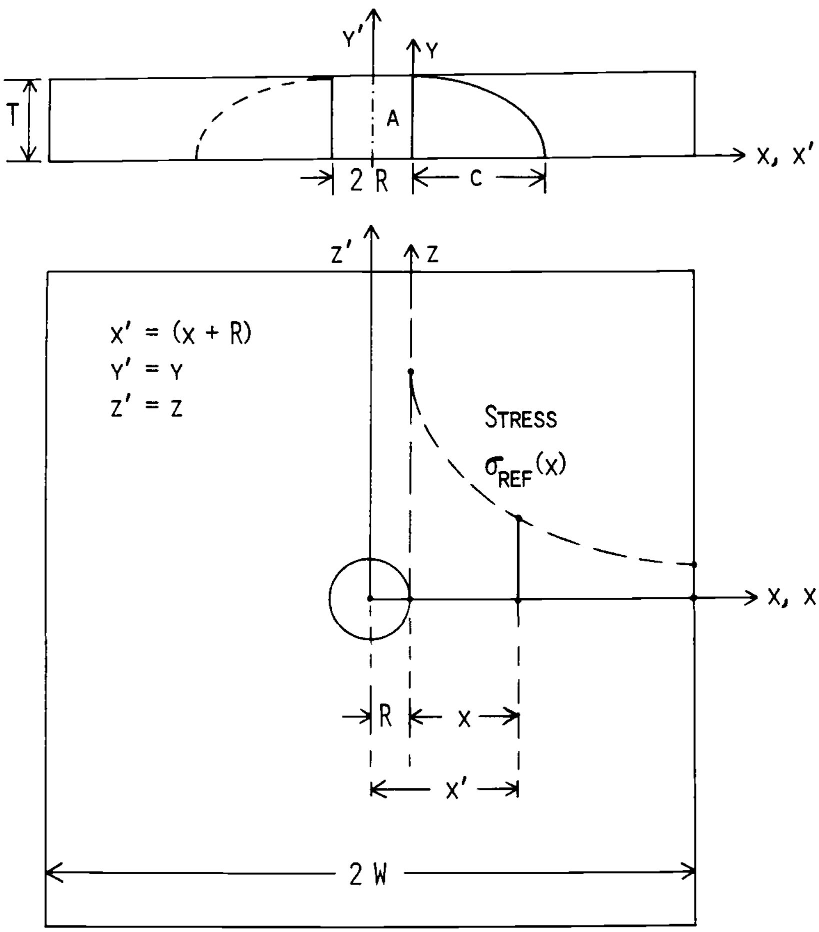

FIG. 16—*Corner crack originating from a circular hole in a plate specimen.*

TABLE 2—*Comparison of effective* K *values for "corner crack at a hole" with* (a/c) = *0.5, under far-field uniform tensile stress of 1 ksi: hole radius,* R = *1.25 in.; thickness,* T = *2.5 in.; width,* W = *10 in.; and scale: 1 ksi = 6.895 MPa (1 in. = 25.4 mm).*

a along T, c along W	K_a (K along Crack Depth a)			K_c (K along Crack Length c)		
Crack Depth Ratio, a/T	Newman and Raju [15, 22] Effective K, ksi$\sqrt{\text{in.}}$	New Weight Function Effective K, ksi$\sqrt{\text{in.}}$	New Weight Function "Simulated Hole" Effective K, ksi$\sqrt{\text{in.}}$	Newman and Raju [15, 22] Effective K, ksi$\sqrt{\text{in.}}$	New Weight Function Effective K, ksi$\sqrt{\text{in.}}$	New Weight Function "Simulated Hole" Effective K, ksi$\sqrt{\text{in.}}$
0.1	1.6901	1.6328	1.7133	1.2515	1.1514	1.2634
0.15	1.9177	1.8533	1.9504	1.3948	1.2541	1.3971
0.2	2.0962	2.0266	2.1461	1.5179	1.3494	1.5246
0.25	2.2561	2.1820	2.3350	1.6381	1.4540	1.6704
0.3	2.4109	2.3328	2.5352	1.7619	1.5726	1.8463
0.35	2.5678	2.4859	2.7578	1.8927	1.7064	2.0596
0.4	2.7309	2.6452	3.0109	2.0325	1.8563	2.3157
0.5	3.0856	2.9920	3.6359	2.3451	2.2072	2.9799
0.6	3.4881	3.3859	4.4641	2.7100	2.6357	3.8994
0.7	3.9470	3.8350	5.5685	3.1371	3.1588	5.1823
0.75	4.2002	4.0826	6.2598	3.3774	3.4637	6.0175

TABLE 3—*Comparison of effective* K *values for "corner crack at a hole" with* (a/c) = *1.0, under far-field uniform tensile stress of 1 ksi: hole radius,* R = *1.25 in.; thickness,* T = *2.5 in.; width,* W = *10 in.; and scale: 1 ksi = 6.895 MPa (1 in. = 25.4 mm).*

a along *T* *c* along *W*	K_a (*K* along Crack Depth *a*)			K_c (*K* along Crack Length *c*)		
Crack Depth Ratio, *a*/*T*	Newman and Raju [*15*, *22*] Effective *K*, ksi$\sqrt{in.}$	New Weight Function Effective *K*, ksi$\sqrt{in.}$	New Weight Function "Simulated Hole" Effective *K*, ksi$\sqrt{in.}$	Newman and Raju [*15*, *22*] Effective *K*, ksi$\sqrt{in.}$	New Weight Function Effective *K*, ksi$\sqrt{in.}$	New Weight Function "Simulated Hole" Effective *K*, ksi$\sqrt{in.}$
0.1	1.5067	1.4502	1.5200	1.3773	1.3674	1.4503
0.15	1.7454	1.6775	1.7649	1.5568	1.5393	1.6429
0.2	1.9224	1.8475	1.9525	1.6882	1.6638	1.7876
0.3	2.1885	2.1011	2.2455	1.8976	1.8577	2.0259
0.4	2.4027	2.3077	2.5148	2.0886	2.0473	2.2826
0.5	2.5981	2.4955	2.7911	2.2841	2.2518	2.5888
0.6	2.7883	2.6781	3.0953	2.4926	2.4775	2.9623
0.7	2.9789	2.8597	3.4325	2.7177	2.7264	3.4185
0.8	3.1715	3.0447	3.8020	2.9606	2.9968	3.9638
0.9	3.3650	3.2312	4.1895	3.2207	3.2924	4.6035
1.0	3.5557	3.4070	4.5861	3.4955	3.5992	5.3526

TABLE 4—*Comparison of effective* K *values for "corner crack at a hole" with* (a/c) = *2.0, under far-field uniform tensile stress of 1 ksi: hole radius,* R = *1.25 in.; thickness,* T = *2.5 in.; width,* W = *10 in.; and scale: 1 ksi = 6.895 MPa (1 in. = 25.4 mm).*

a along T, c along W	K_a (K along Crack Depth a)			K_c (K along Crack Length c)		
Crack Depth Ratio, a/T	Newman and Raju [15, 22] Effective K, ksi$\sqrt{\text{in.}}$	New Weight Function Effective K, ksi$\sqrt{\text{in.}}$	New Weight Function "Simulated Hole" Effective K, ksi$\sqrt{\text{in.}}$	Newman and Raju [15, 22] Effective K, ksi$\sqrt{\text{in.}}$	New Weight Function Effective K, ksi$\sqrt{\text{in.}}$	New Weight Function "Simulated Hole" Effective K, ksi$\sqrt{\text{in.}}$
0.2	1.6119	1.5366	1.5931	1.7557	1.6761	1.7826
0.3	1.8636	1.7766	1.8530	1.9882	1.8961	2.0351
0.4	2.0493	1.9535	2.0547	2.1611	2.0571	2.2329
0.5	2.1988	2.0960	2.2272	2.3078	2.1920	2.4123
0.6	2.3271	2.2183	2.3850	2.4438	2.3163	2.5914
0.7	2.4423	2.3281	2.5351	2.5766	2.4378	2.7803
0.75	2.4966	2.3799	2.6082	2.6432	2.5003	2.8453
0.8	2.5493	2.4302	2.6804	2.7106	2.5615	2.9837
0.9	2.6513	2.5275	2.8205	2.8483	2.6878	3.2031
1.0	2.7502	2.6217	2.9524	2.9914	2.8175	3.4377

excellent agreement with the NR results for all the a/c and a/T ratios considered with differences of 5% or less. This gives another verification of the present work for corner cracks under nonlinear stress gradients.

The problem of corner cracks at a hole was also analyzed using a "simulated hole" method. A quarter elliptical crack is considered at a plate corner that is subjected to a known "ahead-of-circular hole" stress distribution (Eq 13). This stress profile is used as the new stress, σ_{new}, in Eqs 11 and 12 to determine the effective K_a and K_c values. Results obtained in this way are called the "simulated hole" corner crack analyses, and are included in Tables 2 through 4. It could be seen that the simulated hole concept leads to the effective K values that are in very good agreement with the NR solution, but only for the smaller a/T ratios. As the crack size increases, relative to the hole radius, the "simulated hole" K values become much larger than the "corner crack at a hole" K values by Newman and Raju [37,15,22] as well as by the present work. Therefore, the "simulated hole" approximation for corner crack at holes is appropriate only for smaller crack sizes, relative to the hole radius.

Conclusions

The work presented here is a more rigorous improvement of the existing methods for determining weight functions under any general two-dimensional stress gradients on elliptical cracks in three-dimensional structural components. The resulting K solutions compare extremely well with widely accepted results by Newman and Raju [15,22,31,37] for elliptical surface, subsurface, and corner cracks in plates under tension and bending loads. Corner cracks at holes provided additional verification of the computed K values using the "simulated hole" technique for severely nonlinear stress gradients at circular holes.

The weight functions developed here also provide a systematic and self-consistent method for computing crack surface opening displacement fields, by using know reference K solutions for a given loading condition, which are at times needed to calibrate experimental data for part-through surface and corner cracks. The developed method could be included in any residual life prediction code for fatigue crack propagation in structural components.

Acknowledgment

Partial funding for this work was provided by the GE Aircraft Engines' (GEAE) IR&D Program. Discussions and comments on this work by R. H. Van Stone of GEAE are acknowledged. Finally, this paper is dedicated to the memory of author's parents.

References

[1] Petroski, H. J. and Achenbach, J. D., *Journal of Engineering Fracture Mechanics*, Vol. 10, 1978, pp. 257–266.
[2] Mattheck, C., Morawietz, P., and Munz, D., *International Journal of Fracture*, Vol. 23, 1983, pp. 201–212.
[3] Grebner, H. and Strathmeier, U., *Engineering Fracture Mechanics*, Vol. 22, 1985, pp. 1–7.
[4] Bethge, K., Munz, D., and Stamm, H., *Fatigue and Fracture of Engineering Materials and Structures*, Vol. 11, No. 7, 1988, pp. 467–482.
[5] Perez, R., Ray, S. K., and Grandt, A. F., Jr., *Engineering Fracture Mechanics*, Vol. 28, 1987, pp. 283–291.
[6] Perez, R., Grandt, A. F., Jr., and Saff, C. R. in *Surface-Crack Growth: Models, Experiments, and Structures, STP 1060*, W. G. Reuter, J. H. Underwood, and J. C. Newman, Jr., Eds., American Society for Testing and Materials, Philadelphia, 1990.
[7] Cruse, T. A. and Besuner, P. M., *Journal of Aircraft*, Vol. 12, 1975, pp. 369–375.
[8] Besuner, P. M. in *Mechanics of Crack Growth, ASTM STP 590*, American Society for Testing and Materials, Philadelphia, 1976, pp. 403–419.

[9] Fett, T., Mattheck, C., and Munz, D., *International Journal of Fracture*, Vol. 40, 1989, pp. 307–313.
[10] Cruse, T. A., Meyers, G. J., and Wilson, R. B., *Flaw Growth and Fracture, (Tenth Conference), ASTM STP 631*, American Society for Testing and Materials, Philadelphia, 1977, pp. 174–189.
[11] Gorner, F., Mattheck, C., and Munz, D., *Zeitschrift Werkstofftechnik*, Verlag Chemie Gmbh Weinheim, FRG, Vol. 14, 1983, pp. 11–18.
[12] Muller, H. M., Muller, S., Munz, D., and Neumann, J., *Fracture Mechanics: Seventeenth Volume, ASTM STP 905*, J. H. Underwood, R. Chait, C. W. Smith, W. A. Anderson, and J. C. Newman, Eds., American Society for Testing and Materials, Philadelphia, 1986, pp. 625–643.
[13] Mahmoud, M. A., *Engineering Fracture Mechanics*, Vol. 30, 1988, pp. 735–746; and Vol. 36, 1990, pp. 389–395.
[14] Banks-Sills, L., *Fracture Mechanics: Nineteenth Symposium, ASTM STP 969*, American Society for Testing and Materials, Philadelphia, 1988, pp. 620–636.
[15] Newman, J. C., Jr., and Raju, I. S., *Fracture Mechanics: Fourteenth Symposium, Volume I: Theory and Analysis, ASTM STP 791*, J. C. Lewis and G. Sines, Eds., American Society for Testing and Materials, Philadelphia, 1983, pp. I281–I296.
[16] Vainshtok, V. A. and Varfolomeyev, I. V., *International Journal of Fracture*, Vol. 35, 1987, pp. 175–186.
[17] Vainshtok, V. A. and Varfolomeyev, I. V., *Engineering Fracture Mechanics*, Vol. 34, 1989, pp. 125–136.
[18] Raju, I. S., Atluri, S. N., and Newman, J. C., Jr., *Fracture Mechanics: Perspectives and Directions (Twentieth Symposium), ASTM STP 1020*, R. P. Wei and R. P. Gangloff, Eds., American Society for Testing and Materials, Philadelphia, 1989, pp. 297–316.
[19] Yang, C-Y. in *Fracture Mechanics: Nineteenth Symposium, ASTM STP 969*, T. A. Cruse, Ed., American Society for Testing and Materials, Philadelphia, 1988, pp. 657–668.
[20] Polch, E. Z., Cruse, T. A., and Huang, C., *Computational Mechanics*, Vol. 2, 1987, pp. 253–267.
[21] Zhao, W., Wu. X. R., and Yan, M. G., *Engineering Fracture Mechanics*, Vol. 34, 1989, pp. 593–607 and 609–624.
[22] Newman, J. C., Jr., and Raju, I. S. in *Computational Methods in the Mechanics of Fracture*, S. N. Atluri, Ed., North Holland Publishing, Amsterdam, 1986, pp. 312–334.
[23] Schijve, J., *Engineering Fracture Mechanics*, Vol. 22, 1985, pp. 49–58.
[24] Yau, J. F., *Fracture Mechanics: Seventeenth Volume, ASTM STP 905*, J. H. Underwood, R. Chait, C. W. Smith, D. P. Wilhelm, W. A. Andrews, and J-C. Newman, Jr., Eds., American Society for Testing and Materials, Philadelphia, 1986, pp. 601–624.
[25] Pickard, A. C. in *The Application of 3-Dimensional Finite Element Methods to Fracture Mechanics and Fatigue Life Prediction*, Engineering Materials Advisory Services Limited, Wailey, West Midlands, U.K., 1986, pp. 81–116.
[26] Gang, C. Z. and Xing, Z., *Engineering Fracture Mechanics*, Vol. 32, 1989, pp. 419–441.
[27] Wu, X. R., *Engineering Fracture Mechanics*, Vol. 20, 1984, pp. 35–49.
[28] Moraweitz, P., Mattheck, C., and Munz, D., *International Journal of Numerical Methods in Engineering*, Vol. 21, 1985, pp. 1487–1497.
[29] Green, A. E. and Sneddon, I. N., *Proceedings*, Cambridge Philosophical Society, Vol. 47, 1950, pp. 159–164.
[30] Fett, T., *International Journal of Fracture*, Vol. 36, 1988, pp. 55–69.
[31] Raju, I. S. and Newman, J. C., Jr., *Fracture Mechanics: Nineteenth Symposium, ASTM STP 969*, T. A. Cruse, Ed., American Society for Testing and Materials, Philadelphia, 1988, pp. 43–55.
[32] Cruse, T. A. in *The Surface Crack: Physical Problems and Computational Solutions*, J. L. Swedlow, Ed., American Society of Mechanical Engineers, New York, 1972, pp. 153–170.
[33] Cruse, T. A., *Fracture Mechanics: Nineteenth Symposium, ASTM STP 969*, T. A. Cruse, Ed., American Society for Testing and Materials, Philadelphia, 1988, pp. 19–42.
[34] Raju, I. S., Newman, J. C., Jr., and Atluri, S. N., "Crack-Mouth Displacements for Semielliptical Surface Cracks Subjected to Remote Tensile and Bending Loads," in this volume, pp. 19–28.
[35] Shah, R. C. in *Mechanics of Crack Growth, ASTM STP 590*, American Society for Testing and Materials, Philadelphia, 1976, pp. 429–459.
[36] Kobayashi, A. S., Polvanich, N., Emery, A. F., and Love, W. J., *ASME Journal of Engineering for Power*, Vol. 98, 1976, pp. 465–472.
[37] Raju, I. S. and Newman, J. C., Jr., *Fracture Mechanics (Eleventh Conference), ASTM STP 677*, C. Smith, Ed., American Society for Testing and Materials, Philadelphia, 1979, pp. 411–430.
[38] Timoshenko, S. P. and Goodier, J. N., *Theory of Elasticity*, McGraw Hill, New York, 1970, pp. 90–95.

David Ritchie,[1] Cees W. M. Voermans,[1] Mike Bell,[2] and Jan F. deLange[2]

The Application of Line Spring Fracture Mechanics Methods to the Design of Complex Welded Structures

REFERENCE: Ritchie, D., Voermans, C. W. M., Bell, M., and deLange, J. F., "**The Application of Line Spring Fracture Mechanics Methods to the Design of Complex Welded Structures,**" *Fracture Mechanics: Twenty-Second Symposium (Volume II), ASTM STP 1131*, S. N. Atluri, J. C. Newman, Jr., I. S. Raju, and J. S. Epstein, Eds., American Society for Testing and Materials, Philadelphia, 1992, pp. 113–131.

ABSTRACT: Fracture mechanics-based fatigue crack growth prediction methods based on the line spring technique are presented. Developments in the line spring method are described that make it possible to apply the method to realistic welded structures for fatigue design studies. The line spring finite element described in the paper has been formulated to fit between isoparametric brick elements in order to allow shell-to-shell junctions to be represented more accurately. The effect of stress concentrations at weld toes has been also introduced. The accuracy of the line spring approach for the calculation of stress-intensity factors is demonstrated by comparison with three-dimensional finite element fracture mechanics results and empirically estimated values. Prediction of fatigue crack growth in girth welds and tubular connections is compared with observations of cracking in large-scale test specimens. An example of how the fatigue crack growth prediction methods could be applied to the design of welded joints is presented.

KEY WORDS: fatigue (materials), fracture mechanics, finite elements, line spring method, welds, steels, offshore structures, tubular connections

This paper presents fracture mechanics-based fatigue crack growth prediction methods based on the line spring technique. Developments in the line spring method described in the paper make it possible to apply the method to realistic welded structures for fatigue design studies.

Cracking in welded structures is associated generally with local notch-like detail at shell or plate junctions. The finite element [*1*] described in the paper has been formulated to fit between isoparametric brick elements in order to allow shell-to-shell junctions to be more accurately represented. The effect of stress concentrations at weld toes has been also introduced.

The line spring method was originally applied to surface cracks in plates by Rice [*2,3*]. The basis of the method is to represent the compliance of a surface crack in terms of distributed spring stiffnesses coupled to a shell or plate analysis of a structure. The method was extended to Modes II and III [*4*] and was used to formulate a finite element for use with shell elements [*5*]. This type of analysis has been shown to give accurate results, particularly for longer deeper cracks [*1,6,7*] that alter the stiffness of a joint and redistribute stresses in the structure.

[1]Research engineer and research assistant, respectively, Shell Research, Arnhem, The Netherlands.
[2]Students, respectively, Technical University, Delft, The Netherlands.

The accuracy of the line spring approach, both for the calculation of stress-intensity factors and prediction of fatigue crack growth development, is demonstrated for girth welds and tubular connections.

The paper also presents an example of how the methods could be applied to the design of welded tubular connections of the type used in offshore structures.

Formulation of the Line Spring Element

The form of the line spring element is shown in Fig. 1. The relationship between the generalized loads, Q_j, and the relative displacement of the faces at any point, $\overline{q}_i$, can be represented by a compliance relationship

$$\overline{q}_i = C_{ij}Q_j \tag{1}$$

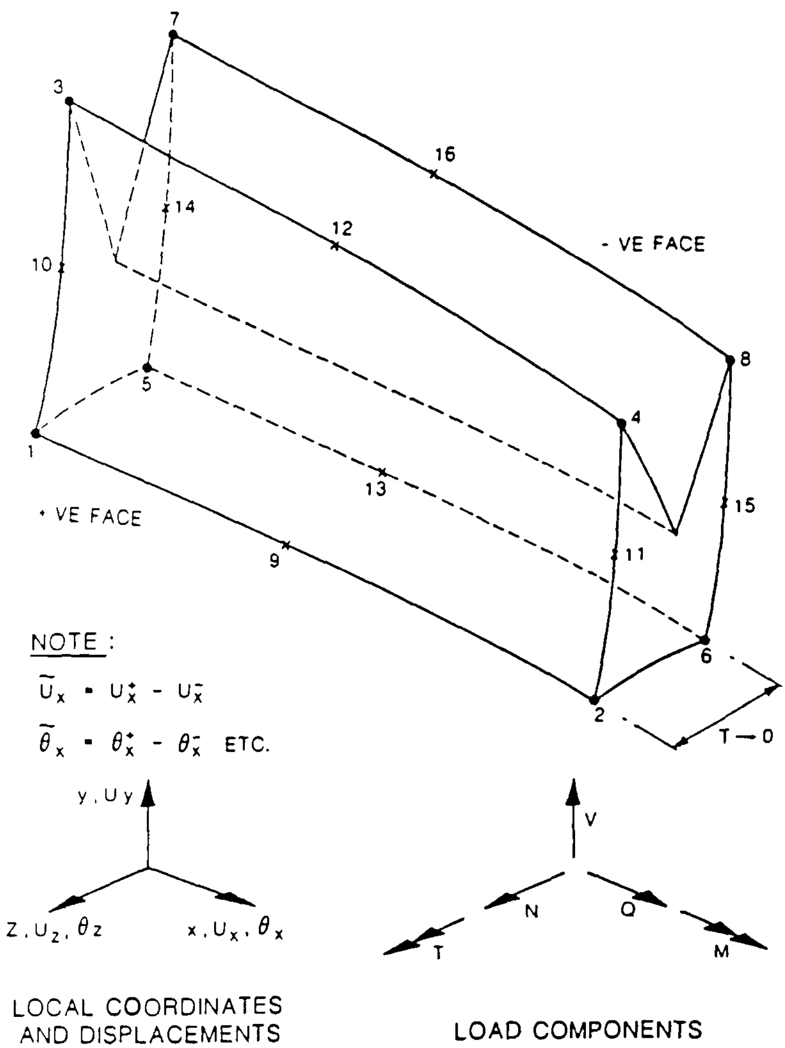

FIG. 1—*Diagram of the line spring finite element.*

The complimentary strain energy, Ω, of the spring can be used to calculate the relative displacements of the crack face by using Castigliano's theorem, that is

$$\bar{q}_i = \frac{\partial \Omega}{\partial Q_i} \tag{2}$$

The complimentary strain energy is related to the strain energy release rate with respect to crack depth, a, as follows

$$J = \frac{\partial \Omega}{\partial a} \tag{3}$$

Integrating Eq 3 with respect to crack depth, a, and substituting the result into Eqs 1 and 2 gives

$$\bar{q}_i = \int_0^a \frac{\partial \Omega}{\partial Q}\, da \tag{4}$$

Modes I, II, and III stress-intensity factors for conditions of plane strain are directly related to the strain energy release rate, that is

$$J = \frac{(K_{\mathrm{I}}^2 + K_{\mathrm{II}}^2)}{E'} + \frac{K_{\mathrm{III}}^2}{2G} \tag{5}$$

where $E' = E/(1 - \mu^2)$.

Substitution of Eq 5 into Eq 4 allows the compliance coefficients to be extracted [*3*]. Mode I can be separated from Modes II and III. Although Modes II and III are coupled, Desvaux [*4*] showed that Modes II and III may be decoupled, and that shear and torsion effects in Mode III can be separated, without any significant loss in accuracy. The result is to reduce the number of compliance coefficients that are necessary to be calculated.

The expressions for stress-intensity factors, used to calculate the strain energy release rate were taken from Ref *8*.

The relative displacements across the element can be related to the nodal displacements by an equation of the form

$$\{\bar{u}\} = [B]\,\{U_i\} \tag{6}$$

The matrix, B, is based on the interpolation functions for the faces of quadratic isoparametric elements [*9*]. In addition to 20-noded solid elements, 15-noded wedge elements are also compatible with the line spring element. Inverting the compliance functions (Eq 1) gives an equation of the form

$$\{Q\} = [S]\,\{\bar{u}\} \tag{7}$$

The stiffness matrix, $[K]$, can be derived by taking Eqs 6 and 7 and using them to calculate the work produced by virtual displacements over the length, l, of the element

$$[K] = \int_0^l [B]^T\,[S]\,[B]ds \tag{8}$$

A typical fatigue crack growth prediction requires several calculations of the stress-intensity factor over the life of the crack. For this reason, the element was not implemented as part of the finite element package, but has been introduced into a post-processing analysis program. The post-processing program is called FRACTEL, and it inserts the line spring elements into the finite element stiffness matrix after all unnecessary degrees of freedom not associated directly with the crack face have been eliminated. The reduction of the stiffness and load matrices can be carried out by any suitable finite element analysis program that generates substructures.

Recovery of the stress-intensity factors is from the stress-intensity factor equations used to calculate J (Eq 5) after the stress resultants have been calculated from the nodal displacements from the solution of the reduced stiffness matrix.

Crack Extension

Crack extension is calculated normal to the surface of the shell. The stress-intensity factors used to calculate the extension of the crack were the values calculated at the element junctions. The stress-intensity factors at the element junctions were interpolated linearly from the element midlength values, which in turn were a linear interpolation from the values calculated at the Gaussian integration points in each element. Surface values of the stress-intensity factors were calculated by extrapolation from the nearest adjacent midlength and element junction values. The surface values of the stress-intensity factors are not used to calculate the growth of the crack along the surface. Extension along the surface was instead calculated by extrapolation of the subsurface crack profile by a parabolic function, as shown in Fig. 2.

In the case where a crack has partially grown across an element, as shown in Fig. 2, the stress-intensity factors over the entire crack front are interpolated between the two cases shown in Fig. 2, described as the inner and outer profiles. Both the inner and outer profiles end at element junctions. Line spring elements outside the crack are held closed. The profiles in the end elements of the inner and outer crack cases are quadratic, and based on the slopes at Points A and B for the inner and outer profiles, respectively. Interpolation of all the stress-intensity factors over the crack front, between the inner and outer cases, is linear and is with respect to the position of the extrapolated profile on the surface in relation to the positions of the inner and outer cases.

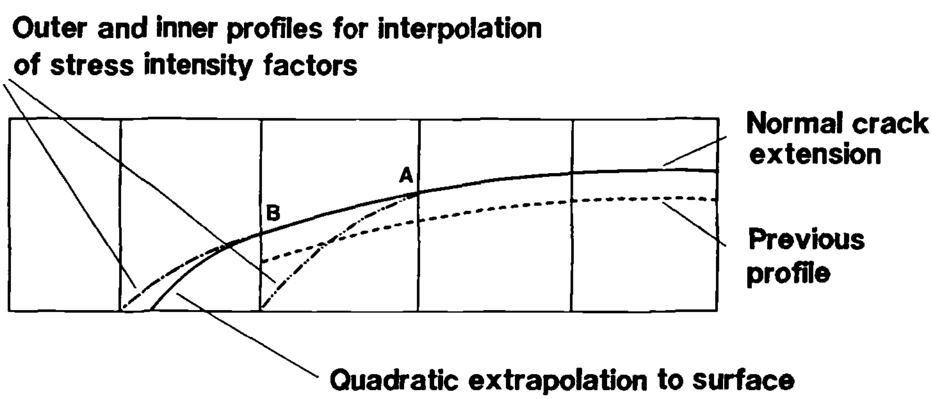

FIG. 2—*Estimation of crack extension.*

Influence of Weld Toe Stress Concentrations

The stress-intensity factors used to estimate the compliance functions do not include the influence of the local weld toe stress fields. The approach used in the paper is to introduce the effect of the stress concentration into the calculation of the stress-intensity factors from the spring stress resultants by means of superposition principles [10]. An advantage of the superposition method is that for stress concentrators with a width less than the shell thickness, the influence of the stress concentration is independent of the shell thickness.

Fatigue Crack Growth Predictions

Thickness Transition Girth Welded Joints

The thickness transition girth weld is a common type of joint in tubular structures. It is used in offshore structures to connect thinner brace or leg members to thicker walled tubes at node connections.

Stress-intensity factors for uniform depth surface cracks in the joint shown in Fig. 3 were calculated using three-dimensional finite element subdivisions with collapsed isoparametric quarter-point solid elements to represent the crack tip. The stress intensities were calculated from the crack face displacements. The finite element model for the line spring analysis is shown in Fig. 4. The reduced load and stiffness matrices were calculated using the MARC finite element package. Comparison between the three-dimensional finite element analysis results and the line spring analysis is shown in Fig. 5. The results compared to within 8% at the center of the crack. The stress-intensity factors were normalized with respect to the nominal extreme fiber bending stress in the thinner cylinder at the joint. The nominal bending stress was calculated from simple bending theory, and does not include the effects of secondary bending due to shell stiffness mismatch, or local notch stresses. The upturn in the stress-intensity factor distribution close to the end of the crack is due to the transition from a straight uniform depth crack front to the arc-shaped profile as the crack front approaches

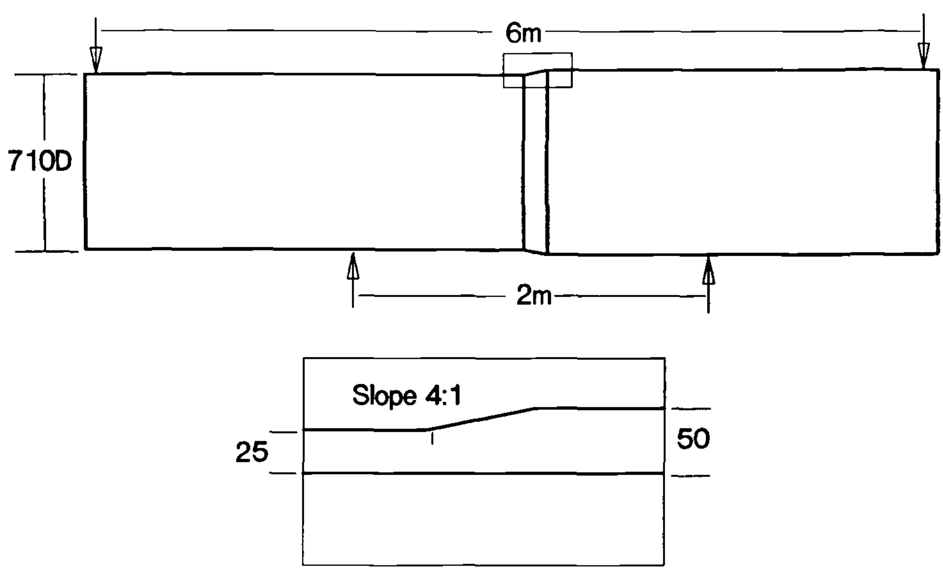

FIG. 3—*A cylinder with a thickness transition girth weld under four-point bending.*

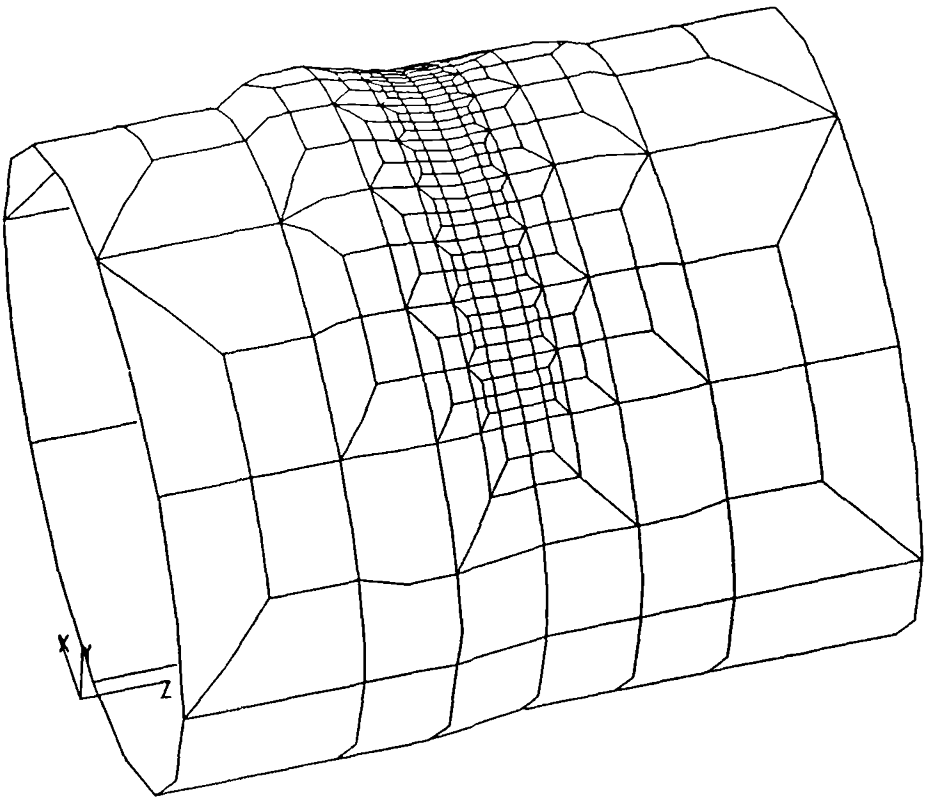

FIG. 4—*Finite element model of the thickness transition girth weld.*

the surface. Although the line spring technique is not intended to represent surface cracks in the area where the crack front meets the surface, the line spring method gave a fair representation of the stress-intensity factor distribution. This region is also a difficult area for three-dimensional finite element fracture mechanics, because the actual elastic singularity loses the square root form assumed in the collapsed quarter-point isoparametric elements used in the analysis.

The thickness transition joint shown in Fig. 3 was a large-scale test joint used to validate the fatigue crack growth method. During the test, fatigue cracking initiated at the weld toe in the thinner shell on the outside of the joint, due to the local bending of the shell produced by the external thickness transition. Fatigue crack development during the test was measured by beachmarking at regular intervals [7], that is, marking the crack front by applying periods of fatigue loading with reduced amplitude.

The first beachmark contained two overlapping cracks that eventually joined into a single crack. Taking the first beachmark as a single crack as the starting point, fatigue crack growth was calculated over the crack front until the point at which the crack penetrated the wall. Comparison between the predicted and observed crack shape development showed the influence of the overlapping crack in Fig. 6. Crack growth was retarded at the overlap, in comparison with the development of the single crack.

Crack growth rates were calculated from the beachmarks, and stress-intensity factors were in turn estimated from the growth rates. Several fatigue crack growth rate correlations were

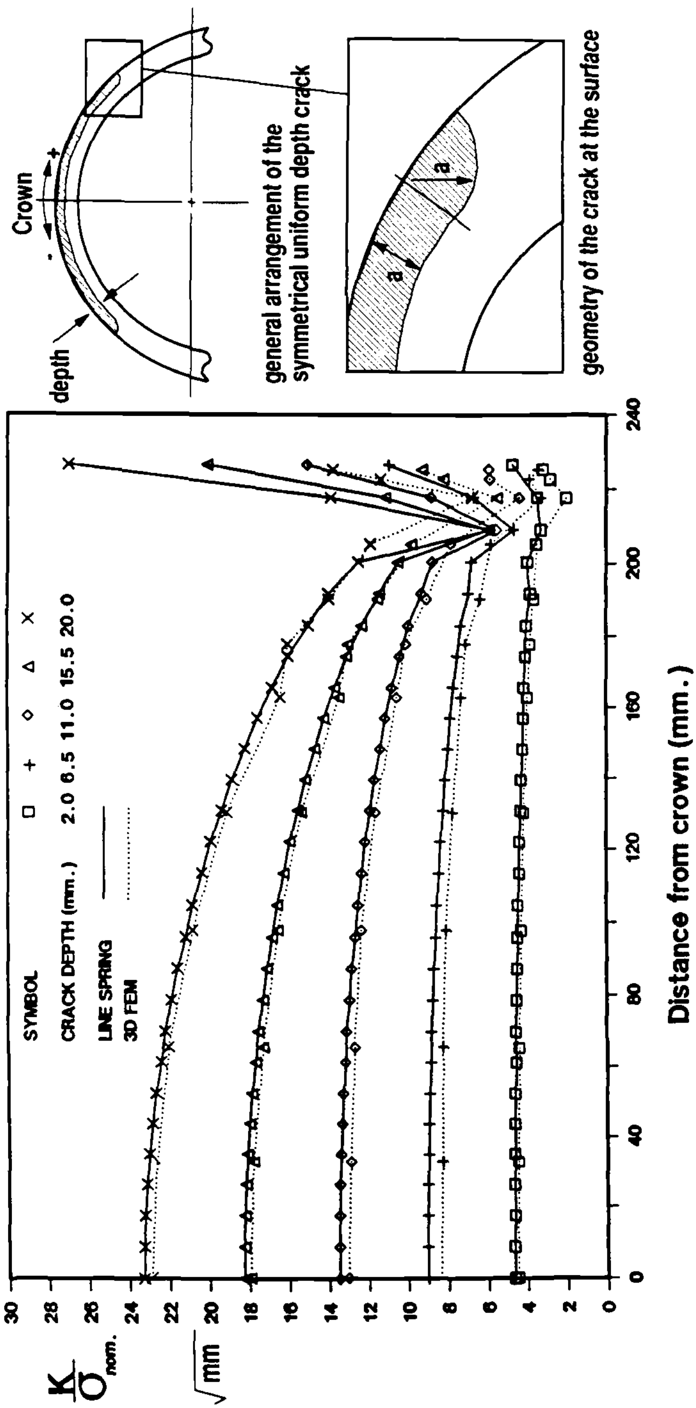

FIG. 5—*Comparison between three-dimensional finite element solutions and line spring results for uniform depth surface cracks.*

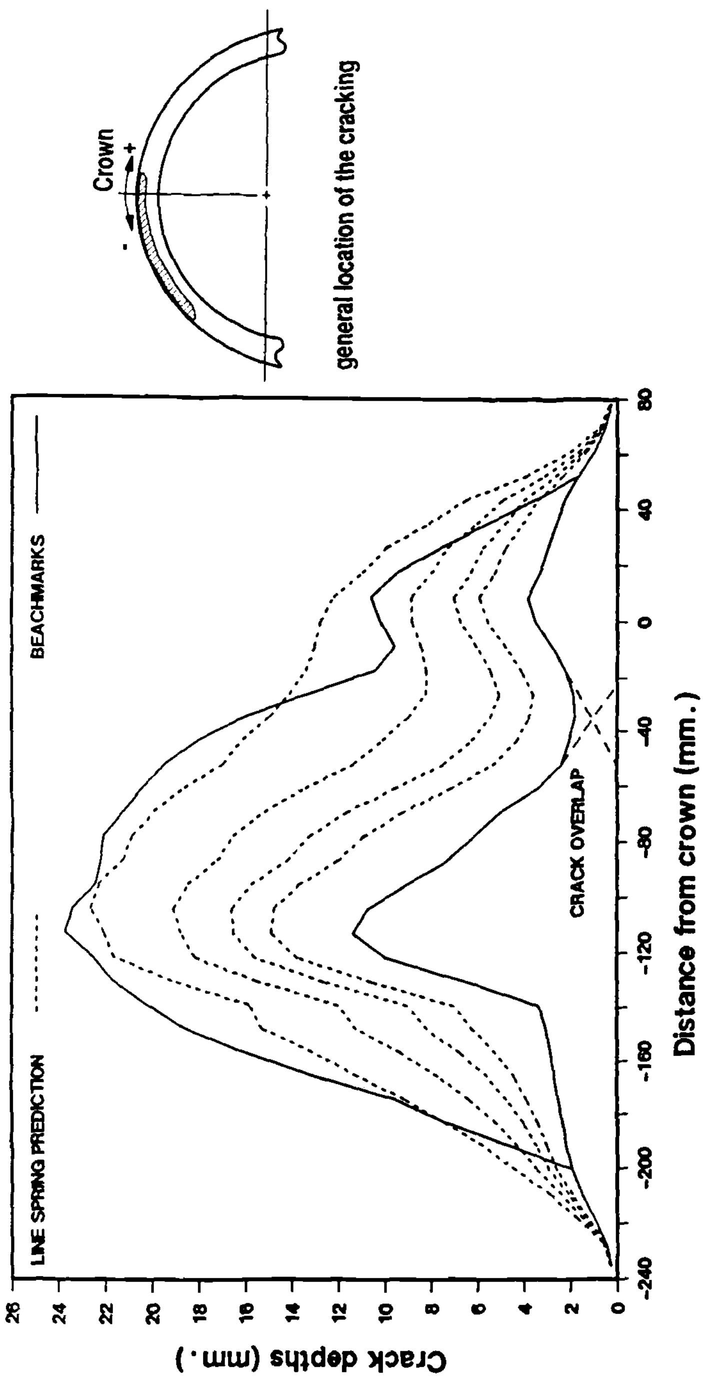

FIG. 6—*Comparison between observed and predicted crack growth in the thickness transition girth joint.*

found in the literature for the material used to fabricate the joint [*11–14*]. Comparison between the line spring results and the experimentally estimated distribution of stress-intensity factors shown in Fig. 7 is typical of the agreement for all the beachmark profiles.

Crack Growth in Tubular Connections

Stress-Intensity Factors—Crack growth in three tubular joint connections has been analyzed and compared with predictions made using the FRACTEL post-processing program. The joints were T [*15*], Y, and K connections loaded under axial loading of the brace, as shown in Fig. 8. Test joints of a similar type have been used to develop empirical *S-N* design rules for offshore structures [*16*]. The joints were all laboratory test joints in which crack growth had been measured by beachmarking.

Stress-intensity factors were calculated using three-dimensional finite element fracture mechanics for the cracks observed in the T-joint [*17*]. Crack growth rates in the T-joint were also used to estimate stress-intensity factors, and a typical comparison between line spring FRACTEL results, three-dimensional finite element results, and empirically estimated stress-intensity factors is shown in Fig. 9. Figure 9 shows the distribution of stress-intensity factors along the front of a particular crack observed in the chord of the joint. The cracking originated at the saddle point, as shown in Fig. 8, which is the area of highest combined local shell bending and membrane stresses.

The line spring mesh for the Y-joint is shown in Fig. 10, and is typical of the meshes used for the T- and K-joint. A typical comparison between line spring FRACTEL results and empirically derived stress intensity factors is also presented in Fig. 11 for the Y-joint. Figure 11 shows a typical distribution of stress-intensity factors along a particular crack profile observed in the joint. The cracking originated at the hot spot in the chord, the region where the combined local shell bending and membrane stresses are highest under the axial brace loads shown in Fig. 8. For a Y-joint, the hot spot lies between the crown and saddle positions. The main crack in the Y-joint was always accompanied by smaller side cracks that grew and coalesced with the main crack. The result of this was to produce a crack profile that has a low angle with respect to the shell as it approaches the surface as shown in Fig. 12. The stress-intensity factor distribution shown in Fig. 11 suggests that the effect of the shallow angle is to produce a reduction in stress-intensity factor as the crack approaches the surface, in contrast with the sharp increases shown in Figs. 5 and 9, where the crack profiles were normal or close to normal at the surface. In Fig. 11, the highest stress-intensity factors are not at the deepest point of the crack.

Crack growth in the K-joint was governed by the coalescence of large overlapping cracks, which left large step marks over much of the depth. Comparison between stress-intensity factors estimated from the crack growth in the K-joint and line spring estimates for a single large nonoverlapped crack indicated that the delaying effect of the overlaps was similar to that observed in the thickness transition girth weld (see Fig. 6).

Crack Growth Predictions—In tubular connections, there is a large amount of local shell bending at the junction. Load shedding around the crack raises the stresses adjacent to the crack. Evidence can be seen on fracture surfaces that the high stresses at the ends of the crack promote the initiation of smaller cracks that grow and coalesce with the main crack. Initiation and coalescence of adjacent cracks generated by a main crack was represented in fatigue crack growth predictions by adding a shallow uniform depth crack on either side of the main crack.

Development of the crack in the T-joint is compared with line spring FRACTEL predictions in Fig. 13. Prediction of crack development in the Y-joint is also good, as shown in Fig. 12. In the case of the K-joint, the crack surfaces were heavily overlapped, and it was

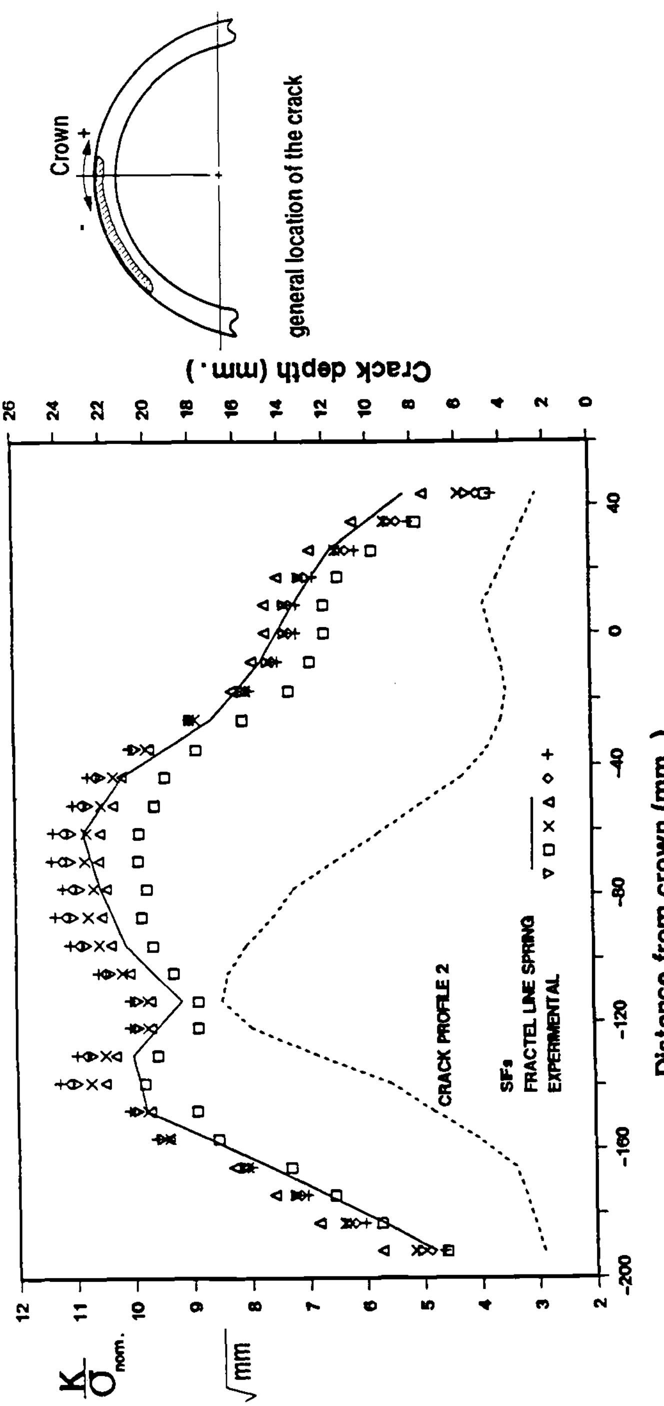

FIG. 7—*A typical stress intensity factor distribution over a crack in thickness transition joint.*

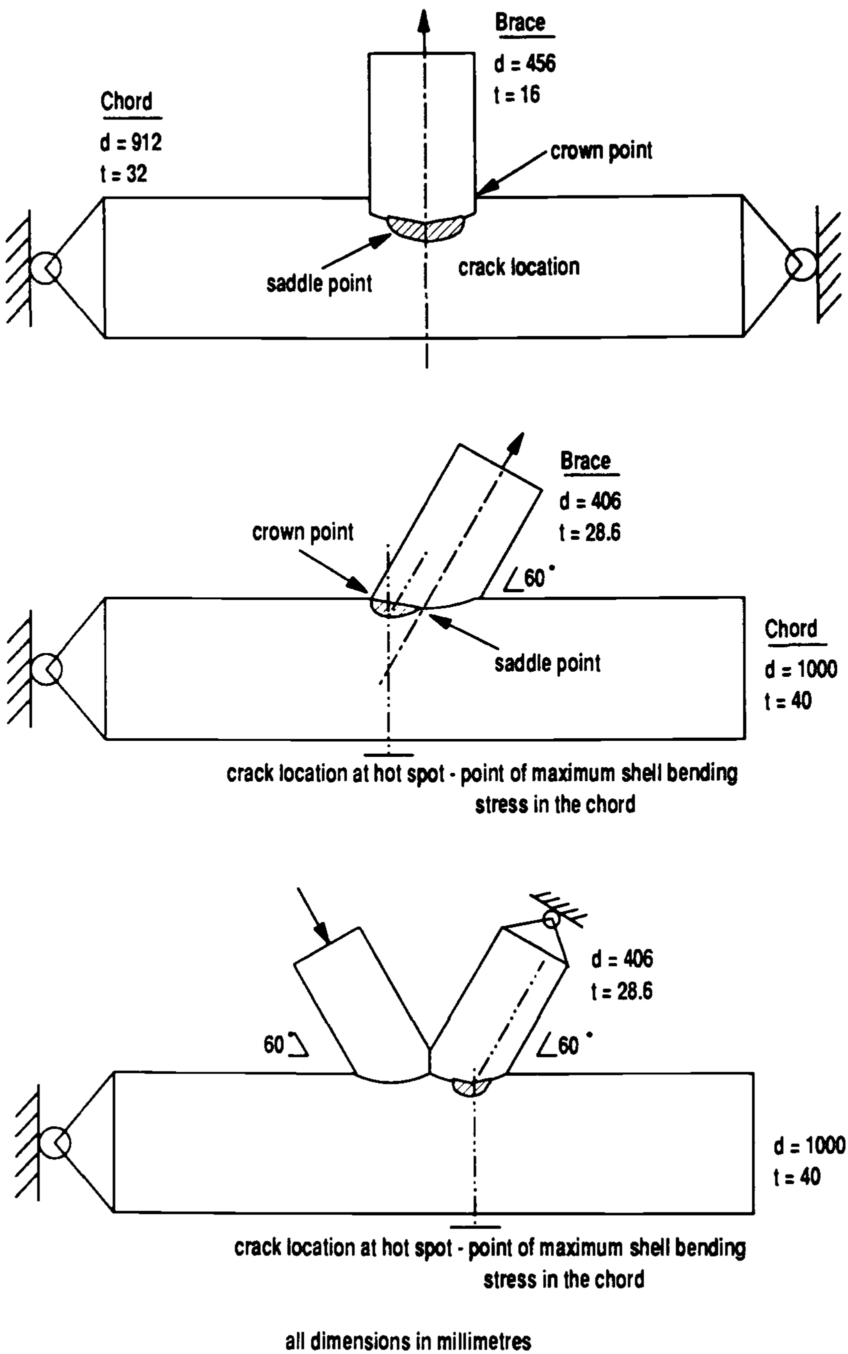

FIG. 8—*Dimensions of the T, Y, and K tubular joints.*

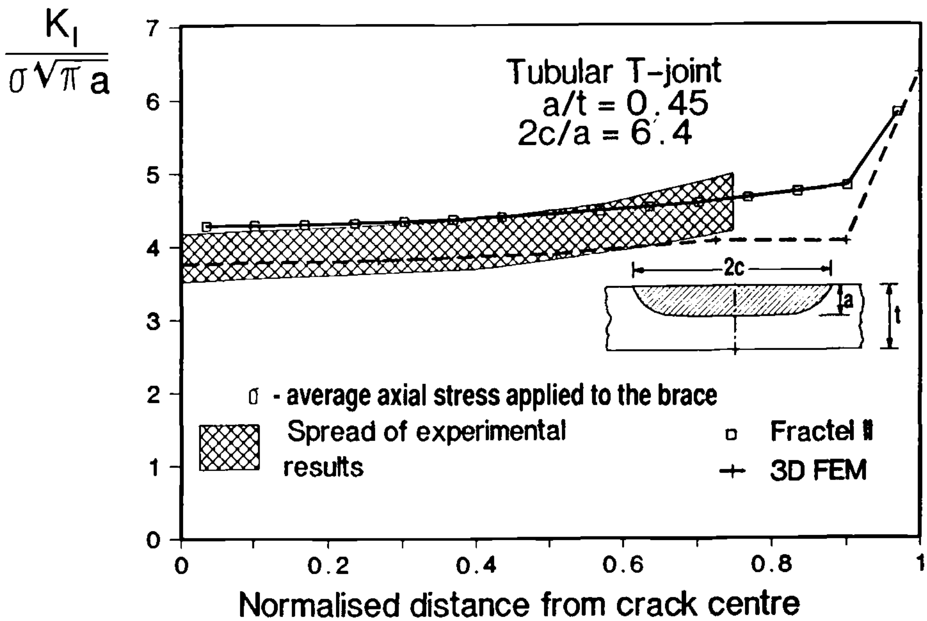

FIG. 9—*A typical comparison between three-dimensional finite element method, line spring, and empirical stress-intensity factor distributions in the T-joint.*

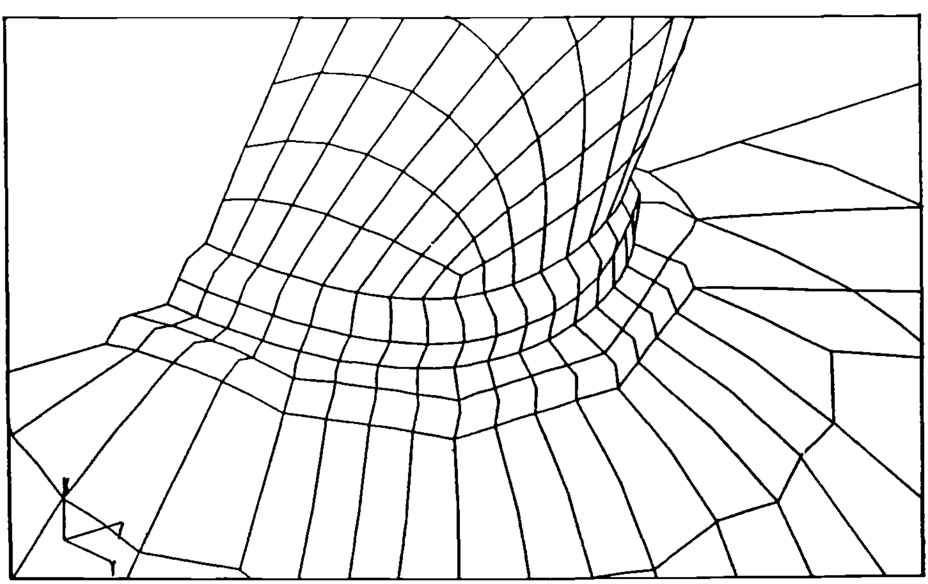

FIG. 10—*Finite element subdivision of the Y-joint.*

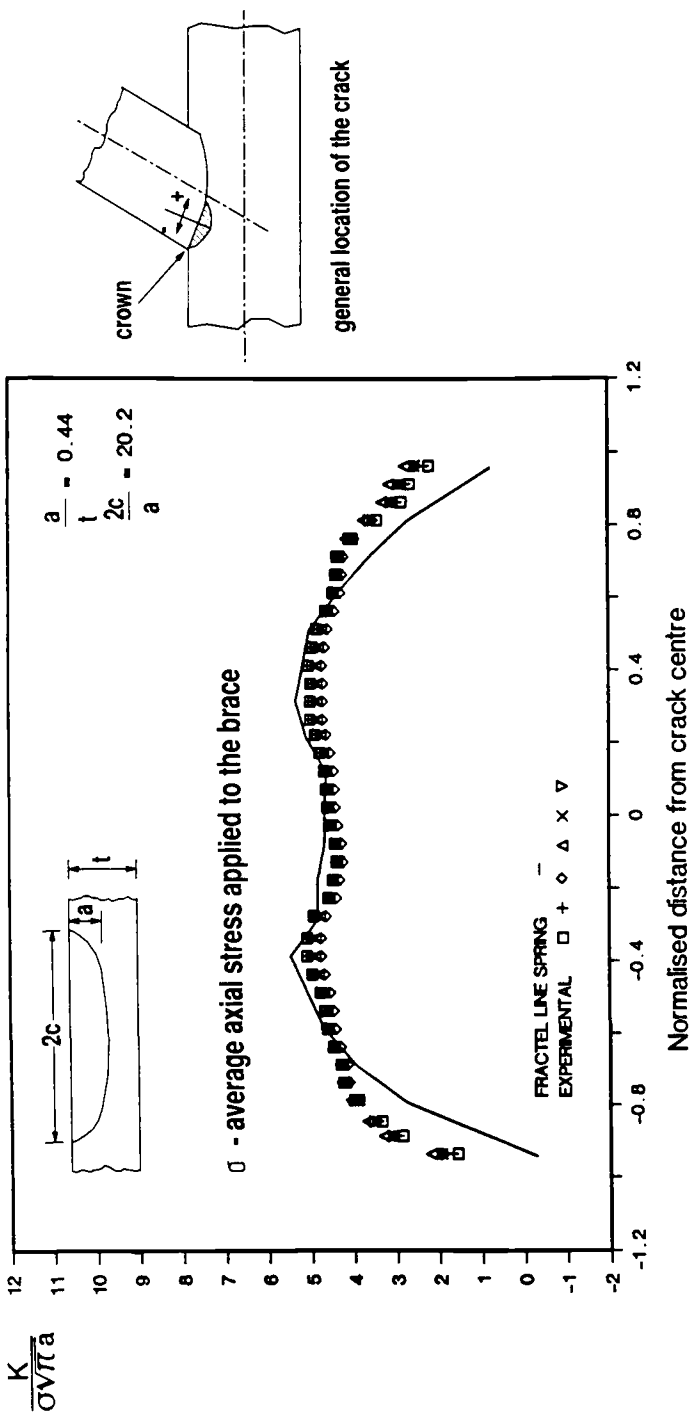

FIG. 11—*A typical agreement between stress-intensity factor distributions estimated from experiments and predicted by line spring methods.*

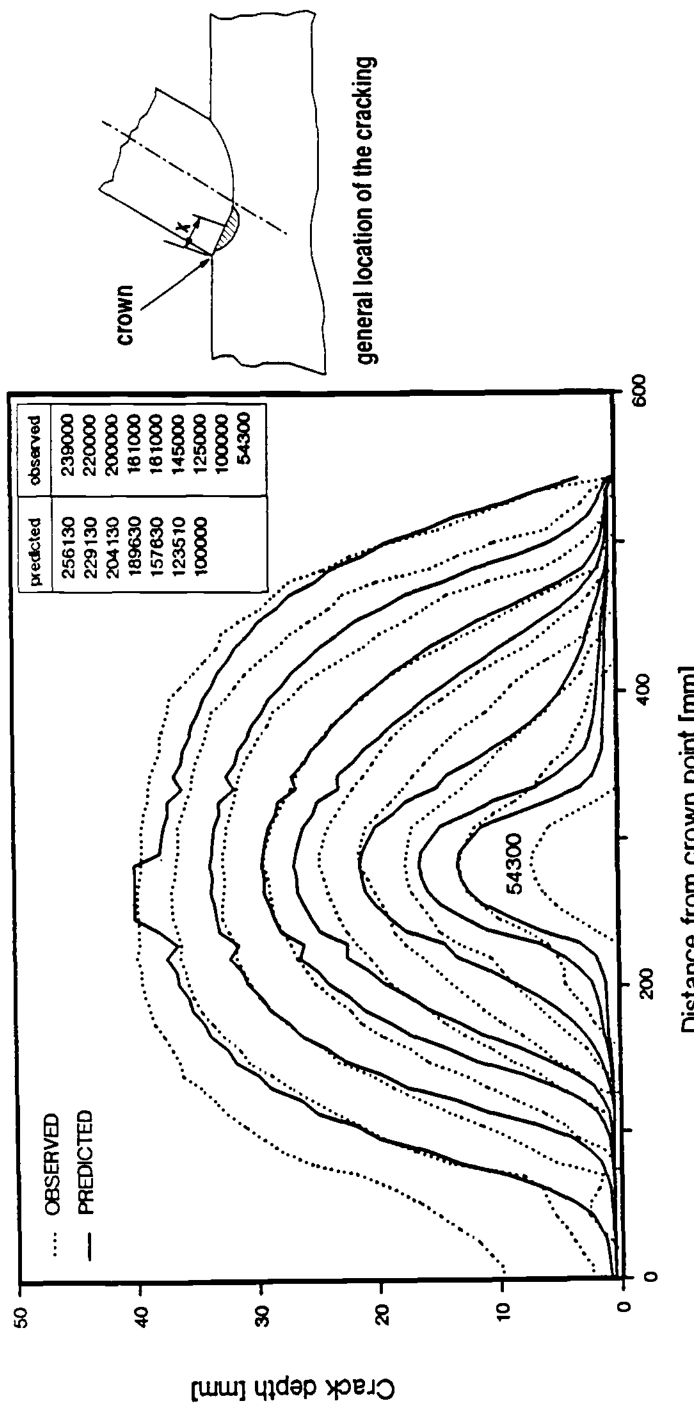

FIG. 12—*Comparison between observed and predicted crack growth in the Y-joint.*

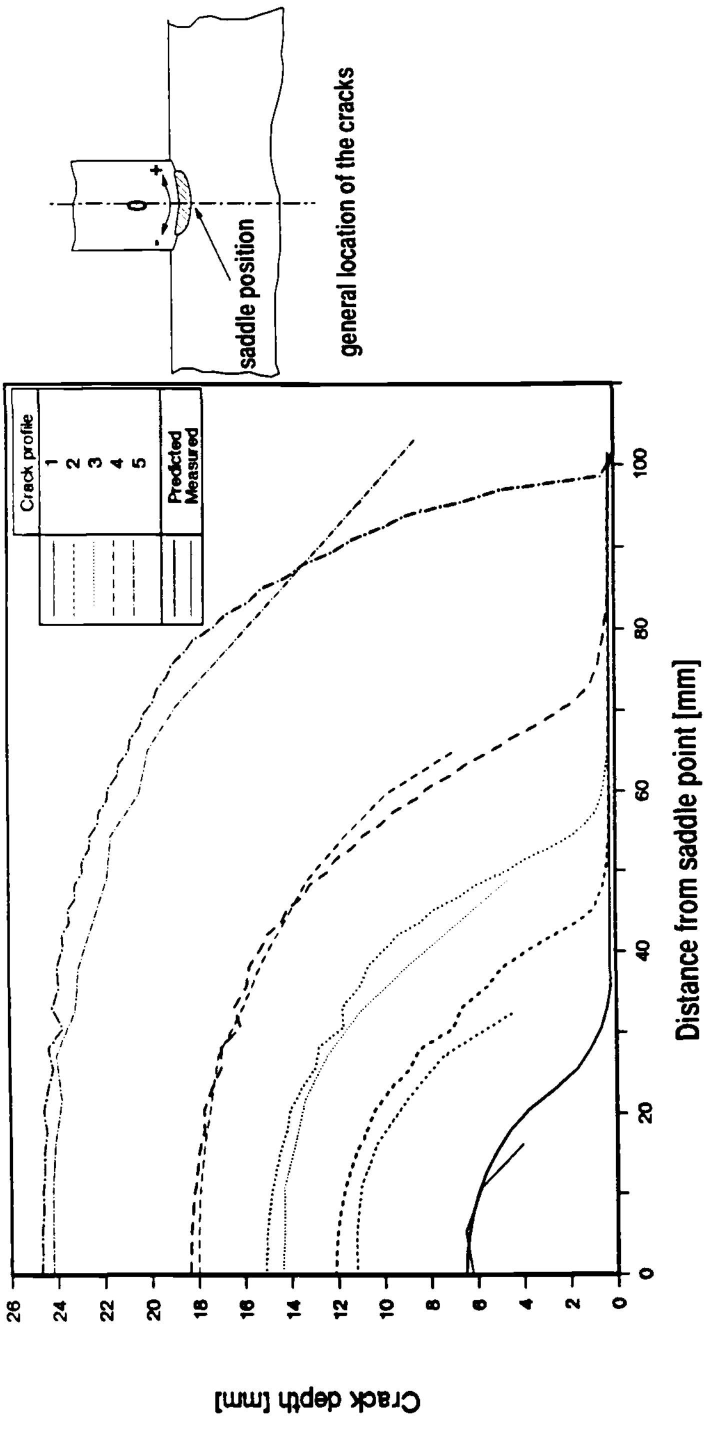

FIG. 13—*Comparison between observed and predicted crack growth in the T-joint.*

not possible to distinguish any consistent pattern of development, or find a clearly distinguishable beachmark that could be used as a starting defect for a crack growth calculation.

Prediction of the actual number of cycles for a crack to grow from an initial size to a final depth depends on the choice of the most appropriate fatigue crack growth correlation data. The scatter in the empirically derived stress-intensity factors shown in Figs. 9 and 11, when translated into crack growth predictions from a calculated stress-intensity factor, could result in a 60% spread in fatigue life predictions. The empirical stress-intensity factor correlation that most consistently agreed with the line spring predictions [11] was used to calculate fatigue crack growth in the T-, Y-, and K-joints.

Design Curves for Offshore Tubular Connections

The strength of fracture mechanics fatigue life prediction methods is that they allow the potential fatigue life to be related to initial defect sizes and local conditions, which in turn enables the specification of standards for local detail and preservice inspection necessary to achieve a minimum required life. Fracture mechanics crack propagation life prediction methods can therefore be used to design joints to be defect tolerant, either as an alternative or as a supplement to the traditional *S-N* methods.

The fatigue life of welded joints have a lower bound set by the behavior of a joint with a sharp weld angle and with a continuous defect. The lower limit to the fatigue life can be estimated for any initial depth of continuous defect. If a joint has even a natural radius at the weld toe, or local welding defects that are not continuous and are shallower than those used in the design life predictions, the joint will have a fatigue performance better than the predicted minimum. The simplest inspection criteria that could be applied to ensure that a weld will have a performance better than the minimum is therefore to ensure that the weld toe is not sharp and that the crack detection method can find continuous defects that exceed the defect size used in the design life predictions.

The most likely source of a continuous defect is a hydrogen crack in the heat-affected zone (HAZ) at the weld toe. Depths of such defects can be in the range of 1 to 2 mm, and for that reason, a 2-mm deep defect, together with a sharp weld toe [10], has been taken as a reasonable basis for the example design curve in this section.

Definition of the end of fatigue life as the point at which a fatigue crack penetrates the wall is used in many empirical design criteria, and is based on a simple experimental observation. In the case of tubular connections, crack growth can decelerate when the crack is about to penetrate the wall. The example shown in Fig. 14, for the T-joint, is a case where the final 12% of wall thickness took up almost 50% of the total crack propagation life. In selecting a defect size that defines the end point of the fatigue crack propagation life, consideration should be given to ductile fracture in thicker sections, and also to more practical considerations such as the difficulties and expense of making reliable repairs in service. Fatigue life curves for the T-, Y-, and K-joints were calculated for continuous defects 2 mm deep. The final crack depth was taken arbitrarily to be at 0.88 of the chord wall.

The fatigue crack growth rate data used to calculate the fatigue lives were that which was found to give consistently good agreement with the line spring stress-intensity factors [11]

$$da/dN = 1.42 \times 10^{-12}(\Delta K)^{2.71} \tag{9}$$

The preceding fatigue crack growth correlation was measured in air. In deriving a realistic design curve, a more appropriate fatigue crack growth correlation derived in cathodically protected seawater should be used. The fatigue crack growth correlation for air was used for comparison with the current *S-N* design rules, which are all based on endurance tests in air.

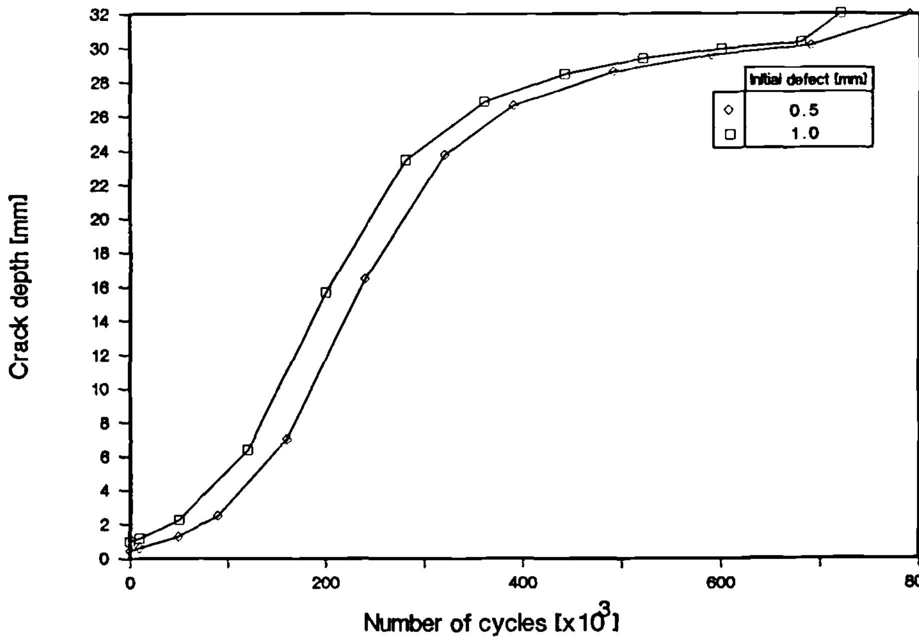

FIG. 14—*Crack growth through the thickness in the T-joint.*

Comparison with the U.K. Department of Energy design curve [*16*] is shown in Fig. 15. The Department of Energy design recommendations base the design of tubular joints on the maximum nominal local bending and membrane shell stresses at the weld, known as the hot-spot stresses, and use a nominal 32-mm wall thickness with a correction for the actual wall thickness. The slope of the fracture mechanics-based curves differ from the *S-N* design curve, due to the slope of the fatigue crack correlation data (Eq 9).

Discussion

Accurate prediction of the surface growth of a crack is necessary for prediction of its growth in depth. The reason is that surface length of a crack affects the stress-intensity factors at the deepest point. Under-prediction of surface growth can lead to nonconservative underestimation of fatigue life. Calculation of stress intensities at the intersection of a crack front with the surface is difficult, even with three-dimensional finite element fracture mechanics [*18*]. Many finite element solutions in this region show that conventional approaches using square root singularities cannot represent the actual singularity [*19*]. Study of the actual nonsquare root singularity in this region is mainly of academic interest, as a crack propagates along the surface by initiation of small side cracks due to high stresses being shed around the main crack. An approach to this problem has been made [*20*] by using *S-N* crack initiation data to predict the development of small side cracks of the order of 1 or 2 mm depth. However, the use, shown in this paper, of uniform depth cracks to represent initiation and growth of side cracks, also appears to be effective.

Another feature of multiple crack initiation was shown in the case of the K-joint, where the overlaps, by connecting the faces of a much larger cracked area, appeared to hinder the growth of the main overall crack. This feature of crack growth raises a question over whether the results of fatigue endurance tests are conservative.

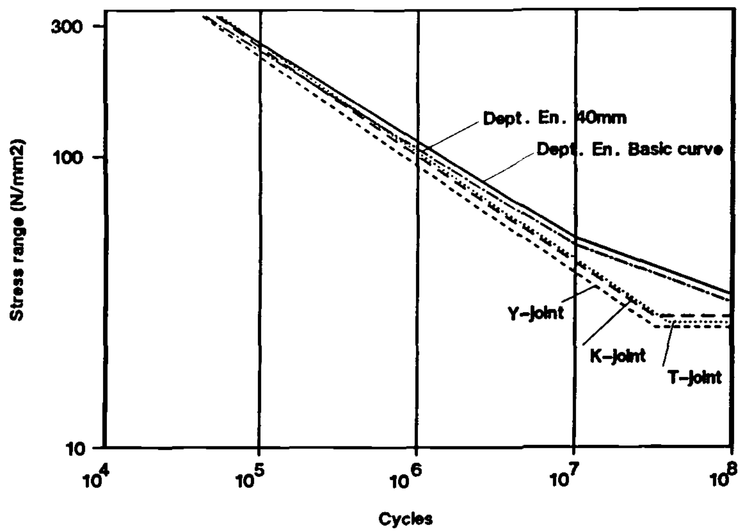

FIG. 15—*Comparison of fracture mechanics-based design curves and U.K. Department of Energy design rules. Fatigue endurance curves for offshore tubular joints.*

The example of derivation of design curves using the fracture mechanics approach requires further development before it can be used to produce general design rules. A wider range of geometries requires further study, and life estimates under random loading are required to check if constant-amplitude design curves could be used to predict fatigue under random loading. Fracture and repair should be considered as end points of the crack propagation life. The example indicates how a defect-tolerant design based on inspection methods could be developed for particular critical joints.

Conclusions

Experience with FRACTEL has shown that the application of line spring fracture mechanics as a post-processing exercise is highly economical, and that the accuracy of stress-intensity solutions is often comparable to three-dimensional finite element fracture mechanics.

Fatigue crack growth can be modeled satisfactorily in complex tubular joints using line spring fracture mechanics.

Further research is required on the prediction of initiation and coalescence of secondary cracking in welds during fatigue.

Acknowledgments

The authors wish to acknowledge the permission of the Shell International Petroleum Maatschapij, Norske Shell, and CONOCO to publish this work.

References

[1] Ritchie, D. and Nicholson, R. W. in *Proceedings*, Fifth International Conference on Numerical Methods in Fracture Mechanics, 23–27 April 1990, Freiburg, FRG, pp. 103–114.

[2] Rice, J. R., *Journal of Applied Mechanics*, Vol. 39, 1972, pp. 185–194.

[3] Rice, J. R. and Levy, N., *The Surface Flaw: Physical Problems and Computational Solutions*, J. L. Swedlow, Ed., American Society of Mechanical Engineers, New York, 1972.
[4] Desvaux, G. J., "The Line Spring Model for Surface Flaw, an Extension to Mode II and Mode III," M.Sc. thesis, Massachusetts Institute of Technology, Cambridge, MA, 1985.
[5] *ABAQUS Theoretical Manual*, Hibbet Karlson and Sorensen Inc., Providence, RI, 1981.
[6] Zhen-Zong, Du and Hancock, J. W., Elastic-Plastic Stress Analysis of Semi-Elliptical Cracks in a Tubular Welded Joint, *Proceedings*, Seventh International Conference on Fracture, Houston, 1989.
[7] Ritchie, D., "A Fatigue Crack Growth Model for Thickness Transition Girth Welds," International Conference on Behaviour of Offshore Structures, Trondheim, Norway, June 1988, pp. 1053–1064.
[8] Tada, H., Paris, P., and Irvin, G., *Stress Analysis of Cracks Handbook*, 2nd ed., Del Research Corp., St. Louis, MO, 1985.
[9] Zienkiewcz, O. C., *The Finite Element Method*, McGraw-Hill, New York, 1977.
[10] Ritchie, D., *International Journal of Fracture*, Vol. 30, R29–R32, 1986.
[11] Bristoll, P. and Roeleveld, J. A., "Fatigue of Offshore Structures: Effect of Seawater on Crack Propagation in Structural Steels," European Offshore Steels Research Seminar, Cambridge, U.K., 27–29 Nov. 1978.
[12] Gall, D. S. and Hancock, J. W., "Fatigue Crack Growth under Narrow Band Random Stationary Loading, Part 2," University of Glasgow, Glasgow, Scotland, 1983.
[13] Thorpe, T. J., "A Simple Model of Fatigue Crack Growth in Tubular Joints," Her Majesties Stationery Office, Report OTH 86 225, 1986.
[14] Maddox, S. J. and Gurney, T. R., "An Investigation of the Influence of Applied Stress Ratio on Fatigue Crack Propagation in Structural Steels," The Welding Institute, Sept. 1986.
[15] Noordhoek, C. and Verheul, A., "Comparison of the ACPD Method of In-Depth Fatigue Crack Growth Monitoring with the Crack Front Marking Technique," Dept. of Civil Engineering Report 6-84-13, Delft University of Technology, Delft, The Netherlands, 1984.
[16] "Background to New Fatigue Design Guidance for Steel Welded Joints in Offshore Structures," Department of Energy, London, U.K., 1983.
[17] Ritchie, D., Voermans, C. W. M., and Vollan, K., *Proceedings*, Fourth International Conference on Numerical Methods in Fracture Mechanics, San Antonio, 23–27 March 1987, pp. 715–726.
[18] Barsoum, R., *Proceedings*, Fifth International Conference on Numerical Methods in Fracture Mechanics, Freiburg, FRG, 23–27 April 1990, pp. 345–354.
[19] Rhee, H. C. and Salama, M. M., *Engineering Fracture Mechanics*, Vol. 28, No. 2, 1987.
[20] Bergez, D., Lebas, G., and Samier, P., *Proceedings*, Third International Conference on Steel in Marine Structures, Delft, The Netherlands, June 1987, pp. 941–949.

Nonlinear Fracture Mechanics and Applications

Mahyar S. Dadkhah,[1] *Albert S. Kobayashi,*[2] *and Winfred L. Morris*[1]

Crack-Tip Displacement Fields and J_R-Curves of Four Aluminum Alloys

REFERENCE: Dadkhah, M. S., Kobayashi, A. S., and Morris, W. L., "**Crack-Tip Displacement Fields and J_R-Curves of Four Aluminum Alloys,**" *Fracture Mechanics: Twenty-Second Symposium (Volume II), ASTM STP 1131*, S. N. Atluri, J. C. Newman, Jr., I. S. Raju, and J. S. Epstein, Eds., American Society for Testing and Materials, Philadelphia, 1992, pp. 135–153.

ABSTRACT: The J_R-curves associated with small crack growth in 0.8-mm-thick 2024-T3, 2024-0, 5052-H32 aluminum and 2091-T3 aluminum-lithium cruciform specimens and 2024-T3 and 2024-0 aluminum single-edge-notched (SEN) specimens are presented. The cruciform specimens were loaded uniaxially and biaxially. The J-integral values were determined directly through contour integration of the stresses and strains using deformation theory of plasticity and power hardening law. The strains were computed from the measured in-plane displacements that were determined experimentally using moiré interferometry. Path independency of the J-integral values were verified by the 5% scatter band for the near- and far-field Js. The J_R results differed substantially from the J-values computed by using the far-field formula of Shih, German, and Kumar. Also the measured crack-tip displacement and strain fields did not agree with the asymptotic solutions of Hutchinson, Rice, and Rosengren computed from the measured J-values. These findings suggest that the current formulas for J calculations may be incorrect and that J may not be a suitable parameter for characterizing the crack tip.

KEY WORDS: J_R-curves, HRR fields, elastic-plastic fracture, aluminum-lithium alloys, u and v displacement fields, ductile fracture, moiré interferometry, three-dimensional nonlinear region, fracture mechanics, fatigue (materials)

There are numerous theoretical and numerical models of the nonlinear plastic behavior at the crack tip: the Dugdale-Barenblatt cohesive zone model, the power law hardening model of Hutchinson, Rice, and Rosengren (HRR) [*1–4*], the finite deformation asymptotic analysis of Knowles and Sternberg [*5,6*], the micromechanical models such as the combination of the J-integral with local constraint (of Kordisch and Sommer) [7], and the continuum damage mechanics model that uses the flow function introduced by Gurson [*8–10*]. Along with high-speed computers have come numerous finite element models [*11–14*]. These models are based on assumed constitutive relationships of the material and attempt to predict the nature of the fracture process based on these assumptions. Such assumptions must be evaluated experimentally by comparing the analytical or numerical results generated by these models with the measured displacement and strain fields.

One of the most popular global ductile fracture criteria of the past two decades is the J-integral concept [*4*] for which enormous developmental efforts have been expended in recent years. The J-integral is heralded by many as a stable crack growth and a ductile

[1]Members of Technical Staff, Mechanics of Materials, Rockwell Science Center, Thousand Oaks, CA 91360.

[2]Professor, Department of Mechanical Engineering, University of Washington, Seattle, WA 98195.

fracture criterion since in its linearly elastic limit, it reduces to the elastic strain energy release rate. The path independency of the J-integral also provides the experimentalist with the convenience of determining the potential energy change due to an incremental crack extension by far-field measurements. The asymptotic analysis of a symmetrically loaded, mathematically sharp crack tip in a power law hardening material leads to a crack-tip field that is contained well within the plastic zone. This field, for plane strain, was given by Hutchinson [2] and Rice and Rosengren [3] and are collectively referred to as the HRR field. Analogous fields for the generalized plane stress, Mixed-Modes I and II plane strain, and Mode III are also known. Hutchinson [2] determined the near-crack-tip fields for plane stress with small-scale yielding. The resulting stresses and strains are singular at the crack tip for a strain hardening material, as no allowance is made for blunting in the analysis.

In addition, if one postulates a power hardening material and the existence of the HRR field [2,3], the crack-tip state can be then characterized by the J-integral. The amplitude of these fields are globally given solely in terms of the value of the local parameter, J, which can be determined by a line integral. Such convenience prompted the use of J-integral for correlating fatigue, creep, void growth, and stable crack growth data in addition to its role of quantifying the onset of ductile fracture. The inherent unloading process associated with crack growth in ductile material, however, violates the postulate of nonlinear elasticity on which the J-integral is founded [4]. Physically, the asymptotic fields cannot dominate too close to the crack tip, due to the effects of crack blunting and the finite geometry changes. Also Hutchinson's model, which is a two-dimensional formulation, does not account for the effects of finite sheet thickness on the deformation and stress fields near a crack tip in a thin elastic-plastic sheet. While a plane stress state exists at the surface of the plate, high stress triaxiality can build up at the midplane near the tip of the crack. In addition to the finite thickness, large geometry changes in the crack-tip region will modify the stress and displacement fields of Hutchinson's [1,2] singular solution. The only nonlinearity introduced into the theoretical derivation of the HRR field is in the stress-strain relationship, and the equations of equilibrium and the strain-displacement relationship are taken to be linear. Also, asymptotically, as the crack tip is approached, the contribution to the strains that depend linearly on stress are neglected compared to the power-law terms.

Extensive numerical analyses [11–13] showed that the J-integral is still a viable far-field parameter for determining the potential energy change under small crack extension and that the HRR field is a reasonable representation of the crack-tip state, where the asymptotic singular field dominates over a distance large in comparison to the crack-tip blunting and fracture process zone. Unfortunately, no comparable experimental verification of the preceding numerical analysis, with the exception of Ref *15* and those of the authors [16–18] exist to date.

The purpose of this study was to use the procedure, which was established previously [16–18], to provide the missing experimental verifications of the path independency of the J-integral and of the existence of an HRR field.

Calculation of Strain from Moiré Fringes

Moiré interferometry was used to record simultaneously the vertical and horizontal inplane displacements with stable crack growth in uniaxially and biaxially loaded aluminum alloys [19–21]. Figure 1 shows specimen configurations and J-integral paths and Table 1 shows the material properties, where σ_0, α, and n are the yield stress and the strain hardening parameters for the Ramberg-Osgood stress-strain relationship of $\varepsilon/\varepsilon_0 = \sigma/\sigma_0 + \alpha(\sigma/\sigma_0)^n$, where ε_0 is the yield strain. Since the moiré fringe patterns represent lines of constant surface displacements, conversion of the displacement field to the corresponding strain field is usually

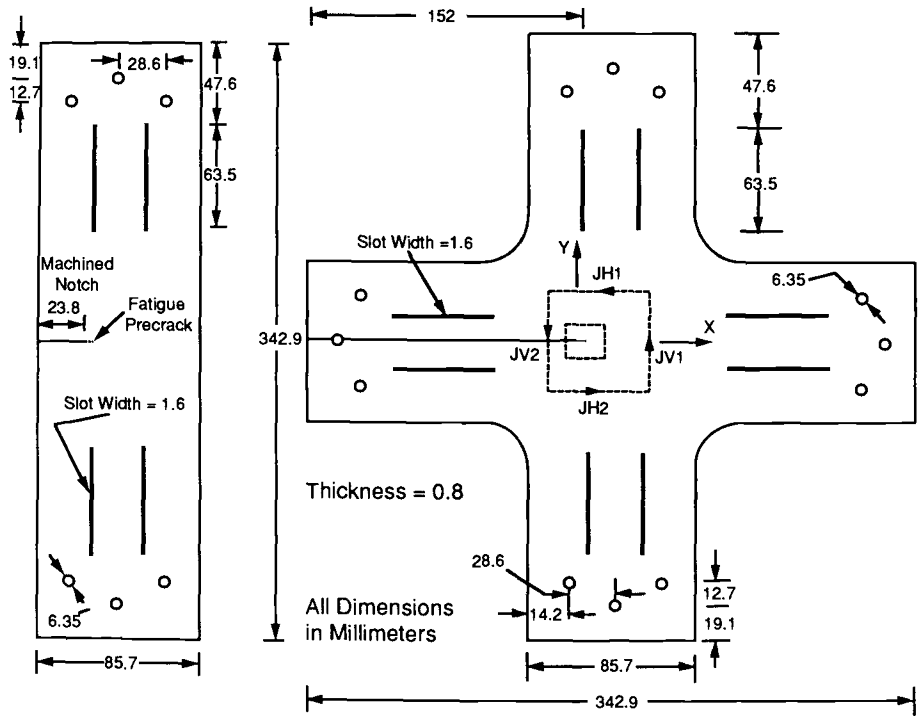

FIG. 1—*Specimen configurations and* J*-integral paths.*

desired. The various techniques that are used to perform this conversion can be grouped roughly into two categories; mechanical differentiation [22] and the displacement-field approach [23]. The method of data reduction used in this paper is based upon the displacement-field approach and is described next.

Data Reduction by the Displacement-Field Approach

The data reduction scheme used in the present study is an automated version of the displacement-field approach. The technique was automated through the use of digitizing equipment and a computer. The two primary pieces of equipment required were an HP ScanJet Plus Digitizer and a Macintosh II computer with a 80 MB hard disk drive and a 40 MB removable hard disk. The moiré patterns were first photographed with a 35 mm or 4 by 5 camera, and 203 by 254 mm (8 by 10 in.) photographic prints were prepared. Since

TABLE 1—*Mechanical properties.*

Aluminum and Al-Li	Yield Stress, σ_0 (MPa)	Modulus of Elasticity, MPa	α	n
2024-O	67	74 200	1.0	4
2024-T3	310	73 087	0.4	12
5052-H32	190	70 000	1.0	16
2091-T3	330	78 000	0.5	8

the area of specimen that was photographed was 25 by 25 mm (1.0 by 1.0 in.), the photographic prints represent a nominal optical magnification of ~ ×9 to ×10. A digital record of the moiré pattern is then obtained using the HP ScanJet Plus Digitizer. Scanning the moiré photographs at a resolution of 12 dots/mm (300 dots/in.); resulting in an effective resolution of about 106 to 118 dots/mm (2700 to 3000 dots/in.). Commercially available image processing software was used to edit the scanned image. The software permits viewing, filtering, and editing of the image at the pixel level. This allows the user to "clean up" any imperfections (such as dust particles and scratches) that appear in the image. Once the image is cleaned to an acceptable level, the image is stored on a disk or a disk backup. An example of the procedure is shown in Figs. 2*a* and *b*. Figure 2*a* shows the original photograph of a moiré pattern recorded for the *u*-displacements induced in an aluminum specimen subjected to a 38-MPa tensile stress. Although this is a high-quality moiré image, note the various scratches and dust particles present. This image was scanned and "filtered," resulting in the digital image shown in Fig. 2*b*.

After the digitization and filtering processes were completed, the moiré data were reduced numerically using two computer programs that were developed in-house, that is, MOIRE and STRREG. MOIRE is used to convert the moiré fringe patterns to strains. STRREG is then used to create a strain contour plot that can be displayed on a computer monitor or plotted using a graphics printer. Details of each program are given in the following sections.

The digitized moiré patterns created using the HP ScanJet Plus system are stored in a bit map file, which in essence contains pixel information for every point on the image. The original 645 mm^2 (1 in.^{2}) grating area is represented by 5 760 000 pixel points in the digitized image. MOIRE computes derivatives in either the horizontal or vertical directions. Normal strain, ε_x, is determined from the *u*-displacement image, that is, $\varepsilon_x = du/dx$; while ε_y is determined from the *v*-displacement image, that is, $\varepsilon_y = dv/dy$. Note that the shear strain, ε_{xy}, can be found by taking the derivatives du/dy and dv/dx and summing as $\varepsilon_{xy} = \frac{1}{2}(du/dy + dv/dx)$. The appropriate derivative is calculated using the fringe center locations of three adjacent fringes. For example, suppose the strain, $\varepsilon_x = du/dx$, is being calculated at Fringe N_i, whose center is located at Position x_i. The derivative is obtained using the fringes immediately to the left and right of Fringe N_i, that is Fringes N_{i-1} and N_{i+1}, and so the derivative, $\varepsilon_x = du/dx$, can be approximated as

$$\varepsilon_x = \frac{\Delta u}{\Delta x} = \left[\frac{1}{f}\frac{(N_{i+1} - N_{i-1})}{(x_{i+1} - x_{i-1})}\right]$$

where, f = virtual reference grating frequency.

Noting that

$$N_{i+1} - N_{i-1} = \pm 2$$

the preceding expression reduces to

$$\varepsilon_x = \left[\frac{1}{f}\frac{2^* \text{ scale}}{(x_{i+1} - x_{i-1})}\right]$$

where scale = scale factor added to account for the difference in size of the original specimen and the computer image.

Strains are calculated at the center of each fringe along the entire row (or column), for every row (or column) in the image. MOIRE evaluates "magnitudes" of strain. The program does not use the actual fringe number when calculating strain, but rather relative fringe

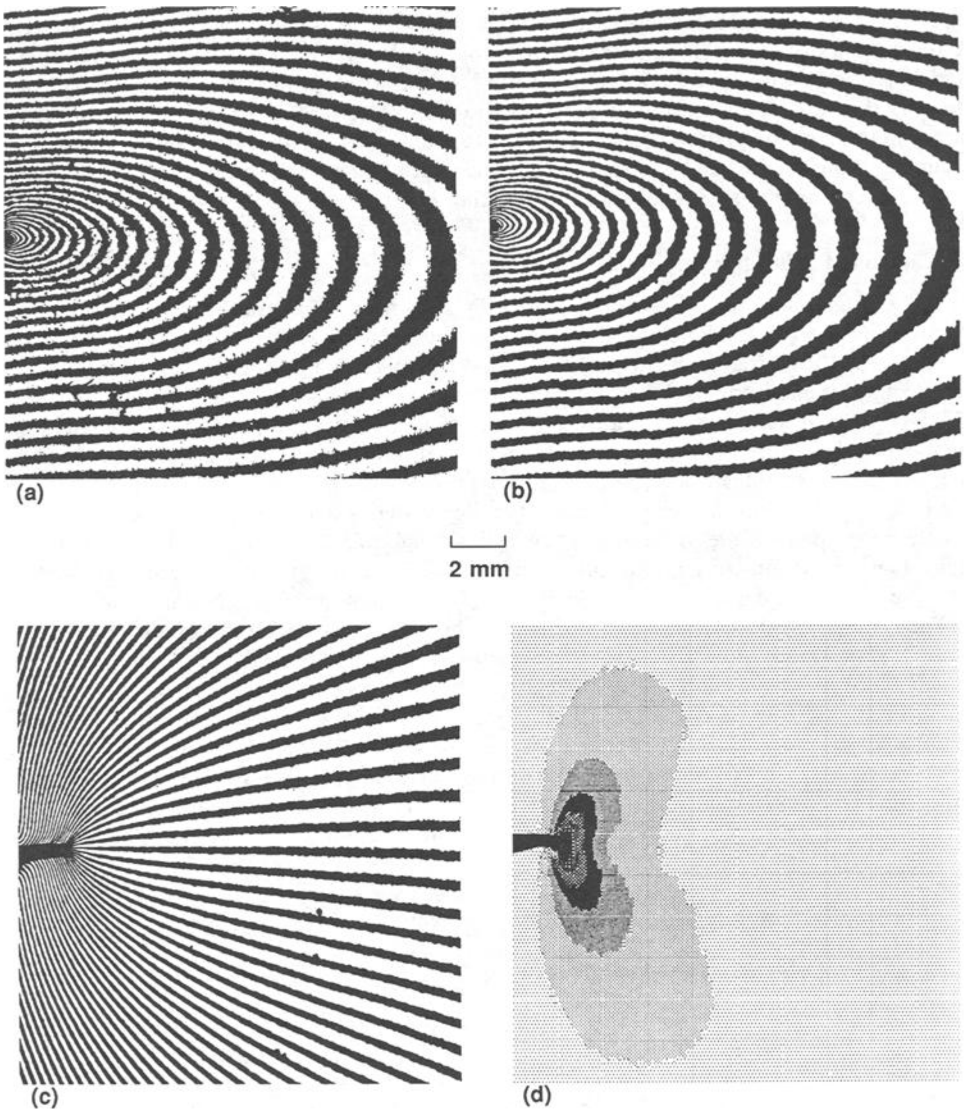

FIG. 2—*Steps required to obtain strain field from moiré fringe patterns:* (a) *original* u-*displacement field;* (b) *filtered and cleaned* u-*displacement field;* (c) *filtered* v-*displacement field; and* (d) *axial strain field map for the corresponding* v-*field.*

numbers, that is, the fringe locations, N_{i-1} and N_{i+1} used to calculate strains, ε_x or ε_y, at Fringe Number N_i.

The strain field map is generated using STRREG from a file that contains the x and y coordinates and either ε_x or ε_y, and from another file containing the maximum and minimum strain values. The total range of strain, as determined using the maximum and minimum strain values, is divided into eight intervals. A distinctive graphics pattern is assigned to each strain interval. Each calculated strain value and the corresponding x- and y-coordinates are read from the strain file. STRREG opens a graphics window in memory, which is slightly larger than the original moiré displacement photograph. The x- and y-coordinates are found in the graphics window. The corresponding graphics pattern is then assigned to that location and is plotted to the next coordinate location. If the local strain value has increased or decreased to a different strain interval, the graphics pattern is changed accordingly. The strain field map is stored in a MacPaint format, allowing for easy editing and printing. An example of the original and digitized moiré fringe pattern and the preceding approach, that is, the corresponding ε_y, is shown in Figs. 2*c* and *d*.

Calculation of *J*-Integral from Moiré Fringes

The evaluation of the J-integral is essentially a numerical integration along a loop encompassing the crack where the three strain components must be evaluated at identical points along the chosen path [*16–18*]. STRAIN calculates strains at fringe center locations, which may or may not be exactly on the chosen path. Thus, an interpolation program (INTRP), which calculates the strains at every pixel point along the contour in the computer image, was developed. The positions of the u and v displacement fields may not be identical in the two photographs, therefore, INTRP requires that offset values be entered relating the relative position of the "origins" in the two fields, that is, du/dx and du/dy are calculated for the given path, while dv/dx and dv/dy are calculated for a path on the v-displacement field that corresponds to the path taken on the u-displacement field. This process ensures that the numeric integration is using three components of strain from the same location.

The J-integral requires the strain components, the stress components, and the strain energy density. The three stress components are calculated using the J_2-deformation theory of plasticity for multiaxial states with a power hardening stress-strain relationship. A Newton-Raphson routine was used to solve the three coupled nonlinear constitutive equations. The strain energy density, W, is determined using the stress and strain components just calculated.

The J-measurement, which was derived for rectangular contours surrounding the crack tip, is divided into line integrals along the vertical and horizontal segments shown in Fig. 3. The integral value of J along the vertical segments is

$$J_V = \int_{V1}\left[W - \left(\sigma_{xx}\frac{\partial u}{\partial x} + \tau_{xy}\frac{\partial v}{\partial x}\right)\right]dy - \int_{V2}\left[W - \left(\sigma_{xx}\frac{\partial u}{\partial x} + \tau_{xy}\frac{\partial v}{\partial x}\right)\right]dy \quad (1)$$

and along the horizontal segments the value of J is

$$J_H = -\int_{H1}\left(\sigma_{yy}\frac{\partial v}{\partial x} + \tau_{xy}\frac{\partial u}{\partial x}\right)dx + \int_{H2}\left(\sigma_{yy}\frac{\partial v}{\partial x} + \tau_{xy}\frac{\partial u}{\partial x}\right)dx \quad (2)$$

$$J = J_V + J_H \quad (3)$$

Accuracy of this J-evaluation procedure was assessed by evaluating Eqs 1 and 2 along a closed contour, which did not enclose the crack tip, and was 0.4% of the corresponding J-value in this paper.

Results and Discussion

Displacement Fields

Figures 3*a* and *b* show a typical moiré fringe pattern corresponding to the simultaneous vertical and horizontal displacements, v and u, of an aluminum lithium (Al-Li) specimen. Figures 4 and 5 show plots of v and u versus the radial distance, r, at a crack-tip polar angle of $\theta = 45°$. For the power hardening exponent of $n = 8$ for 2091-T3 aluminum-lithium

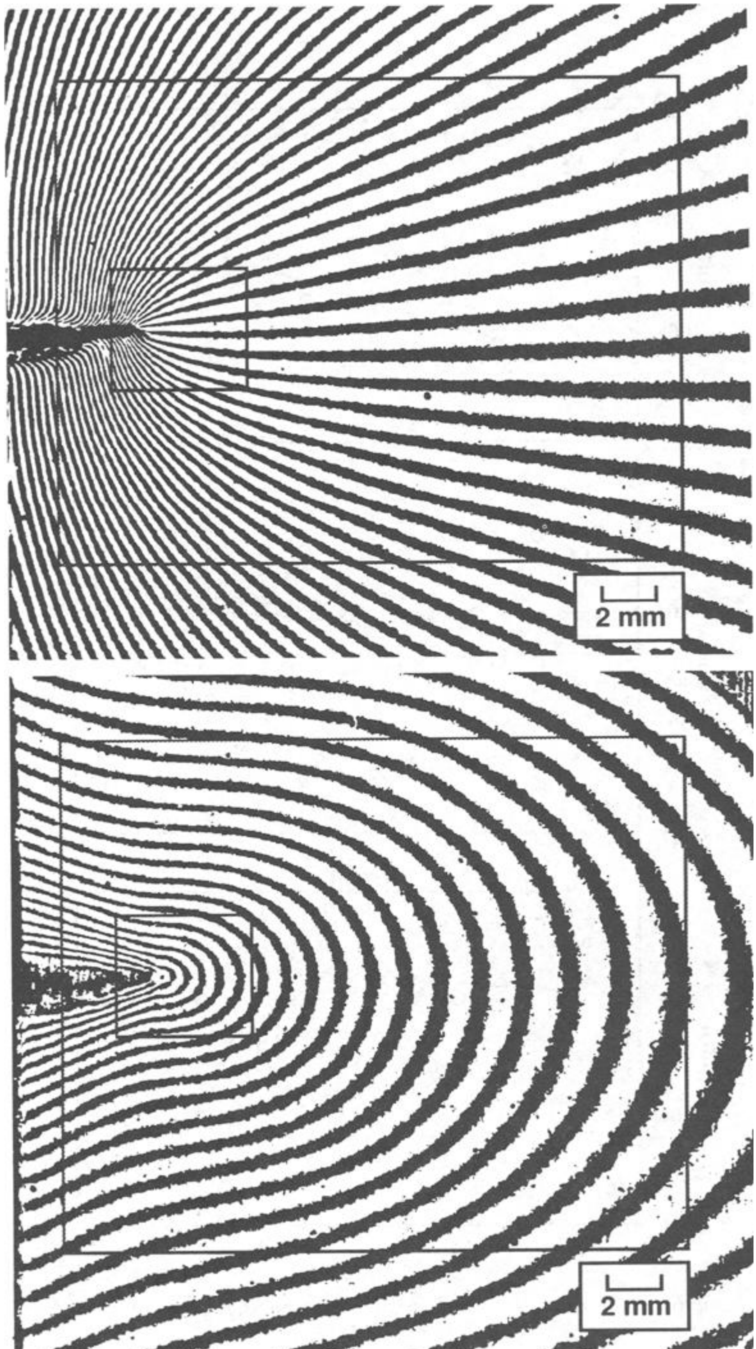

FIG. 3—*Simultaneous moiré fringe patterns of the vertical and horizontal displacements,* v *and* u, *of 2091-T3 Al-Li.*

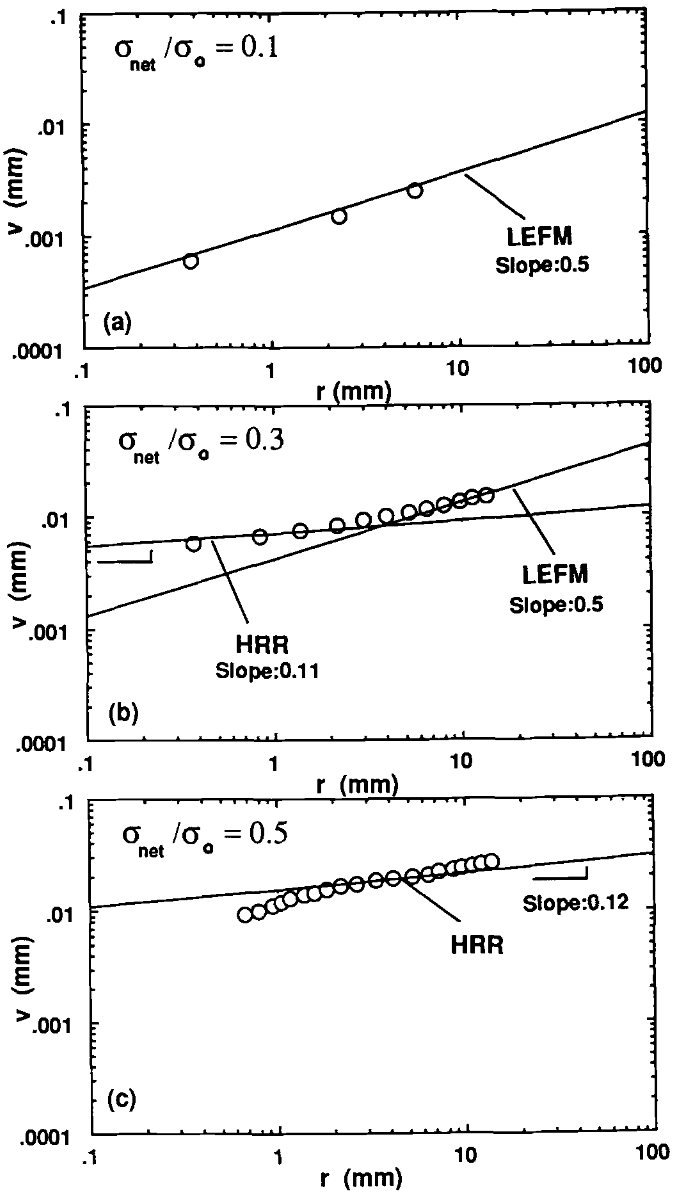

FIG. 4—*Comparison of the* v*-displacement variation from moiré experiment with LEFM and HRR predictions at different load levels at* $\theta = 45°$ *for 2091-T3 Al-Li.*

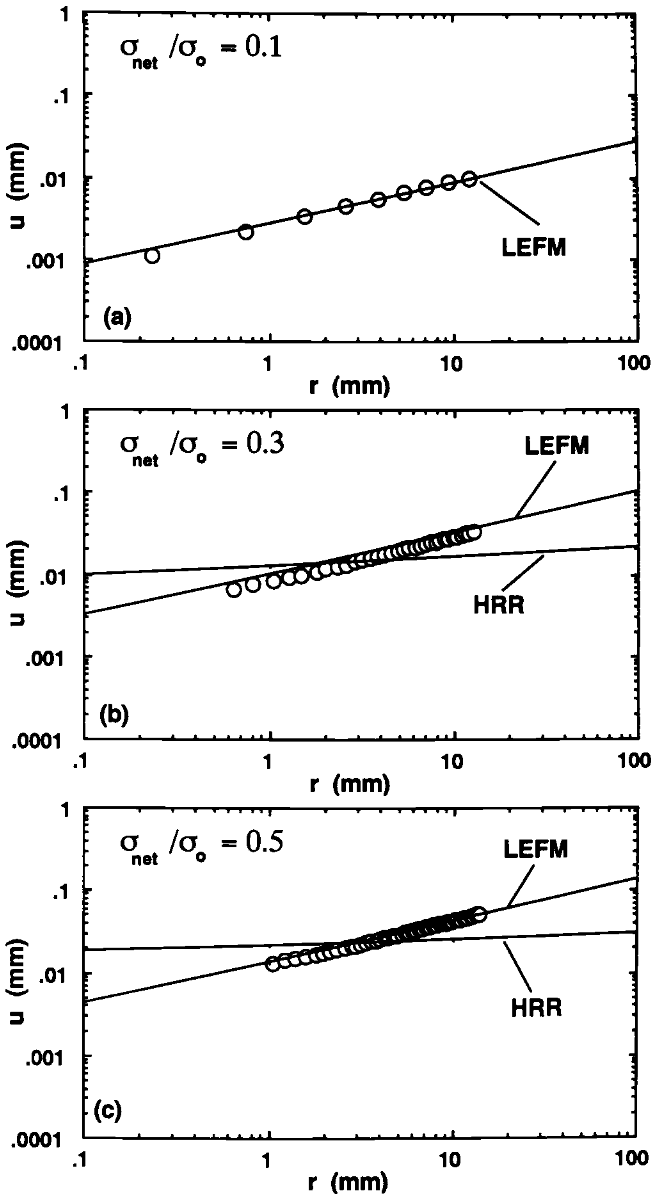

FIG. 5—*Comparison of the* u-*displacement variation from moiré experiment with LEFM and HRR predictions at different load levels at* $\theta = 45°$ *for 2091-T3 Al-Li.*

alloy, the HRR field predicts a slope of 0.12 in the log-log plots of the v and u versus r-curves. For the linear elastic fracture mechanics (LEFM) field, the curves of log-log of u and v should be a family of straight lines with a slope of ½. Figures 4*a* through *c* and 5*a* through *c* show the variations of v and u at $\theta = 45°$ for three applied load levels of $\sigma_{net}/\sigma_0 = 0.1$ to $\sigma_{net}/\sigma_0 = 0.5$, where σ_{net} is the nominal stress along the remaining ligament of the specimen and σ_0 is the yield stress of the aluminum alloy. Also shown are the log-log plots of displacement versus radial distance, r, of LEFM and HRR fields at a crack-tip polar angle of $\theta = 45°$. The displacements for the HRR field were calculated by using the average J-integral values obtained through contour integration of the moiré data. The corresponding displacement fields for the LEFM crack tip were obtained by equivalent plane-stress stress-intensity factors computed from these J-integral values.

Plots in Figs. 4*a* through *c* indicate that the v-field exhibited a nearly LEFM field at $\sigma_{net}/\sigma_0 = 0.1$, which later, near the crack tip, changed to HRR field as the plastic zone size increased for the intermediate load level, $\sigma_{net}/\sigma_0 = 0.3$. The HRR zone moved further ahead of the crack tip and was replaced by the three-dimensional nonlinear region (3D

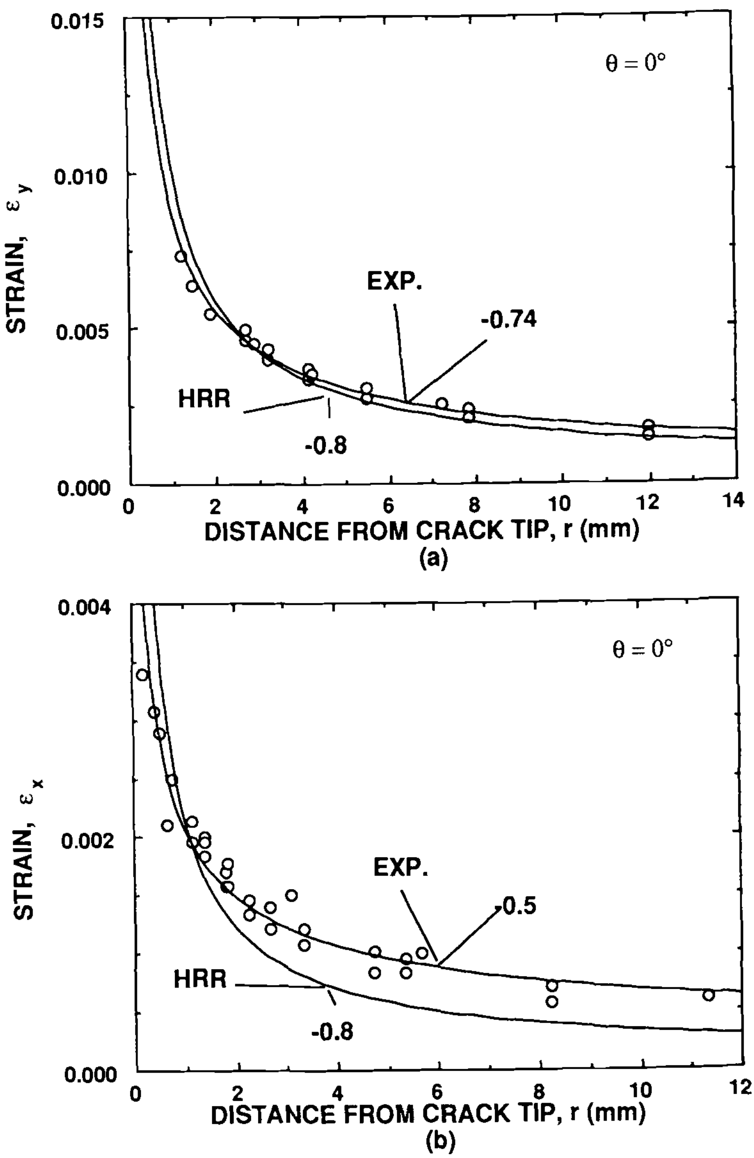

FIG. 6(*a* and *b*)—*Variations of* ε_y *and* ε_x *near crack tip, 2024-O aluminum specimen at* $\theta = 0°$.

NLR), near the crack tip, at a higher load of $\sigma_{net}/\sigma_0 = 0.5$. The u-field, (Figs. 5*a* through *c*), on the other hand, exhibited a nearly LEFM field throughout the increasing applied load.

The many log-log plots for all other aluminum alloys showed that the predicted power of $1/n + 1$ of r for the HRR crack-tip displacement was more or less replicated by the measured v-displacement but the measured u-displacement field consistently indicated a power of ≈ 0.5 of the radial distance, r [*16–18*].

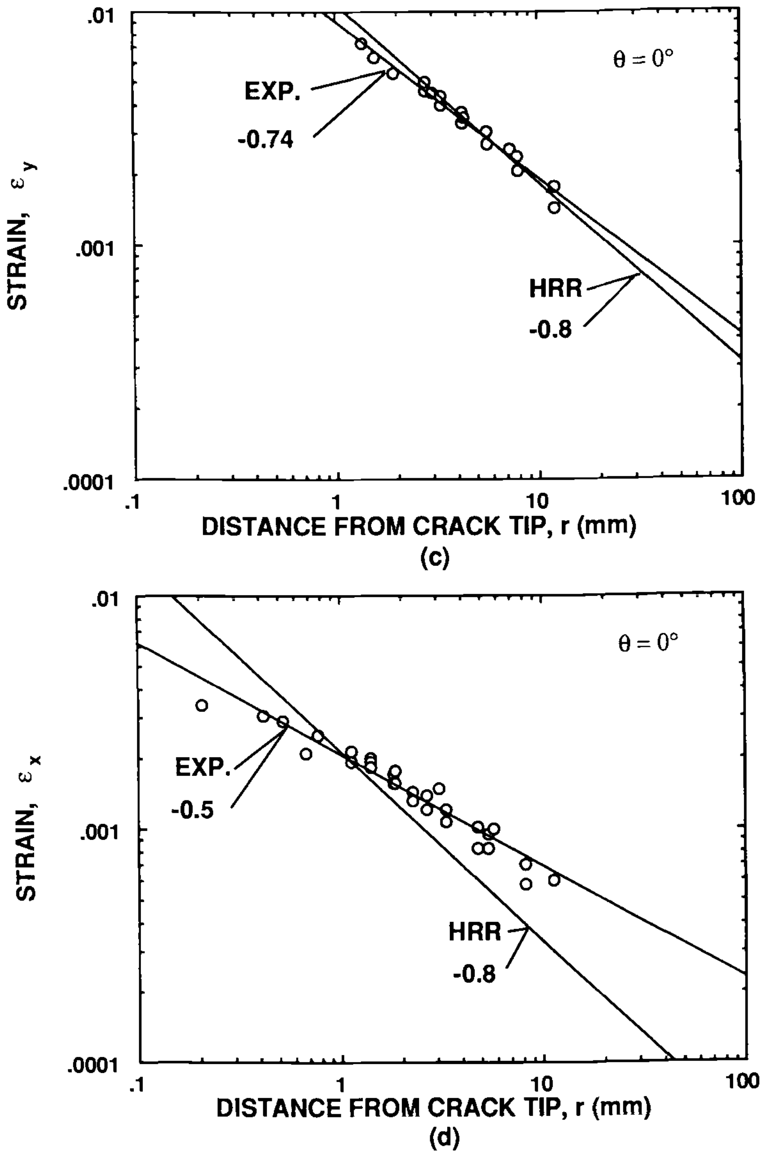

FIG. 6(*c* and *d*)—*Log-log plots of* ε_y *and* ε_x *near crack tip, 2024-O aluminum specimen at* $\theta = 0°$.

Strain Fields

The correct representation of the displacement fields as $r \to 0$ is

$$u_i - \hat{u}_i = \alpha\varepsilon_0 r \left(\frac{J}{\alpha\sigma_0\varepsilon_0 I_n r}\right)^{n/n+1} \tilde{u}_i(\theta,n) \tag{4}$$

The dimensionless function of $\tilde{u}_i(\theta,n)$ and the normalizing constant, I_n, depend on the mode, n, and on whether plane strain or plane stress is assumed. The $\hat{u}_i$ allows for a possible

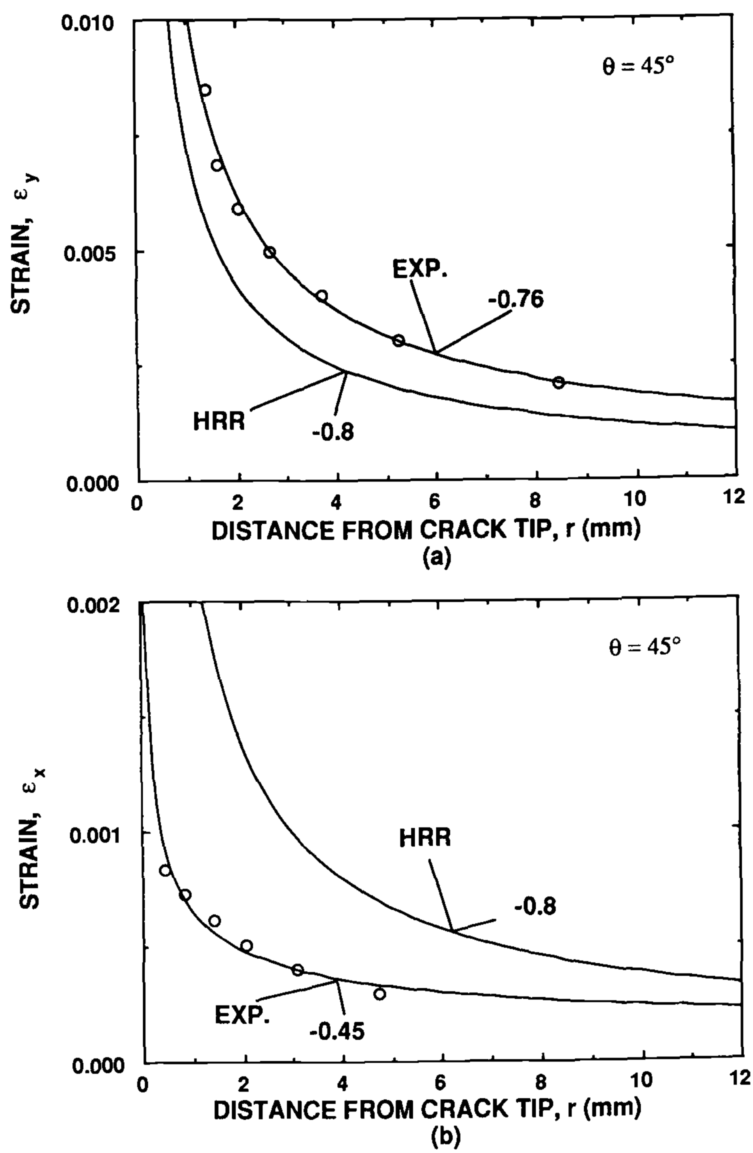

FIG. 7—*Variations of ε_y and ε_x near crack tip, 2024-O aluminum specimen at $\theta = 45°$.*

translation of the crack tip itself. Or, equivalently, a constant displacement term, $\hat{u}_i$, should be subtracted from the absolute displacement fields. Moiré interferometry measures the relative displacements and is blind to a constant translation. Obviously, this rigid body displacement does not contribute to the strains [24,25]. In order to dispel any doubts on the contributions of the rigid body displacements to log-log plots of displacement fields, we turn to the strain fields derived from moiré interferometry.

Figures 6 through 8 show the variations of ε_x and ε_y for two different strain hardening materials, 2024-O and 2024-T3, with hardening components of $n = 4$ and 12, respectively.

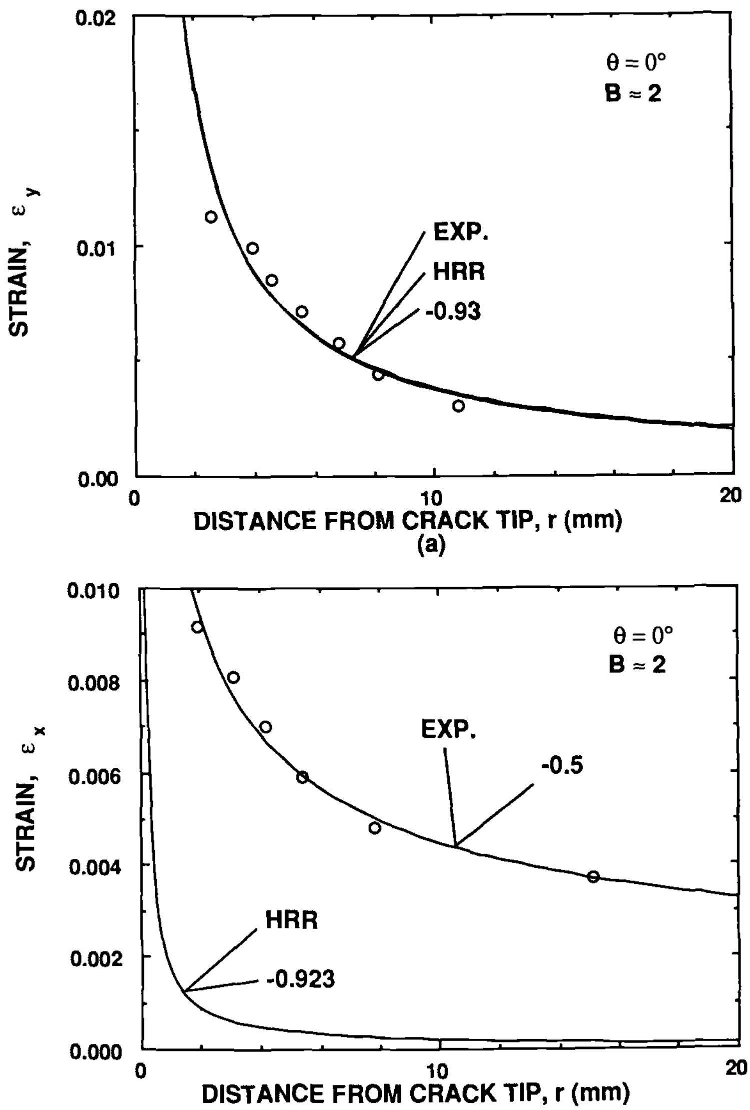

FIG. 8—*Variations of ε_y and ε_x near crack tip, 2024-O aluminum specimen at $\theta = 0°$ and $B \approx 2$.*

Also shown are the log-log plots of the strain versus radial distance, r, of the HRR fields. The HRR field requires a $r^{-n/n+1}$ singularity in the strains. The strains for the HRR field were calculated by using J-integral values obtained through contour integrations of the moiré data. Figures 6a and b show plots of ε_x and ε_y versus the radial distance, r, for an angular orientation of $\theta = 0°$ (for 2024-O aluminum). The magnitude of the predicted strains in both vertical and horizontal directions are close to the measured strains at $\theta = 0°$.

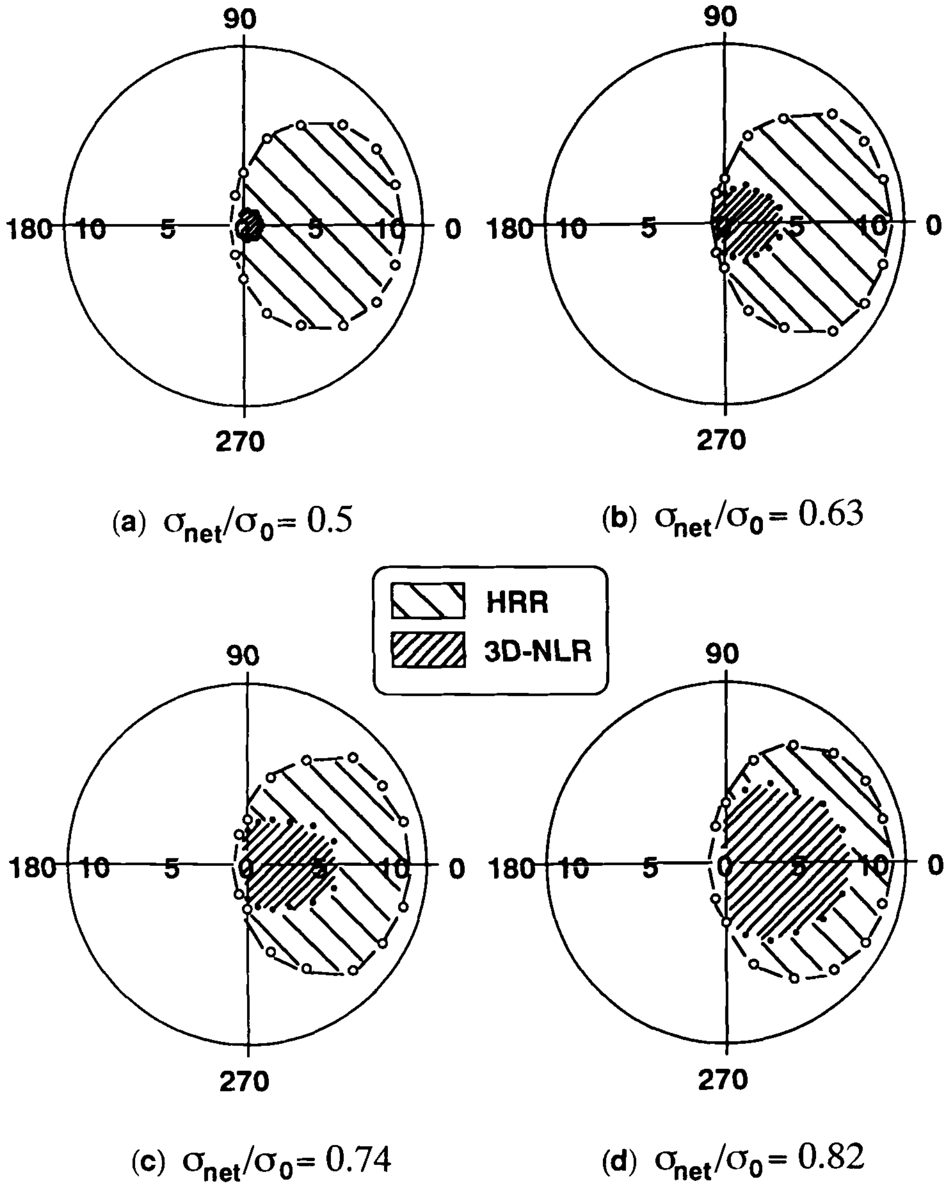

FIG. 9—*Zone of HRR-dominance and three-dimensional nonlinear region (3D-NLR) of the* v-*displacement fields as a function of increasing load. No corresponding dominance exists for the* u-*displacement field. Dimensions are in millimetres.*

Figures 6*c* and *d* show the log-log plots of Figs. 6*a* and *b*. Moiré results show that the ε_y variation agrees with the HRR prediction, where the slope of the log-log plot is $-n/(n + 1) = -0.74$ and the HRR slope is -0.8. In contrast, the ε_x variation does not agree with the HRR prediction and the slope of the log-log plots are nearly -0.5. Since we are looking at the plane stress condition, strain measurement along $\theta = 0°$ is valid for HRR field calculations. Figures 7*a* and *b* show plots of ε_x and ε_y of 2024-O aluminum for an angular orientation of $\theta = 45°$, which are consistent with plots at $\theta = 0°$. The magnitude of ε_x predicted from the HRR field underestimates the experimental ε_x at $\theta = 45°$. Figures 8*a* and *b* show the plots of strain for 2024-T3 aluminum alloy at a biaxiality ratio of $B = Fx/Fy \approx 2$ loading [*17,18*]. Due to external load along the crack plane, the magnitude of ε_x is higher than the calculated HRR field, but the $-n/(n + 1)$ singularity value is consistent with the previous uniaxial tests where they all show a slope of about -0.5.

The associated HRR crack-tip displacements and strains in all specimens were in agreement with the measured displacements and strains vertical to the crack, but consistently differed in magnitude and order of singularity with measured displacement and strain parallel to the crack.

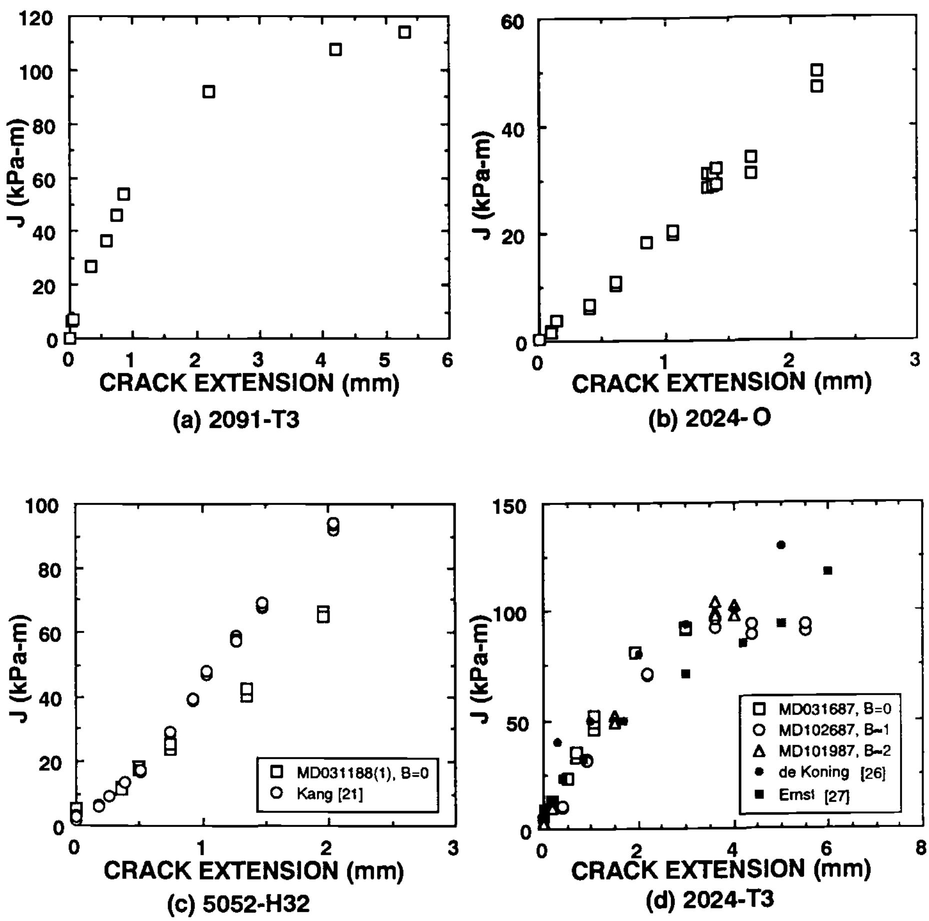

FIG. 10—J_R *curves of 2091-T3, 2024-0, 5052-H32, and 2024-T3 aluminum specimens.*

HRR Field Dominance

Figures 9*a* through *d* show the zone of dominance of the HRR field with respect to the external loads for the v-displacement field. Also shown are the boundaries of the process zone or regions of three-dimensional nonlinear zone (3D-NLR). Note that in Fig. 4, for $\sigma_{net}/\sigma_0 = 0.5$, the slope of log($v$)-log($r$) near the crack tip is high, that is, about 0.8 to 1.0. This is the region of finite strain and fracture process zone (3D-NLR) in which the microscopic process of separation occurs. From Fig. 9, it is shown that the v-displacement indicates a large range of HRR dominance. Figures 9*a* through *d* also show that the three-dimensional nonlinear region grows larger as the load increases and the HRR dominance zone is insensitive to increase in the applied load or crack extension. Recent numerical results of Zhang and Ravi-Chandar [*14*] also show that the HRR dominance is not very sensitive to increase in the applied loading. As the magnitude of load increases, the size of the HRR region

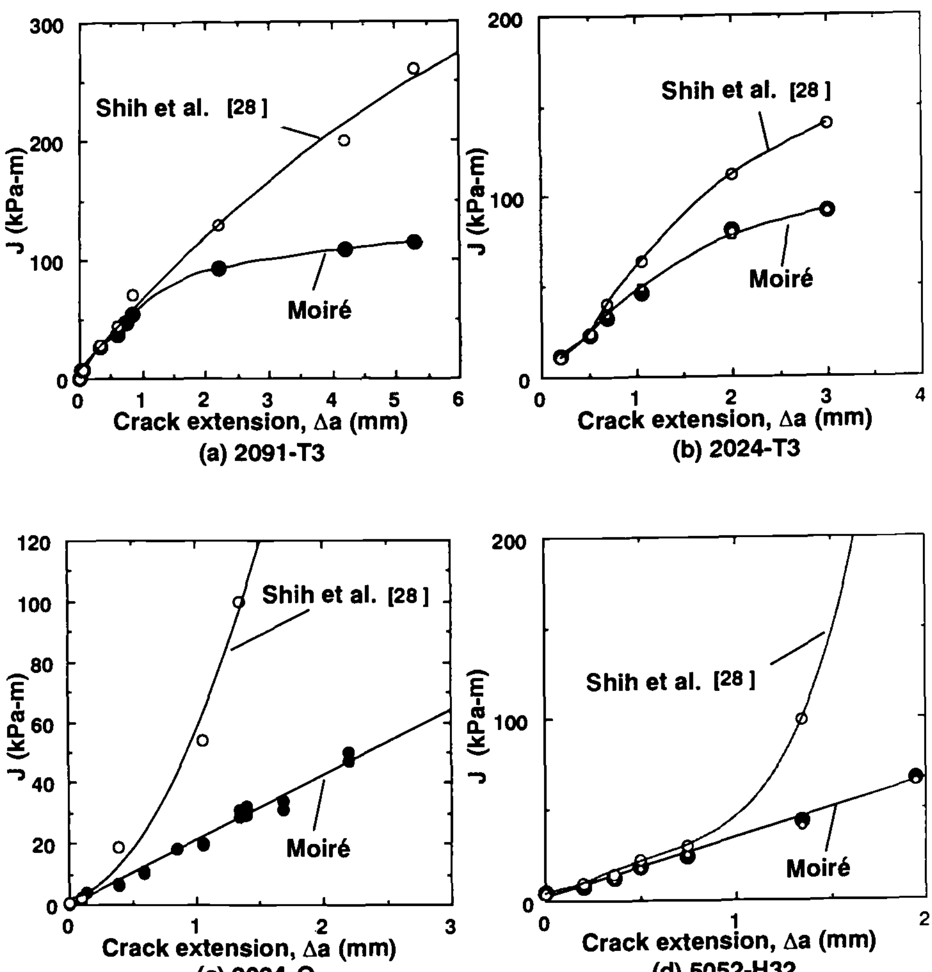

FIG. 11—J_R *curves of 2091-T3, 2024-T3, 2024-O, and 5052-H32 aluminum specimens compared with predicted* J_R *curves of Refs* 28 *or* 29.

increases, but beyond some limit load the size of HRR region remains unchanged. On the other hand, the 3D-NLR or the process zone grows continuously and annihilates the HRR zone as the load increases. It should be noted that the *u*-field has no range of HRR dominance throughout the loading process from LEFM to elastic-plastic fracture.

J_R *Curves*

Figures 10*a* through *d* show the J_R-curves for 2091-T3 aluminum-lithium, 2024-T3, 2024-O, and 5052-H32 aluminum specimens, respectively. Despite the maximum differences of 4.4 cm in the length of integration paths, the *J*-values for each crack length differed at the most

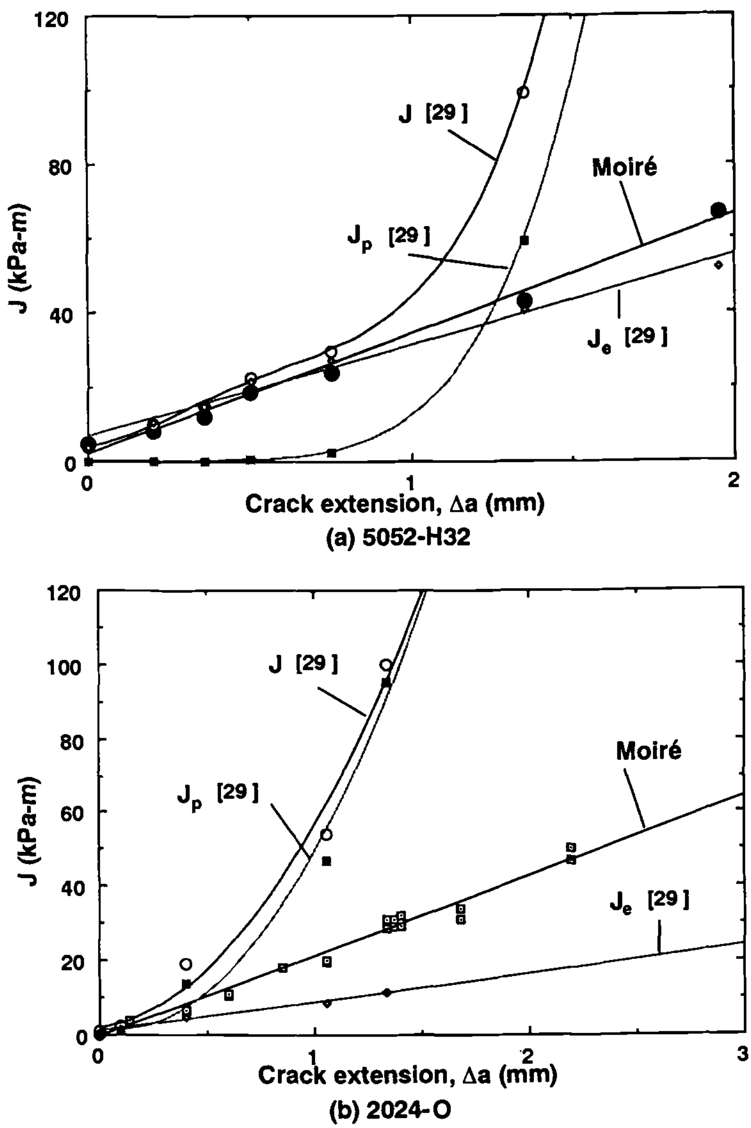

FIG. 12—J_R *curves of 5052-H32 and 2024-O compared with predicted* J, J_e, *and* J_p *of Refs* 28 *or* 29.

by 5%. The extrapolated J_R-curves inferred a critical J of 8 to 10 MPa m for 2091-T3, 6 to 7 MPa m for 5052-H32, and 9 to 10 MPa m for 2024-T3; there was no recognizable critical J for 2024-O. Figure 10*c* shows the J_R-curves for the approximate [*21*] and exact [*16*] J-values obtained from 2024-O small and large single-edge-notched (SEN) specimens, respectively. Figure 10*d* shows the J_R-curves for 2024-T3 tests during stable crack growth. Also shown is the J-resistance curve obtained by deKoning [*26*] for a 2024-T3 and Ernst [*27*] for 2024-T351. Figures 11*a* and *b* compare the measured J_R-curves and the J_R-curves predicted by using the J-prediction method by Shih et al. [*28*]. Shih's J-prediction method was obviously meant for a stationary crack, and the estimated J deviates substantially from the measured J-values at the larger crack extension, that is, $\Delta a > 0.6 \sim 1.0$ mm.

Figures 12*a* and *b* show the $J_e(\Delta a)$ and $J_p(\Delta a)$, which were calculated using the EPRI estimation technique [*28* or *29*] compared with the measured $J(\Delta a)$ curves using moiré interferometry. Since the crack tip is surrounded by large plastic deformation in 2024-0 and 5052-H32 aluminum specimens, the fully plastic estimation would be expected to be used. The predicted J_p, however, differed substantially from the measured J in both alloys.

These findings raise some key issues regarding elastic-plastic fracture mechanics: Are the current formulas for J calculations incorrect? Even though the J is path independent, is it really a suitable parameter for characterizing the crack-tip fields?

Conclusions

1. Moiré interferometry was used successfully to measure the displacement and strain fields around stably growing cracks in four aluminum alloys. One of the advantages of moiré interferometry is that it does not involve a priori assumptions regarding the displacement and strain fields.
2. Path independency of J is shown and the J_R-curves associated with small crack extension in thin (0.8 mm) aluminum specimens are presented.
3. These J_R results differed substantially from the J-values computed by using the far-field formula of Shih, German, and Kumar.
4. The u crack-tip displacement and strain fields did not agree with the asymptotic solutions of Hutchinson, Rice, and Rosengren computed from the measured J-values.

Acknowledgment

The research support from the Office of Naval Research and Rockwell International Independent Research and Development is gratefully acknowledged.

References

[*1*] Hutchinson, J. W., "Singular Behavior at the End of a Tensile Crack in a Hardening Material," *Journal of Mechanics and Physics of Solids*, Vol. 16, 1968, pp. 13–31.

[*2*] Hutchinson, J. W., "Plastic Stress and Strain Fields at a Crack Tip," *Journal of Mechanics and Physics of Solids*, Vol. 16, 1968, pp. 337–347.

[*3*] Rice, J. R. and Rosengren, G. F., "Plane Strain Deformation Near a Crack Tip in a Power-Law Hardening Material," *Journal of Mechanics and Physics of Solids*, Vol. 16, 1968, pp. 1–12.

[*4*] Rice, J. R., "A Path Independent Integral and the Approximate Analysis of Strain Concentration by Notches and Cracks," *Journal of Applied Mechanics*, Vol. 35, Series E, American Society of Mechanical Engineers, June 1968, pp. 379–386.

[*5*] Knowles, J. K. and Sternberg, E., "An Asymptotic Finite-Deformation Analysis of the Elastostatic Field Near the Tip of a Crack," *Journal of Elasticity*, Vol. 3, No. 2, 1973, pp. 67–107.

[*6*] Knowles, J. K. and Sternberg, E., "Finite-Deformation Analysis of the Elastostatic Field Near the Tip of a Crack: Reconsideration and Higher-Order Results," *Journal of Elasticity*, Vol. 4, 1973, pp. 201–233.

[7] Kordisch, H. and Sommer, E., "3D-Effects Affecting the Precision of Lifetime Predictions," *Fracture Mechanics: Nineteenth Symposium, ASTM STP 969*, T. A. Cruse, Ed., American Society of Testing and Materials, Philadelphia, 1988, pp. 73–87.
[8] Gurson, A. L., "Continuum Theory of Ductile Rupture by Void Nucleation and Growth: Part I—Yield Criteria and Flow Rules for Porous Ductile Media," *Journal of Engineering Materials Technology*, Vol. 99, 1977, pp. 2–15.
[9] Needleman, A. and Tvergaard, V., "An Analysis of Ductile Rupture Modes at the Crack Tip," *Journal of Mechanics and Physics of Solids*, Vol. 35, 1987, pp. 151–183.
[10] Sun, D. Z., Siegele, D., Voss, B., and Schmitt, W., "Application of Local Damage Models to the Numerical Analysis of Ductile Rupture," *Fatigue and Fracture of Engineering Materials and Structures*, Vol. 12, No. 3, 1989, pp. 201–212.
[11] Shih, C. F., deLorenzi, R. G., and Andrews, W. R., "Studies on Crack Initiation and Stable Crack Growth," *Elastic-Plastic Fracture, ASTM STP 668*, J. D. Landes, J. A. Begley, and G. A. Clarke, Eds., American Society for Testing and Materials, Philadelphia, 1979, pp. 65–120.
[12] Shih, C. F. and German, M. D., "Requirements for a Single Parameter Characterization of a Crack Tip Field by HRR Singularity," *International Journal of Fracture*, Vol. 17, 1981, pp. 27–43.
[13] Shih, C. F., "*J*-Dominance under Plane Fully Plastic Conditions: The Edge Crack Panel Subjected to Combined Tension and Bending," *International Journal of Fracture*, Vol. 29, 1985, pp. 73–84.
[14] Zhang, Y. and Ravi-Chandar, K., "A Finite Element Investigation into the Foundation of Elastic-Plastic Fracture Mechanics, Part 1: Dominance of the HRR Field," *Journal of Mechanics and Physics of Solids*, to be published.
[15] Chiang, F. P. and Hareesh, T. V., "Experimental Studies of Crack-Tip Deformation and the HRR Singularity Field," *Proceedings*, 1986 SEM Spring Conference on Experimental Mechanics, 1968, pp. 782–783.
[16] Dadkhah, M. S., Kobayashi, A. S., Wang, F. X., and Graesser, D. L., "*J*-integral Measurements Using Moiré Interferometry," *Proceedings*, VI International Congress on Experimental Mechanics, 1988, pp. 227–234.
[17] Dadkhah, M. S. and Kobayashi, A. S., "HRR Field of a Moving Crack, An Experimental Analysis," *Engineering Fracture Mechanics*, Vol. 34, 1989, pp. 253–262.
[18] Dadkhah, M. S. and Kobayashi, A. S., "Further Studies in the HRR Field of a Moving Crack, An Experimental Analysis," *International Journal of Plasticity*, Vol. 6, 1990, pp. 635–650.
[19] Dadkhah, M. S., Wang, F. X., and Kobayashi, A. S., "Simultaneous On-Line Measurement of Orthogonal Displacement Fields by Moiré Interferometry," *Experimental Techniques*, Vol. 12, 1988, pp. 28–30.
[20] Kang, B. S.-J., Kobayashi, A. S., and Post, D., "Stable Crack Growth in Aluminum Tensile Specimens," *Experimental Mechanics*, Vol. 27, 1987, pp. 234–245.
[21] Kang, B. S.-J. and Kobayashi, A. S., "*J*-estimation Procedure Based on Moiré Interferometry Data," *Journal of Pressure Vessel Technology*, Vol. 110, American Society of Mechanical Engineers, Aug. 1988, pp. 291–300.
[22] Post, D., "Moiré Interferometry," *Handbook of Experimental Mechanics*, A. S. Kobayashi, Ed., Prentice Hall, Englewood Cliffs, NJ, 1987.
[23] Dally, J. W. and Riley, W. F., *Experimental Stress Analysis*, McGraw-Hill Book Company, New York, 1978.
[24] Hutchinson, J. W., "Fundamentals of the Phenomenological Theory of Nonlinear Fracture Mechanics," *Journal of Applied Mechanics*, Vol. 50, 1983, pp. 1042–1051.
[25] Hutchinson, J. W., private communication.
[26] de Koning, A. U., "A Contribution to the Analysis of Quasi-Static Crack Growth," *Fracture 1977, Proceedings*, Fourth International Conference on Fracture, Vol. 3A, Pergamon Press, Elmsford, NY, 1978, pp. 25–31.
[27] Ernst, H. A., "Material Resistance and Instability Beyond *J*-Controlled Crack Growth," Scientific Paper 81-107-JINF-P6, Westinghouse R&D Center, Pittsburgh, Dec. 3, 1981.
[28] Shih, C. F., German, M. D., and Kumar, V., "An Engineering Approach for Examining Crack Growth and Stability in Flawed Structures," *International Journal of Pressure Vessel & Piping*, Vol. 9, 1981, pp. 159–196.
[29] Kumar, V., Shih, C. F., and German, M. D., "An Engineering Approach for Elastic-Plastic Fracture Analysis," EPRI NP-1931, Project 1237-1 Topical Report, Electric Power Research Institute, Palo Alto, CA, July 1981.

Pin Tong,[1] Robert Greif,[2] and Li Chen[3]

Application of the Hybrid Finite Element Method to Aircraft Repairs

REFERENCE: Tong, P., Greif, R., and Chen, L., "**Application of the Hybrid Finite Element Method to Aircraft Repairs**," *Fracture Mechanics: Twenty-Second Symposium (Volume II), ASTM STP 1131*, S. N. Atluri, J. C. Newman, Jr., I. S. Raju, and J. S. Epstein, Eds., American Society for Testing and Materials, Philadelphia, 1992, pp. 154–169.

ABSTRACT: A hybrid finite element approach is presented for the analysis of cracked panels with riveted doublers in airframe structures. The method uses the super element developed by Tong to model the cracked panel with rivet holes, springs to model the rivets, and regular finite elements to model the doubler. The super element accurately models the crack and rivet holes of the skin while the regular finite element method provides the versatility to take into account the variety of doubler designs. Numerical results are presented to demonstrate the efficiency and accuracy of this approach, and to compare different doubler designs.

KEY WORDS: fracture mechanics, fatigue (materials), finite element method, aircraft structures, aircraft repairs

In December 1978, the Federal Aviation Administration of the United States (FAA) issued the Amendment 45 to the FAR 25.571, Fatigue Evaluation of Flight Structure, requiring that the structure of all new transport category airplanes certificated in the United States be designed to damage tolerant principles. This is a requirement [*1*] that methods of advanced fracture mechanics be applied to evaluating the structural integrity of aircraft to ascertain that the airframe will not experience catastrophic failure due to fatigue, corrosion, or accidental damage under the expected load spectra throughout the operating life of the aircraft. In 1981, the FAA further issued advisory circula AC 91.56 providing guidance for development of the Supplemental Inspection Documents (SIDs) based on the damage tolerant philosophy for existing large transport category airplanes. Since then, aircraft manufacturers have carried out damage tolerant evaluations to define inspection programs for both new designs and the existing older transport category airplanes.

Damage tolerant evaluation is not normally performed for repairs and modifications to principal structural elements. The current practice generally assures that repairs or modifications would have an equal or better static strength as compared to the original design. In Ref *2*, Swift shows how these repairs and modifications can degrade the damage tolerance of the structure. The main causes for the degradation are due to the bearing loads and stress concentration induced on the rivet holes at the location of repair and the reduced inspect-

[1]Professor and head, Mechanical Engineering Department, Hong Kong University of Science and Technology, Hong Kong. Dr. Tong is currently on leave from the Volpe National Transportation Systems Center, U.S. Department of Transportation, Cambridge, MA 02142.

[2]Transportation Systems Center, U.S. Department of Transportation, Cambridge, MA 02142; also, Professor of Mechanical Engineering, Tufts University, Medford, MA 02155.

[3]Graduate student, Department of Mechanical Engineering, Tufts University, Medford, MA 02155.

ability of these holes because they are covered by the doubler. He has suggested a number of approaches to improve the design of these repairs to reduce the rivet forces, improve the inspectability, and consequently increase the fatigue life and damage tolerance of the repaired basic structure.

Swift uses the displacement compatibility method to determine the rivet forces and the bearing stresses in the holes of built-up panels. The present paper presents a hybrid method for the analysis of cracked panels with riveted doublers. The method uses the super-element developed in Ref *3* with a slight modification to model the cracked panel with rivet holes, springs to model the rivets, and regular finite elements to model the doublers. The super-element accurately models the crack and rivet holes of the skin while the regular finite method provides the versatility to take into account the variety of doubler designs.

As mentioned in Ref *3*, the standard finite element method is versatile enough to take into account the effects of complex geometry variations, and different stiffener and fastener configurations. However, in order to account for the stress singularities at crack tips and rapid stress variations near rivet holes, enormous amounts of elements are required to model the structure with any degree of accuracy. Thus for an efficient finite element solution, it is natural to employ a hybrid super-element to account for the singular behavior. It is seen from Ref *4*, that the use of the hybrid superelement to solve problems for structural components with cracks is extremely accurate and efficient in comparison to the standard finite element method.

Hybrid Formulation

Airframe structures often involve skins with bonded or riveted stiffeners. If the skin is damaged, a doubler(s) is riveted over the damaged area. Loads are transferred out of the skin to the doubler through the rivets. The bearing stress induced in the rivet holes will degrade the fatigue life of the skin. Therefore, it is essential to determine the rivet loads in order to quantify the effects of repairs on the damage tolerance of the structure. The hybrid finite element method is ideal for analysis that can accurately calculate the singular stresses at the crack tips and the nearly singular stresses around the rivet holes.

Following the formulation given in Ref *3*, we approximate the skin as an infinite panel with a centrally located crack of length $2a$ (Fig. 1). Remote stresses, σ_{11}°, σ_{22}°, and σ_{12}°, are applied. The panel is also subjected to loads, P^k, along the surfaces of small holes at z_k, $k = 1, 2, \ldots$ Complex variables are used in this formulation where

$$z = x + iy$$

$$P^k = X^k + iY^k \tag{1}$$

in which X^k and Y^k denote the load per unit thickness in the x and y directions, respectively. The load at z_k is applied on the hole surface of radius $|z - z_k| = \varepsilon$ where ε is small as compared to any characteristic dimension (such as the half crack length) of the problem. The applied forces are in self-equilibrium, that is

$$\sum_k P^k = 0 \tag{2}$$

$$Im\left(\sum_k P^k \bar{z}_k\right) = 0 \tag{3}$$

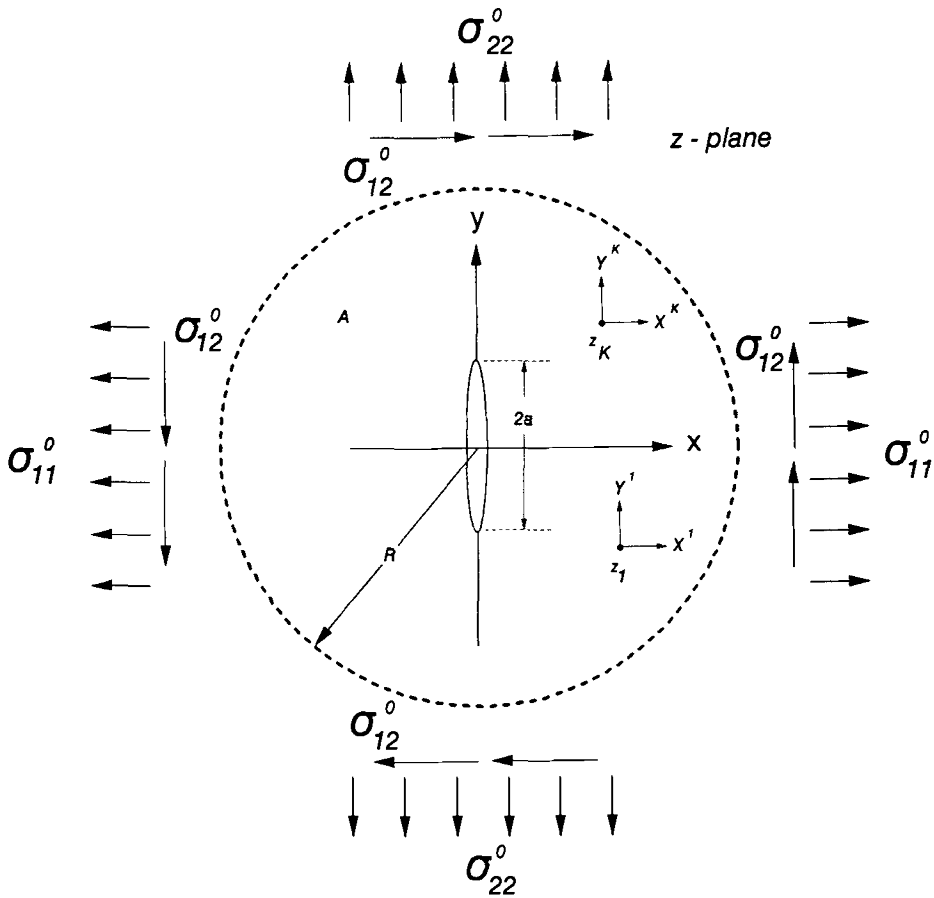

FIG. 1—*Concentrated loads and remote stresses on a cracked panel.*

Equations 2 and 3 are, respectively, the force and the moment equilibrium equations, and *Im*( ) denotes the imaginary part.

A hybrid variational functional for the panel can be written as

$$\pi_p = \sum_k \int_{|z-z_k|=\epsilon} tT_i\tilde{u}_i ds - t\left(\int_A U(\sigma_{ij})dA - \int_A U(\sigma^\circ_{ij})dA\right)$$

$$+ \int_{R\to\infty} tT_i u^\circ_i ds - \int_{R\to\infty} tT^\circ_i u^\circ_i ds \tag{4}$$

where t is the panel thickness; u_i are the displacements; $T_i(=\sigma_{ij}\nu_j)$ and σ_{ij} are, respectively, the boundary tractions and stresses; and $U(\sigma_{ij})$ is the complementary energy per unit volume. In Eq *4*, we required that σ_{ij} satisfy a priori the equilibrium conditions in A and the traction-free conditions at the crack surface. The superscript, $(\ )^\circ$, denotes the known quantities associated with the solution of a cracked panel without holes subjected to given remote stresses. Therefore, the second term in the parenthesis and the last term on the right side are constants that have no effect on the functional variation. The $\tilde{u}_i$ are the displacements of the skin at the hole surface, $|z - z_k| = \varepsilon$, and are independent functional variables of π_p. The Euler equations for the panel can be derived through the first variation of π_p. They are the compatibility equations in A, at the hole surfaces, and at $R(\rightarrow \infty)$.

Let us write

$$\sigma_{ij} = \hat{\sigma}_{ij} + \sigma_{ij}^{\circ}$$

$$T_i = \hat{T}_i + T_i^{\circ} \tag{5}$$

In addition, we will choose σ_{ij} to satisfy also a priori the compatibility equation in A. In other words, σ_{ij} are selected such that an associated compatible displacement field, u_i, in A exists. Writing u_i in the form

$$u_i = \hat{u}_i + u_i^{\circ} \tag{6}$$

substituting both Eqs 5 and 6 into Eq 4, and converting the area integration to line integration, π_p becomes

$$\pi_p = t\left[\sum_k \int_{|z-z_k|=\varepsilon} \left(T_i\tilde{u}_i - \hat{T}_i\hat{u}_i^{\circ} - \frac{1}{2}\hat{T}_i\hat{u}_i\right) ds - \frac{1}{2}\int_{R\rightarrow\infty} \hat{T}_i\hat{u}_i dS\right] \tag{7}$$

The detailed derivation of σ_{ij} and u_i are given in Ref *3*, which expresses the solution in terms of two stress functions (ϕ,ψ).

The remote stress solution without holes [5] is

$$\phi^{\circ}(\zeta) = \frac{a}{8}\left[\sigma_{22}^{\circ}\left(\zeta - \frac{1}{\zeta}\right) + \sigma_{11}^{\circ}\left(\zeta + \frac{3}{\zeta}\right) + \frac{4i\sigma_{12}^{\circ}}{\zeta}\right]$$

$$\psi^{\circ}(\zeta) = \frac{a}{4}\left[\sigma_{22}^{\circ}\left(\zeta - \frac{1}{\zeta}\right) - \sigma_{11}^{\circ}\left(\zeta - \frac{1}{\zeta} + \frac{4\zeta}{1+\zeta^2}\right) + 2\sigma_{12}^{\circ}i\left(\zeta + \frac{1}{\zeta} - \frac{2\zeta}{1+\zeta^2}\right)\right] \tag{8}$$

where ζ and z are related by

$$z = \frac{a}{2}\left(\zeta - \frac{1}{\zeta}\right)$$

$$\zeta = \frac{z}{a} + \sqrt{1 + \left(\frac{z}{a}\right)^2} \tag{9}$$

The branch of the square root in Eq 9 is chosen to ensure that $|\zeta| \geq 1$. The transformation in Eq *9* maps the cracks surface in the z-plane to the unit circle centered at the origin in the ζ-plane.

The solution for a panel with a crack and concentrated load, P^k, at ζ^k is [3,6]

$$\phi^k(\zeta) = -\frac{P^k}{2(\kappa+1)\pi}\ln(\zeta-\zeta_k) - \frac{\kappa P^k}{2(\kappa+1)\pi}\ln\left(\frac{1}{\zeta}-\bar{\zeta}_k\right) - \frac{\bar{P}^k}{2(\kappa+1)\pi}\,\frac{\bar{\zeta}_k\left(\zeta_k-\dfrac{1}{\zeta_k}+\bar{\zeta}_k-\dfrac{1}{\bar{\zeta}_k}\right)}{(1+\bar{\zeta}_k^2)(1-\zeta\bar{\zeta}_k)} - \frac{\bar{P}^k}{2\pi(\kappa+1)}\,\frac{4\bar{\zeta}_k^2\varepsilon^2}{(1+\bar{\zeta}_k^2)^2a^2}\,\frac{1}{(1-\zeta\bar{\zeta}_k)^2} + \frac{P^k}{2\pi(\kappa+1)^2}[\ln(-\zeta_k)+\kappa^2\ln(-\bar{\zeta}_k)] + \frac{\bar{P}^k}{2\pi(\kappa+1)^2}\left[\frac{\left(\zeta_k-\dfrac{1}{\zeta_k}\right)\bar{\zeta}_k-2}{1+\bar{\zeta}_k^2}\right] \tag{10}$$

and

$$\psi(\zeta) = -\bar{\phi}\left(\frac{1}{\zeta}\right) - \frac{\zeta(1-\zeta^2)}{1+\zeta^2}\phi'(\zeta) \tag{11}$$

where ε is the radius of the hole at ζ_k and

$$\kappa = \frac{3-\nu}{1+\nu} \quad \text{for plane stress}$$
$$= 3-4\nu \quad \text{for plane strain} \tag{12}$$

in which ν is the Poisson's ratio. The short bar over ϕ denotes the complex conjugate of ϕ, but not the independent variable itself.

For the case that the radii of the rivet holes are sufficiently small, we can approximate the stress functions for σ_{ij} as the sum of the solutions for concentrated loads at ζ_k, that is

$$\phi(\zeta) = \sum_k \phi^k(\zeta)$$
$$\psi(\zeta) = \sum_k \psi^k(\zeta) \tag{13}$$

The expression in Eq 10 is the same as that of Eq 21 of Ref *3* except for the last three terms. The first of these three terms is added to ensure that the 0(1) displacements of (u_1, u_2) on the rivet hole surfaces are independent of θ, the local angle defining each rivet hole. The last two terms are constants having no effects on the stress distribution and are added for the convenience of programming so that the **H** flexibility matrix in Eq 24 is symmetric.

Returning to Eq 7, recall that T_i and u_i are the tractions and displacements associated with the equilibrating and compatible stress field, σ_{ij}, which also satisfies the traction-free conditions at the crack surface. The integration over $R \to \infty$ is zero [3]. If the radii of the holes are sufficiently small, the integration over $|z - z_k| = \varepsilon$ can be carried out explicitly.

Because $\tilde{u}_i$ and u_i° have no singularity in A, as $\varepsilon \to 0$, we have

$$\int_{|z-zk|=\varepsilon} T_i\tilde{u}_i ds = X^k(\tilde{u})_k + Y^k(\tilde{v})_k + 0(\varepsilon^2)$$

$$\int_{|z-zk|=\varepsilon} \hat{T}_i u_i^\circ ds = X^k(u^\circ)_k + Y^k(v^\circ)_k + 0(\varepsilon^2) \tag{14}$$

where $(\tilde{u}, \tilde{v})_k$ and $(u^\circ, v^\circ)_k$ are the values of $(\tilde{u}_1, \tilde{u}_2)$ and (u_1°, u_2°) at z_k, respectively. We have

$$2\mu(u_1^\circ + iu_2^\circ) = \sigma_{11}^\circ \frac{a}{8}\left[\kappa\left(\zeta + \frac{3}{\zeta}\right) - \frac{\left(\zeta - \frac{1}{\zeta}\right)}{1 + \bar{\zeta}^2}(\bar{\zeta}^2 - 3) + 2\left(\bar{\zeta} - \frac{1}{\bar{\zeta}} + \frac{4\bar{\zeta}}{1 + \bar{\zeta}^2}\right)\right]_k$$

$$+ \sigma_{22}^\circ \frac{a}{8}\left[(\kappa - 1)\left(\zeta - \frac{1}{\zeta}\right) - 2\left(\bar{\zeta} - \frac{1}{\bar{\zeta}}\right)\right]_k + \sigma_{12}^\circ \frac{ai}{2}\left[\frac{\kappa}{\zeta} - \frac{\zeta - \frac{1}{\zeta} + \bar{\zeta} - \frac{1}{\bar{\zeta}}}{1 + \bar{\zeta}^2} + \bar{\zeta}\right]_k$$

The integration of $\hat{T}_i\hat{u}_i$ over $|z - z_j| = \varepsilon$ with $\varepsilon \to 0$ can be performed easily in polar coordinates in the z-plane, that is

$$\int_{|z-z_j|=\varepsilon} \hat{T}_i\hat{u}_i ds = Re \int_0^{2\pi} - (\hat{\sigma}_{rr} - i\hat{\sigma}_{r\theta})(\hat{u}_r + i\hat{u}_\theta)\varepsilon\, d\theta \tag{15}$$

in which Re denotes the real part of a complex function, and

$$\hat{u}_r + i\hat{u}_\theta = e^{-i\theta}(\hat{u}_1 + i\hat{u}_2) = \frac{e^{-i\theta}}{2\mu}\left(\kappa\phi - z\overline{\frac{d\phi}{dz}} - \bar{\psi}\right)$$

$$\hat{\sigma}_{rr} - i\hat{\sigma}_{r\theta} = \frac{d\phi}{dz} + \overline{\frac{d\phi}{dz}} - e^{2i\theta}\left(\bar{z}\frac{d^2\phi}{dz^2} + \frac{d\psi}{dz}\right) \tag{16}$$

where μ is the shear modulus.

Using Eqs 10, 11, and 13, we find

$$\hat{\sigma}_{rr} - i\hat{\sigma}_{r\theta} = -\bar{P}^j\frac{e^{i\theta}}{2\pi\varepsilon} + 0(1) \tag{17}$$

at $z = z_j + \varepsilon e^{i\theta}$. Similarly, we obtain

$$\hat{u}_r + i\hat{u}_\theta = e^{-i\theta}\sum_k \{P^k[d^k(\zeta_j) + f^k(\zeta_j)] + \bar{P}^k[e^k(\zeta_j) + g^k(\zeta_j)]\} + 0(\varepsilon) \tag{18}$$

The functions $d^k(\zeta)$, $e^k(\zeta)$, $f^k(\zeta)$, and $g^k(\zeta)$ are defined as follows. For $\zeta \neq \zeta_k$,

$$f^k(\zeta) = \frac{1}{4(\kappa+1)\mu\pi}\left[-\ln\left(1-\frac{1}{\zeta_k\bar{\zeta}}\right) - \kappa^2\ln\left(1-\frac{1}{\bar{\zeta}_k\zeta}\right) + \frac{\left(\zeta-\frac{1}{\zeta}+\bar{\zeta}-\frac{1}{\bar{\zeta}}\right)\left(\zeta_k-\frac{1}{\zeta_k}+\bar{\zeta}_k-\frac{1}{\bar{\zeta}_k}\right)\bar{\zeta}^2\zeta_k^2}{(1+\bar{\zeta}^2)(1+\zeta_k^2)(1-\bar{\zeta}\zeta_k)^2}\right] \tag{19}$$

$$g^k(\zeta) = \frac{1}{4(\kappa+1)\mu\pi}\left[\frac{2(\overline{\zeta\zeta_k}-1)}{(1+\bar{\zeta}^2)(1+\bar{\zeta}_k^2)} - \frac{\kappa\bar{\zeta}_k\left(\zeta_k-\frac{1}{\zeta_k}+\bar{\zeta}_k-\frac{1}{\bar{\zeta}_k}\right)}{(1+\bar{\zeta}_k^2)(1-\bar{\zeta}\zeta_k)} - \frac{\kappa\bar{\zeta}\left(\zeta-\frac{1}{\zeta}+\bar{\zeta}-\frac{1}{\bar{\zeta}}\right)}{(1+\bar{\zeta}^2)(1-\bar{\zeta}\zeta_k)}\right]$$

$$d^k(\zeta) = -\frac{\kappa}{4(\kappa+1)\mu\pi}\ln(\zeta-\zeta_k)(\bar{\zeta}-\bar{\zeta}_k)$$

$$e^k(\zeta) = \frac{1}{4(\kappa+1)\mu\pi}\left[\frac{\left(\zeta-\frac{1}{\zeta}\right)\bar{\zeta}^2}{1+\bar{\zeta}^2} - \frac{\left(\zeta_k-\frac{1}{\zeta_k}\right)\bar{\zeta}_k^2}{1+\bar{\zeta}_k^2}\right]\frac{1}{\bar{\zeta}-\bar{\zeta}_k} \tag{20}$$

and if $\zeta \cong \zeta_k$

$$d^k(\zeta_k) = -\frac{\kappa}{4(\kappa+1)\mu\pi}\ln\left[\frac{4\varepsilon^2\bar{\zeta}_k^2\zeta_k^2}{a^2(1+\bar{\zeta}_k^2)(1+\zeta_k^2)}\right]$$
$$e^k(\zeta_k) = \frac{1}{4(\kappa+1)\mu\pi}\frac{2\left(\zeta_k-\frac{1}{\zeta_k}\right)\bar{\zeta}_k}{(1+\bar{\zeta}_k^2)^2} \tag{21}$$

The functions d, e, f, and g are each different from those of Eqs 28 through 30 of Ref *3* by a constant that has no effect for the stress distribution.

A substitution of Eqs 17 through 21 into Eq 15 yields

$$\int_{|z-z_j|=\varepsilon}\hat{T}_i\hat{u}_i\,ds = Re\left[\bar{P}^j\sum_k\left(P^kD_j^k+\bar{P}^kE_j^k\right)\right] + 0(\varepsilon^2) \tag{22}$$

where

$$D_j^k = d^k(\zeta_j) + f^k(\zeta_j)$$
$$E_j^k = e^k(\zeta_j) + g^k(\zeta_j) \tag{23}$$

It is noted that the integration of 0(1) terms in the integrand is zero. After some algebraic manipulations, we get

$$\sum_j \int_{|z-z_j|=\varepsilon} \hat{T}_i \hat{u}_i ds = (\mathbf{X}^T \mathbf{Y}^T) \begin{pmatrix} \mathbf{H}_{1R} & \text{sym} \\ \mathbf{H}_{1I} & \mathbf{H}_{2R} \end{pmatrix} \begin{pmatrix} \mathbf{X} \\ \mathbf{Y} \end{pmatrix} \tag{24}$$

where $(\ )^T$ denotes the transpose, the subscripts $(\ )_R$ and $(\ )_I$ respectively denote the real and imaginary parts, $(\ )$ denotes a vector or a matrix, and

$$\mathbf{X}^T = (X^1, X^2, \ldots .)$$

$$\mathbf{Y}^T = (Y^1, Y^2, \ldots .)$$

$$\mathbf{H}_1 = [D_j^k + E_j^k]$$

$$\mathbf{H}_2 = [D_j^k - E_j^k] \tag{25}$$

It is noted that

$$\mathbf{H}_{1R} = \mathbf{H}_{1R}^T$$

$$\mathbf{H}_{2R} = \mathbf{H}_{2R}^T$$

$$\mathbf{H}_{1I} = -\mathbf{H}_{2I}^T \tag{26}$$

so that the flexibility matrix $\mathbf{H}$ of Eq 24 is symmetric.

Hybrid Functional for Repaired Panel

The repaired panel shown in Fig. 2 consists of three parts: the skin, rivets, and a doubler.[4] The variational functional of the panel is simply the sum of the functional of the three components. Each of the rivets is modeled as a series of springs representing the flexibility of the rivet stem and the adjacent holes of the skin and doubler. The stiffness of each spring element is shown in Fig. 3*a*, where E_s, E_r, and E_d are, respectively, the Young's moduli of the skin, rivet, and doubler; D is the rivet diameter; and t and t_d are the thickness of the panel and the doubler, respectively. The constants A_1 and A_2 are obtained empirically through tests [*2*] and are, respectively, 5 and 0.8 for aluminum rivets, and 1.666 and 0.86 for steel fasteners. The compliance coefficient of the rivet is

$$\alpha = \left(\frac{A_1}{E_r D} + \frac{A_2}{E_s t} + \frac{A_2}{E_d t_d}\right) \tag{27}$$

Using the complementary energy formulation [*3*], the variational functional for the rivets can be written as

$$\pi_r = \sum_k \left[(u_d - \tilde{u})_k F_x^k + (v_d - \tilde{v})_k F_y^k - \frac{1}{2}\alpha[(F_x^k)^2 + (F_y^k)^2] \right] \tag{28}$$

[4]The original data used non-SI units.

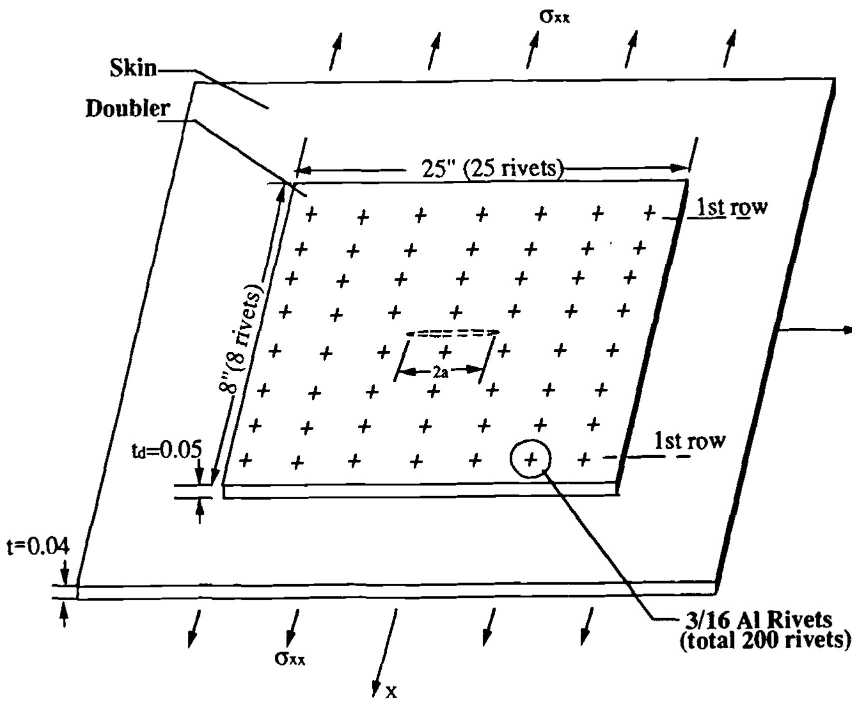

FIG. 2—*Cracked skin with single doubler.*

where (F_x^k, F_y^k) are the forces on the rivet, $(\tilde{u}, \tilde{v})_k$ are the skin displacements around the rivet hole, and $(u_d, v_d)_k$ are the doubler displacements at z_k.

Let us model the doubler by the regular finite-element method. The strain energy of the doubler is

$$\pi_d = t_d \int_A \frac{1}{2} \mathbf{e}^T \mathbf{C} \mathbf{e} \, dA \tag{29}$$

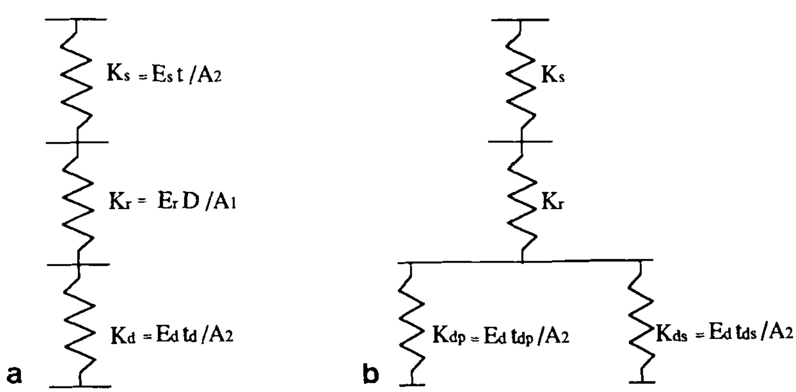

FIG. 3—*Spring models for rivets:* (a) *single doubler design and* (b) *double doubler design.*

where $\mathbf{e}$ is the strain vector, $\mathbf{C}$ is the elastic coefficient matrix per unit thickness, and A is the area of the doubler.

Using Eqs 7, 28, and 29, we have the functional for the repaired panel

$$\pi = \pi_p + \pi_d + \pi_r \tag{30}$$

which can be used to derive the finite element equations. The number of unknowns of the finite element equations can be reduced by eliminating the rivet displacements at the skin $(\bar{u}, \bar{v})_k$, and the rivet forces, (F_x^k, F_y^k). We shall consider the following two doubler designs.

(a) Single Doubler (Fig. 2)

The first variation of π with respect to (F_x^k, F_y^k) and $(\bar{u}, \bar{v})_k$ gives

$$\begin{aligned} \alpha F_x^k &= (u_d)_k - (\bar{u})_k \\ \alpha F_y^k &= (v_d)_k - (\bar{v})_k \end{aligned} \tag{31}$$

and

$$\begin{aligned} F_x^k &= tX^k \\ F_y^k &= tY^k \end{aligned} \tag{32}$$

Requiring that the relationships between (F_x^k, F_y^k) and (X^k, Y^k) are satisfied a priori, Eq 30 reduces to

$$\begin{aligned} \pi = & -\sum_k t\left[X^k(u^\circ)_k + Y^k(v^\circ)_k + \int_{|z-z_k|=\varepsilon} \frac{1}{2}\hat{T}_i\hat{u}_i ds\right] \\ & + \sum_k t\left\{X^k(u_d)_k + Y^k(v_d)_k - \frac{1}{2}\alpha t[(X^k)^2 + (Y^k)^2]\right\} + \pi_d \end{aligned} \tag{33}$$

The independent field variables for Eq 33 are the doubler deflections $(u_d, v_d)_k$ and the stress functions (ϕ, ψ) with the nodal values of the deflection and rivet loads (X^k, Y^k), respectively, being the unknowns for the finite-element equations.

(b) Doubler Lamination: Two-Side Doublers (Fig. 4)

This is a design that can be used to reduce the abrupt change of bending rigidity at the edge of the doubler and, hence, minimize the induced bending stresses on the skin. This design also reduces the forces of the rivets of the first row to improve the life of the skin. For this design, we can model the flexibility around the holes of the doublers as two parallel springs (Fig. 3*b*). The variational functional for the rivets can be written as

$$\begin{aligned} \pi_r = \frac{1}{2}\sum_k [& K(\tilde{u} - \bar{u})^2 + K(\tilde{v} - \bar{v})^2 + K_{ds}(u_{ds} - \bar{u})^2 \\ & + K_{ds}(v_{ds} - \bar{v})^2 + K_{dp}(u_{dp} - \bar{u})^2 + K_{dp}(v_{dp} - \bar{v})^2]_k \end{aligned} \tag{34}$$

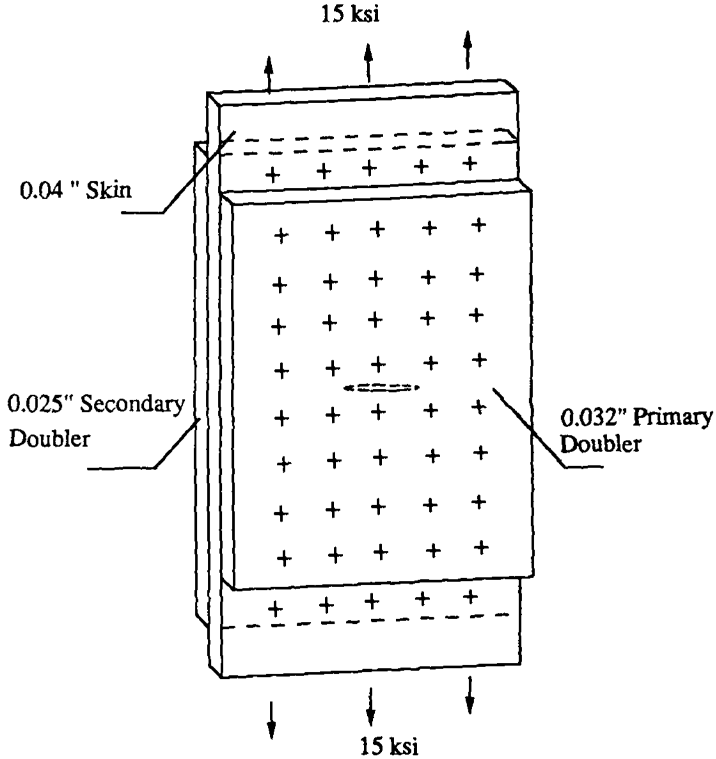

FIG. 4—*Two-side doubler lamination.*

where $(\bar{u}, \bar{v})_k$ are the fictitious displacements between the springs representing the rivet stem and the doubler holes and

$$\frac{1}{K} = \frac{A_2}{E_s t} + \frac{A_1}{E_r D} \quad \text{(rivet stem and skin in series)}$$

$$K_{ds} = \frac{E_d t_{ds}}{A_2}$$

$$K_{dp} = \frac{E_d t_{dp}}{A_2} \tag{35}$$

are stiffnesses of the spring elements with the subscripts, s and p, denoting quantities associated with the secondary and primary doublers.

The functional for the doublers is in the same form as that in Eq 29 except that the domain of integration now includes the area of both doublers. The first variation of π with respect to the displacements $(\tilde{u}, \tilde{v})_k$, and $(\bar{u}, \bar{v})_k$ gives

$$tX = K(\bar{u} - \tilde{u})$$

$$tY = K(\bar{v} - \tilde{v}) \tag{36}$$

$$K(\bar{u} - \tilde{u}) + K_{ds}(\bar{u} - u_{ds}) + K_{dp}(\bar{u} - u_{dp}) = 0$$
$$K(\bar{v} - \tilde{v}) + K_{ds}(\bar{v} - v_{ds}) + K_{dp}(\bar{v} - v_{dp}) = 0 \tag{37}$$

In Eqs 36 and 37 and in the subsequent discussion, the subscripts and superscripts, k, are dropped for convenience. We can solve for $(\tilde{u}, \tilde{v})$ and $(\bar{u}, \bar{v})$ in terms of (X, Y), (u_{ds}, v_{ds}), and (u_{dp}, v_{dp}). Eliminating $(\tilde{u}, \tilde{v})$ and $(\bar{u}, \bar{v})$, the functional, π, then becomes

$$\pi = \pi_d - \sum_k t\left[X^k(u^\circ)_k + Y^k(v^\circ)_k + \int_{|z - z_k| = \varepsilon} \frac{1}{2}\hat{T}_i\hat{u}_i ds\right]$$
$$+ \frac{1}{2}\sum_k \left\{(X, u_{ds}, u_{dp})\,\mathbf{K}\begin{pmatrix} X \\ u_{ds} \\ u_{dp}\end{pmatrix} + (Y, v_{ds}, v_{dp})\,\mathbf{K}\begin{pmatrix} Y \\ v_{ds} \\ v_{dp}\end{pmatrix}\right\}_k \tag{38}$$

where $\mathbf{K}$ is given by the matrix

$$\mathbf{K} = \begin{pmatrix} -t^2\left(\frac{1}{K} + \frac{1}{K_{ds} + K_{dp}}\right) & & \text{sym} \\ \frac{tK_{ds}}{K_{ds} + K_{dp}} & \frac{K_{ds}K_{dp}}{K_{ds} + K_{dp}} & \\ \frac{tK_{dp}}{K_{ds} + K_{dp}} & \frac{-K_{ds}K_{dp}}{K_{ds} + K_{dp}} & \frac{K_{ds}K_{dp}}{K_{ds} + K_{dp}} \end{pmatrix} \tag{39}$$

The independent variables for the functional are the doubler deflections $(u_{dm}, v_{dm})_k$ where $m = s$ and p, and the loads (X^k, Y^k), the rivet loads on the panel per unit thickness. The nodal values of these quantities are the unknowns for the finite-element equations.

Examples

Figure 5 shows the results for a fuselage skin of thickness 1 mm (0.04 in.) with a crack of length $2a$. A doubler of thickness 1.27 mm (0.05 in.) is riveted over the damaged area with four rows of rivets on each side of the crack in the x direction. Each row contains 25 rivets, running from $y = -304.8$ mm (-12 in.) to $y = +304.8$ mm ($+12$ in.). The rivet diameter is 4.76 mm ($\frac{3}{16}$ in.) and the rivet pitch is 25.4 mm (1 in.). The results for rivet forces, F_x, are shown in Fig. 5 for the case that the skin, rivets, and doublers are all made of aluminum ($E = 10^7$ psi, $\nu = 0.33$) with a crack length of $2a = 50.8$ mm (2 in.). It is seen that the higher rivet loads are at the first row of rivets ($x = +88.9$ mm) ($+3.5$ in.) that connects the doubler to the skin, with the highest force of 103 kg (227 lb) at the corner rivet ($x = 3.5$ in., $y = 12$ in.) where both edges of the doubler come together.

As a comparison to these rivet loads, the results of Swift [2] that are based on the displacement compatibility method are also shown. Although the rivet loads from Ref 2 are based on a skin without a crack, the present finite element results for a small crack, $a = 1$ in., are an adequate comparison. The maximum rivet load, F_x, from Ref 2 is 85 kg (187 lb), which is 18% less than the present result of 103 kg (227 lb). This difference is mainly due to the inclusion of two-dimensional effects in the present finite element analysis, in comparison to the one-dimensional effects of the displacement compatibility method. Since the finite element results accurately model the effects at the first row of the doubler/skin

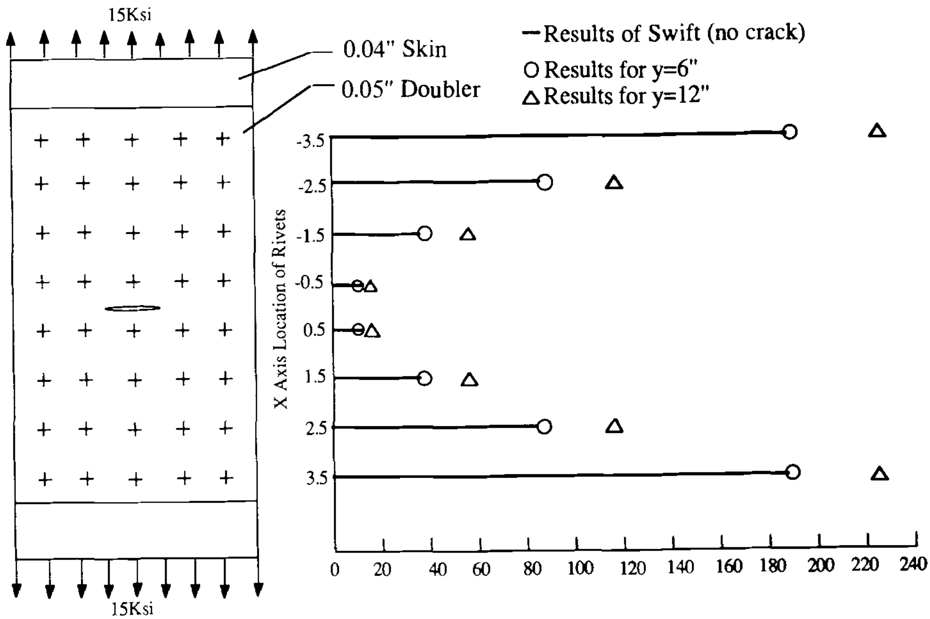

FIG. 5—*Rivet load distribution (lb),* F_x, *single doubler, crack length* $2a$ = *2 in. (50.8 mm).*

intersection, it is physically most plausible to compare with Ref 2 halfway along this edge row of rivets at y = 152.4 mm (6 in.), which minimizes the effects of both the crack and the corner effect where the edges of the doubler come together. At this location, the present finite element technique produces a rivet load of 85.4 kg (188 lb). As seen in Fig. 5, the comparison of rivet loads at y = 152.4 mm (6 in.) shows excellent agreement. Another factor of importance is the effect of rivet load in the y direction, that is, normal to direction of applied stress of 103.4 MPa (15 ksi). For the maximum rivet load of $F_{x,\max}$ = 103 kg (227 lb), there is also a load component in y direction of 34.5 kg (76 lb), so that the resultant rivet load is actually 108.5 kg (239 lb).

The effect of crack length on the maximum rivet load, F_x, for the corner rivet, x = 88.9 mm (3.5 in.), y = 304.8 mm (12 in.), is shown in Fig. 6. For a doubler thickness of 1.27 mm (0.05 in.), F_x reaches 134.4 kg (296 lb) when the crack length $2a$ is 609.6 mm (24 in.), that is, the crack reaches all the way to the edge of the doubler. The additional rivet force in the y direction is small and has little effect on the resultant rivet load.

An important indicator of fatigue life is the skin peak bearing stress that is calculated from the maximum rivet force at the corner rivet

$$\sigma_{br} = \frac{F_{\max}}{tD} \tag{40}$$

where t is the skin thickness and D is the rivet diameter. For the crack length of 50.8 mm (2 in.), the peak bearing stress is calculated as σ_{br} = 239/(0.04)(0.1875) = 219.7 MPa (31 867 psi), while for a crack length of 609.6 mm (24 in.) the bearing stress is 272.4 MPa (39 500 psi). The ratio of bearing stress to the gross stress of 103.4 MPa (15 000 psi) is then 2.12 and 2.63 respectively, for 50.8 and 609.6 mm (2 and 24 in.) crack lengths. If the skin is made of 2024-T3, the fatigue life of the basic structure with open holes and a stress ratio

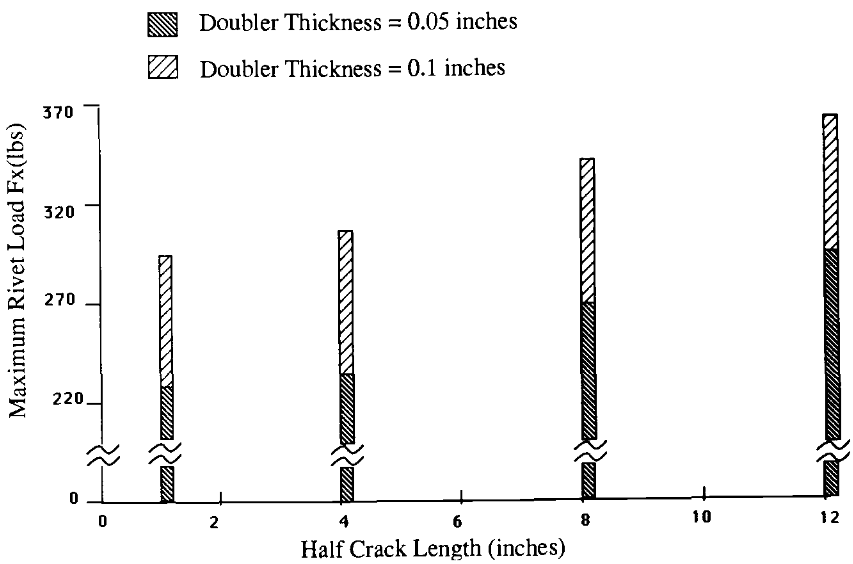

FIG. 6—*Maximum rivet load* F_x *for different crack lengths, single doubler.*

of $R = 0$ is 160 000 cycles, but this fatigue life is reduced with increasing ratio of bearing stress to gross stress [2]. With the 1.27 mm (0.05 in.) doubler, the fatigue life is reduced to about 39 000 cycles and 30 000 cycles, respectively, for 50.8 and 609.6 mm (2 and 24 in.) crack lengths, based upon open hole *S-n* data of Ref *2*.

As the thickness of the doubler increases, the rivets in the first (edge) row carry an increasing portion of the load transferred to the doubler. In Fig. 6, the maximum rivet load, F_x, for the corner rivet is plotted as a function of crack length, for a doubler thickness of 2.54 mm (0.10 in.), as well as for 1.27 mm (0.05 in.). The increase in rivet load with crack length, from $a = 25.4$ mm (1 in.) to $a = 304.8$ mm (12 in.), is 17 and 30%, respectively, for a doubler thickness of 2.54 and 1.27 mm (0.10 and 0.05 in.). For a crack length of 609.6 mm (24 in.), the maximum corner rivet force for a 2.54 mm (0.10 in.) doubler is 166.2 kg (366 lb), which is 24% higher than the 134.4 kg (296 lb) force for the 1.27 mm (0.05 in.) doubler. Consequently, the fatigue life of the skin is reduced further by the thicker doubler, even though a thicker doubler can be stronger statically. The effect of doubler thickness on maximum rivet load (corner rivet) is shown in Fig. 7 for 1 mm (0.040 in.) rivet skin thickness. It is seen that the rivet load is affected strongly by the doubler thickness in the range from 1 to 2.5 mm (0.04 to 0.10 in.), rising 45% in this range, which is similar to the result of Swift [2].

A doubler design configuration that can be used to reduce fastener loads in the first doubler row is the use of a multiple doubler as shown in Fig. 4. Placing a secondary doubler on the inside of the panel and extending it one fastener row so that the outer rivet row of the skin only has a single doubler connection, produces a significant advantage in terms of load transfer and inspectability. Consider the case with a 0.63 mm (0.025 in.) inner (secondary) doubler and a 0.81 mm (0.032 in.) outer (primary) doubler. For this configuration and a crack length of $2a = 50.8$ mm (2 in.), the corner rivet load, F_x, $x = 114$ mm (4.5 in.), $y = 304.8$ mm (12 in.), is reduced 22% to 79.9 kg (176 lb) as compared to 103 kg (227 lb), $x = 88.9$ mm (3.5 in.), $y = 304.8$ mm (12 in.), for the 1.27 mm (0.05 in.) single doubler shown in Fig. 5. The skin bearing stress is reduced to 162 MPa (23 466 psi) and the ratio

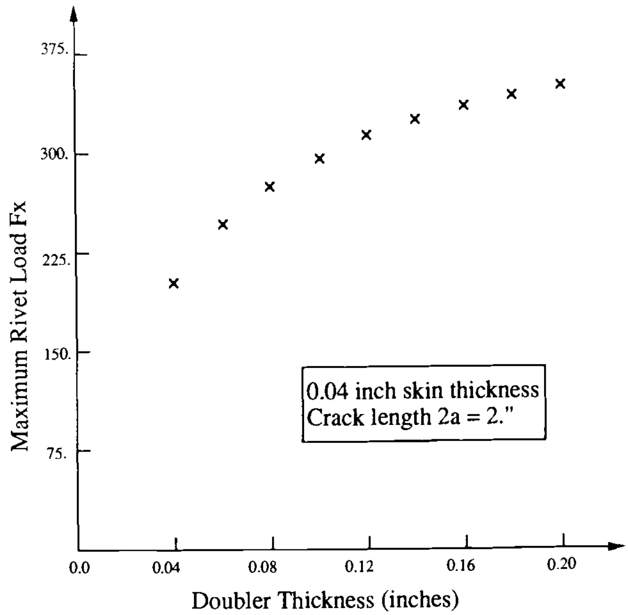

FIG. 7—*Effect of doubler thickness on maximum rivet load (corner rivet), single doubler.*

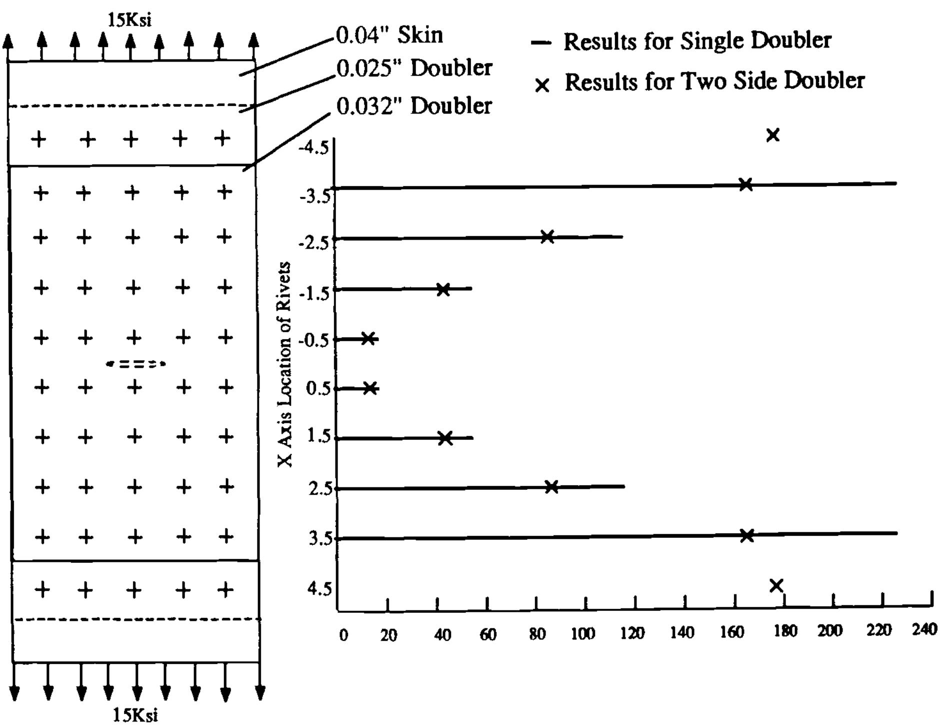

FIG. 8—*Rivet load distribution (lb),* F_x*, two-side doubler, crack length 2*a *= 2 in. (50.8 mm).*

of bearing stress to gross stress is 1.56, producing an enhanced fatigue life of 55 000 cycles. Additionally, inspectability of this type of doubler repair is improved since a crack in the first rivet row will now be visible. In Ref *2*, the critical rivet load, without a crack, is calculated as 55 kg (122 lb), which should be compared to the present rivet load of 66 kg (146 lb) located halfway along the edge row of rivets at y = 152.4 mm (6 in.). The difference in this result is due to alternate modeling of the rivet compliance in Ref *2* and the present analysis. The row-by-row rivet load distribution for this two-sided doubler configuration is shown in Fig. 8 for a crack length of 50.8 mm (2 in.).

Acknowledgment

This work was supported by the Federal Aviation Administration Technical Center.

References

[*1*] Swift, T., "Damage Tolerance Analysis of Redundant Structures," AGARD Lecture Series No. 97, Fracture Mechanics Design Methodology, Advisory Group for Aerospace Research and Development, Jan. 1979.

[*2*] Swift, T., "Repairs to Damage Tolerant Structures," Structural Integrity of Aging Airplanes, S. N. Atluri, Sampath, and P. Tong, Eds., Springer Serves in Computation Mechanics, Springer-Verlag, New York, 1991, pp. 433–489.

[*3*] Tong, P., "A Hybrid Finite Element Method for Damage Tolerance Analysis," *Computers and Structures*, Vol. 19, No. 1–2, 1984, pp. 263–269.

[*4*] Tong, P., Pian, T. H. H., and Lasry, S., "A Hybrid Finite Element Approach to Crack Problems in Plane Elasticity," *International Journal for Numerical Methods in Engineering*, Vol. 7, 1973, pp. 297–308.

[*5*] Muskhelishvilli, N. I., *Some Basic Problems of Mathematical Theory of Elasticity*, P. Noordhoff, Leyden, The Netherlands, 1953.

[*6*] Greif, R., "The Plane Stress Solution of a Concentrated Load in the Presence of a Crack," private communication.

Toshihisa Nishioka,[1] Toshihisa Fujimoto,[1] and Keigo Sakakura[1]

A Hybrid Numerical-Experimental Method for Caustic Measurements of the T^*-Integral

REFERENCE: Nishioka, T., Fujimoto, T., and Sakatura, K., "**A Hybrid Numerical-Experimental Method for Caustic Measurements of the T^*-Integral**," *Fracture Mechanics: Twenty-Second Symposium (Volume II), ASTM STP 1131*, S. N. Atluri, J. C. Newman, Jr., I. S. Raju, and J. S. Epstein, Eds., American Society for Testing and Materials, Philadelphia, 1992, pp. 170–182.

ABSTRACT: This paper presents a methodology of direct experimental measurement of the T^*-integral, which has great potential as a nonlinear (elastoplastic) fracture mechanics parameter. A hybrid numerical-experimental method was developed to measure the T^*-integral by the size of reflected caustic pattern. To this end, the formation process of the caustic pattern for an elastoplastic crack tip in a compact tension specimen was simulated by a previously developed finite element simulation technique aided by computerized symbolic manipulation. Experimental measurement of the caustic pattern in the compact tension specimen was also carried out. Both simulated and actual caustic patterns agreed very well. The relations between the T^*-integral and the size of caustic pattern were obtained for various optical setup.

KEY WORDS: elastic-plastic fracture mechanics, method of caustics, finite element simulation, T^*-integral, path independent integral, generalized J-integral

In recent years, nonlinear fracture mechanics methodology for safety design against ductile fracture in structural components has been the object of intense study. In nonlinear fracture mechanics, consideration of integral type crack-tip parameters is essential due to a finite extent of a process zone or damaged zone near the crack tip. These integral type parameters, however, are usually difficult to evaluate experimentally and mathematically. Therefore, nonlinear fracture mechanics relies heavily on finite-element simulation technologies and appropriate integral-type crack-tip parameters.

Among the integral-type crack-tip parameters proposed in literature, the path independent T^*-integral derived by Atluri, Nishioka, and Nakagaki [*1*] has great potential as a unified crack-tip parameter, since the T^*-integral is the most natural extension of the so-called (Rice's static) J-integral [*2*] and the nonlinear dynamic J-integral (J') [*3*], to nonlinear static and nonlinear dynamic crack problems.

The method of caustics, which also is known as the shadow spot method, has many advantages, such as the simplicity of equipment and measurement, applicability to static as well as dynamic crack problems, and so forth. For these reasons, the method of caustics has been used to measure static and dynamic stress-intensity factors in many cases.

However, only a few attempts [*4,5*] have been done to extend the method of caustics for the measurement of elastic-plastic crack-tip parameters. The present authors [*6*] have developed a finite element simulation technique aided by computerized symbolic manipulation

[1]Professor, graduate student, and technician, respectively, Kobe University of Merchantile Marine, Higasinada-ku, Kobe, 658 Japan.

for the formation process of reflected caustic pattern in an elastic-plastic material. This technique showed great ability to obtain simulated caustic patterns precisely.

In the present study, based on the aforementioned numerical method aided by computerized symbolic manipulation, a hybrid numerical-experimental method is developed to measure the T^*-integral by the size of reflected caustic pattern. Experimental measurement of the caustic pattern in the compact tension specimen is also carried out. In order to assure the accuracy of the present method, the simulated caustic patterns are compared with the actually measured caustic patterns.

Nonlinear Fracture Parameter T^*-Integral

Consider a crack in an elastic-plastic body as shown in Fig. 1. For elastoplastic crack problems, a finite element analysis based on an incremental flow theory of plasticity is usually used. Therefore, it is natural to consider an incremental measure of the strength of the crack-tip field. First, based on this idea, Atluri, Nishioka, and Nakagaki [*1*] have derived a general form of path independent integral T^*, which is valid for any material-constitutive relation under quasi-static as well as dynamic conditions. For static crack problems, the T^*-integral can be written as

$$T_k^* = \sum \Delta T_k^* \tag{1}$$

$$\Delta T_k^* \equiv \int_{\Gamma_\varepsilon} [\Delta W n_k - (t_i + \Delta t_i)\Delta u_{i,k} - \Delta t_i u_{i,k}]dS \tag{2a}$$

$$= \int_{\Gamma + \Gamma_c} [\Delta W n_k - (t_i + \Delta t_i)\Delta u_{i,k} - \Delta t_i u_{i,k}]dS$$

$$+ \int_{V_\Gamma - V_\varepsilon} \left[\Delta\sigma_{ij}\left(\varepsilon_{ij} + \frac{1}{2}\Delta\varepsilon_{ij}\right)_{,k} - \Delta\varepsilon_{ij}\left(\sigma_{ij} + \frac{1}{2}\Delta\sigma_{ij}\right)_{,k}\right]dV \tag{2b}$$

where Σ denotes the summation along the loading history; $\Delta W = (\Delta\sigma_{ij} + \frac{1}{2}\Delta\sigma_{ij})\Delta\varepsilon_{ij}$ is the incremental stress working density; σ_{ij} and ε_{ij} are the stress and the strain, respectively; n_k the outward normal direction cosines; t_i and u_i are the traction and the displacement, respectively; ( ), k denotes $\partial(\ )/\partial x_k$. The general expression of the T^*-integral including dynamic crack problems is given in Ref *1*. The path independence of the T^*-integral can be shown easily without using a constitutive relation. Therefore, the T^*-integral is valid for any constitutive model, including plasticity, creep, and viscoplasticity.

The T^*-integral can be also expressed in a total form as follows

$$T_k^* \equiv \int_{\Gamma_\varepsilon} [W n_k - t_i u_{i,k}]dS \tag{3a}$$

$$= \int_{\Gamma + \Gamma_c} [W n_k - t_i u_{i,k}]dS$$

$$+ \int_{V_\Gamma - V_\varepsilon} [\sigma_{ij}\varepsilon_{ij,k} - W_{,k}]dV \tag{3b}$$

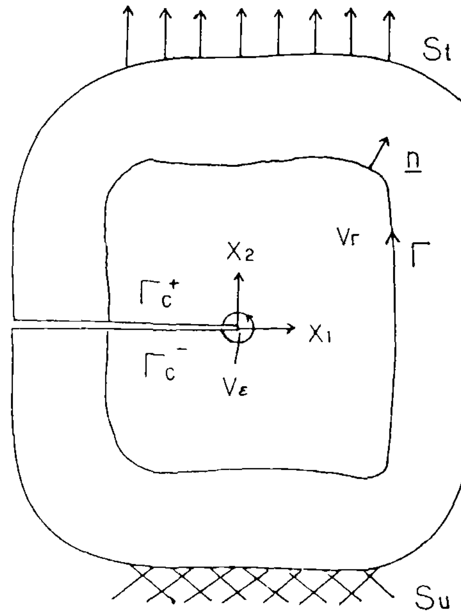

FIG. 1—*Nomenclature for a cracked body.*

The near-field path Γ_ε in Eqs 2 and 3 will be taken along the boundary of a fracture process zone [*7*]. Usually the size of fracture process zone may be finite for growing cracks in ductile (elastic-plastic) materials.

However, in brittle materials, the process zone should be very small, compared to the size of the crack itself. For this reason, an infinitesimally shrinking path to the crack tip can be used. It is also noted that, in numerical analyses for stationary cracks, $V_\varepsilon = 0(\Gamma_\varepsilon = 0)$ can be used, as demonstrated in Ref *8*.

Note that in an elastic-plastic material under arbitrary loading history, W is the total accumulated increments of stress working density. Since σ_{ij} is not a single-valued function of ε_{ij}, in general, we have $W_{,k} \neq \sigma_{ij}\varepsilon_{ij,k}$.

For elastic materials, since W corresponds to the strain energy density, the T_k^*-integrals reduce to the J_k'-integrals derived by Nishioka and Atluri [*3*] for elastodynamic cases. Moreover, for elastostatic cases, the T_k^* integrals reduce to the J_k integrals derived by Budiansky and Rice [*9*] for elastostatic cases. Thus, the T^*-integral is a natural extension of the so-called (Rice's static) J-integral and the dynamic J-integral J'. For these reasons, the T^*-integral may be considered as the generalized J-integral and has good features as a unified crack-tip parameter for various types of fracture mechanics.

The T_k^*-integrals can be regarded as the x_k components of the vector integral $\mathbf{T}^*$ emanating from the crack tip. Accordingly, the ordinary coordinate transformation rule of vector can be used for the T_k^*-integrals [*10*].

Physical and Mathematical Principles in the Formation of Reflected Caustic Pattern

Consider a family of parallel light rays incident on an opaque specimen containing a crack as illustrated in Fig. 2. Here, we consider the optical setup for the method of reflected caustics.

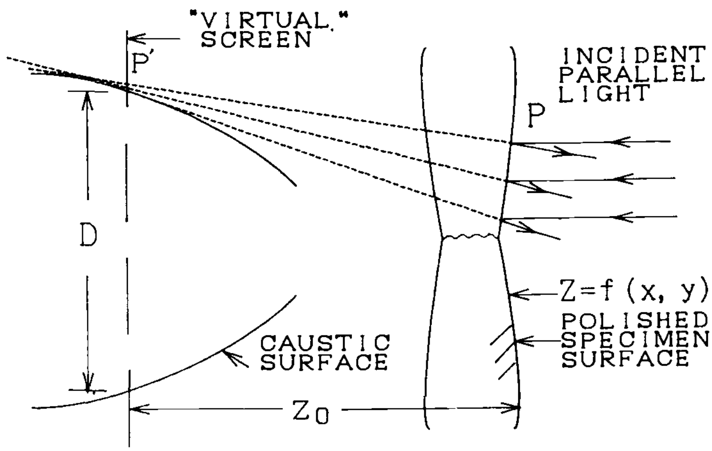

FIG. 2—*Optical relations in reflected caustic method.*

The stress concentration around the crack tip causes a reduction of the thickness of the specimen as shown in Fig. 2. As a consequence, the polished surface of the specimen near the crack tip acts similar to a concave mirror. Thus, the light ray reflected from the Point P (Fig. 3) on the specimen is deflected inward and reaches the Point P' on a virtual screen behind the specimen. As can be seen in Fig. 3, the position vector $\mathbf{W}$ of the image point P' is given by

$$\mathbf{W} = \lambda \mathbf{r} + \mathbf{w} \tag{4}$$

where λ is the magnification factor of the optical apparatus. λ takes a unit value (1.0) for a parallel light beam.

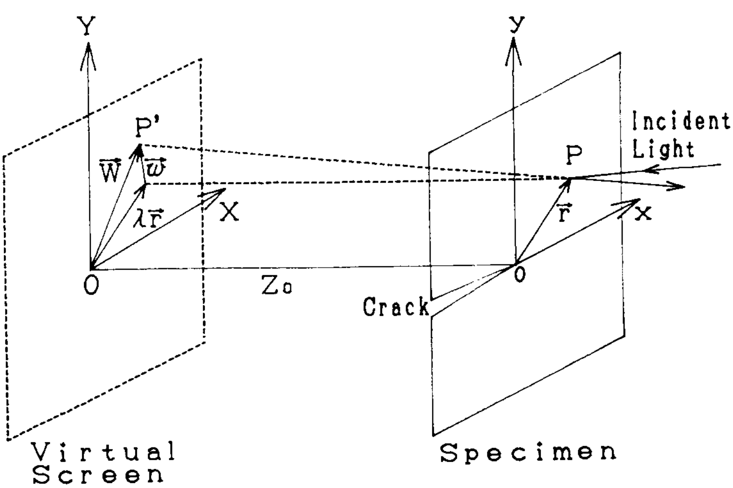

FIG. 3—*Schematic of the optical setup for caustic by reflection.*

The vector $\mathbf{w}$, which indicates the deviation of the light ray on the screen, is given as [4,11]

$$\mathbf{w} = -2z_0 \operatorname{grad} f(x,y) \tag{5}$$

where z_0 is the distance between the screen and the specimen, and $f(x,y)$ is the total displacement of the specimen surface in the thickness direction x_3.

The outward deviation of the reflected image rays around the crack tip creates a dark spot on the virtual screen. This dark spot is surrounded by a bright light concentration, which is called the "caustic curve." The caustic curve consists of a series of the light rays passing through a particular curve on the specimen. This curve is called the "initial curve" of the caustic. Usually the initial curve for an elastostatic crack problem represents a circle around the crack tip. The initial curve can be determined by the condition where the mapping is not invertible between $\mathbf{r}$ on the specimen and $\mathbf{W}$ on the screen. Mathematically this condition can be expressed by the vanishing point of Jacobian

$$J = \frac{\partial(W_x,W_y)}{\partial(x,y)} = \begin{vmatrix} \dfrac{\partial W_x}{\partial x} & \dfrac{\partial W_x}{\partial y} \\ \dfrac{\partial W_y}{\partial x} & \dfrac{\partial W_y}{\partial y} \end{vmatrix} = 0 \tag{6}$$

where W_x and W_y are the components of the vector $\mathbf{W}$ with respect to x and y, respectively. Then, substitution of the determined initial curve into Eq 4 leads to the expression for the caustic curve.

The surface deformation $f(x,y)$ can be calculated by the three-dimensional finite element analysis. However, for thin plates, it is convenient to evaluate $f(x,y)$ by using the generalized plane stress condition, as follows

$$f(x,y) = \Sigma\Delta f(x,y) \tag{7}$$

and

$$\begin{aligned} \Delta f(x,y) &= \int_0^{B/2} \Delta\varepsilon_{33}(x,y)dx_3 \\ &= \frac{B}{2}\left[(\Delta\sigma_{11} + \Delta\sigma_{22})\frac{1-2\nu}{E} - (\Delta\varepsilon_{11} + \Delta\varepsilon_{22})\right] \end{aligned} \tag{8}$$

where Σ will be taken over the loading steps or time steps, and B is the specimen thickness.

In the present paper, the surface deformation $f(x,y)$ was calculated at the Gaussian integration points (3×3) in each eight-noded isoparametric element. In a previous paper [8], the formation of reflected caustic pattern was simulated using reflected light beams from the Gaussian points. However, this method was difficult to obtain initial curves and precise caustic curves. To overcome the difficulties, the authors [6] have developed a finite element simulation technique aided by computerized symbolic manipulation. In the new simulation technique, the surface deformation data at the Gaussian points first were smoothed by a least squares fitting of the following function

$$f(r,\theta) = \sum_{m=1}^{6}\sum_{n=1}^{3} C_{mn} r^{(m/2)-1}\theta^{2(n-1)} \tag{9}$$

where r,θ are the polar coordinate centered at the crack tip, and C_{mn} are the coefficients to be determined by the least squares method.

To obtain the initial and caustic curves from Eq 9, Eq 6 should be solved after substituting Eq 9 into Eqs 4 through 6. In this process, numerous algebraic manipulations are required. Approximately 300 terms will appear in the algebraic expression of Eq 6. Therefore, the use of a computerized symbolic manipulation system, which is based on an artificial intelligence technique, is indispensable. Moreover, the algebraic expressions of the partial derivatives appeared in Eqs 5 and 6 can be obtained easily if the computerized symbolic manipulation system is used.

The initial curve Eq 6 can be rewritten substituting Eq 9 into Eqs 4 through 6, as

$$\sum_{n=0}^{10} A_n(\theta)R^n = 0 \tag{10}$$

where $R = r^{1/2}$; $A_n(\theta)$ is the coefficient of the R^n term, and a function of the angle θ. In the previous paper [6], algebraic expressions of $A_n(\theta)$ were determined by a computerized symbolic manipulation system (REDUCE). To solve Eq 10 numerically, the angle range $(-\pi \leq \theta \leq \pi)$ around the crack tip was divided into small segments. Then, for each respective angle, the 10^{th} order polynomial Eq 10, was solved numerically by Bairstaw method. The solutions in terms of R were converted to those of the polar coordinate system, with $r = R^2$. The locus of r represents the initial curve. The caustic curve can be evaluated by the use of the data of r into Eqs 4 and 5.

Hybrid Numerical-Experimental Method for the T^*-Integral Caustic Measurement

The present authors [6] have developed a finite element simulation technique aided by computerized symbolic manipulation for the formation process of caustic pattern in an elastoplastic material. This technique was also used to establish the relation between the T^*-integral and the size of caustic pattern for the nuclear pressure vessel A508K′ steel (heat-treated with heating at 890°C for 1 h, oil quenching, and tempering at 250°C for 1 h) [12]. Experimental measurement of the caustic pattern in the A508K′ compact tension specimen was also carried out. Figure 4 shows the geometry of the CT specimen. To validate the

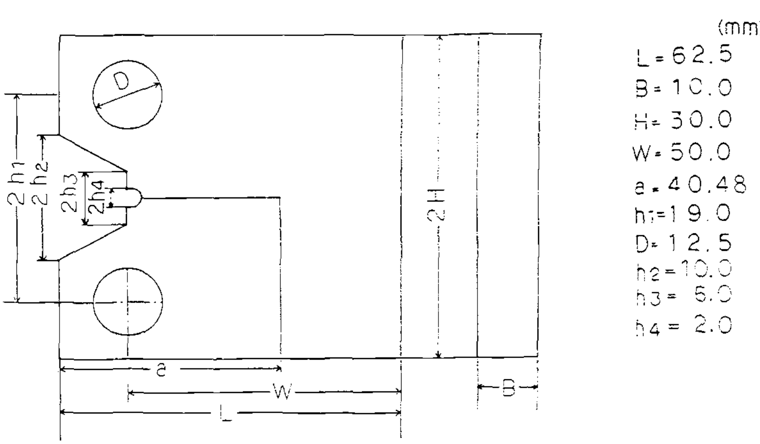

FIG. 4—*Compact tension specimen.*

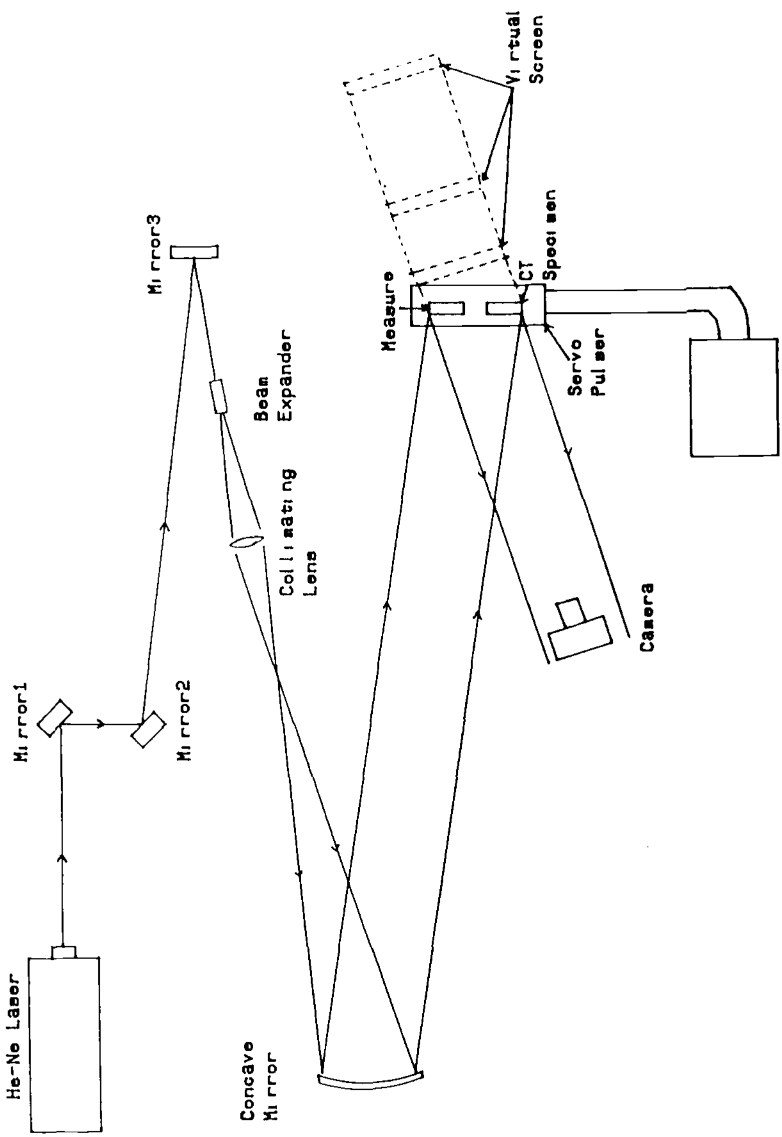

FIG. 5—*Experimental setup for reflected caustics under static loading.*

generalized plane stress condition, the reduced thickness of $B = 10$ mm was employed, while otherwise the same dimensions of 1TCT specimen were used.

The material properties of A508K′ steel are Young's modulus $E = 244.7$ GPa, Poisson's ratio $\nu = 0.3$, and the initial yield stress $\sigma_0 = 800$ MPa. After yielding, the experimental stress-strain curve exhibited the strain hardening of Ramberg-Osgood, as follows

$$\sigma/\sigma_0 = \alpha(\varepsilon_p/\varepsilon_0)^{1/n} \tag{11}$$

where ε_0 and ε_p are the initial yield strain and plastic strain, respectively, and the material constant α and n are $\alpha = 1.21$ and $n = 5.97$.

Figure 5 shows the experimental setup for the measurement of reflected caustic pattern with a parallel light ($\lambda = 1.0$). To evaluate the maximum size of caustic pattern D at virtual screens behind the specimen, the caustic patterns were photographed together with a measure (Fig. 6). The crack opening displacement (COD) δ at the load line was monitored by a COD clip gage. Displacement controlled load was applied such that, in the loading stage, δ increases from zero to 1.0 mm, and in unloading stage, δ decreases from 1.0 mm to a certain value at the zero load. The photographs of caustic pattern were taken at the various loading stages including unloading stages. Figure 7 shows the experimental results for the sizes of the caustic pattern at various loading stages.

To obtain the T^* versus D relation, the finite element simulation aided by computerized symbolic manipulation was carried out evaluating both the simulated caustic pattern and the T^*-integral in the A508K′ compact tension specimen. The finite element mesh breakdown with the eight-noded isoparametric elements for this simulation is shown in Fig. 8. Broken lines in the figure indicate the far-field paths for the calculation of the T^*-integral. Figure 9 shows the development of plastic zone around the crack tip at the various loading stages ($\delta = 0.2$, 0.4, 0.6, 0.8, 1.0 mm). A fairly large plastic zone is seen at the maximum loading.

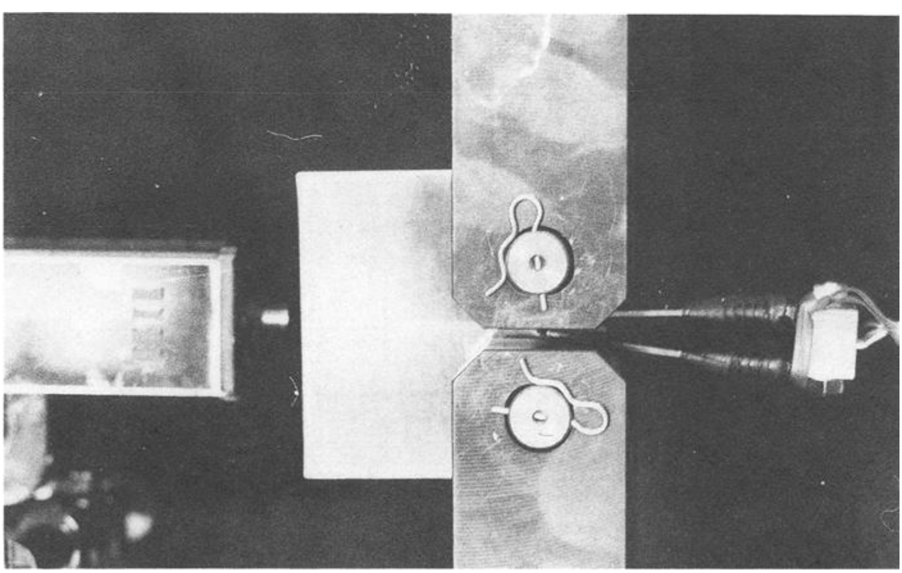

FIG. 6—*Photograph of experimental setup.*

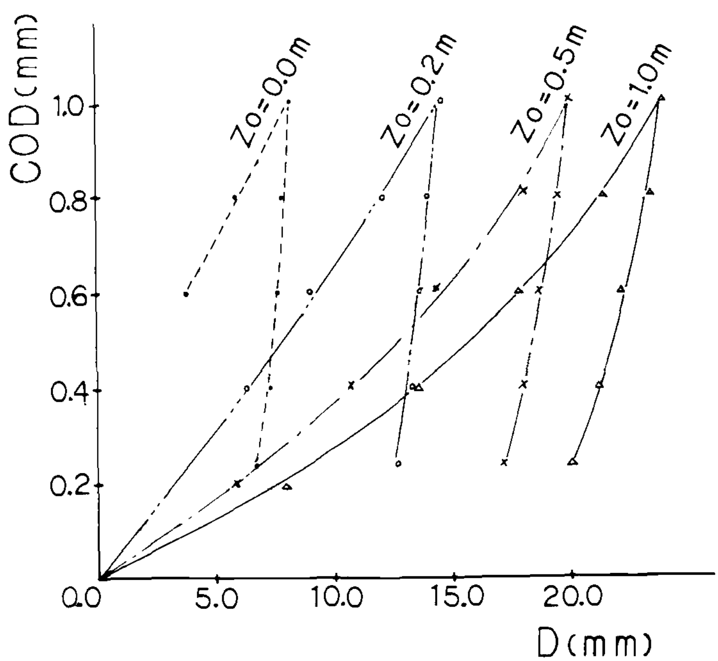

FIG. 7—*Experimental results for the size of caustic pattern.*

The simulated caustic patterns are shown in Fig. 10 comparing with the photographs of the actual caustic patterns. The projection of the shadow pattern appeared in the photograph for δ = 0.2 mm is caused by a marking line of a scriber for machining the initial notch. The simulated caustic patterns agree very well with the actual caustic patterns. The initial curves obtained by the simulation are also indicated by broken lines. The caustic curves on the virtual screen are created by the light beams incident to these initial curves on the specimen.

Figure 11 shows the variations of the size of caustic pattern D in the loading and unloading stages. Numerical results agree excellently with the experimental results. Agreement in both

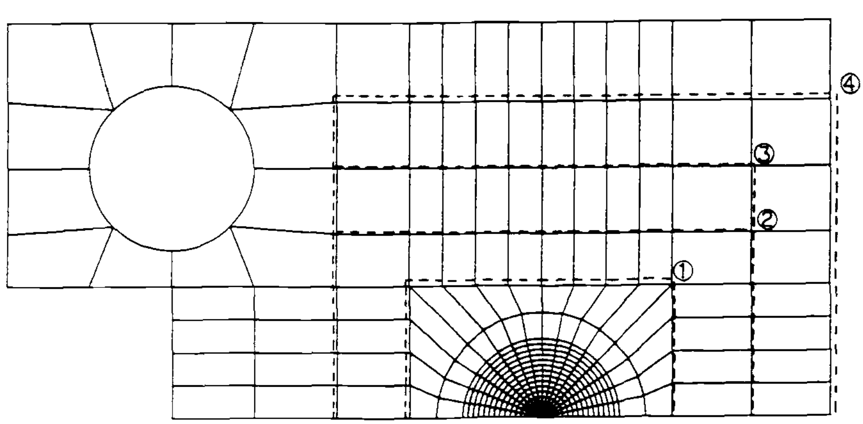

FIG. 8—*Finite element mesh for the compact tension specimen.*

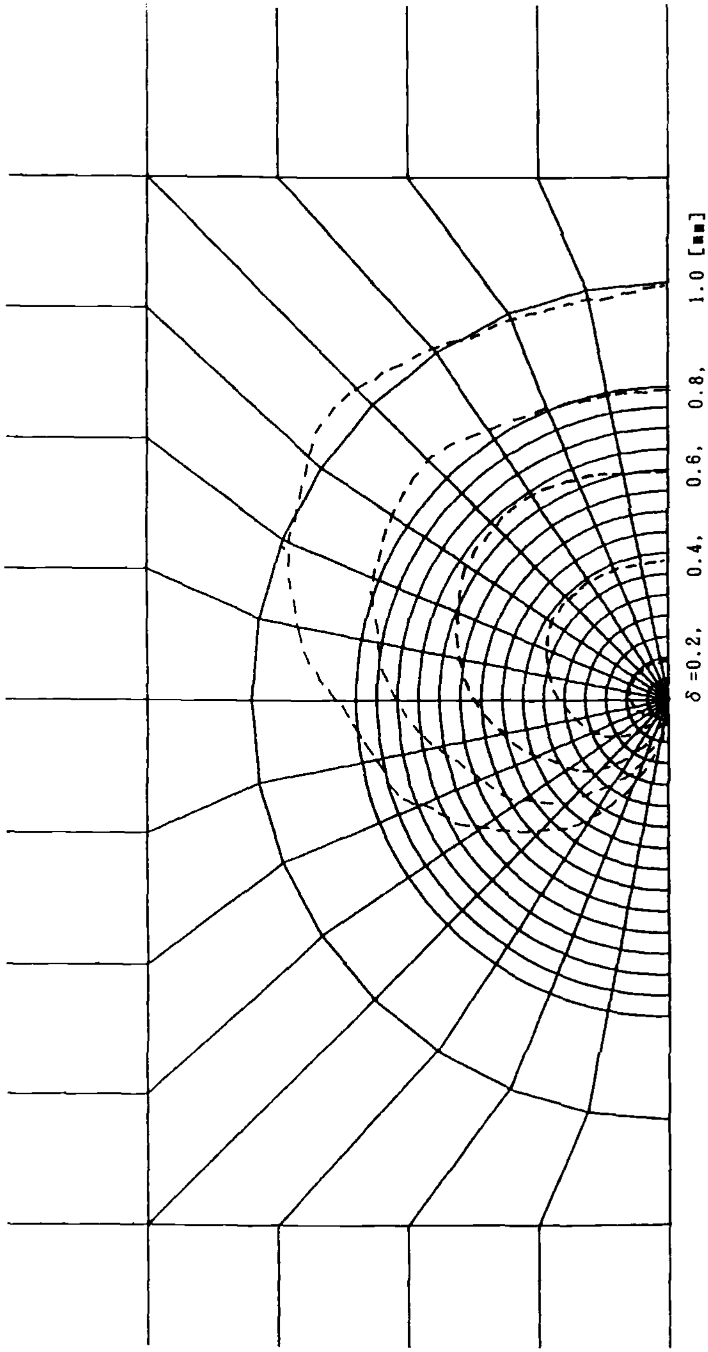

FIG. 9—*Development of plastic zone around the crack tip.*

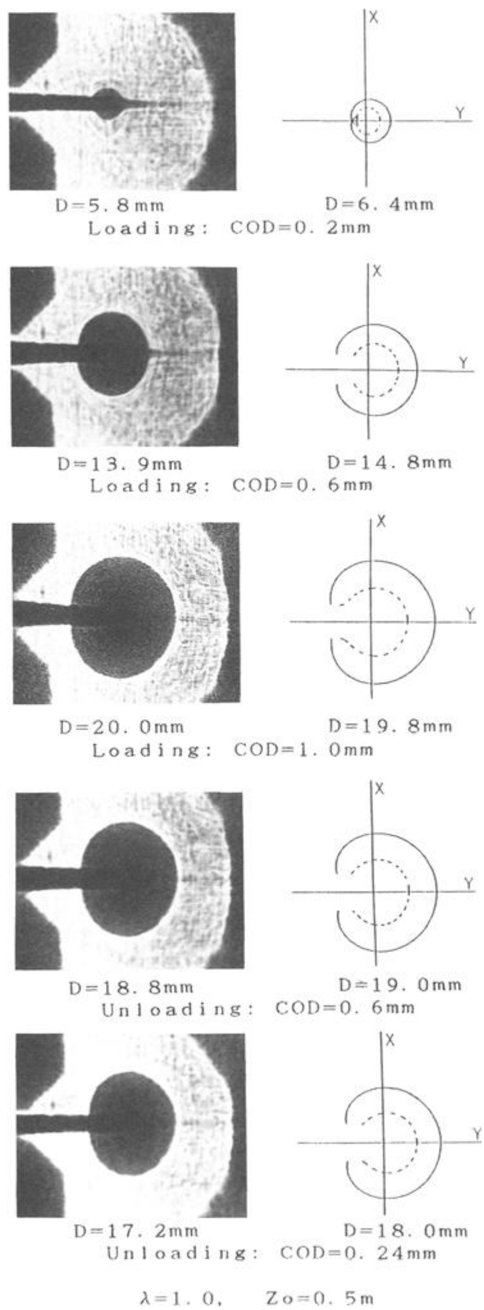

FIG. 10—*Comparison of actual caustic patterns and simulated caustic patterns.*

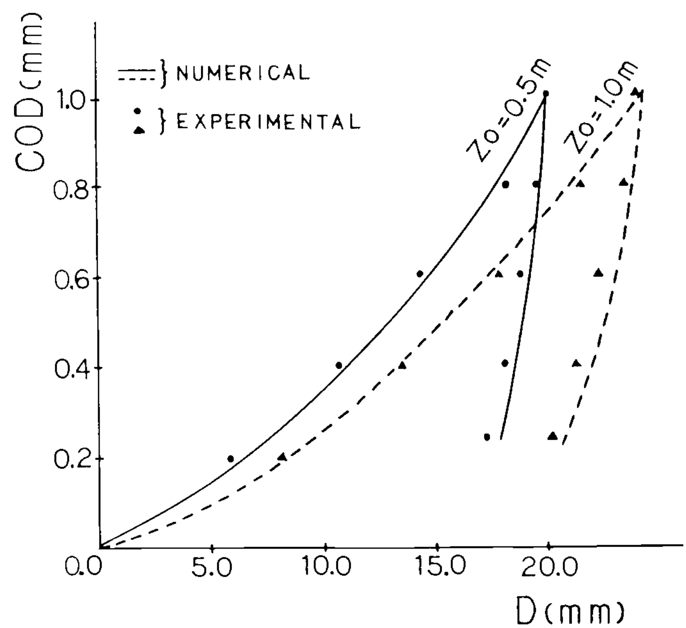

FIG. 11—*Comparison of numerical and experimental results for* D *versus COD curves.*

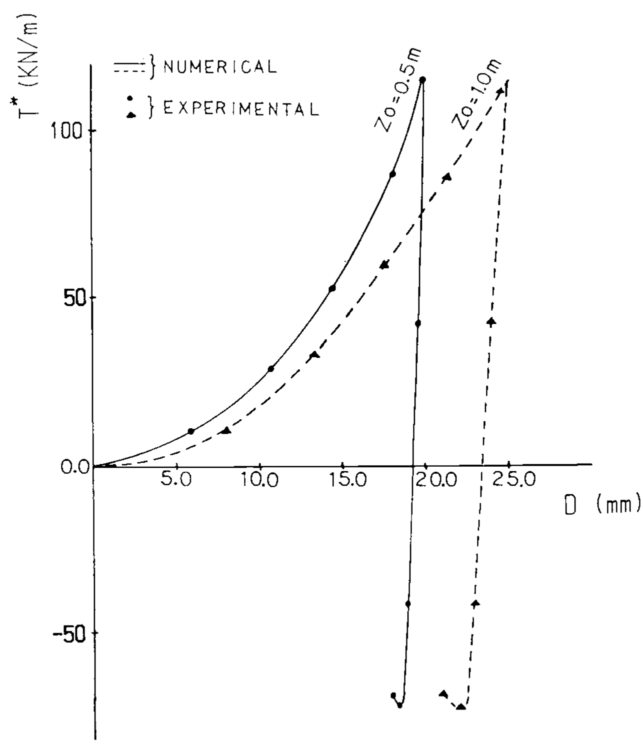

FIG. 12—*Relations between the* T* *integral and the size of caustic pattern* (λ = *1.0, B* = *10 mm).*

simulated and actual caustic patterns assures that the T^* versus D relation obtained by the simulation can be used for the direct experimental measurement of the T^*-integral in a sense of the hybrid numerical-experimental method [*13,14*].

Figure 12 shows the simulated T^* versus D relation for the parallel light ($\lambda = 1.0$) used in the experiment.

Concluding Remarks

First, the actual reflected caustic patterns in the A508K′ CT specimen were measured. From this experiment, the relations between the size of caustic pattern D and the crack opening displacement δ were determined.

Next, the formation process of the caustic pattern in the CT specimen was simulated by the previously developed finite element simulation technique aided by computerized symbolic manipulation. From this numerical simulation, the relations among the T^* integral, the caustic size D, and the crack opening displacement δ were obtained. The simulated caustic patterns agreed very well with the actual caustic patterns.

The presently developed hybrid numerical-experimental method made it possible to measure optically the T^*-integral.

Acknowledgment

The present study was supported by the Science and Technology Grant from Toray Science Foundation.

References

[*1*] Atluri, S. N., Nishioka, T., and Nakagaki, M., *Engineering Fracture Mechanics*, Vol. 20, No. 2, 1984, pp. 209–244.
[*2*] Rice, J. R., *Journal of Applied Mechanics*, Vol. 35, 1968, pp. 376–386.
[*3*] Nishioka, T. and Atluri, S. N., *Engineering Fracture Mechanics*, Vol. 18, No. 1, 1983, pp. 1–22.
[*4*] Rosakis, A. J. and Freund, L. B., *Journal of Engineering Material and Technology*, Vol. 104, 1982, pp. 115–120.
[*5*] Nishioka, T., Fujimoto, T., and Atluri, S. N., *Nuclear Engineering and Design*, Vol. 111, 1988, pp. 309–319.
[*6*] Nishioka, T. and Fujimoto, T., *Transactions*, Japan Society of Mechanical Engineers, Vol. 56, No. 522, Series A, 1990, pp. 310–316.
[*7*] Nishioka, T. and Yagami, H., *Engineering Fracture Mechanics*, Vol. 31, No. 3, 1988, pp. 481–491.
[*8*] Nishioka, T., Kobashi, M., and Atluri, S. N., *Computational Mechanics*, Vol. 3, 1988, pp. 331–342.
[*9*] Budiansky, B. and Rice, J. R., *Journal of Applied Mechanics*, Vol. 40, 1973, pp. 201–203.
[*10*] Nishioka, T. and Atluli, S. N., *Engineering Fracture Mechanics*, Vol. 20, 1984, pp. 193–208.
[*11*] Beinert, J. and Kalthoff, J. F., *Experimental Evaluation of Stress Concentration and Intensity Factors*, Chapter 5, G. C. Sih, Ed., Martinus Nijhoff, The Hague, The Netherlands, 1981, pp. 281–330.
[*12*] Nishioka, T., *A Study of Evaluation of Intensity of Primary System of Light Water Reactor Using Fracture Mechanics (Part III)*, Report of Atomic Energy Research Committee, JWES-AE-8603, Japan Welding Engineering Society, 1987, pp. 105–110.
[*13*] Kobayashi, A. S., *Experimental Mechanics*, Vol. 23, No. 3, 1983, pp. 338–347.
[*14*] Atluri, S. N. and Nishioka, T., *Unification of Finite Element Methods*, Chapter 3, H. Kadestuncer, Ed., Elsevier, New York, 1984, pp. 65–95.

Christian Franco[1] *and Philippe Gilles*[1]

Three-Dimensional Elastic-Plastic Analysis of Small Circumferential Surface Cracks in Pipes Subjected to Bending Load

REFERENCE: Franco, C. and Gilles, P., "**Three-Dimensional Elastic-Plastic Analysis of Small Circumferential Surface Cracks in Pipes Subjected to Bending Load,**" *Fracture Mechanics: Twenty-Second Symposium (Volume II)*, S. N. Atluri, J. C. Newman, Jr., I. S. Raju, and J. S. Epstein, Eds., American Society for Testing and Materials, Philadelphia, 1992, pp. 183–205.

ABSTRACT: This study presents the elastic-plastic behavior of a circumferentially surface-cracked pipe using the finite element method based on a three-dimensional model.

The action of a pure bending load on the pipe is analyzed for three crack depths with a/t equal to 0.25, 0.5, and 0.75, and their eccentricities, a/c, being 0.2, 0.4, and 0.6, respectively.

The material obeys a Ramberg-Osgood power law. The goals are to determine the stress-strain fields and the values of J on the crack front, to define the different plastic deformation stages reached as the load on the crack is increased, and to validate the Central Electricity Generating Board (U.K.) (CEGB) two-criteria rule for circumferential surface flaws on the basis of the J results.

KEY WORDS: ductile fracture, elastic-plastic behavior, cracked pipe, semielliptical surface crack, pure bending, J-values, estimation scheme, RH/R6 rule, three-dimensional meshes, fracture mechanics, fatigue (materials)

Defect assessment is of increasing importance in nuclear power plant piping systems for safety and economic reasons.

Most cracked pipe geometries may be analyzed by considering either a circumferential or a longitudinal small surface crack in a pipe section. FRAMATOME has developed a large set of stress-intensity factor (SIF) solutions [*1,2*] for such surface cracks. However SIFs are parameters only valid for linear elastic fracture mechanics (LEFM) analyses. Since pressure vessels and primary piping systems are made of highly ductile steels, such as Type A533 carbon steel or Type 316 stainless steel, their failure modes occur very often under large-scale yielding conditions. This fracture behavior requires elastic-plastic fracture mechanics (EPFM) analyses to be conducted.

In LEFM, accounting for three-dimensional effects is the major difficulty. Nonlinear fracture processes are more complex and time-dependent. On one hand, they call for greater care in validation of criteria, on the other hand, EPFM parameter computations are usually very expensive. At a time when the need for engineering methods providing low-cost and fast defect assessment remains acute, whatever the material behavior, it seems much harder to develop simplified methods in EPFM than in LEFM.

In response to this problem, FRAMATOME conducts its work in fracture mechanics on three different but related levels: basic, advanced, and design applications.

[1]Mechanical engineer and expert, Fracture Mechanics, respectively, FRAMATOME, Tour Fiat, Cedex 16, 92084 Paris-La Defense, France.

1. Since the use of a global approach based on a single parameter, J, is questionable in some EPFM analyses (see examples in Refs *3* and *4*), FRAMATOME is contributing to the development of local approaches for brittle [*5*] and ductile fracture [*6,7*]. This level of investigation is aimed at gaining a better understanding of fracture behavior and working out related criteria.
2. At the second level, the discussion no longer concerns the type of criteria but their utilization. The question is how to validate an approach chosen with a view to industrial applications. This may be done through very accurate computations of the fracture parameter variations (see computations conducted in Refs *8* or *9* as a basis for a J-estimation method) and, if need be, by definition of corrective coefficients accounting for basic research results (like in Ref *10*).
3. In a third step advantage can be taken of the derivation of such reference solutions in order to build engineering formulae for global criteria based on J or crack-tip opening displacement (CTOD).

These second and third types of development are illustrated in the present J analysis (for application of the fracture criterion proposed by Broberg [*11*] and Begley and Landes [*12*], or the crack stability criterion defined by Paris et al. [*13*]) of small circumferential inner surface cracks in a pipe subjected to simple loadings. Three cases are considered, where the pipe geometry, and the semielliptical shape and length of the crack are fixed: three pipes in pure bending with different crack depths.

The objectives are the following:

1. Computation of accurate stress-strain fields and J-values.
2. Detailed explanation of the changes in fracture behavior under increasing load.
3. Application of the J results to validation of the R6 rule simplified method [*14*] for circumferential surface cracks.

Three-Dimensional Finite Element Model

For analyzing these three cracked pipes, a three-dimensional incremental elastic-plastic finite element procedure has been used. The CASTEM code developed by the French Atomic Energy Commission (CEA) [*15*] facilitates mesh generation with its object-oriented programming environment.

The mesh size and shape may be modified to create pipes with different crack depths from a simple cracked plate model (Fig. 1).

Following a brief description of the material characteristics, the cracked pipe geometry and the finite element model, two justifications of the model are presented based on published results; one in LEFM, the other in EPFM.

Model Description

The material characteristics have been chosen to represent a stainless steel in use in a French pressure water reactor (PWR) primary loop and to allow the comparison with other computational results. The stress-strain behavior follows a Ramberg-Osgood law according to Eq 1

$$\frac{\varepsilon}{\varepsilon_0} = \frac{\sigma}{\sigma_0} + \alpha\left(\frac{\sigma}{\sigma_0}\right)^n \tag{1}$$

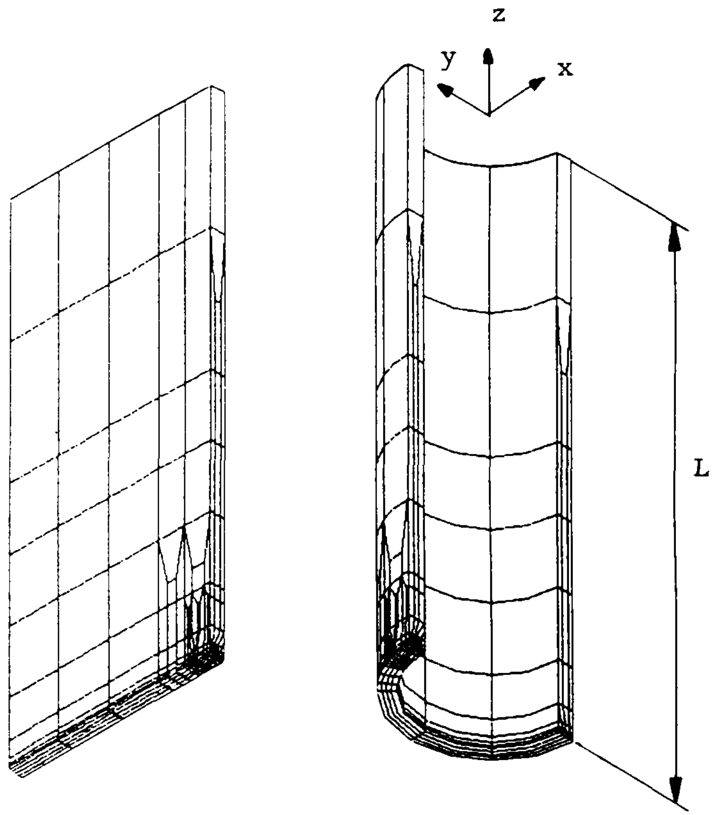

FIG. 1—*Plate cylinder transformation.*

where $\varepsilon_0 = \sigma_0/E$, E is the Young's modulus, and σ_0 is chosen equal to the 0.2% offset yield strength, σ_y. Poisson's ratio; the elastic properties, σ_y and E; and the plastic properties, α and n, take the following values indicated at room temperature

$$E = 177\,000 \text{ MPa} \qquad \nu = 0.3$$

$$\sigma_y = 120 \text{ MPa}$$

$$\alpha = 3 \qquad n = 5$$

This represents the behavior of a highly ductile metal, and the Ramberg-Osgood form greatly accentuates the offset from the elastic slope for this value of α.

The cracked pipe geometry is a right circular cylinder whose mean radius, R_m, is 300 mm and thickness is 60 mm. This makes a very thick pipe with a curvature ratio, $R_m/t = 5$, representative of the primary loop pipe. The pipe length has been fixed at 2 m, after a detailed study of the minimum length-to-diameter ratio making the J solution almost independent of the length.

This length criterion is presented in the Appendix.

The present study concerns mainly defect assessment, thus only short cracks have a realistic size. We have decided to keep the crack length, its elliptical shape, and the material characteristics constant, and to concentrate our investigation on the effect of the crack depth.

The half crack angle, γ, value of 14.3° corresponding to one quarter of the c/R_m ratio, the radius, R, and the length, $2L$, are kept constant. Three cracked pipe geometries are defined by their relative crack depths, a/t, with respective values of 0.25, 0.50, and 0.75 (the corresponding a/c values are 0.2, 0.4, and 0.6).

These three cracked pipes are subjected to increasing pure bending.

The finite element method, based on small geometry change assumptions, is used to analyze these three configurations. For reasons of symmetry, only a quarter of the pipe (which is designated in the following as the cylinder) is meshed. We have selected isoparametric elements consisting essentially of 20-node cubes and 15-node prisms. To preclude any overestimate of the yield extension around the crack front, a finer mesh is used in the portion of the cylinder surrounding the crack. The "crack block" is 20 times shorter than the cylinder, its width being one sixteenth of the circumference.

Since the stress and strain fields are singular at the crack tip, a fine mesh was developed consisting of tunnels surrounding the crack.

Furthermore, a comparison of finite element analyses of surface cracked pipes [*16*] has shown that mesh refinement in the ligament has a strong influence on the accuracy of J-values.

The same reference stipulates that the justification of the mesh using linear elastic results is not sufficient and also that nine nodes in the ligament can be considered as the minimum required.

Thus Fig. 2 shows that a very large number of nodes (24) exists in the ligament and around the crack front in every direction. The whole mesh has 624 cubes, 66 prisms, and one 10-node tetrahedron element, which gives a total of 3554 nodes. Two-thirds of these nodes are concentrated in the crack block.

Model Justification

As stated before, the mesh for an elastic-plastic problem has to be justified both inside and outside the elastic domain. To our knowledge at the beginning of this analysis, no reference study matching the aforementioned criteria relative to mesh concentration was available for a thick cylinder with an elliptical surface crack. However, taking advantage of the object-oriented programming capabilities of CASTEM, we generated the mesh of the cracked cylinder from a surface-cracked plate. We decided then to base our comparisons on two well-established solutions for a surface-cracked plate subjected to tension [*17,18*]. These two finite element analyses consider a surface semielliptical crack in a finite thickness plate whose material behavior is respectively linear elastic or fully plastic.

For the detailed description of these two cases, the aforementioned papers should be referred to. We will only mention the results and the conclusions of the comparisons. In both cases, the height and width of the plate are much larger than the crack length and depth, so that free boundaries other than the plate face perpendicular to the thickness direction have no effect on the crack driving force.

(a) Comparison with the Linear-Elastic Solution of I. S. Raju and J. C. Newman [17]
The crack size is defined by $a/t = 0.6$ and $a/c = 0.4$.

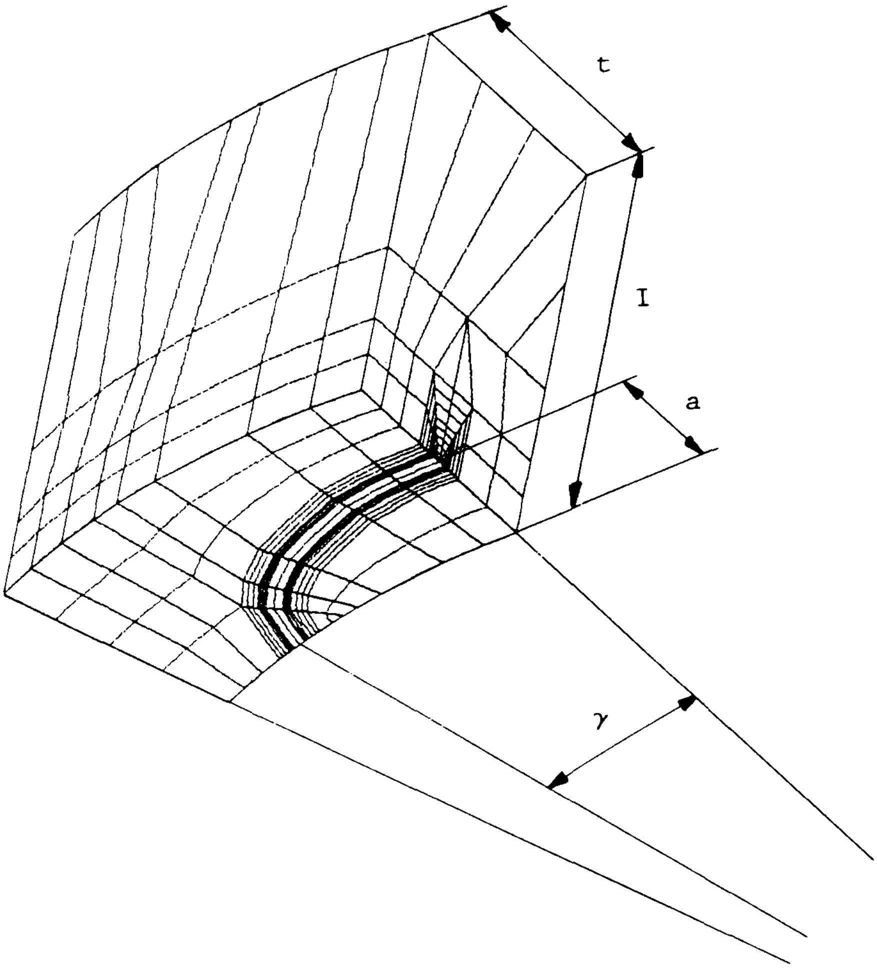

FIG. 2—*Mesh of crack block.*

Figure 3 compares our results to the influence functions

$$F\left(\frac{a}{t}, \frac{a}{c}, \phi\right)$$

that represent the ratio of the SIF, K, to a reference SIF, K_0, ϕ being the parametric angle of the ellipse. This SIF, K_0, is defined to make K/K_0 independent of the load level and to reduce the effects of the crack size and shape

$$K_0 = \sigma_T \sqrt{\frac{\Pi a}{Q}}$$

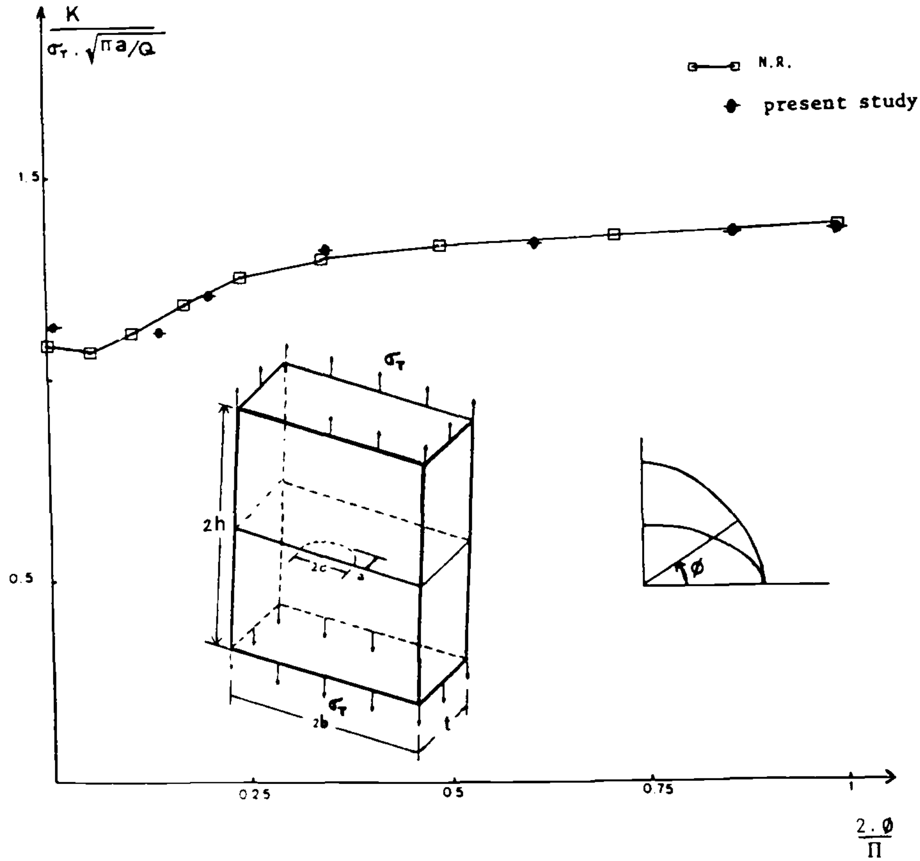

FIG. 3—*The influence function,* F(a/t, a/c, ϕ), *on the crack front versus the parametric angle,* ϕ.

where

σ_T = applied stress,
a = crack depth, and
Q = shape factor for an ellipse.

A very good approximation to Q as a function of the a/c ratio is given in Ref *19*. For a/c < 1, this formula is

$$Q = 1 + 1.464 \left(\frac{a}{c}\right)^{1.65}$$

The agreement between the K/K_0 results obtained with our 3500-node mesh and the functions, $F(0.6, 0.4, \phi)$, is excellent. Therefore, we may consider that the mesh is validated for the elastic case. It should be noted that the same mesh is used for the cracked cylinder: the only differences concern the crack size and the transformation of the plate into a cylinder.

(b) Comparison with the Inelastic Analysis of G. Yagawa, H. Ueda, and Y. Takahashi [18]

In this study, referred to here as the Y-U-T solution, the same type of configuration as in the previous paragraph has been chosen: a plate with a semielliptical crack having $a/t = 0.6$ and $a/c = 0.4$ subjected to uniform tensile loading. However, the material behavior is totally different: fully plastic instead of linear. To model this behavior, the authors consider an incompressible, nonlinear elastic material characterized by the power-law hardening equation

$$\frac{\varepsilon}{\varepsilon_0} = \alpha \left(\frac{\sigma}{\sigma_0}\right)^n \tag{2}$$

where α, ε_0, σ_0, and n are material constants.

The J-values can be normalized, so that the resulting influence functions depend only, for a given type of loading, on the parameters of the elliptical crack, a/t, a/c, ϕ, and on the hardening exponent, n. Thus, α, ε_0, and σ_0 values need not be specified. We have chosen $n = 5$ and taken $\alpha = 1$ for reasons of convenience. As usual, $\varepsilon_0 = \sigma_0/E_0$, where E_0 is Young's modulus.

Using the J_2 deformation plasticity theory, Yagawa et al. transform Eq 1 into a relationship between von Mises equivalent strain, $\bar{\varepsilon}$, and stress, $\bar{\sigma}$.

Such an approach gives a correct approximation of the stress-strain field derived by the flow theory of plasticity if the structure is subjected to a monotonically increasing proportional loading. Also, it is much less expensive.

However, for treating the incompressibility, the FEM technique has to be modified and Yagawa et al. have developed for that purpose a "selective reduced integration/penalty function method." The CASTEM code is based on flow theory of plasticity and does not allow Poisson's ratio, ν, to reach the limit value of 0.5 corresponding to incompressible materials. Furthermore, this code requires the stress-strain curve to have a finite slope at the origin because the finite element procedure does not converge if strain values are very small. In order to solve these problems at low cost, we set the ν-value at 0.495 and split the stress-strain curve into two parts, linear and nonlinear

$$\varepsilon = \frac{\sigma}{E_F} \qquad \text{for } \varepsilon < \varepsilon_F$$

$$\frac{\varepsilon}{\varepsilon_0} = \left[\frac{\sigma}{\sigma_0}\right]^5 \qquad \textit{for } \varepsilon > \varepsilon_F$$

where E_F is a fictitious Young's modulus having a very high value and ε_F is the strain representing the limit of linear elastic behavior.

The consequences of this modification of the stress-strain law are examined by comparing the Y-U-T solution to the results obtained with different linear parts. In the first case, E_{F1} is very high and $\varepsilon_{F1} = 10^{-4}$; in the other one, E_{F2} is huge and ε_{F2} is limited to 10^{-6}. The Case 1 J results differ from the Y-U-T solution for σ/σ_0 lower than 0.7, but above this threshold, the agreement is excellent (Fig. 4).

In the second case, the scatter of J-values reduces to 5% for $\sigma/\sigma_0 = 0.25$. However, when the stress ratio, σ/σ_0, increases, convergence problems appear, showing that the upper limit for E_F is reached. In any case, as soon as the stress-strain curves become close to each other, our mesh gives the same J-values as the Y-U-T solution. This justifies our mesh for an inelastic stress-strain law.

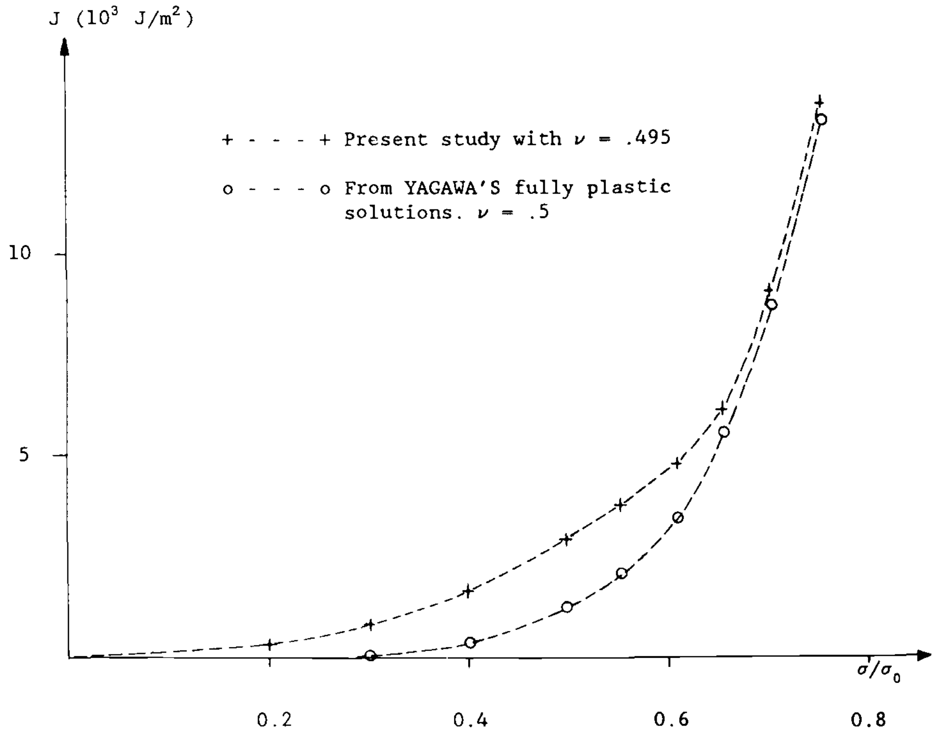

FIG. 4—J-*values at the deepest crack point with increasing load.*

Presentation of Results of Investigation

A rotation is imposed on the pipe. Rather than defining four-point bending, with one fixed point and one moving point (for the quarter-cylinder), we have introduced a displacement field on the end surface of the pipe conforming to a bending state (see Fig. 5). This produces a state of constant pure bending in all the right cross sections, minimizing the length of the pipe.

The calculations are performed in small displacements and the angle of rotation, Φ, increases gradually up to a threshold beyond which the load plastifies the end cross section so further analysis is meaningless.

For each cracked pipe, the load has been applied in 30 steps, the run time being close to 5 h on a CRAY-XMP.

Figure 6 records the change in moment with the rotation exerted on the end of the pipe, for the flaws under consideration. The crack depth has practically no effect on the resulting moment, which would seem extremely plausible considering the size of the crack (γ = 14.3°) and the rotations involved.

Plastic Flow Behavior

For all three flaw depths, the plastic behavior develops in three stages during the crack loading process. First, yielding remains contained within the ligament between the deepest point of the crack and the outer wall (Fig. 7*a*).

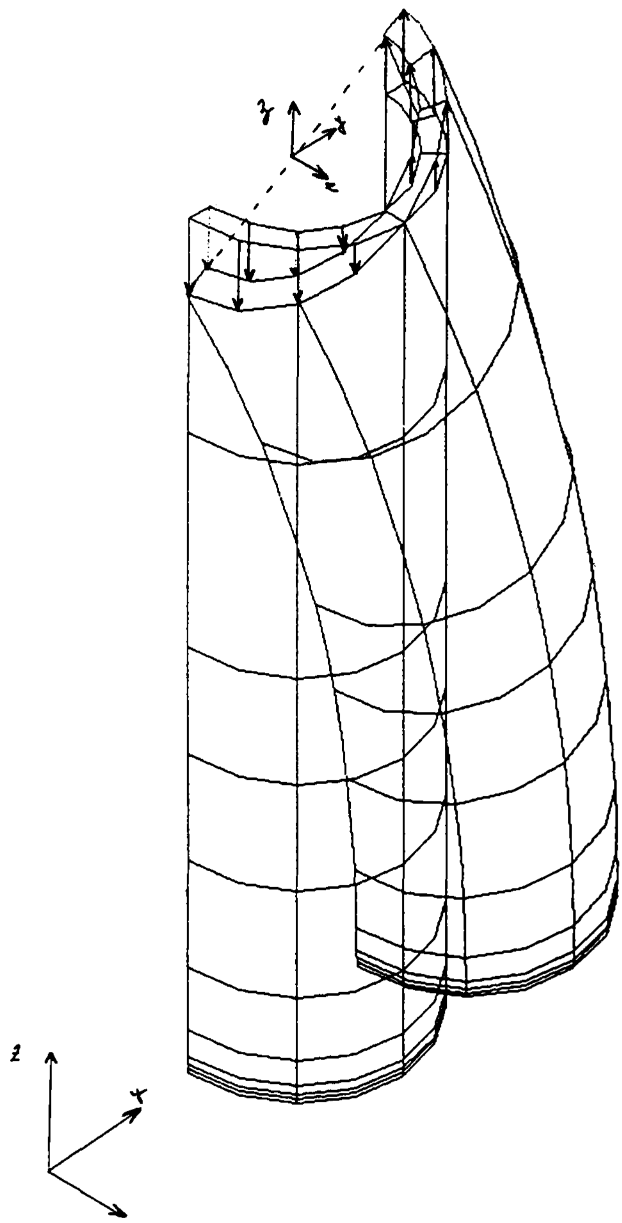

FIG. 5—*Pipe mesh in pure bending.*

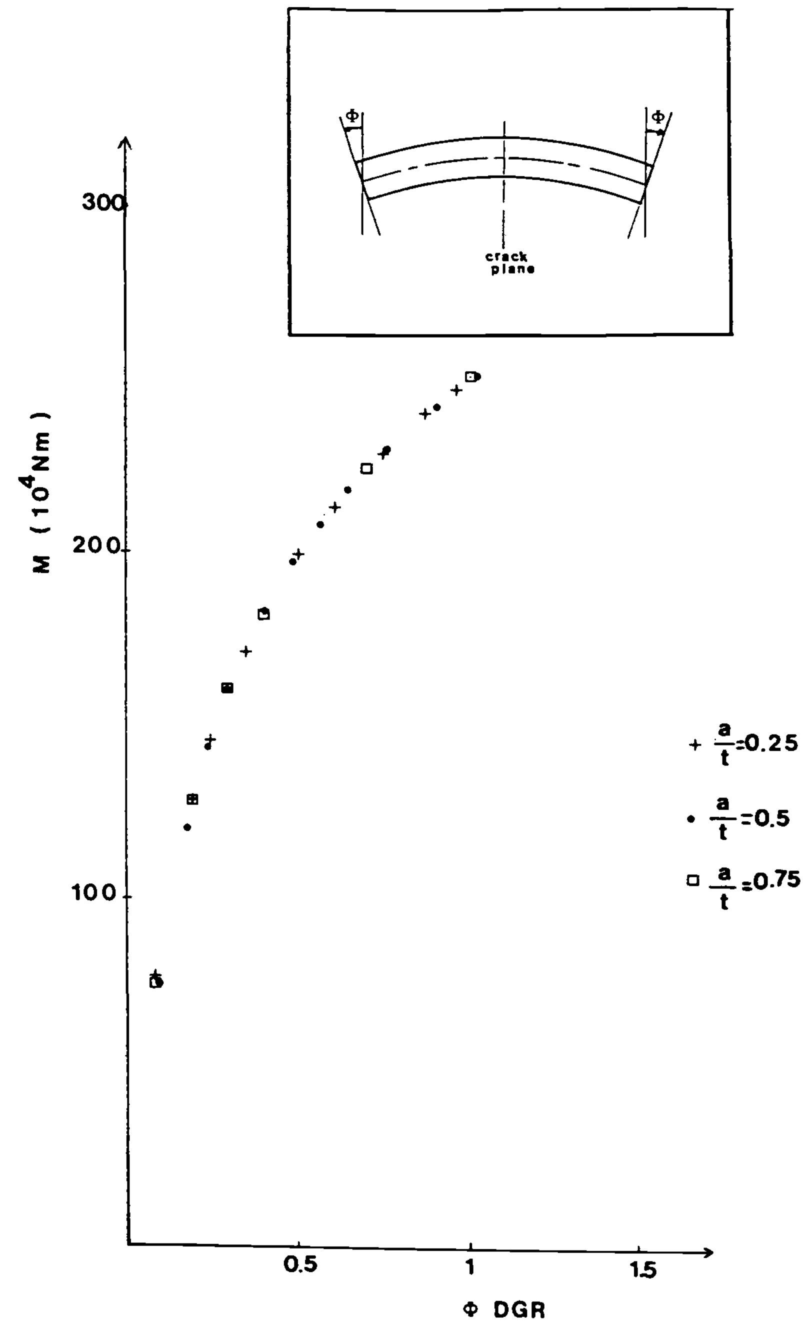

FIG. 6—*Computed moment versus applied rotation.*

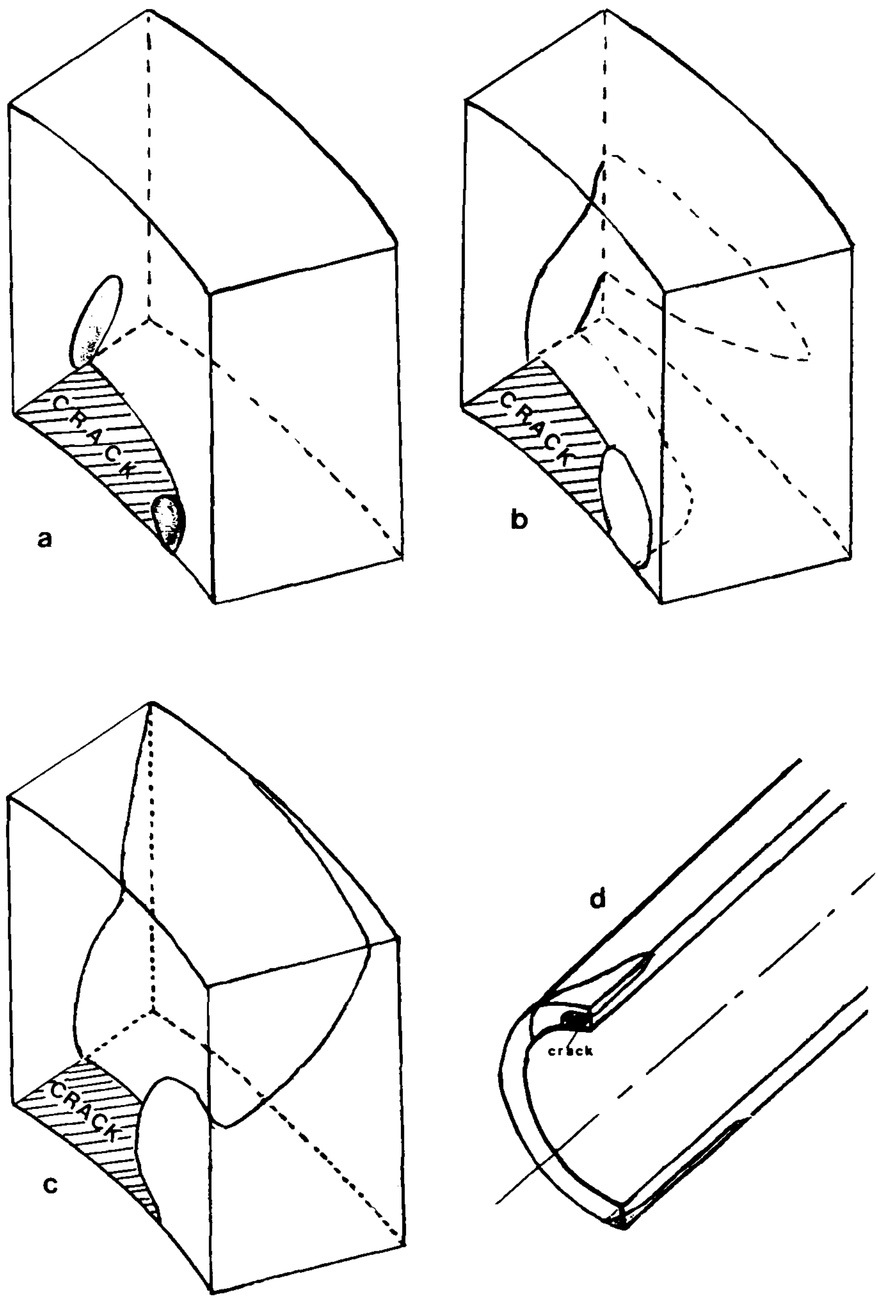

FIG. 7—*Plastic flow deformation of crack block at three characteristic loading steps:* (a) *small-scale yielding,* (b) *ligament yielding* (*local yielding*), (c) *large-scale yielding, and* (d) *formation of a mechanism* (*global yielding*).

At the deepest point, the plastic "wing" takes on the shape of an elongated butterfly's wing oriented at 45° in the radial plane perpendicular to the crack plane. This justifies the plane strain hypothesis that is considered usually to apply at the crack tip. However, the plastic wing at the surface point of the crack reveals a plane stress field, with the plastic wing being much more compact (almost circular, the diameter of this zone being bigger than the maximum size of the plane strain plastic zone) and oriented in the axial direction.

In a second stage, the ligament becomes plastic but remains contained within globally elastic surroundings (Fig. 7*b*).

Finally, yielding spreads throughout the crack block (Fig. 7*c*) and the diametrically opposite region (Fig. 7*d*) revealing the compression zone that is characteristic of a bending load. Subsequently, there is a gradual evolution until the pipe limit load is reached (plastic hinge mechanism).

J-Integral Calculations

The J–integral calculations were performed by the virtual crack extension method [*20*]. The rate of decrease of the potential energy, $\Delta\Pi$, during an infinitesimal increase in the crack is first calculated and then J is defined as the ratio

$$J = \frac{\Delta\Pi}{\Delta A}$$

where ΔA represents the virtual crack extension.

In the following computations, only one node has been shifted.

Figures 8, 9, and 10 record the evolution of the J-integral with changing moment at the deepest and surface points of the crack, respectively, for the three depths, $a/t = 0.25$, 0.5, and 0.75. For all the crack sizes processed, the value of J at the deepest point is always larger than J at the surface point.

When yielding remains contained in the ligament (see Fig. 7*a*), J may be approximated by applying a plasticity correction to J_e calculated elastically. This value will be written J_{cp}. The previous three curves display the J-value corrected using Irwin's [*21*] plastic zone correction given here as used in the RCC-M Code [*22*]

$$J_{cp} = \alpha^2 \left(1 + \frac{r_y}{a}\right) J_e \tag{3}$$

where

$$r_y = \frac{1}{6\Pi}\left[\frac{K(a)}{\sigma_y}\right]^2 \qquad \text{for plane strain}$$

and such that

$$\alpha = 1 \qquad \text{for } r_y < 0.05\ (t - a)$$

and

$$\alpha = 1 + 0.15\left[\frac{r_y - 0.05\ (t - a)}{0.035\ (t - a)}\right]^2 \qquad \text{for } 0.05(t - a) \leq r_y \leq 0.085(t - a)$$

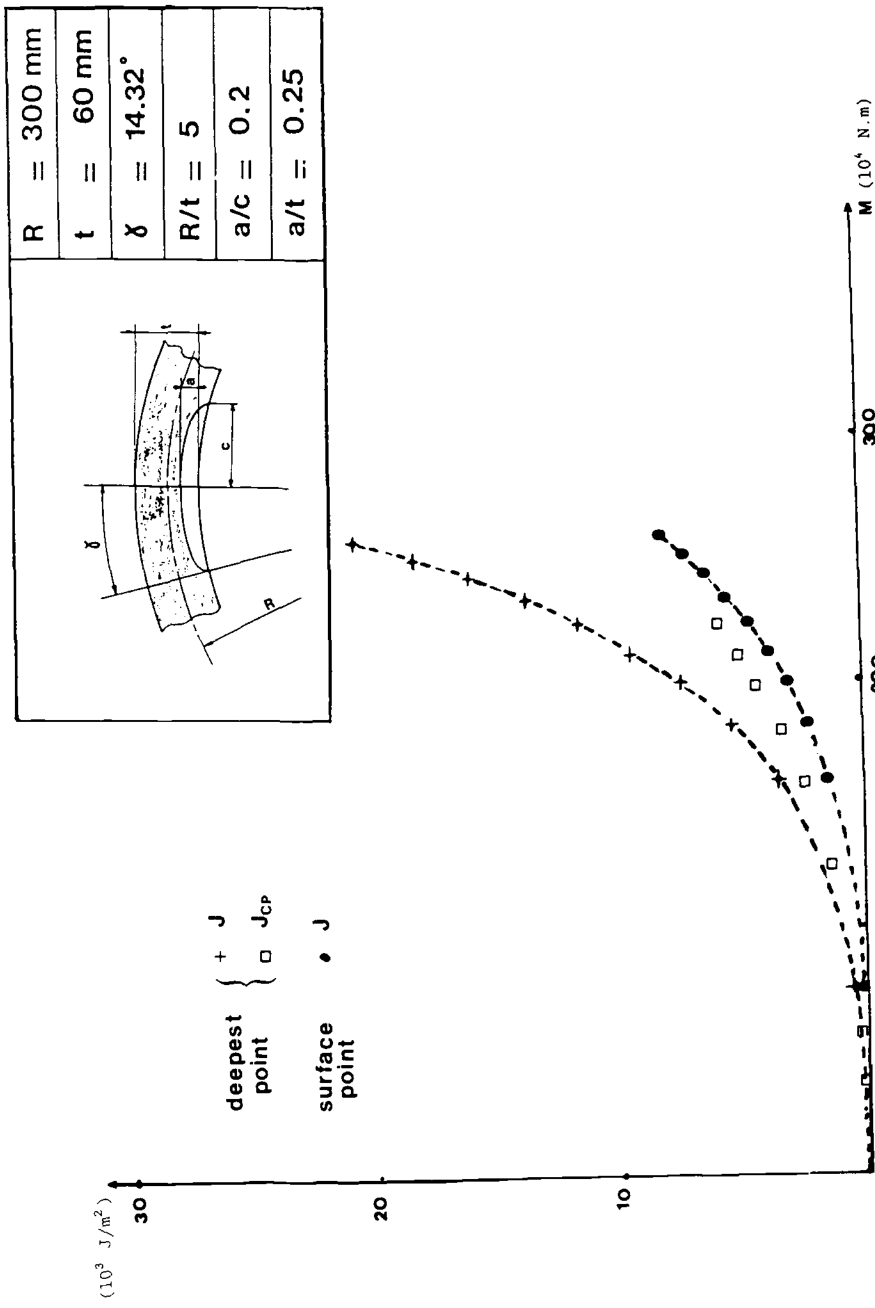

FIG. 8—*Comparison of J versus moment variations for the shallow crack.*

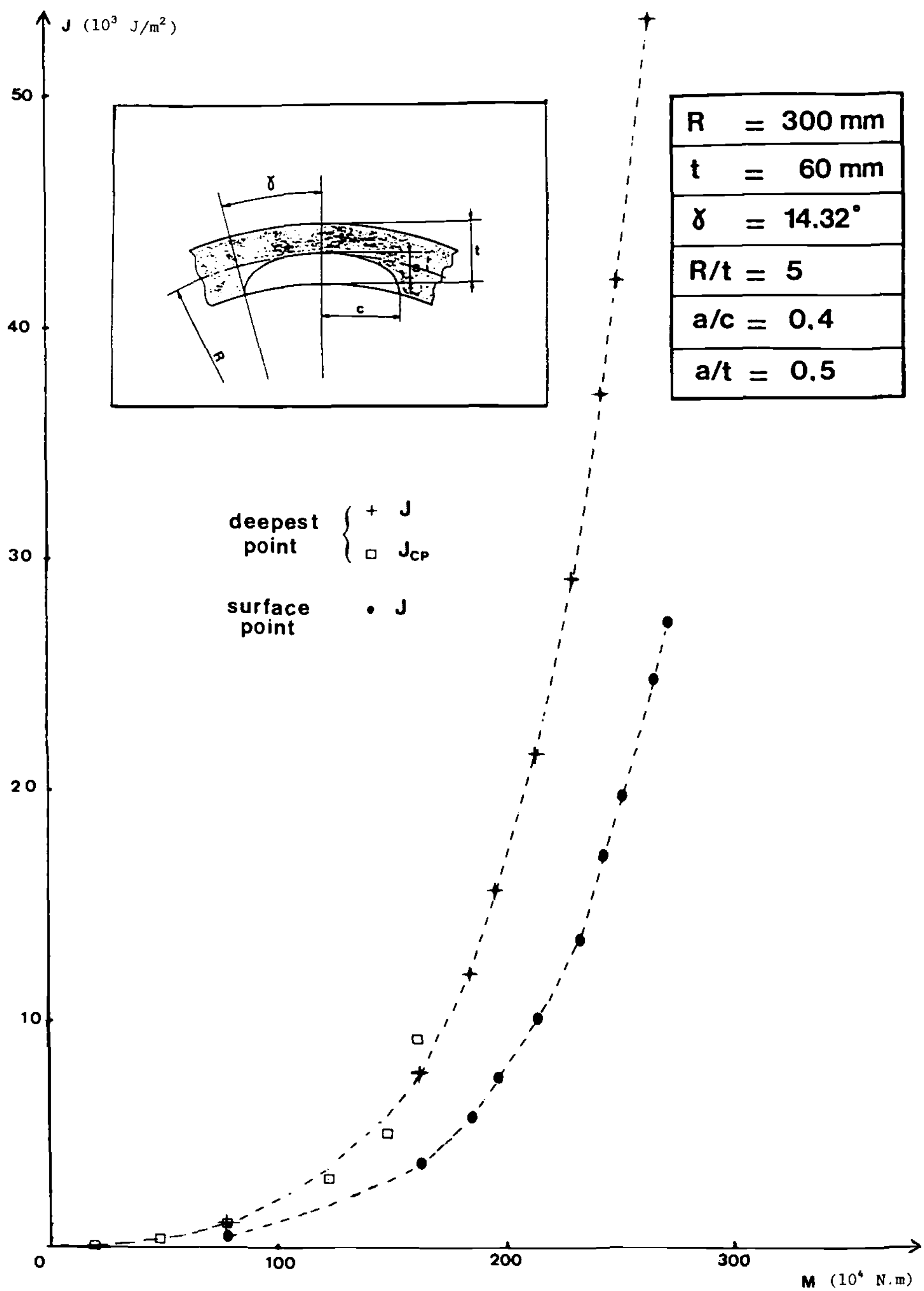

FIG. 9—*Comparison of* J *versus moment variations for the medium-depth crack.*

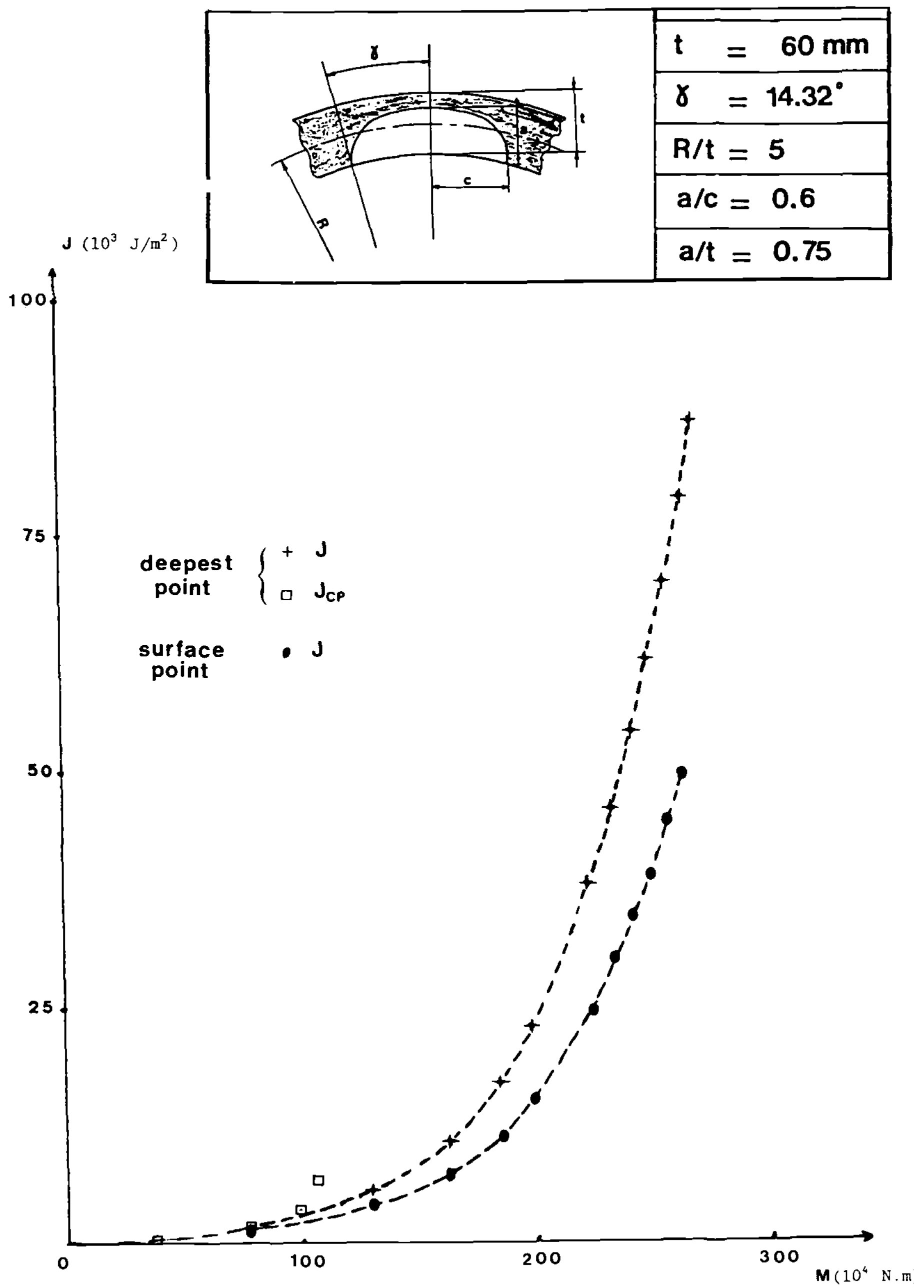

FIG. 10—*Comparison of* J *versus moment variations for the deep crack.*

Beyond, this approximation is no longer valid.

When the flaw is deep ($a/t = 0.5$ or 0.75), J_{cp} approaches elastic-plastic J in a satisfactory manner for r_y meeting the conditions just defined.

For the flaw having a depth defined as one quarter of the thickness, the correction made to J_e supplies unconservative results (see Fig. 8). In fact, when the ligament is large ($t - a = 45$ mm), the moment load that satisfies the condition that $r_y = 0.085 \cdot (t - a)$, becomes large compared to the pipe's global limit load. The deformations then develop within the structure independently of the presence of the crack [*4*]. So it is necessary to define another, more restrictive, validity limit for shallow defects.

When yielding is generalized throughout the ligament (see Fig. 7*b*), and then through the pipe (see Fig. 7*c* and *d*), the elastic approach just described no longer gives a valid estimate of elastic-plastic J. It becomes necessary to define limit load criteria that adequately represent strain levels in the pipe. The two-criteria approach of the Central Electricity Generating Board (CEGB) [*14*] provides solutions that are presented in the last section of our study.

Application in Accordance with the Two-Criteria Approach

CEGB Two-Criteria Approach

Of the three alternatives proposed in Ref *14*, we describe Option 2 here, whose failure assessment diagram (FAD) determination is based on the Electric Power Research Institute (GE-EPRI) method [*23*] and represented by the evolution of the parameter

$$K_R = \sqrt{\frac{J_e}{J}}$$

versus

$$L_R = \frac{\text{applied load}}{\text{limit load}} = \frac{P}{P_0}$$

J_e and J represent the elastic and total J-integrals, respectively.

When the material behaves according to the Ramberg-Osgood law

$$\frac{\varepsilon}{\varepsilon_0} = \frac{\sigma}{\sigma_0} + \alpha \left(\frac{\sigma}{\sigma_0}\right)^n \tag{4a}$$

it is possible to write, per the GE-EPRI method [*23*]

$$J = \frac{K^2(a_e)}{E'} + \alpha\sigma_0\varepsilon_0 c h_1 \left(\frac{a}{t}, \gamma, n, R/t\right) \left(\frac{P}{P_0}\right)^{n+1} \tag{4b}$$

where $c = t - a$, a_e is a plastic zone corrected crack length, h_1 is a coefficient obtained by the finite element method, and P_0 is a conventional limit load.

The dependence of the n parameter in Eq 4*b* leads Ainsworth to propose several changes in order to define a FAD that is independent of n [*24*]. His main modification in the definition consists of a reference stress, $\sigma_{\text{ref}} = P/P'_0 \cdot \sigma_0$ based on the "true" (for the given configuration) limit load expression, P'_0, such that h_1 (n) is almost a constant.

Ainsworth makes the conservative assumption that there is a plastic zone corresponding to the case of an infinite plate under tension in plane stress.

He thus obtains

$$K_R = \left\{ E \frac{\varepsilon_{ref}}{\sigma_{ref}} + 0.5 \frac{L_R^2}{1 + L_R^2} \right\}^{-1/2} \tag{5}$$

that defines the FAD of the two-criteria rule, Option 2.

The hypothesis underlying the normalization of the ratio, $h_1(n)/h_1(1)$ is based, as we have seen, on a reference stress defined on the basis of a global limit load.

This hypothesis has been validated by Ainsworth for plane geometries. Miller [*25*] has extended the analysis to three-dimensional surface defect configurations in pipes using published J results, in particular for a cylinder with a circumferential flaw under tension [*26*] or again for a pressurized cylinder with an axial flaw [*27*].

It is proposed later in the study to fill out the discussion with the J results obtained on our model.

Analysis to Choose the Limit Load

The three-dimensional case of a surface flaw in a pipe raises the problem of deciding which limit load should be considered. There are two possible approaches:

1. The plasticity is confined to the vicinity of the crack. The limit load is a local limit load whose various formulations have been reviewed and compared by Miller [*25*] depending on the type of geometry (plate, test specimen, or cylinder) and loading (tension or pressure).
2. Plastic flow is generalized in the cracked section of the tube. In that case the global limit load on the structure is considered.

We need to know which instability criterion most closely meets Ainsworth's normalization hypothesis.

As in the two approaches just described, we use the formulation developed by the Battelle Institute as the local instability criterion [*28*].

The containment loss factor, Q, is then written [*29*]

$$Q = \frac{A_0 - A_e}{A_0 - A_e/M} \tag{6}$$

where A_e represents the crack area, A_0 is the cross-sectional area of a $2(c + t)$ long pipe section, and M is the bulging factor.

Eiber's expression, established empirically [*30*] from burst tests when pressure is applied to the sides of the crack, gives

$$M = \sqrt{1.61 \frac{c^2}{R_m t}} \tag{7}$$

When there is a loss of plasticity containment, the global limit load referred to is the load on a circumferentially cracked pipe, calculated with a perfectly plastic rigid model. Deformation occurs at the elastic limit stress shown in Fig. 11.

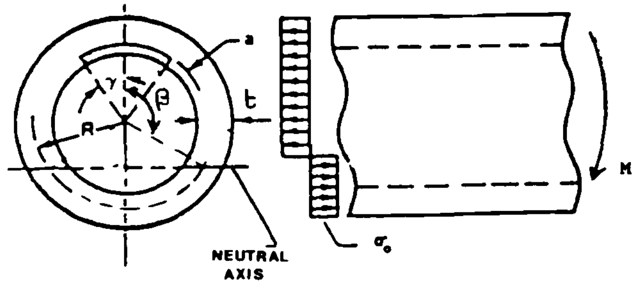

FIG. 11—*Deformation at the elastic limit stress.*

The expression for the limit moment [*28* or *31*] is

$$M_0 = 4\sigma_0 R_m^2 t\left(\cos\beta - \frac{1}{2}\frac{a}{t}\sin\gamma\right) \tag{8}$$

where

$$\beta = \frac{a}{t}\gamma/2$$

The values of K_R at the deepest and surface points, as a function of L_R depending on the type of limit load, have been recorded in Tables 1, 2, and 3 for the three flaw depths (a/t = 0.25, 0.5, and 0.75). The corresponding figures at the deepest point (Figs. 12*a*, *b*, and *c*) show that, whatever the flaw depth, the reference stress calculated from the global limit load on the structure gives a (K_R, L_R) line very close to Ainsworth's FAD. On the other hand, the reference stress based on the local limit load gives a (K_R, L_R) line located well beyond Ainsworth's FAD.

The results agree with the study by Miller [*25*] and show that the global limit load is more appropriate as a means of satisfying Ainsworth's normalization hypothesis, $h_1(n)/h_1(1)$, as opposed to the local limit load approach that displays excessive conservatism.

TABLE 1—K_R *and* L_R *values for crack depth* a/t = *0.25 with increasing bending.*

	L_R		$K_R = \sqrt{\frac{J_e}{J}}$	
Φ, deg	Local Collapse	Global Collapse	Deepest Point	Surface Point
0.1	0.376	0.3	0.99	0.98
0.3	0.79	0.64	0.81	0.81
0.4	0.9	0.725	0.74	0.75
0.5	0.99	0.79	0.69	0.7
0.6	1.06	0.85	0.65	0.67
0.7	1.11	0.89	0.62	0.64
0.8	1.16	0.93	0.60	0.61
0.9	1.21	0.97	0.57	0.59
1.0	1.25	1.0	0.55	0.57
1.1	1.28	1.03	0.54	0.55

TABLE 2—K_R *and* L_R *values for crack depth* a/t = *0.5 with increasing bending.*

	L_R		$K_R = \sqrt{\frac{J_e}{J}}$	
Φ, deg	Local Collapse	Global Collapse	Deepest Point	Surface Point
0.1	0.395	0.32	1.	0.96
0.3	0.83	0.665	0.76	0.78
0.4	0.94	0.76	0.69	0.72
0.48	1.0	0.81	0.65	0.682
0.6	1.09	0.88	0.6	0.63
0.69	1.14	0.92	0.57	0.61
0.75	1.175	0.95	0.55	0.59
0.9	1.245	1.	0.52	0.55
1.0	1.29	1.035	0.5	0.535
1.2	1.36	1.09	0.47	0.50
1.3	1.39	1.12	0.46	0.49

Conclusions

This study presents the elastic-plastic behavior of a circumferentially surface-cracked pipe using the finite element method based on a three-dimensional model.

The results show that the plastic flow in a pipe subjected to rotation goes through three stages:

1. yielding is contained within the ligament,
2. the loss of containment of yielding inside the ligament remains concentrated in an elastic environment, and
3. yielding becomes generalized throughout the cracked section until the component global limit load is reached.

When yielding is contained within the ligament, the calculation of elastic J with Irwin's plastic zone correction [*21*] produces a satisfactory approach to J for flaws with depths of

TABLE 3—K_R *and* L_R *values for crack depth* a/t = *0.75 with increasing bending.*

	L_R		$K_R = \sqrt{\frac{J_e}{J}}$	
Φ, deg	Local Collapse	Global Collapse	Deepest Point	Surface Point
0.05	0.21	0.17	0.985	1.0
0.1	0.41	0.33	0.95	0.97
0.2	0.69	0.55	0.82	0.87
0.3	0.86	0.69	0.73	0.78
0.4	0.97	0.78	0.66	0.72
0.49	1.05	0.85	0.61	0.67
0.7	1.19	0.96	0.53	0.59
0.8	1.24	1.0	0.51	0.56
0.9	1.29	1.04	0.49	0.54
1.0	1.33	1.07	0.47	0.52
1.1	1.37	1.1	0.45	0.505

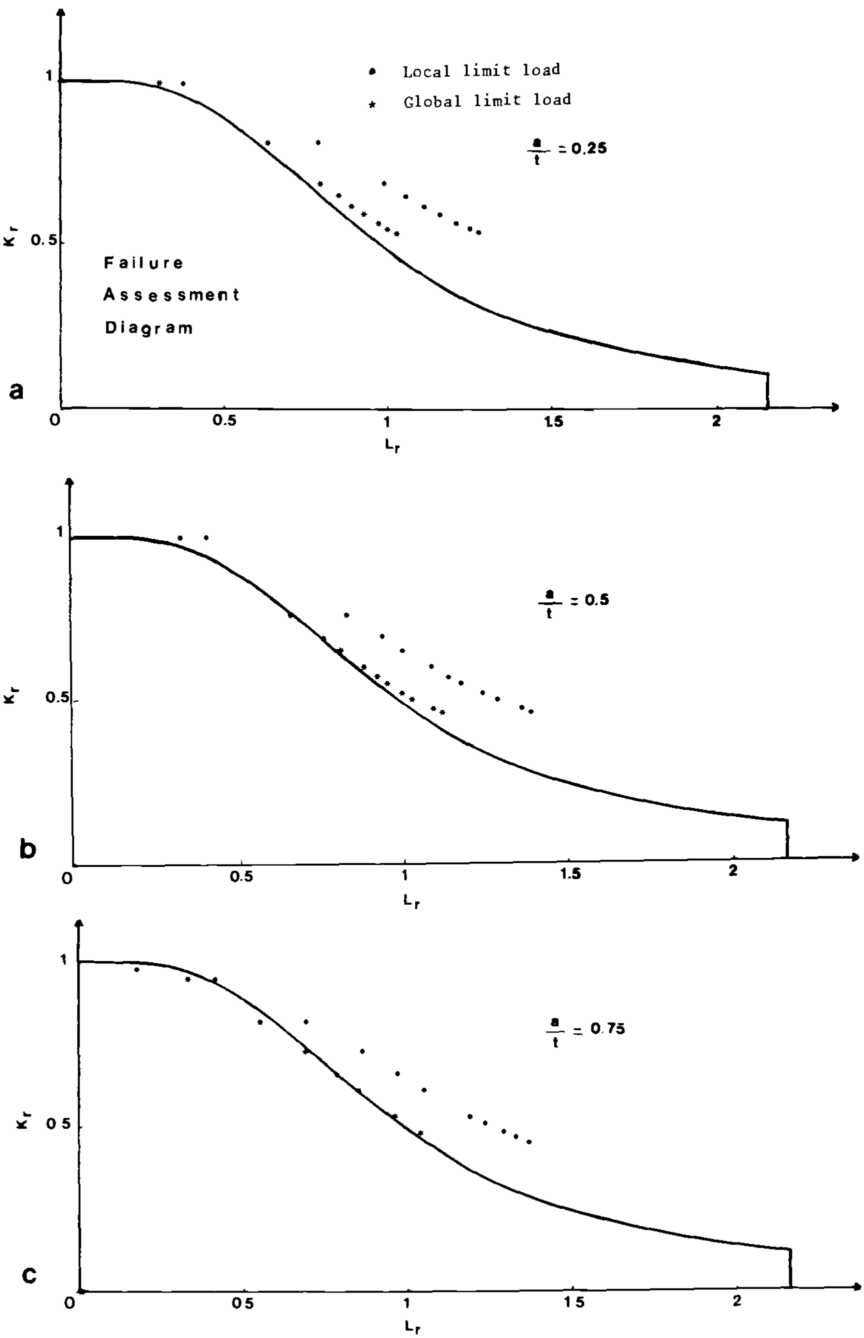

FIG. 12—K_R *and* L_R *values at the deepest crack point:* (a) *with* a/t = *0.25,* (b) *with* a/t = *0.5, and* (c) *with* a/t = *0.75.*

half or three-quarters the thickness, if the RCC-M Code validity formulae [22] are applied.

This approach is no longer conservative for the shallow flaw, and it is necessary to define a more restrictive validity limit.

When loss of containment of plasticity within the ligament occurs, the elastic approach is no longer valid and a criterion governing plastic instability has to be introduced to come near to J. For this purpose, the CEGB two-criteria rule [14] is applied and the method is validated for circumferential surface flaws by defining a reference stress on the basis of the pipe's global limit load. The local limit load produces excessively conservative results.

APPENDIX

Minimum Pipe Length Criterion

Different SIFs of J finite element methods solutions for the same configuration are easier to compare if end effects are avoided.

In the case of a circumferentially cracked pipe, this requires fixing a minimum distance between the crack plane and any loading point. This distance, Z, depends on a large number of factors: the pipe and crack geometry, the material behavior, the type of loading, and to a large extent, the model.

A detailed analysis of several results obtained for uncracked, through-wall-cracked or surface-cracked pipes subjected to tension or bending and behaving elastically or inelastically has led us to several general conclusions that are summarized here.

A pipe is free from end effects if its length, $2Z$, verifies the inequality

$$\frac{Z}{2R} > \lambda \left(\frac{R}{t}, \begin{array}{l} \text{crack size, material behavior,} \\ \text{mesh refinement, type of elements} \end{array} \right)$$

where λ is almost independent of the type of loading.

1. For cracked pipes, λ is increasing with R/t.
2. The larger the crack, the greater is λ.
3. λ values are smaller for surface cracks than for through-wall cracks having the same length.
4. λ is slightly larger in EPFM than in LEFM.
5. Isoparametric elements are strongly recommended.
6. For short cracks, three-dimensional elements are recommended.
7. **For a thick pipe, with a short circumferential crack provided that the fineness of the mesh ensures a good approximation of the stress-strain field.**

$$\frac{Z}{2R} > 3$$

References

[1] Heliot, J., Labbens, R., and Pellissier-Tanon, A., "Semi-Elliptical Cracks in a Cylinder Subjected to Stress Gradients," *Fracture Mechanics (Eleventh Conference), ASTM STP 677*, American Society for Testing and Materials, Philadelphia, 1979, pp. 347–364.

[2] Heliot, J., Labbens, R., and Pellissier-Tanon, A., "Application of the Boundary Integral Equation Method to Three Dimensional Crack Problems," *Proceedings*, ASME-PVP Conference, San Francisco, 12–15 Aug. 1980-80-CZ/PVP-119, American Society of Mechanical Engineers, New York, 1980.
[3] Pineau, A., "A Review of Global and Local Approaches of Ductile and Brittle Fracture of Steels," *Proceedings,* European Symposium on Elastic-Plastic Fracture Mechanics: Elements of Defect Assessment," 9–12 Oct. 1989, Freiburg, FRG, to be published.
[4] Dodds, R. H., Jr., Anderson, T. L., and Kirk, M. T., "Numerical Correlation of Size Effects on Elastic-Plastic Fracture Toughness (J_c)," *Proceedings*, Fifth International Conference on Numerical Methods in Fracture Mechanics, 23–27 April 1990, Freiburg, FRG, A. R. Luxmoore and D. R. J. Owen, Eds., Pineridge Press Ltd, Swansea, U.K.
[5] Beremin, F. M., "A Local Criterion for Cleavage Fracture of a Nuclear Pressure Vessel Steel," *Metallurgical Transactions*, Vol. 14, A, 1983, p. 2277.
[6] Rousselier, G., Devaux, J.-C., Mottet, G., and Devesa, G., "A Methodology for Ductile Fracture Analysis Based on Damage Mechanics: An Illustration of a Local Approach of Fracture," *Nonlinear Fracture Mechanics, Volume II: Elastic-Plastic Fracture, ASTM STP 995*, J. D. Landes, A. Saxena, and J. G. Merkle, Eds., American Society for Testing and Materials, Philadelphia, 1989, pp. 332–354.
[7] Perrin, G., Leblond, J. B., and Devaux, J., "Strain Hardening Effects in Ductile Porous Metals," *Proceedings*, ECF8 Fracture Behavior and Design of Materials and Structures, Turino, Italy, July 1990.
[8] Kumar, V. and German, M. D., "Elastic-Plastic Fracture Analysis of Through-wall and Surface Flaws in Cylinders," EPRI Report NP-5596, Electric Power Research Institute, Palo Alto, CA, 1988.
[9] Yagawa, G., Ye, G. W., Kitajima, Y., and Yoshimura, S., "Three Dimensional Fully Plastic Solutions and Related Probabilistic Fracture Mechanics Analysis," *Proceedings*, Fifth International Conference on Numerical Methods in Fracture Mechanics, 23–27 April 1990, Freiburg, FRG, A. R. Luxmoore and D. R. J. Owen, Eds., Pineridge Press Ltd, Swansea, U.K.
[10] Klemm, W., Memhard, D., and Schmitt, W., "Experimental and Numerical Investigation of Surface Cracks in Plates and Pipes," *Proceedings*, IAEA Specialists' Meeting on Large Scale Testing, May 1988, Stuttgart, FRG.
[11] Broberg, K. B., "Crack-growth Criteria and Non-Linear Fracture Mechanics," *Journal of the Mechanics and Physics of Solids*, Vol. 19, 1971, pp. 407–418.
[12] Begley, J. A. and Landes, J. D., "The *J* Integral as a Fracture Criterion," *Fracture Toughness, ASTM STP 514*, American Society for Testing and Materials, Philadelphia, 1972, pp. 1–23.
[13] Paris, P. C., Tada, H., Zahoor, A., and Ernst, H., "The Theory of Instability of the Tearing Mode of Elastic-Plastic Crack Growth," *Elastic-Plastic Fracture, ASTM STP 668*, J. D. Landes, J. A. Begley, and G. A. Clarke, Eds., American Society for Testing and Materials, Philadelphia, 1979, pp. 5–36.
[14] Milne, I., Ainsworth, R. A., Dowling, A. R., and Stewart, A. T., "Assessment of the Integrity of Structures Containing Defects," Internal Report R/H/R6, Rev. 3, Central Electricity Generating Board, U.K., 1986.
[15] CASTEM Finite Element System, June 1988 version, "CISI INGENIEURIE," C.E.N. Saclay BP 249 1190—Gif-sur-Yvette, France.
[16] Wilkowski, G. M., "Elastic Plastic Fracture Mechanics Applications to Nuclear Piping," Ph.D thesis in Nuclear Engineering, Tokyo University, Japan, Feb. 1988.
[17] Raju, I. S. and Newman, J. C., Jr., "Stress-Intensity Factor for a Wide Range of Semi-Elliptical Surface Cracks in Finite Thickness Plates," *Engineering Fracture Mechanics*, Vol. 11, No. 4, 1979, pp. 817–829.
[18] Yagawa, G., Ueda, H., and Takahashi, Y., "Numerical and Experimental Study on Ductile Fracture of Plate with Surface Crack," *Proceedings*, ASME PVP, Vol. 103, PVP Conference, Chicago, 20–24 July 1986, American Society of Mechanical Engineers, NY, 1986, pp. 43–48.
[19] "A Critical Evaluation of Numerical Solutions to the 'Benchmark' Surface Law Problem," *An Assessment of the Precision of Stress-Intensity Distributions for Surface Flaw Problems of Specified Geometry from Numerical Models and Comparison with Limited Experimental Results*, Benchmark Editorial Committee, J. J. McGowan, Ed., Society for Experimental Stress Analysis, U.K., 1980.
[20] Parks, D. M., "The Virtual Crack Extension Methods for Nonlinear Material Behavior," *Computer Methods in Applied Mechanics and Engineering*, Vol. 12, 1977, pp. 353–364.
[21] McClintock, A. and Irwin, G. R., "Plasticity Aspects of Fracture Mechanics," *Fracture Toughness Testing and Its Applications, ASTM STP 381*, American Society for Testing and Materials, Philadelphia, 1965, pp. 84–113.

[20] Parks, D. M., "The Virtual Crack Extension Methods for Nonlinear Material Behavior," *Computer Methods in Applied Mechanics and Engineering*, Vol. 12, 1977, pp. 353–364.

[21] McClintock, A. and Irwin, G. R., "Plasticity Aspects of Fracture Mechanics," *Fracture Toughness Testing and Its Applications, ASTM STP 381*, American Society for Testing and Materials, Philadelphia, 1965, pp. 84–113.

[22] "RCC-M Règles de conception et de construction applicables aux matériels mécaniques des îlots nucléaires," Annexe ZG, AFCEN, Paris, France.

[23] Kumar, V. and Shih, C. F., "Fully Plastic Crack Solutions, Estimation Scheme, and Stability Analyses for the Compact Specimen," *Fracture Mechanics (Twelfth Conference), ASTM STP 700*, American Society for Testing and Materials, Philadelphia, 1980, pp. 406–438.

[24] Ainsworth, R. A., "The Assessment of Defects in Structures of Strain Hardening Material," *Engineering Fracture Mechanics*, Vol. 19, No. 4, 1984, pp. 633–642.

[25] Miller, A. G., "*J* Estimation for Surface Defects," CEGB Internal Report TPRD/B/0811/R86, Central Electricity Generating Board, Berkeley, Gloucestershire, UK, July 1986.

[26] Yagawa, G., Ueda, H., and Takahashi, Y., "Surface Crack Behaviour in Ductile Materials," *Proceedings*, Eighth SMIRT Conference, Brussels, Paper G6/2, North Holland Publishing, Amsterdam, The Netherlands, 1985.

[27] Wilkening, W. W., de Lorenzi, H. G., and Barishpolsky, M., "Elastic-Plastic Analyses of Surface Flaws in a Reactor Vessel," *Journal of Pressure Vessel Technology*, Vol. 106, Aug. 1984, pp. 247–254.

[28] Wilkowski, G. M. and Kanninen, M. F., "Fracture of Circumferentially Cracked Type 304 Stainless Steel Pipe in Bending—The Net Section Collapse Analysis," Report on 15th National Symposium of Fracture Mechanics, College Park Maryland, July 1982, Battelle Memorial Institute, Columbus, OH.

[29] Harrison, R. P., Loosemore, K., and Milne, I., "Assessment of the Integrity of Structures Containing Defects," CEGB Report R/H/R6, Central Electricity Generating Board, UK, 1976.

[30] Eiber, R. J., Maxey, W. A., Duffy, A. R., and Atterbury, J. J., "Investigation of the Initiation and Extent of Ductile Pipe Rupture," BMI 1908 Report, Battelle Memorial Institute, Columbus, OH, 1971.

[31] Miller, A. G., *Review of Limit Loads of Structures Containing Defects*, 3rd ed., CEGB-TPRD/B/0093/N82 Rev. 2, Central Electricity Generating Board, UK, 1987.

Frederick W. Brust,[1] Jalees Ahmad,[2] and Samir Naboulsi[3]

Elastic-Plastic Crack-Tip Fields Under History-Dependent Loading

REFERENCE: Brust, F. W., Ahmad, J., and Naboulsi, S., "**Elastic-Plastic Crack-Tip Fields Under History-Dependent Loading,**" *Fracture Mechanics: Twenty-Second Symposium (Volume II), ASTM STP 1131*, S. N. Atluri, J. C. Newman, Jr., I. S. Raju, and J. S. Epstein, Eds., American Society for Testing and Materials, Philadelphia, 1992, pp. 206–224.

ABSTRACT: Elastic-plastic behavior of a cracked structure subjected to cyclic loading is evaluated through a series of finite element analyses of a test specimen geometry. A specimen of an extremely ductile material (Type 304 stainless steel) is loaded to just below the J_i value at crack initiation, then unloaded and reloaded using R-ratios of 0.0, −0.5, and −1.0 including the effects of crack face contact. The crack-tip asymptotic fields, tensile and compressive plastic zones, and crack-tip parameters such as crack-tip-opening displacement and the J- and T^*-integrals are evaluated and discussed in the context of cyclic loading for a stationary crack.

KEY WORDS: elastic-plastic behavior, cyclic loading, crack closure, J-integral, T^*-integral, asymptotic fields, crack initiation, fracture mechanics, fatigue (materials)

The elastic-plastic behavior of cracked structures subjected to monotonically applied loads can now be predicted with engineering accuracy using the J-integral concept. This is because the J-integral may be interpreted as the strength of the asymptotic crack-tip fields, or the Hutchinson, Rice, and Rosengren fields (HRR), for a stationary crack in a monotonically loaded body. Often, even if gross violation of the limits of valid J-tearing theory as developed by Hutchinson and Paris [*1*] are made, reasonable and conservative engineering predictions of maximum load usually result (see the large data set developed by Wilkowski, et al. [*2*] for cracked pipes monotonically loaded to failure). Even for surface cracked structures where constraint effects are currently an issue of great interest and concern, conservative and reasonable predictions of crack instability may be made as long as the structure is monotonically loaded to failure [*2*].

In many practical instances, cracked structures that fail via ductile rupture experience cyclic tearing rather than monotonic tearing to failure. Here we distinguish between fatigue crack growth and cyclic tearing by defining the latter to occur when the value of J is near or greater than the initiation valve, J_i.

In situations where ductile cracked structures experience history-dependent crack-tip damage, the J-integral approach does not perform adequately. History-dependent damage at the crack tip will accumulate if the component experiences significant cyclic fatigue or tearing, as occurs in many structures such as nuclear pipe subjected to an earthquake spectrum. J cannot characterize history-dependent damage during cyclic loading because it loses its significance as the strength of the asymptotic crack-tip fields. Ductile crack growth analyses

[1]Senior research scientist, Battelle Memorial Institute, Columbus, OH 43201.
[2]Director of research, Ad Tech Systems Research, Dayton, OH, 45432.
[3]Graduate student, Engineering Mechanics Department, The Ohio State University, Columbus, OH 43210.

based on J can lead to nonconservative failure load predictions depending upon the applied load history (see Ref *3*, for instance). Indeed, this unpredictability renders current methods ineffective without further study.

The focus of the present study is to further examine the cyclic tearing process by performing detailed finite element analyses of a compact tension specimen that experiences gross plastic deformation both during the loading and the unloading phases. We focus our attention on a high hardening, high-toughness steel (Type 304 stainless steel at 280°C) since qualitative experimental data exists on this material for loading levels that induce cyclic tearing. Wilkowski [*4*] has observed that when a through-wall cracked pipe of Type 304 stainless steel is loaded to a level producing a J-value just below initiation and then completely unloaded ($R = -1.0$) and reloaded, crack growth initiation occurs at load levels much lower than expected for the corresponding monotonically loaded pipe. In addition, for an unload level to $R = 0$, crack growth initiation resistance upon reloading occurs at the load level expected during monotonic loading of a virgin pipe (that is, at $J = J_i$). In other words, the cyclic tearing damage induced at the crack tip for $R = -1.0$ greatly reduces the crack initiation resistance of the pipe during subsequent reloading. For $R = 0$, little cyclic tearing damage occurs and crack growth initiation during reloading occurs as for virgin undamaged material. With these experimental observations in mind, the present paper attempts to determine if this behavior can be predicted using classic continuum theory.

Background

Before describing the analysis results, a brief discussion of previous studies of cyclic tearing behavior for cracked bodies is presented in order to bring the current study into focus. Note that conflicting results have been obtained from the different researchers.

Experimental

Clark et al. [*5*] showed that 10% unloadings produce virtually no effect on ductile fracture resistance. These observations led to the original unloading compliance method for monitoring crack growth in fracture specimens before potential drop methods became popular. Kaiser [*6*] proposed a linear summation model for predicting crack growth behavior during cyclic tearing conditions. Under this framework, crack growth per cycle is estimated by separating the growth into cyclic fatigue and tearing components. The cyclic fatigue component is estimated by extrapolating fatigue data developed at low load levels to ΔK (or ΔJ) levels that are typical of cyclic tearing, while the tearing component per cycle is estimated using classical J-tearing theory.

Since Kaiser's model was proposed, a number of researchers have examined the appropriateness of the model through experimental efforts and have obtained conflicting results. Landes and McCabe [*7*] show that the linear summation model performs adequately for HY130 steel and poorly for A508 steel. Their tests were for ratios of minimum to maximum load level (R) less than zero. Landes and Liaw [*8*] produced experimental results that suggest that the linear summation model performs adequately for R ratios greater than zero and performs poorly for $R < 0$. Joyce [*9*] developed experimental data on A710 Grade A steel for ratios of $R = -1.0$. These data suggest that a linear summation model may be appropriate under load control, but is not at all useful for experimental data developed under complete crack opening displacement (COD) reversals. These results suggest that Kaiser's model is not general, but rather is perhaps appropriate for certain materials and up to certain load levels (or R ratios).

Analytical

Most of the analytical studies that have been performed to date are concerned with cyclic fatigue; that is, the load levels are low and the corresponding plastic zone sizes are small compared with those corresponding to cyclic tearing. Many of the analysis efforts may be found in *ASTM STP 982* [*10*] and references cited therein. In addition, Chan et al. [*11*] and Kubo et al. [*12*] have examined crack-tip field parameters including J (or ΔJ) under cyclic fatigue conditions. From these efforts, we may conclude that the J-integral (or ΔJ) is very much path dependent within the plastic zone, and, of course, path independent outside this zone.

From these efforts, combined with the experimental studies just discussed, it appears that for low toughness materials where the plastic zone is relatively small a linear summation model for predicting cyclic tearing behavior may be adequate for engineering purposes. However, for high-toughness materials where large plastic zones develop during the cyclic tearing process, a linear summation model is likely to be inadequate. This conclusion is also supported by the results of Ref *3*, which showed that nonconservative results may result if the prediction of cyclic behavior is made using the J-tearing theory.

Cyclic Tearing Analysis

As just stated, many of the elastic-plastic cyclic load analysis results of cracked bodies were performed to study fatigue crack growth where relatively low loads and corresponding small plastic zones prevail. Here, the cyclic elastic-plastic behavior of a stationary cracked body (compact tension specimen) is examined under conditions of large-scale yielding.

The standard 0.75 T compact tension specimen shown in Fig. 1*a* was modeled. The three loading sequences illustrated in Fig. 1*b* were modeled via the finite element method. The horizontal axis of Fig. 1*b* represents a time-like parameter that will be used to correlate the load at each part of the analysis sequence in subsequent figures. As seen in Fig. 1, the effect of the differing amount of damage induced for $R = 0$, -0.5, and -1.0 is considered.

This particular compact specimen and the corresponding dimensions were chosen since they are typical of J-resistance curves developed for through-wall cracked pipes.

Finite Element Model

The symmetric finite element model utilized for all analyses is illustrated in Fig. 2. The positive or negative loading was applied to the top or bottom triangular elements, respectively, to simulate the load pin action on the holes. As seen in Fig. 2*c*, the mesh refinement in the crack-tip region is 0.002 C, where C is the uncracked ligament (C = 17.02 mm, see Fig. 1*a*). This mesh is about two times less refined than that used by Shih and German [*13*] in their finite element asymptotic studies. As discussed later, the refinement used here is quite adequate for capturing the monotonic and cyclic asymptotic crack-tip fields.

Here we utilize one node at the crack tip. It is known that using multiple nodes at the crack tip, each of which may deform independently, results in a $1/r$ singularity in crack-tip strains, and no singularity in stress. This type of singularity is produced only in an elastic-perfect plastic material model. The material here is modeled as a power law hardening model and thus produces a singularity of the order of $-1/(n + 1)$, with n the hardening coefficient. Here, we choose to not introduce a $1/r$ singularity, but recognize that an underprediction of crack-tip-opening displacements may result by using a single crack-tip node.

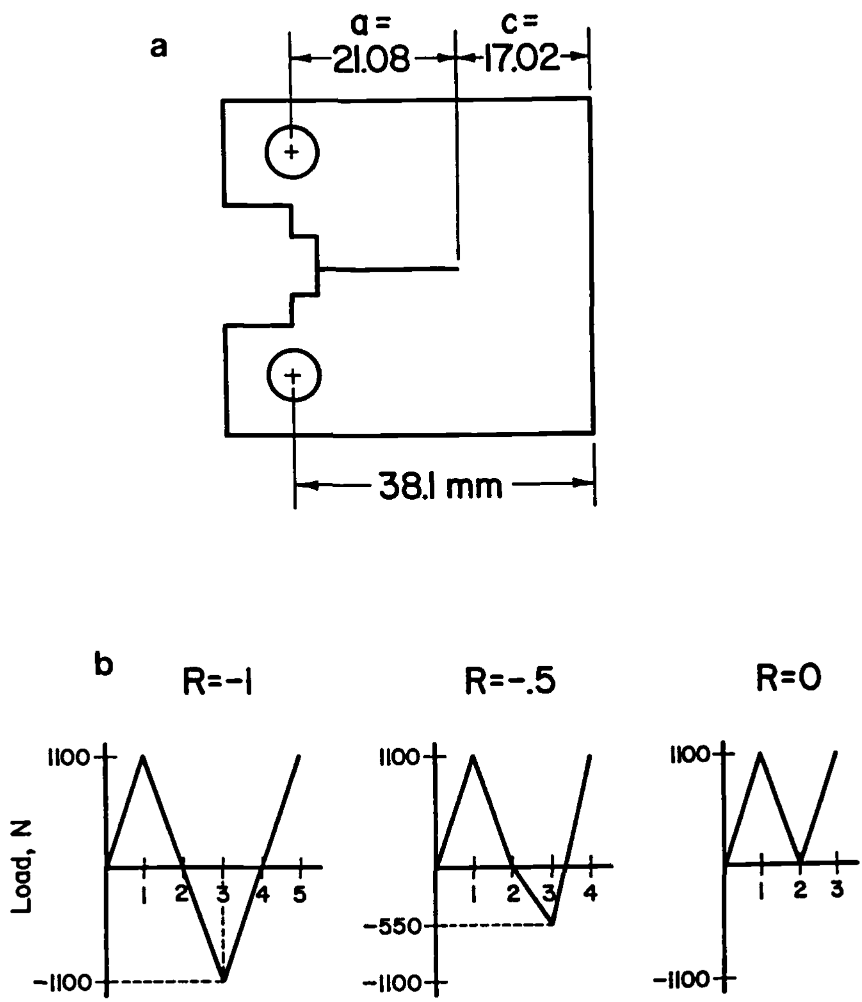

FIG. 1—(a) *Analysis geometry; and* (b) *Analysis load definition. The horizontal axis is a time parameter that will be used to define the load sequence definition in later figures. The maximum load of 1100 N corresponds to an applied* J_i.

The material was modeled as a Ramberg-Osgood power law hardening material, written in normalized form as

$$\frac{\varepsilon}{\varepsilon_0} = \frac{\sigma}{\sigma_0} + \alpha \left(\frac{\sigma}{\sigma_0}\right)^n \tag{1}$$

where

$\sigma_0 = 135$ MPa,
$\alpha = 6$,
$n = 3.6$,
$\varepsilon_0 = \sigma_0/E$, and
$E = 192\ 000$ MPa.

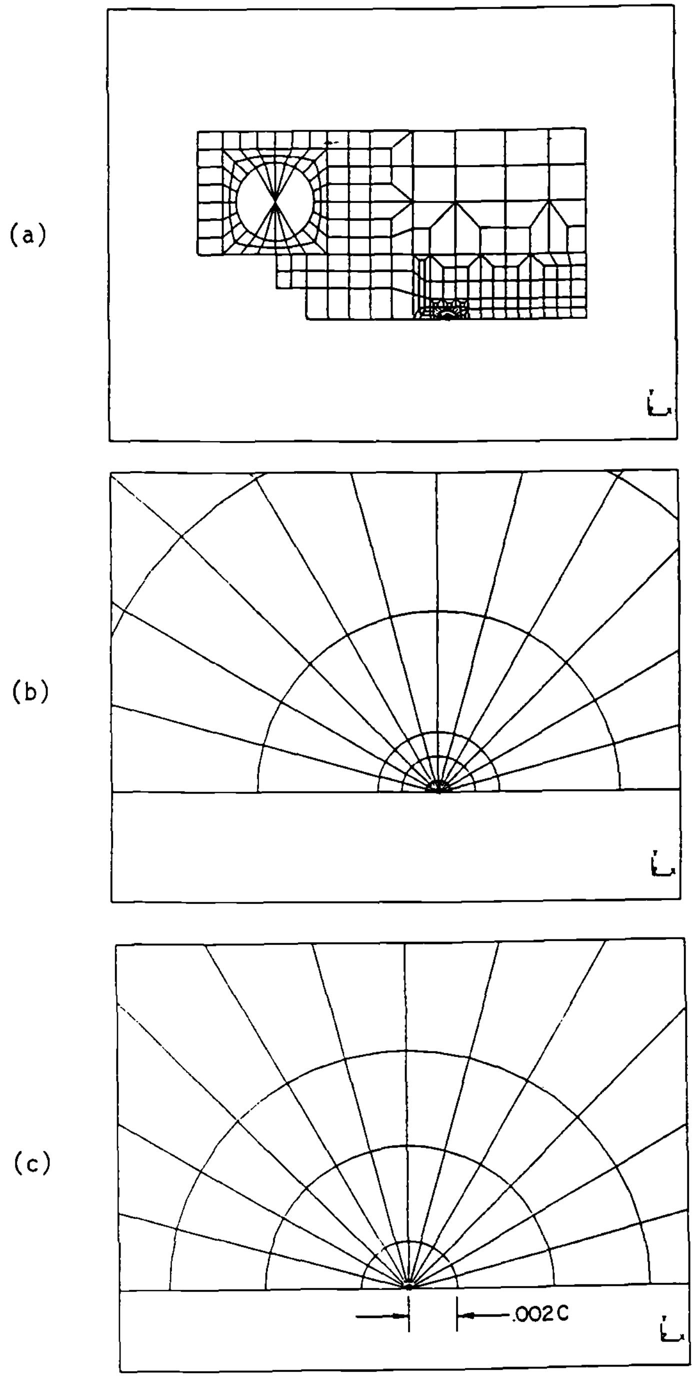

FIG. 2—*Finite element mesh.*

The tensile properties were developed from a specimen cut from pipe. Classical flow theory of plasticity and small strain theory were utilized for all analyses. For the material considered here, which is a very tough stainless steel, a nonneglibible zone of large strains and rotations develops near the crack tip at maximum load. However, since the *J*-tearing theory is based upon small strain theory (*J*-resistance curves and estimation schemes are developed as such), these analyses are performed neglecting large strains. Implications regarding this assumption appear later in the discussion section.

The value for *J* at crack initiation is between 550 and 650 N/mm, determined from a compact tension specimen cut from pipe (see Ref *2*). For this material, corresponding material properties were used since qualitative experimental results exist for a through-wall cracked pipe loaded cyclically at high loads [*4*]. The maximum load applied (*P*) for each analysis was 1100 N, which corresponds to a *J*-value of about 600 N/mm. ABAQUS [*14*] was used for all analyses. Isotropic hardening was assumed. Plane-strain analyses using the mixed element with separate displacement and pressure unknowns were used. A VAX cluster computer system was used for the analyses.

Results

Observe from Fig. 1*b* that for all three analyses, the load is 1100 N at a parametric time equal to one. For times greater than one, the loads vary for the different analyses (R = 0.0, −0.5, and −1.0). The half crack-tip-opening displacement (CTOD) profile at the maximum monotonic load point (1100 N) for all three analyses is shown in Fig. 3. Significant crack-tip blunting suggests that a zone exists near the crack tip in which large deformation effects play an important role. The CTOD, defined using the convention of Rice [*15*] as the intersection of the included 90° angle and the blunted crack faces, is about 1.2 mm. The CTOD predicted from the elastic-plastic handbook [*16*] is about 1.35. The *J*-integral, which was calculated on 15 different paths each encircling a different ring of elements in Fig. 2, was path independent and its magnitude was 610 N/mm. The corresponding handbook [*16*] value is about 620 N/mm.

Plastic Zones

The magnitude of the plastic zone extent can be observed in Fig. 4. This is an equivalent stress (von Mises) contour plot. The contour values (1 through 6) are listed at the bottom, with the minimum value equal to the yield stress of 135 MPa. The "dot" in the figure inset identifies the point on the load versus parametric time plot that represents the results in Fig. 4. Figure 4 then can be used to identify the extent of the plastic zone at the maximum monotonic load (with no unloading). The hatched regions in Fig. 4 thus represent regions in the specimen that have not yielded. The gross plastic deformation of the specimen is evident.

Figures 5*a* and *b* show contour plots of the plastic strain developed during unloading (for parametric time >1, see figure insets) for the $R = 0$ and $R = -1.0$ analyses, respectively. These plots represents the additional amount of plastic deformation developed between Times 1 and 2 for the $R = 0$ analysis and Times 1 and 3 for the $R = -1.0$ analysis. Therefore, these contour plots reveal the extent of reverse plastic deformation that occurs during the unloading phase for the $R = 0$ and $R = -1.0$ cases. The cross-hatched regions represent the reverse plastic deformation zone. The results for the $R = -0.5$ analysis are between these two results and are not shown here. A reverse plastic zone (compressive) very near the crack tip begins to develop almost immediately after reversing the load very

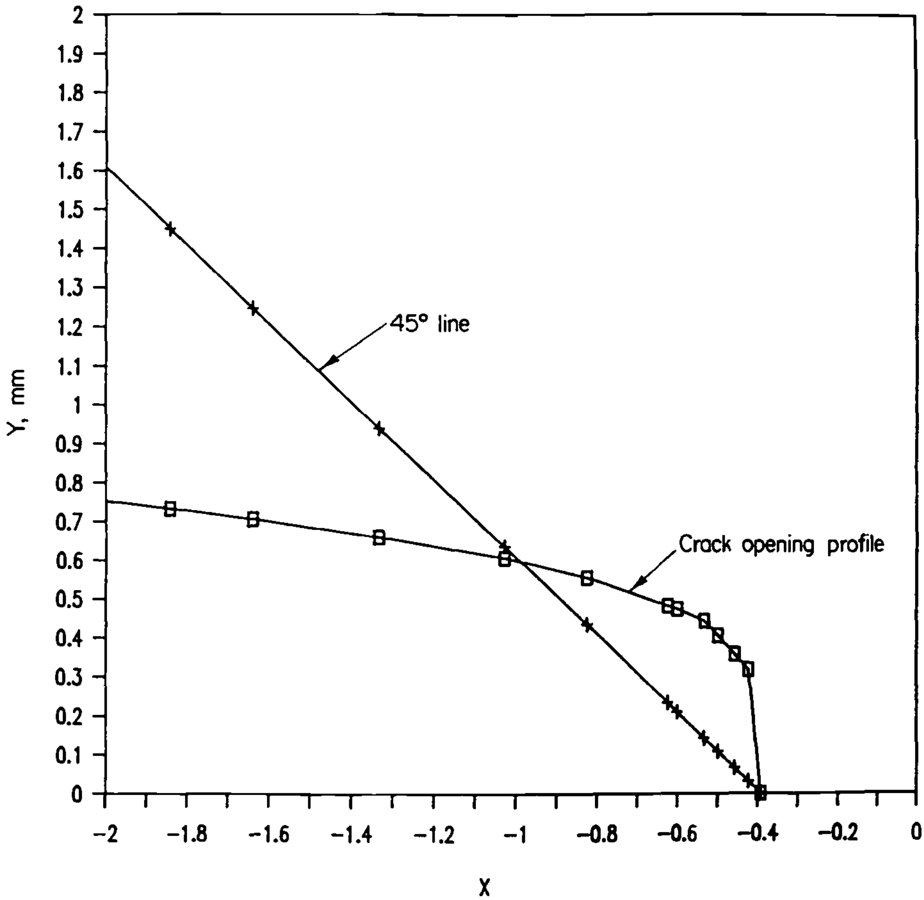

FIG. 3—*Crack tip at maximum monotonic load.*

near the crack tip. However, the extent of the compressive zone near the crack tip is not extensive when the load is eliminated completely (Fig. 5*a*). As unloading continues, the crack-tip compressive zone rapidly extends until, at the $R = -1.0$ point (load = −1100 N), net section gross reverse plastic deformation is experienced (Fig. 5*b*).

The extent of the large compressive plastic zone that develops near the crack tip may affect the crack-tip damage and subsequent crack initiation point during reloading. By predicting the extent of this zone, one may possibly develop simple techniques for predicting cyclic tearing damage in cracked bodies. However, within the limits of this analysis (small strain theory, isotropic hardening, classical continuum constitutive plasticity theory), we should not expect to predict cyclic damage and history-dependent crack growth using the J-tearing theory.

During unloading to $R = -1.0$, no crack face contact was experienced. This is because the crack tip was stretched and blunted so severely that upon unloading a large amount of reverse plastic deformation would have to be achieved to overcome the tensile load plastic strains. While this is partially an artifact of the isotropic hardening assumption, this lack of crack face contact upon unloading for this material was also observed in through-wall cracked-

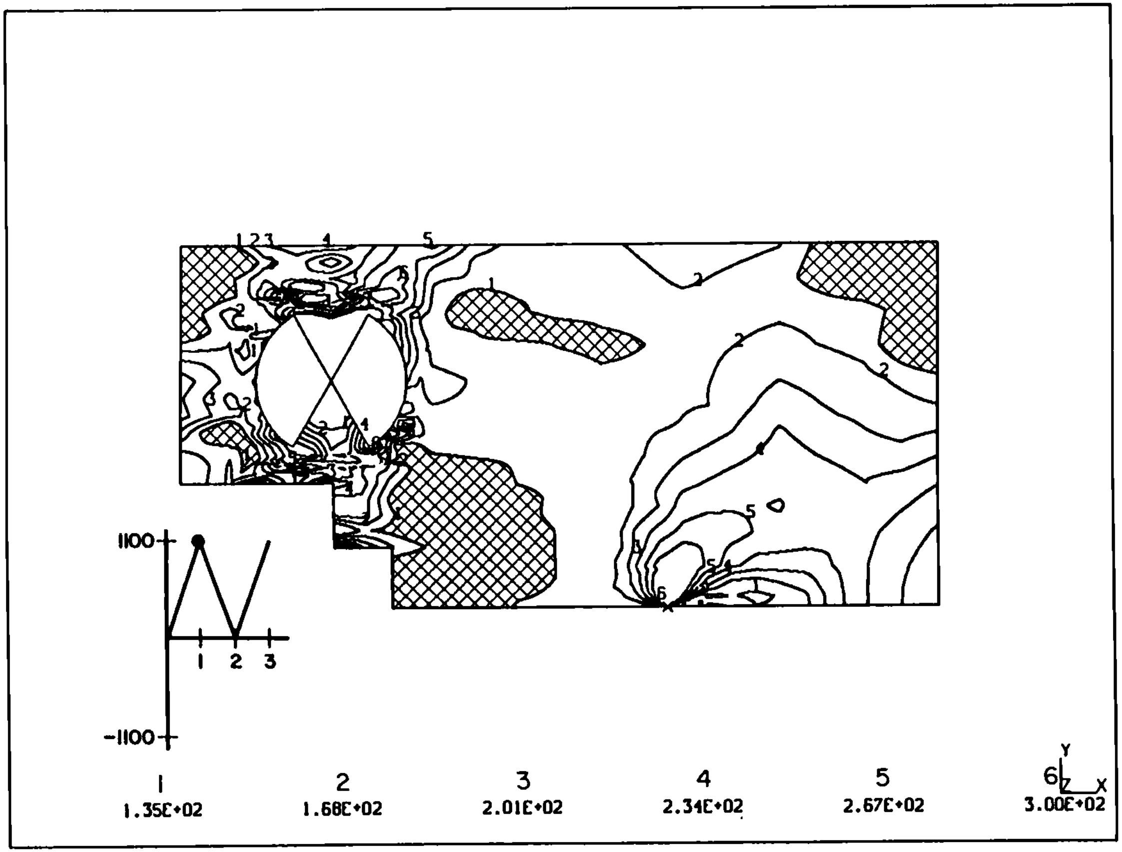

FIG. 4—*Equivalent stress contour plots. The hatched regions represent regions that* **have not** *yielded as yet. The figure inset describes the load-time history point represented by this plot.*

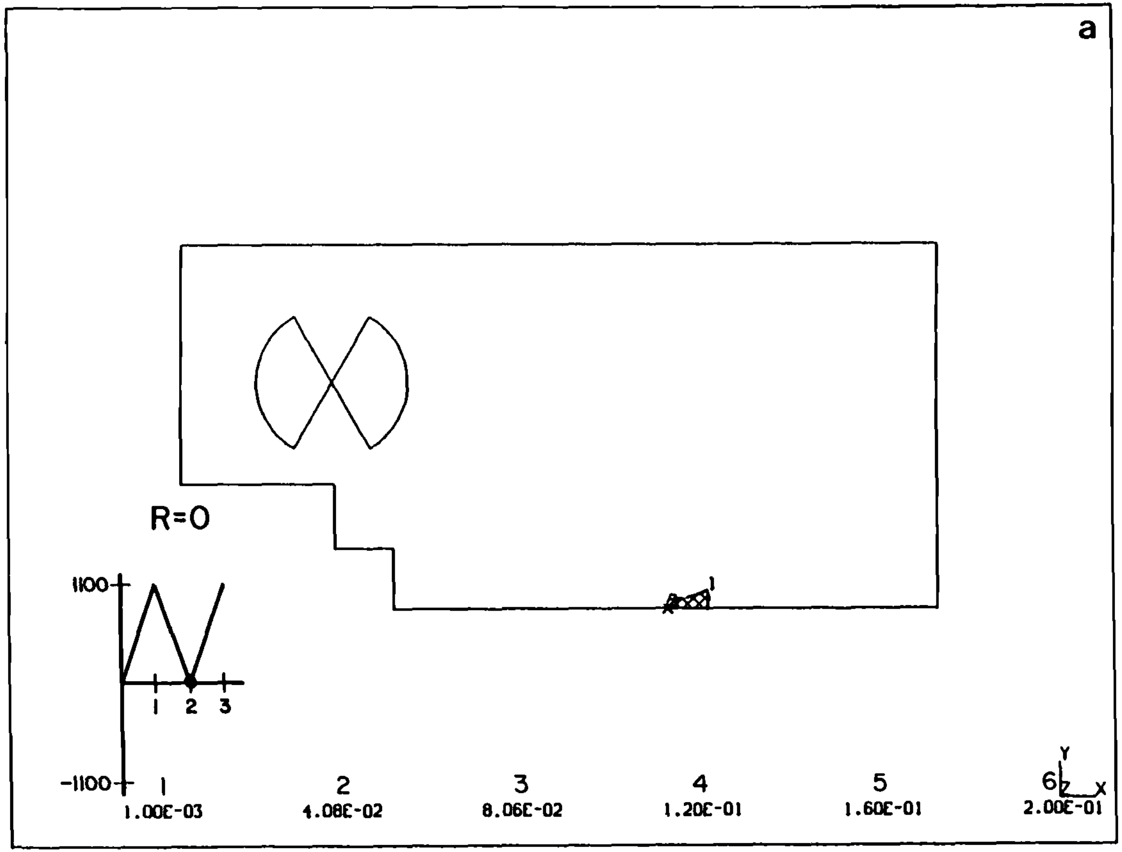

FIG. 5—*Reverse plastic deformation zone contour plots* (a) *the plastic zone developed between Times 1 and 2* (*inset*), *and* (b) *the additional plastic zone developed between Times 1 and 3* (*inset*).

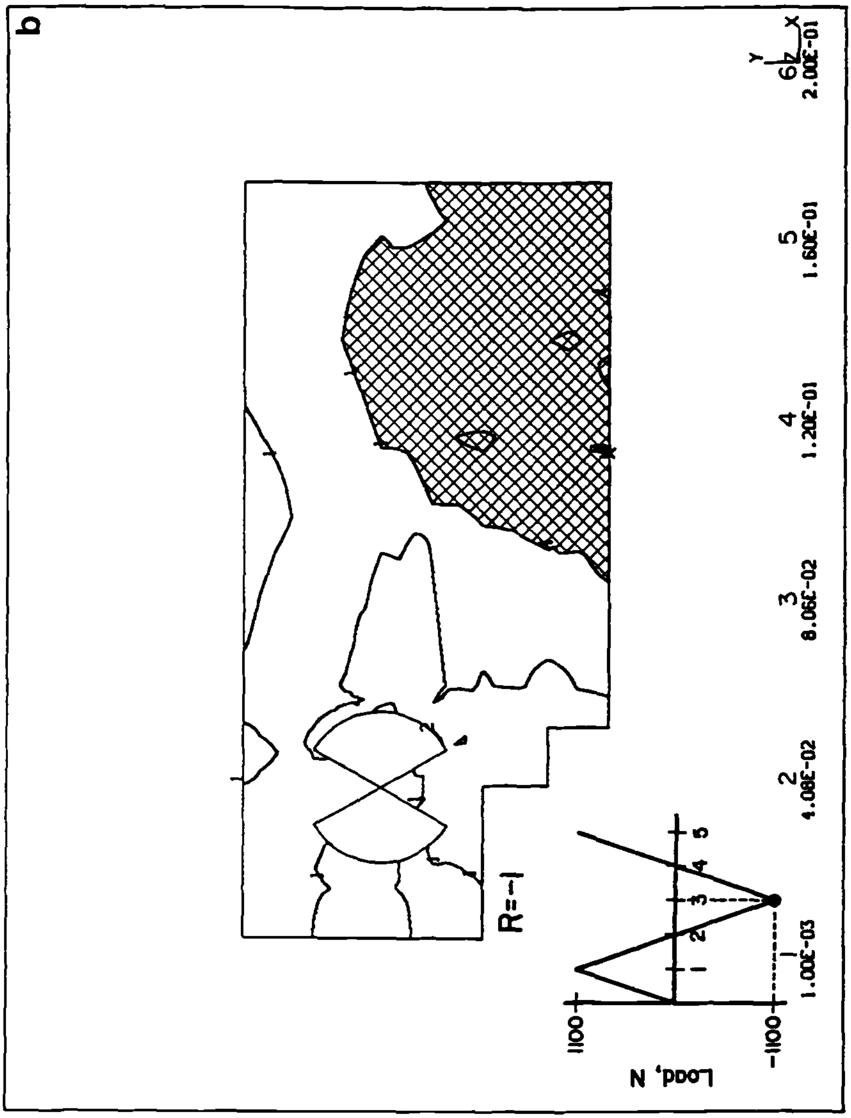

FIG. 5—Continued

pipe cyclic bending experiments when the tensile load level produces an applied J-value near J_i [4]. This will be further elaborated upon in the discussion section.

Asymptotic Crack Field Stresses

The stresses are compared with the corresponding HRR field stresses at different points in the analysis in Figs. 6 and 7 at 90° to the crack plane. Figure 6 provides the radial stresses as a function of radial distance from the crack tip at the monotonic load point, the completely reversed load point, and the reload point (Points A, B, and C of the Fig. 6 inset) for the $R = -1.0$ case. At the monotonic load point (Point A, inset) stresses compare very well with the HRR field up to about two crack-tip-opening displacements (recall $\delta_i \cong 1.2$ mm) from the tip.

At Point B, the complete unload point in the load history, the stress state is entirely compressive. In Fig. 6, the absolute value of the radial stresses at 90° from the crack plane are plotted. Rather remarkably, these compressive stresses compare quite well with a negative of the HRR field. Finally, after one cycle of unload-reload, with full account of the history dependence of flow theory of plasticity provided for, the stresses again compare quite well with the monotonic, history-independent HRR field.

Figure 7 shows a similar comparison for the $R = 0$ case, where again the HRR field is preserved even after one cycle of unload-reload. This is not as surprising as the $R = -1.0$ results since the size of the reverse plastic deformation zone (Fig. 5*a*) is not large and the effect of history dependence is less pronounced. Again, the HRR field is preserved up to a distance several times δ_i from the crack tip.

Figures 8 and 9 provide stresses compared with the HRR field for the intermediate load history of $R = -0.5$. Figure 8 shows $\sigma_{\theta\theta}$ stresses at $\theta = 0$ in front of the crack tip. For the monotonic load point (Point A indicated by the + symbol), the stress field compares with the HRR field up to about 1.5 mm (about 1.25 δ_i) ahead of the crack tip if we (arbitrarily) choose a 10% tolerance on the stresses compared to HRR stresses to define the point where divergence from the HRR field begins. The corresponding monotonic load stresses (Fig. 9) compare quite well with the HRR field at $\theta = 90°$ up to more than 2 δ_i from the tip. This was the general trend of all analysis results; that is, the stresses (all components) compare favorably with the HRR field for a shorter distance from the crack tip at $\theta = 0°$ compared with $\theta = 90°$.

After one complete cycle of unload, the stresses in front of the crack tip are, of course, nearly identical to the monotonic load stress (Figs. 8 and 9). In addition, the HRR field is also maintained near the crack tip as if no unloading has occurred. Also plotted in these figures (open squares) are the absolute value of the stresses at the complete unload point of the load history. Here, it is seen that the comparison to the "negative" of the HRR field occurs over a much shorter distance from the crack tip compared with the $R = -1.0$ case (Fig. 6).

It is quite interesting to observe that the HRR field is preserved for a stationary crack taken through one complete cycle of load reversal for all three R-ratios considered here. Of course, the simplified constitutive law (isotropic hardening) and the small strain analysis assumption contribute to this effect.[4] However, it should be expected that, at Points A and C of Figs. 6 through 9, the value of the crack driving force as measured by J should not be affected significantly by the unload cycle as the near field stresses are not significantly affected. This is discussed next.

[4]Observe (Figs. 3 to 5) that a significant amount of reverse plastic deformation does occur, especially for the case of $R = -1.0$.

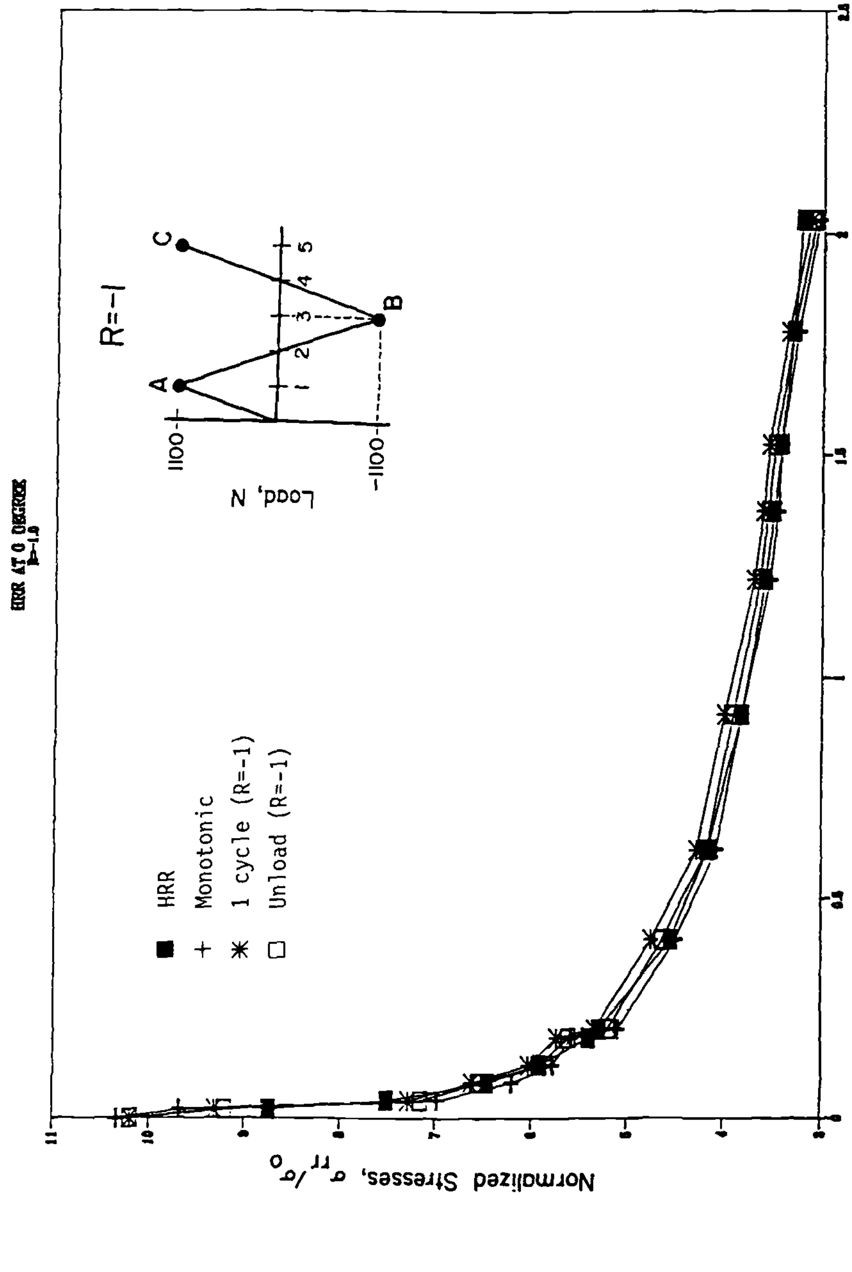

FIG. 6—*Radial stress components (at 90° from the crack plane) compared to HRR field stresses. Monotonic (MONTNC), one cycle (1 cy), and unload (UNL) correspond to Points A, C, and B, respectively, in the figure inset. (Note: the absolute value of the stress is plotted for unload (Point B) since these are negative.)*

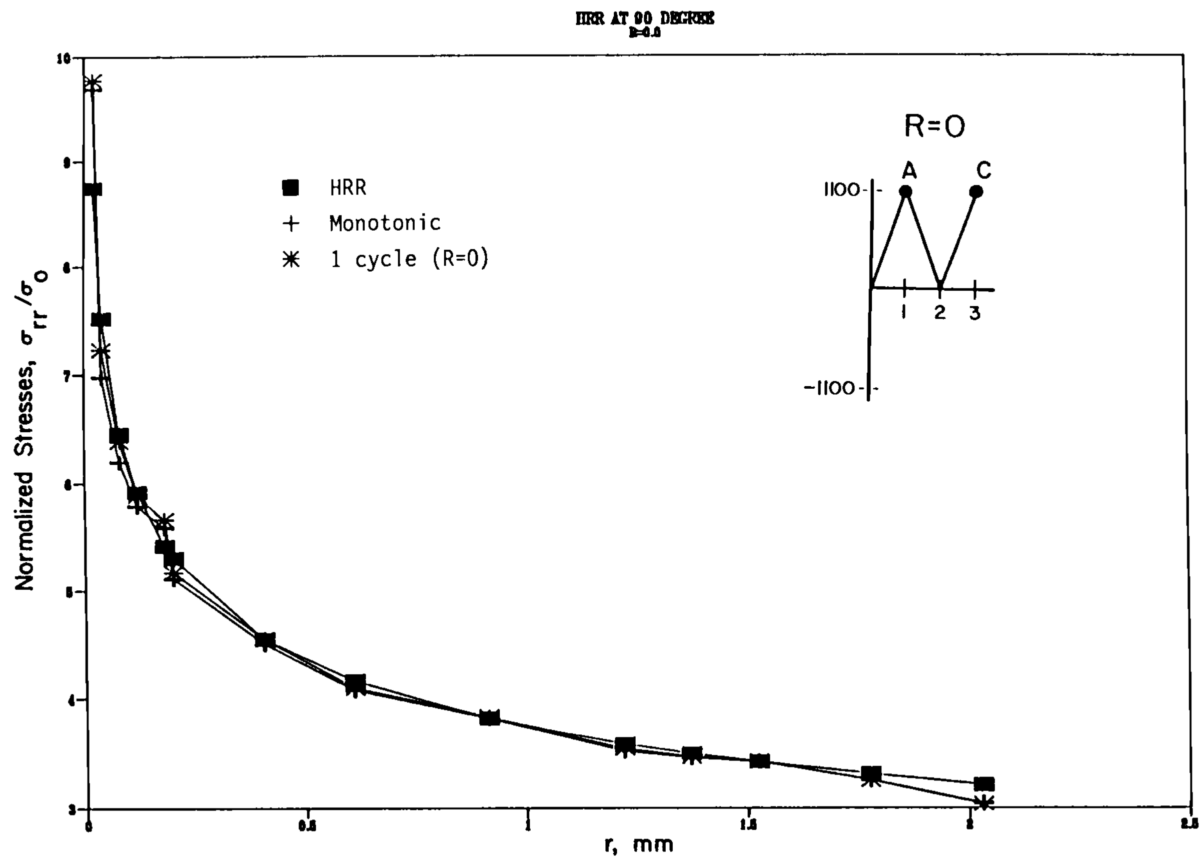

FIG. 7—*Radial stress components (at 90° from the crack plane) compared to HRR field stresses. Monotonic (MONTNC) and one cycle (1 CY) correspond to Points A and C in the figure inset.*

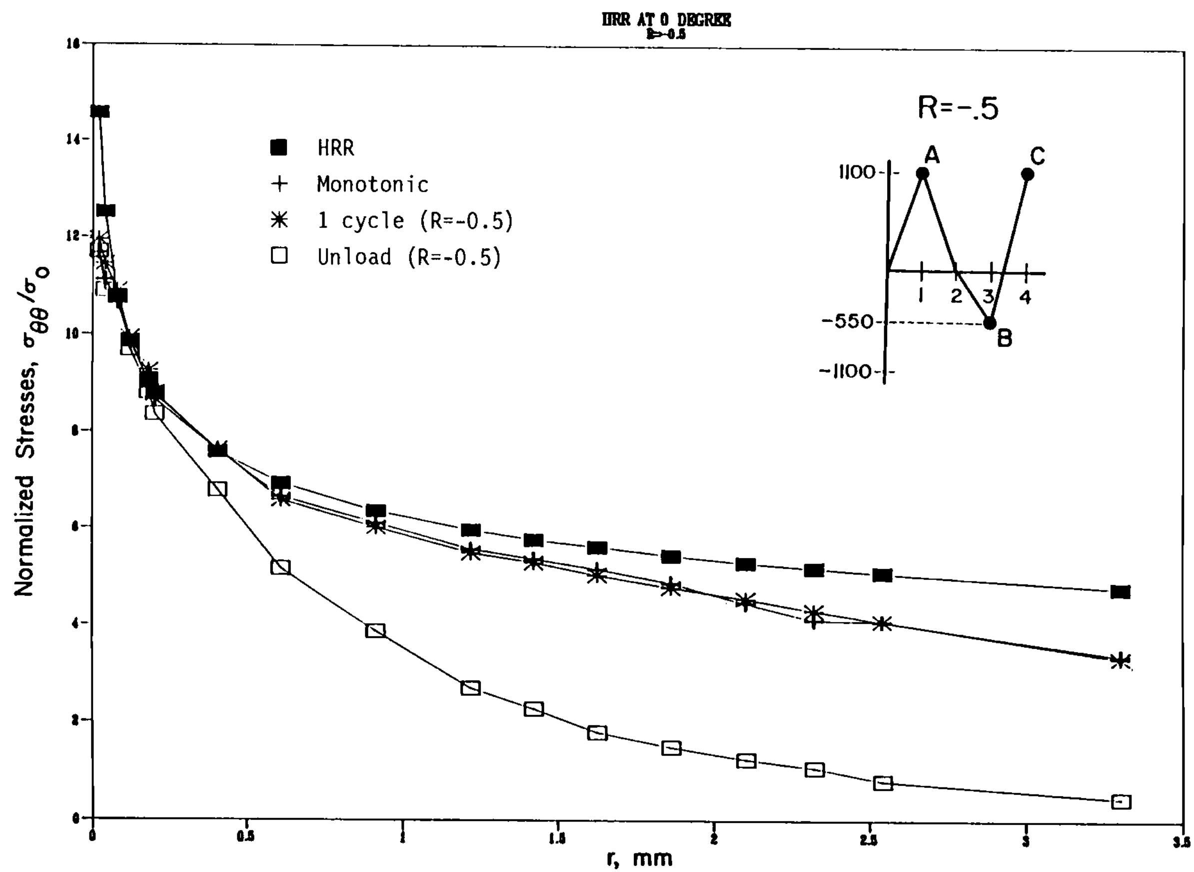

FIG. 8—*Hoop stresses* ($\sigma_{\theta\theta}$) *in front of the crack tip at* $\theta = 0°$ *compared to HRR field. Montonic (MONTNC), one cycle (1 CY), and unload (UNL) correspond to Points A, C, and B, respectively. (Note: the absolute value of the stress is plotted for unload Point B since these stresses are negative.)*

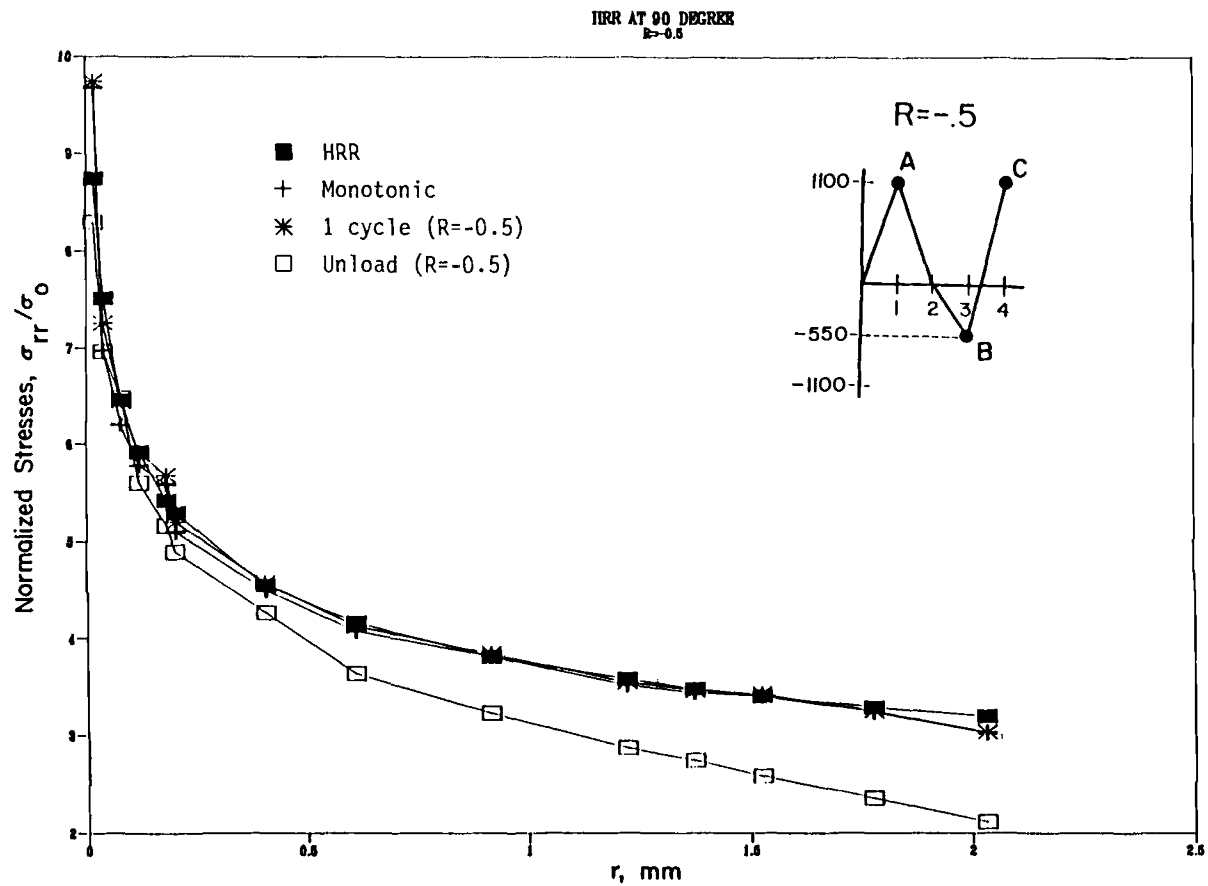

FIG. 9—*Radial stresses* (σ_{rr}) *in front of the crack tip compared to HRR field. Monotonic* (*MONTNC*), *one cycle* (*1 CY*), *and unload* (*UNL*) *correspond to Points A, C and B, respectively.* (*Note: the absolute value of the stress is plotted for unload Point B since these stresses are negative.*)

Crack Driving Force

The J-integral[5] was evaluated along 15 different paths ranging from very close to the crack tip to the far boundaries of the specimen (see Fig. 2). During the original monotonic loading portion of all analyses, J was basically path independent, along all but the first path (and slightly in error along the second path). The value of J at the maximum load of 1100 N is 610 N/mm. During the unloading portions of all analyses, J decreased, became negative for the $R = -1.0$ and $R = -0.5$ cases, and was very much path dependent. However, upon reloading for all three R-ratio cases analyzed, J along all paths became path independent by the time the maximum load of 1100 N was again reached. Moreover, the value of J at maximum reload was again about 610 N/mm. This means that, within the context of the J-tearing theory confined by the assumptions inherent in this analysis, no history effect is predicted to occur.

Discussion

Monotonic Loading

The specimen dimensions chosen for these analyses are shown in Fig. 1. Typically, specimens between 0.5 T and 2 T compact tension specimens are cut from pipe in order to develop J-resistance curves. The specimens are made to have a thickness close to the pipe thickness. The rationale for this approach is that a compact tension specimen J-resistance curve is a lower bound curve, and thus when it is used in a predictive analysis, the results will be conservative. Wilkowski et al. [2] have used this methodology to predict the behavior of numerous through-wall cracked-pipe experiments using a J-estimation scheme procedure with reasonable results.

These analyses produce very good predictions despite several violations of the classic J-tearing theory, as lucidly described by Hutchinson [*17*]. These violations include crack growth beyond the limits imposed by Hutchinson and Paris [*1*] and violation of the HRR dominance as prescribed by the asymptotic studies of Shih and German [*13*], Parks [*18*],

McMeeking [*19*], from the finite strain analysis of the small-scale yielding problem, found large strains of order unity directly in front of the blunted crack tip. This leads to a reduction in stress triaxiality near the tip and corresponding great reduction of the stress state compared with the singular small strain HRR field. These large strains persist for a distance of about one δ_t ahead of the crack tip ($\varepsilon_p > 0.15$) for the elastic perfectly plastic limit of $n \to \infty$. The zone of large strains (greater than 0.15) decreases as the material hardening increases (n decreases). Moreover, large deformation effects are important in terms of their effect on the stress state for a distance of about 2 or so δ_t ahead of the blunted crack tip. The classic J-dominance argument is that the small strain HRR field controls the large deformation process zone at the blunted crack tip, and hence controls the fracture process if the HRR field is experienced for a distance greater than 2 δ_t ahead of the crack tip. For bend-type cracked geometries, Refs *13* and *18* through *20* suggest that HRR field dominance occurs if the uncracked ligament, C, is greater than about 25 (J/σ_0), which is about 110 mm for the present case. From Fig. 1, C is 17 mm from this case, and will clearly always miss the limit of 110 mm for any 1 T or 2 T specimen cut from pipe. From Figures 6 to 9, we also see that the HRR field is realized for less than 2 δ_t, in general.

[5] J was evaluated using a post-processor written especially for use with ABAQUS using the equivalent domain integral procedure. The J-integral module of ABAQUS assumes proportional loading is valid that results in the elimination of one term. For nonproportional loading, which occurs here, this term is not zero, and necessitates the use of the new post-processor.

limit of 110 mm for any 1 T or 2 T specimen cut from pipe. From Figures 6 to 9, we also see that the HRR field is realized for less than 2 δ_t, in general.

Thus, based on this discussion, J should not control the fracture process if the resistance curves are developed from small specimens. However, as just mentioned, Wilkowski et al. [2] have numerous practical examples showing that, for monotonic loading to failure, the J-tearing theory gives good predictions of failure load in pipe. Why does J work here when it appears to be inadequate?

If we examine the path dependence of J from McMeeking's [19] results, we find that J varies from near zero at the blunted crack tip to its far-field value at about 0.5 δ_t from the tip. Beyond this point, J is only slightly lower than its far-field value.[6] Thus, while large strain effects are important to the stress field up to about 2 δ_t or more distances from the crack tip, J is affected greatly only for distances of 0.5 δ_t and less from the tip. In addition, Papaspyropoulos [21] performed a series of finite element analyses on 1 T, 3 T, and 10 T compact tension specimen experiments of the same plan-form thickness. In these numerical tests, the displacement versus crack growth record from a series of experiments served as input to the finite element analyses. The J-resistance curves developed did not differ much from each other at crack initiation and for small amounts of crack growth. Note that the 10 T specimen is the only one that satisfies the strict HRR field J-dominance requirements ($C \geq 110$ mm). It appears that the strict requirements on valid J-tearing theory application may be relaxed for practical applications.

Cyclic Loading

The present finite element analysis examined the cyclic tearing behavior in a practical engineering material (Type 304 stainless steel). This material is well suited for application of the J-tearing theory because of its high hardening characteristics ($n = 3.6$). A 0.75 compact tension specimen was analyzed as being subjected to three different cyclic load controlled conditions; $R = 0, -0.5, -1.0$. The maximum load applied before unloading produces a J-value near the expected crack initiation value of $J_i = 600$ N/mm.

The results indicate that the HRR field is preserved after one cycle of loading is completed. This suggests that J should be a useful parameter to describe and predict this behavior. J became nearly path independent after one complete cycle of loading. In addition, after reloading the specimens for all three R-ratio analyses, J again approached the monotonic value of J_i. This behavior is in disagreement with experimental observations of Wilkowski [4] that for initial monotonic loading of through-wall crack pipe of Type 304 stainless steel (288°C) to near J_i (600 N/mm) for $R = -1.0$ case, the crack should initiate at about one-half the load for virgin material, while an $R = 0$ case is almost unaffected by cyclic damage.

There are several possible reasons why our analysis does not appear to model reality.

1. The use of isotropic hardening is an unrealistic constitutive representation of cyclic plasticity. However, for one cycle of load, this hardening model should not perform extremely poorly. In Ref 3, an isotropic hardening model was used to model an unload cycle after an appreciable amount of crack growth had occurred. During reloading the near-field value of J (called T^*-integral in Ref 3) predicted the crack reinitiation behavior of the experimental data quite well. In that analysis, J was extremely path dependent upon reloading. It is believed that the difference between the situation modeled in Ref 3 and that here is the crack growth. In Ref 3, an appreciable plastic

[6]The lower the Ramberg-Osgood power coefficient, the more path independent J is beyond 0.5 δ_t from the tip. For stainless steel, which is a high hardening material, n generally ranges between 3 and 5.

wake developed along the flanks of the growing crack and appreciable local crack-tip nonproportional loading occurs while global loading continues. Here, for the stationary crack, local and global unloading/loading occur synchronously; that is, a kind of global proportional loading/unloading occurs. This may be why HRR fields are once again produced after the reload cycle, and J becomes path independent. Finally, in some recent preliminary results to be reported elsewhere, we have found that kinematic and isotropic hardening assumptions do not produce results appreciably different from those observed here if near- or far-field J is used as a crack growth criterion.

2. The use of a classic continuum constitutive theory may not be appropriate for predicting cyclic damage observed in the experiments. It may be more appropriate to utilize a Gurson-type model for analyzing cyclic damage, as, for example, Needleman [*22*] used for monotonic loading to failure. Indeed, after loading to an applied J-level near J_i, voids have developed in front of the blunted crack tip. During unloading, the voids may crease along their edges to different amounts depending on the applied R-ratio. Upon reloading, microcracks should be expected to develop at the void edges previously creased. This should lead to crack reinitiation predictions at a lower load level compared with undamaged material.
3. The near- or far-field J-integral may be inappropriate for predicting cyclic damage and crack initiation. If this is the case, then efforts to develop cyclic J-resistance curves and separable fatigue/J-tearing methods may not be warranted.
4. In the monotonic loading discussion section, we argue that large deformation effects and the corresponding J-dominance criterion can be relaxed. However, it may be that large deformation/strain effects play an important role in characterizing cyclic damage accumulation. Large deformation, large-strain finite element analyses of an initially blunted crack tip (in the spirit of McMeeking [*19*]) are under way and will be reported elsewhere.

The results presented here are expected to be reproduced for other, less tough, materials. As discussed earlier, the initiation value of J for Type 304 stainless steel at 288°C is about 600 N/mm, and this represents one of the highest toughness values expected for steel (see Ref *2* and the material property studies referred to therein). If the analyses had been performed for a carbon steel, say A106-B with $J_i \cong 200$ N/mm, similar results as produced here should be expected. Reviewing the finite element results produced here for a level of $J = 200$ N/mm where the CTOD (δ_t) is about one third, the stress field compares with the HRR field for distances more than 3 δ_t from the tip. Thus, the region dominated by large strains is contained within the small strain HRR field. Although not done here, after loading to $J_i = 200$, unloading and reloading, one would expect results similar to those presented in Figs. 6 to 9; that is, reproduction of the HRR field for a distance equal to that before unloading. Therefore, it appears that Reason 4 concerning large deformation effects may play a less significant role in being able to predict cyclic tearing damage. This is encouraging since the development of an engineering approach to predict cyclic tearing damage is simplified if large-strain effects can be neglected. This observation is consistent with earlier comments where we note that the stress field is affected up to 2 δ_t, while J is influenced up to 0.5 δ_t. Hence, one of the main purposes of this paper is to point up that currently accepted views regarding monotonically loaded elastic-plastic tearing cannot be extended easily to cyclic tearing without more work.

Finally, these results perhaps raise more questions than produce answers, and work is continuing to addresses all four points just described.

Acknowledgments

This effort was supported by Battelle internal research and development funds.

References

[1] Hutchinson, J. W. and Paris, P. C. in *Elastic-Plastic Fracture, ASTM STP 668*, J. D. Landes, J. A. Begley, and G. A. Clarke, Eds., American Society for Testing and Materials, Philadelphia, 1979, pp. 37–64.

[2] Wilkowski, G. M. et al., "Degraded Piping Program—Phase II," Final Report, NUREG/CR-4082, U.S. Nuclear Regulatory Commission, Washington, DC. Vol. 8, March 1989.

[3] Brust, F. W., McGowan, J. J., and Atluri, S. N., "A Combined Numerical/Experimental Study of Ductile Crack Growth after a Large Unloading Using T*, J, and CTOA Criteria," *Engineering Fracture Mechanics*, Vol. 23, No. 3, 1986, pp. 537–550.

[4] Wilkowski, G. M., unpublished data in an ongoing investigation at Battelle Memorial Institute, Columbus, OH.

[5] Clarke, G. A., Andrews, W. R., Paris, P. C., and Schmidt, D. W., "Single Specimen Tests for J_{Ic} Determination," *Mechanics of Crack Growth, ASTM STP 590*, American Society for Testing and Materials, Philadelphia, 1976, pp. 27–42.

[6] Kaiser, S., "On the Relation Between Stable Crack Growth and Fatigue," *Fatigue of Engineering Materials and Structures*, Vol. 6, No. 1, 1983, pp. 33–49.

[7] Landes, J. D. and McCabe, D. E., "Load History Effects on the J_R-Curve," *Elastic-Plastic Fracture: Second Symposium, Volume II: Fracture Curves and Engineering Applications, ASTM STP 803*, C. F. Shih and J. P. Gudas, Eds., American Society for Testing and Materials, Philadelphia, 1983, pp. II–723–II–738.

[8] Landes, J. D. and Liaw, P. K., "Effect of Cyclic Loading on Fracture Toughness of a Modified 4340 Steel," *Proceedings*, Symposium on Effects of Load and Thermal Histories on Mechanical Behavior of Materials, P. K. Liaw and T. Nicholas, Eds., American Institute of Mining, Metallurgical and Petroleum Engineers, to be published.

[9] Joyce, J. A., "Characterization of the Effects of Large Unloading Cycles on the Ductile Tearing Toughness of HSLA Steel," *Advances in Fracture and Fatigue for the 1990's, Vol. 1, Load History Effects On Fracture Resistance*, American Society of Mechanical Engineers, New York, Vol. 166, 1989.

[10] *Mechanics of Fatigue Crack Closure, ASTM STP 982*, J. C. Newman and W. Elber, Eds., American Society for Testing and Materials, Philadelphia, 1988.

[11] Chan, K. S., Lankford, J., and Davidson, D. L., "A Comparison of Crack-Tip Field Parameters For Large and Small Fatigue Cracks," *Engineering Materials and Technology*, Vol. 108, 1986, pp. 206–213.

[12] Kubo, S. et al., "Investigation on Path-Integral Expression of the J-Integral Range Using Numerical Simulations of Fatigue Crack Growth," *Transactions*, Japan Society of Mechanical Engineers, *Series I*, Vol. 32, No. 2, 1989.

[13] Shih, C. F. and German, M. D., "Requirements for a One Parameter Characterization of Crack Tip Fields by the HRR Singularity," *International Journal of Fracture*, Vol. 17, No. 1, Feb. 1981.

[14] *ABAQUS User's Manual*, Hibbitt, Karlsson, and Sorensen, Inc., Providence, RI, 1990.

[15] Rice, J. R., "Mathematical Analysis in the Mechanics of Fracture," *Fracture*, Vol. II, H. Liebowitz, Ed., Academic Press, New York, 1968, pp. 191–311.

[16] Kumar, V. et al., "Advances in Elastic-Plastic Fracture Analysis," EPRI Final Report NP-3607, Electric Power Research Institute, Palo Alto, CA, Aug. 1984.

[17] Hutchinson, J. W., "Fundamentals of the Phenomenological Theory of Nonlinear Fracture Mechanics," *Journal of Applied Mechanics*, Vol. 50, 1983, pp. 1042–1051.

[18] Parks, D. M., "The Dominance of the Crack Tip Fields of Inelastic Continuum Mechanics," *Proceedings*, Second International Conference on Numerical Methods in Fracture Mechanics, July 1980, Hinton and Owen, Eds., Pineridge Press, Swansea, U.K.

[19] McMeeking, R. M., "Finite Deformation Analysis of Crack-Tip Opening in Elastic-Plastic Materials and Implications for Fracture," *Journal of the Mechanics and Physics of Solids*, 1977, Vol. 25, pp. 357–381.

[20] McMeeking, R. M. and Parks, D. M., "On Criteria for J-Dominance of Crack-Tip Fields in Large-Scale Yielding," *Elastic-Plastic Fracture, ASTM STP 668*, J. D. Landes, J. A. Begley, and G. A. Clarke, Eds., American Society for Testing and Materials, Philadelphia, 1979.

[21] Papaspyropoulos, V. et al., "Predictions of J-R Curves with Large Crack Growth From Small Specimen Data," NUREG/CR-4575, U.S. Nuclear Regulatory Commission, Washington, DC, Sept. 1986.

[22] Needleman, A., "Numerical Studies of Ductile Fracture Processes," *Proceedings*, 5th International Conference on Numerical Methods in Fracture Mechanics, Freiburg, 23–27 April 1990, Pineridge Press, Swansea, U.K.

Fu-Pen Chiang,[1] Shen Li,[1] and Yin Yang Wang[1]

Experimental Study of Near-Crack-Tip Deformation Fields

REFERENCE: Chiang, F.-P., Li, S., and Wang, Y. Y., "**Experimental Study of Near-Crack-Tip Deformation Fields,**" *Fracture Mechanics: Twenty-Second Symposium (Volume II), ASTM STP 1131*, S. N. Atluri, J. C. Newman, Jr., I. S. Raju, and J. S. Epstein, Eds., American Society for Testing and Materials, Philadelphia, 1992, pp. 225–245.

ABSTRACT: Stationary crack-tip singularity fields of strain-hardening material, Al 2024-0, are investigated by combined moiré and moiré interferometry techniques as a crack goes through elastic and plastic deformation. The experimental results are compared with the corresponding theories at different stages, K field and HRR field, respectively. A two-dimensional finite element computation is also carried out at plastic deformation stage to aid the analysis.

KEY WORDS: K field, HRR field, geometric moiré, moiré interferometry, three-dimensional zone, plastic zone, fracture mechanics, fatigue (materials)

The singularity fields at the crack tip are characterized differently for different materials. For linear elastic materials or when materials deform at the linear elastic stage, the stress and strain singularity fields are characterized by the stress-intensity factor, K, with the singularity of $r^{-0.5}$, where r is the distance measured from the crack tip as derived by Williams in 1955 [*1*]. The singularity field is different if the material undergoes extensive plastic deformation prior to the crack initiation. Fracture in low-to-intermediate strength metals are of this nature. For strain hardening materials, Hutchinson, Rice, and Rosengren [*2,3*] contributed the two-dimensional asymptotic solutions for a monotonically loaded stationary crack tip of Mode I, which is referred to as the Hutchinson, Rice, and Rosengren (HRR) field. In the HRR solution, a path-independent integral, the J-integral [*4*], is assumed to be a measure of the intensity of deformation outside a process zone in the vicinity of the crack tip. The singularity form in this case depends on the hardening index, n.

It is well known that linear-elastic deformation surrounding the crack tip can be described by the K solution over a zone within 10% of characteristic dimensions of the specimen [*5*]. The existence of the HRR field requires that materials must possess a strain hardening property and that the deformation be well approximated by the small deformation theory either under small- or large-scale yielding. As emphasized by Hutchinson [*6*], the HRR field should be of a size scale large compared with the near-tip finite strain zone and be well contained in the plastic zone.

The results of HRR field studies are mostly computational and for the state of plane strain deformation. McMeeking [*7*] points up that the size of the finite strain zone is about 2 to $3\delta_t$, where δ_t is the crack-tip-opening displacement. Since the size of crack process zone is assumed to be comparable to that of the finite strain zone, the HRR field exists beyond $3\delta_t$. Shih [*8*] relates quantitatively the crack-tip-opening displacement to the J-integral.

[1]Leading professor and graduate students, respectively, Department of Mechanical Engineering, State University of New York at Stony Brook, Stony Brook, NY 11794.

Numerical computations [9,10] indicate that under small-scale yielding, the crack-tip deformation can be approximated by the HRR equation within 20 to 25% of plastic zone size while under fully plastic yielding, it is about 0.01 to 0.07 times of uncracked ligament depending whether it is under tensile or bending configuration.

Experiments on HRR field under the state of plane stress are done quite recently. Measurements are made mostly on the specimen surface. Dadkhah and Kobayashi [11] tested different aluminum alloys by applying the moiré interferometry method and evaluated J-integral [12] from fringe patterns and compared the displacement along 45° with the HRR equation. Rosakis et al. [13,14] used an interferometry technique to obtain full-field out-of-plane displacement and associated the experimental results with computation to investigate the HRR field. Chiang et al. [15,16] applied the inplane moiré technique and compared certain deformation components with the HRR solution at selected angles. Both experiments [13,15] and computations [17] show that a strong three-dimensional effect is found at $r \leq 0.5t$ in front of the crack tip, where t is the specimen thickness. At $r = 1$ to $1.5t$, the deformation transits from three-dimensional to a two-dimensional state as indicated by computation [17] and experiment [15,16]. Narasimhan and Rosakis reported that a much larger J-dominant zone or the HRR zone was found under plane-stress condition than under plane-strain condition [14,18] in a three-point-bend specimen with hardening index, $n = 22$. The same phenomenon of larger HRR zone is also observed in other experiments [15,16].

In this paper, we study the crack-tip deformation at both the elastic and plastic stages and compare them with both the K and HRR fields. We wish to know the extend of the HRR zone when extensive plastic deformation has occurred in most parts of the specimen. We would like to know the relative dimensions of the crack-tip three-dimensional zone, K zone, HRR zone, and plastic deformation zone. To aid the analysis, a detailed two-dimensional finite element computation is also carried out by employing the ABAQUS finite element code. The computed distributions of strain component, ε_{yy}, in front of the crack tip are compared with the experiment and HRR solution.

Experiment

The specimens are made of aluminum alloy, Al 2024-0. The material is assumed to be strain hardening and follow the Ramberg-Osgood law

$$\frac{\varepsilon}{\varepsilon_0} = \frac{\sigma}{\sigma_0} + \alpha\left(\frac{\sigma}{\sigma_0}\right)^n \tag{1}$$

where

ε_0 and σ_0 = yield strain and yield stress, respectively;
α = a constant; and
n = hardening index.

α and n are determined by fitting measured stress and strain into Eq 1 with the elastic term neglected. This is justified because elastic deformation is not considered in the derivation of HRR equations.

The Ramberg-Osgood equation can be written into the form of a piecewise power law, that is

$$\frac{\varepsilon}{\varepsilon_0} = \begin{cases} \dfrac{\sigma}{\sigma_0} & \varepsilon \leq \varepsilon_0 \\ \alpha\left(\dfrac{\sigma}{\sigma_0}\right)^n & \varepsilon \geq \varepsilon_0 \end{cases} \tag{2}$$

Equations 1, 2, and experimental results are plotted in Fig. 1. The data points are closer to the piecewise relationship especially near the yield point.

To have a better appreciation of the HRR field, a high strain-hardening material (n = 3.0) was selected in the experiment since the size of the HRR field is greater in this case. The geometry of the specimen is given in Fig. 2. A long crack equal to 50% of the specimen width was made in order to introduce bending to the crack, because the HRR field is greater under bending than simple stretching. It was designed in such a way that all length dimensions are much greater than the specimen thickness (3.2 mm). As a result, it may be safe to assume that the state of plane stress prevails everywhere except near the crack tip. The crack was first machined by a notch with a 60° V-shaped end horizontal to 3 mm less than the half width of the specimen. A fatigue crack about 3 mm long was initiated by applying cyclic loading. In order to measure both elastic and plastic crack-tip deformation fields, two optical methods were employed. On one side of the specimen surface, we used moiré interferometry with a grating density equal to 2400 lines/mm to record the elastic deformation. On the other surface the method of geometric moiré with a grating density equal to 20 or 40 lines/mm was applied to measure the plastic deformation.

The specimens were loaded by applying tensile forces at the two ends. Three specimens were tested in the experiment. A typical load versus crosshead displacement curve is shown in Fig. 3. Moiré fringe patterns were recorded at selected load levels. Moiré interferometric fringes were recorded first, until they were too dense to be distinguishable with the experiment set up similar to that described in Ref *19*. When large plastic deformation occurred, the crack-tip deformation was recorded by geometric moiré. These fringe patterns are

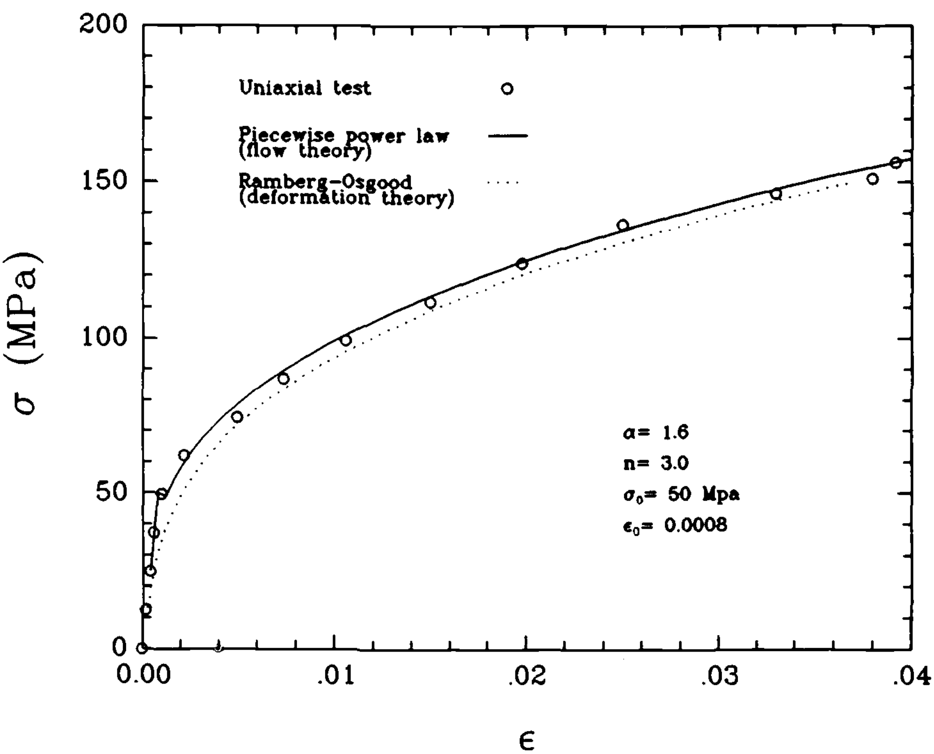

FIG. 1—*Stress-strain relationship of AL 2024-0.*

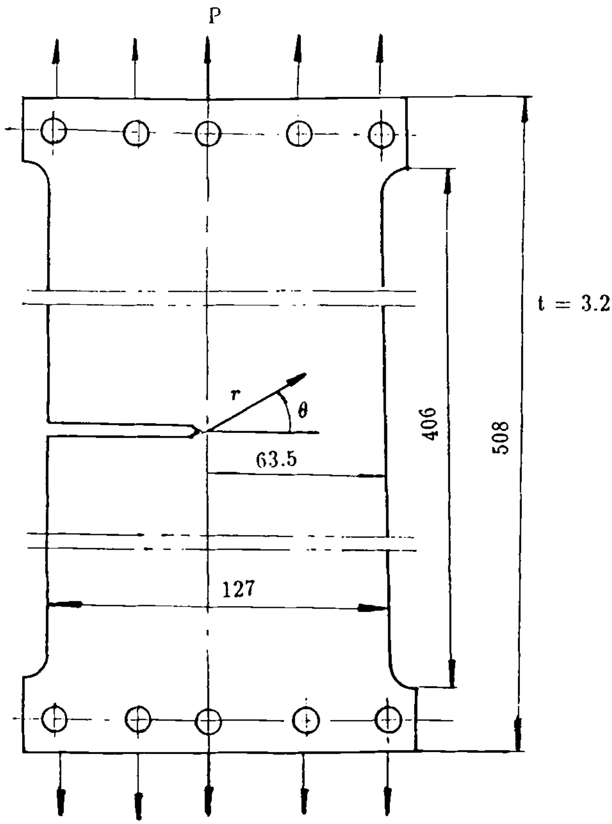

FIG. 2—*Specimen geometry (mm).*

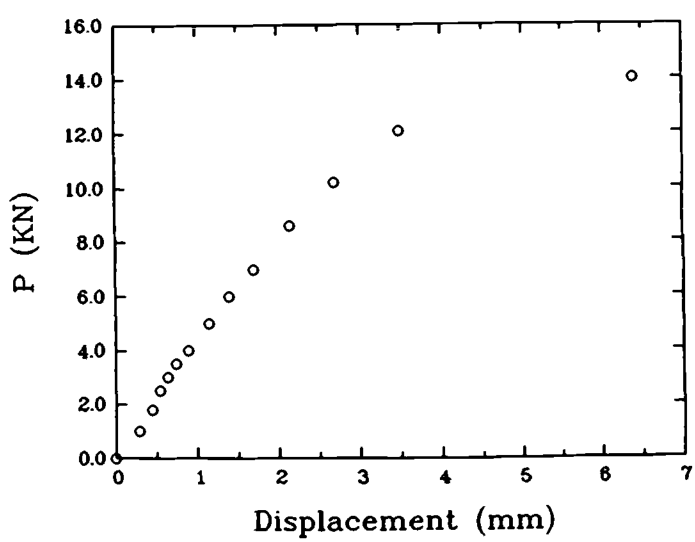

FIG. 3—*Load versus crosshead displacement curve.*

contours of displacement component resolved along the principal direction of the grating. A typical set of fringe patterns obtained from moiré interferometry and geometric moiré method are given in Figs. 4 and 5, respectively.

The equations that relate fringes with displacements are

$$\begin{aligned} u &= N_x p_x \\ v &= N_y p_y \end{aligned} \tag{3}$$

where

N_x and N_y = fringe orders;
p_x and p_y = grating pitches with grating normal along x and y directions, respectively.

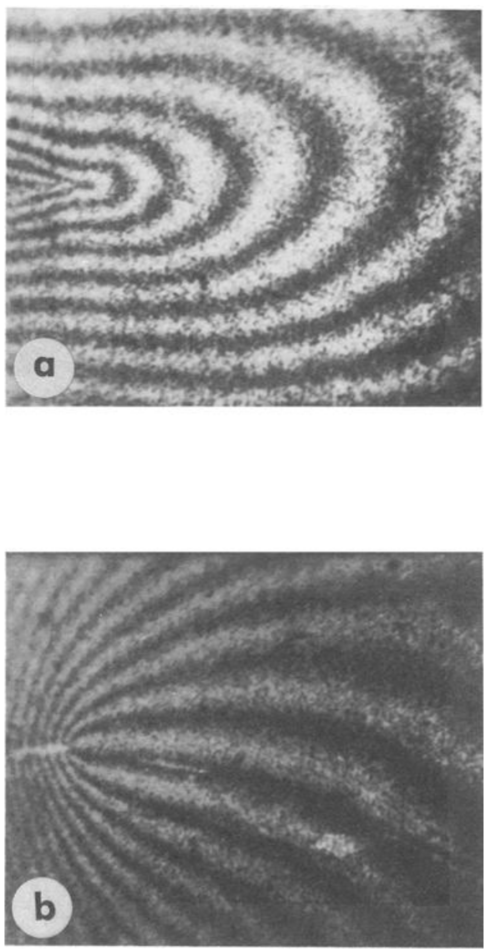

FIG. 4—*Moiré interferometry fringe patterns* (a) *displacement in* x *direction and* (b) *displacement in* y *direction* (P = *1.22 kN, scale 2.4:1, 2400 lines/mm*).

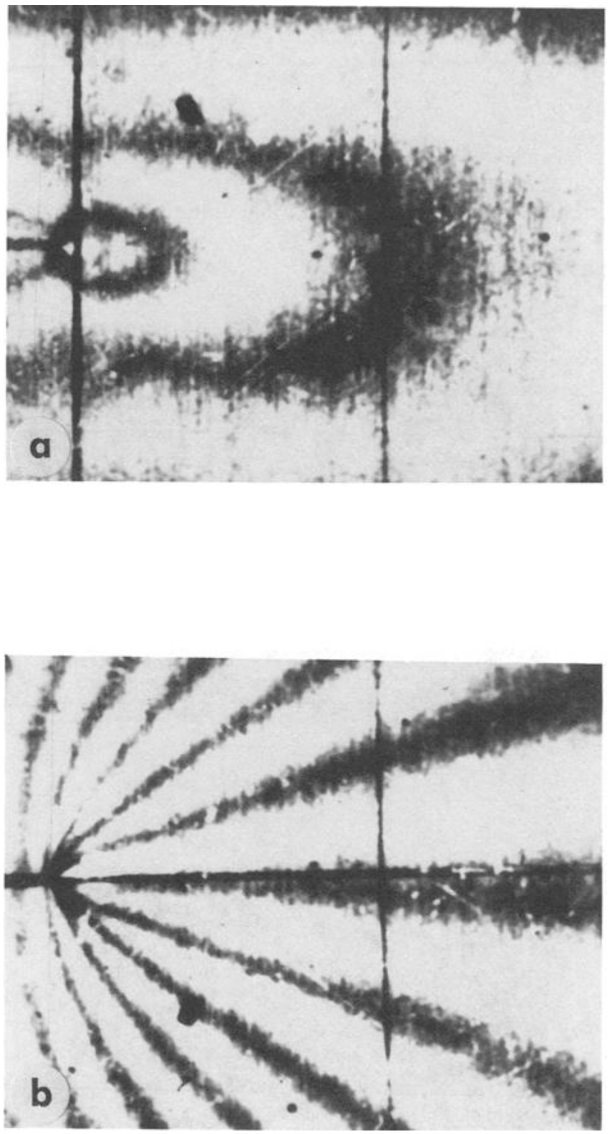

FIG. 5—*Geometry moiré fringe patterns* (P = *9.66 kN, scale 4.2:1, 20 lines/mm*); (a) *displacement in* x *direction and* (b) *displacement in* y *direction.*

In our experiments, we have selected p_x to be equal to p_y. Strain components can be thus evaluated by the following equations

$$\begin{aligned}
\varepsilon_{xx} &= \frac{\partial u}{\partial x} = \frac{\partial N_x}{\partial x} p_x \\
\varepsilon_{yy} &= \frac{\partial v}{\partial y} = \frac{\partial N_y}{\partial y} p_y \\
\varepsilon_{xy} &= \frac{1}{2}\left(\frac{\partial u}{\partial y} + \frac{\partial v}{\partial x}\right) = \frac{1}{2}\left(\frac{\partial N_x}{\partial y} p_x + \frac{\partial N_y}{\partial y} p_y\right)
\end{aligned} \tag{4}$$

Comparison with the *K*-Field

The stress, displacement, and strain fields for a linear elastic solid under Mode I loading are, respectively

$$u_i = \frac{K_\mathrm{I}}{2G}\left(\frac{r}{2\pi}\right)^{1/2} f_i^u(\theta)$$

$$\varepsilon_{ij} = \frac{1}{E}\frac{K_\mathrm{I}}{(2\pi r)^{1/2}} f_{ij}^{\varepsilon}(\theta) \tag{5}$$

and

$$\sigma_{ij} = \frac{K_\mathrm{I}}{(2\pi r)^{1/2}} f_{ij}^{\sigma}(\theta)$$

where

K_I = stress-intensity factor,
E = Young's modulus,
G = shear modulus, and
r = distance measured from the crack tip.

The stress-intensity factor, K_I, was evaluated by assuming a uniform remote stress distribution applied to an edge-cracked panel [5]. Since the experiment results were in terms of displacement contours, comparison with the theory were done using the vertical displacement component, v, along selected angles. However, along $\theta = 0°$, the crack line, $v = 0$. As a consequence, we used ε_{yy} for the comparison. Figure 6 shows the result for $K_\mathrm{I} = 7.5$ MN/m$^{3/2}$. As can be seen, the segment within which there is a reasonable agreement between theory and experiment varies from angle to angle, but does not exceed 10% of the ligament (~6.4 mm) except at $\theta = 30°$, where the limit is a little over 9 mm (about 14% of the ligament).

Comparison with the HRR Field

The theoretical model to describe the stationary crack-tip singularity field of a strain hardening material under large plastic deformation is the HRR solution for which the

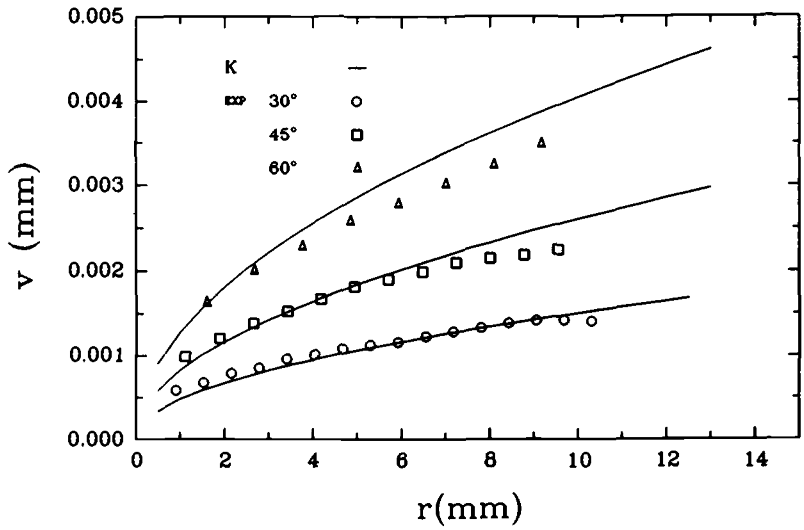

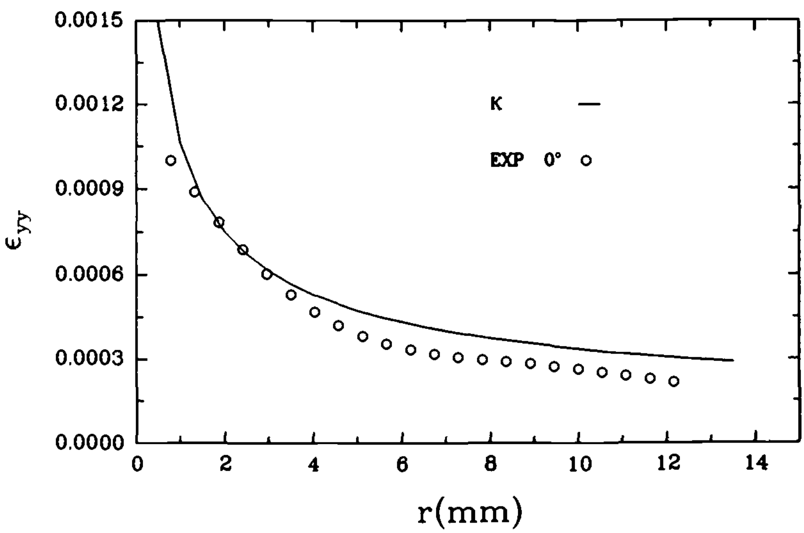

FIG. 6—*Experimental comparison with* K *field* (K = *7.5 MN/m*$^{1.5}$).

expressions for displacement, strain, and stress are, respectively

$$u_i = \alpha\varepsilon_0 r \left[\frac{J}{\alpha\varepsilon_0\sigma_0 I_n r}\right]^{n/(n+1)} \tilde{u}_i(\theta, n) \tag{6}$$

$$\varepsilon_{ij} = \alpha\varepsilon_0 \left[\frac{J}{\alpha\varepsilon_0\sigma_0 I_n r}\right]^{n/(n+1)} \tilde{\varepsilon}_{ij}(\theta, n) \tag{7}$$

$$\sigma_{ij} = \sigma_0 \left[\frac{J}{\alpha \varepsilon_0 \sigma_0 I_n r} \right]^{1/(n+1)} \tilde{\sigma}_{ij}(\theta, n) \tag{8}$$

where J is Rice's path independent integral; I_n, $\tilde{u}_i$, $\tilde{\varepsilon}_{ij}$, and $\tilde{\sigma}_{ij}$ depend on the hardening index, n, and whether a state of plane-stress or plane-strain prevails. The latter three quantities are also a function of polar angle, θ, with the coordinate origin being at the crack tip. All these parameters have been calculated and tabulated in Ref *20*.

J-*Integral Estimation*

The intensity of the near-tip field in the HRR solution is measured by the path independent J-integral, which has the form

$$J = \int_\Gamma (Wn_x - \sigma_{ij} u_i u_{i,j}) ds \tag{9}$$

where Γ represents any contour encircling the crack tip, u_i is the displacement vector, s is the length along the contour, n_i is the unit normal to Γ, and W is the strain energy density.

The J-integral may be estimated using a procedure proposed in Ref *15*. Using a rectangular contour surrounding the crack tip as shown in Fig. 7, the contour integration can be divided into line integrals along the vertical and horizontal segments as follows.

$$J = \int_{V1,V2} Wdy - \int_\Gamma \sigma_{ij} n_j u_{i,j} ds$$

$$= \int_{V1,V2} Wdy - \left(\int_{V1,V2} \sigma_{ix} u_{i,x} dy + \int_{H1,H2} \sigma_{iy} u_{i,x} dx \right)$$

$$= \int_{V1,V2} (W - \sigma_{xx} u_{x,x} - \sigma_{xy} u_{y,x}) dy + \int_{H1,H2} (\sigma_{xy} u_{x,x} + \sigma_{yy} u_{yx}) dx \tag{10}$$

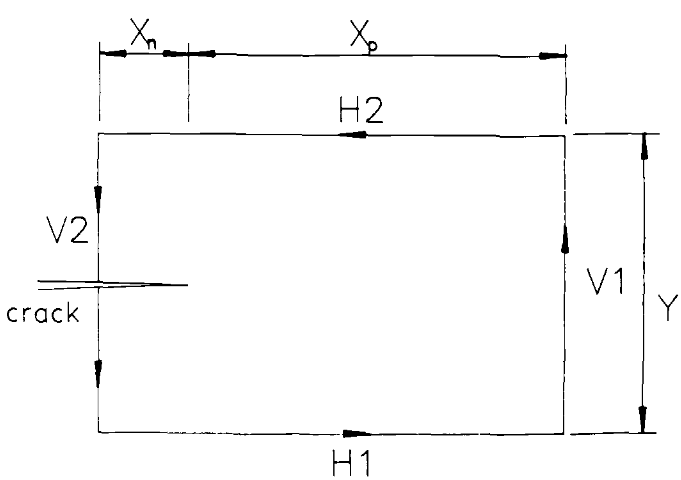

FIG. 7—*Rectangular path of* J-*integral.*

where $u_{i,x}$ can be calculated from the fringe patterns.

By applying linear elasticity and deformation plasticity to a strain hardening material subjected to small deformation, the strain components are

$$\varepsilon_{ij} = \frac{1 + \nu}{E}\sigma_{ij} - \frac{\nu}{E}\sigma_{kk} + \frac{3}{2}\frac{\varepsilon_0}{\sigma_0}\alpha\left(\frac{\sigma_e}{\sigma_0}\right)^{n-1} s_{ij}$$

and stress components are derived as

$$\sigma_{ij} = \frac{\varepsilon_{ij}}{F(\sigma_e)} + \left[\frac{E}{3(1 - 2\nu)} - \frac{1}{3F(\sigma_e)}\right]\varepsilon_{kk}\delta_{ij} \tag{11}$$

where

$$F(\sigma_e) = \frac{(1 + \nu)}{E} + \frac{3\alpha}{2E}\left(\frac{\sigma_e}{\sigma_0}\right)^{n-1}$$

with effective strain

$$\varepsilon_e = \sqrt{\frac{2}{3}e_{ij}e_{ij}}$$

and effective stress

$$\sigma_e = \sqrt{\frac{3}{2}s_{ij}s_{ij}}$$

And strain energy density is

$$W = \frac{1 + \nu}{2E}\sigma_{ij}\sigma_{ij} - \frac{\nu}{2E}\sigma_{kk}^2 + \frac{n}{n + 1}\alpha\sigma_0\varepsilon_0\left(\frac{\sigma_e}{\sigma_0}\right)^{n+1} \tag{12}$$

where

s_{ij} = deviatoric stress,
e_{ij} = deviatoric strain,
E = Young's modulus, and
ν = Poisson's ratio.

Although the out-of-plane strain component is not available, its value was estimated from the plane-stress condition. ε_{zz} is determined by an iteration procedure to let σ_{zz} approach zero. Thus, all the deformation components in Eq 10 can be calculated.

Three paths were chosen for the integration as in Fig. 7 with x_p ranging from 7 to 15 mm, x_n ranging from 1 to 2.5 mm, and y ranging from 10 to 30 mm for each set of fringe patterns. In addition, a closed path not surrounding the crack was selected to further test the path independent nature of the J-integral. Only v fringe contours were used in the evaluation because u fringe contours are so sparse that their contribution may be ignored.

This approach of calculating the J-integral suffers from a number of errors. First, the contribution from the u field is neglected although it is usually very small relative to the v

field. Second, the integrations can not be evaluated continuously. Error also arises while calculating the displacement derivatives. To offer a comparison, another estimation of the J-integral is made by measuring the crack-tip-opening displacement δ_t, which is also a measure of crack damage. Shih [8] related δ_t to J-integral by

$$\delta_t = d(\alpha, \varepsilon_0) \frac{J}{\sigma_0} \tag{13}$$

where

$$d(\alpha, \varepsilon_0) = (\alpha\varepsilon_0)^{1/n} D_n$$

D_n is a dimensionless quantity tabulated in Ref *20*. δ_t is defined as the separation where 45° lines intersect the crack faces as shown in Fig. 8. In our calculation, δ_t was estimated by counting the fringe numbers from the v field fringe patterns at the positions of the 45° intersection lines. A plot of δ_t versus load for one specimen is given in Fig. 9. Figure 10 shows a plot of load versus J-integral where the experimental points were converted from that shown in Fig. 9 and the solid line is obtained from a finite element calculation (to be described later).

The J-values for three different loadings as obtained from the two approaches are listed in Table 1. The first column is the resulting δ_t-values for the three loads. The second column is the J-values obtained using measured δ_t, and the third column is the J-values calculated by approximated contour integration. The last column is the values obtained from an arbitrary closed path integration that did not enclose the crack tip.

It is seen that the two sets of J-values agree with a 10% error. The J-value for an arbitrary closed loop is, however, quite off. We felt that the J-values from δ_t measurements were more accurate because the procedure was simple and less error prone. As a result, these J-values were used in the evaluation of the HRR field for the subsequent comparison.

Experimental Comparison with the HRR Field

The coarse grating densities used in the experiment could produce sufficient fringes for calculation only when the specimens were subject to large plastic deformation. As a result, the comparisons were made at high loads (P = 8.82 kN to P = 10.56 kN) but no obvious crack growth had occurred. Plastic deformation was believed to have extended well over 50% of the ligament at P = 8.82 kN as can be deduced from the ε_{yy} plot shown in Fig. 11.

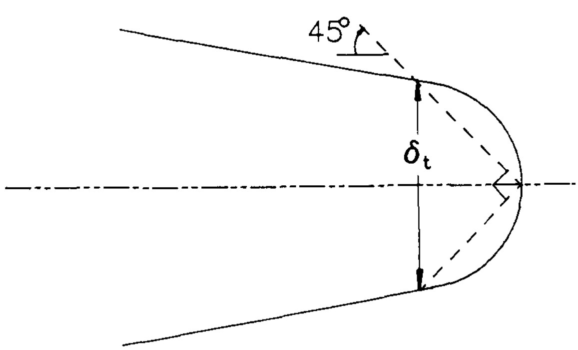

FIG. 8—*Crack-tip opening.*

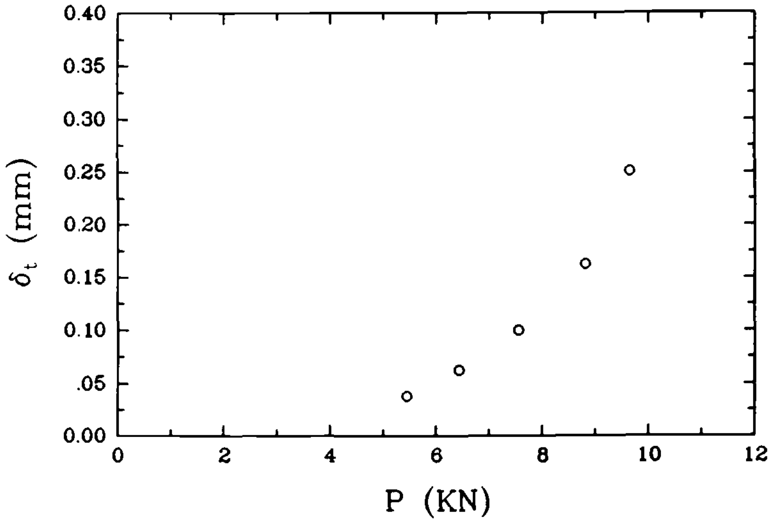

FIG. 9—*Load versus crack-tip-opening displacement.*

It is seen that at $r = 30$ mm ($r/t \sim 10$), ε_{yy} is about 0.0021 while the yield strain ε_0 is 0.0008. Large plastic zones were evident in the finite element calculation given in the next section. The v-field displacement was compared with the theory at selected angles from the crack tip. The strain, ε_{yy}, was compared at $\theta = 0°$ as $v = 0$ in this direction. The comparisons were plotted as shown in Figs. 11 to 13, where the distance, r, was normalized by the specimen thickness, t.

For comparison between theoretical and experimental results, we selected the following arbitrary criteria. For displacement component, v, we allowed one-fourth fringe error. That

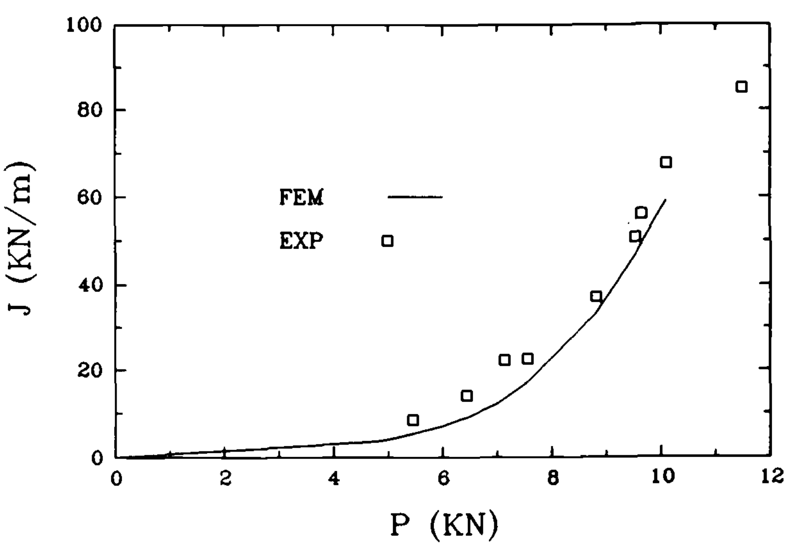

FIG. 10—*Load versus* J*-integral.*

TABLE 1—*J-values.*

δ_t, mm	J, kN/m (δ_t)	J, kN/m (moiré)	J, kN/m (arbitrary path)
0.175	39.5	37.0	0.16
0.25	56.4	53.5	0.43
0.3	67.7	61.8	2.1

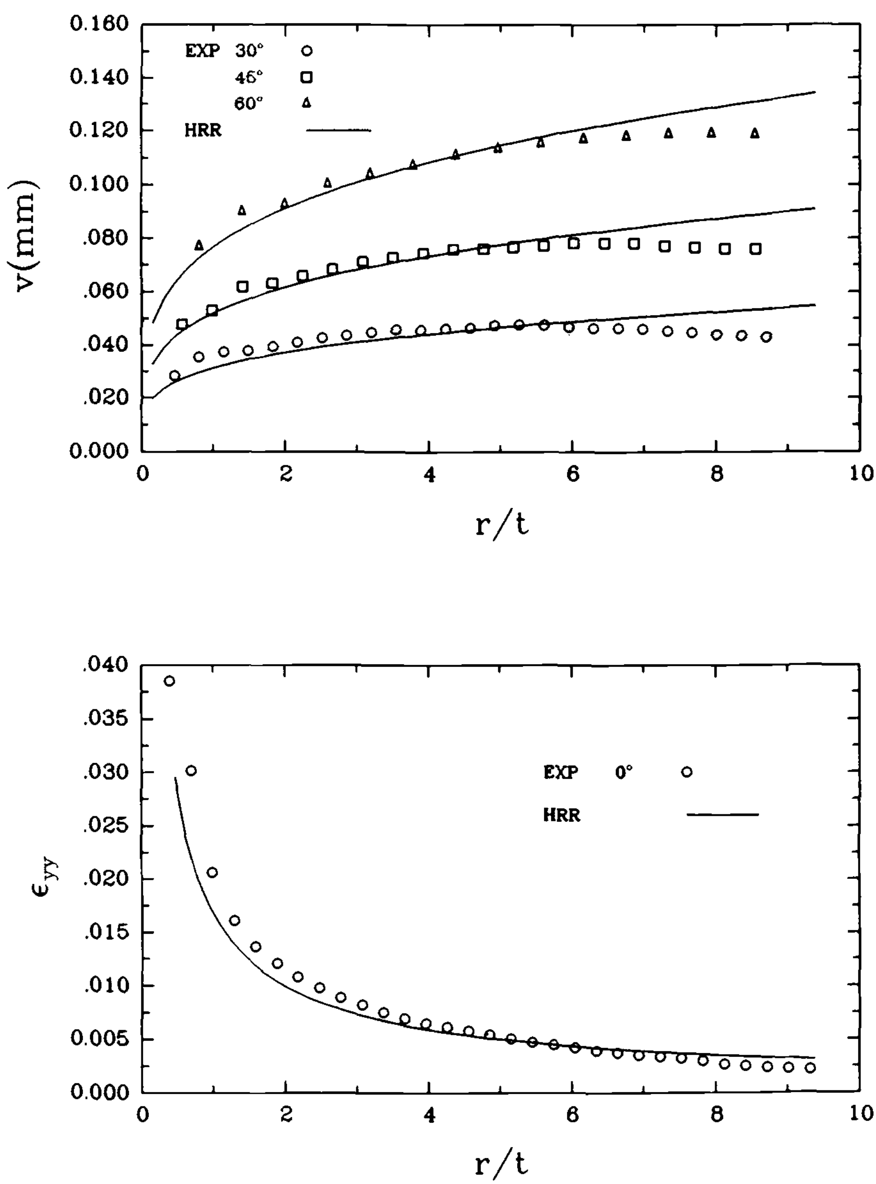

FIG. 11—*Experimental comparison with the HRR field at* P = *8.82 kN.*

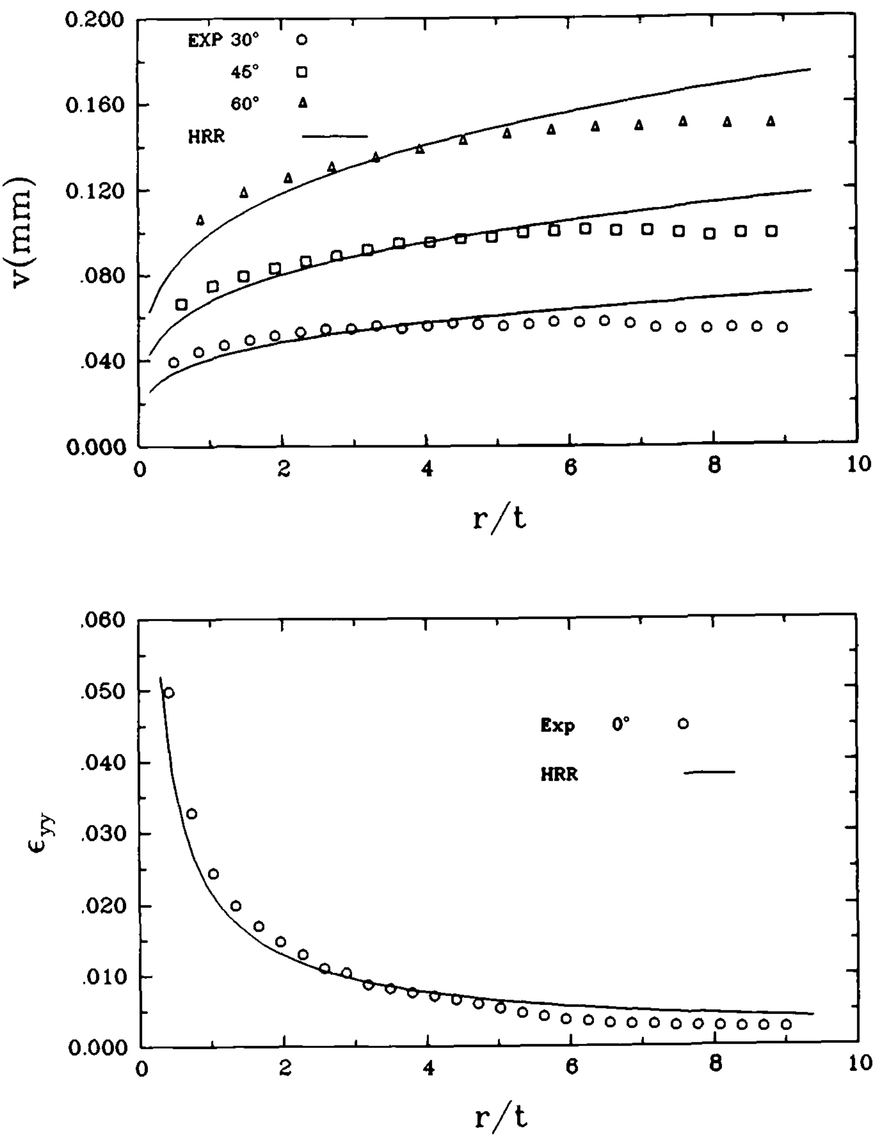

FIG. 12—*Experimental comparison with the HRR field at* P = *9.54 kN.*

corresponds to a distance of 0.00625 mm from the theoretical curve. For the strain component, ε_{yy}, we assumed that agreement was reached when the ratio of the experimental to the theoretical values was with 95%. And we found that at P = 8.82 kN, the HRR field extends around r/t = 6.2 to 7 depending on the angle, θ. At P = 9.54 kN, it varies from 4.4 to 6.2. Errors in J will result in the shifting of the entire theoretical curve. A case in point is shown in Fig. 13 where the result of P = 10.56 kN is presented. Due to the error in J, the experimental result appears to agree with the theory within the three-dimensional zone. To determine the HRR region experimentally, it is crucial that the J-value be evaluated

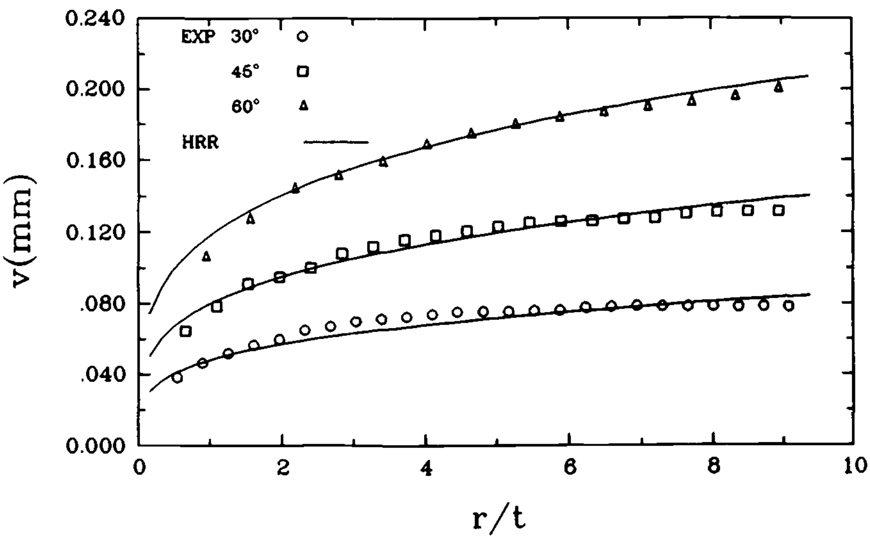

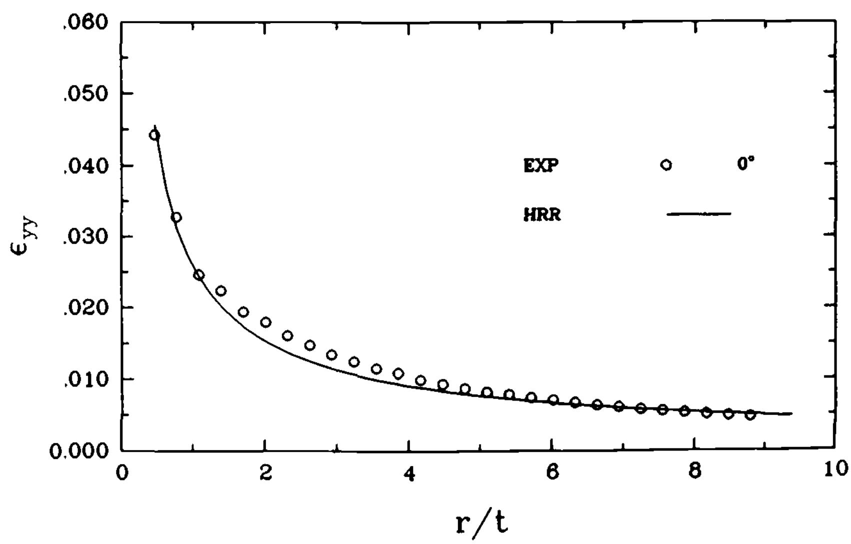

FIG. 13—*Experimental comparison with the HRR field at* P = *1056 kN.*

correctly. However, from the multiple experimental results we have obtained using v and ε_{yy}, we can conclude that the HRR field exists up to r/t = 5.0 to 6.0.

Finite Element Analysis

To provide a comparison, an finite element analysis of the problem was also performed. The ABAQUS finite element code was utilized. Eight-node biquadratic plane-stress elements were used and the mesh arrangement is as shown in Fig. 14. Due to the symmetric

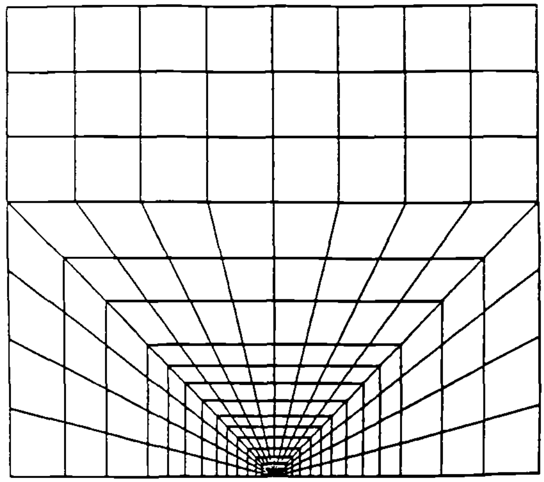

FIG. 14—*Mesh for finite element calculation.*

nature of the problem, only half of the specimen was modeled. A piecewise strain-hardening relationship was assumed, since it was closer to the actual stress-strain relationship as shown in Fig. 1. The horizontal strain distribution at a section 110 mm above the crack line was measured by strain gages, the result of which is given in Fig. 15. The stress distribution was determined at these positions through Hooke's law. Such stress distribution was employed as the load boundary condition in the finite element calculations. The computed strain component, ε_{yy}, in front of the crack tip was plotted and is shown in Figs. 16 and 17 for different loads together with experimentally measured values at the same load levels. Theoretical HRR curves were plotted by applying the J-integral obtained from the finite element computation.

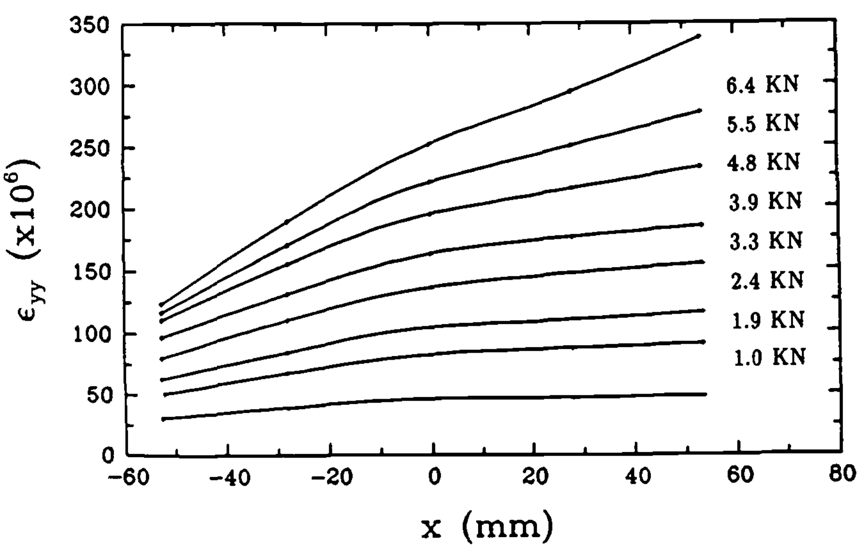

FIG. 15—*Strain distribution at a section 110 mm above crack line obtained from strain gages.*

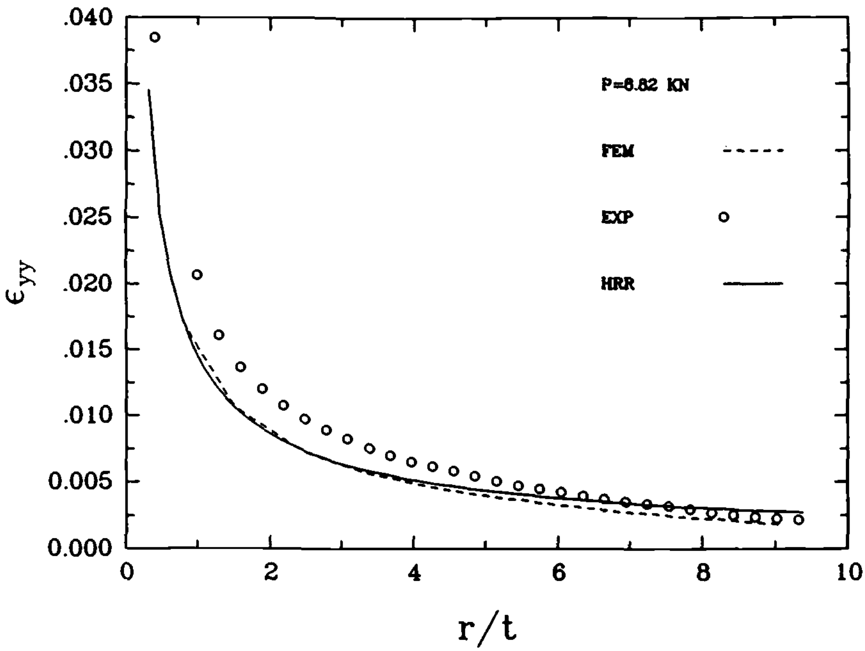

FIG. 16—*HRR field comparison with the results of computation and experiment at* $\theta = 0°$, P = *8.82 kN.*

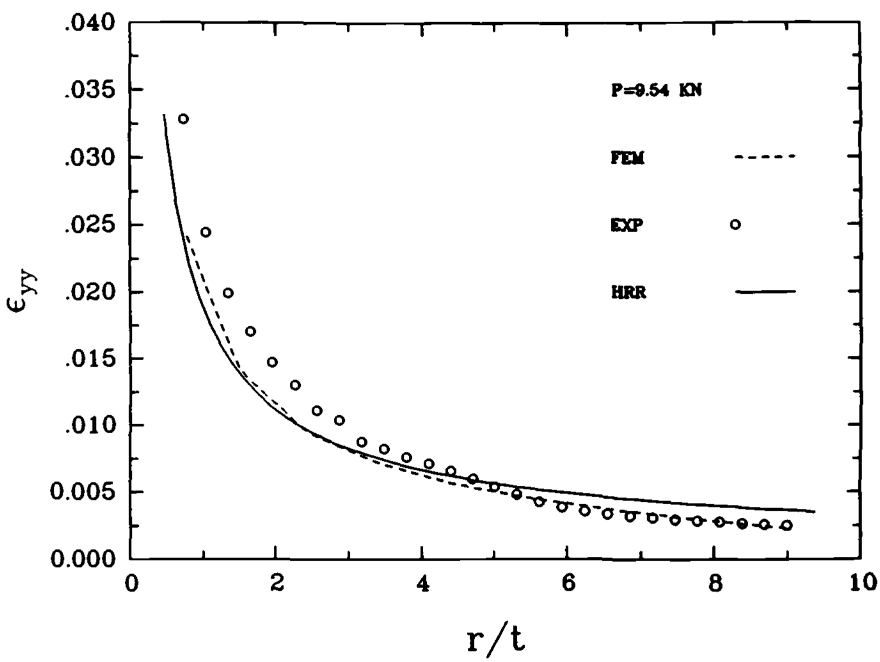

FIG. 17—*HRR field comparison with the results of computation and experiment at* $\theta = 0°$, P = *9.54 kN.*

The results show that large differences between the computation and experiment are found at the crack tip within $r/t = 1.5$ that are attributed to the three-dimensional effects. The finite element computation was based on a two-dimensional model. However, recent research [13,15,17] shows that a three-dimensional zone near the crack tip exists at about 1 to 1.5 times of the plate thickness, which is 3.2 to 4.8 mm in the specimens investigated. Some residual plastic deformation introduced during the precrack process also exists within this region. Relatively large differences between the finite element and experimental results are also seen at $r/t = 1.5$-3. Since strain values in this region are rather high, the deformation in the region may not exactly follow the deformation behavior with the determined material constants, α and n. Also, at high strain levels, slight variation of stress will introduce a large variation of strain for power-law hardening materials. These factors are believed to be the reason for the large difference between computational and experimental results in this region. One would expect smaller errors if the comparison were made between stress components.

Better agreement between the two is found at around $r/t = 3$ to 5. Both results are also fairly close to the plane-stress HRR solution. These facts buttress the conclusions reached in the previous section concerning the extent of the HRR field.

At a greater distance away from the crack tip, the computational result is very close to that of the experiment. It is especially true at $P = 9.54$ kN as shown in Fig. 17. The deviation seen in Fig. 16 may be due to the error in reading the load. When the testing machine was stopped to record the load, a small elastic unloading took place resulting in a load drop. The actual load would be slightly higher.

The plastic zone can not be obtained from the experimental results because the recordings did not cover a large enough region. However, it was computed from the finite element analysis by finding the boundary along which the effective stress reaches the yield stress. The results at two load levels are presented in Fig. 18. It is seen that the plastic deformation occurs in quite a large region. It covers the entire ligament, except at the transition region, where the specimens are loaded by compression.

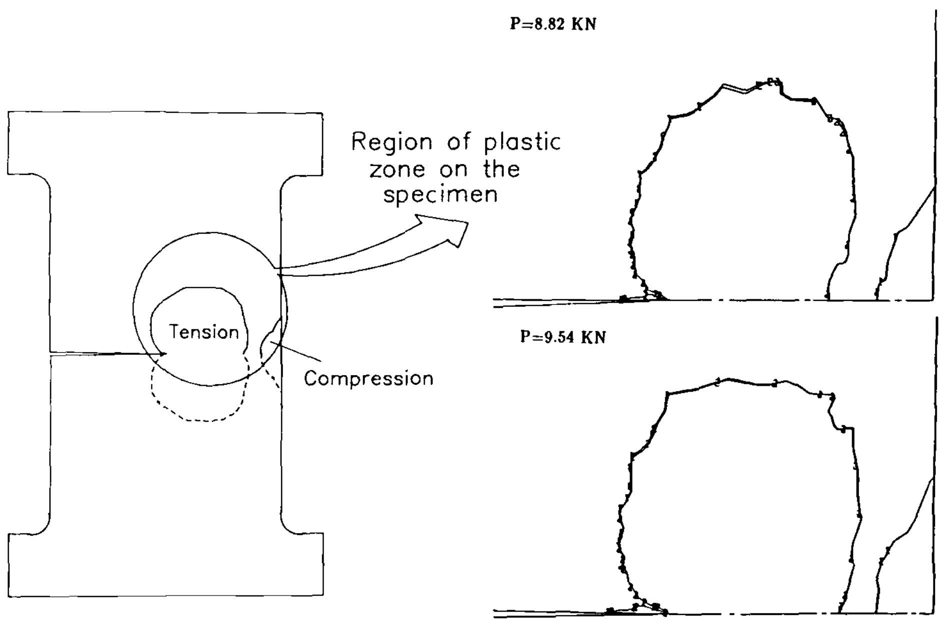

FIG. 18—*Plastic zone at different loads obtained from finite element computation.*

Discussion and Conclusion

By combining the method of moiré interferometry and geometric moiré, we have investigated the crack-tip singularity field of a strain-hardening material, Al 2024-0, under the Mode I plane-stress condition. Since the grating densities of the two optical methods are either 120 or 60 times different, the deformation information is not available at certain ranges of loading before large plastic deformation has already occurred.

We find that at low-load levels, a K field exists at the crack tip and its size is about 10% of the ligament or crack length in this case. Under large-scale yielding, the experiment shows that the displacement component, v, and the strain component, ε_{yy}, could be approximated by the plane-stress HRR equation up to r/t = 4.0 to 6.0 from the crack tip, which is about 40% of plastic zone. The results in Fig. 18 indicate that the boundary of the plastic zone does not progress much after P = 8.82 kN. The outer boundary of the HRR zone obtained from the experiment at P = 9.54 kN was mapped as shown in Fig. 19. At this load level, the experiment also has fairly good agreement with the computation beyond r/t = 3. The boundary of the HRR zone is determined by using the same criterion as described in the previous section of experimental comparison with the HRR field. The extent of the three-

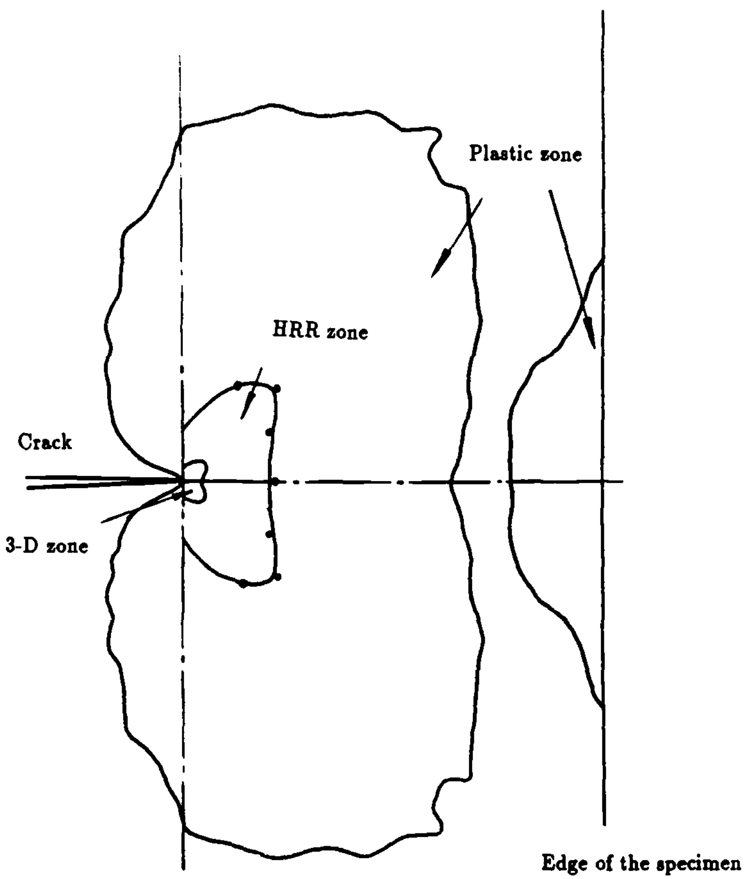

FIG. 19—*Graphic representation of the HRR zone within the plastic zone* (P = *9.54 kN*) (*three-dimensional zone taken from Ref* 15).

dimensional zone taken from Ref *15* was also plotted. Since data at 90° are sparse, the boundary at the edges was only an estimation. From the plotting, we see that the shape of the HRR zone is quite similar to that of the plastic zone. The HRR zone reaches $r/t = 4.4$ ($r = 14$ mm) or 35% of the plastic zone size at 0°. The maximum r/t of 6.2 ($r = 19.8$ mm) is found at 45°, which extends to about 33% of the plastic zone.

This result is rather consistent with that of Chiang et al. [*15,16*], where the outer boundary of the HRR zone was also found around 13 to 15 mm from the crack tip. Crack length in the experiments of Ref *15* was only 18% of the specimen width while the current ratio is 50%. This introduces more bending to the ligament resulting in a greater HRR zone. Since the plane-strain HRR zone is about 20 to 25% of plastic zone under contained yielding and 1 to 7% of ligament under full yielding [*9,10*], the HRR zone under the plane-stress condition as shown by our results is much greater than that of plane strain.

Large plane-stress HRR zones are also reported in Ref *18*. In this study, the experimental boundary conditions were used in a finite element calculation of a three-point-bend specimen made of a weak hardening material ($n = 22.0$) under large-scale yielding. The plane stress HRR field extends to nearly $r = 20J/\sigma_0$ when the plastic deformation intensity parameter, $C\sigma_0/J$, reaches 70, where C is the uncracked ligament. These two equations lead to an r-to-ligament ratio of 28.6%. Our current result shows an HRR zone of around 25 to 30% of the uncracked ligament under a combination of bending and stretching. In general, since the HRR zone increases with decreasing n (the hardening exponent), the result suggests that the size of the HRR zone under a plane-stress condition is also greatly dependent upon crack configuration.

Acknowledgment

We thank the financial support provided by the Office of Naval Research, Solid Mechanics Division, through Grant No. N0001482K0566 (Dr. Yapa D. S. Rajapakse, scientific officer).

References

[*1*] Williams, M. L., *Journal of Applied Mechanics*, Vol. 24, 1957, pp. 109–114.
[*2*] Hutchinson, J. W., *Journal of the Mechanics and Physics of Solids*, Vol. 16, 1968, pp. 13–31.
[*3*] Rice, J. R. and Rosengren, G. F., *Journal of the Mechanics and Physics of Solids*, Vol. 16, 1968, pp. 1–12.
[*4*] Rice, J. R., *Journal of Applied Mechanics*, Vol. 35, No. 1, 1968, pp. 379–386.
[*5*] Hellan, K., *Introduction to Fracture Mechanics*, McGraw-Hill, New York, 1984, p. 244.
[*6*] Hutchinson, J. W., *Journal of Applied Mechanics*, Vol. 50, 1983, pp. 1042–1051.
[*7*] McMeeking, R. M., *Journal of the Mechanics and Physics of Solids*, Vol. 25, 1977, pp. 357–381.
[*8*] Shih, C. F., *Journal of the Mechanics and Physics of Solids*, Vol. 29, 1981, pp. 305–326.
[*9*] Shih, C. F., *International Journal of Fracture*, Vol. 29, 1985, pp. 73–34.
[*10*] Shih, C. F. and German, M. D., *International Journal of Fracture*, Vol. 17, No. 1, 1981, pp. 27–43.
[*11*] Dadkhah, M. S. and Kobayashi, A. S., "HRR Field in an Aluminum SEN Specimen," Technical Report, UWA/DME/ATR-89/69, University of Washington, Seattle, 1989.
[*12*] Kang, B. S-J. and Kobayashi, A. S., "J-Estimation Procedure Based on Moiré Interferometry Data," Technical Report, UWA/DEM/TR/87-58, University of Washington, Seattle, 1987.
[*13*] Rosakis, A. J. and Ravi-Chander, K., *International Journal of Solids Structures*, Vol. 22, No. 2, 1986, pp. 121–134.
[*14*] Zehnder, A. T. and Rosakis, A. J., "Three-Dimensional Effects Near a Crack Tip in a Ductile Three Point Bend Specimen—Part II: An Experimental Investigation Using Interferometry and Caustics," Division of Engineering and Applied Science, California Institute of Technology, Pasadena, CA, SM Report 88-7, 1988.
[*15*] Chiang, F. P. and Hareesh, T. V., *International Journal of Fracture*, Vol. 36, 1988, pp. 143–257.

[16] Chiang, F. P., Hareesh, T. V., Liu, B. C., and Li, S., *Optical Engineering*, Vol. 27, 1988, pp. 625–629.
[17] Nakamura, T. and Parks, D. M., *Journal of the Mechanics and Physics of Solids*, Vol. 38, No. 6, 1990, pp. 787–812.
[18] Narasimhan, R. and Rosakis, A. J., "Three Dimensional Effects Near a Crack Tip in a Ductile Three Point Bend Specimen—Part I: Numerical Investigation," Division of Engineering and Applied Science, California Institute of Technology, Pasadena, CA, SM Report 88-6, 1988.
[19] Post, D., "Moiré Interferometry," *Handbook on Experimental Mechanics*, A. S. Kobayashi, Ed., Society for Experimental Mechanics, Inc., Bethel, CT, 1987, pp. 334–384.
[20] Shih, C. F., "Tables of Hutchinson-Rice-Rosengren Singular Field Quantities," Report MRLE-147, Materials Research Laboratory, Brown University, Providence, RI, 1983.

Inhoy Gu[1]

An Engineering Approach for Crack-Growth Analysis of 2024-T351 Aluminum Alloy

REFERENCE: Gu, I., "**An Engineering Approach for Crack-Growth Analysis of 2024-T351 Aluminum Alloy,**" *Fracture Mechanics: Twenty-Second Symposium (Volume II), ASTM STP 1131*, S. N. Atluri, J. C. Newman, Jr., I. S. Raju, and J. S. Epstein, Eds., American Society for Testing and Materials, Philadelphia, 1992, pp. 246–256.

ABSTRACT: A simple methodology is suggested to analyze the crack growth of a body up to maximum load, by integrating the step-like increments of applied load and crack extension. The crack-growth criterion is the critical rate of crack-tip opening displacement (CTOD) increase versus effective crack extension of plastic-zone-size adjustment. Formulations of linear elastic fracture mechanics and limit-load expressions are used in the calculation. The analysis also presents a K-resistance (K_R) curve equation, which is complete with constants of fracture initiation toughness and crack-growth resistance. The proposed method is applied to 2024-T351 aluminum alloy specimens in plane stress, for which experimental data are available. The calculated maximum loads are in reasonable agreement with the failure loads.

KEY WORDS: fracture initiation, crack growth, resistance (K_R) curve, effective crack length, maximum load, fracture mechanics, 2024-T351 aluminum alloy

One of the fundamental problems concerning use of a flawed structure or design against structural failure is to predict its critical state in terms of operating conditions. For small-scale yielding fracture, the fracture toughness of the ASTM Test Method for Plane-Strain Fracture Toughness of Metallic Materials (E 399-83) is a useful parameter in the determination of critical loads or crack lengths. Further, metallic materials of stable crack growth are characterized in the R-curve of the ASTM Recommended Practice for R-Curve Determination (E 561-86). It is a continuous record of crack extension resistance, K_R in terms of stress-intensity factor as a function of crack extension. The K_R-curve is regarded as a material property independent of original crack length and crack configurations for a given specimen thickness. The fracture instability of a specimen is predicted so that a crack-extension-force curve in units of stress-intensity factor, K, develops tangency with the K_R-curve. This practice has been developed for use on ultra-high-strength sheet materials. However, McCabe and Schwalbe [*1*] showed that the K_R-curve method can be applied to handle the ductile structural grades of materials by using effective crack length instead of physical crack length. The effective crack length is the physical crack size augmented for the effects of plastic deformation at a crack tip. The loading compliance of secants drawn to the test record of load-deflection is compared with the elastic compliance function to estimate effective crack sizes. The present analysis adopts this practice.

This paper presents a method that allows easy determination of K_R-curve from a test result, by deriving a K_R-curve equation. An analytical procedure is presented for the calculation of loads against effective crack extensions up to maximum load, either in fracture

[1]Associate professor, Department of Mechanical Engineering, Chung-Ang University, Seoul, 156-756, Korea.

instability or in plastic instability at limit load. The method is simple enough not to require specialized analytical or computational techniques of the J-resistance (J_R) crack approach [2]. It can be applied to any specimen configuration with expressions of stress-intensity factor and limit load. Moreover, a microscopic crack-growth criterion associated with the K_R-curve method is suggested with a material constant. Thus, direct comparison of crack-growth resistance between materials is made possible quantitively in the suggested method. The method is applied to various specimens of 2024-T351 aluminum alloy in plane stress. The calculated maximum loads are compared with experimental data in the literature, from which the accuracy of the suggested method may be assessed.

Formulations

A cracked body of metallic material under a continuously increased load, P, may follow the stages of fracture initiation, stable crack growth, and fracture or plastic instability. The fracture initiation toughness can be evaluated in the critical value, K_i, of stress-intensity factor or its equivalent parameters. Up to then, crack-tip blunting occurs with crack advance, negligibly small compared with total crack length. After fracture initiation, the crack-extension force for slow stable crack growth is expressed in terms of crack-tip opening displacement (CTOD), V_t, defined with respect to the extended crack tip. The present analysis assumes crack growth in the step-like behavior of crack extension and load increment. Thus, the CTOD increment in a step is written as follows from the function, $V_t\ (P,a)$, of applied load, P, and current crack length, a

$$dV_t = \frac{\partial V_t}{\partial a}\,da + \frac{\partial V_t}{\partial P}\,dP \tag{1}$$

Here, the first term on the right is due to crack extension without load increment and the second is due to load increase with a crack length fixed. The CTOD in linear elastic fracture mechanics is related to the stress-intensity factor, K, elastic modulus, E, and flow stress, σ_0

$$V_t = K^2/\sigma_0 E \tag{2}$$

The stress-intensity factor is a function of crack length, available for specimen types in handbooks, for instance Murakami [3]

$$K = Pf(a) \tag{3}$$

A crack-growth criterion is proposed so that a crack tip extends an incremental length, da, when the crack tip attains a critical CTOD increment. This critical rate of CTOD increment versus crack extension is termed crack-growth resistance constant

$$dV_t/da = I_c \tag{4}$$

When the CTOD increases linearly with the J-integral value, the criterion is consistent with the tearing-modulus approach [4] where material's resistance to crack extension, da, is evaluated with an increase in J-resistance value, dJ, and the ratio, dJ/da, is constant. Figure 1 shows a schematic of the crack-growth process. For a crack tip at 0_1, consider that the crack-growth criterion is met at Point A, then the crack tip advances by an increment, da, to Point 0_2. During the time the CTOD at Point B increases $(\partial V_t/\partial a)da$, and it should be

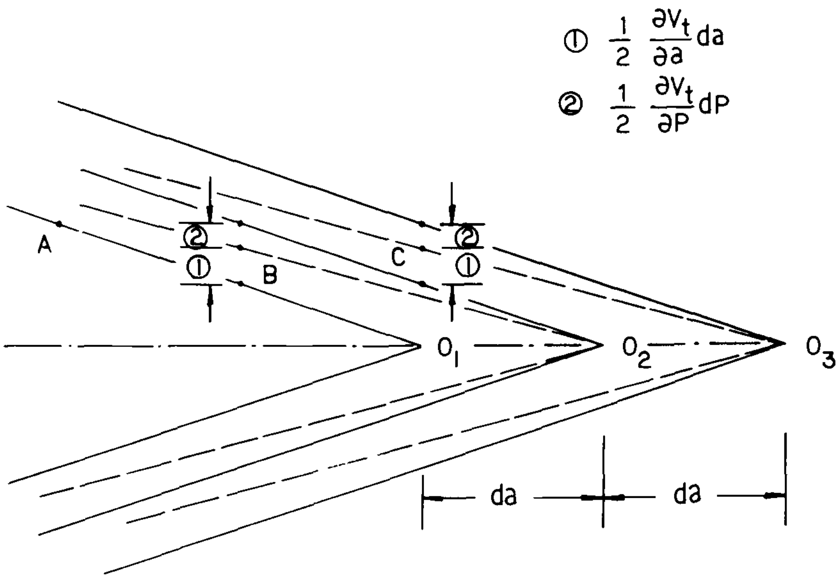

FIG. 1—*Schematic of step-like crack-growth process.*

further increased with load by $(\partial V_t/\partial P)dP$. When the combined CTOD increment at Point B reaches a critical value, the crack tip advances to Point 0_3, rendering a CTOD increase $(\partial V_t/\partial a)da$ at Point C. This crack-growth process, assumed to continue repeatedly, is step-like or finite-incremental rather than continuous. As there may be a CTOD before the current step of crack extension, the proposed criterion is different from those based on total CTOD, such as a critical CTOD or crack-tip opening angle (CTOA) criterion. The value, I_c, is not a measurable quantity in the conventional sense, but a derived quantity. Substituting Eqs 2, 3, and 4 into Eq 1, we get a load increment needed for an incremental crack extension

$$dP = \frac{1}{2Pf(a)^2}\left[E\sigma_0 I_c - 2P^2 f(a)\frac{df}{da}\right]da \tag{5}$$

Starting from an initial load, P_i, at an original crack length, a_0, the load in Eq 5 is integrated numerically for a plot of load versus crack length. The plot does not change with different sizes of finite differential increment, *da*. That agrees with a physical sense because crack-growth increments in the step may be of small, variable sizes. Significantly enough, the constants associated with material properties constitute a single term, $E\sigma_0 I_c$, in Eq 5. Thus, even though a constant coefficient is considered in Eq 2, that does not make a difference as far as the coefficient is used consistently in the evaluation of the parameters and their applications.

The other consequence from the present crack growth analysis is the K resistance curve. Substituting Eq 2 into the criterion, Eq 4, and integrating it from the fracture initiation toughness, K_i, at the crack length, a_0, gives

$$K_R^2 = K_i^2 + E\sigma_0 I_c(a - a_0) \tag{6}$$

The K_R-curve equation, unlike Eq 5, is independent of specimen type and crack configurations and complete with parameters, K_i and $\sigma_0 I_c$. The fracture instability in ASTM E 561-

86 is defined by letting a crack-extension-force curve of stress-intensity factor, K, be tangent to the K_R-curve. The tangent point is used to determine the fracture toughness, K_c for high strength and low ductility materials. Instead of the graphical procedure, they can be calculated in the K_R-curve equation as follows

$$\frac{dK}{da} = \frac{dK_R}{da} \tag{7}$$

$$K = K_R \tag{8}$$

Multiplying two equations (Eqs 7 and 8) and substituting Eqs 2 and 6 gives the crack-growth criterion (Eq 4), so the criterion is compatible with the instability condition in the K_R-curve method. Moreover, calculating the maximum load by integrating Eq 5 is easier than solving Eqs 7 and 8 directly for the load and crack length at fracture instability. The fracture instability load for a given K_R-curve does not depend on the flow stress of material. However, in other situations, the load may attain the limit load on the specimen before reaching the condition, $dP/da = 0$, in the integrated Eq 5. Then the limit load is the maximum load, beyond which fracture instability may occur in a stroke-controlled test. Materials of an identical K_R-curve may not yield the same maximum load on a specimen when their flow stresses are different. Whether the maximum load is attained at fracture instability or plastic instability, as the present formulation uses the expressions of the linear elastic fracture mechanics, the analysis is not applicable to the fracture analysis beyond maximum load. The two possible ways of attaining maximum loads are depicted schematically in Fig. 2, where the solid line is for applied loads calculated from Eq 5. First for low-ductility materials or structures, the limit-load curve (1) does not intersect with the applied-load curve, and the maximum load is the peak load, P_1, corresponding to the instability condition in the K_R-curve method of ASTM E 561–86. Low-ductility structures may have a small ratio of initial crack length to specimen width. Second, for ductile materials or structures, the limit-load curve (2) in Fig. 2 intersects with the applied-load curve, and the maximum load is a limit load, P_2, at the intersection point. This case is not included in the ASTM E 561–86.

As mentioned earlier, the crack length is the effective crack length of plastic-zone-size adjustment rather than the physical crack length. Schwalbe and Setz [5] showed that effective crack size is valid up to the ligament yield load in bend specimens. The effective crack length is obtained in the loading compliance method of the ASTM E 561–86. However, for large-scale yielding specimens under limit load, the effective crack length is determined in the limit-load equation.

Applications

For a standard compact specimen of thickness, B, width, W, and crack length, a, of the configuration in Fig. 3, the stress-intensity factor in the ratio $\lambda = a/W$ is

$$K = \frac{P}{B\sqrt{W}} \frac{(2 + \lambda)}{(1 - \lambda)^{3/2}} (0.886 + 4.64\lambda - 13.32\lambda^2 + 14.72\lambda^3 - 5.6\lambda^4) \tag{9}$$

Using the published experimental data [6] of loads and effective crack lengths for three compact specimens of 2024-T351 aluminum alloy, we get K_R-values in Eq 9. They are plotted up to maximum loads in Fig. 4, with relevant mechanical properties in the caption. The

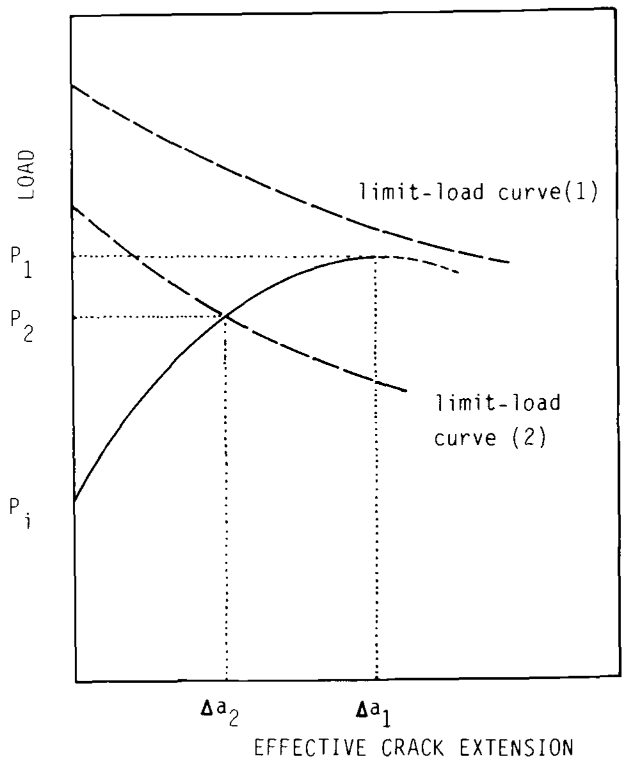

FIG. 2—*Schematic of two cases of attaining maximum load.*

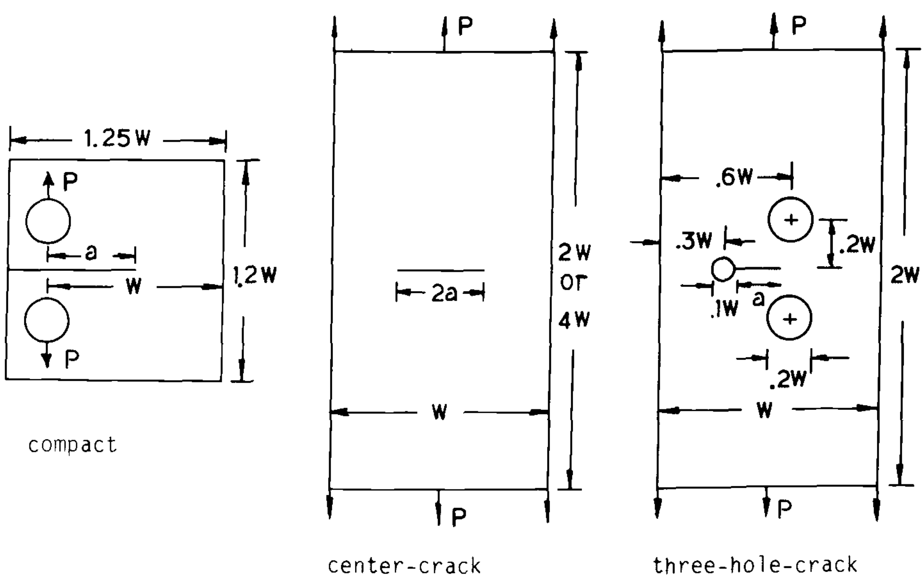

FIG. 3—*Specimen configurations analyzed in the proposed method.*

data on three different-size specimens have an evident consistency. The effective crack extensions are the mean of two compliance measurements at load line and crack mouth up to maximum load. These baseline data of initial crack length-to-width ratio, $a_0/W = 0.5$, were supplied for the determination of material properties in an extensive round-robin test program (ASTM Subcommittee E24.06.02). Accordingly, they are also used to determine the material constants, K_i and $\sigma_0 I_c$, so that the calculated loads against crack length from Eq 5 may be best fit to the test records of load against effective crack length. This procedure is the same as letting the K_R-curve, Eq 6, be fit to the measured K_R data plotted against effective crack length. Then the determined constants are K_i = 34 MN/$m^{3/2}$ and $\sigma_0 I_c$ = 12.2 MPa for the plate of about a 12.7 mm (0.5 in.) thickness. The last crack-extension data for each specimen is disregarded in the evaluation, for the crack may extend significantly at the maximum load. The K_R-equation (Eq 6) of the constants is also plotted in the solid curve in Fig. 4, with a reasonable representation of the experimental data. Since ductile fracture is assumed on this material, it is needed to separate the flow stress, σ_0, from the constant I_c of crack-growth resistance. Thus, the flow stress determines that a maximum load is a limit load. In other words, loads and crack lengths are calculated in Eq 5 using the unse-

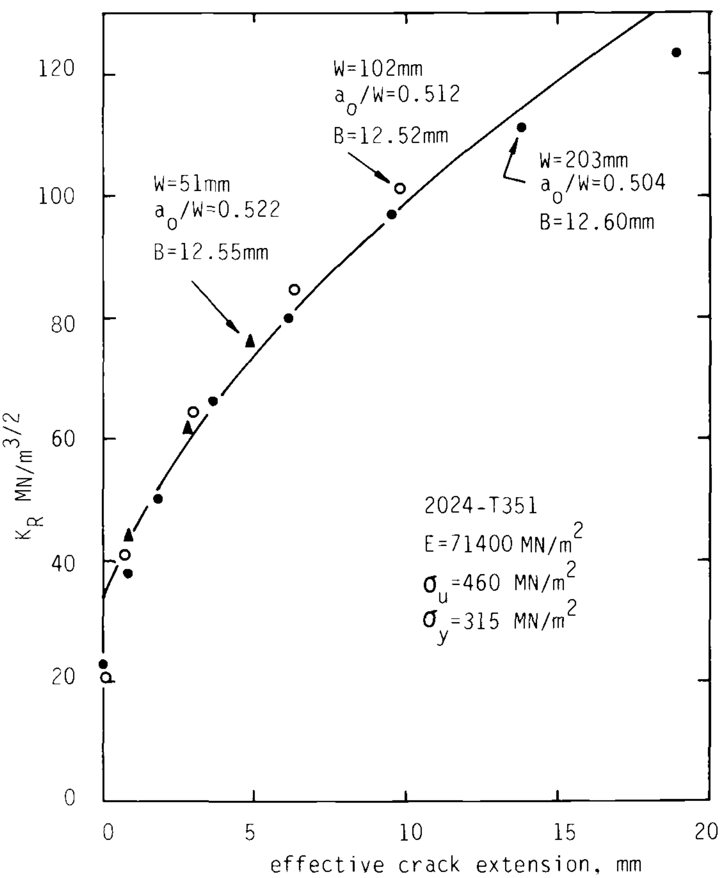

FIG. 4—*Crack-growth resistance* (K_R) *curve for 2024-T351 aluminum alloy with data from compact specimens. A* K_R*-curve equation (Eq 6) is plotted in the solid line.*

parated constant up to an experimental failure load, and its final crack length is used to determine the flow stress in the limit-load expression. Even though the conventional estimate of the flow stress in the middle of yield and tensile strength can be a first approximation, the flow stress in the preceding method gives a better estimate of maximum loads. This difference in estimating flow stress may be due to the lack of rigorous fundamentals in applying the limit-load expression of nonhardening flow stress to the hardening material of the 2024-T351 aluminum alloy. The limit load on the compact specimen in plane stress is given as follows in Ref *2*

$$c = W - a$$

$$\eta = [(2a/c)^2 + 2(2a/c) + 2]^{1/2} - (2a/c + 1)$$

$$P_L = 1.071\eta\sigma_0 cB \tag{10}$$

The flow stress (σ_0 = 339 MPa) is determined so that the failure load on a compact specimen (W = 203 mm) among the baseline data specimens can be a limit load in Eq 10. Consequently, the crack-growth resistance constant is I_c = 0.036.

Using the determined material constants, the maximum loads on various specimens of Fig. 3 are predicted and compared with experimental failure loads in Table 1. These experimental data, aside from the baseline data, were provided to evaluate the fracture analysis methods in the round-robin test [*6*]. The results on compact specimens are plotted in Fig. 5, where solid lines are calculations. All specimens of the ratio a_0/W = 0.3, 0.5, and 0.7

TABLE 1—*Comparison between calculated* (P_c) *and experimental* (P_f) [5] *maximum loads on 2024-T351 aluminum alloy specimens where* Δa *is the calculated effective crack extension at the maximum load.*

B, mm	W, mm	a_0, mm	Δa, mm	P_c, kN	P_f, kN
		COMPACT SPECIMEN			
12.4	51	16.1	4.74	27.4	29.8
12.6	51	26.5	2.52	13.6	14.2
12.3	51	36.2	0.90	4.87	5.22
12.5	102	31.4	10.69	54.3	54.7
12.5	102	51.9	6.33	26.7	28.8
12.6	102	71.2	3.11	9.90	10.1
12.5	203	61.8	22.45	107.0	98.5
12.6	203	102.4	13.82	53.0	52.1
12.5	203	142.9	7.12	17.9	18.6
		CENTER-CRACKED SPECIMEN			
12.6	127	26.2	3.37	289.9	302
12.6	254	51.2	8.07	578.7	581
		THREE-HOLE-CRACK TENSION SPECIMEN			
12.6	254	13.9	7.54	759.5	754
12.5	254	25.7	9.40	753.4	738
12.5	254	38.6	8.48	753.4	735
12.5	254	51.8	5.64	725.8	718
12.6	254	64.3	3.23	688.5	696
12.6	254	75.8	2.21	643.4	660
12.5	254	90.0	2.91	575.2	580
12.5	254	101.5	4.85	518.2	505

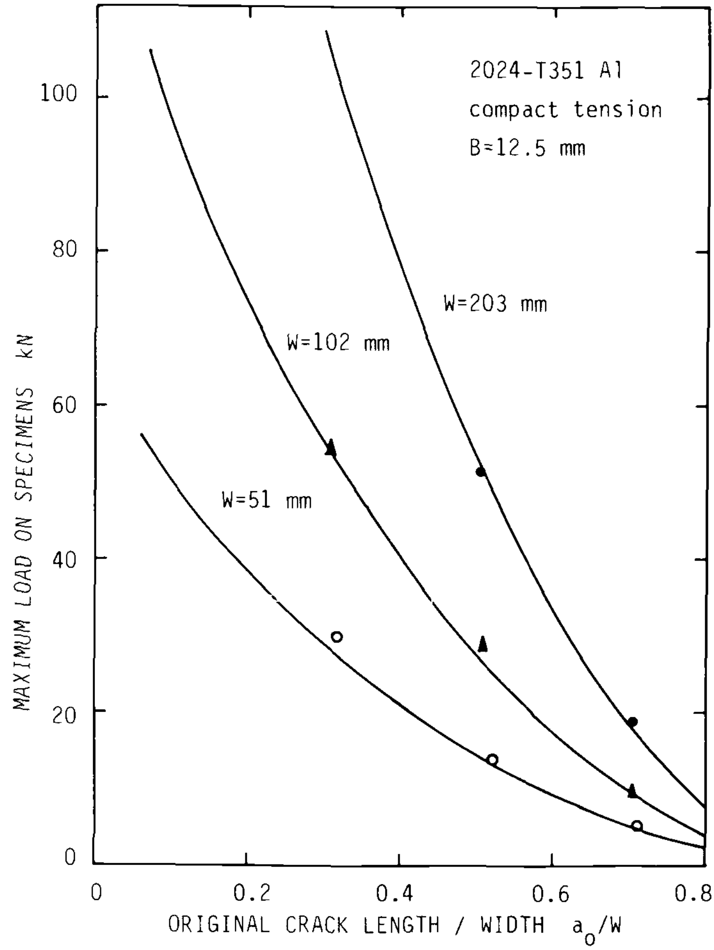

FIG. 5—*Comparison between predicted (solid lines) and experimental maximum loads on compact specimens of 2024-T351 aluminum alloy.*

for three specimen widths attained the maximum loads with limit load. The effective crack extensions at the maximum loads are also calculated and given in Table 1 as well as in Fig. 6. These may be used to obtain the load-line displacements from the elastic compliance functions, available in Ref *3*, for instance. There seems to be no geometrical proportionality between different-size specimens at the maximum loads. Note that in Fig. 6 the normalized crack extension at maximum load increases with specimen size. As the crack extension becomes large, the possibility of fracture instability increases in Fig. 2. This appears to explain the specimen-size dependence of fracture mode. The expressions for stress-intensity factor and plane-stress limit-load on center-cracked specimens of width, *W*, thickness, *B*, and crack length, 2*a*, shown in Fig. 1 are, respectively

$$K = (P/BW)\sqrt{\pi a \sec(\pi a/W)} \tag{11}$$

$$P_L = \sigma_0 B(W - 2a) \tag{12}$$

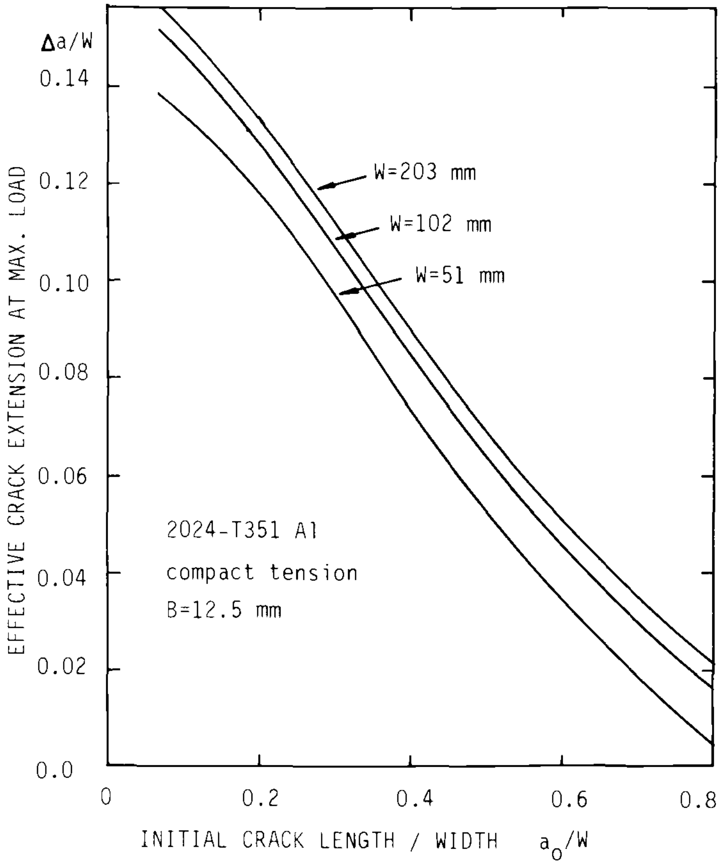

FIG. 6—*Calculated effective crack extensions at maximum loads on compact specimens for three specimen widths.*

For the three-hole-crack tension specimen in Fig. 1, the stress-intensity factor expression is derived by Newman [6] with the finite element method

$$K = (P/WB)\sqrt{\pi a}\, F \tag{13}$$

where

$$F = \sum_{i=1}^{4} \sum_{j=1}^{2} \frac{A_{ij}(1 - a/b)^{-1/2}}{(1 + a/r)^{i-1}\,[(y_0/x_0)^2 + (a/x_0 - 1)^2]^{(j-1)/2}} \tag{14}$$

$A_{11} = 2.02$	$A_{12} = -9.17$	$A_{21} = -62.37$	$A_{22} = 287.72$
$A_{31} = 1025.8$	$A_{32} = -2845.1$	$A_{41} = -8270.6$	$A_{42} = 11927.3$
$r = 12.7$ mm	$b = 165$ mm	$x_0 = 63.5$ mm	$y_0 = 50.8$ mm

The limit load is approximated in the net-ligament yield load

$$P_L = 0.7\sigma_0 BW \qquad \text{for } a/W \leqslant 0.2$$

$$P_L = \sigma_0 B(0.9W - a) \text{ for } a/W \geqslant 0.2 \tag{15}$$

Table 1 as well as Fig. 7 show good agreement between calculated and experimental loads on the three-hole-crack tension specimens of initial crack lengths ranging from $a_0/W = 0.05$ to $a_0/\mathrm{W} = 0.4$.

Conclusions

Crack growth is considered a process of alternating the increase of applied load and crack extension, based on the criterion of a critical rate, I_c, of CTOD increase versus crack extension. Ductile fracture analysis is made possible by determining the effective crack length of plastic-zone-size corrections and limit-load expressions. The derived K_R-curve

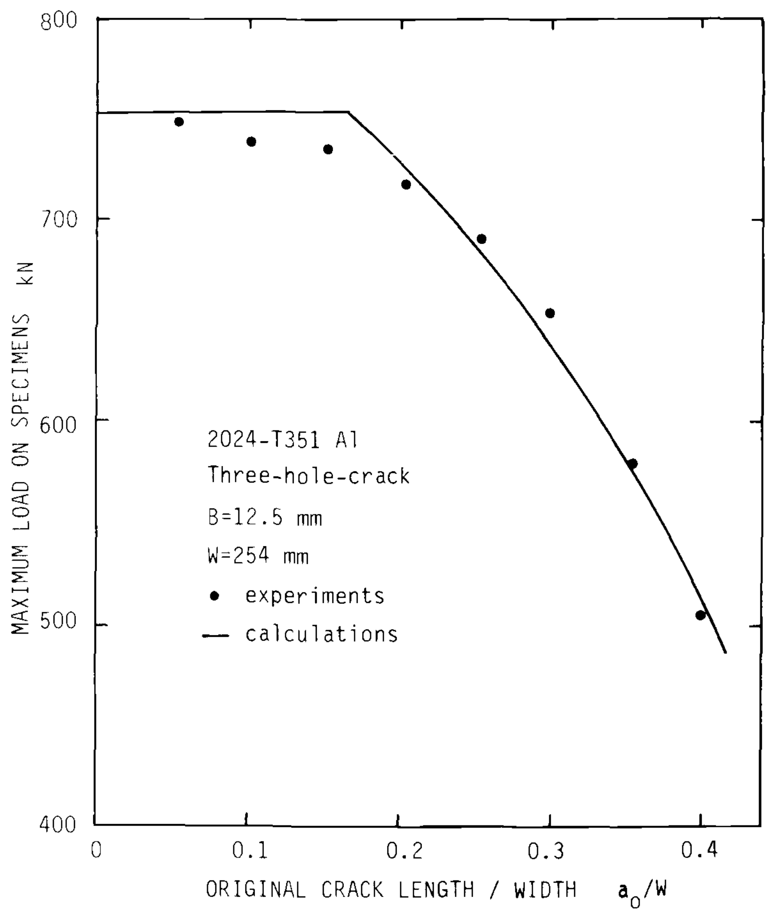

FIG. 7—*Comparison between predicted and experimental maximum loads on three-hole-crack specimens of 2024-T351 aluminum alloy.*

equation is independent of specimen configurations. It is used to determine the material constants of the analysis, among which the flow stress, σ_0, of material is presumably related to the limit load on the specimen of extended crack length. With test data on three compact specimens of 2024-T351 aluminum alloy, the constants are estimated in fracture initiation toughness, K_i = 34 MNm$^{3/2}$, flow stress, σ_0 = 339 MPa, and crack-growth resistance, I_c = 0.036. The proposed method with the constants is applied to other compact specimens, center-cracked specimens, and three-hole-crack tension specimens of various crack lengths and specimen sizes. All of the calculated maximum loads are in reasonable agreement with available experimental failure loads, with an error of less than 10%. The stable crack extensions at maximum load are also calculated, and they, normalized to specimen width, increase with specimen size. The proposed method does not require a specialized computational or experimental technique. Nevertheless, it can be used to predict failure loads with reasonable accuracy.

References

[1] McCabe, D. E. and Schwalbe, K. H., "Prediction of Instability Using the K_R-Curve Approach," *Elastic-Plastic Fracture Mechanics Technology, ASTM STP 896*, J. C. Newman, Jr., and F. J. Loss, Eds., American Society for Testing and Materials, Philadelphia, 1985, pp. 99–113.

[2] Kumar, V., German, M. D., and Shih, C. F., "An Engineering Approach for Elastic-Plastic Fracture Analysis," EPRI Topical Report NP-1931, Electric Power Research Institute, Palo Alto, CA, 1981.

[3] Murakami, Y., *Stress Intensity Factors Handbook*, Pergamon Press, Oxford, 1987.

[4] Paris, P. C., Tada, H., Zahoor, A., and Ernst, H., "The Theory of Instability of the Tearing Mode of Elastic-Plastic Crack Growth," *Elastic-Plastic Fracture, ASTM STP 668*, J. D. Landes, J. A. Begley, and G. A. Clarke, Eds., American Society for Testing and Materials, Philadelphia, 1979, pp. 5–36.

[5] Schwalbe, K. H. and Setz, W., "*R*-Curve and Fracture Toughness of Thin Sheet Materials," *Journal of Testing and Evaluation*, Vol. 9, No. 4, July 1981, pp. 182–194.

[6] Newman, J. C., Jr., "An Evaluation of Fracture Analysis Methods," *Elastic-Plastic Fracture Mechanics Technology, ASTM STP 896*, J. C. Newman, Jr., and F. J. Loss, Eds., American Society for Testing and Materials, Philadelphia, 1985, pp. 5–96.

Padraic E. O'Donoghue,[1] *Melvin F. Kanninen,*[2] *Carl F. Popelar,*[2] *and Carl H. Popelar*[3]

Advanced Fracture Mechanics Analyses of the Service Performance of Polyethylene Gas Distribution Piping Systems

REFERENCE: O'Donoghue, P. E., Kanninen, M. F., Popelar, C. F., and Popelar, C. H., "**Advanced Fracture Mechanics Analyses of the Service Performance of Polyethylene Gas Distribution Piping Systems,**" *Fracture Mechanics: Twenty-Second Symposium (Volume II), ASTM STP 1131*, S. N. Atluri, J. C. Newman, Jr., I. S. Raju, and J. S. Epstein, Eds., American Society for Testing and Materials, Philadelphia, 1992, pp. 257–273.

ABSTRACT: Most of the plastic gas distribution pipe now in service is polyethylene (PE). While this material has an excellent safety record, due to a variety of abnormal loadings that can arise in long-time service, some slow crack growth (SCG) related field failures have occurred. Accelerated test procedures to accurately predict the long-term performance of PE gas pipes are therefore required for the evaluation of existing gas piping systems and to qualify new pipe materials prior to installation. In addition, particularly as interest in the use of larger diameter and higher pressure polyethylene pipes increases, rapid crack propagation (RCP) can occur in a gas piping system at the site of an SCG failure, or as a result of third party damage, or by other similarly unforeseeable mechanisms, attention must be given to the possibility of RCP. Accordingly, dynamic fracture mechanics research aimed at preventing RCP in PE gas distribution pipelines has also been carried out. This paper reviews current advanced fracture mechanisms research on PE gas pipe materials that investigates both SCG and RCP events.

KEY WORDS: fracture, fracture mechanics, gas pipelines, slow crack growth, rapid crack propagation, viscoelasticity, fatigue (materials)

There are about 640 000 km (400 000 miles) of plastic pipe in gas distribution service in the United States, a substantial portion of which is polyethylene (PE) piping. Given a 50-year design life, some 2% of this total (12 000 km) needs to be replaced each year. This amount is in addition to the requirements for expanding the current gas distribution piping system to accommodate consumer demand that is currently about 24 000 km (15 000 miles) annually. Therefore, with the large amount of piping that is needed, there is clearly a considerable incentive for cost-effective and failure-free design and maintenance procedures for PE gas pipes.

While the vast majority of the present PE gas piping system has been trouble free, field failures have occurred as a result of abnormal loadings such as improper squeeze-off, rock impingement, and excessive bending. In many instances, the failures have occurred after many years of service through a "brittle" slow crack growth (SCG) mechanism. Quantitative knowledge of SCG therefore is needed to help ensure that the pipe materials selected for

[1]College lecturer, University College Dublin, Dublin, Ireland,
[2]Program director and research engineer, respectively, Southwest Research Institute, San Antonio, TX 78228.
[3]Professor, The Ohio State University, Columbus, OH 43210.

new installations will not be susceptible to SCG, and thereby to assist the gas industry in making cost effective judgments on existing piping systems. In addition, due to the trend towards higher pressure and larger diameter piping systems, the possibility of rapid crack propagation (RCP) in distribution pipes arises. Taking the point of view that, if the conditions required for a long-running crack can be precluded, crack arrest will occur, crack arrest fracture mechanics principles are applicable to assess the integrity of engineering structures where fracture instability cannot be absolutely prevented. The primary motivation for the development of this technology has been experience with gas transmission pipelines subjected to third party damage where long-running crack propagation is entirely possible.

A number of studies have been carried out recently both in Europe [*1–4*] and in this country [*5,6*] to investigate the possibility of RCP in PE pipes used in gas distribution service. While this work was successful in obtaining extensive experimental data, less effort was expended in the development of theoretical models for the prediction of crack propagation and arrest. The limited modeling was due in part to the lack of a suitable computational analysis for the complex fluid/structure behavior that occurs. In this regard, one of the first efforts was conducted by Kanninen et al. [*7*]. A portion of the experimental data was examined and, with the aid of finite element analyses and the fracture mechanics principles for steel transmission pipelines, a preliminary model for the prediction of RCP arrest was developed.

Several issues involved in both SCG and RCP events in PE gas distribution piping systems call for the use of advanced fracture mechanics treatments. Because of their desire to bring the best available technology to the service of the industry, the Gas Research Institute (GRI) has enabled advances to be made in several areas. This paper reviews the work that has been performed recently in the development and validation of viscoelastic fracture mechanics for application to SCG, and in dynamic fracture mechanics for application to RCP of PE pipes.

Background

A difficulty that exists in quantifying the SCG behavior of PE gas distribution pipe materials arises from a competition between a "ductile" failure process that predominates at short times and high load levels and the long time "brittle" failure SCG mechanism that manifests itself only at lower loads. Unfortunately, as is now well-established, extrapolations of failure times based on ductile failure data generally provide anticonservative results. This has led to the successful development of accelerated, high temperature tests that reproduce the observed SCG failure morphology. However, the analyses of data obtained from such tests are difficult for two reasons. First, because PE is viscoelastic, creep and crack growth occur simultaneously. Second, at the high stress levels that occur at the tips of defects (notches and cracks), PE exhibits a local ratification process known as "crazing." The occurrence of this extreme nonlinear type of behavior significantly compounds the problem.

In accelerating a test to obtain brittle SCG failures in short time intervals to be of practical use, the ancillary complications due to manufacturing and extrusion variations must be treated while residual stresses are eliminated. Hence, the test should employ actual extruded pipe materials. While several candidate SCG tests have been developed [*8,9*], only a few qualify on this basis. One such procedure is the three-point bend SCG test developed for GRI by Battelle [*10*]. Through the application of existing fracture mechanics principles and procedures, it will be shown later that valid test data generated over one week can be used successfully for making service predictions that are reliable for many years.

In regard to applications of fracture mechanics to gas distribution piping, it should be recognized that field failures are virtually always caused by external forces. Documented instances are those arising from rock impingement, squeeze-off or improper installation that act in concert with internal pressure and residual stresses. With this in mind, a lifetime prediction methodology has been developed that quantifies the performance of the pipe. The robustness of this procedure will be demonstrated by analyzing a representative service condition that consists of an axial flaw produced during a squeeze-off process.

Slow Crack Growth Testing and Analysis

While several different types of test specimens have been proposed, because most of these require use of molded material, the test developed by Battelle [*10*] on a pipe segment is more appealing. The use of similar arc-shaped specimens for metals is discussed by Underwood et al. [*11*]. Battelle SCG test specimens were produced by machining 17.78 mm (0.7 in.) wide rings from 50.8 mm (2 in.) SDR11 PE pipes. (SDR is the ratio of the outer diameter to the wall thickness of the pipe.) Each ring was further cut into three 120° sectors and centrally notched. In order to minimize test procedure differences, the Battelle approach [*8*] for slicing the starter notch into the specimen was followed. All notches were nominally 2.54 mm (0.10 in.) deep. Both room temperature and elevated temperature (40 and 60°C) tests were conducted with load levels varying from 4.5 to 9 kg (10 to 20 lb) [*12*].

The key measurement in these tests is the time dependent load point displacement under constant load. It reflects changes in the compliance of the specimen due to combined creep and crack growth. Typical elevated temperature load point displacement histories on a recently manufactured PE gas pipe resin are presented in Fig. 1. A similar trend is evident at room temperature, but here it can be many weeks before crack growth initiates.

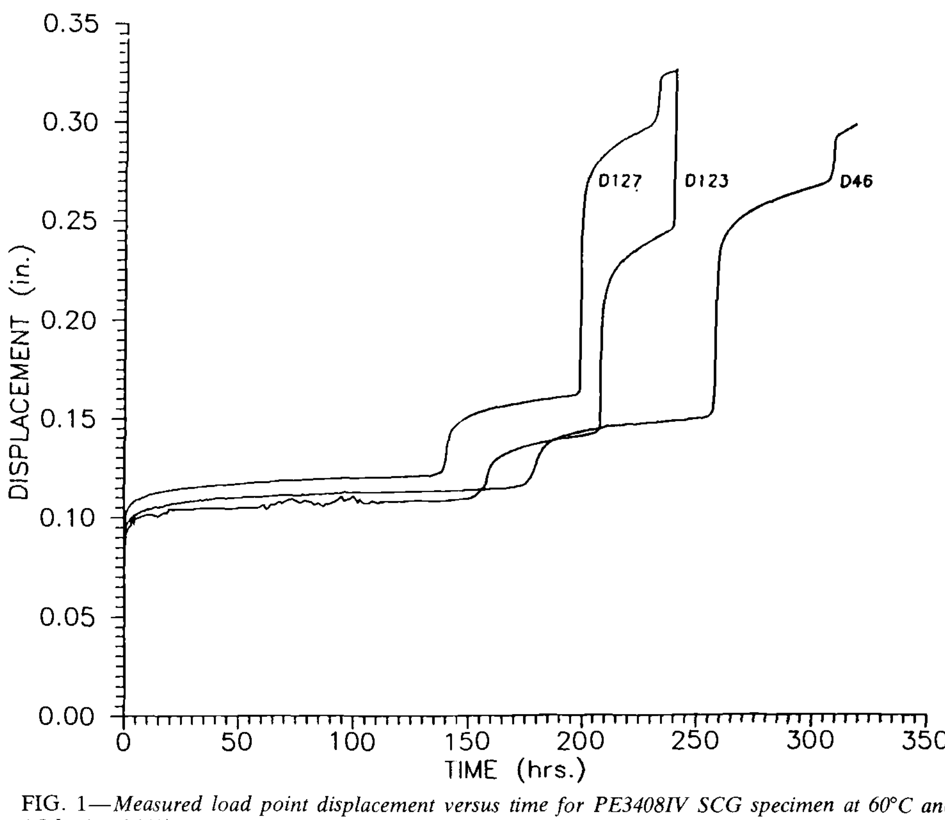

FIG. 1—*Measured load point displacement versus time for PE3408IV SCG specimen at 60°C and ~4.5 kg (10.04 lb).*

An examination of the fracture surface in conjunction with the load point displacement histories of these specimens revealed that the SCG process was discontinuous, consisting of rather abrupt crack extensions followed by arrests. Thus, there is a sequence of crack growth re-initiations and arrests until final collapse. The measured load point displacement history for an older PE gas pipe resin tested at room temperature and a load of 9 kg (20 lb) is shown in Fig. 2. Crack growth initiated after 38 h. It is apparent that the local point displacement record is appreciably smoother than those observed in Fig. 1. This implies that the crack growth rates are likewise more continuous. A similar trend has been observed for other older resins.

It is clear that there are significant differences between the behavior of newer and older PE materials. The latter appears to exhibit more continuous crack growth while the former clearly exhibits more discontinuous crack growth in this test configuration. The measured craze lengths for these materials were also distinctly different, that is, four times longer for the newer than the older PE material.

A detailed viscoelastic finite element analysis of these tests was performed, and this included nonlinear geometric and material behavior. Many complicating effects including anisotropy, residual stresses, large geometry changes, and nonlinear viscoelastic material behavior were treated. In order to circumvent the additional difficulty of crack growth, the analysis was focused on the preinitiation phase of the process. It was determined for the older resins (typified by the record in Fig. 2) that a linear viscoelastic analysis did a very good job in matching the measured load point displacement records. In contrast, a fully nonlinear viscoelastic analysis was required to match the load point displacement record for the newer resin given in Fig. 1 [*13,14*].

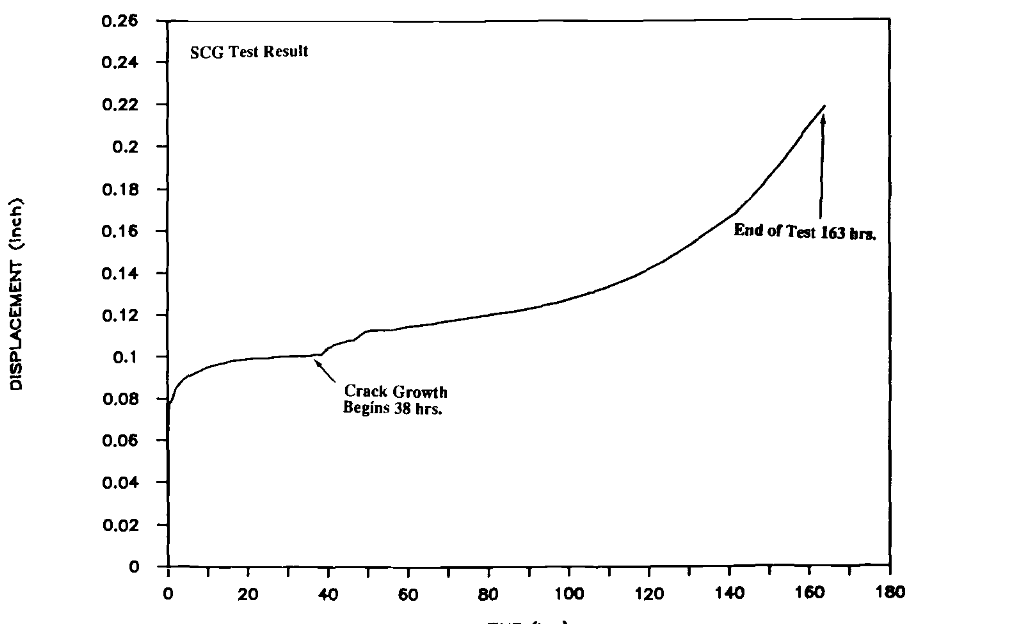

FIG. 2—*Measured load point displacement versus time for PE2306I SCG specimen at room temperature and 9 kg (20 lb).*

A Fracture Mechanics Assessment of the SCG Test

A valid fracture mechanics methodology for use in the interpretation of SCG test data and for predicting PE gas pipe fracture behavior requires establishing the size of the zone of dominance of the singular stress field at the crack (notch) tip. For example, in linear elastic fracture mechanics (LEFM), the region of dominance must contain the inelastic zone at the crack tip. Another requirement on the size of this dominant region size is that it must be smaller than the characteristic dimensions of the structure. It is essential to establish the size of this region to ensure the transferability of fracture data obtained from laboratory specimens to the structure; for example, from an SCG specimen to a pipe.

The focus of this analysis is the size of the region of dominance for the SCG specimen based on the linear elastic fracture mechanics methodology. Once the extent of the region has been determined, it can be then compared with the craze lengths measured in the SCG experiments. A linear viscoelastic analysis, with a very fine mesh in the immediate vicinity of the crack tip, was performed to establish the size of this region. A graded mesh with the smallest elements being approximately 0.001 b, where b is the length of the remaining ligament, was used. This mesh refinement permitted very precise determinations of the stress field in this region.

The extent of the region of dominance is established conventionally by comparing the numerically determined full-field stresses (from the finite element results) for the specimen with the asymptotic or singular stress field [*15*]. For LEFM, the latter field has a $r^{-1/2}$ character, where r denotes the distance from the crack tip. Using the finite element solution, the stress-intensity factor is calculated. More specifically, in a LEFM approach, the singular stress component in the crack-tip region is given by

$$\sigma_s = K/\sqrt{2\pi r} \tag{1}$$

The numerically computed values for the ratio of the full-field stress on the plane ahead of the crack to σ_s as a function of distance from the crack tip are given in Fig. 3.

An estimate of the dominance of the singular stress field can be made by invoking the criterion used by Shih [*16*] in the development of elastic-plastic fracture mechanics. In his work, the zone of dominance is that region in which the full-field stresses are within 90% of the singular stresses. Figure 3 indicates that the zone of dominance then extends approximately 6% of the ligament ahead of the crack tip. This value is in agreement with determinations of LEFM analysis of other specimens [*17*]. The 80 and 70% limits are also shown here for comparison purposes. They represent dominant regions of 10 and 16%, respectively, of the remaining ligament.

For a 50.8-mm (2-in.) SDR11 SCG specimen, based on a ligament length of 3 mm (0.12 in.), 6% of the ligament translates to 0.2 mm (0.008 in.) as the extent of this region. A comparison of this length with the measured craze lengths in the newer resins (designated here as PE2306IX) [*12*] and those measured by Battelle [*10*] for older resins designated as (PE2306II) is made in Fig. 4. Note that, while the 70 and 80% limits are also shown here, because it is conservative, the conclusions that are drawn will utilize the 90% limit.

It is evident from Fig. 4 that the craze lengths for the older material used in the earlier Battelle tests [*10*] are about five times shorter than those measured for the present PE2306IX material for a given load. Also, as a general rule, the craze lengths for PE2306II are less than the extent of the region of dominance of the singular field, particularly at lower load levels. In contrast, the PE2306IX material exhibits craze lengths that extend beyond the region dominated by the crack-tip singularity. The solid lines (PE2306IX) lie above the 90% limit region of dominance. Craze lengths for other newer PE materials were also found to be greater than the size of the dominant region.

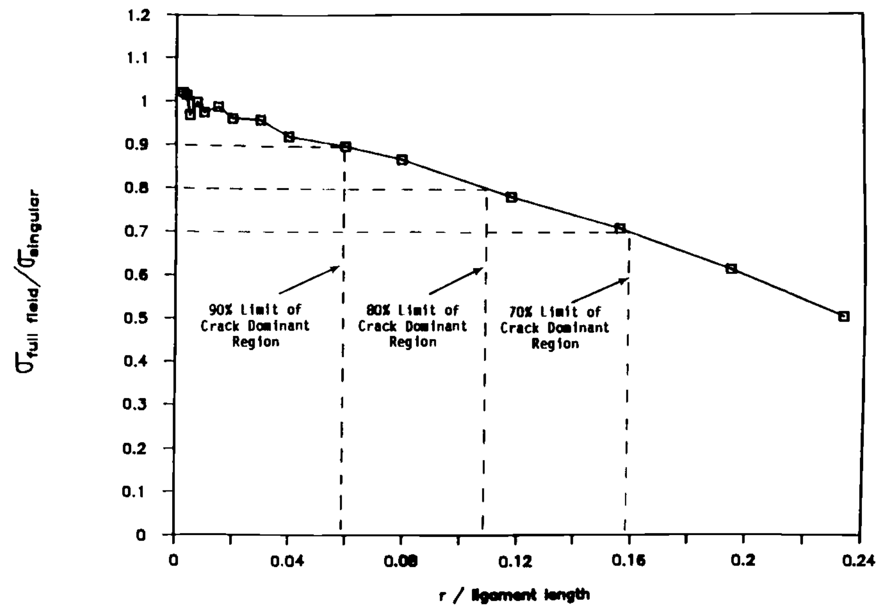

FIG. 3—*Determination of the region of dominance for a linear viscoelastic material for the SCG test specimen.*

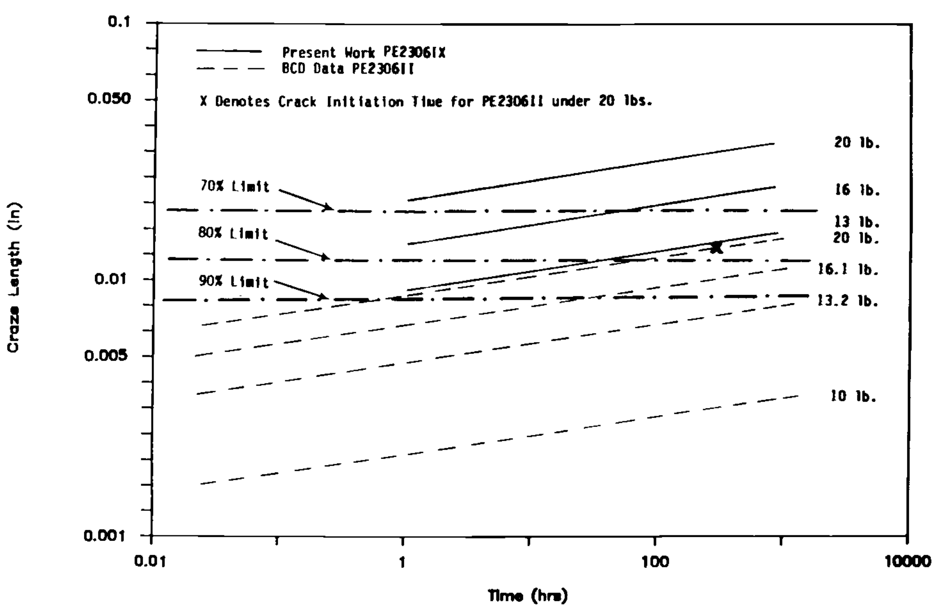

FIG. 4—*Craze length comparison with region of dominance size for PE2306 at room temperature.*

The implication of this finding is that the principles of LEFM are applicable for interpreting SCG data having short craze lengths and smooth crack growth. For such materials, generally the older PE resins, the correlation of crack growth data with the stress-intensity factor for the SCG specimen can be expected to be transferable to pipes having the same crack-tip constraint. However, for materials having longer craze lengths such as PE2306IX, LEFM conditions do not hold. Here, a more sophisticated analysis model that explicitly includes the crazed region must be developed to interpret SCG data and apply it to PE gas pipes of this type. Thus, the comparison typified by Fig. 4 therefore provides one of the most important results of this research, since it places the results from the Battelle SCG specimen on a firm theoretical foundation.

Application of the SCG Test Data to Lifetime Predictions for PE Pipe

A relatively straightforward approach that uses SCG data to predict the useful service life of PE pipes involves a two-part approach. In the first portion of the computation, a procedure to determine the crack growth characteristics for a PE material from SCG data has been developed. The second part consists of using this information in an example analysis of a pipe under service loadings. Because the approach is based on LEFM principles, it strictly valid only for materials with short craze lengths. In addition, as the "dwell" time required for crack incubation and initiation of growth is not yet being taken into account, the results provide a conservative estimate of the actual leak time.

Development of a Lifetime Prediction Methodology for PE Pipes

An engineering analysis model, based on the principles of linear viscoelasticity, has been developed recently by Popelar and his co-workers. This estimates the crack length from the load point displacement record, and the details are presented in Ref *12* and *18*. This is combined with an analytical procedure that evaluates the stress-intensity factor for the SCG specimen.

At the heart of the methodology is a relationship between the crack growth rate and the stress-intensity factor that is assumed to take the following form

$$\frac{da}{dt} = AK^m \qquad (2)$$

where A and m are material constants and a is the crack length. This corresponds to a linear plot on a log-log scale where m is the slope and A is the intercept with the axis. Thus, a linear fit is made to the data to determine these constants.

In the computer code that has been developed, the program will automatically calculate the material parameters, A and m. These constants quantify the slow crack growth behavior for the particular material tested. They can now be applied to a pipe in a service situation and used to make an estimate of the safe operating life of the pipe. This represents the transition from the short-term laboratory test (160 h) to long-term prediction for the pipe (many years).

In addition to the material constants, A and m, lifetime prediction requires knowledge of the pipe geometry and loading to make an estimate of the safe operating period for the pipe. The present procedure takes account of several different loading situations including internal pressure, soil backfill, residual stresses from the extrusion process, rock impingement, and squeeze off. The latter two correspond to severe loading situations and are most likely to result in pipe failure from SCG. In the analysis, it is assumed that a small flaw exists in the axial direction. In practice, this only occurs in the case of an extremely severe load. The time taken for this crack to propagate through the wall corresponds to the lifetime of the pipe.

Through a series of finite element computations for a range of pipe sizes, the stress-intensity factors under the various field loads have been computed as a function of crack length. Using the results of these computations, empirical expressions have been developed for the stress-intensity factors arising from the different loads. Therefore, once the load and crack length are known, the stress-intensity factor may be calculated easily. Since a LEFM approach is adopted here, the K contributions from the various loads can be added directly.

The next step is to determine t_f, the portion of the total time to failure spent in crack growth for a given initial crack length. This is found by integrating Eq 2. The result is

$$t_f = \int_{a_0}^{h} \frac{da}{AK^m} \tag{3}$$

where h is the wall thickness and a_0 is the initial flaw size. It is relatively straightforward to estimate t_f by numerically integrating Eq 3.

Example Lifetime Prediction for PE Pipe

Field failures are generally caused by external force arising from rock impingement, squeeze-off, or improper installations that act in concert with internal pressure and residual stresses. The combined effect of these forces intensifies the stress that acts on defects (for example, inferior cold joint, knit lines, deep scratches) contained in the pipe wall. These defects can act as initiation sites for crack growth that in turn could lead to failure of the pipe. A limited amount of data is available on pipe failures due to the SCG mechanism, for example, as contained in Battelle's *Field Failure Reference Catalog* [*19*].

In order to illustrate the predictive capability of the analysis procedures just described, a preliminary investigation has been conducted on damage resulting from squeeze-off on the service life of gas distribution piping. Squeeze-off takes place during pipe repair when a pipe is squeezed to prevent gas flow. If done improperly, severe damage can be imparted to the pipe resulting in SCG [*19*].

In a recent example of a squeeze-off related failure, a small axial flaw developed on the inner surface of a pipe during a repair procedure. The pipe went into service in 1974 and the squeeze-off operation took place in 1980. At this stage, the crack began to grow and eventually failed in 1988. It is assumed that the crack initiated during squeeze-off and thereafter began to grow in a slow fashion.

Examination of the fracture surface indicated that an SCG failure occurred. Figure 5*a* contains a view of the fracture surface, showing a series of rings that appear to be centered around a point on the inner surface. This is the crack initiation site. The rings are likely due to crazing that takes place during short pauses in the crack growth process, similar to the discontinuous growth features that have been observed in laboratory specimens. A close-up view of the initiation region is given in Fig. 5*b*. Examination of this revealed the initial flaw was 0.127 mm (0.005 in.) deep in the pipe wall.

The pipe in this case was a PE2306I, 76.2 mm (3-in.) IPS pipe with an SDR of 11.5 (wall thickness = 7.73 mm). The SCG results in Fig. 2 are for the same type of material. Thus, the crack growth properties from that test are appropriate for this service situation. From an analysis of that data, $m = 1.83$ and $A = 1.96 \times 10^{-12}$ (mm/s)(kPa $\text{m}^{0.5})^{-1.83}$ [9.2×10^{-14} (in./s)(psi $\text{in.}^{0.5})^{-1.83}$]. The service loads acting on the pipe during the crack growth phase were (1) an average internal pressure of 0.28 MPa (40 psi), (2) a soil load due to 600

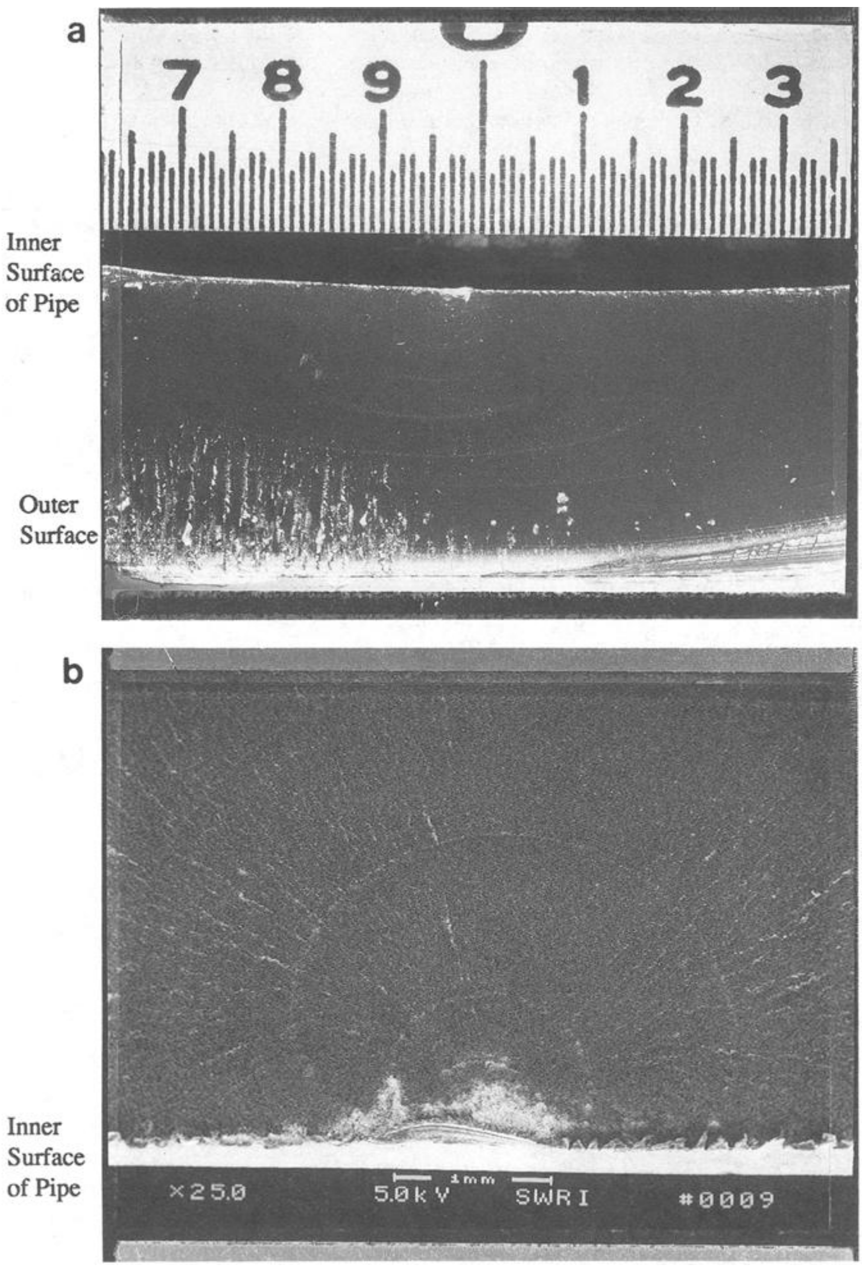

FIG. 5—(a) *Enlarged view of fracture surface showing progress of SCG in a squeeze-off region; agnification* ×6. (b) *Close-up view of crack initiation site arising from squeeze-off; magnification* ×25.

mm (2 ft) of backfill that corresponded to 0.012 MPa (1.73 psi), and (3) residual stresses in the pipe wall with the stress on the outside being 0.86 MPa (125 psi). For this loading situation, the predicted safe operating life for the pipe was 6.4 years. As the actual failure was likely to have occurred prior to the detection of the leak, this compares very favorably with the nominal lifetime of 8 years, beyond the squeeze-off. This example serves both to validate the analysis and also to illustrate the usefulness of the procedure. The result also illustrates that the SCG specimen is appropriate for obtaining useful crack growth data for PE pipe.

RCP Analysis Approach

Slow crack growth is just one of the failure processes that can occur in PE pipes. A potentially more serious situation can occur if a through-wall crack developed in an SCG mechanism provides the initiation site for a rapidly running axial crack. Third party damage is another possible cause of rapid crack propagation. The likelihood of a rapid crack in the axial direction, initiating from the site of a through-wall crack developed after SCG, becomes important as larger diameter pipes are used by the gas industry. Based on an extensive analysis of SCG failures, it has been estimated that the resulting damage is often a through-wall axial crack with a length roughly equaling two thirds of the pipe diameter. The stress-intensity factor variation with diameter is plotted in Fig. 6 for an SDR11 pipe under internal pressures of 0.28 and 0.56 MPa (40 and 80 psi). This uses the expression for a through-wall crack in a pressurized pipe developed by Folias [20].

It is estimated that fracture initiation toughnesses for older PE materials are about 2.2 MPa $m^{1/2}$ (2 ksi in.$^{1/2}$). For existing piping systems, having diameters of less than 200 mm (8 in.) and pressures of less than 0.28 MPa (40 psi), crack initiation is not very likely. However, with the anticipated use of large diameter (up to 400 mm) and higher pressures (up to 0.7 MPa), it is clear that RCP initiation is an important consideration.

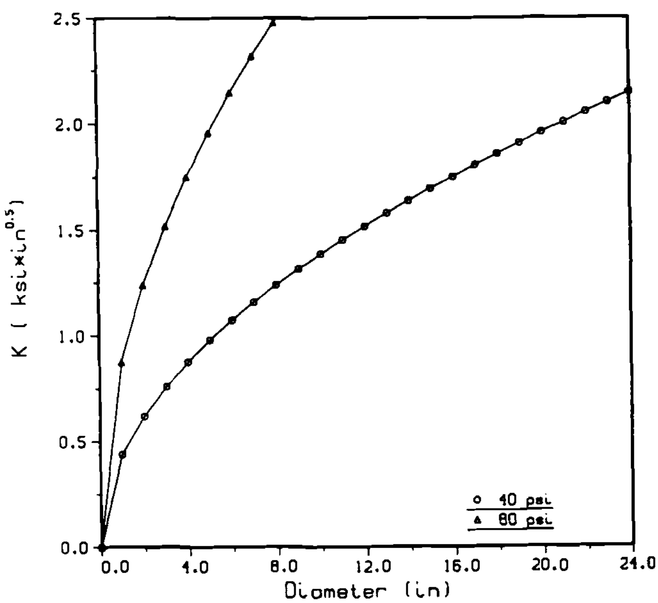

FIG. 6—*Stress intensity factor variation with diameter for a through-wall crack.*

While PE is a viscoelastic material, the time frame for RCP is usually short enough such that the material behavior can be considered as elastic, provided an appropriate dynamic modulus is used. Therefore, dynamic crack propagation in PE pipes is governed by the relationship

$$K(V, D, h, p, E_D) = K_D(V, T) \tag{4}$$

where K is the computed dynamic stress-intensity factor and K_D is the dynamic fracture propagation resistance, a material property dependent on crack speed, V, and temperature, T. As indicated by Eq 4, K is a function of crack speed, the mean pipe diameter, D, the wall thickness, h, the internal pressure, p, and the dynamic Young's modulus, E_D.

In addition to propagation, Eq 4 also indicates the conditions needed for crack arrest; for example, when the minimum value of K_D exceeds K because the crack propagates into a tougher piece of material. The arrest toughness, K_A, is defined as the minimum value of K_D. Unfortunately, arrest toughnesses have not been measured for the PE materials of interest. As an alternative, the absorbed energy in the Charpy impact test (C_V) is used. One of the deficiencies of the present work is that C_V is only loosely connected to K_A.

Earlier work [7] has shown that, over a range of admissible crack speeds, the steady-state driving force has a maximum value, K_{max}, for a given diameter, wall thickness, pressure, and dynamic Young's modulus. Thus, the boundary between propagate and arrest behavior for PE gas pipes is given by

$$K_{max} = K_A \tag{5}$$

Through a recently completed Southwest Research Institute (SwRI) internal research project, a three-dimensional fully coupled fluid/structure interaction code PFRAC (Pipeline FRacture Analysis Code) was developed for flawed fluid containment vessels [21]. In the case of axial crack propagation in pipes, very complex interactions take place as the gas escapes from the breach and as the flaps open behind the crack tip. The initial verification was done by simulating full-scale burst tests for large (1400 mm diameter) steel gas transmission pipelines. PFRAC consists of two primary portions; one to model the structural behavior and the second to model the gas flow, in addition to an interface routine that couples these modules together.

Computational Simulations of RCP in PE Pipes

A series of computational simulations of RCP in PE pipe were performed using PFRAC. The primary quantity of interest in these analyses is the stress-intensity factor that is calculated from the energy release rate, G, using the well-known relationship

$$K = \sqrt{E_D G} \tag{6}$$

A typical computational result showing the stress-intensity factor as a function of propagation distance is given in Fig. 7.

As shown in Fig. 7, as the crack begins to propagate from a plane of symmetry, the stress-intensity factor rises until steady-state conditions are achieved. After this, the driving force remains relatively constant. This plateau value is referred to as the steady-state stress-intensity factor. Some of the perturbations evident here are due to a finite element mesh dependency. An example of a deformed pipe shape during the steady-state phase of the

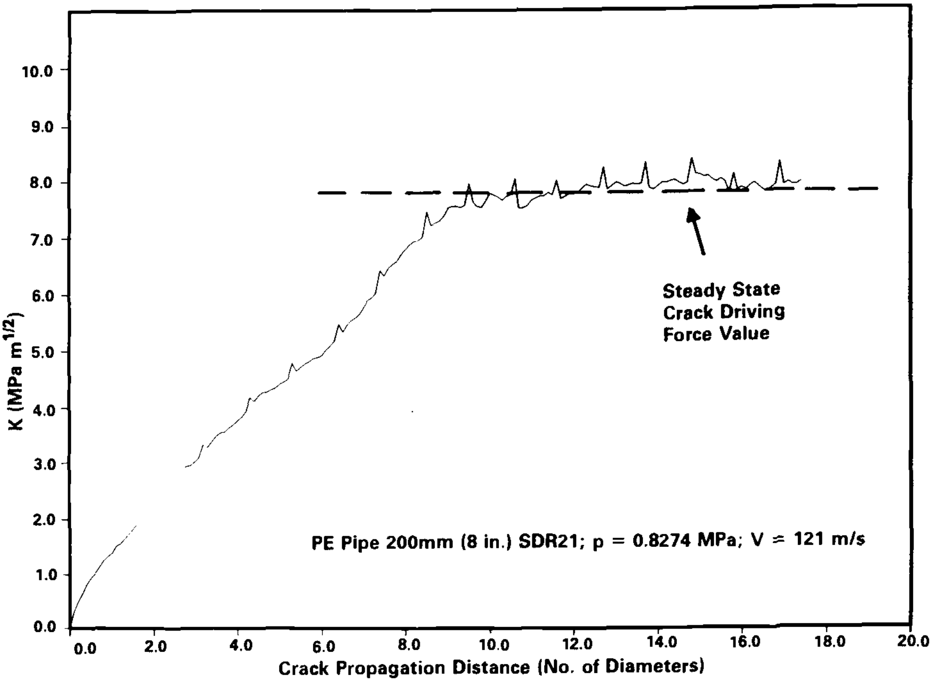

FIG. 7—*Stress intensity factor variation with distance during RCP for a PE pipe.*

propagation is illustrated in Fig. 8. This clearly shows the opening of the flaps behind the crack tip.

To investigate the variation of the steady-state stress-intensity factor with velocity, a series of analyses was carried out. The results are shown in Fig. 9. In all of these computations, the crack was allowed to propagate a distance that was sufficient for a clearly identifiable steady-state plateau to form. It is important to note that in these analyses a constant crack speed has been imposed. However, it is recognized that RCP may not occur at each speed under service conditions. The results are plotted in the normalized form of K/K_0, where K_0 is given by

$$K_0 = \frac{p_L}{2}\left(\pi \frac{D}{2}\right)^{1/2} (\text{SDR} - 1) \tag{7}$$

where p_L is the line pressure. The expression given by Eq 7 has been referred to by a number of names including the Irwin-Corten relationship, the critical stress formula, and the British Gas formula. It corresponds to the assumption that the pressure is constant ahead of the propagating crack tip and zero behind.

It is evident from Fig. 8 that a maximum driving force is obtained as a function of the assumed crack speed. This value is denoted as K_{max}. It is important to recognize that there is a unique K_{max} value for every combination of p_L, D, and SDR. That a maximum value as a function of crack speed exists can be understood by recognizing that, at low velocities, the crack-tip pressure is small and the inertia effects are unimportant. The crack-tip pressure is higher at increased velocities resulting in a larger value of K. However, when inertia

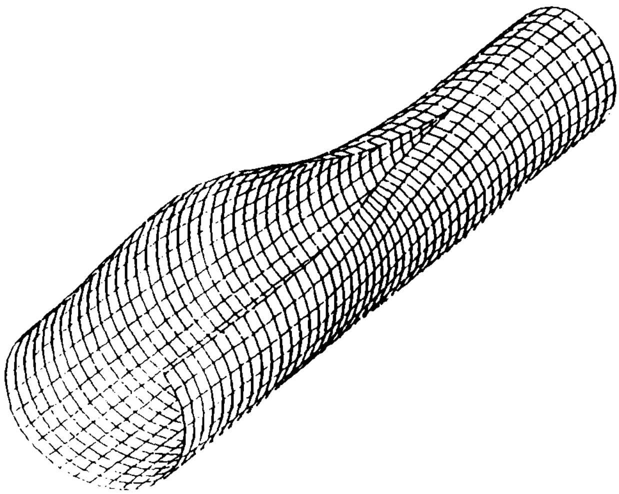

FIG. 8—*Deformed shape of a PE pipe during steady-state phase of RCP; 300-mm diameter;* p = *0.83 MPa;* v = *152 m/s.*

effects become significant at high velocities, K begins to drop again. Indeed, previous work has shown [15] that there is a limiting crack speed given by

$$V_1 = \frac{3}{4} C_0 \left(\frac{h}{D}\right)^{1/2} \tag{8}$$

where $C_0 = (E/\rho)^{1/2}$ is the elastic bar wave speed.

The maximum crack driving force for a given set of conditions is obviously a very important quantity. When inserted into the left-hand side of the crack propagation/arrest Eq 4, it establishes a bound on the arrest condition; see Eq 5. It is desirable to establish an analytical expression for the dependence of K_{max} on the diameter, SDR, pressure, and dynamic Young's modulus. Accordingly, a series of parametric studies were carried out where the various design quantities were varied. Using these results, the maximum driving force is assumed to take the form

$$K_{max} = K_0\hat{K} \tag{9}$$

where

$$\hat{K} = C\,(D/D_0)^n\,(\text{SDR} - 1)^m\,(E_D/E_S)^r \tag{10}$$

and C, n, m, and r are dimensionless constants. For convenience, D_0 and E_S are taken as 25.4 mm and 689.5 MPa (100 ksi), respectively. This leads to following values for the constants [22]

$$\begin{aligned} C &= 1.45 \\ n &= 0.67 \\ m &= -0.58 \\ r &= 0.79 \end{aligned}$$

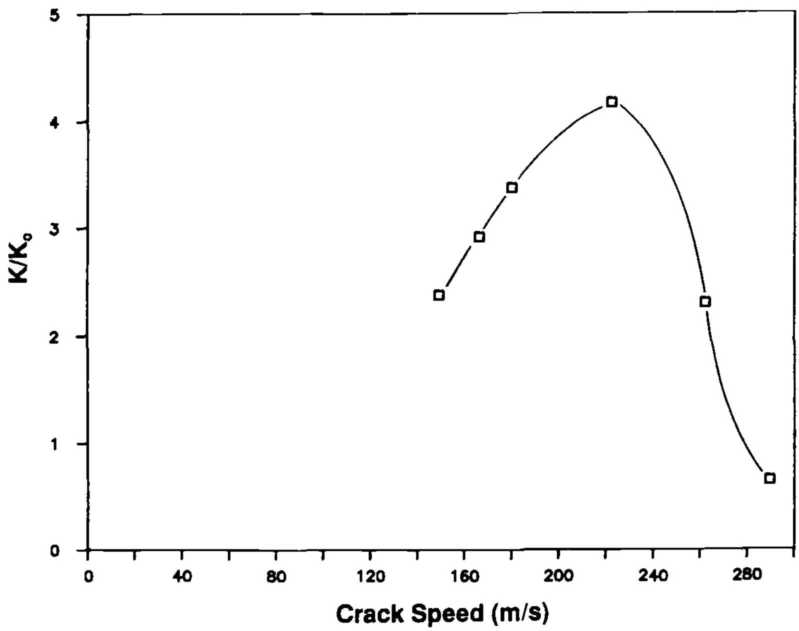

FIG. 9—*Parametric study of steady-state stress-intensity factor variation with assumed crack speed.*

Equation 9 can be used conveniently to estimate the maximum available stress-intensity factor for a given range of operating conditions. Thus, it will not be necessary to perform an extensive set of numerical computations for each proposed design option.

Development of a Crack-Arrest Criterion for PE Pipes

It was mentioned earlier that a significant amount of rapid crack propagation and arrest data exist that cover a wide range of materials. Since fracture toughness data are not available, Charpy energy can be used as an alternative. It is assumed that a crack will arrest when

$$K_{max} < A\ (E_s\ C_V)^{1/2} \tag{11}$$

where A is a dimensionless constant that remains to be determined. The quantity E_s is included for dimensional convenience. For all PE materials considered, it is taken as 689.5 MPa (100 ksi).

To determine Constant A in Inequality 11, a comparison was made with a diverse range of experimental data. This included many examples of both crack propagation and arrest for different pipe sizes and materials. These data were obtained from four independent sources: British Gas [*2*], Battelle [*5*], Du Pont [*6*], and Washington Gas Light [*23*]. In all cases, cracks were initiated, but in some cases they arrested after a few diameters. These are termed "arrests," while long running cracks are termed as "propagations." Figure 10 illustrates a plot of K_{max} against $(E_sC_V)^{1/2}$ for these data, with K_{max} calculated from Eq 9.

A well-defined demarcation between propagation and arrest in Fig. 10 is indicated by the solid line in the figure. From this plot, a value of 8.3 was estimated for Constant A. That

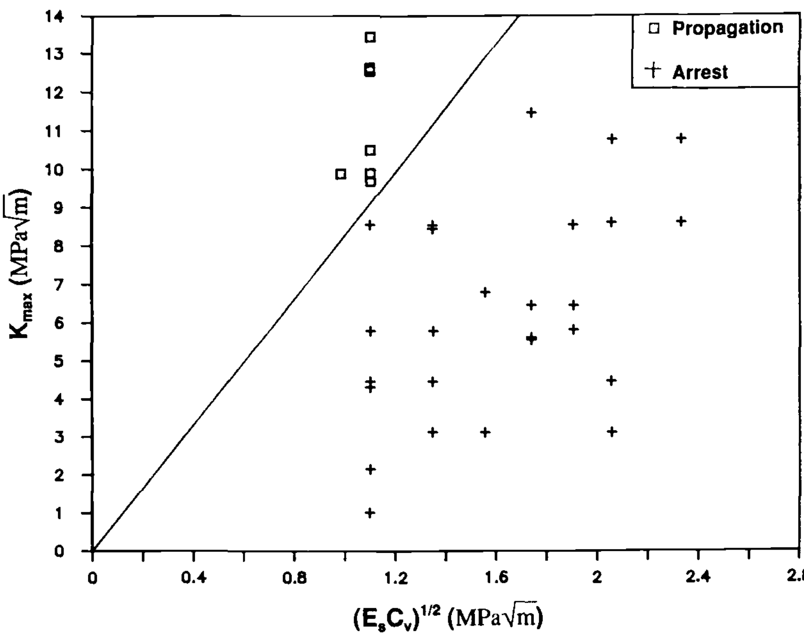

FIG. 10—*Experimental propagate and arrest data comparison for PE pipe.*

a simple straight line relationship, as given by the insertion of an equality sign in Inequality 11, has been obtained to separate all the propagation and arrest data demonstrates the fidelity of the RCP arrest relationship. Hence, the methodology developed here can be used conveniently in the design of PE distribution piping systems to prevent long running rapid cracks, even if initiation occurs. For example, with a specified set of pipeline conditions, pressure, diameter, etc., the maximum driving force can be estimated using Eq 9. Then, Inequality 11 can be used to calculate the minimum Charpy energy for the PE material at the lowest expected temperature that is necessary to prevent crack propagation.

Conclusions

While data representative of the SCG process in PE gas pipe materials can be obtained, the manner in which fracture mechanics principles and computational methods are applied to interpret the test results is an issue independent of the test procedure. In this regard, it was found that the commonly used linear elastic fracture mechanics interpretation is appropriate for those PE gas pipe materials having short craze lengths. Specifically, a necessary condition for the transferability of LEFM-based SCG data for the assessment of the long-term performance of PE pipes has been established in this work. This condition has quantified the permissible size of the craze attending the crack tip at the onset of crack growth such that it is within the zone of dominance of the LEFM crack-tip fields in the SCG specimen. Thus, this research has established that data obtained from the SCG test can be valid for making long-term performance assessments of slow crack growth in PE gas pipe materials.

To be sure of using SCG data correctly, it is necessary to estimate the craze zone length at the onset of cracking. This size must then be less than 6% of the ligament width. It remains to develop crack growth analysis procedures for materials where nonlinear viscoelastic behavior takes place.

In the course of the RCP work, two very useful expressions were developed. The first relates the maximum crack driving force to pipe quantities such as diameter, SDR, and E_D. A link between this quantity and the absorbed Charpy energy for the pipe material was then used to delineate between crack propagation and arrest. Both expressions agree very well with available experimental and computational results. Thus, the extremely encouraging results from this study represent a significant step forward in the design of PE pipes against rapid crack propagation. It also appears likely that similar procedures can be used in the design of the larger steel gas transmission pipelines.

These results also confirm earlier beliefs that a maximum driving force exists over a range of typical crack propagation velocities. Another pleasing aspect is that the model appears valid for a wide range of pipe materials. Equations 9 and 11 can be used as guidelines to prevent RCP in the design of PE pipes. However, a short-coming of the present RCP prevention criterion is that it is based on Charpy energy. There is no fundamental connection between this quantity and the arrest toughness. The obvious way to remedy this is to develop a small-scale test procedure for measurement of valid fracture toughness values for current and contemplated PE gas pipe materials. This work is presently underway and involves the use of a compact PE specimen placed between two pressure bars [*24*]. When completed, this will lead to a more fundamentally based fracture criterion.

Acknowledgments

The work on slow crack growth was performed for the Gas Research Institute (GRI) under Contract No. 5087-271-1483 to SwRI. The work on RCP has drawn upon results obtained for the Pipeline Research Committee of the American Gas Association through Contracts RA 182-527 and PR 15-526. The Advisory Committee for Research at SwRI supported the development of PFRAC and the application to RCP in PE pipes described in this paper. Support for the subsequent studies of the RCP problem is being provided by GRI under Contract No. 5088-271-1822 to SwRI. The authors would particularly like to express their appreciation to Dr. M. M. Mamoun of GRI for his many useful suggestions on the technical approach and for his overall encouragement for the use of sound technology for gas piping applications. The authors are also thankful for the assistance of Dr. R. Gillot in the use of the computer facilities at MPA, Stuttgart.

References

[*1*] Grieg, J. M. and Skiplorne, I. C., "Impact Fracture Toughness (Kc) Measurements of Polyethylene Gas Pipes," British Gas Engineering Research Station Report No. E428, Newcastle, U.K., April 1985.

[*2*] Grieg, J. M., "Fracture Propagation in 250 mm and 315 mm Polyethylene Gas Pipes," British Gas Engineering Research Station, Report No. E472, Newcastle, U.K., Dec. 1985.

[*3*] Gaube, E. and Muller, W. E., "Rapid Crack Propagation and Stoppage in PE Gas Pipes," Kunststoffe, Munich, FRG, Vol. 70, 1980, pp. 72–75.

[*4*] Usclat, D. and Nussbaum, M., "Evaluating Criteria for Characterizing the Mechanisms of Rapid Crack Propagation in PE Pipes," Gaz de France Report, undated.

[*5*] Krishnaswamy, P., Maxey, W., Leis, B., and Hulbert, L., "A Design Procedure and Test Method to Prevent Rapid Crack Propagation in Polyethylene Gas Pipe," Battelle Columbus Division Report to the Gas Research Institute, Oct. 1986.

[*6*] Palermo, E. F., private communication to Southwest Research Institute, San Antonio, Dec. 1988.

[*7*] Kanninen, M. F., Cardinal, J. W., and Morrow, T. B., "An Analysis of Rapid Crack Propagation in Polyethylene Gas Distribution Pipes," Topical Report to the Gas Research Institute under Contract 5087-271-1483 (draft), Southwest Research Institute, San Antonio, TX, Dec. 1987.

[8] Lu, X. and Brown, N., "The Relationship of the Initiation Stage to the Rate of Slow Crack Growth in Linear Polyethylene," *Journal of Materials Sciences*, Vol. 21, 1986, pp. 2423–2429.
[9] Moet, A. and Chudnovsky, A., "A Theory for Accelerated Slow Crack Propagation in Polyethylene Fuel Pipes," Final Report, GRI Report No. 87/0232, prepared by Case Western Reserve University, Cleveland, for the Gas Research Institute, Aug. 1987.
[10] Leis, B., et al., "Investigation of the Validity of the Slow Crack Growth Test," Topical Report, GRI Report No. 88/O131, prepared by Battelle Columbus Division, Columbus, for the Gas Research Institute, May 1988 (draft).
[11] Underwood, J. H., Kapp, J. A., and Witherell, M. D., "Fracture Testing with Arc Bend Specimens," *Fracture Mechanics: Seventeenth Volume, ASTM STP 905*, J. H. Underwood et al., Eds., American Society for Testing and Materials, Philadelphia, 1986, pp. 279–296.
[12] Kanninen, M. F., O'Donoghue, P. E., Popelar, C. H., and Kenner, V. H., "A Fracture Mechanics Assessment of the Slow Crack Growth Test for Predicting Long Time Performance Polyethylene Gas Pipes," Final Report to GRI under Contract No. 5087-271-1483, Southwest Research Institute, San Antonio, TX, May 1988 (draft).
[13] Kanninen, M. F., O'Donoghue, P. E., Popelar, C. H., and Kenner, V. H., "A Viscoelastic Fracture Mechanics Assessment of Slow Crack Growth in Polyethylene Gas Distribution Pipe Materials," *Engineering Fracture Mechanics*, in press.
[14] Kanninen, M. F., O'Donoghue, P. E., Cardinal, J. W., Green, S. T., Curr, R. M., and Williams, J. G., "A Fracture Mechanics Analysis of Rapid Crack Propagation and Arrest in Polyethylene Gas Pipes," *Proceedings*, Eleventh Plastic Gas Pipe Symposium, American Gas Association, 3–5 Oct. 1989.
[15] Kanninen, M. F. and Popelar, C. H., *Advanced Fracture Mechanics*, Oxford University Press, New York, 1985.
[16] Shih, C. F., "J-Dominance under Plane Strain Fully Plastic Conditions: The Edge Crack Panel Subject to Combined Tension and Bending," *International Journal of Fracture*, Vol. 29, 1985, pp. 73–84.
[17] Knott, J. F., *Fundamentals of Fracture Mechanics*, Butterworths, London, 1979.
[18] Popelar, C. H., Kenner, V. H., and Popelar, C. F., "Slow Crack Growth in Polyethylene Pipe Materials: Part 2. Analysis," *Advances in Fracture Research*, K. Salama, K. Ravi-Chandar, D. M. R. Taplin, and P. Rama Rao, Eds., Pergamon, New York, Vol. 4, 1989, pp. 2861–2869.
[19] Hulbert, L. E., et al., *Field Failure Reference Catalog for Polyethylene Gas Piping*, First Edition, January 1980–December 1984, GRI Report No. 84/O235.1, prepared by Battelle Columbus Division, Columbus, OH, March 1986.
[20] Folias, E. S., "A Finite Line Crack in a Pressurized Cylinder," *International Journal of Fracture Mechanics*, Vol. 1, 1965, pp. 104–113.
[21] Kanninen, M. F., O'Donoghue, P. E., Green, S. T., Freitas, C. J., Morrow, T. B., Dexter, R. J., and Bowles, P. K., "The Development and Verification of Dynamic Fracture Mechanics Analysis Procedures for Flawed Fluid Containment Boundaries," Final Report to the Southwest Research Institute Internal Research Committee on Project 06-9452, San Antonio, TX, Dec. 1989.
[22] Kanninen, M. F., O'Donoghue, P. E., Cardinal, J. W., Green, S. T., Curr, R. M., and Williams, J. G., "A Fracture Mechanics Analysis of Rapid Crack Propagation and Arrest in Polyethylene Gas Pipes," *Proceeding*, Eleventh Plastic Gas Pipe Symposium, American Gas Association, 3–5 Oct. 1989, pp. 334–343.
[23] Gunther, K., "Usage of Large Diameter Polyethylene Pipe at Washington Gas Light Company," Eleventh Plastic Fuel Gas Pipe Symposium, San Francisco, Oct. 1989.
[24] Couque, H., Dexter, R. J., and Hudak, S. J., "Using Small Specimens to Measure Dynamic Fracture Properties of High Toughness Steels," Symposium on Rapid Load Fracture Testing, San Francisco, 1990, (accepted for publication by ASTM).

Wen-Hwa Chen[1] *and Chin-Cheng Huang*[1]

Three-Dimensional Analysis of Thermoelastic Fracture Problems

REFERENCE: Chen, W-H. and Huang, C-C., "**Three-Dimensional Analysis of Thermoelastic Fracture Problems,**" *Fracture Mechanics: Twenty-Second Symposium (Volume II), ASTM STP 1131*, S. N. Atluri, J. C. Newman, Jr., I. S. Raju, and J. S. Epstein, Eds., American Society for Testing and Materials, Philadelphia, 1992, pp. 274–285.

ABSTRACT: This paper deals with three-dimensional thermoelastic fracture problems using both analytical and numerical results. The analytical temperature distribution of an infinite solid with an embedded elliptical insulated crack subjected to an uniform heat flow solved by the authors is first described briefly to provide a verification for the three-dimensional finite element model with collapsed quarter-point singular elements around the crack front. To determine the thermal stress-intensity factors, the three-dimensional path-independent integrals that are physically the energy release rates per unit area of crack extension along respective directions of crack growth are employed and computed for three-dimensional realistic thermoelastic fracture problems.

To evaluate the influence of geometry and Poisson's ratio on the computation of temperature distributions and thermal stress-intensity factors for various thermal conditions, several representative examples are presented. The variations of pure and mixed-mode thermal stress-intensity factors along the crack front are also studied for both through and part-through cracks in finite elastic solids.

Good agreements between the computed results and referenced solutions show the validity and accuracy of the present analysis.

KEY WORDS: thermoelastic fracture analysis, path-independent integral, thermal stress-intensity factor, part-through crack, fracture mechanics, fatigue (materials)

Many structural components such as turbines, combustion chambers, nuclear reactors, pipelines, storage tanks, etc. are often serviced in severe temperature environments. Since unavoidable cracks or crack-like defects can occur during the manufacturing process of structures, the local thermal stresses at the regions near the imperfections are elevated even under normal thermal conditions and may initiate crack propagation or breakdown of the structures. As is commonly known, the geometries of such cracks or crack-like defects are usually complicated and a three-dimensional analysis is required to study the thermoelastic fracture behaviors of the cracked structure.

The two-dimensional thermoelastic fracture problems with various types of heat transfer conditions on the crack surfaces have been discussed extensively in the literature [*1–9*]. However, the work that is devoted to the study of three-dimensional problems is still limited. Using the Hankel transform technique, Florence et al. [*10*] studied the thermoelastic fracture problem of an infinite solid with a penny-shaped insulated crack subjected to a uniform heat flow. The local intensification of the temperature gradient accompanied by intensified thermal stresses near the crack front was solved. Bregman and Kassir [*11*] analyzed fracture

[1]Professor and graduate student, respectively, Department of Power Mechanical Engineering, National Tsing Hua University, Hsinchu, Taiwan, 30043, Republic of China.

behaviors of dissimilar media containing an interface penny-shaped insulated crack. Tsai [12] and Singh et al. [13] extended the study to a transversely isotropic medium with a penny-shaped crack and an external circular crack, respectively. In addition, Uchiyama and Tsuchida [14] obtained an analytical solution of a long cylinder with a penny-shaped insulated crack subjected to a steady uniform heat flow, and the effects of free boundary on the computation of thermal stress-intensity factors were discussed. However, those studies [10–14] were solved only for axisymmetric type problems. Hence, a more general study needs to be made for realistic three-dimensional thermoelastic fracture problems.

The objective of this work is thus devoted to deal with three-dimensional thermoelastic fracture behaviors for a general elastic solid containing a through or part-through crack under various thermal conditions. An analytical solution of the three-dimensional temperature field for an infinite solid with an embedded elliptical insulated crack subjected to a steady uniform heat flow, as obtained by the authors earlier, is presented to verify the solution obtained by a three-dimensional finite-element model with collapsed quarter-point singular elements [15] around the crack front. Based on the accurate model of computing the temperature field, the thermoelastic fracture behavior of the structure is then studied. To predict the fracture behaviors of cracked structures, accurate determinations of stress-intensity factors are essential. Among various methods in evaluating stress intensity factors, the use of crack-tip integral fracture parameters becomes one of the most effective ways [9]. Based on the authors' previous work without using a specified smooth function needed for a standard equivalent domain integral (EDI) method [16,17], a simpler and more accurate approach of using three-dimensional path-independent integrals that are physically the energy release rates per unit area of crack extension along respective directions of crack growth is employed here.

Several examples with through or part-through cracks under various thermal conditions are presented to evaluate the influence of crack geometry and Poisson's ratio on the computation of temperature field and thermal stress-intensity factors. Good agreements between the computed results and referenced solutions show the validity and applicability of the present analysis.

Analytical Solution of Three-Dimensional Temperature Fields

To verify the numerical results obtained in this study for completeness, the analytical solution for a three-dimensional temperature field, as solved in the authors' previous work [18], is described here briefly. Consider an infinite solid with an embedded elliptical insulated crack subjected to a steady uniform heat flow with temperature gradient, q, as shown in Fig. 1, the crack region on the midplane, $z = 0$, is denoted as $x^2/a^2 + y^2/b^2 \leq 1$. Here, (x,y,z) are the Cartesian coordinates, and a and b are the half length of the major and minor axes of the elliptical crack. Due to the existence of the crack, the elevated temperature gradient near the crack front may be induced. Using the conformal mapping technique, the elliptical crack region can be first mapped conformally onto a penny-shaped crack for which the solution of the temperature field on the crack surface is available. After solving the heat conduction equation, the thermal boundary conditions on the crack plane are then satisfied through the use of inverse Fourier transformation. The complete solution of the temperature field, $\theta(x,y,z)$, is thus quoted as (a detailed derivation can be seen in Ref *18*)

$$\theta(x,y,z) = qz + \frac{2ab^2q}{\pi E(k)} \int_0^\infty \int_0^\infty \frac{\sin p - p\cos p}{p^3} \cos\lambda x \cos\xi y \, e^{-z\sqrt{\lambda^2+\xi^2}} \, d\lambda d\xi \tag{1}$$

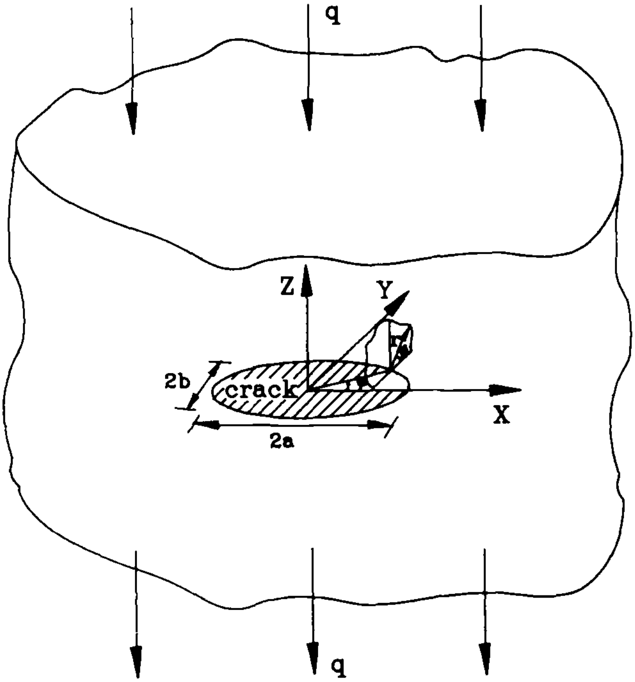

FIG. 1—*An infinite solid with an elliptical crack subjected to uniform heat flow.*

where $E(k)$ is the complete elliptical integral of the second kind ($= \int_0^{\pi/2}\sqrt{1 - k^2\sin^2\eta}\,d\eta$), $k^2 = 1 - b^2/a^2$, λ and ξ are real constants, and $p = \sqrt{a^2\lambda^2 + b^2\xi^2}$. The second term of the right-hand side of Eq 1 denotes the variation of temperature disturbed by the crack. As a result, the temperature distribution on the elliptical crack surface can be further expressed as

$$\theta(x,y,0) = \frac{b}{E(k)}q\sqrt{1 - \left(\frac{x^2}{a^2} + \frac{y^2}{b^2}\right)}$$

For the case of the penny-shaped crack, say $a = b$, $\theta(x,y,0) = 2q/\pi\sqrt{a^2 - (x^2 + y^2)}$, which is same as that obtained by Florence et al. [*10*].

In addition, based on the coordinate system (r,ϕ,φ) along and around the crack front (see Fig. 1), the near-field temperature distribution (taking r as a small value) on the elliptical crack plane (that is, $z = 0$) can be rewritten as

$$\theta(r,\pi,\varphi) = \frac{bq}{E(k)}\left\{\frac{2r(a^2\sin^2\varphi + b^2\cos^2\varphi)^{1/2}}{ab} + \frac{r^2(a^4\sin^2\varphi + b^4\cos^2\varphi)}{a^2b^2(a^2\sin^2\varphi + b^2\cos^2\varphi)}\right\}^{1/2}$$

$$\text{for } \frac{x^2}{a^2} + \frac{y^2}{b^2} < 1,\ z = 0$$

and

$$\theta(r,0,\varphi) = 0 \quad \text{for } \frac{x^2}{a^2} + \frac{y^2}{b^2} \geq 1,\ z = 0$$

As seen here, the $r^{1/2}$ type behavior of the near-field temperature distribution and $r^{-1/2}$ type singularity of temperature gradient on the crack surface are observed.

Calculation of Thermal Stress-Intensity Factors

To calculate the thermal stress-intensity factors, the path-independent integrals, $\tilde{J}_1$, $\tilde{J}_2$, and $\tilde{G}_3$, that are physically the energy release rates per unit area of crack extension along respective directions of crack growth in the volume surrounding the crack front increment derived by the authors [*19*] are employed. Selecting a thin slice of cracked structure as shown in Fig. 2, the local orthogonal coordinates (X_1,X_2,X_3) denote the normal, binormal, and tangential front increments, respectively, and the origin, o, is located at the midpoint of the crack front increment. These path-independent integrals at the midpoint, o, are shown as follows

$$\tilde{J}_k = \frac{1}{B}\left[\int_V \frac{\partial W_e}{\partial X_k}\,dV - \int_{A+A_s} T_i \frac{\partial u_i}{\partial X_k}\,dA + \int_V \sigma_{ij}\frac{\partial \varepsilon_{ij}^*}{\partial X_k}\,dV\right] \tag{2}$$

and

$$\tilde{G}_3 = \frac{1}{B}\left[\int_V \frac{\partial W_e^{(3)}}{\partial X_1}\,dV - \int_{A+A_s} T_3 \frac{\partial u_3}{\partial X_1}\,dA + \int_V \sigma_{3j}\frac{\partial \varepsilon_{3j}^*}{\partial X_1}\,dV\right] \tag{3}$$

where the subscript index $_k$ = 1,2 and $_{i,j}$ = 1,2,3; W_e is the elastic strain energy density, u_i is the displacement vector, and σ_{ij} is the stress tensor; ε_{ij}^* is the thermal strain tensor and denoted as $\varepsilon_{ij}^* = \alpha\delta_{ij}\Delta\theta$; α is the thermal expansion coefficient, δ_{ij} is kronecker delta, and

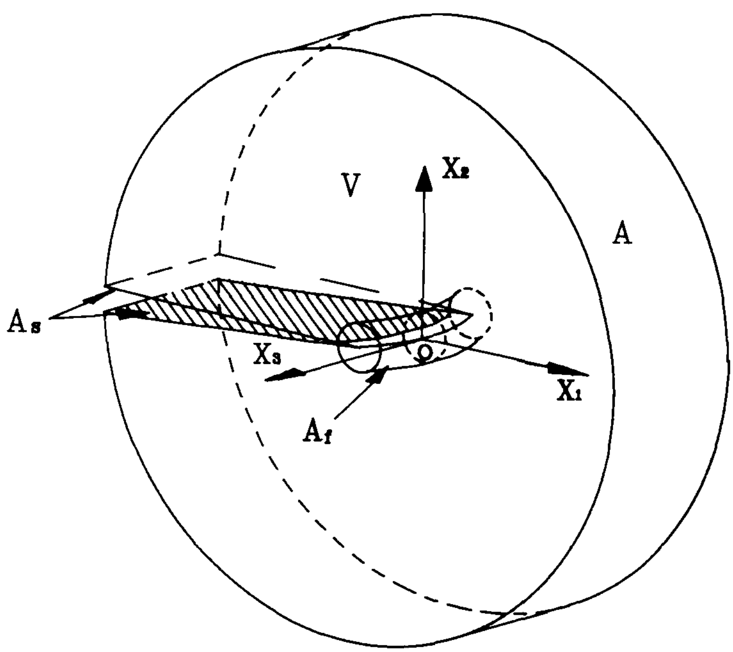

FIG. 2—*Integration domains of path-independent integrals* $\tilde{J}_1$, $\tilde{J}_2$, *and* $\tilde{G}_3$.

$\Delta\theta$ is the temperature variation; $W_e^{(3)}$ is part of the elastic strain energy density that is calculated using stress, σ_{3j}, and strain components, ε_{3j}, say, $W_e^{(3)} = \frac{1}{2}\,\sigma_{3j}\varepsilon_{3j}$; B denotes the length of the crack front increment considered; V is the volume of the slice enclosing the crack front increment except the small volume surrounded by the assumed fracture region, A_f. Hence, the first terms in Eqs 2 and 3 are integrable. A denotes the entire surface enclosing the slice of the cracked structure except the crack surface, A_S, and fracture region, A_f. The detailed formulation of the path-independent integrals as stated in Eqs 2 and 3 can be referred to in the authors' previous work [19]. The path-independence of $\tilde{J}_k$ and $\tilde{G}_3$ has been also tested numerically.

To calculate the thermal stress-intensity factors indirectly, the relationship between the thermal stress-intensity factors and path-independent integrals, $\tilde{J}_1$, $\tilde{J}_2$, and $\tilde{G}_3$, can be expressed as [19]

$$K_{\mathrm{I}} = \frac{1}{2}\sqrt{\frac{E}{1-\nu^2}}\left(\sqrt{\tilde{J}_1 - \tilde{J}_2 - \tilde{G}_3} + \sqrt{\tilde{J}_1 + \tilde{J}_2 - \tilde{G}_3}\right)$$

$$K_{\mathrm{II}} = \frac{1}{2}\sqrt{\frac{E}{1-\nu^2}}\left(\sqrt{\tilde{J}_1 - \tilde{J}_2 - \tilde{G}_3} - \sqrt{\tilde{J}_1 + \tilde{J}_2 - \tilde{G}_3}\right)$$

and

$$K_{\mathrm{III}} = \sqrt{2\mu\tilde{G}_3}$$

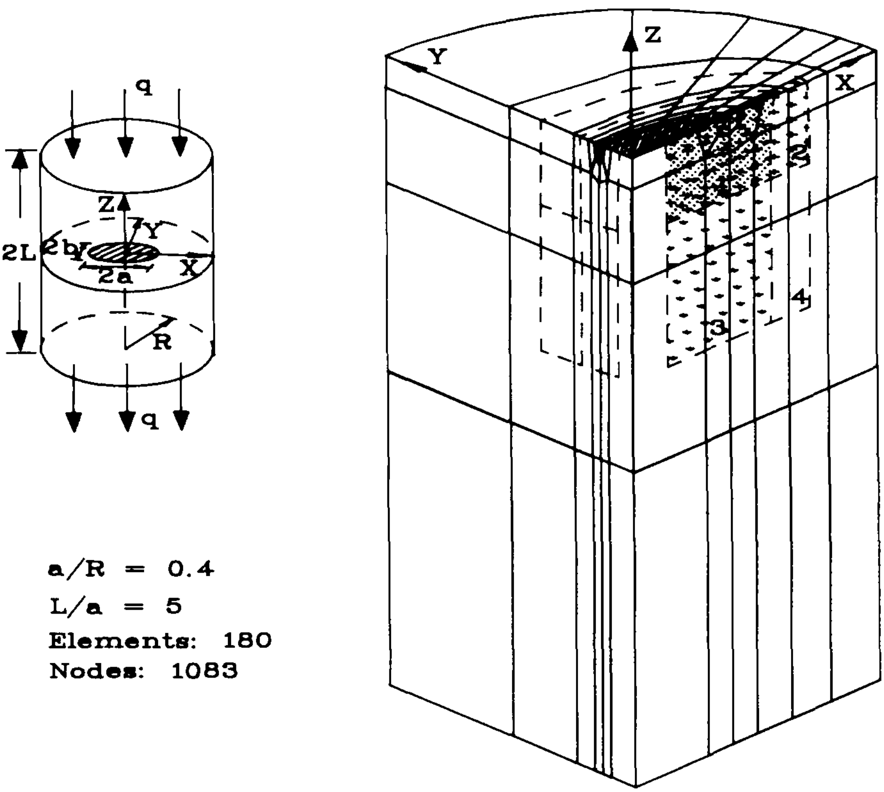

FIG. 3—*Finite element model of a cylinder with an embedded elliptical crack.*

where K_I, K_{II}, and K_{III} represent the thermal stress-intensity factors for opening, sliding, and tearing modes, respectively; E is the Young's modulus; ν is the Poisson's ratio; and μ is the shear modulus.

Fracture Mechanics Analysis of Three-Dimensional Thermoelastic Problems

To evaluate the applicability of the present analysis, several representative examples with through or part-through cracks are solved using the finite element method. The geometry and Poisson's effect that have been recognized as the important factors for evaluating the strength of three-dimensional problems are also studied in the work.

A Long Cylinder with an Embedded Elliptical Insulated Crack Subjected to Uniform Heat Flow

In industrial applications, a crack due to material imperfection embedded in a solid (for example, a transmission shaft) is often found during the manufacturing process. Because of the geometric discontinuity, the heat conduction and radiation between the upper and lower crack surfaces are negligible and the embedded crack can be treated as an insulated crack. To study such thermoelastic fracture behaviors, a long cylinder with an embedded elliptical insulated crack subjected to a steady uniform heat flow, as displayed in Fig. 3, is modeled. Due to the symmetry of geometry, only one eighth is treated and antisymmetric thermal loading is taken. There are 180 elements (including 24 collapsed quarter-point singular elements and 156 conventional brick elements) and 1083 nodes employed in the analysis. The temperature distribution on the elliptical crack surface is first verified with the analytical solution obtained earlier in this paper where a is the half length of the major axis of the crack and R is the radius of the cylinder. As seen in Fig. 4, the variation of normalized

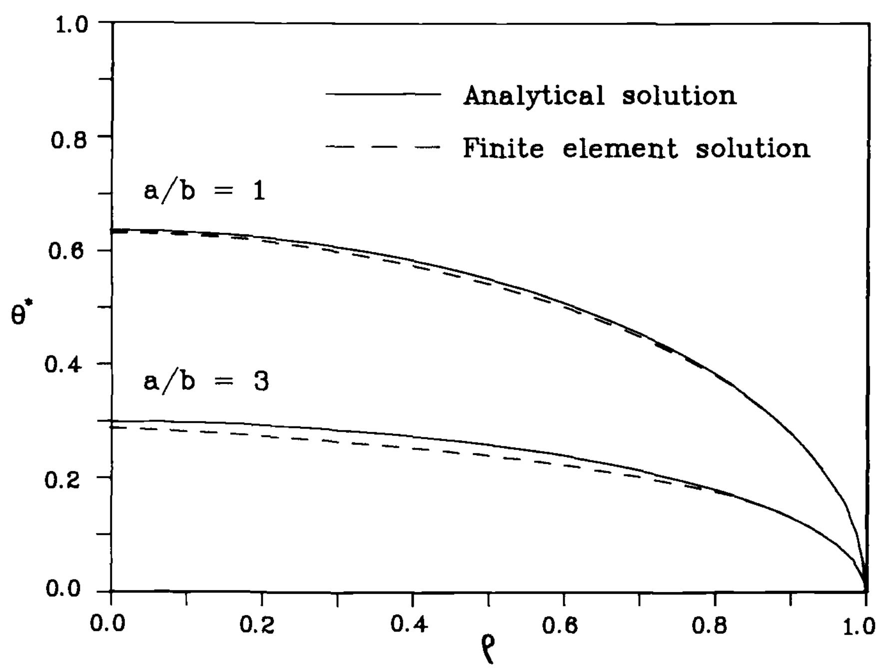

FIG. 4—*Normalized temperature distribution on the crack surface.*

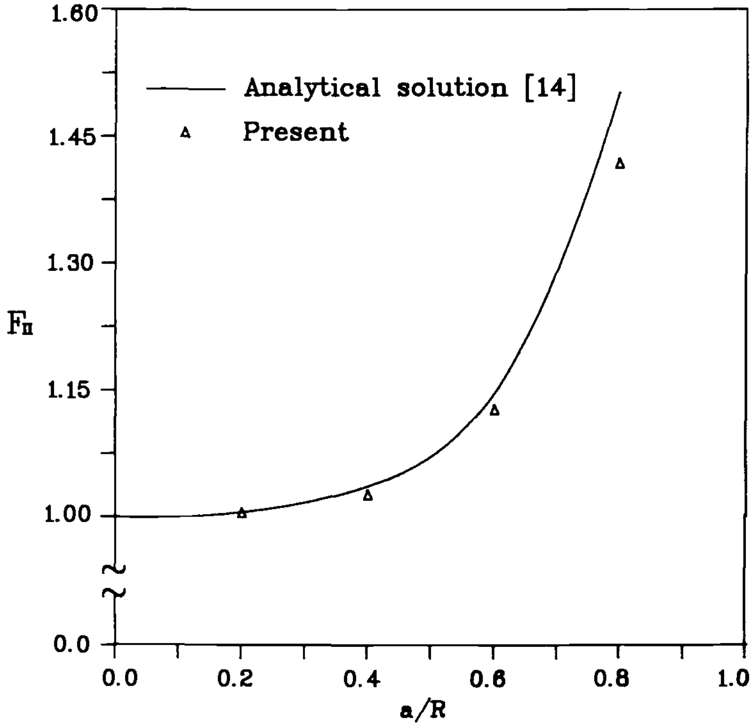

FIG. 5—*Normalized thermal stress-intensity factor,* F_{II}, *versus nondimensional radius of penny-shaped crack.*

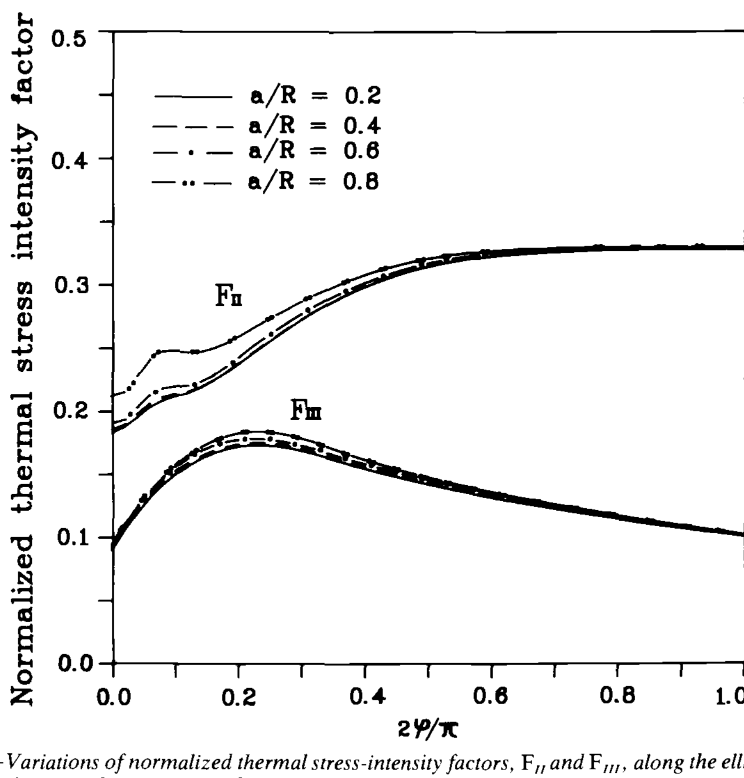

FIG. 6—*Variations of normalized thermal stress-intensity factors,* F_{II} *and* F_{III}, *along the elliptical crack front for various nondimensional radius.*

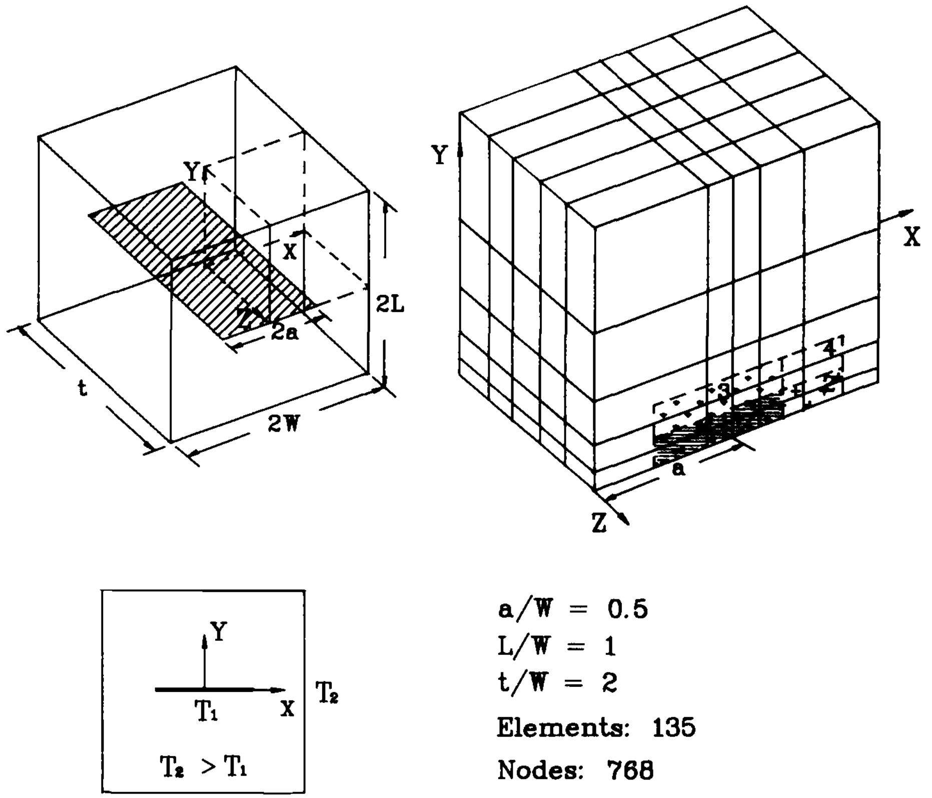

FIG. 7—*Finite element model of a thick plate with a through central crack.*

temperature, $\theta^* = \theta/qa$, on the crack surface versus normalized radius $\rho = \sqrt{x^2/a^2 + y^2/b^2}$ for $a/b = 1$ and 3 is displayed (a is constant). The singular characteristics of temperature gradient near the crack front as ρ approaches 1 is observed. It is noted that the maximum normalized temperatures are always found at the center of the crack surface. Good correlations between the computed results and obtained analytical solutions show the accuracy of the present finite element model. The fracture behaviors of the long cylinder are also studied. To calculate the path-independent integrals, the integration domains selected surrounding the crack front of each slice are also displayed in Fig. 3. The effect of the free lateral boundary of the cylinder on the computation of thermal stress intensity factors is also considered for $a/R = 0.2$, 0.4, 0.6, and 0.8, respectively. For comparison purposes, the pure Mode II problem is solved for the case of $a/b = 1$. The variation of normalized Mode II thermal stress-intensity factor, $F_{II} = K_{II}/K_{II\infty}$ versus a/R is shown in Fig. 5. $K_{II\infty} = E\alpha q a^{3/2}/3(1 - \nu)\sqrt{\pi}$ is the analytical solution of an infinite solid with a penny-shaped crack [14]. Good agreements between present computed results and referenced solutions [14] are observed with the largest discrepancy about 6% at $a/R = 0.8$. The larger influence of free lateral boundaries is obtained as a/R increases. F_{II} is equal to 1 as a/R approaches zero for the case of the crack embedded in an infinite solid, and F_{II} tends to infinite as a/R approaches 1. Figure 6 displays the variation of F_{II} and F_{III} ($= K_{III}/K_{II\infty}$) along the crack front for the case of elliptical crack with $a/b = 3$ versus various values of a/R. For all a/R, F_{II} is maximum at the minor axis and minimum at the major axis. However, the maximum value of F_{III} occurs near $2\varphi/\pi = 0.2$. Again, the mixed-mode normalized

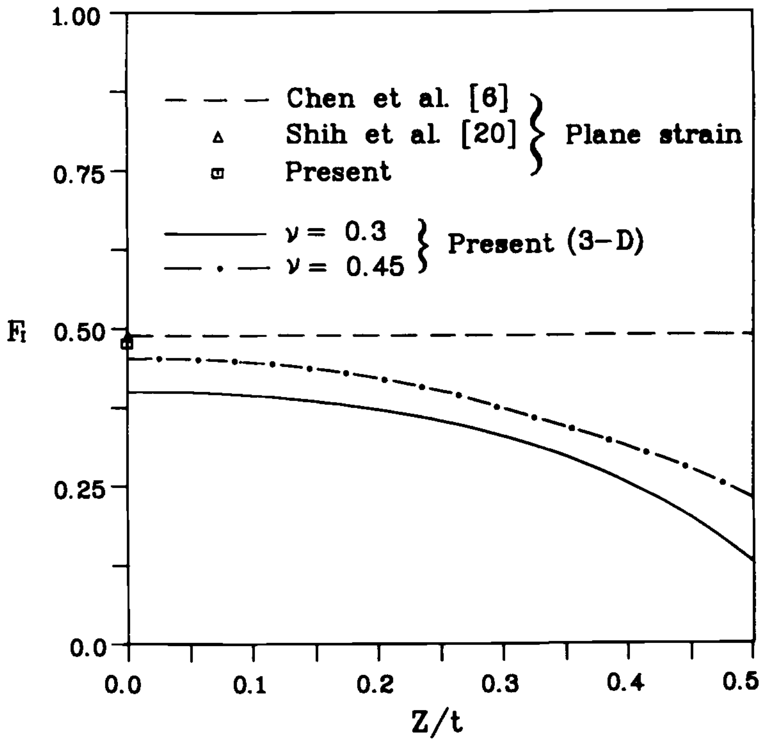

FIG. 8—*Variations of normalized thermal stress-intensity factor, F_I, across the thickness of plate with different Poisson's ratios.*

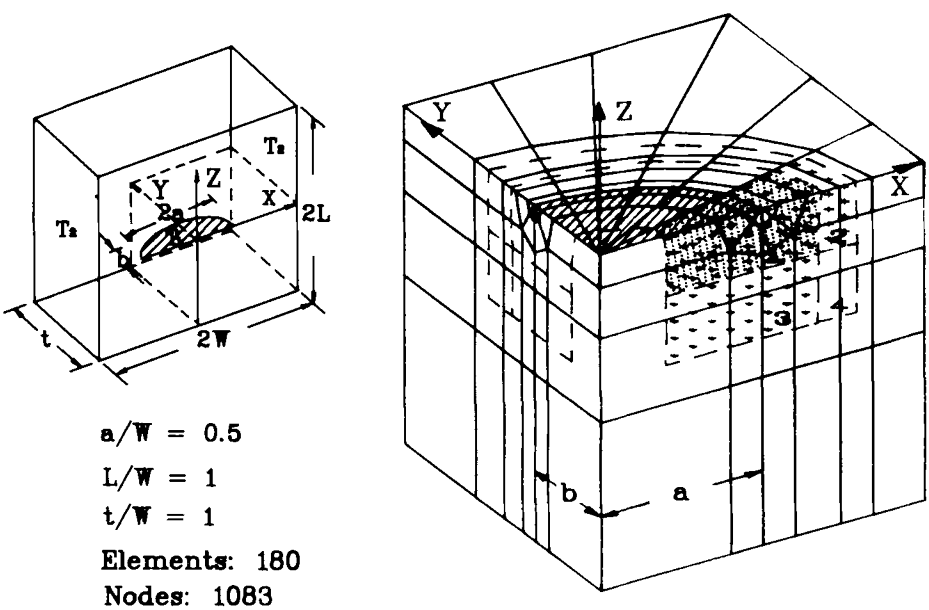

FIG. 9—*Finite element model of a thick plate with a part-through surface crack.*

thermal stress-intensity factors, F_{II} and F_{III}, increase as a/R increases. Due to the influence of the free boundary that occurred near the major axis, remarkable variations of F_{II} can be obtained while there is nearly no change for F_{II} and F_{III} near the minor axis.

A Thick Plate with a Through Central Crack

A thick plate with a through central crack subjected to specific thermal loadings is solved for different Poisson's ratios. As seen in Fig. 7, only one eighth of the problem is modeled due to the symmetry of geometry and loading conditions. There are 135 elements (including 20 collapsed quarter-point singular elements and 115 conventional brick elements) and 768 nodes employed. Four different integration domains are selected in the model. Figure 8 displays the variations of normalized Mode I thermal stress-intensity factor, F_I ($= K_I/E\alpha(T_2 - T_1)\sqrt{w}$) across the thickness of the plate for $a/w = 0.5$. The difference between the three-dimensional and plane strain solutions is noted. For comparison purposes, the plane strain solutions obtained using the procedure developed by Shih et al. [*20*], Chen et al. [*6*], and present technique for the case of $\nu = 0.3$ are also shown, respectively. The location of the largest F_I is found at the middle plane ($z = 0$) of the plate. The influence of the magnitude of Poisson's ratio on the computation of thermal stress intensity factors is also noted.

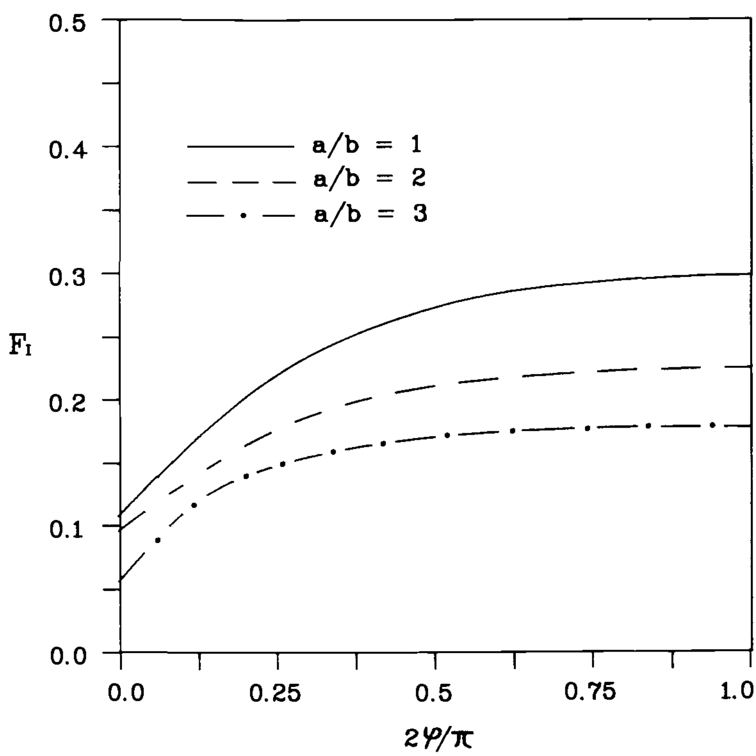

FIG. 10—*Variations of normalized thermal stress-intensity factor,* F_I, *along the surface crack front versus crack aspect ratios* ($\nu = 0.3$).

A Thick Plate with a Part-Through Surface Crack

A thick plate with a part-through crack, for example, a semielliptical surface crack subjected to given thermal loadings is then solved. As seen in Fig. 9, the temperature on the crack surface is T_1 and on the surfaces at $x = \pm w$ is T_2, $T_2 > T_1$. The other faces of the plate are insulated. Again, due to the symmetry of geometry and loading conditions, only one quadrant of the problem is modeled using 180 elements (including 24 collapsed quarter-point singular elements and 156 conventional brick elements) and 1083 nodes. Figures 10 and 11 show the variations of F_I along the crack front with various crack aspect ratios (a is kept constant) and Poisson's ratios for $a/w = 0.5$, respectively. In these cases, maximum F_I is found at the minor axis of the crack, say, $2\varphi/\pi = 1$, and minimum F_I is observed at the major axis. It is noted that F_I decreases as the aspect ratio, a/b, increases mainly due to the change of the area of crack region. As would be expected, as $a,b \rightarrow \infty$, since there is no crack found in the plate, F_I approaches to zero. Further, larger results of F_I are obtained for larger ν.

Conclusions

The complete analytical solution of the temperature field for an infinite solid with an embedded elliptical insulated crack subjected to a steady uniform heat flow has been presented for the verification of the three-dimensional finite element analysis model devised. To calculate the thermal stress-intensity factors, the three-dimensional path-independent

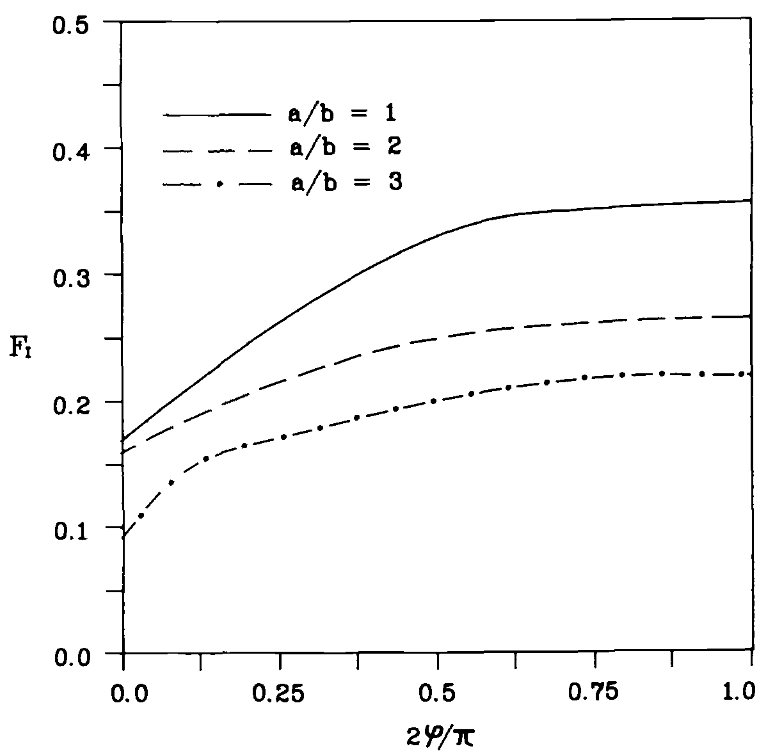

FIG. 11—*Variations of normalized thermal stress-intensity factor,* F_I, *along the surface crack front versus crack aspect ratios* ($\nu = 0.45$).

integrals that are physically the energy release rates per unit area of crack extension along respective directions of crack growth have been employed successfully and computed for several three-dimensional thermoelastic fracture problems containing through or part-through cracks. The effects of thickness, boundary, and Poisson's ratio on the computation of thermal stress-intensity factors along the crack front are also investigated thoroughly. The analysis procedure developed in this work has been demonstrated as an efficient tool in dealing with three-dimensional thermoelastic fracture problems.

References

[1] Sih, G. C., *Transactions*, American Society of Mechanical Engineers, *Journal of Applied Mechanics*, Vol. 29, 1962, pp. 587–589.

[2] Sekine, H., *Engineering Fracture Mechanics*, Vol. 9, 1977, pp. 499–507.

[3] Hellen, T. K. and Cesari, F., *Engineering Fracture Mechanics*, Vol. 12, 1979, pp. 469–478.

[4] Emery, A. F., Neighbors, P. K., Kobayashi, A. S., and Love, W. J., *Transactions*, American Society of Mechanical Engineers, *Journal of Pressure Vessel Technology*, Vol. 100, 1977, pp. 100–105.

[5] Wilson, W. K. and Yu, I. W., *International Journal of Fracture*, Vol. 15, No. 4, 1979, pp. 377–387.

[6] Chen, W. H. and Ting, K., *Nuclear Engineering and Design*, Vol. 90, 1985, pp. 55–65.

[7] Ting, K. and Chen, W. H., *Journal*, American Institute of Aeronautics and Astronautics, Vol. 26, No. 1, 1987, pp. 119–121.

[8] Chen, W. H. and Ting, K., *Computational Mechanics*, Vol. 4, 1989, pp. 1–10.

[9] Brust, F. W., Nakagaki, M., and Springfield, C., *Engineering Fracture Mechanics*, Vol. 33, No. 4, 1989, pp. 561–579.

[10] Florence, A. L. and Goodier, J. N., *International Journal of Engineering Sciences*, Vol. 1, 1963, pp. 533–540.

[11] Bregman, A. M. and Kassir, M. K., *International Journal of Fracture*, Vol. 10, No. 1, 1974, pp. 87–98.

[12] Tsai, Y. M., *Journal of Thermal Stresses*, Vol. 6, 1983, pp. 379–389.

[13] Singh, B. M., Danyluk, H. T., and Selvadurai, A. P. S., *International Journal of Solids and Structures*, Vol. 23, No. 3, 1987, pp. 403–412.

[14] Uchiyama, T. and Tsuchida, E., *Bulletin*, Japan Society of Mechanical Engineers, Vol. 29, No. 253, 1986, pp. 2007–2014.

[15] Barsoum, R. S., *International Journal for Numerical Methods in Engineering*, Vol. 10, 1976, pp. 25–37.

[16] Shih, C. F., Moran, B., and Nakamura, T., *International Journal of Fracture*, Vol. 30, 1986, pp. 79–102.

[17] Nikishkov, G. P. and Atluri, S. N., *Engineering Fracture Mechanics*, Vol. 26, 1987, pp. 851–867.

[18] Chen, W. H. and Huang, C. C., "Three-Dimensional Thermal Analysis of an Infinite Solid Containing an Elliptical Surface Crack," *International Journal of Fracture*, to be published.

[19] Chen, W. H. and Huang, C. C., "Analysis of Three-Dimensional Thermoelastic Fracture Problems Using Path-Independent Integrals," *Engineering Fracture Mechanics*, Vol. 39, No. 3, 1991, pp. 581–589.

[20] Shih, C. F., deLorenzi, H. G., and German, M. D., *International Journal of Fracture*, Vol. 12, 1976, pp. 647–651.

Novel Mathematical and Computational Methods

Genki Yagawa,[1] Shinobu Yoshimura,[1] Akira Yoshioka,[1] and Chang-Ryul Pyo[1]

Analysis of Growing Ductile Cracks Using Computer Image Processing

REFERENCE: Yagawa, G., Yoshimura, S., Yoshioka, A., and Pyo, C.-R., "**Analysis of Growing Ductile Cracks Using Computer Image Processing,**" *Fracture Mechanics: Twenty-Second Symposium (Volume II), ASTM STP 1131*, S. N. Atluri, J. C. Newman, Jr., I. S. Raju, and J. S. Epstein, Eds., American Society for Testing and Materials, Philadelphia, 1992, pp. 289–313.

ABSTRACT: This paper is concerned with a study of growing crack-tip behaviors in ductile materials using the hybrid experimental and numerical method by means of a computer image processing technique.

Here, a displacement field near a crack tip is first measured by the image processing technique. Combined with a finite element technique, the strain, the stress, the near-crack-tip J-integral, and the crack-tip singular field are evaluated from the measured displacement field. In this procedure, elastic unloading phenomena occurring around a growing crack tip, which may play important roles in the near-crack-tip behaviors, are also evaluated and are taken into account in evaluating the near-crack-tip J-integral.

The present method is applied to the analyses of a growing ductile crack in a tensile (CT) specimen made of Type 304 stainless steel. The transition behaviors of the crack-tip singular field, the elastic unloading, and the near-crack-tip J-integral in accordance with crack growth are discussed in detail through the comparison between experimental and theoretical results.

KEY WORDS: fracture mechanics, fatigue (materials), ductile crack growth, image processing, compact tension specimens, stainless steels, J-integral, elastic unloading effects, crack-tip behavior, HRR singular field

For the assessment of fracture behaviors of structural components, various fracture mechanics parameters have been proposed to date. Among them, the J-integral [*1*] may be one of the most promising parameters because of its applicability to linear as well as nonlinear fracture phenomena. The reasons why the J-integral has been popularly utilized may be summarized as follows.

First of all, the J-integral is essentially the same as the energy release rate for fracture problems of elastic materials, and the J-integral preserves path independence under conditions such as the deformation theory of plasticity or nonlinear elasticity [*1*]. In addition, if the crack-tip state in a strain-hardening material of Ramberg-Osgood power-hardening type can be represented by the Hutchinson, Rice, and Rosengren (HRR) field [*2,3*], the J-integral becomes the amplitude of this crack-tip singular field. Some recent numerical studies [*4–6*] have also shown that the crack-tip field near a stationary crack on bimaterial interfaces can be a kind of the HRR field in an elastic-plastic regime. Owing to the path independence feature of the J-integral, the integrity assessment of structures based on the J-integral concept and numerical analyses such as the finite element method is applicable to complicated structures such as nuclear pressure vessels and piping [*7,8*].

[1]Professor, associate professor, and graduate students, respectively, Department of Nuclear Engineering, University of Tokyo, Bunkyo, Tokyo 113, Japan.

On the other hand, for experimental fracture mechanics, some simple procedures for J-integral evaluation [*9,10*] enable us to estimate the fracture toughness of elastic-plastic materials from load versus load-line displacement records.

Although the J-integral has been applied to various integrity studies of structures, it should be noted also that this parameter still possesses some theoretical limitations. When cyclic loading is applied to a cracked body of an elastic-plastic material, or when a stable crack grows, the crack under the large-scale yielding condition is necessarily accompanied by nonproportional loading and elastic unloading [*11*]. As a result of this, the J-integral loses those attractive features previously mentioned. Some detailed analyses of crack-tip fields by the elastic-plastic finite element method have shown that the crack-tip field can be represented by the HRR field when an amount of crack growth is sufficiently small in comparison with ligament length [*12*]. Thus, the tearing modulus concept that treats stability of stable crack growth controlled by the J-integral was proposed in Ref *13* and has been used in the LBB (leak before break) assessment of nuclear piping systems. However, the tearing modulus criterion and the J-integral have sometimes been used beyond their theoretical limitations. Therefore, various attempts have been made to develop some fracture mechanics theories applicable to large-scale crack growth phenomena.

Some nonlinear fracture mechanics parameters, which coincide with the conventional J-integral under the proportional loading condition and still possess path independence even under a condition of large-scale crack growth [*14,15*], were proposed as some of these attempts, and their characteristics have been studied using the finite element method [*16–18*]. These parameters may be simply regarded as examples of the extended J-integrals, and their definitions can be summarized as follows:

(*a*) The parameters are similar to the conventional J-integral in formulation, but defined along the near-crack-tip path that is a very small contour set in the vicinity of a crack tip.
(*b*) The line integral calculated along the near-crack-tip path equals the line integral with an area integral portion calculated along a far-field path. This feature is also regarded as "path independence" in those advanced parameters. The effects of nonproportional loading, elastic unloading, body force, and inertia force (none of which are considered in the original J-integral) are taken into account in the area integral portion.
(*c*) Sophisticated numerical techniques such as the finite element method have been indispensable to evaluate the parameters up to now.

Thus, it is an interesting and important subject to experimentally evaluate the advanced parameters during large-scale ductile crack growth.

The authors have studied an application of a computer image processing technique for experimental analyses of various structural behaviors. This method was first successfully applied to the measurement of strain distributions near a crack tip under elevated temperature creep conditions [*19*] and under dynamic loading conditions [*20*]. Combined with a stereo-vision technique, this method was applied to the strain measurement of a curved body such as pipes and bellows under elevated temperature conditions [*21,22*]. Recently, the data smoothing technique, which is utilized in the present method, was improved by developing the modified least-squares method based on the Sobolev norm and finite elements [*23*]. The improved method was applied to fracture mechanics analyses of stationary ductile cracks [*24–26*]. The series of nonlinear fracture mechanics studies has shown that the present method enables us to experimentally evaluate nonlinear crack-tip behaviors, such as the J-integral, or the singular fields although slight difference was observed between the results measured on specimen surface and average values in the thickness direction [*26*]. Similar trends were also obtained in the three-dimensional finite element analyses of compact tension (CT) specimens [26–28].

In the present study, this hybrid method is applied to the analyses of large-scale crack growth behaviors, such as crack-tip singular fields, elastic unloading, and the near-crack-tip J-integral, in practical structural materials such as Type 304 stainless steel. Experimental studies on the singular field near a crack tip and the J-integral for growing cracks in center-cracked tension (CCT) specimens made of aluminum alloys have been conducted using moiré interferometry by some researchers [29,30]. However, in these studies, elastic unloading effects on crack-tip behaviors due to large-scale crack growth were not considered, which might play important roles in large-scale crack growth in ductile materials such as Type 304 stainless steel. In the present study, the elastic unloading phenomena and their effects on the near-crack-tip J-integral are discussed in detail.

Nonlinear Fracture Mechanics Analyses Using the Image Processing Technique

Outline of the Method

First, the displacements of a number of small marks printed near a crack tip (Fig. 1) are measured directly using an image processing technique. Second, the displacement distribution is obtained by interpolating and smoothing the mark displacements with the help of finite element interpolation. The crack-tip singularity can be examined directly from the displacement distribution against a polar coordinate centered at a growing crack tip. The strain and the stress distributions near the crack-tip are calculated from the displacement distribution. A shape of an elastic unloading region around the crack-tip is evaluated through the examination of strain histories at a number of points in accordance with crack growth. The J-integral evaluated along a near-crack-tip path, which is called "the near-crack-tip J-integral," is evaluated by the line integration technique that is widely used in the finite element analysis. The flow of the present analysis is summarized in Fig. 2.

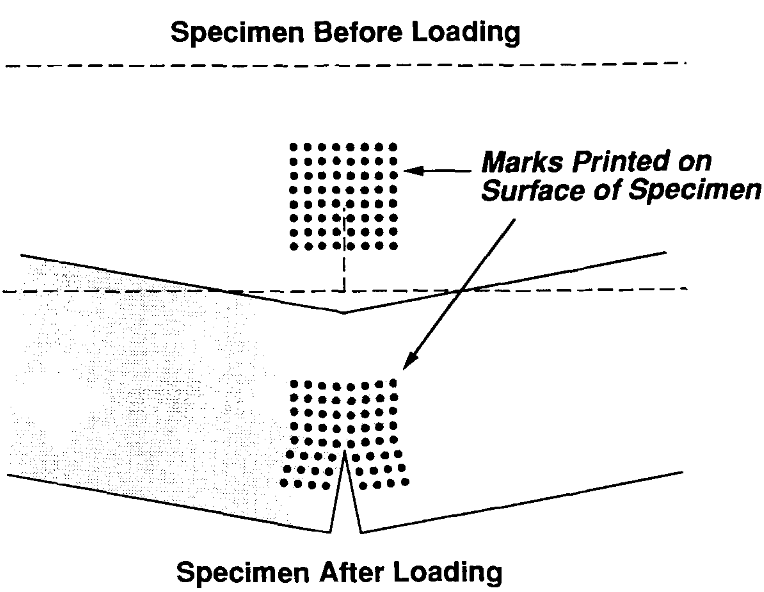

FIG. 1—*Artificially printed marks before and after deformation.*

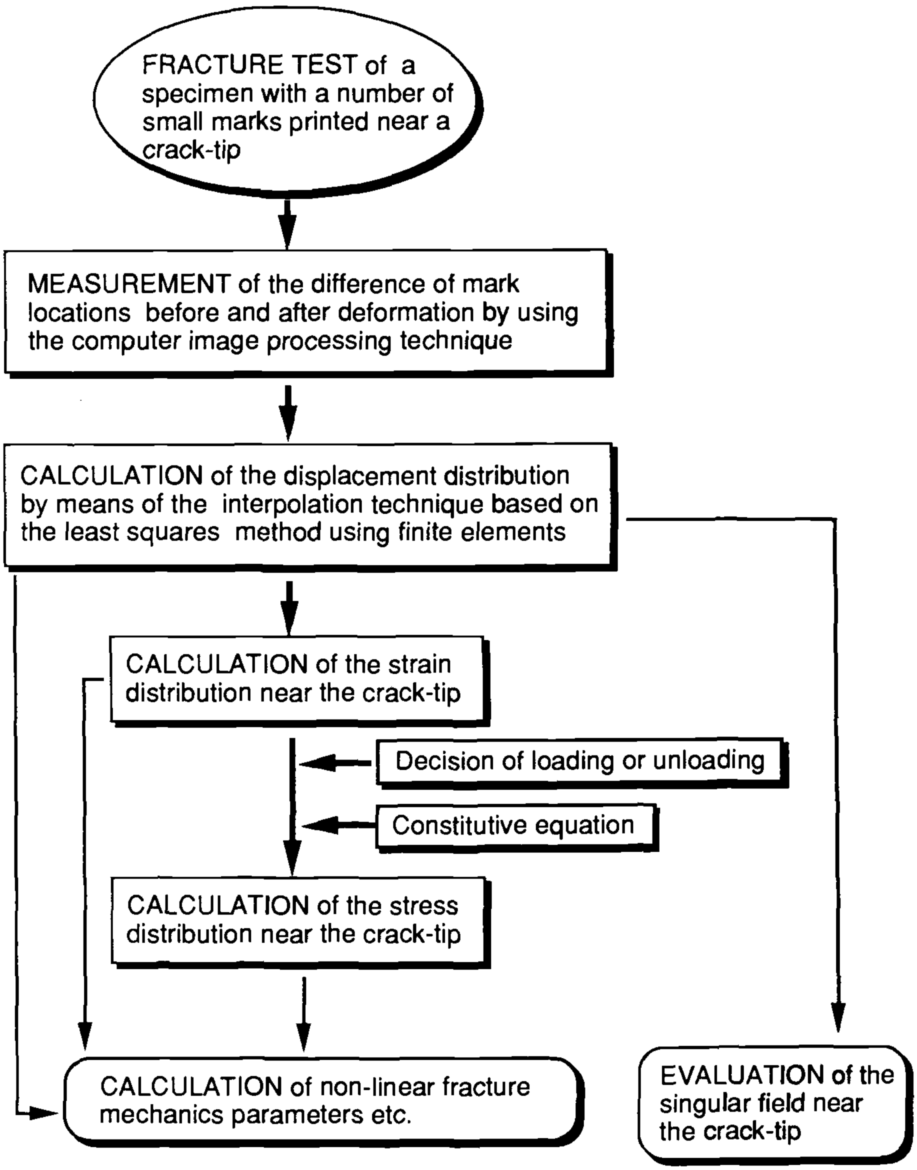

FIG. 2—*Flow of analyses.*

Mark Displacement

Figure 1 shows a schematic example of a specimen before and after loading, when hundreds of small marks are printed on a surface of the specimen. The images of the marks are photographed before and after deformation. Mark locations are determined automatically by the computer image processing technique, the details of which have been published in Refs *24* to *26*. The displacement of each mark is the difference of the mark location before and after deformation.

Interpolation of Mark Displacements

The least-squares method using polynomial interpolation functions, finite elements, and the spline functions are often utilized to interpolate discrete data such as mark displacements [*19,20,31–35*]. Most of the interpolation processes intend to maintain the continuity of derivative values among segmented interpolation functions or finite elements. Nevertheless, since these methods interpolate discrete data too precisely (even if the data involve random measurement errors), undesirable oscillation could be sometimes caused in derivative values. Therefore, the authors have proposed a new interpolation technique based on the least-squares method using both the Sobolev norm and finite elements [*23*].

The key idea of the present method can be summarized as follows.

By analogy to the Sobolev norm, we employ the following error measure

$$\phi = \frac{\alpha'}{2}\sum_{i=1}^{ND}\{u(x_i) - \bar{u}(x_i)\}^2 + \frac{1}{2}\sum_{k=1}^{DIM}\int_A \left(\frac{\partial u}{\partial x_k} - \overline{\frac{\partial u}{\partial x_k}}\right)^2 dA \tag{1}$$

where ND is the number of measured points, DIM is the dimension number, $u(x_i)$ and $\bar{u}(x_i)$ are the interpolated and the measured displacements at Point x_i, and $\partial u/\partial x_k$ and $\overline{\partial u/\partial x_k}$ the derivatives of the interpolated and the measured values with respect to x_k, respectively. α' is the coefficient to adjust dimensions of two terms in Eq 1 and is defined as follows

$$\alpha' = \frac{A}{L^2} \tag{2}$$

where L is a representative length of a measured domain, and A is a size of the domain.

In this interpolation method, a measured domain is subdivided into a number of finite elements independent of mark locations as schematically shown in Fig. 3, and then nodal displacements are determined by minimizing the error measure of Eq 1.

Strain and Stress Distributions

A displacement distribution is obtained by both the image processing technique and the interpolation technique with finite elements. Since the displacement is given as nodal values through this interpolation process, one can easily calculate strain and stress distributions using common numerical techniques.

The distributions of infinitesimal strain and Green's strain are calculated through numerical differentiation of the displacement field. A stress distribution is obtained from the strain distribution, assuming an appropriate constitutive equation of material such as the incremental or the deformation theory of plasticity.

In general, the incremental theory of plasticity with the consideration of loading history is more reasonable to describe the deformation phenomena around a growing ductile crack than the deformation theory of plasticity. Nevertheless, the deformation theory of plasticity can still give us good approximation under the limited conditions such as proportional loading. Then, stress values are basically calculated based on the deformation theory of plasticity until elastic unloading occurs.

In the deformation theory of plasticity, the total stress tensor, σ_{ij}, is directly related to the total strain tensor, ε_{ij}, as follows

$$\sigma_{ij} = \frac{2G}{1 + 3G/H_s}\left(\varepsilon_{ij} + \frac{\nu + (1+\nu)G/H_s}{1 - 2\nu}\delta_{ij}\varepsilon_{mm}\right) \tag{3}$$

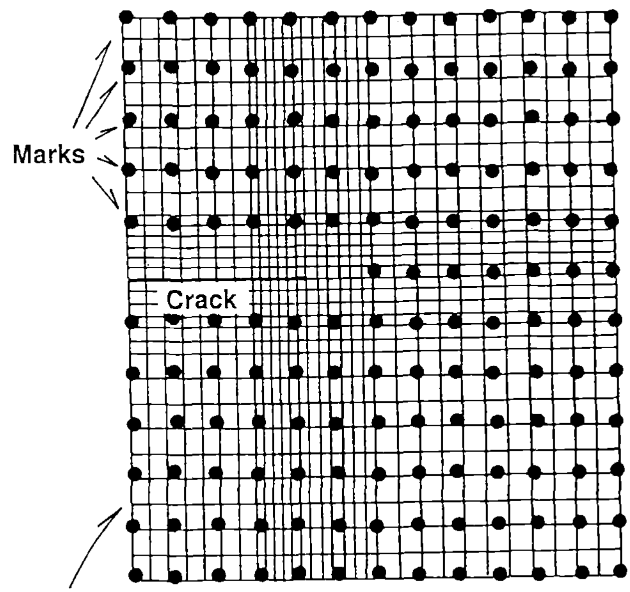

Mesh used in the smoothing process

FIG. 3—*Mark locations and overlapped finite element.*

where G is the elastic shear modulus, H_s is the plastic secant modulus, ν is Poisson's ratio, and δ_{ij} is Kronecher's delta. H_s is written in terms of the Mises-type equivalent stress, $\bar{\sigma}$, and the equivalent plastic strain, $\bar{\varepsilon}^p$, as

$$H_s = \frac{\bar{\sigma}}{\bar{\varepsilon}^p} \tag{4}$$

Since Eq 3 is nonlinear with respect to stress, the total stress tensor corresponding to the total strain tensor is obtained by applying a simple iterative substitution method to Eqs 3 and 4.

Elastic Unloading

Ductile crack growth is, of course, accompanied by elastic unloading. The behavior of such elastic unloading was studied theoretically in Ref *11* for steady-state crack growth in an elastic perfectly-plastic material under the two-dimensional plane-strain condition. However, any comparable experimental studies on elastic unloading have not yet been performed.

As has been already emphasized, the deformation theory of plasticity utilized in the present analysis does not model elastic unloading. Therefore, a shape of an elastic unloading region is evaluated experimentally as follows.

First, the histories of equivalent strains at a number of points near a crack tip are plotted against crack growth as shown in Fig. 4. When a value of equivalent strain reaches almost a constant value at any point after it increases monotonously, it is judged that elastic unloading starts to occur at that point. It should be also noted that detailed processes of stress and strain reduction due to elastic unloading are not evaluated here because the

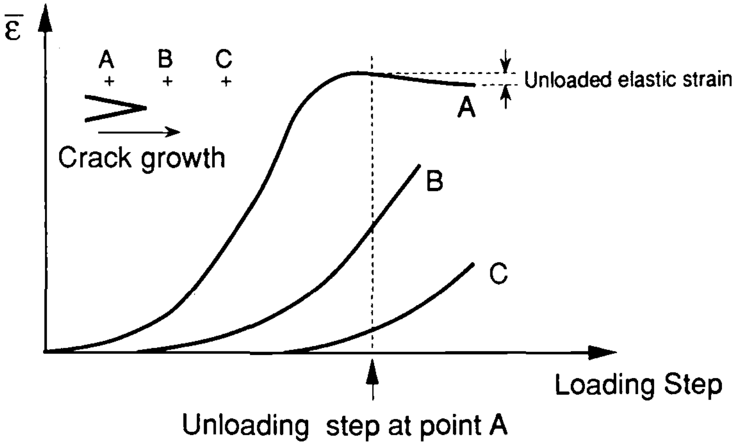

FIG. 4—*Strain histories at points beside a growing crack.*

present method is not so accurate to measure decreasing elastic strain less than an order of 0.1%. The accuracy of the present measurement method will be discussed in more detail later.

Crack-Tip Displacement Singularity

In power-law hardening materials, the J-integral possesses a meaning of the amplitude of the crack-tip singular fields, which are referred to as the HRR singular fields [*2,3*]. For example, the crack-tip displacement field is expressed as follows

$$U_i = \alpha\varepsilon_0\left(\frac{J}{\alpha\varepsilon_0\sigma_0}\right)^{n/n+1} r^{1/n+1}F_i(\theta,n) \tag{5}$$

where J is the J-integral, ε_0 is the yield strain, σ_0 is the yield stress, $F_i(F_r$ or $F_\theta)$ is a dimensionless function of θ and n, and (r,θ) are the polar coordinates centered at the crack tip as shown in Fig. 5. The hardening exponent, n, and the material constant, α, are determined with the following Ramberg-Osgood type stress-strain relationship

$$\frac{\varepsilon}{\varepsilon_0} = \frac{\sigma}{\sigma_0} + \alpha\left(\frac{\sigma}{\sigma_0}\right)^n \tag{6}$$

Experimental results of the dimensionless functions, F_r and F_θ, for a stationary ductile crack can be found in Refs *24* to *26*.

Near-Crack-Tip J-integral

Considering the two-dimensional crack problem and the path, Γ, shown in Fig. 5, the J-integral is defined as

$$J = \int_\Gamma \left(Wn_1 - \sigma_{ij}n_j\frac{\partial u_i}{\partial x_1}\right) d\Gamma \tag{7}$$

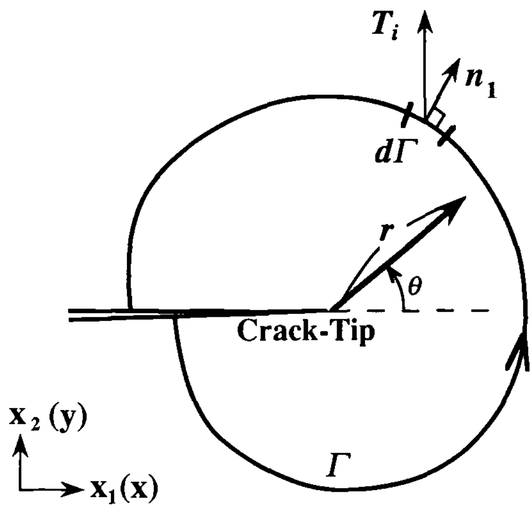

FIG. 5—*Crack-tip coordinates for the definition of* J*-integral.*

with

$$W = \int_0^{\varepsilon_{ij}} \sigma_{ij} d\varepsilon_{ij} \tag{8}$$

where W is the strain energy density, n_i is the x_i component of the outward normal vector on Γ, and u_i is the displacement vector. The J-integral is evaluated numerically by the path integration technique that is popularly used in the finite element fracture analysis.

As described previously, ductile crack growth phenomena are necessarily accompanied by elastic unloading, whose effects are taken into account in the evaluation of Eq 7 as follows.

The strain energy density term, W, and the traction force term, $T_i = \sigma_{ij}n_j$, include the total stress tensor, σ_{ij}. W is simply evaluated by using the total stress value directly calculated with Eq 3 on the assumption that a fraction of released elastic strain energy in the whole strain energy is negligible in the vicinity of a largely deformed ductile crack tip.

On the other hand, an evaluation of the traction force term in Eq 7 is a little more complicated than that of W. Stress values are simply calculated with Eq 3 at the integration points where equivalent strain values are still increasing. A certain amount of stress reduction has to be taken into account at the integration points where elastic unloading occurs. However, it is difficult to measure such stress reduction due to elastic unloading by the present method although the boundary between loading and elastic unloading regions is measurable. In addition, it is expected that the stress values in an elastic unloading region may be very small in comparison with those in a loading region. Thus, as the first order approximation, stress values are simply taken to be zero at the integration points where elastic unloading occurs. In other words, elastic unloading effects are overestimated here.

It should be noted here that the preceding definition of the near-crack-tip J-integral in this study is similar to that of the T^*-integral [*15–18*] in the following two senses. First, both integrals are defined along a near-crack-tip path. Second, both are considering elastic unloading effects although there are slight differences in the treatment of stress reduction as described earlier. Thus, it is expected that the present study will be able to examine experimentally how and how much elastic unloading affects the behaviors of the near-crack-tip J-integral and, indirectly, the T^*-integral.

Experiment

Experimental Procedure

Figure 6 shows a CT specimen made of Type 304 stainless steel, in which a mechanical notch is machined and then a fatigue precrack is given up to a total crack length of 115 mm. The measured stress versus plastic strain relationship of this material at room temperature is shown in Fig. 7, together with a bilinear approximation and the power-law hardening-type approximation that is obtained by the Ramberg-Osgood data fit for the stress-strain data ranging from 0 to about 30%. The material properties determined here are as follows: Young's modulus, $E = 1.9 \times 10^2$ GPa; Poisson's ratio, $\nu = 0.27$; the yield stress, $\sigma_0 = 234.0$ MPa; the yield strain, $\varepsilon_0 = 0.00126$; the hardening exponent, $n = 2.4$; and the constant, $\alpha = 12.6$, respectively.

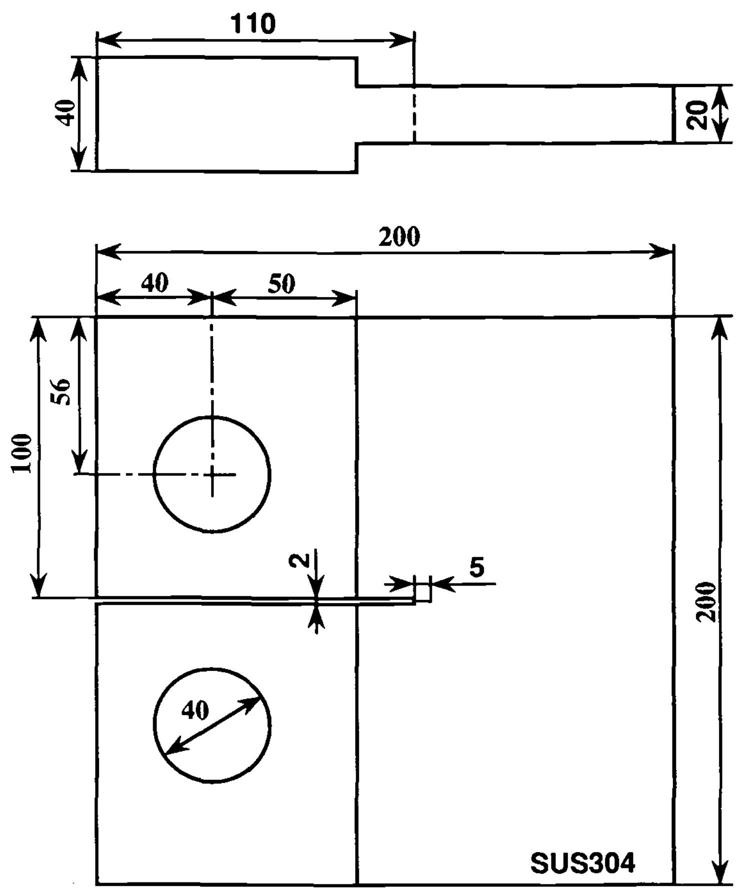

FIG. 6—*Configuration and dimension of specimen.*

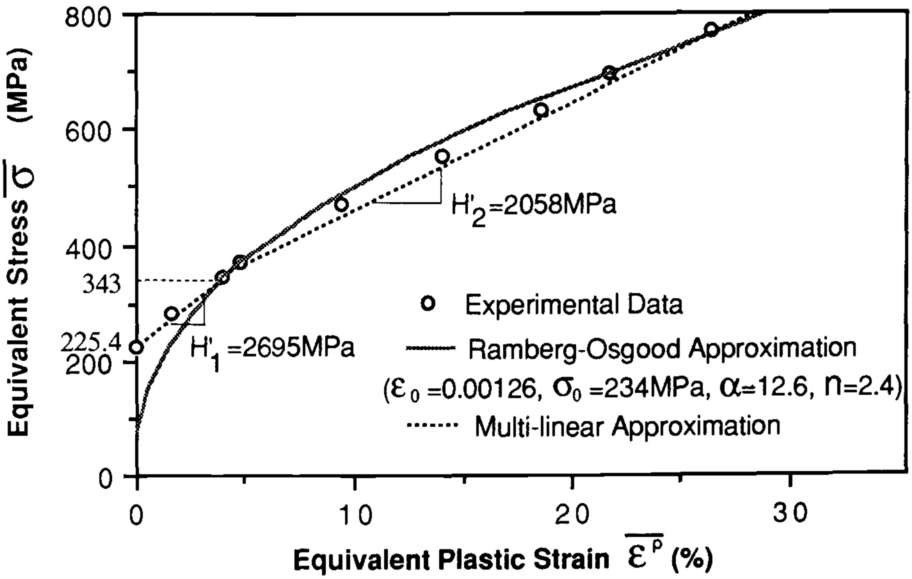

FIG. 7—*Uniaxial stress-strain relationship of Type 304 stainless steel at room temperature.*

Hundreds of small marks are printed on the specimen surface by a photochemical etching technique.

Displacement-controlled loading is applied statically to the specimen using a servohydraulic MTS machine. The photographs of marks around a crack tip are taken with an autofocus camera while maintaining the applied load level at several loading steps. Focus and position of the camera are adjusted before loading starts. After this adjustment, the magnification factor of the photographs is completely fixed irrespective of deformation and crack growth to avoid the undesirable complexity of optical compensation.

Color film is used in the experiment to easily distinguish marks from noise.

Measured Loading Record and Mark Photographs

Figure 8 shows the measured load versus load-line displacement curve. Small open circles indicate the loading steps where the mark photograph is taken while maintaining an appropriate loading level. For example, Figs. 9*a*, *b*, and *c* show the mark photographs taken at Step 13 (Δa = 0.21 mm), at Step 19 (Δa = 0.80 mm), and at Step 24 (Δa = 7.61 mm), respectively.

The figures include three kinds of marks. Among them, the smallest and medium marks are utilized in the present measurement. The diameter and distance of the smallest marks are 0.1 and 0.2 mm, and those of the medium marks are 0.2 and 1.0 mm, respectively.

It can be seen that the marks are clearly distinguished from noise, irrespective of the large deformation in the vicinity of the crack tip and of a large amount of crack growth.

Results and Discussions

Measurement Error of Displacement and Strain

A distance of neighboring smallest marks is 0.2 mm, and about 60 pixels are placed between neighboring marks in the image processing technique. A distance of neighboring

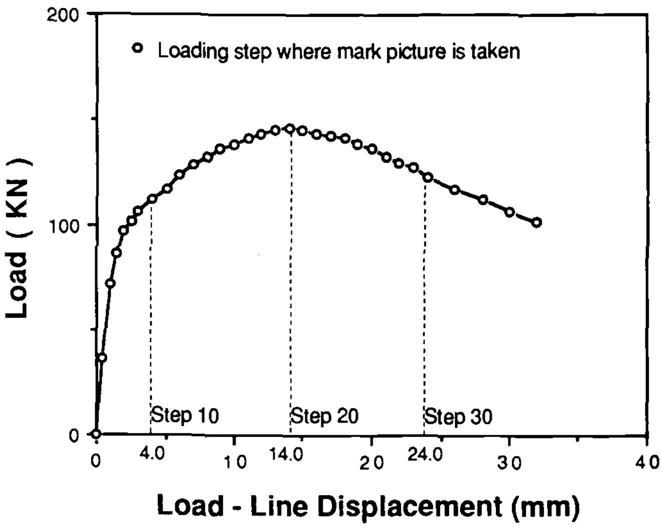

FIG. 8—*Load versus load-line displacement curve.*

medium marks is 1.0 mm, and about 60 pixels are also placed between neighboring marks. The lower measurable limit of the technique is a movement of one pixel. Then, the measurement error of mark displacement is estimated to be about 0.0033 mm in the former case, while it is about 0.017 mm in the latter case.

In this experiment, out-of-plane motion occurs and would influence the inplane motion. To measure the out-of-plane motion is, however, difficult during the experiment. Instead of on-line measurement, we measured the residual out-of-plane deformation of the fractured specimen. This result is illustrated schematically in Fig. 10. If elastic unloading effects are neglected (this assumption seems to be correct because here significant plastic deformation occurs near a crack tip during ductile crack growth), the inplane displacement that was directly measured by the image processing technique should be corrected by the factor of $1/\cos(10.8°) = 1.018$ in the region ranging from $r = 0$ to 6 mm, while corrected by the factor of $1/\cos(3.8°) = 1.002$ in the region ranging from $r = 6$ to 30 mm. It is considered that neglecting the out-of-plane motion would lead only to a 1 or 2% error at most to the inplane motion.

To examine the accuracy of the interpolation technique, Fig. 11*a* shows the distribution of displacement in the y-direction, v, along the uncracked ligament, that is, in the x-direction. In the figure, open circles denote the measured mark displacements, while a solid line shows the interpolated displacement. For the purpose of reference, the used mesh subdivision in the x-direction is shown in the same figure. Figure 11 indicates that the present interpolation technique leads to a 2 or 3% error in this case. Figure 11*b* shows the distribution of $\partial v/\partial x$ along the uncracked ligament obtained through differentiation of the smoothed displacement shown in Fig. 11*a*. For the purpose of comparison, Fig. 11*b* also shows average gradient, $\Delta v/\Delta x$, which is simply calculated as the ratio of the difference of the measured displacements of neighboring marks to their distance. This figure clearly demonstrates that the present interpolation technique gives us medium results smoothly interpolating oscillated average gradients of measured displacements.

From such error estimation, it is expected that the present method can neither measure elastic strain nor stress reduction due to elastic unloading.

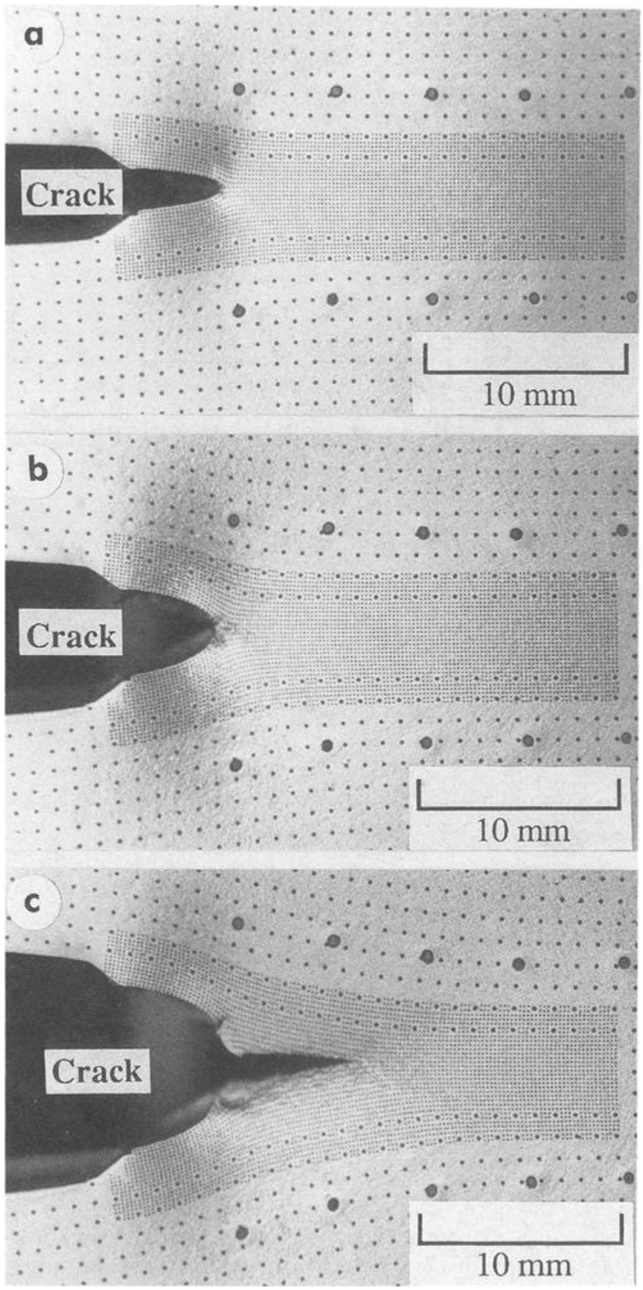

FIG. 9—(a) *Mark picture around a crack tip (Step 13, $\Delta a = 0.21$ mm);* (b) *mark picture around a crack tip (Step 19, $\Delta a = 0.80$ mm); and* (c) *mark picture around a crack tip (Step 28, $\Delta a = 7.61$ mm).*

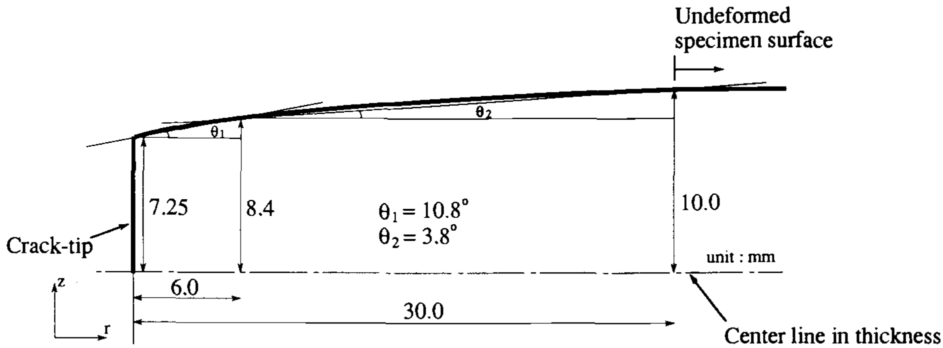

FIG. 10—*Schematic of the deformed shape of the near-crack-tip field measured from the fracture specimen.*

Strain Distribution

Figures 12*a* and *b* show the distribution of infinitesimal strain in the y-direction and that of Green's strain at Step 13, that is, Δa = 0.21 mm. In Fig. 12*a*, very large strain values, over 50%, are observed in the vicinity of the crack tip. It is found by comparing both figures that the maximum value of Green's strain is about 20% larger than that of infinitesimal strain at the very vicinity of the crack tip, but that the difference between both strains is not so significant in other regions. For the purpose of simplicity, the subsequent analyses are performed based on infinitesimal strain.

Elastic Unloading Behavior Near Crack Tip

Figure 13 shows the measured transition behavior of an elastic unloading region in accordance with crack growth of up to about Δa = 1.0 mm. The "+" symbols in the figure denote the points at which the decision of loading or elastic unloading is made through the examination of the history of equivalent strain.

This figure shows that the boundary between loading and elastic unloading regions is inclined about 90° against the direction of crack growth just after the crack initiation, but that the boundary gets slanted backward in accordance with crack growth. For reference, the theoretical result obtained for steady-state crack growth in an elastic perfectly-plastic material under the plain-strain condition, that is, 115° [*11*], is depicted with dashed lines. It can be estimated from the figure that after a certain amount of crack growth, the present experimental result approaches the theoretical one in a steady state.

Crack-Tip Displacement Field

Figures 14*a*, *b*, *c*, and *d* show the distributions of u_r displacement against a polar coordinate centered at a growing crack tip. Figure 14*a* shows the result when a ductile crack is about to grow after large blunting. Figures 14*b*, *c*, and *d* show the results of Δa = 0.80 mm, 3.06 mm, and 7.61 mm, respectively. Here, u_r displacements in the range of $\theta < 60°$ were too small to be measured with sufficient accuracy. By the same reason, u_θ displacements in the range of $0° < \theta < 90°$ are not presented here. Although the measured results are limited, the following nature of a near-crack-tip displacement field might be estimated from Figs. 14*a* through *d*.

The near-crack-tip displacement field can be divided roughly into two regions. As shown in Fig. 14*a*, the near-crack-tip region is mostly characterized by the HRR singularity just

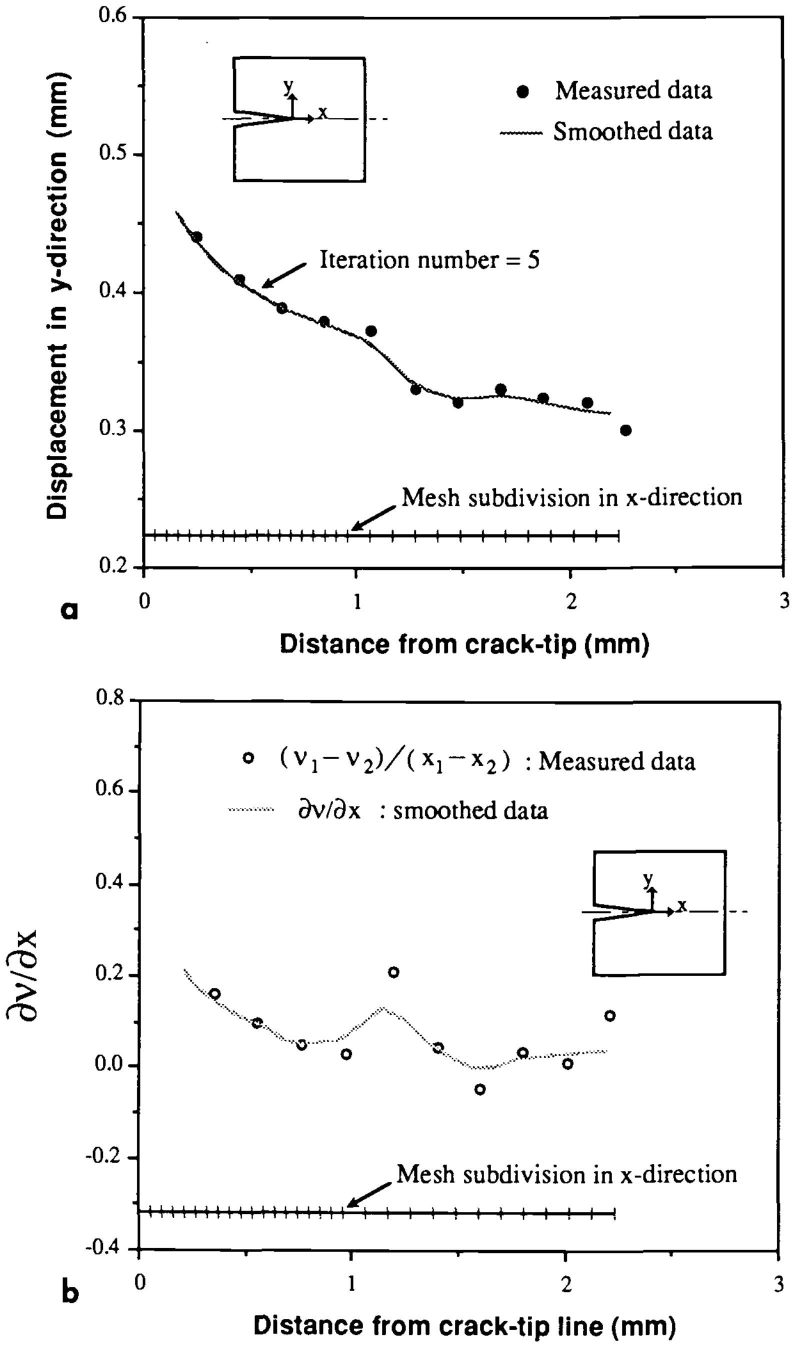

FIG. 11—(a) *Distribution of v along uncracked ligament (Step 13,* $\Delta a = 0.21$ *mm) and* (b) *distribution of* $\partial v/\partial x$ *along uncracked ligament (Step 13,* $\Delta a = 0.21$ *mm).*

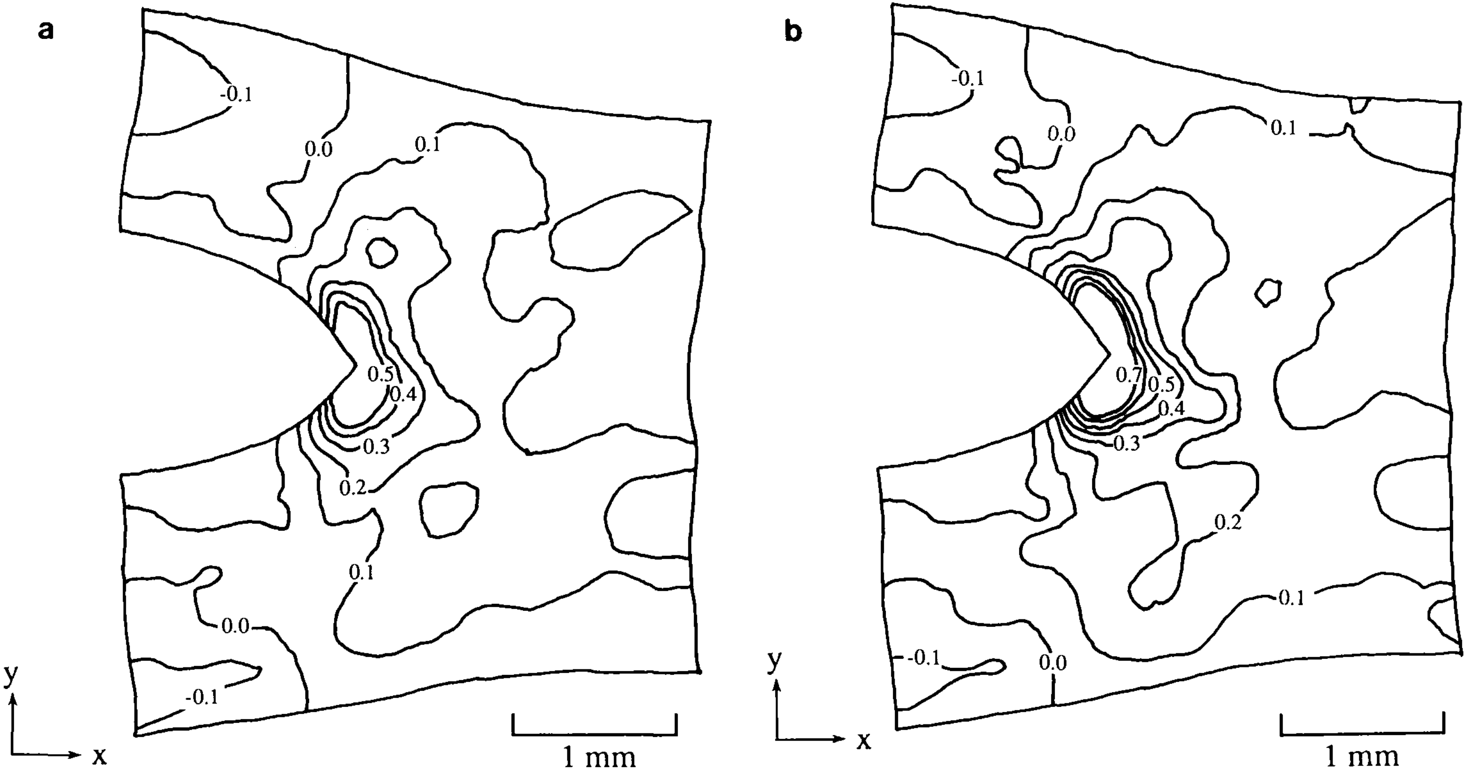

FIG. 12—(a) *Distribution of infinitesimal strain in* y-*direction (Step 13,* Δa *= 0.21 mm), and* (b) *distribution of Green's strain in* y-*direction (Step 13,* Δa *= 0.21 mm).*

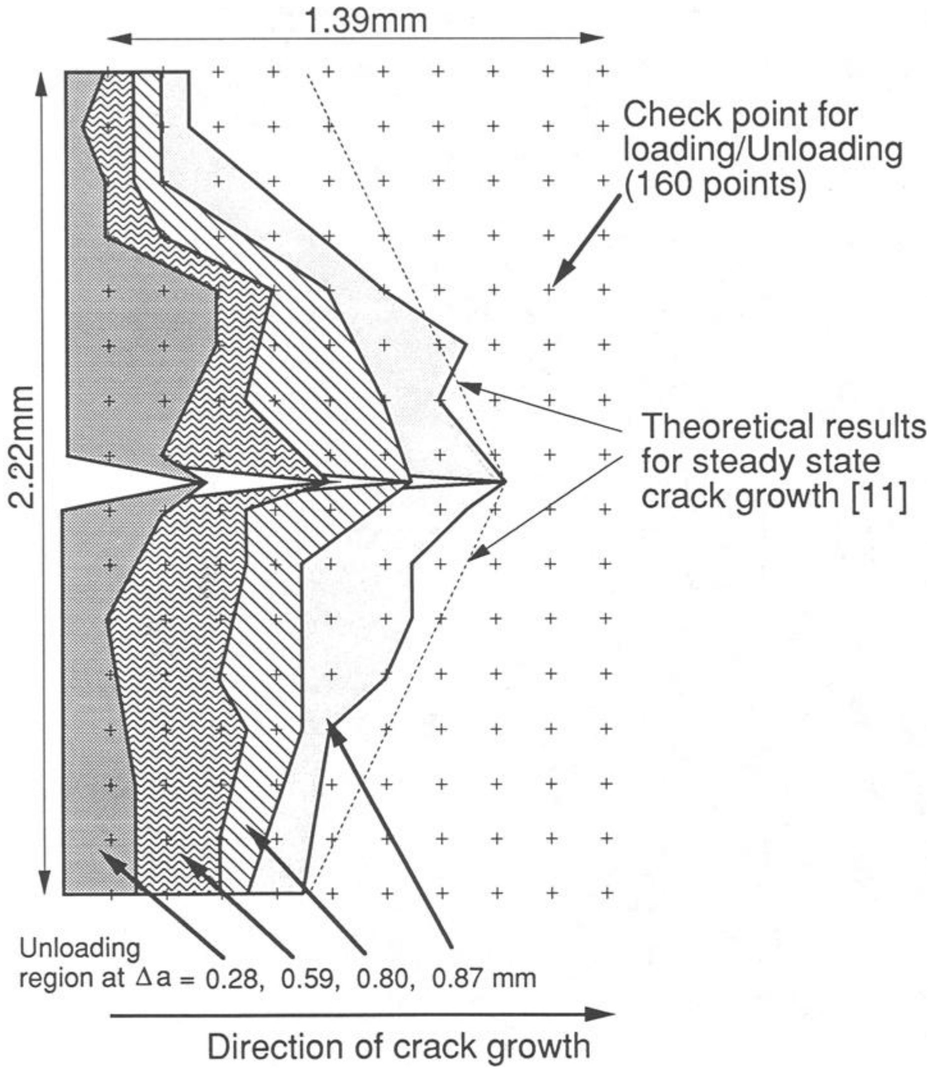

FIG. 13—*Extension of elastic unloading region in accordance with crack growth.*

after crack initiation. Until a certain amount of crack growth, the small region where the slope of the displacement field is steeper than the HRR field expands over $r = 1$ mm as shown in Figs. 14*b*, *c*, and *d*. This small region is named, "a nonlinear field," following Ref *30*. On the other hand, as a crack grows larger, the HRR displacement field disappears and a quasi-linear elastic singular field appears. It can be seen from the comparison between Fig. 14*c* and *d* that this quasi-linear elastic field moves in accordance with the movement of the crack tip during a large amount of ductile crack growth. The phenomenon shown in Figs. 14*a* and *b* may be basically the same as those observed in the crack growth in aluminum alloys that were measured with moiré interferometry [*30*]. On the other hand, the phenomenon shown in Figs. 14*c* and *d* is first observed in the present study. This reappearance of

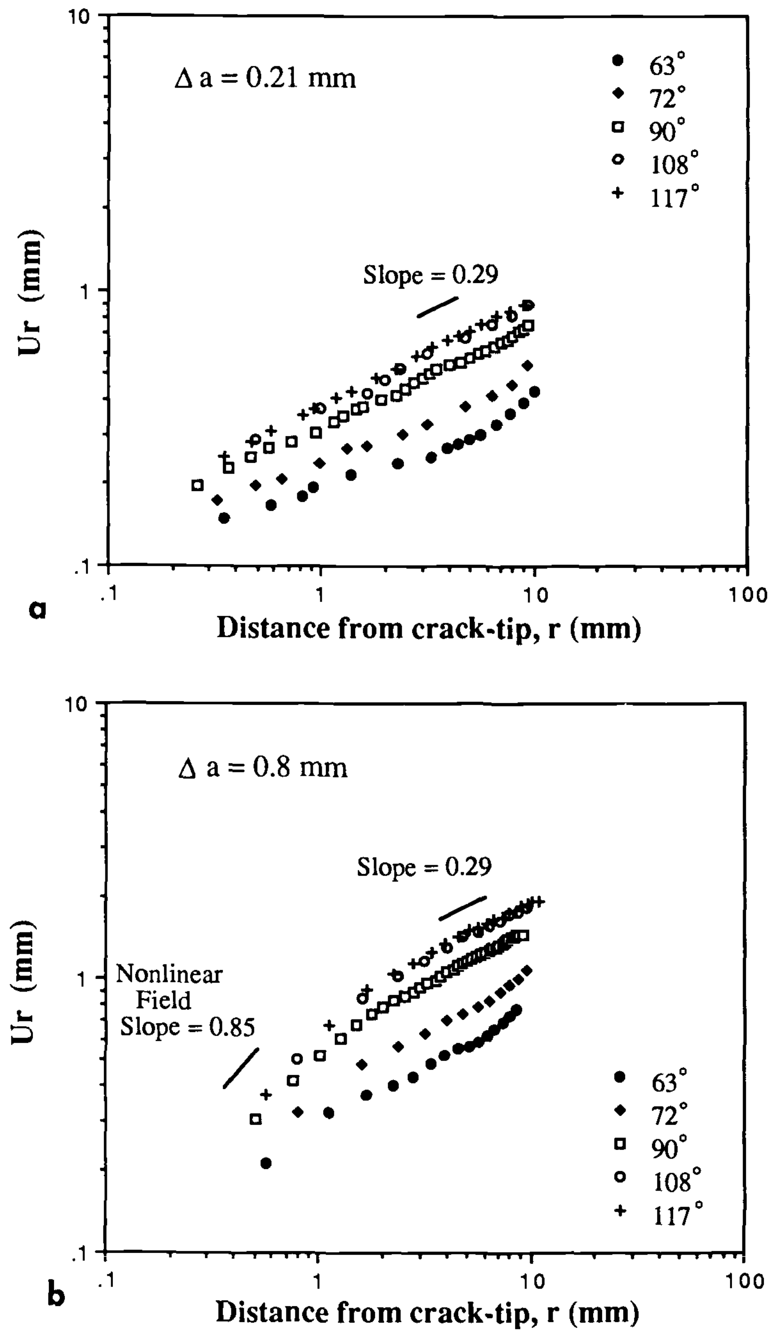

FIG. 14—(a) *Displacement field near a crack tip (Step 13,* $\Delta a = 0.21$ *mm) and* (b) *displacement field near a crack tip (Step 19,* $\Delta a = 0.80$ *mm).*

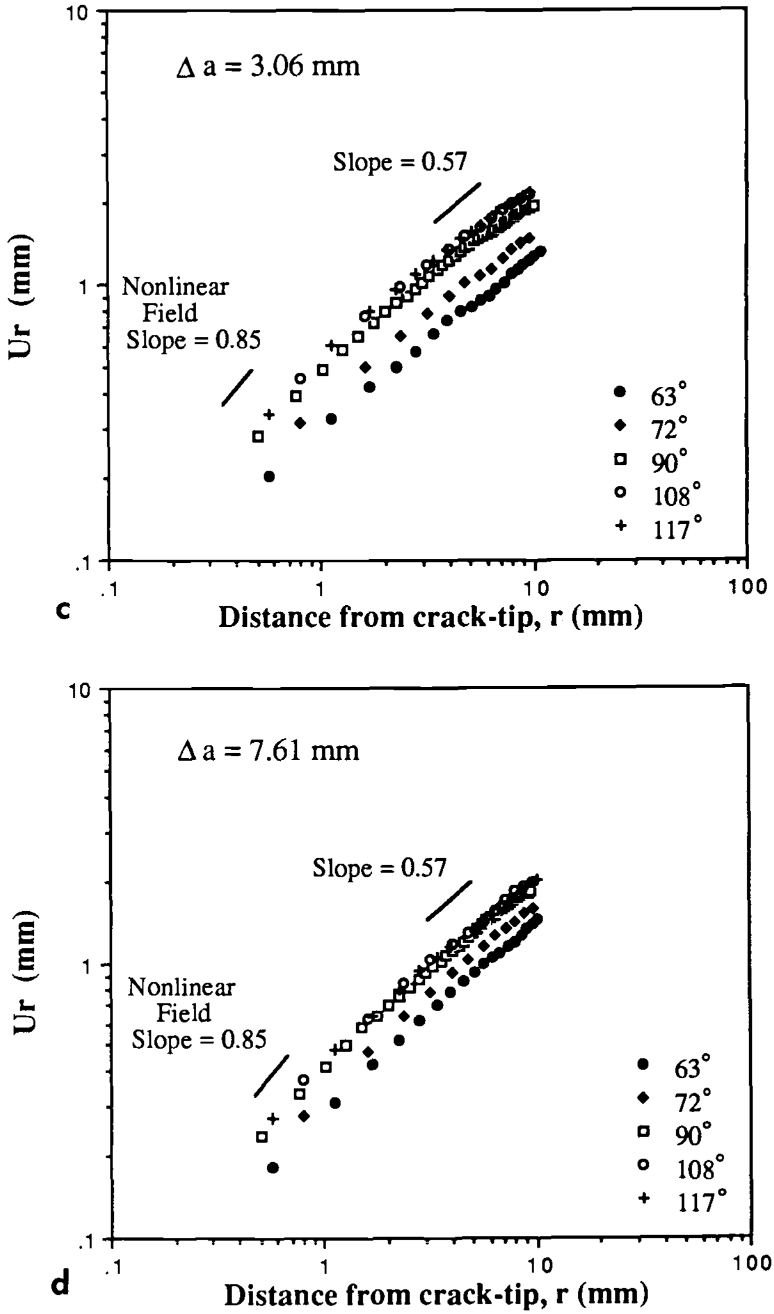

FIG. 14—(c) *Displacement field near a crack tip (Step 24,* Δa = *3.06 mm) and* (d) *displacement field near a crack tip (Step 28,* Δa = *7.61 mm).*

a quasi-linear elastic singular field and its self-similar transition may be related to constant behaviors of the crack-tip opening angle (CTOA) and the T^*-integral in steady-state ductile crack growth [36,37].

The present method cannot measure the distribution of a crack-tip displacement singular field in the thickness direction. However, three-dimensional finite element analyses of crack-tip singular fields for stationary cracks in a CT specimen [27,28] have shown that the near-crack-tip fields on the center plane of a CT specimen is the same as the plane strain HRR solutions, and that the near-crack-tip fields near the specimen surface are a little smaller than the plane strain HRR solution. Numerical results of dimensionless functions, F_i, near the specimen surface agreed well with the experimental results obtained by the present method [26–28].

Near-Crack-Tip J*-Integral*

The near-crack-tip J-integral is evaluated by using the line integration technique along several small paths set near a crack tip, as shown in Fig. 15, which move together with a growing crack tip. Figures 16*a*, *b*, and *c* show the near-crack-tip J-integral plotted against a distance from the growing crack tip. For the purpose of comparison, the experimental J-integral value evaluated using the Merkle-Corten's formula [10] is drawn in the figure with a broken straight line.

Those figures clearly indicate that the near-crack-tip region can be roughly divided into two regions. As shown in Fig. 16*a*, when a specimen's deformation is small, the near-crack-tip J-integral holds good path independence in the whole near-crack-tip region. However, when being deformed further, this J-integral strongly depends on path location in the bor-

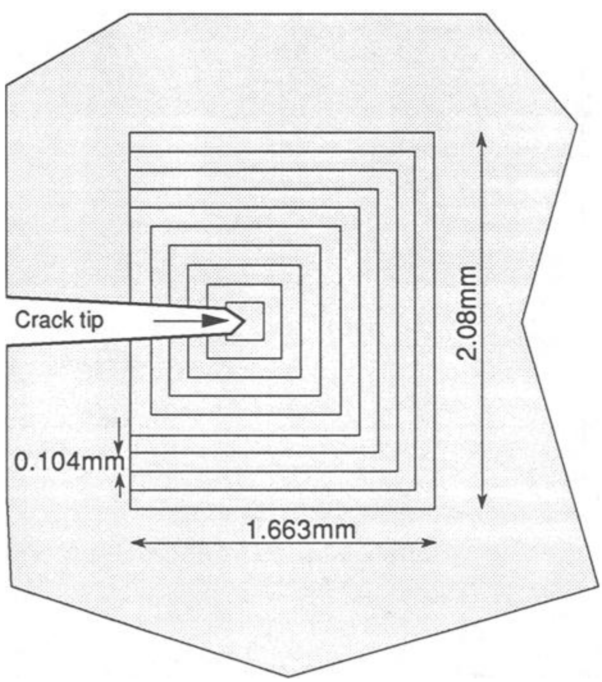

FIG. 15—*Integration paths for* J*-integral calculation.*

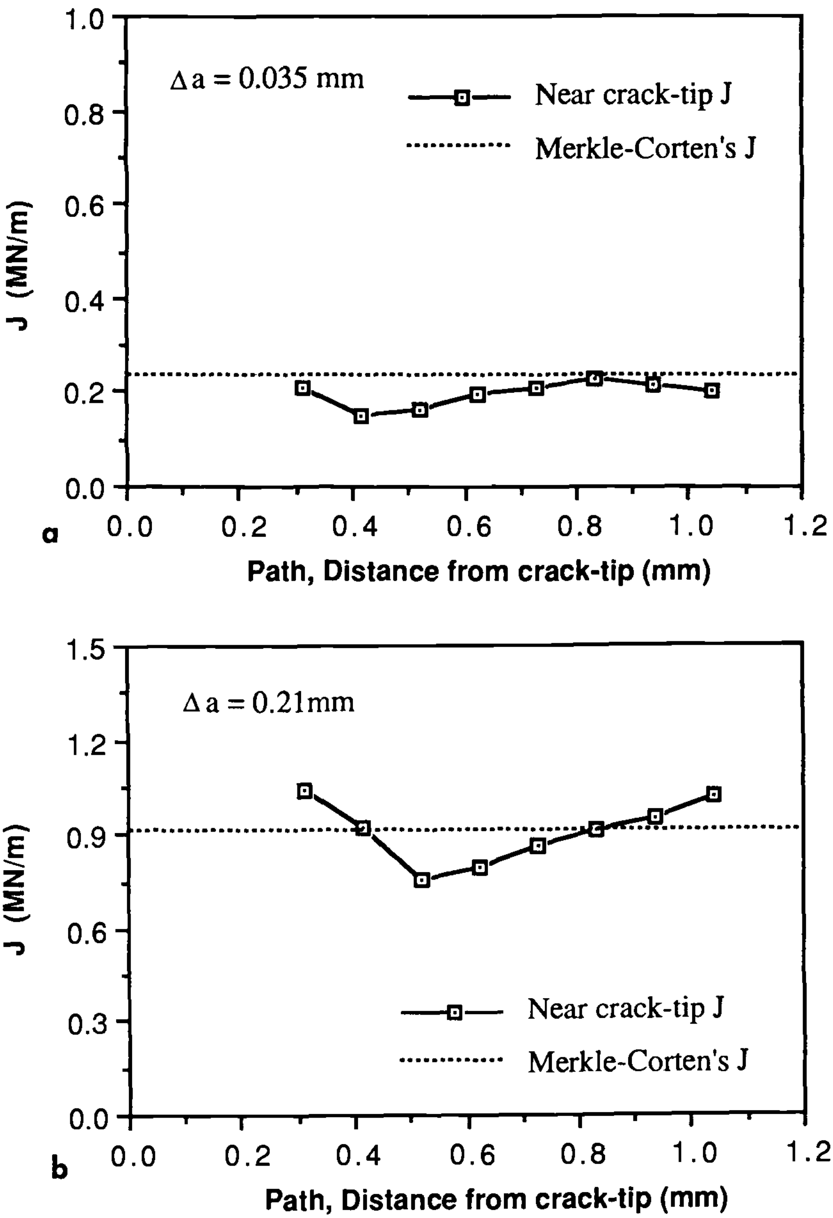

FIG. 16—(a) *Distribution of* J-*integral (Step 08,* Δa = *0.035 mm) and* (b) *distribution of* J-*integral (Step 13,* Δa = *0.21 mm).*

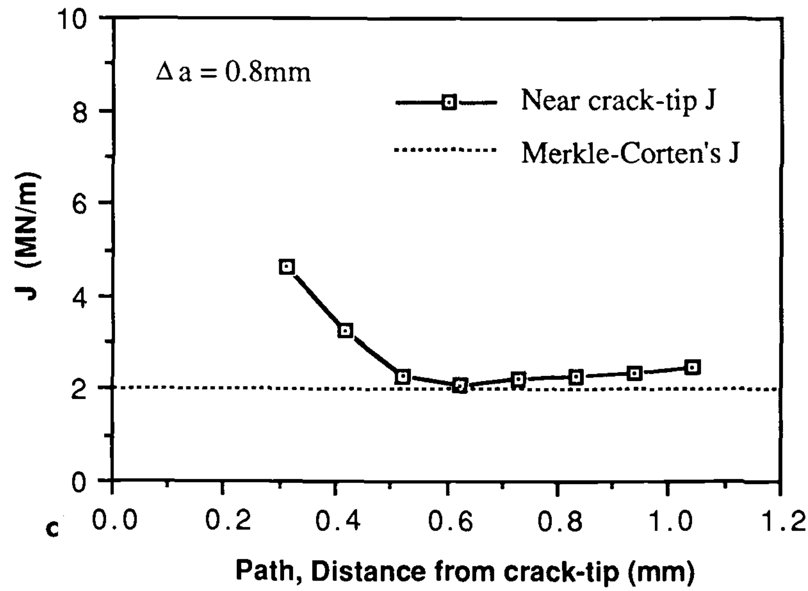

FIG. 16—(c) *Distribution of* J-*integral (Step 19,* Δa = *0.80 mm).*

dering near-crack-tip region, while path independence is held outside that region to some extent. This feature of the near-crack-tip J-integral corresponds to numerical results obtained from various finite element analyses [*12,17*].

Figure 17 shows the measured crack resistance curve, that is, the relationship between the near-crack-tip J-integral and crack growth measured on the specimen surface, with open circles and a solid line. The plotted value is an average value of the near-crack-tip J-integrals calculated along five paths set over $r = 0.6$ mm. The maximum difference among the five values is indicated also with an error bar. For the purpose of comparison, open square marks and a broken line indicate the conventional experimental J-integral obtained with the Merkle-Corten's formula, while cross marks and a dashed line indicates the conventional J-integral obtained with the formula by Ernst et al. [*38*], that is, the deformed J. The observations in this figure are summarized as follows:

(*a*) Crack growth of up to several millimetres does not cause much difference between the Merkle-Corten's J and the deformed J, both of which are evaluated using load versus load-line displacement records.
(*b*) The conventional J-integrals continue to increase in accordance with crack growth.
(*c*) The near-crack-tip J-integral obtained by the present method agrees well with those of the conventional experimental J-integrals within about 20% difference in the range of crack growth of up to about $\Delta a = 1$ mm.
(*d*) The near-crack-tip J-integral then starts to decrease and reaches almost a constant value of about 1.2 MN/m, when $\Delta a = 2.0$ mm, after about a 40% reduction from the maximum value.

Such behaviors of the near-crack-tip J-integral during large-scale ductile crack growth, which is evaluated along a near-crack-tip path considering elastic unloading, are similar to those of the T^*-integral [*37*]. As mentioned previously, the present near-crack-tip J-integral may

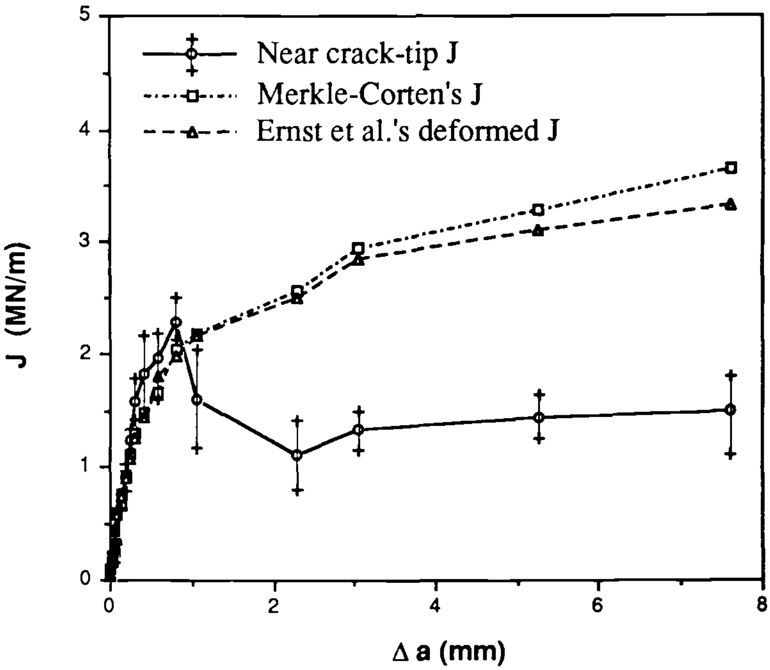

FIG. 17—*Crack growth resistance curve.*

overestimate the effects of elastic unloading than the T^*-integral because stress values are assumed to be completely zero in the elastic unloading region. This overestimation might cause the sudden decrease of the present J-integral around $\Delta a = 0.8$ to 1.5 mm. Nevertheless, this constant behavior of the present J-integral after a certain amount of crack growth, which is estimated to be corresponding to the self-similar transition of the quasi-linear elastic singular displacement field, may give us experimental proof for one of the key features of the T^*-integral.

Conclusions

Using the displacement field obtained by the computer image processing technique, the crack-tip singular displacement field, the elastic unloading behavior, and the near-crack-tip J-integral are evaluated experimentally for large-scale ductile crack growth. The main conclusions given in the present study are summarized as follows:

(*a*) The HRR singularity of the crack-tip displacement field seems to exist outside a smaller nonlinear region of $r < 1$ mm in Type 304 stainless steel, even if a crack is largely blunted and a short ductile crack grows.

(*b*) The quasi-linear elastic singularity of the displacement field seems to exist near a crack tip after large-scale ductile crack growth, that is, in a steady state.

(*c*) The shape of elastic unloading produced due to ductile crack growth is experimentally evaluated, and it is found that the unloading region, after a certain amount of crack growth, coincides with the theoretical results for steady-state crack growth [*11*].

(*d*) The near-crack-tip J-integral evaluated by the present method shows good path independence outside the smaller nonlinear region.

(*e*) The near-crack-tip J-integral agrees well with the conventional experimental J-integrals in the range of a small amount of crack growth.
(*f*) The near-crack-tip J-integral reaches almost a constant value after large-scale ductile crack growth just like the T^*-integral.

Acknowledgments

This study was performed under the Study on Elastic-Plastic Fracture Mechanics in Inhomogeneous Materials and Structures (EPI program), and was financially supported by Japanese utilities and fabricators, and the U.S. Nuclear Regulatory Commission (USNRC) and Martin Marietta Energy Systems, Inc., under Subcontract No. 19X-SD561V.

References

[*1*] Rice, J. R., *Journal of Applied Mechanics*, Vol. 35, 1968, pp. 376–386.
[*2*] Rice, J. R. and Rosengren, G. F., *Journal of the Mechanics and Physics of Solids*, Vol. 16, 1968, pp. 1–12.
[*3*] Hutchinson, J. W., *Journal of the Mechanics and Physics of Solids*, Vol. 16, 1968, pp. 13–31.
[*4*] Shih, C. F. and Asaro, R. J., *Journal of Applied Mechanics*, Vol. 55, 1988, pp. 299–316.
[*5*] Shih, C. F. and Asaro, R. J., *Journal of Applied Mechanics*, Vol. 56, 1989, pp. 763–779.
[*6*] Aoki, S., Kishimoto, K., and Takeuchi, N., *Transactions*, Japan Society of Mechanical Engineers, Vol. 56A, 1990, pp. 638–645 (in Japanese).
[*7*] Yagawa, G., Takahashi, Y., and Ueda, H., *Journal of Applied Mechanics*, Vol. 52, 1985, pp. 319–325.
[*8*] Yagawa, G. and Ishihara, K., *Journal of Pressure Vessel Technology*, Vol. 111, 1989, pp. 241–246.
[*9*] Rice, J. R., Paris, P., and Merkle, J. in *Progress in Flaw Growth and Fracture Toughness Testing, ASTM STP 536*, American Society for Testing and Materials, Philadelphia, 1973, pp. 231–245.
[*10*] Merkle, J. G. and Corten, H. T., *Journal of Pressure Vessel Technology*, Vol. 96, 1974, pp. 286–292.
[*11*] Rice, J. R., Drugan, W. J., and Sham, T-L. in *Fracture Mechanics (Twelfth Conference), ASTM STP 700*, American Society for Testing and Materials, Philadelphia, 1980, pp. 189–221.
[*12*] Hutchinson, J. W. and Paris, P. C. in *Elastic-Plastic Fracture, ASTM STP 668*, J. D. Landes, J. A. Begley, and G. A. Clarke, Eds., American Society for Testing and Materials, Philadelphia, 1979, pp. 37–64.
[*13*] Paris, P. C., Tada, H., Zahoor, A., and Ernst, H. A. in *Elastic-Plastic Fracture, ASTM STP 668*, J. D. Landes, J. A. Begley, and G. A. Clarke, Eds., American Society for Testing and Materials, Philadelphia, 1979, pp. 5–36.
[*14*] Aoki, S., Kishimoto, K., and Sakata, M., *Journal of Applied Mechanics*, Vol. 48, 1981, pp. 825–829.
[*15*] Atluri, S. N., Nishioka, T., and Nakagaki, M., *Engineering Fracture Mechanics*, Vol. 20, 1984, pp. 209–244.
[*16*] Brust, F. W., Nishioka, T., Atluri, S. N., and Nakagaki, M., *Engineering Fracture Mechanics*, Vol. 22, 1985, pp. 1079–1103.
[*17*] Nishioka, T. and Yagami, T., *Engineering Fracture Mechanics*, Vol. 31, 1988, pp. 481–491.
[*18*] Yoshimura, S., Yagawa, G., and Atluri, S. N., *Nuclear Engineering and Design*, Vol. 111, 1989, pp. 273–289.
[*19*] Yagawa, G. and Matsuura, S., *Nuclear Engineering and Design*, Vol. 83, 1984, pp. 259–265.
[*20*] Yagawa, G. and Yoshimura, S., *Nuclear Engineering and Design*, Vol. 97, 1986, pp. 195–209.
[*21*] Yagawa, G., Miyoshi, A., and Yoshioka, A., *Engineering with Computer*, Vol. 3, 1988, pp. 149–156.
[*22*] Yoshioka, A., Yagawa, G., Miyoshi, A., and Soneda, N., *International Journal*, Japan Society of Mechanical Engineers, Vol. 31, 1988, pp. 233–239.
[*23*] Yagawa, G., Yoshioka, A., Yoshimura, S., and Soneda, N. in *Proceedings*, International Computer in Engineering Conference, Anaheim, CA, American Society of Mechanical Engineers, Vol. 2, 1989, pp. 267–272.
[*24*] Yagawa, G., Soneda, N., and Yoshimura, S. in *Proceedings*, Sixth International Congress on Experimental Mechanics, Portland, The Society for Experimental Mechanics, 1988, pp. 241–245.

[25] Yagawa, G., Soneda, N., and Yoshimura, S. in *Proceedings*, Seventh International Conference on Fracture, Houston, Vol. 3, Pergamon Press, New York, 1989, pp. 2059–2067.
[26] Yagawa, G., Yoshioka, A., Yoshimura, S., and Soneda, N. in *Proceedings*, Tenth Structural Mechanics in Reactor Technology, Anaheim, CA, The American Association for Structural Mechanics in Reactor Technology, Vol. 6, 1989, pp. 1–12.
[27] Kikuchi, M. and Yano, K., *International Journal*, Japan Society of Mechanical Engineers, Series I, Vol. 33, 1990, pp. 179–185.
[28] Kikuchi, M. in *Proceedings*, Fifth International Conference on Numerical Methods in Fracture Mechanics, Freiburg, FRG, Pineridge Press, Swansea, U.K., 1990, pp. 533–544.
[29] Kang, B. S. and Kobayashi, A. S., *Transactions*, American Society of Mechanical Engineering, *Journal of Pressure Vessel Technology*, Vol. 110, 1988, pp. 291–300.
[30] Dadkhah, M. S. and Kobayashi, A. S., *Engineering Fracture Mechanics*, Vol. 34, 1989, pp. 253–262.
[31] Engelstad, M. J., Chambless, D. A., Swinson, W. F., and Turner, J. L., *Experimental Mechanics*, Vol. 27, 1987, pp. 23–30.
[32] Lee, C. A., Richard, T. G., and Rowlands, R. E., *Experimental Mechanics*, Vol. 28, 1988, pp. 409–416.
[33] AbdelMohsen, H. H., Huang, Y. M., and Rowlands, R. E., *Experimental Mechanics*, Vol. 29, 1989, pp. 474–480.
[34] Gu, C., Bates, D. M., Chen, Z., and Wahba, G., *Journal of Matrix Analysis*, Vol. 10, 1989, pp. 457–480.
[35] Sirkis, J. S. and Taylor, C. E., *Experimental Mechanics*, Vol. 30, 1990, pp. 26–33.
[36] Yagawa, G., Takahashi, Y., and Kashima, K., *Engineering Fracture Mechanics*, Vol. 19, 1984, pp. 755–769.
[37] Brust, F. W., Nishioka, T., Atluri, S. N., and Nakagaki, M., *Engineering Fracture Mechanics*, Vol. 22, 1985, pp. 1079–1103.
[38] Ernst, H. A., Paris, P. C., and Landes, J. D. in *Fracture Mechanics (Thirteenth Conference), ASTM STP 743*, R. Roberts, Ed., American Society for Testing and Materials, Philadelphia, 1981, pp. 476–502.

DISCUSSION

M. A. Sutton (written discussion)—The authors presented surface displacement data for a region very close to the tip of a growing crack in a Type 304 stainless steel specimen. It is well known that the surface dimpling in the crack-tip vicinity is substantial. Since the authors imaged the dots onto a CCD or other type array, the motion of the dots recorded by the camera has all three components of displacements in the data!

Of course, under certain situations, the effect of the out-of-plane motion on the inplane data can be reduced to a value that is in the noise of the system and hence immeasurable. I believe that the authors should conclusively show by a baseline experiment or analytical work or both on their optical system how much the out-of-plane motion affects the inplane measurements! That is, they should provide an error band for their data due to the presence of significant out-of-plane motion. Otherwise, their data cannot be used with any confidence.

G. Yagawa, S. Yoshimura, A. Yoshioka, and C-R. Pyo (authors' closure)—Since some other reviewers pointed up the same thing, we have added a section, Measurement Error of Displacement and Strain, in the revised paper. Please refer to it.

M. A. Sutton (written discussion)—I should also note that much work has been done by Dr. Jim Sirkis (now at the University of Maryland) on dot patterns and how to accurately track their motion. The authors may wish to include his work in their references.

G. Yagawa, S. Yoshimura, A. Yoshioka, and C-R. Pyo (authors' closure)—We would like to refer to the work on dot patterns by Dr. Jim Sirkis and other researchers' works on data smoothing in the section, Interpolation of Mark Displacements, of the revised paper.

Thank you very much for your kind suggestion.

[1]Department of Mechanical Engineering, University of South Carolina, Cola, SC 29208.

Thomas A. Cruse[1] *and Giorgio Novati*[2]

Traction Boundary Integral Equation (BIE) Formulations and Applications to Nonplanar and Multiple Cracks

REFERENCE: Cruse, T. A. and Novati, G., "**Traction Boundary Integral Equation (BIE) Formulations and Applications to Nonplanar and Multiple Cracks,**" *Fracture Mechanics: Twenty-Second Symposium (Volume II), ASTM STP 1131,* S. N. Atluri, J. C. Newman, Jr., I. S. Raju, and J. S. Epstein, Eds., American Society for Testing and Materials, Philadelphia, 1992, pp. 314–332.

ABSTRACT: The hypersingular Somigliana identity for the stress tensor is used as the basis for a traction boundary integral equation (BIE) suitable for numerical application to nonplanar cracks and to multiple cracks. The variety of derivations of hypersingular traction BIE formulations is reviewed and extended for this problem class. Numerical implementation is accomplished for piecewise-flat models of curved cracks, using local coordinate system integrations. A nonconforming, triangular boundary element implementation of the integral equations is given. Demonstration problems include several three-dimensional approximations to plane-strain fracture mechanics problems, for which exact or highly accurate numerical solutions exist. In all cases, the use of a piecewise-flat traction BIE implementation is shown to give excellent results.

KEY WORDS: analytical methods, stress intensity factors, three dimensions, linear elastic fracture mechanics, boundary integral equations, boundary element methods, fracture mechanics, fatigue (materials)

Fracture mechanics formulations in the standard boundary integral equation (BIE) format suffer from a well-known problem of degeneracy when the two crack surfaces become one mathematical plane [*1*]. The reason for the degeneracy is that the formulation of elastic equilibrium must be able to distinguish between two surfaces, and the standard BIE cannot do this for cracks. Three well-established approaches to circumvent this degeneracy include the multiregion approach [*2*], the special Green's function approach [*3*], and the displacement discontinuity approach [*4*].

The multiregion approach has the drawback of needing to model the continuum ahead of the crack, between the crack front(s) and the external surface(s) of the body. The accuracy of the solution is compromised by the modeling; further, the need to initially model an internal surface limits the utility of this approach for fatigue crack growth modeling.

The special Green's function approach seems inherently limited to two dimensions. The required Green's function is a solution to the elastic field equations for the case of an internal crack in the infinite body, subject to loading from a Kelvin (point load) singularity imposed at an arbitrary internal location. While such a solution is conceivable in three dimensions, such a closed-form solution in all but the most elementary three-dimensional problems seems unlikely.

[1]H. Fort Flowers Professor of Mechanical Engineering, Vanderbilt University, Nashville, TN 37235.
[2]Assistant professor, Politecnico di Milano, Milan, Italy.

The displacement discontinuity (DD) method is the formulation now favored by most investigators as offering real advantages for complex three-dimensional fracture mechanics solutions with great flexibility in crack shape and form. However, the basic BIEs for this problem are hypersingular (unbounded integrals) and require special attention to the formulation and to the numerical implementation. The current report will make some observations on these difficulties, and will extend one of the earlier approaches to the case of multiple and nonplanar internal cracks. The application of the formulation to surface cracks is straightforward and will be the subject of future reports.

Displacement Discontinuity Formulations

The following derivations address recent developments on the application of three different, but related, displacement discontinuity (DD) formulation strategies. The DD is defined as a surface across which the displacement vector is discontinuous and is represented by the jump in the displacement vector, denoted as $\Delta u_i(Q)$, where $Q(y)$ is a point on the surface of displacement discontinuity, Γ. The surface of the DD is taken to be nonplanar and may be composed of a finite set of discrete surfaces. In some of the formulations, the surface is taken to be piecewise flat. The bounding curve for the DD is denoted $\partial\Gamma$ and is assumed to be piecewise smooth.

The stresses at any point not on Γ are denoted by $\sigma_{kj}(p)$, where $p(x)$ is the stress solution point. When $p(x) \rightarrow \Gamma$, the stress solution point is denoted as $P(x)$. The stresses in an infinite body due to an arbitrary surface of DD are given by the following Somigliana identity

$$\frac{8\pi}{\mu}\sigma_{kj}(p) = \int_\Gamma \left\{\frac{2\nu}{1-\nu}\delta_{kj}F_{,i} + \delta_{ik}F_{,j} + \delta_{ij}F_{,k}\right\}\Delta u_i(Q)dS(Q)$$

$$+ \int_\Gamma \left\{-\frac{2}{1-\nu}n_l r_{,ijkl} + n_k\nabla^2 r_{,ij} + n_j\nabla^2 r_{,ik} + \frac{2\nu}{1-\nu}n_i\nabla^2 r_{,kj}\right\}\Delta u_i(Q)dS(Q)$$

$$= \frac{8\pi}{\mu}\{\sigma^0_{kj} + \sigma^*_{kj}\} \tag{1}$$

where

$$F(p,Q) = \nabla^2\frac{\partial r}{\partial n} = \left(\frac{2}{r(p,Q)}\right)_{,l} n_l(Q) \tag{2}$$

and where

$$r(p,Q) = r(x,y) = \sqrt{(x_i - y_i)(x_i - y_i)}$$

$$r_{,i} = \frac{\partial r}{\partial y_i} = \frac{y_i - x_i}{r(x,y)} = -\frac{\partial r}{\partial x_i} \tag{3}$$

The Somigliana identity for the DD, Eq 1, is valid for any piecewise smooth surface, Γ, upon which the applied tractions are in local equilibrium, $\Delta\sigma_{kj}(P) = \sigma_{kj}(+) - \sigma_{kj}(-) = 0$, for each point on the upper $(+)$ and lower $(-)$ surfaces of Γ. The DD identity is hypersingular. By this we mean that the identity contains unbounded terms as $p(x) \rightarrow P(x)$.

The various mathematical treatments in the literature report on different, but largely equivalent, approaches to coping numerically with the hypersingular nature of Eq 1.

The first numerical application known to these authors of a form of this set of equations was made to the case of a circular crack loaded by normal pressures [5]. At a slightly later time, Weaver published an application for rectangular cracks [4], and Bui [6] published a more general approach for cracks of arbitrary, planar shape. However, the numerical results of Bui were quite limited in terms of accuracy, an issue later seen to be related to the hypersingular nature of the governing equations. Somewhat earlier, Cruse [7] published a general formulation for flat cracks that is generally of the same approach as Bui, but without numerical results. Those numerical results were long in coming, in part due to the hypersingularity issues on numerical implementation [8].

The first paper to operationally address the hypersingular Somigliana identity, Eq 1, reported on the limiting form of this identity for the interior point taken, in the limit, to the surface of the body [9]. Cruse showed that one could regularize the Somigliana stress identity by subtracting a rigid body displacement term from the displacement field, such that the displacement value at the limiting surface point is zero. However, such a local regularization process does not apply to the DD integral equation formulation contained in Eq 1.

Three different approaches to reducing the hypersingular nature of Eq 1 will now be presented. The first approach [10] is a direct evaluation of Eq 1 for $P(x)$ on Γ. Each term in the hypersingular integrals is integrated for an assumed, continuous DD field on Γ. The authors found that if the DD is continuous at $P(x)$ and has a unique set of derivatives at $P(x)$, then all unbounded contributions had zero integrals, due to zero-valued integrals of the angular variations of the integrands. This result occurs because the integral operator has zero-valued integrals at $P(x)$, on the exclusion surface (see the Appendix) for the singularity, Γ_ε at $P(x)$.

While the authors state that they are using the finite part (FP) approach to treating the hypersingular integral equations, this is not strictly true. The concept of the finite part of a hypersingular integral is developed in the Appendix to this paper. The essential element of the FP proof is that, for continuous integral operators, the unbounded results on the exclusion surface cancel the unbounded results arising from the remainder of the surface, $\Gamma - \Gamma_\varepsilon$. Nevertheless, we will refer to their work as a direct FP interpretation of the Somigliana identity for the DD.

Given that the interior stresses and the hypersingular operator are continuous as $p(x) \rightarrow P(x)$, the FP of the hypersingular Somigliana identity may be written in the following form

$$\frac{8\pi}{\mu}\sigma_{kj}(P) = \fint_\Gamma \left\{\frac{2\nu}{1-\nu}\delta_{kj}F_{,i} + \delta_{ik}F_{,j} + \delta_{ij}F_{,k}\right\}\Delta u_i(Q)dS(Q)$$

$$+ \fint_\Gamma \left\{-\frac{2}{1-\nu}n_l r_{,ijkl} + n_k\nabla^2 r_{,ij} + n_j\nabla^2 r_{,ik} + \frac{2\nu}{1-\nu}n_i\nabla^2 r_{,kj}\right\}\Delta u_i(Q)dS(Q) \qquad (4)$$

where the double slash through the integral sign denotes the finite part of the integral. The resulting FP integral equation (Eq 4) may be converted to the equivalent traction BIE by taking the stress tensor to operate on the local normal to Γ at $P(x)$. The integral identity then relates the local tractions on the crack to the global distribution of the DD on the same crack surface.

The use of the direct FP integral equation reduction, as in Eq 4, to a quadrature of the integral equations "requires" the use of closed-form integrations of the kernel functions.

Closed-form integrals are required to assure an exact FP interpretation of the resulting quadratures. The use of numerical integrations generally does not result in zero-valued multipliers of the unbounded terms. Further comments on the direct FP approach will be given in the discussion on numerical implementation of the traction BIE. The direct approach also magnifies the numerical errors in the BIE solution with the FP of the hypersingular integral operator, as found in Ref *9*.

A recent manuscript [*11*] has also applied a FP approach to the hypersingular Somigliana identity, this time for the problem of acoustic scattering at a surface of DD. In this FP development, the integral operator is first regularized through the use of continuity conditions on the DD and then interpreted in the FP sense. The resulting traction BIE is analytically equivalent to the development previously cited, but is more suitable for numerical quadrature of the resulting traction BIE, because of the regularization. Further, the hypersingular integrals are isolated in such a way that the finite part interpretation can be applied more obviously than was done in Ref *10*. However, the resulting equations are also more extensive as a consequence of the additional regularization steps taken in the formulation.

The approach used in Ref *11* begins by taking the DD to be locally smooth, and given in terms of the first-order Taylor series expansion about the point $P(x)$

$$\Delta u_i(Q) \approx \Delta u_i(P) + \Delta u_{i,\alpha}|_Q\{\zeta_\alpha(Q) - \zeta_\alpha(P)\} = \Delta u_i(P) + \Delta u_{i,\alpha}|_Q\bar{\zeta}_\alpha \tag{5}$$

where α denotes the two orthogonal directions tangent to Γ at $P(x)$.

The series expression for the DD is substituted into the Somigliana identity for the DD, which results in the following expression, which again may be interpreted as a traction BIE for the DD on Γ by operating this equation on the normal to Γ at $P(x)$.

$$\frac{8\pi}{\mu}\sigma_{kj}(p) = \int_\Gamma \Sigma_{kji}(p,Q)\{\Delta u_i(Q) - \Delta u_i(P) - \Delta u_{i,\alpha}\bar{\zeta}_\alpha\}dS(Q)$$

$$+ \Delta u_i(P)\int_\Gamma \Sigma_{kji}(p,Q)dS(Q) + \Delta u_{i,\alpha}(P)\int_\Gamma \Sigma_{kji}(p,Q)\bar{\zeta}_\alpha dS(Q) \tag{6}$$

The first integral in Eq 6 can be shown to be regular (that is, weakly singular) at $P(x)$, in the sense given in the Appendix. As such, the first integral is amenable to numerical quadrature. The second integral has a FP integral result in terms of a path integral of the DD. The third integral contains both continuous and discontinuous singular integral operators; as such it must be treated as a Cauchy principal value integral as $p(x) \rightarrow P(x)$. Unlike the direct FP approach, the implementation of Eq 6 in Ref *11* is more like the use of integration by parts to regularize the hypersingular traction BIE, than like the direct FP approach used in Ref *10*. The use of numerical quadrature of the traction BIE identity (Eq 6) requires such regularization, as will be further detailed in the discussion of numerical implementations.

A (third) FP approach will now be applied to the static Somigliana identity for the DD, Eq 1. The integral operator will be manipulated into forms for which the divergence theorem and Stoke's theorem provide a transformation from surface integrals into path integrals, for which the FP proofs are given in the Appendix. The approach is not limited to planar cracks and is easily implemented for multiple cracks.

The formulation begins by taking the first term in the top line integral in Eq 1; this term can be modified in form so as to take advantage of Stoke's theorem in the area integration.

The modifications are given as follows

$$\int_\Gamma \delta_{kj} F_{,i} \Delta u_i dS = \int_\Gamma \delta_{kj} \left(\frac{2}{r}\right)_{,il} n_l \Delta u_i dS$$

$$= 2\int_\Gamma \delta_{kj} \left[n_l \left(\left(\frac{1}{r}\right)_{,l} \Delta u_i \right)_{,i} - n_l \left(\frac{1}{r}\right)_{,l} \Delta u_{i,i} - n_i \left(\left(\frac{1}{r}\right)_{,l} \Delta u_i \right)_{,l} + n_i \left(\left(\frac{1}{r}\right)_{,l} \Delta u_i \right)_{,l} \right] dS \qquad (7)$$

The y_i derivative in the second integral in Eq 7 is taken outside the terms involving the distance $r(x,y)$ and the displacement discontinuity, Δu_i, but not outside the normal vector, n_l, thereby including the case of nonflat cracks. As given in the second line, the change in the derivative is canceled by the following, negative term. A third term is then subtracted from the first, to form a combination that can be integrated through Stoke's theorem. The fourth term in the integral cancels the term included for application of Stoke's theorem. The integral operator is continuous as $p(x) \to P(x)$, and the FP interpretation for Stoke's theorem is written for a smooth surface Γ as

$$\int_\Gamma (F_{,i} n_j - F_{,j} n_i) dS = \varepsilon_{mji} \oint_{\partial\Gamma} F dx_m \qquad (8)$$

where ε_{mji} is the permutation symbol. The resulting integral for the first term in Eq 1 may then be written as

$$\int_\Gamma \delta_{kj} F_{,i} dS = \oint_{\partial\Gamma} \delta_{kj} \varepsilon_{mli} \left(\frac{1}{r}\right)_{,l} \Delta u_i dx_m - \int_\Gamma \delta_{kj} n_l \left(\frac{1}{r}\right)_{,l} \Delta u_{i,i} dS + \int_\Gamma \delta_{kj} n_i \nabla^2 \left(\frac{1}{r}\right) \Delta u_i dS \qquad (9)$$

The FP of Eq 9 exists for $p(x) \to P(x)$, based on the development in the Appendix, for continuous DD. The result requires that the DD have a unique set of derivatives at $P(x)$. Implementation of Eq 9 can be made to problems with discontinuous DD fields at points other than $P(x)$ by the inclusion of the line integral term, in the preceding equation. This will be discussed briefly in the numerical implementation section, Eqs 18 to 20.

The preceding process of substitution and integration may be performed for each of the three terms in the first integral in Eq 1. When complete, it can be seen that the set of path integrals is zero for continuous DD on Γ, and the terms corresponding to the first surface integral in Eq 9 combine to form the discontinuity of the stress tensor ($\Delta\sigma_{kj} = 0$) from the upper to the lower surface of Γ. This latter interpretation holds only for the case that the derivatives of the DD exist uniquely at $P(x)$. The Laplacian of $(1/r)$ is zero for all interior points; for the case of taking the interior point to the surface Γ, the FP of the operator is also zero, as shown in the Appendix. The first integral from Eq 1 is then given by the result

$$\frac{4\pi}{\mu} \sigma^0_{kj}(p) = \int_\Gamma \left[\frac{2\nu}{1-\nu} \delta_{kj} n_i + \delta_{ik} n_j + \delta_{ij} n_k \right] \left(\frac{1}{r}\right)_{,l} \Delta u_{i,l}(Q) dS(Q) \qquad (10)$$

The resulting equation is no longer hypersingular, as one of the derivatives has been transferred to the DD term on Γ. The result has a zero Cauchy principal value, so long as the derivatives of the DD are uniquely defined at all points $P(x)$ on Γ. The gradient operation on the DD involves the normal derivative in the case of nonflat cracks. In such cases, the normal derivative of the displacement will have to be eliminated through Hooke's law in order to have a true BIE formulation. This substitution poses no problems for the nonflat crack case.

Following a similar process, the first three terms in the second integral in Eq 1 may be written in terms of path integrals of the DD at the crack front (zero values, except for surface crack problems), and additional terms. The terms arising from the first integration-by-parts terms combine to cancel the last term in the second integral in Eq 1. The complete results for the second integral are then found to be given by

$$\frac{8\pi}{\mu}\sigma_{kj}^{*}(p) = \int_{\Gamma}\left\{\frac{2}{1-\nu}r_{,jkl}[n_l\Delta u_{i,i} - n_i\Delta u_{i,l}]\right.$$

$$\left. + \nabla^2 r_{,j}[n_i\Delta u_{i,k} - n_k\Delta u_{i,i}] + \nabla^2 r_{,k}[n_i\Delta u_{i,j} - n_j\Delta u_{i,i}]\right\}dS(Q) \tag{11}$$

It is to be noted that both Eqs 10 and 11 are true for any crack surface, so long as the surface is regular (for example, piecewise smooth). Further, the results are totally regular as $p(x) \rightarrow P(x)$. It can also be shown, using local coordinates, that the results in Eq 11 only involve derivatives in the surface Γ, and not normal to it, as shown in different form in Ref *12*. This is a common result of the integration-by-parts approach, although the forms are different. Thus, these results combine to form another traction BIE for the DD problem.

The results obtained by combining Eqs 10 and 11 may be applied to the case of a piecewise-flat crack in order to compare the form of the terms to earlier formulations. We take the plane of the crack, Γ, to be given by the two coordinates x_β, $\beta = 1,2$. The normal is taken to be in the $-x_3$ direction, such that $n_i = -\delta_{i3}$. It is convenient to write $\sigma_{kj}(x)$ in terms of the terms that correspond to the tractions on Γ, σ_{33}, and $\sigma_{\beta 3}$ as follows

$$\frac{8\pi}{\mu}\sigma_{33}(p) = -\frac{4}{1-\nu}\int_{\Gamma}\Delta u_{3,l}\left(\frac{1}{r}\right)_{,l}dS - \frac{2}{1-\nu}\int_{\Gamma}[r_{,333}\Delta u_{\alpha,\alpha} - r_{,33\alpha}\Delta u_{3,\alpha}]dS(Q) \tag{12}$$

and as

$$\frac{8\pi}{\mu}\sigma_{\beta 3}(p) = -\int_{\Gamma}\nabla^2 r_{,\alpha}\Delta u_{\beta,\alpha}(Q)dS(Q) - \int_{\Gamma}\nabla^2 r_{,3}\Delta u_{\beta,3}(Q)dS(Q)$$

$$-\int_{\Gamma}\left[\left(\frac{2}{1-\nu}r_{,33\beta} - \nabla^2 r_{,\beta}\right)\Delta u_{\alpha,\alpha}(Q) - \frac{2}{1-\nu}r_{,3\alpha\beta}\Delta u_{3,\alpha}(Q) + \nabla^2 r_{,3}\Delta u_{3,\beta}(Q)\right]dS(Q) \tag{13}$$

These relationships hold for any point off the crack. The condition of local crack surface stress equilibrium ($\Delta\sigma(x) = \sigma(x^+) - \sigma(x^-) = 0$) is imbedded in the traction BIE. The limiting form for points on the crack surface is obtained by setting $x_3 = 0$, recognizing that the kernel terms with odd-order derivatives with respect to x_3 are zero for $P(x) \in \Gamma$. The final forms of Eqs 12 and 13 are then obtained as the following principal value (PV) integrals (see the Appendix)

$$\frac{8\pi}{\mu}\sigma_{33}(P) = \frac{2}{1-\nu}\int_{<\Gamma>}\left[2\left(\frac{1}{r^2}\right)r_{,\alpha} + r_{,33\alpha}\right]\Delta u_{3,\alpha}(Q)dS(Q) \tag{14}$$

and

$$\frac{4\pi}{\mu}\sigma_{\beta 3}(P) = -\int_{<\Gamma>}\left[\nabla^2 r_{,\alpha}\Delta u_{\beta,\alpha}(Q) + \frac{2}{1-\nu}r_{,33\beta}\Delta u_{\alpha,\alpha}(Q) - \nabla^2 r_{,\beta}\Delta u_{\alpha,\alpha}(Q)\right]dS(Q) \tag{15}$$

where the derivative term $r_{,33\alpha} = -(1/r^2)r_{,\alpha}$. The PV for the exclusion surface, Γ_ε, is zero in this case due to the zero value integral of the first-order trigonometric functions, $r_{,\alpha}$, in each term.

The preceding results are suitable traction boundary integral equations for the crack surface, Γ, subject to applied crack surface tractions. As has been shown in Ref *8*, the limiting forms of these equations for the field point taken to Γ results in the Cauchy principal value interpretation for the integrals, so long as the DD has continuous inplane derivatives at the limiting point. Otherwise, the final forms of Eqs 14 and 15 are unchanged from those given.

All of the integration-by-parts approaches appear to produce the same traction BIE for the normal stress, while the results for the shear tractions differ in their detailed forms. However, these authors believe that it is possible to transform all such traction BIE results into the same final form without affecting the numerical integration issues. We also believe, but have not proven, that all of the various forms of the traction BIE, so derived, are applicable to piecewise-flat cracks, so long as the integration is performed in a local coordinate system.

Numerical Quadrature Issues

Reference *8* reviews the numerical quadrature problems for traction BIE formulations found by earlier authors. The central issue in developing numerical quadrature algorithms, that was not properly treated in some of the earliest work, is the need for unique values of the derivatives of the DD at the collocation point $P(x)$ on the crack surface, Γ. The work reported in Ref *8* found an additional problem in traction BIE quadrature having to do with the principal value interpretation of the integrals. When using Gaussian integration (or other, numerical quadratures) for a principal value area integral, the Gauss points must be placed symmetrically around the singularity. If the points are not symmetric, the local integration on the area around $P(x)$ does not satisfy the principal value requirement, resulting in significant numerical errors at the collocation point.

The two recent FP approaches to the traction BIE formulation [*10,11*] resolve these problems in unique and creative ways. In the first [*10*], the need for single-valued derivatives of the DD is accounted for by a smooth interpolation of these variables over a polygon "centered" at $P(x)$. The authors then use exact integrations of the BIE kernel functions for the interpolation of the DD over Γ.

Reference *11* uses curved isoparametric boundary element interpolations, as did Ref *8*. The regularization process used on the hypersingular integrand is essentially equivalent in numerical terms to that used in Ref *8* to assure a proper numerical treatment of the principal value integrands, although the details of that statement require extensive comparisons of each paper's algorithms. The requirement for single-valued derivatives of the DD at $P(x)$ is satisfied by using nonconforming boundary elements for which the collocation points are not at the nodes of the elements, but are at interior points of the element. A result of the use of nonconforming elements is the need to account for discontinuities in the DD along element edges, by including the line integrals of the DD terms, such as in Eq 9.

The current paper attempts to combines the best of these approaches to quadrature of the traction BIE, based on a form of the integral equations developed by an integration-by-parts strategy. The boundary elements are linear triangular elements for which exact integrations of the integral equation kernel functions are available [*13*]. The boundary collocation points are taken at interior points in the triangular elements, resulting in a nonconforming interpretation of the DD on Γ. As indicated earlier, previous authors have used a variety of paths to the integration-by-parts of the traction BIE formulation. The second author of this paper has recently developed another regularization process [*14*] that makes use of clear, physically based sets of integration-by-parts substitutions, thereby removing some of the ad hoc elements of the derivations in Ref *7*. The approach in Ref *13* is the one actually used for the numerical examples contained herein.

The Somigliana identity, Eq 1, is again the basis of the new formulation. The formulation considers the potential for multiple cracks by taking two source points, $P(\xi,\eta)$, where (ξ,η) refer to two surfaces, Γ_ξ and Γ_η. The traction at the location of each surface due to the DD at the other surface is given as

$$\hat{t}_k(\xi) = \hat{\sigma}_{kj}(\xi)n_j(\xi) = n_j(\xi)\int_{\Gamma_\eta} \Sigma_{kji}(\xi,Q_\eta)\Delta u_i(Q_\eta)dS(Q_\eta) \tag{16}$$

and as

$$\check{t}_k(\eta) = \check{\sigma}_{kj}(\eta)n_j(\eta) = n_j(\eta)\int_{\Gamma_\xi} \Sigma_{kji}(\eta,Q_\xi)\Delta u_i(Q_\xi)dS(Q_\xi) \tag{17}$$

As shown in Ref *13*, each of these Somigliana identity equations can be regularized in the local crack surface coordinate systems such that they apply for points off the cracks and in the cracks. The Somigliana identities are then integrated-by-parts to obtain the following general traction BIE results

$$t_j(p) = \int_\Gamma K_{ji\alpha}(p,Q)\Delta u_{i,\alpha}(Q)dS(Q) + \oint_{\partial\Gamma} G_{ji}(p,Q)\Delta u_i(Q)ds(Q) \tag{18}$$

The boundary is next divided into triangular elements over which the displacement discontinuity varies linearly. For the nth triangle, Γ^n, we represent the DD and its inplane derivative in the "local" coordinate system using interpolation operators $\underline{D}$, and $\underline{N}$ as

$$\Delta u_i(Q) = \underline{N}^T(Q)\Delta\underline{u}_i^n$$

$$\Delta u_{i,\alpha} = \underline{D}_\alpha^T(Q)\Delta\underline{u}_i^n \tag{19}$$

where $\Delta\underline{u}_i^n$ is evaluated at the three vertices of the nth triangle. The underlined symbol denotes a matrix operator. The DD is included in this implementation for each element boundary, except at the crack front, due to use of nonconforming boundary elements.

Then, the traction BIE for a given surface of DD can be written in the following operational form

$$t_j(p) = \left[-\int_{\Gamma^n} A_i^{\alpha j} \underline{D}_\alpha^T ds \right] \Delta u_i^n + \left[\oint_{\partial\Gamma^n} A_i^{\alpha j} \underline{N}^T d\sigma n_\alpha^n \right] \Delta u_i^n \tag{20}$$

or in more compact form as

$$t_j(p) = g_i^j \Delta u_i^n \tag{21}$$

This result applies for each of the crack surfaces. The terms in Eq 20 have been integrated exactly such that the required principal value interpretation is fully and exactly accounted for. This is in the same spirit as done in Ref *10*. The resulting traction BIE may be applied to curved cracks by representing each as a set of piecewise-flat cracks. It is only necessary to collocate each of the traction results over each of the crack surfaces, at the n boundary element collocation points

$$\underline{t}^n = \underline{g}^{nn} \Delta \underline{u}^n \tag{22}$$

In Eq 22, $\underline{t}^n$ is a $3c^n$ row vector, where c^n is the set of traction collocation points; $\Delta \underline{u}$ is a $3d^n$ column vector, where d^n denotes the number of vertices on the element at which the DD field is unknown.

For piecewise-flat models of curved cracks, we let $\underline{R}^n$ denote the orthogonal matrix that transforms vector representations in the local-crack surface reference frame into the global coordinate system, denoted by upper-case symbols. Then

$$\underline{t}^n = \underline{G}^{nn} \Delta \underline{u}^n \tag{23}$$

where

$$\underline{G}^{nn} = \underline{R}^n \underline{g}^{nn} \underline{R}^{nT}$$

At this point, the DD on each of the m crack surfaces is simultaneously treated through superposition of all the traction BIE's for each DD by the summation

$$\underline{t}^h = \sum_{m=1}^{M} \underline{G}^{hm} \Delta \underline{u}^m \tag{24}$$

In order to obtain a square set of equations, we take three collocation points for each of the triangular elements. The three collocation points in each triangular element are taken to be along the axes connecting the element centroid to the vertices, at 60% of the distance from the centroid to the vertex. Fewer collocation points are needed for the elements along the crack front, where the DD at the crack front vanishes, in order to retain a square system of equations. The selection of the coordinates of these points in the triangle is based on numerical experience described in detail in Ref *13*.

Numerical Results for Multiple and Nonplanar Cracks

The present numerical results are relevant to the analysis of cracks imbedded in an infinite medium subjected to a remote loading and are mainly intended to demonstrate the applicability of the traction BIE to the case of nonplanar and multiple cracks. All the examples considered are for three-dimensional cracks whose geometries simulate two-dimensional angled and curved cracks (plane strain) in order that direct comparison to known solutions is possible. The case of a plane, isolated crack is also considered with the purpose of assessing the performance of the adopted technique in a simple situation. A planar crack surface "strip," parallel to the x_2 axis, is used to model each crack surface segment in the two-dimensional cross sections shown in Fig. 1. Each strip, as defined in Fig. 2, is of variable width conforming to the maps in Fig. 1. Each strip is modeled symmetrically with respect to the plane, $x_2 = 0$, by eight triangular elements, keeping the strip mesh along the x_2 direction unaltered in each example. The strips are taken to have very great length in the x_2 direction in order that plane strain conditions are modeled. This modeling approach in no way detracts from the three-dimensional character of the solution algorithm, even though the models clearly are most accurate only near the axis, $x_2 = 0$. Further, while three of the crack geometries are symmetric with respect to $x_1 = 0$, no symmetry is assumed in the numerical implementation of the traction BIE for these examples.

A remote applied stress of $\sigma_{33}^{\infty} = 1000$ (stress units) has been considered in all examples. The applied stress of $\sigma_{13}^{\infty} = 1000$ was also considered in the first example to validate the shear loading solution. The following values of material constants have been adopted: $E = 10^6$ (stress units), $\nu = 0.3$.

Unless otherwise specified, the DD results reported are average values obtained by weighting the DD values at adjacent element vertices (incompatible model). The weighting factors are the amplitudes of the element vertex angles, normalized by 360°. The weighted DD values are denoted by Δu_i^{av}. The quantity

$$\delta_i = \max_k \left| \frac{[\Delta u_i^{\text{av}} - (\Delta u_i)_k]}{\Delta u_i^{\text{av}}} \right| \tag{25}$$

represents the maximum discrepancy between the weighted DD and the nodal DD, for k-elements surrounding the mesh point (element vertex) of interest. The discrepancy between the reported DD results and the reference values of DD will be denoted by

$$d_i = \frac{(\Delta u_i^{\text{ref}} - \Delta u_i^{\text{av}})}{\Delta u_i^{\text{ref}}} \tag{26}$$

Example I

The isolated straight crack in Fig. 1a, in which $a = 5$ units, is modeled by 14 strips of elements, the mesh points on the x_1 axis being located at $x_1 = 0.0, \pm 1.5, \pm 3.0, \pm 4.0, \pm 4.8, \pm 4.9, \pm 5.0$. The discretization consists of 75 mesh points and 112 elements with 312 DD unknowns. Table 1 displays the solution results, δ, d, for representative mesh-points along the x_1 axis given remote applied tension and shear stresses. The reference solution is the exact two-dimensional DD solution given by

$$\Delta u_i = [4(1 - \nu^2)/E]\sigma_{3i}^{\infty}(a^2 - x_1^2)^{1/2} \quad (i = 1, 3) \tag{27}$$

Table 1 clearly indicates the discrepancies that exist in nodal estimates of the local DD using the incompatible element modeling approach, especially near the crack tip. However, Table 1 also indicates that the weighted average values of the nodal DD are quite accurate, even without the use of a special crack-tip interpolation in the current numerical imple-

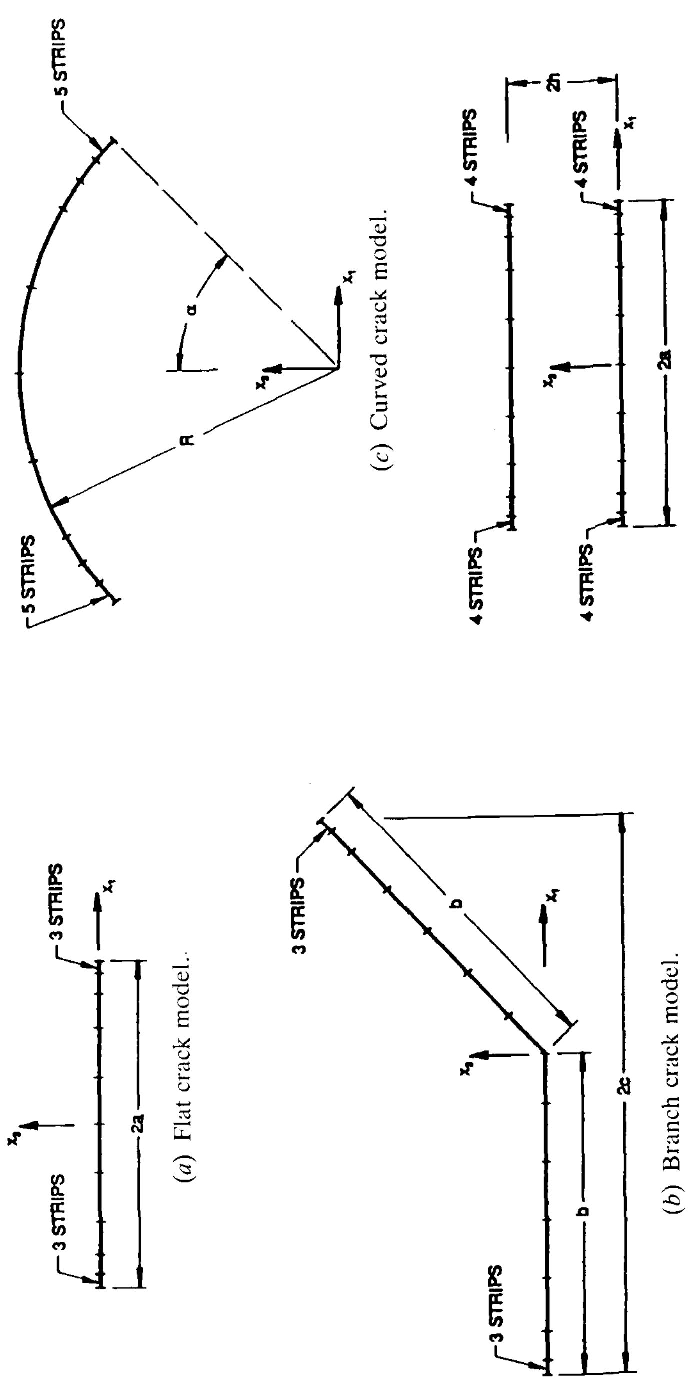

FIG. 1—*Cross sections of the simulated two-dimensional cracks using the crack segment models shown in Fig. 2.*

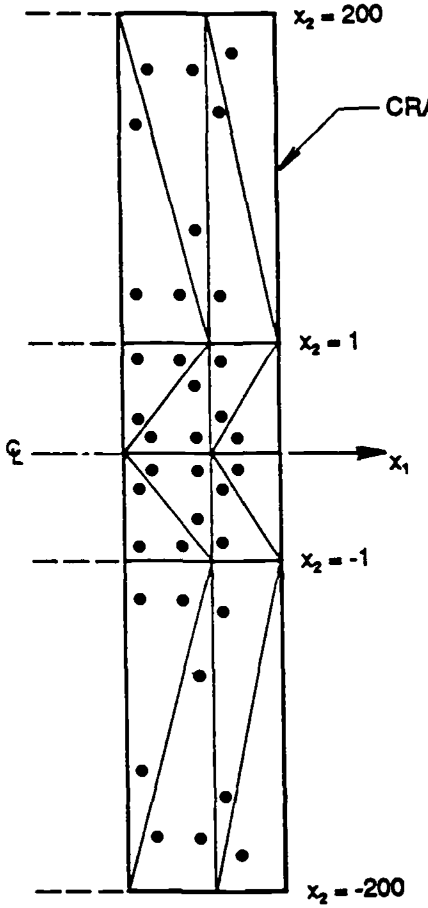

FIG. 2—*Two representative planar crack surface element strips showing collocation points as heavy dots; crack front elements are at maximum* x_1.

mentation. The normal stress and shear stress solutions are of essentially the same degree of accuracy, as expected.

Example II

This example considers the angled crack in Fig. 1*b*, for which $b = 10$ and $2c = 10 + 10\sqrt{2}/2$. The meshes used on the horizontal and inclined (45°) portion of the crack surface are identical. The mesh points along the x_1 axis are located at $x_1 = -10.0, -9.9, -9.8, -9.5, -8.6, -7.0, -5.2, -3.4, -1.6, 0.0$. The total BEM mesh includes 144 elements with 95 mesh points. The number of DD unknowns is 1224.

A reference solution for the corresponding two-dimensional DD problem has been obtained using the code BIECRX [3] that uses a Green's function approach to modeling the stress-free crack. In the BIECRX model considered, the horizontal portion of the crack is modeled as an open notch with a notch surface separation of 0.45 distance units. The crack branch is exactly modeled with the imbedded Green's function in BIECRX. A similar

TABLE 1—*DD solution comparisons for Example I.*

x_1/a, $x_2 = 0$	δ_3, %	d_3, %	δ_1, %	d_1, %
0.0	0.26	−0.55	0.26	−0.55
0.8	0.39	−0.82	0.5	−0.73
0.92	0.70	−0.04	0.73	0.07
0.96	0.44	2.5	0.48	2.6
0.98	4.1	2.5	4.1	2.6

modeling strategy was demonstrated for other branched crack problems [*15*]. The stress-intensity factors (SIFs) $K_{\rm I}$ and $K_{\rm II}$ at the inclined crack tip as well as the DD along the upper surface of the branched crack are computed with comparable accuracy (for points away from the notch surfaces).

Table 2 compares the SIF solutions obtained by BIECRX with the results of Tada [*16*]. The results are in essential agreement, given that both are numerical results. DD values obtained from BIECRX along the upper half of the crack branch, segment BC, are used as reference values for the present three-dimensional traction BIE results. The results are given in Table 3.

The results in Table 3 clearly demonstrate the good accuracy for the branched crack solution that was obtained with the traction BIE code. The solution becomes mode accurate away from the crack tip, but in all cases the comparison is satisfactory. As the angle of the crack branch increases, we can expect the percent error in d_1 to increase, as the actual DD in the normal direction decreases and the DD error remains at about the same magnitude.

Example III

The circular crack geometry is shown in Fig. 1*c* with $R = 10$ and $\alpha = 45°$. The crack is modeled with 18 element strips. The locations for the 10 mesh points with $x_2 = 0$, $x_1 > 0$ is given by mapping onto a constant radius circle with angles of 0, 15, 30, 35, 40° from the vertical through the center; the last five nodes approaching the crack tip are equidistant from each other and lie on a straight line segment of length = 0.4, tangent to the original crack shape at the crack tip (and hence at a slope of 45°). Thus, there are four coplanar element strips in the vicinity of each crack front. The size of the discretized problem is the same as for Example II.

The analysis of this example focused on the evaluation of the SIFs through extrapolation from the DD values relevant to the mesh points (with $x_2 = 0$) located on the four coplanar strips along the crack edge. Exact plane strain reference values for the SIFs is again available from Tada [*16*]. The stress intensity factors are taken for the DD problem from the usual DD asymptotic solution near the crack tip

$$\begin{Bmatrix} K_{\rm I}^* \\ K_{\rm II}^* \end{Bmatrix} = \frac{G}{4(1-\nu)} \sqrt{2\pi/r} \begin{Bmatrix} \Delta u_n \\ \Delta u_t \end{Bmatrix} \tag{28}$$

TABLE 2—*Stress-intensity factor comparisons for the branched crack, Example II.*

	BIECRX	Ref *16*
$K_{\rm I}/(\sigma_{33}^{\infty}\sqrt{\pi c})$	0.565	0.569
$K_{\rm II}/(\sigma_{33}^{\infty}\sqrt{\pi c})$	0.638	0.641

TABLE 3—*Comparison of the DD results with the BIECRX data for Example II.*

r	r/b	$\Delta u_1 \cdot 10^4$	$\Delta u_3 \cdot 10^3$	$\Delta u_1 \cdot 10^4$ BIECRX	$\Delta u_3 \cdot 10^3$ BIECRX	$d_1,\%$	$d_3,\%$
0.1	0.01	2.352	3.990	2.456	4.046	4.23	1.38
0.2	0.02	3.340	5.656	3.480	5.709	4.02	0.93
0.5	0.05	5.426	9.140	5.540	8.970	2.06	−1.90
1.4	0.14	9.293	14.999	9.446	14.719	1.62	−1.90
3.0	0.30	14.176	21.046	14.247	20.763	0.50	−1.36
4.8	0.48	18.530	25.359	18.405	25.086	−0.68	−1.10

where Δu_n and Δu_t are the weighted averaged normal and tangential DD components at one of the mesh points. The distance from the crack front is denoted by r. A linear extrapolation of these effective stress-intensity factor values in Eq 28 for $r \rightarrow 0$ is performed using a least-squares fit, and provides the estimated crack-tip SIFs. The results are given in Table 4 where $K_0 = \sigma_{33\infty} \sqrt{\{\pi(R\pi/4)\}}$, the SIF solution for a flat crack of the width $R\pi/2$. The value of K_0 for this problem ($R = 10$) is 4967.3 SIF units. The least square linear fit of the effective SIF data in Table 4 is then extrapolated to the crack front to obtain estimated SIF solutions. The extrapolated values are given by $K_{\mathrm{I}} = 2486.3$ SIF units, and $K_{\mathrm{II}} = 2757.8$ SIF units. The solutions from Tada *[16]* are 2563.6 and 2861.5 SIF units, respectively. The errors are then 3 and 4%, respectively. These results are quite satisfactory and demonstrate the applicability of the traction BIE implementation for curved cracks.

Example IV

The multiple crack configuration is shown in Fig. 1*d*, with $a = 5$. Two cases have been studied, with $h/a = 1$ and $h/a = 0.2$. Each of the two plane surfaces is discretized by a mesh of 16 element strips derived from the mesh of Example I by simply subdividing each of the two edge strips into two 0.05 unit width strips. Additional mesh points are taken at $x_1 = 4.95$. For the overall model, there are 170 mesh points, 256 elements, and 2160 DD unknowns.

As in the previous example, the SIF solutions are obtained by extrapolation to the crack front. Comparison is made to the reference solution *[17]*. The reference solutions are cited to be 1% accurate. Table 5 summarizes the comparisons with the traction BIE solutions. For this example, $K_0 = \sigma^\infty \sqrt{(\pi a)} = 3963.3$ SIF units. The extrapolation of the effective SIF data in Table 5 is based on the four points nearest the crack tip, and does not use the $r = 1$ data. The solution from Ref *17* is given for the two ratios in Tables 5 in 6. The Mode I values are seen to be in excellent agreement between the two solution results. However, the Mode II results are less accurate on an absolute basis. The results suggest that the

TABLE 4—*Extrapolated stress-intensity factors for curved crack, Example III.*

r	K_{I}^*	K_{II}^*	K_{I}^*/K_0	K_{II}^*/K_0
0.1	2510.8	2780.9	0.5055	0.5598
0.2	2494.7	2757.9	0.5022	0.5552
0.3	2514.5	2774.8	0.5062	0.5586
0.4	2543.8	2804.1	0.5121	0.5645

TABLE 5—*Comparisons of stress-intensity factor solutions for the multiple crack, Example IV.*

		$h/a = 0.2$				$h/a = 1.0$			
r	r/a	$\delta_3,\%$	$\delta_1,\%$	K_I^*/K_0	K_{II}^*/K_0	$\delta_3,\%$	$\delta_1,\%$	K_I^*/K_0	K_I^{*1}/K_0
1.0	0.20	0.61	1.1	0.6057	0.1245	0.47	0.77	0.7985	0.0512
0.4	0.08	0.80	1.1	0.6755	0.1532	0.72	0.89	0.8317	0.0578
0.2	0.04	0.50	0.53	0.6909	0.1574	0.47	0.49	0.8295	0.0588
0.1	0.02	0.52	0.52	0.6908	0.1572	0.50	0.52	0.8184	0.0586
0.05	0.01	3.9	3.9	0.6985	0.1587	3.8	3.9	0.8217	0.0592
Extrapolated values				0.7002	0.1594			0.8188	0.0593

TABLE 6—*Reference* 16 *stress-intensity factor results.*

$h/a = 0.2$		$h/a = 1.0$	
K_I/K_0	K_{II}/K_0	K_I/K_0	K_{II}/K_0
0.700	0.170	0.835	0.065

amount of numerical error is the same for both modes, but is magnified on a relative basis, as the Mode II solutions are about one order of magnitude smaller than the Mode I values. Regardless, the comparison demonstrates that the implementation of the traction BIE is also valid for the case of multiple cracks.

Acknowledgments

Both authors gratefully acknowledge the support of the Southwest Research Institute (SwRI) during the employment of the first author at SwRI and the visiting position of the second author. The first author also acknowledges the SwRI Internal Research Advisory Committee for partial financial support of the research. The second author also acknowledges the support provided by a NATO-CNR fellowship during his stay at SwRI, where the bulk of this work was performed.

APPENDIX

The elastic Somigliana identity may be regularized through the use of FP results for various terms in the hypersingular integral equation for the DD. The FP of a hypersingular integral is a generalization of the concept of the Cauchy principal value of a singular integral. In the general case, let us define the value of a (hyper)singular integral in the following manner

$$I(P) = \lim_{p \to P} \int_{\Gamma} \{. . .\} dS(Q) = \lim_{p \to P} \int_{\Gamma - \Gamma_\varepsilon} \{. . .\} dS(Q) + \lim_{p \to P} \int_{\Gamma_\varepsilon} \{. . .\} dS(Q) \tag{29}$$

where Γ_ε is taken to be a piecewise-smooth surface "centered" at the singular point $r(p,Q) = 0$. If the term in the brackets is weakly singular and the third integral is zero, then the integrals are weakly singular, but regular. If the third term is finite (say, equal to C), then the singular integral is discontinuous and has a Cauchy principal value. If the second and third integrals are unbounded in the limit, then the integral is said to be hypersingular. We will now consider this case for integrals that can be transformed by Stoke's theorem or by the divergence theorem into path integrals.

Hypersingular Integrals

Assume first that the hypersingular integral can be written in the form of the Stoke's integral theorem

$$\int_{\Gamma} (F_{,i}n_j - F_{,j}n_i)dS = \varepsilon_{mji} \oint_{\partial\Gamma} F dx_m \tag{30}$$

where the integrand, F, must be continuous and have continuous derivatives. Let the integrand also be hypersingular (for example, $0(1/r^{n+1})$; $n \geq 2$ for three-dimensional problems). Let $P(x)$ be on Γ, adjacent to an "interior" point, $p(x)$, such that the distance between the points is Δ, and $0 < \Delta \ll \varepsilon$. Equation 30 applies to any singular, differentiable function of $r(p,Q)$, so long as $\Delta \neq 0$.

Question 1

What is the order, in terms of Δ, of the following equation written for the surface Γ_ε, where $\varepsilon > 0$?

$$I_3 = \int_{\Gamma\varepsilon} \left(\frac{\partial F(p,Q)}{\partial x_i} n_j(Q) - \frac{\partial F(p,Q)}{\partial x_j} n_i(Q) \right) dS(Q) - \varepsilon_{mji} \oint_{\partial\Gamma\varepsilon} F(P,Q) dx_m(Q) \tag{31}$$

For $\Delta > 0$, the integrand in Eq 31 can be transformed by Stoke's theorem, such that

$$I_3 = \varepsilon_{mji} \oint_{\partial\Gamma\varepsilon} \{F(p,Q) - F(P,Q)\} d\sigma(Q) = 0\left(\frac{\Delta}{\varepsilon^{n+1}}\right) \tag{32}$$

where O(●) indicates the order of magnitude of the contained term. Thus, in the limit as $\Delta \to 0$, the integral is continuous at $P(x)$ and $I_3 = 0$ for any finite ε, and any piecewise-smooth surface Γ_ε.

The hypersingular integral operator may also contain terms that can be written in terms of the Laplacian operator, which in turn may be transformed to a line integral through the divergence theorem. Again, the integrand is taken to be a hypersingular function of $r(p,Q)$. This case results in the following question, with $n \geq 2$.

Question 2

What is the order, in terms of Δ, of the following equation written for the surface Γ_ε, where $\varepsilon > 0$?

$$I_4 = \int_{\Gamma\varepsilon} \nabla^2 F(p,Q) dS(Q) - \oint_{\partial\Gamma\varepsilon} \frac{\partial F(P,Q)}{\partial n} d\sigma(Q) \tag{33}$$

For $\Delta > 0$, the first term in Eq 33 is continuous as $p(x) \rightarrow P(x)$, and can be transformed by the divergence theorem, such that

$$I_4 = \oint_{\partial\Gamma\varepsilon} \left(\frac{\partial F(p,Q)}{\partial n} - \frac{\partial F(P,Q)}{\partial n}\right) d\sigma(Q) = 0\left(\frac{\Delta}{\varepsilon^n}\right) \tag{34}$$

Thus, as before, the integrand is continuous at $P(x)$ and the limit of Eq 34 as $\Delta \rightarrow 0$ is zero, for any $\varepsilon > 0$, and for any piecewise-smooth Γ_ε.

Thus, since the hypersingular integrands are continuous at $P(x)$, we may apply Stoke's theorem and the divergence theorem without restriction for $\Delta > 0$, and take the limit as $\Delta \rightarrow 0$, for *any order hypersingularity* in $r(p,Q)$ with the results

$$\lim_{\Delta\rightarrow 0} \left\{ \int_{\Gamma\varepsilon} (F_{,i}n_j - F_{,j}n_i) dS(Q) \right\} = \varepsilon_{mji} \oint_{\partial\Gamma\varepsilon} F(P,Q) dx_m(Q)$$

$$\lim_{\Delta\rightarrow 0} \left\{ \int_{\Gamma\varepsilon} \nabla^2 F dS(Q) \right\} = \oint_{\partial\Gamma\varepsilon} \frac{\partial F(P,Q)}{\partial n} d\sigma(Q) \tag{35}$$

The integrands in Eq 29 over the regular surface $\Gamma - \Gamma_\varepsilon$ are nonsingular and continuous for $\varepsilon > 0$; thus, it is easily shown that the following identities also hold

$$\int_{\Gamma-\Gamma\varepsilon} (F_{,i}n_j - F_{,j}n_i) dS = \varepsilon_{mji} \left\{ \oint_{\partial\Gamma} F(P,Q) dx_m - \oint_{\partial\Gamma\varepsilon} F(P,Q) dx_m \right\}$$

$$\int_{\Gamma-\Gamma\varepsilon} \nabla^2 F dS = \oint_{\partial\Gamma} \frac{\partial F(P,Q)}{\partial n} d\sigma - \oint_{\partial\Gamma\varepsilon} \frac{\partial F(P,Q)}{\partial n} d\sigma \tag{36}$$

where, in Eq 36, the path/normal is taken in the same sense as those in Eq 35. We may therefore combine the equations, seeing that the opposite terms cancel on Γ_ε. The resulting hypersingular equations are then given for any evaluation point by

$$I(P) = \lim_{\Delta\rightarrow 0} \left\{ \int_{\Gamma} (F_{,i}(p,Q)n_j - F_{,j}(p,Q)n_i) dS(Q) \right\} = \varepsilon_{mji} \oint_{\partial\Gamma} F(P,Q) dx_m(Q)$$

$$I(P) = \lim_{\Delta\rightarrow 0} \left\{ \int_{\Gamma} \nabla^2 F(p,Q) dS(Q) \right\} = \oint_{\partial\Gamma} \frac{\partial F(P,Q)}{\partial n} d\sigma \tag{37}$$

Equation 37 defines the finite part integrals for the hypersingular integrals, as the nonsingular result of the cancellation of the area integral on Γ_ε with the path integral $\partial\Gamma_\varepsilon$ from the integral on $\Gamma - \Gamma_\varepsilon$. Such FP results may be denoted by the double slash on the integral symbol

$$⨎_{\Gamma} (F_{,i}n_j - F_{,j}n_i) dS \doteq \varepsilon_{mji} \oint_{\partial\Gamma} F(P,Q) dx_m$$

$$⨎_{\Gamma} \nabla^2 F dS \doteq \oint_{\partial\Gamma} \frac{\partial F(P,Q)}{\partial n} d\sigma \tag{38}$$

The essential common element of all evaluations of hypersingular integrals is the requirement of continuity of the operator for $p(x) \rightarrow P(x)$, and the identification of all unbounded terms and their subsequent discarding. The assurance that these unbounded terms can be disregarded is given in the proofs such as given in this Appendix.

Cauchy Principal Value (PV)

In the case that the integrand in Eq 29 is singular ($n = 1$), the application of Stoke's theorem in Eq 30 or the divergence theorem in Eq 33 results in the following limiting approximations

$$I_3 = \varepsilon_{mji} \oint_{\partial\Gamma\varepsilon} \{F(p,Q) - F(P,Q)\} d\sigma(Q) = 0\left(\frac{\Delta}{\varepsilon}\right) \tag{39}$$

$$I_4 = \oint_{\partial\Gamma\varepsilon} \left(\frac{\partial F(p,Q)}{\partial n} - \frac{\partial F(P,Q)}{\partial n}\right) d\sigma(Q) = 0(1) \tag{40}$$

In the case of Eq 39, the integral operator is continuous as $p(x) \rightarrow P(x)$, and both of the two questions used for the hypersingular case also hold for the PV case. However, the results are usually presented as Cauchy PV results with a zero contribution on Γ_ε due to a zero-value result of integrating the trigonometric part of the integrand. In the case of Eq 40, we have the result for a *discontinuous* integrand; that is, the result is zero for $P(x)$, and of O(1) for $\Delta > 0$. For these cases, the results are presented as PVs of the integrals in the following form

$$I(P) = \underset{\varepsilon \to 0}{\text{limit}} \left\{\int_{\Gamma - \Gamma\varepsilon} \{. \, . \, .\} dS(Q)\right\} + C \doteq \int_{<\Gamma>} \{. \, . \, .\} dS(Q) + C \tag{41}$$

where $<\Gamma>$ denotes the PV interpretation of the area integral.

References

[1] Cruse, T. A., *Boundary Element Analysis in Computational Fracture Mechanics*, Kluwer Academic Publishers, The Netherlands, 1988.

[2] Blandford, G. E., Ingraffea, A. R., and Liggett, J. A., "Two Dimensional Stress Intensity Factor Computations Using the Boundary Element Method," *International Journal of Numerical Methods in Engineering*, Vol. 17, 1981, pp. 387–404.

[3] Cruse, T. A., "Two Dimensional BIE Fracture Mechanics Analysis," *Applied Mathematics and Modeling*, Vol. 2, 1978, pp. 287–293.

[4] Weaver, J., "Three Dimensional Crack Analysis," *International Journal of Solids Structures*, Vol. 13, 1977, pp. 321–330.

[5] Guidera, J. T. and Lardner, R. W., "Penny-Shaped Cracks," *Journal of Elasticity*, Vol. 5, 1975, pp. 59–73.

[6] Bui, H. D., "An Integral Equations Method for Solving the Problem of a Plane Crack of Arbitrary Shape," *Journal of Mechanics and Physics of Solids*, Vol. 25, 1977, pp. 29–39.

[7] Cruse, T. A., "Boundary Integral Equation Method for Three Dimensional Elastic Fracture Mechanics Analysis," AFOSR-TR-75-0813, Accession No. ADA-11060, 1975, pp. 13–20.

[8] Polch, E. Z., Cruse, T. A., and Huang, C.-J., "Traction BIE Solutions for Flat Cracks," *Computer Mechanics*, Vol. 2, 1987, pp. 253–267.

[9] Cruse, T. A. and Van Buren, W., "Three Dimensional Elastic Stress Analysis of a Fracture Specimen with an Edge Crack," *International Journal of Fracture Mechanics*, Vol. 7, 1971, pp. 1–15.

[10] Gray, L. J., Martha, L. F., and Ingraffea, A. R., "Hypersingular Integrals in Boundary Element Fracture Analysis," *International Journal of Numerical Methods in Engineering*, Vol. 29, 1990, pp. 1135–1158.

[11] Krishnasamy, G., Schmerr, L. W., Rudolphi, T. J., and Rizzo, F. J., "Hypersingular Boundary Integral Equations: Some Applications in Acoustic and Elastic Wave Scattering," *Journal of Applied Mechanics*, Vol. 57, 1990, pp. 404–414.

[12] Sladek, V. and Sladek, J., "Three Dimensional Curved Crack in an Elastic Body," *International Journal of Solids Structures*, Vol. 19, No. 5, 1983, pp. 425–436.

[13] Cruse, T. A., "An Improved Boundary-Integral Equation Method for Three Dimensional Elastic Stress Analysis," *Computers & Structures*, Vol. 4, 1974, pp. 741–754.

[14] Novati, G. and Cruse, T. A., "A Regularized Integral Equation Approach for Nonplanar, Piecewise-Flat, Three-Dimensional Cracks," submitted for publication.

[15] Chan, K. S. and Cruse, T. A., "Stress Intensity Factors for Anisotropic Compact Tension Specimens with Inclined Cracks," *Engineering Fracture Mechanics*, Vol. 23, 1986, pp. 864–874.

[16] Tada, H., Paris, P., and Irwin, G., *The Stress Analysis of Cracks Handbook*, Del Research Corporation, St. Louis, MO, 1985.

[17] Rooke, D. P. and Cartwright, D. J., *Compendium of Stress Intensity Factors*, Her Majesty's Stationery Office, London, England, Figs. 79 and 81.

Roshdy S. Barsoum[1] *and Tzi-Kang Chen*[2]

Evaluation of Three-Dimensional Singularities by the Finite Element Iterative Method (FEIM)

REFERENCE: Barsoum, R. S. and Chen, T.-K., **"Evaluation of Three-Dimensional Singularities by the Finite Element Iterative Method (FEIM),"** *Fracture Mechanics: Twenty-Second Symposium (Volume II), ASTM STP 1131*, S. N. Atluri, J. C. Newman, Jr., I. S. Raju, and J. S. Epstein, Eds., American Society for Testing and Materials, Philadelphia, 1992, pp. 333–346.

ABSTRACT: The three-dimensional asymptotic singularity fields for surface cracks and corner at a bimaterial interface are evaluated by the finite element iterative method (FEIM). The FEIM approach to three-dimensional cases is described and extended to evaluate the second singular term. The results for the bimaterial surface crack are correlated with experimental results, and the implications of the corner singularity on adhesive failure are discussed. It is shown that surface singularities are stronger than two-dimensional singularities in both cases, which means that commonly used plain-strain conditions at interfaces are nonconservative.

KEY WORDS: asymptotic fields, singularity, three-dimensional singularities, free surface, interfaces, bimaterials, adhesives, delamination, finite element method, eigenvalue analysis, numerical methods, fracture mechanics, fatigue (materials)

Nomenclature

E_1, E_2	Elastic modulus
U, $\{U\}$	Displacement field
i	Imaginary number $= \sqrt{-1}$
K	Stress intensity
k_1, k_2	Real and imaginary parts of the stress intensities
σ	Stress tensor
λ	Stress singularity
α, ε	Real and imaginary parts of the stress singularity
Θ, ϕ	Spherical angles
$R_e\{\cdot\}$	Real part of the function
ν	Poisson's ratio
r, R_s, R_b	Radial distance from point of singularity
F, G	Displacement eigenfunction
Σ	Summation sign
Λ	Eigenvalue
X, Y	Eigenfunction

Fracture failure is truly a three-dimensional phenomena. Since the inception of fracture mechanics, two-dimensional plain-strain approximations were used. This has carried the field to its current successful achievements. In dealing with homogeneous media, two-

[1]Manager, Solid Mechanics Program, Office of Naval Research, Arlington, VA 22217.
[2]Mechanical engineer, U.S. Army Material Technology Laboratory, Watertown, MA 02172.

dimensional analyses are satisfactory and in most cases lead to conservative results. As demonstrated here, this two-dimensional analysis could be nonconservative in nonhomogeneous media. It is therefore argued that three-dimensional fracture analyses are fundamental in the understanding of failure processes at interfaces and the development of fracture criteria. In addition, since measurements are usually performed at the surface, three-dimensional fracture mechanics analyses are needed for the interpretation of tests results.

Evaluating three-dimensional singularities of the asymptotic field are among the most difficult eigenvalue problems in fracture mechanics, therefore numerical methods represent the only practical means for their calculation. In spite of the fact that analytical solutions (such as the eigenfunction expansion method) were performed for the evaluation of the three-dimensional singularity at the free surface of an elastic homogeneous media, analytical methods are not general enough to deal with the complex problem of bimaterial fracture. In addition, since no closed-form solution can be found for cases involving nonhomogeneous media, the asymptotic field is a function of the material properties and therefore the analysis has to be performed for each specific case. The need for a numerical method to evaluate the asymptotic field (eigenvalue problems) as well as the stress-intensity factors is becoming more apparent as in the cases of cracks in composite materials and at interfaces. Crack-tip elements are successful in representing the singular field in homogeneous media when the singularity is known a priori, and the only parameters to be evaluated are the stress-intensity factor, J-integral, or the energy release rate. Still, difficulties arise in the use of such solutions, especially in anisotropic media because of the complexity of the expressions of the analytical solutions of the asymptotic field [*1*]. Therefore, the need for solving eigenvalue fracture problems in these cases and in bimaterial interfaces cannot be overemphasized.

In the treatment of nonhomogeneous media and cracks at interfaces, the finite element iterative method (FEIM) was used in evaluating both the asymptotic field and the fracture parameters [*2–4*]. The method has the capability to handle two-dimensional and three-dimensional problems as well as plates and shells. FEIM relies on the use of general purpose finite element (FE) programs that should have the desired library of elements. It should be noted that FEIM requires no additional modification to the FE programs other than the ability to manipulate the results in an iterative manner. The global-local nature of the method, its generality, and ease of its use, makes the method attractive for the analyst as well as the designer. Application of general numerical methods such as FEIM is even more desirable in most problems of complex material systems, such as in the micromechanics of composite materials, polycrystaline interfaces, and interfaces of adhesives and thin films, where analytical methods cannot be performed.

In this paper, we will give a brief review of the FEIM, its use in three-dimensional singularities, and its accuracy in the case of homogeneous media. The results for surface singularity near the terminal point of an interface crack at the free surface of an elastic bimaterial are discussed. It is shown that the bimaterial surface crack possesses a super singularity (that is, $>r^{-0.5}$). These three-dimensional FEIM results are then compared with experimental results and observations. Implications on failure in adhesive joints and bimaterials are also discussed. The case of a three-dimensional corner bimaterial interface is also discussed. In this case where no crack exists, the singularity could reach $r^{-0.5}$ for ν = 0.499. Implications of these results on the failure of composites and adhesives are also discussed.

The Finite Element Iterative Method (FEIM) for Three-Dimensional Cases

In applying the FEIM to three-dimensional singularity problems, a spherical mesh is constructed with its center at the point of the singularity of interest. Figure 1 shows typical

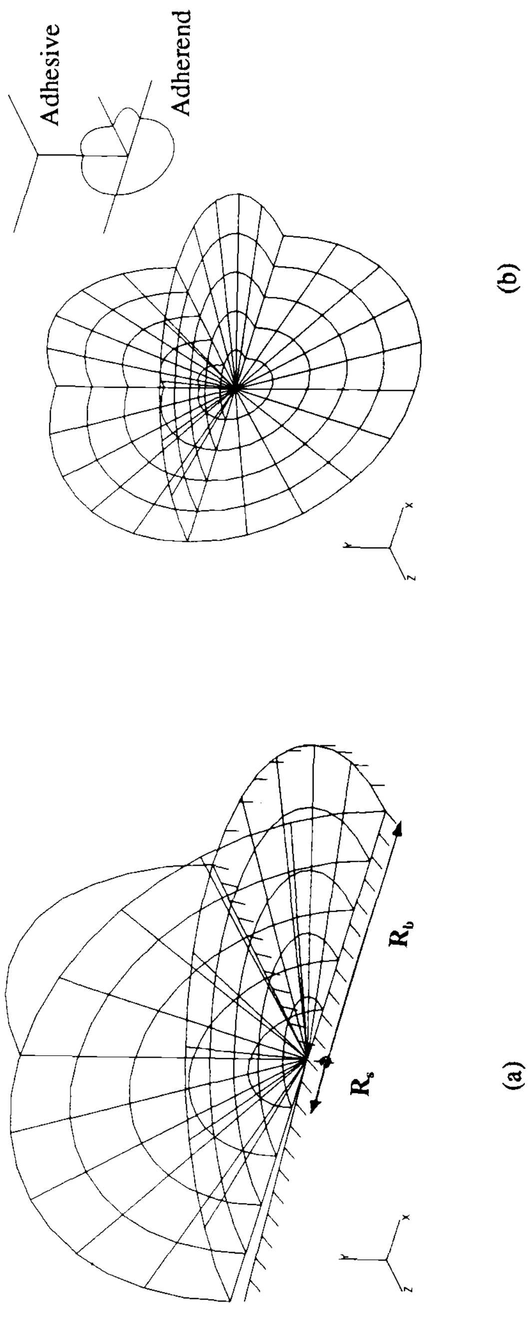

FIG. 1—(a) *FEIM three-dimensional mesh for interface surface crack, and* (b) *FEIM three-dimensional mesh for corner singularity.*

meshes for surface cracks and corners. The mesh consists of layers of spherical shells, at radial distances that are increasing quadratically from the origin of the singularity. References *2* and *3* give in detail the technique and its theoretical basis. For eigenvalue analysis, an arbitrary displacement field, U_{Rb}, is imposed first on the outermost shell, designated in Fig. 1 by the radius, R_b. However, since the power of the singularity of the three-dimensional asymptotic fields could depend on the loading mode (Modes I, II, or III), the imposed displacement field should reflect the mode of interest. An analysis is then carried out and the resulting displacements, U_{Rs}, at an inner radius, R_s, close to the singularity are scaled by A_1 to make a crack opening displacement (COD) = 1.0 applied at the outer boundary, R_b, and the analysis is repeated again. This procedure is repeated several times until convergence is achieved according to the following condition [*2*]

$$\alpha\{U^j_{Rb}\} + \beta\{U^k_{Rb}\} + \gamma\{U^l_{Rb}\} = 0,\ \alpha,\ \beta,\ \gamma = \text{constants} \tag{1}$$

where j, k, and l are any iteration number after convergence. It should be emphasized that the basic results of the analysis, U_{Rb}, are obtained from any general-purpose FE program. The FEIM operations involve only post-processing of these results. In the FEIM, the asymptotic displacement field is assumed to be of the form

$$U = \sum_{m=1}^{n} U^m = k_1 r^{1-\lambda_1} F^1(\nu,\Theta,\phi) + \sum_{m=2}^{n} k_m r^{1-\lambda_m} F^m(\nu,\Theta,\phi) \tag{2}$$

where $\lambda_1 > \lambda_2 > \lambda_3 \ldots\ldots > \lambda_n$.

For the most general cases, k_m, λ_m, and F^m are complex numbers and complex functions. In the case of a bimaterial interface crack, the first term is of the form [*5*]

$$U = R_e\{(k_1 + ik_2) r^{(1-\alpha+i\epsilon)}[F(\nu,\Theta,\phi) + iG(\nu,\Theta,\phi)]\} \tag{3}$$

Similar expressions can be written for the following weaker singularity terms that follow. This form of singular field is termed an oscillatory singular field since the stresses tend to oscillate with larger amplitudes as one approaches the singular point. They also lead to overlap and crack closure at small distances from the tip. Discussions regarding this solution form can be found elsewhere [*17*].

On the other hand, if the singularity is real, the asymptotic field is given by

$$U = K r^{(1-\lambda)} F(\nu,\Theta,\phi) \tag{4}$$

It was shown in Ref *3* that after m iterations the FEIM reduces the results to those obtained by the power sweep of an eigenvalue problem of a transfer matrix $[T]$.

$$\{U_{Rs}\} = [T]\,\{U_{Rb}\} \tag{5}$$

Therefore, the resulting displacements can be expressed in terms of the linear combination of the complete set of the fundamental eigenfunctions of the matrix $[T]$

$$\{U^m_{R_b}\} = \Lambda^m_1 \alpha_1 x_1 + \overline{\Lambda}^m_1 \overline{\alpha}_1 \overline{x}_1 + \sum_{l=3}^{n} \Lambda^m_l \alpha_l x_l \tag{6}$$

where the bars represent the conjugate functions. At convergence, $\Lambda_1 > \Lambda_2 > \Lambda_3$, the results of the iteration reduce to

$$\{U^m_{R_b}\} = \Lambda_1^m \alpha_1 x_1 + \bar{\Lambda}_1^m \bar{\alpha}_1 \bar{x}_1 \tag{7}$$

Using Eq 7, the m, $m + 1$, and $m + 2$ iterations can be written in the form

$$\beta_1\{U^m_{R_b}\} + \beta_2\{U^{m+1}_{R_b}\} + \beta_3\{U^{m+2}_{R_b}\} = 0 \tag{8}$$

from which the characteristic equation for Λ is obtained

$$\beta_1 + \beta_2\Lambda_1 + \beta_3\Lambda_1^2 = 0 \tag{9}$$

The stress singularity, $\lambda = (\alpha + i\varepsilon)$, is evaluated from the roots of Eq 9, and as discussed in Ref *3*

$$\Lambda_1 = (R_s/R_b)^{1-\lambda} \tag{10}$$

The resulting displacements after convergence can then be used to construct the asymptotic field as follows [*2*]

$$X_1 = Z_1 + iW_1 = \frac{1}{2}\left[\{U^m_{R_b}\} + i(\xi_1\{U^m_{R_b}\} - \frac{1}{A_1}\{U^{m+1}_{R_b}\})/\eta_1\right] \tag{11}$$

and $\Lambda_1 = \xi_1 + i\eta_1$, and A_1 = scaling factor.

The preceding analysis leads to the evaluation of the first eigenvalue, or the strongest singularity. Using FEIM, it is also possible to investigate the form of the singularity of the second term of the expansion (Eq 2). For cases where the first singularity is real, an orthogonalization to the first eigenvector in the power sweep method is used. Therefore, the new trial vector, U_{s+1}, to be imposed on the outer boundary in the iteration, will be

$$U_{s+1} = V_{s+1} - (V_{s+1} \cdot X_1)X_1 \tag{12}$$

where X_1 is the normalized first eigenvector, $X_1^TX_1 = 1$, and V_{s+1} is the resulting vector from any iteration. The preceding orthogonalization is proper only for the case of self-adjoint problems. Most interface crack problems are nonself-adjoint, and, therefore, they possess complex singularities (oscillatory singularities). In this case, the scheme should be of the form

$$U_{s+1} = V_{s+1} - (V_{s+1} \cdot Y_1)X_1 \tag{13}$$

where $X_1^TY_1 = 1$ and $\lambda_1 \cdot Y_1 = [T]^TY_1$. Y_1 is the left-handed eigenvector and satisfies the preceding properties, and X_1 can be calculated from Eq 11. In most of the cases studied here, $[T]^T \simeq [T]$, therefore $Y_1 = X_1$, and, therefore, Eq 12 is sufficiently accurate for calculating the second eigenvalue.

Three-Dimensional Surface Crack

From an engineering design point of view, the analysis of surface cracks is probably more important than those in the interior, because of environmental effects. In addition, from the experimental point of view, almost all measurements are performed at the surface. The homogeneous material surface crack was analyzed by FEIM [*9*] and agreed well with other analytical and numerical results [*6,7*]. This was also verified recently by Smith [*8*].

Bimaterial three-dimensional surface cracks were recently investigated using the FEIM [*9*]. The mesh shown in Fig. 1*a* was used to evaluate the singularity at the free surface of an elastic material bonded to a rigid substrate. The singularity was generally shown to be of a complex power, Eq 3. The real part, α, was found to be greater than 0.5 (or the case of plane strain) and a strong function of Poisson's ratio, ν. It increases from $\alpha = 0.5$ for $\nu = 0.0$ to $\lambda = 0.7$ for $\nu = 0.48$. Such behavior is usually termed a super singularity. The imaginary part starts at $\varepsilon = 0.174$, which is the same value as plane strain at $\nu = 0.0$, and becomes zero at $\nu > 0.25$.

The fact that the real part of the singularity is greater than 0.5 leads to an unbounded strain energy flux and *J*-integral at the surface. However, the strain energy density is still bounded, since $0 < \lambda < 3/2$. Similar results were obtained for Modes II and III for surface cracks in homogeneous media [*7*]. In the case of interfacial cracks, the stress field is always a mixed mode, therefore, this super singularity will persist for any mode of loading. FEIM analysis has confirmed this conclusion for any selection of the initial $\{U_{Rb}\}$. This singularity means that the crack would propagate at the surface before the interior (that is, the usual thumbnail is reversed). Correlation with experimental results is discussed later.

In order to investigate the nature of the singularity of the second term of the asymptotic field, Eq 12 was used for the cases of $\varepsilon = 0$, that is, $\nu > 0.25$.

The results show that the second singularity, λ_2, is very close to 0.5. The values are $\lambda_2 = 0.507$ for $\nu = 0.3$, $\lambda_2 = 0.513$ for $\nu = 0.4$, and $\lambda_2 = 0.523$ for $\nu = 0.48$.

It is well known that the accuracy of the power sweep method deteriorates for the second eigenvalue. Therefore, one might be inclined to assume that the second singularity is approximately equal to 0.5. In the boundary value problem, the dominate stress field will depend on the stress intensities associated with the first and second singularities. If the second stress intensity is much larger than the first, the influence of the super singularity or unbounded energy flux will be confined to a very small distance from the surface point, and the second singularity will dominate at a distance of the material grain size.

Comparison with Experimental Results

The comparisons discussed in this section are based only on the calculated singularity and the experimental observations. To perform a one-to-one correspondence between the analytical results and the experiments, the corresponding boundary value problem must be solved also. This however is not the subject of this paper. Therefore, we will refer to some other boundary value problem solutions in the literature [*10–12*] in order to substantiate comparison between the results.

1. Surface Angle of a Propagating Interfacial Crack

In Ref *13* (Fig. 10), duplicated here in Fig. 2, a thin film of polyimide of the order of 35 μm thick is bonded to a glass plate approximately 2 mm thick, and a straight cut is made. Observations of the cut test, which were performed on polyimide thin film, showed that the decohered region could be pinned along the cut or it could run along the cut, as shown in Fig. 2. Here, the lower part of this decohered region has two smaller decohesion regions that appear to be pinned at a point along the cut. The angle was found to be approximately 48° with the free edge of the cut. It was observed that when the crack front was at angles

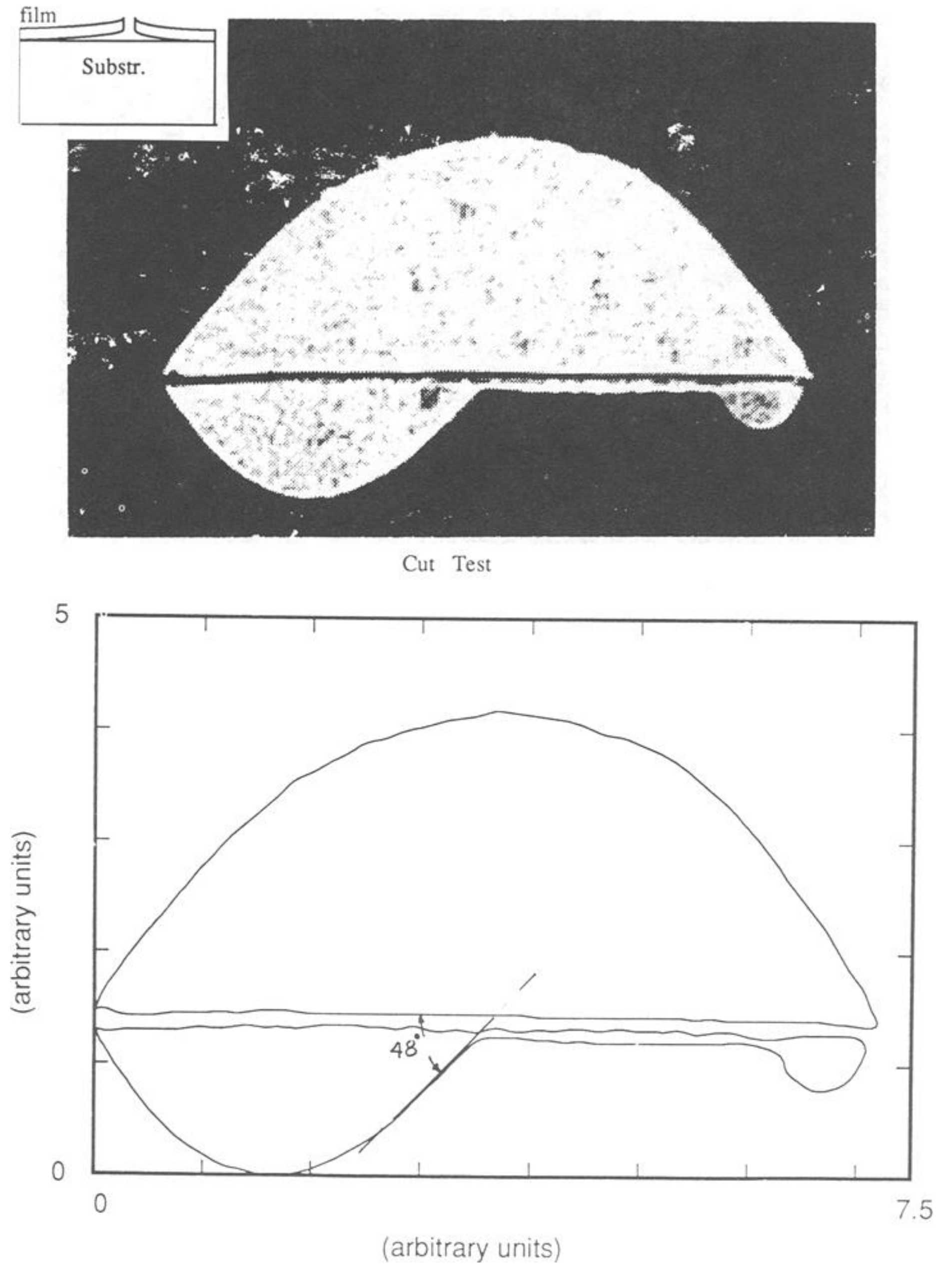

FIG. 2—*Schematic of the cut test* [13]. *Decohesion region from straight cut, glass plate with a film of polyimide.*

greater than 48°, the crack front would not be pinned and would propagate all along the free edge of the cut, as in the upper region of Fig. 2.

The delamination fracture of such films is based on the analysis of the delamination geometry of the upper portion only in Fig. 2, which does not involve the free surface. It was shown in Ref *13* that such delamination is governed by a mode-dependent interface toughness based on a critical energy release rate. This energy release rate is of special form, and it depends on two phase angles, which depend not only on the loading but also on local quantities including the singularity that governs the crack tip. This means that fracture of thin film interfaces depends not only on global quantities, but also on local processes at small distances from the crack tip. The behavior of the lower portion of the delamination in Fig. 2, depends on the free surface singularity along the cut. The three-dimensional singularity of such material ($\nu = 0.48$), at the vertex of the free surface of the cut, will depend on the angle of the crack front with the cut. It was found that an $r^{-1/2}$ singularity occurs at 48° for $\nu = 0.49$. At angles greater than 48°, the singularity power is greater than $-\frac{1}{2}$ and reaches approximately -0.7 for a 90° crack front as was shown in Ref *9*. Singularities greater than $-\frac{1}{2}$ would thus lead to an unstable vertex (crack front) and would not pin the crack at the cut. These analytical results are therefore consistent with the preceding experimental observations, showing that crack fronts with angles greater than 48° are unstable and propagate to the shape of the upper portion of Fig. 2.

Results of the boundary value problem of a thin film with free surface interface are not available. However, in Ref *11*, a three-dimensional analysis was performed using *p*-version finite element calculations to show that the corner (vertex) singularity region of dominance, in a nearly incompressible homogeneous media, is very strongly dependent on the boundary conditions and incompressibility. The region of dominance for a semielliptical surface crack (at the vertex) in a homogeneous media was found to be valid over distances of the order of 3% of the thickness of a compact tension specimen, and can reach 15% for incompressible materials. Delamination at interfaces poses a more complex and highly confined boundary condition, in addition to the polyimide incompressibility. Thus, it may lead to a large scale of dominance to apply to the free surface of a thin film. Therefore, these results have a bearing on the pinned front of the decohered region at distances of the order of micrometres to millimetres, where they can be related to a $-\frac{1}{2}$ singularity.

A second experiment discussed in Ref *14* can be also used for comparison with the results of FEIM given in Ref *9*. In this experiment, a bimaterial double cantilever specimen is fractured at the interface. The bimaterial is made of glass bonded to aluminum. When side grooves were used, the crack propagation resulted in the normal thumbnail front. On the other hand, when flat surface specimens were tested, the propagation occurred at the surface ahead of the interior, that is, reversed thumbnail, and the crack propagation angle was approximately 27°. Figure 3 shows these results. The boundary value problem of this configuration was not performed. However, interpolation between the singular results of the FEIM in Ref *9* is used here. One finds that the angle of propagation for an elastic material of $\nu = 0.30$, on a rigid substrate ($E_1/E_2 = 0.0$), is 31°. Extrapolating the results to the case of glass bonded to aluminum, this angle should be reduced, since E_1/E_2 is not zero, which agrees with these experimental results.

2. *Surface Displacements of an Interface Crack*

Chiang et al. [*15*] performed surface displacement measurements on a thick aluminum plate using the moiré interferometry method. The specimen had a single-edge sharp crack of half the width, crack length of 63.5 mm (2.5 in.) and thickness of 3.175 mm (⅛ in.). The boundary value problem for this case was analyzed in Refs *10* through *12*. The results of Ref *10* indicate that the effect of the weak vertex singularity at the free surface drops to zero within a boundary layer region of thickness of the order of 3% of the thickness of the plate. On the other hand, accurate measurements and analysis using the frozen stress photoelasticity and high-density moiré interferometry [*12*] indicate that the thickness of the

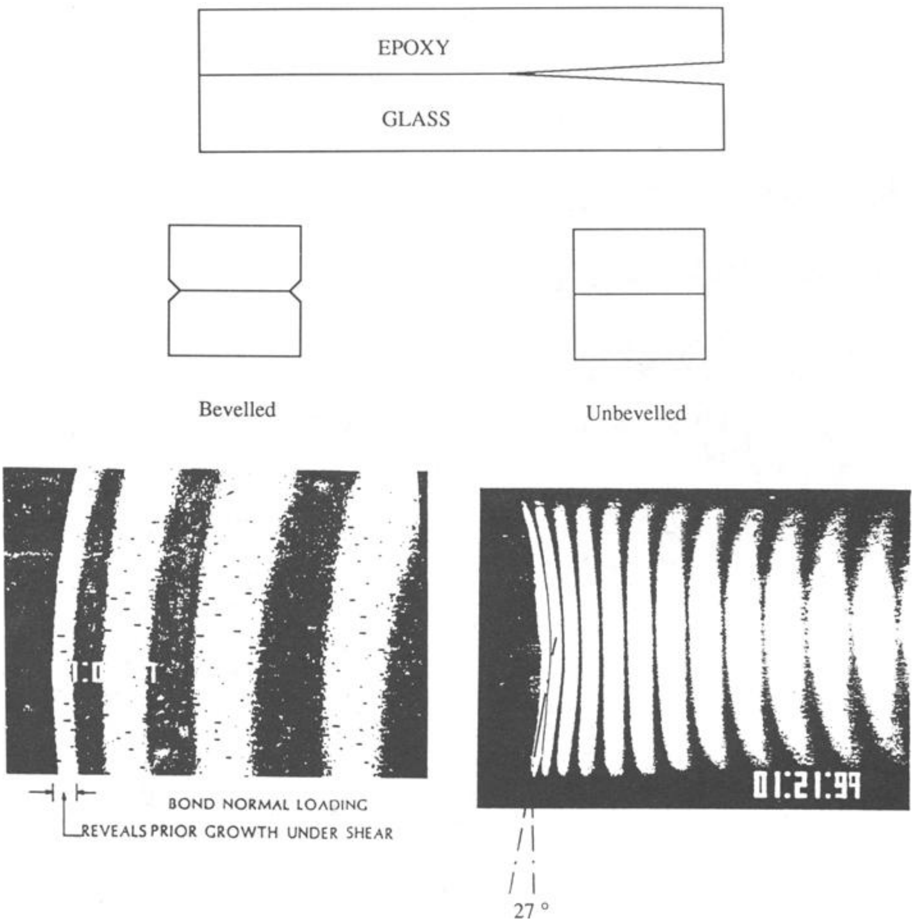

FIG. 3—*Crack front geometry for glass bonded to aluminum, double cantilever beam* [14].

boundary layer exceeds 10%, that is, 0.31 mm ($\frac{1}{80}$ in.). The surface displacement results of Ref *14* are shown in Fig. 4. They were obtained at very small loads to guarantee elastic behavior. The moiré photographs in Fig. 4 are magnified four times. Figures 4*c* and *d* show the corresponding FEIM results for the same free-surface displacements for $\nu = 0.30$ of the asymptotic field. This serves as a further correlation with the three-dimensional FEIM results that were reported previously in Ref *9*. These results were also compared with the theoretical and numerical analysis of Benthem [*7*] and Bazant and Estenssoro [*7*] in Ref *9*.

The stronger singularity associated with bimaterial surface cracks was recently examined by Chiang et al. [*16*] using a white light speckle method where the surface displacements were measured and the singularity was calculated by extrapolation. These results also indicate that the surface singularity is stronger than $r^{-0.5}$ as just discussed.

Corner Singularity for an Adhesive Lap Joint

In practice, it is usually common to find cracks at the adhesive corner of a lap joint, see Fig. 5. Investigation of the 90° corner singularity has not been possible in the past because

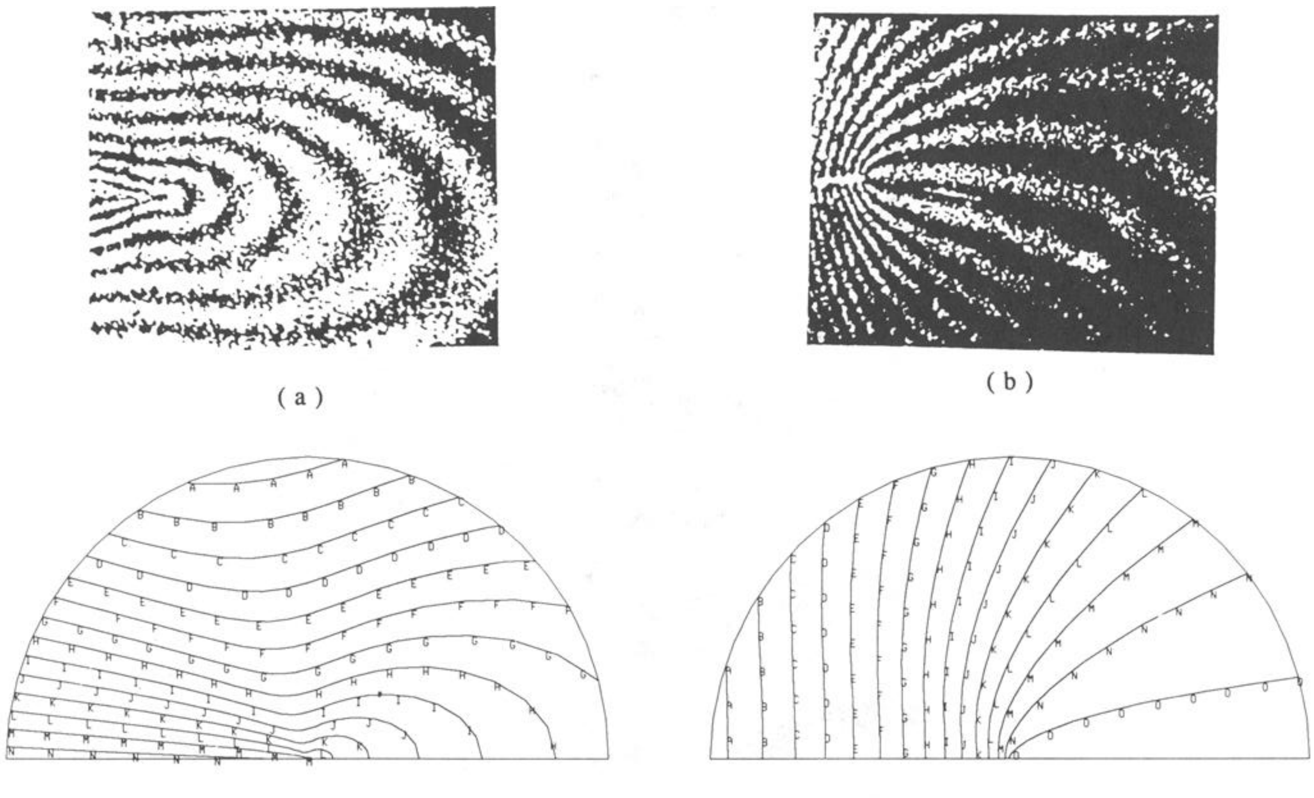

(a) (b) (c) (d)

FIG. 4—(a,b) *Surface displacement field* U, V, *after Ref* 15. (c,d) *Surface displacement field* U, V, *calculated by FEIM for* $\nu = 0.3$, *after Ref* 9.

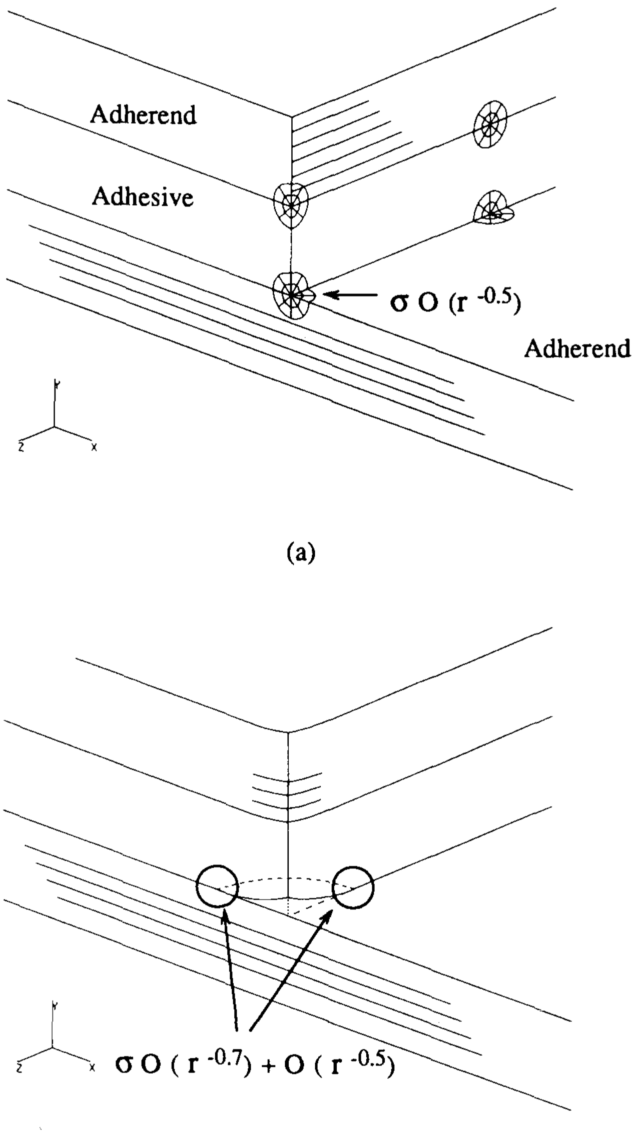

FIG. 5—(a) *Corner singularity in adhesive lap joint, and* (b) *failure at the corner.*

of the three-dimensional nature of the problem. The FEIM was applied to this problem and the singularity was found to be real and in the form

$$U = Kr^{(1-\lambda)}F(\nu,\ E_1/E_2,\ \Theta,\ \phi) \tag{14}$$

where the values of $(1 - \lambda)$ are given in Table 1 for different values of adhesive and adherent elastic properties.

TABLE 1—*Singularity at a corner interface.*

Case No.	E_1/E_2	ν_1	ν_2	$(1 - \lambda)$
1	0.01	0.0	0.3	1.0
2	0.01	0.15	0.3	0.7462
3	0.01	0.3	0.3	0.6310
4	0.01	0.48	0.3	0.5477
5	0.0	0.48	. . .	$\approx$0.5
6	0.1	0.0	0.3	1.0
7	0.1	0.15	0.3	0.8388
8	0.1	0.3	0.3	0.7347
9	0.1	0.48	0.3	0.6624

Implications of Surface Singularity at a 90° Corner

The stress singularity in all the cases in Table 1 is weaker than a crack. However, in Case 5, which represents the approximate properties of an adhesive and a typical adherent, the 90° corner singularity is close to that of a sharp crack, that is, $r^{-0.5}$, a result not commonly recognized by adhesive designers. It is therefore anticipated that an elastomer or an adhesive with high Poisson's ratio (that is, close to $\nu = 0.5$) will initially fail at the corner rather than the interior. Once an interface crack at the surface is generated, a larger singularity will ensue (that is, the super singularity of a three-dimensional free-surface interface crack). This will aggravate the situation, leading to further propagation. Unless the stress intensity, K, in Eq 2 drops substantially, allowing the second singularity ($\sim r^{-0.5}$) to take over, the interface surface crack will thus continue to propagate. This stress state coupled with the out-of-plane tension at the free surface are thought to be responsible for most of the edge failures in adhesive lap joints. The sketch in Fig. 5 shows such a failure scenario.

Global Formalism of the Finite Element Iterative Method (FEIM)

From the preceding discussion, it is essential to evaluate the stress-intensity factors for most of these three-dimensional cases. When the FEIM is used in stress-intensity calculation, that is, full boundary value problems, the initial boundary conditions $\{U_{Rb}\}$ for the spherical substructure are obtained from the global structure. One then can proceed to evaluate the asymptotic field as previously discussed, and the associated stress intensities can be calculated as subsequently shown.

Evaluation of Stress Intensities

It was shown in Ref *3* that the resulting eigenvector, X_1, from the iteration process in Eq 11 could be used in evaluating the real and imaginary parts of the displacement function, that is

$$X_1 = Z + iW = (k_1 + ik_2)(F + iG) \tag{15}$$

In carrying out the iterations in FEIM, one has to keep in mind that each iteration has a scaling factor of $(R_s/R_b)^3$ [*18*] that is essential in calculating the stress intensity factors (this scaling is ignored in the eigenvalue problem discussed in the previous sections).

If the analytical functions, F and G, are known (as given in Ref 5), then the stress intensities, k_1 and k_2, can be calculated from

$$k_1 = (ZF + WG)/(FF + GG)$$

$$k_2 = (WF - ZG)/(FF + GG) \tag{16}$$

However, if these analytical eigenfunctions are not known, a remote loading on an infinite domain must be analyzed first and the functions, F and G, are calculated using the definitions in Ref 5. Equation 16 would have the numerical values of F and G.

In many cases, one is only interested in the relative values of k_1 and k_2 in a specific material system under different loading conditions or geometric configurations of the specimen. For two cases, designated as I and II, one can relate the intensities using Eq 16. It was shown in Ref 3 that the relative values of the stress intensities can be then calculated from

$$\begin{bmatrix} Z^{II}Z^{II} & -W^{II}Z^{II} & -Z^{I}Z^{II} & W^{I}W^{II} \\ W^{II}Z^{II} & Z^{II}Z^{II} & -W^{I}Z^{II} & -Z^{I}Z^{II} \\ Z^{II}W^{II} & W^{II}W^{II} & -Z^{I}W^{II} & W^{I}W^{II} \\ W^{II}W^{II} & Z^{II}W^{II} & -W^{I}W^{II} & -Z^{I}W^{II} \end{bmatrix} \begin{Bmatrix} K_1^{I} \\ K_2^{I} \\ K_1^{II} \\ K_2^{II} \end{Bmatrix} = 0 \tag{17}$$

The procedure for calculating the stress-intensity factors from Eq 16 is general and can be applied also to mixed-mode fracture in homogeneous materials by dropping the imaginary parts. It is also more accurate than evaluating intensities from individual points because it is an inner product that is similar to a contour integral around the singularity. Its accuracy should be even better than the J-integral because only the displacements are used in the calculations instead of strains.

Conclusion

Three-dimensional interfacial surface cracks and interfacial corner singularities were evaluated using the finite element iterative method. It was shown that the interfacial surface crack singularity possesses a super singularity (greater than $1/\sqrt{r}$). This singularity reaches $r^{-0.7}$ for a material with a Poisson's ratio, $\nu = 0.48$, bonded on a rigid substrate. The calculated asymptotic displacement field of free-surface vertex was compared with moiré interferometry measurements. Predicted crack propagation at the free surface rather than the plain-strain condition in the interior compared favorably with experimental results of glass aluminum interface cracks.

A result of practical importance was presented on the three-dimensional interfacial 90° corner, it was found that the singularity approaches $r^{-0.5}$ that is the same as a plain-strain crack. This singularity is also higher than a two-dimensional 90° corner (approaches a maximum of $r^{-0.4}$). These results lead to the conclusion that an adhesive lap joint would fail at the free surface before the plane-strain center.

It was concluded from the bimaterial free-surface singularity results discussed here that two-dimensional analysis at interfaces is nonconservative and three-dimensional analysis must be used. The FEIM was demonstrated to offer a general global-local approach for evaluating the asymptotic field as well as the stress-intensity factors.

References

[1] Sih, G. C. and Chen, E. P., *Mechanics of Fracture—Cracks in Composite Materials*, Martinus Nijhoff, The Hague, The Netherlands, 1981.

[2] Barsoum, R. S., "Theoretical Basis of the FEIM for the Eigenvalue Problems of Stationary Cracks," *International Journal of Numerical Methods in Engineering*, Vol. 25, 1988, pp. 531–539.

[3] Barsoum, R. S., "Applications of the FEIM to the Eigenvalue Problems of a Crack Between Dissimilar Media," *International Journal of Numerical Methods in Engineering*, Vol. 25, 1988, pp. 541–554.

[4] Williams, M. L., "The Stresses Around a Fault or Crack in Dissimilar Media," *Bulletin*, Seismic Society of America, Vol. 49, 1959, pp. 199–204.

[5] Rice, J. R. and Sih, G. C., "The Plain Problems of Cracks in Dissimilar Media," *Journal of Applied Mechanics*, American Society of Mechanical Engineers, Vol. 32, 1965, pp. 400–402.

[6] Benthem, J. P., "State of Stress at Vertex of a Quarter Infinite Crack in Half Space," *International Journal of Solids and Structures*, Vol. 13, 1977, pp. 479–492.

[7] Bazant, Z. and Estenssoro, L. F., "Surface Singularity and Crack Propagation," *International Journal of Engineering Science*, Vol. 15, 1979, pp. 405–426.

[8] Smith, C. W., "Experimental Determination of Fracture Parameters in Three-Dimensional Problems," in this volume.

[9] Barsoum, R. S. and Chen, T-K., "Three Dimensional Interface Singularity of an Interface Crack," *International Journal of Fracture*, to be published.

[10] Nakamura, T. and Parks, D. M. "Three Dimensional Stress Field Near the Crack Front of a Thin Elastic Plate," *Journal of Applied Mechanics*, Vol. 55, Dec. 1988, pp. 805–813.

[11] Blom, A. F. and Anderson, B., "On the Semielliptical Surface Crack Problem: Detailed Numerical Solutions for Complete Elastic Stress Fields," *Surface-Crack Growth: Models, Experiments, and Structures, ASTM STP 1060*, W. G. Reuter, J. H. Underwood, and J. C. Newman, Jr., American Society for Testing and Materials, Philadelphia, 1990, pp. 77–98.

[12] Smith, C. W., Rezvani, M., and Chang, C. W., "Analysis of Optical Measurements of Free-Surface Effects on Natural Surface and Through Cracks," *Surface Crack Growth Models, Experiments and Structures, ASTM STP 1060*, W. G. Reuter, J. H. Underwood, and J. C. Newman, Jr., American Society for Testing and Materials, Philadelphia, 1990, pp. 99–111.

[13] Jensen, H. M., Hutchinson, J. W., and Kim, K.-S., "Decohesion of a Cut Prestressed Film on a Substrate," Harvard University, Division of Engineering, Report No. MECH-143, May 1989.

[14] Liechti, K. M. and Chai, Y.-S., "Three Dimensional Effects in Interfacial Crack Growth," 11th U.S. National Congress of Applied Mechanics, Tuscon, AZ, May 1990.

[15] Chiang, F. P., Li, S., and Wang, Y. Y., "Experimental Study of Near-Crack-Tip Deformation Fields," in this volume.

[16] Chiang, F. P., Yan, X. T., and Lu, H., "Measurement of Three-Dimensional Deformation of an Interfacial Crack in a Bimaterial," ASTM Twenty-Second National Symposium on Fracture Mechanics, Atlanta, GA, June 1990.

[17] Rice, J. R., "Elastic Fracture Mechanics Concepts for Interfacial Cracks," *Journal of Applied Mechanics*, Vol. 55, 1988, pp. 98,103.

[18] Barsoum, R. S., "Finite Element Solution of the Eigenvalue Problem Associated with the Fracture of Composites," Fourth International Conference on Numerical Methods in Fracture Mechanics, San Antonio, TX, 23–27 March 1987.

An-Yu Kuo,[1] Simon Shvarts,[1] and Randall B. Stonesifter[2]

An Analytical Solution for an Elliptical Crack in a Flat Plate Subjected to Arbitrary Loading

REFERENCE: Kuo, A.-Y., Shvarts, S., and Stonesifer, R. B., "**An Analytical Solution for an Elliptical Crack in a Flat Plate Subjected to Arbitrary Loading,**" *Fracture Mechanics: Twenty-Second Symposium (Volume II), ASTM STP 1131*, S. N. Atluri, J. C. Newman, Jr., I. S. Raju, and J. S. Epstein, Eds., American Society for Testing and Materials, Philadelphia, 1992, pp. 347–367.

ABSTRACT: An elliptical or partial-elliptical crack (either embedded or surface) of any orientation in a flat plate subjected to arbitrary crack surface loading is studied in this paper. Based on two analytical solutions, an elliptical crack embedded in an infinite space subjected to arbitrary crack surface loading and an uncracked flat plate subjected to arbitrary loading on its bounding surfaces, an alternating analytical procedure has been developed by the authors for the three-dimensional crack problem. The alternating analytical technique for the elliptical crack problem has been also implemented into a user-friendly computer software for use in mainframe and personal computers.

KEY WORDS: linear elastic fracture mechanics, mixed-mode fracture, partial-elliptical crack, surface crack, embedded crack, flat plate, alternating technique, analytical solutions, three-dimensional problems, fracture mechanics, fatigue (materials)

Many fracture mechanics problems associated with structural components such as pressure vessels and airplane fuselages can be idealized as an elliptical or partial-elliptical crack in a flat plate, as illustrated in Figs. 1 and 2. An elliptical or partial-elliptical crack is often a good approximation and bounding geometry for an arbitrarily shaped crack.

There have been numerous researchers working on the three-dimensional crack problem. A number of technical papers presenting results for the problem under various loading and geometry combinations are available in the literature. Atluri [*1,2*] has provided a good and thorough review on this topic. Until 1981, analytical solutions for an elliptical crack embedded in an infinite space were available only for polynomial crack surface loads up to the sixth order. A general solution for an embedded elliptical crack in an infinite space subjected to polynomial crack surface loads of any order was first obtained by Vijayakumar and Atluri [*3*] and then by Nishioka and Atluri [*4*]. This solution has been often referred to as the VNA solution.

For the problem of an elliptical or partial-elliptical crack in a more practical, finite thickness flat plate, an exact solution similar to that of Refs *3* and *4* is very difficult if not impossible to derive. Numerical methods such as the finite element method (FEM) and the boundary integral evaluation (BIE) have been used by many researchers, for example, Raju and Newman [*5*], to obtain the three-dimensional fracture mechanics solutions. However, such

[1]Associate and engineer, respectively, Structural Integrity Associates, Inc., San Jose, CA 95118.
[2]President, Computational Mechanics, Inc., Julian, PA 16844.

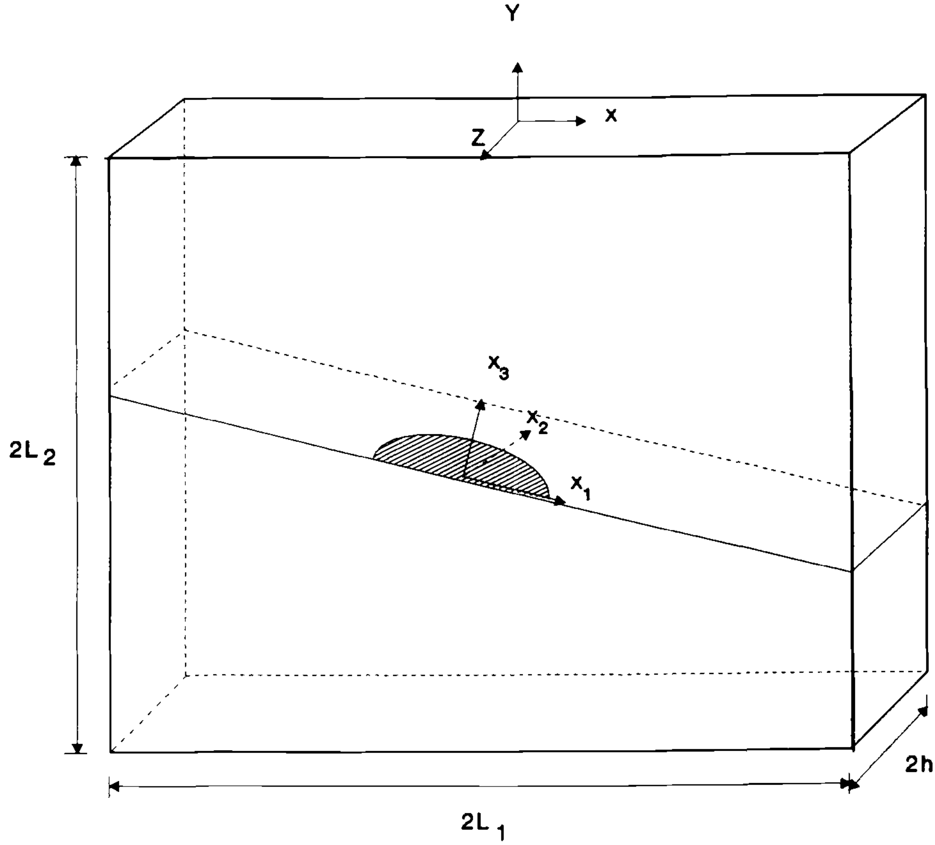

FIG. 1—*An elliptical (or partial-elliptical) crack in a flat plate.*

conventional numerical methods as FEM and BIE often require not only a lengthy computation time but also a large amount of manpower in preparing the mesh. Worst of all, for problems involving different geometries or sometimes loading conditions, the labor intensive numerical procedure just mentioned has to be repeated for each case. Nishioka and Atluri [*4*] have demonstrated successfully the concept of an alternating finite element method for the problem of an elliptical crack in a structure component of any shape. With this alternating finite element method, the computation and the modeling time can be greatly reduced relative to usual numerical methods since only an uncracked structure needs to be analyzed in the finite element analysis. However, the alternating finite element method proposed by Nishioka and Atluri [*4*] requires (1) manpower to prepare a three-dimensional FEM mesh for the uncracked plate for each crack geometry, (2) a numerical package separate from the finite element program to do a fairly complex mathematical manipulation for the problem of an elliptical crack embedded in an infinite space, (3) a nodal force generator to convert the residual stresses on the free surfaces resulting from the VNA solution into nodal forces for the next iteration of the finite element analysis, and (4) an automated computer program to carry out the iterative procedure of the alternating finite element method.

In this study, we have developed an analytical alternating procedure as well as a user-friendly computer program for problems of an elliptical or partial-elliptical crack in an infinite

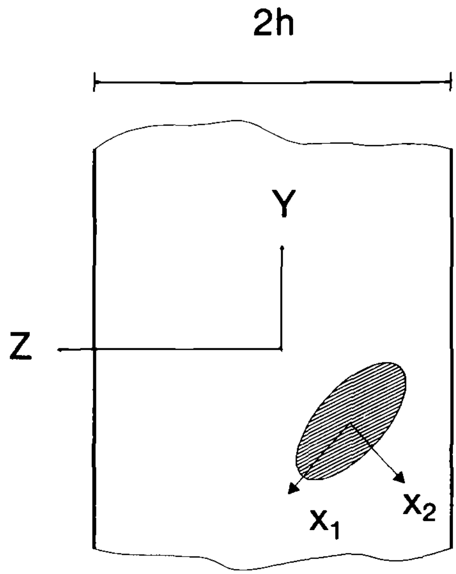

FIG. 2—*An elliptical (or partial-elliptical) crack at arbitrary location.*

flat plate. The cracked plate is assumed to be subjected to a set of arbitrarily applied crack surface tractions. The objective of this study is to enable researchers to simply enter plate thickness, crack location and orientation relative to the plate, crack dimensions, and crack surface loads to obtain K_I, K_{II}, and K_{III} solutions at the crack front without going through the previously mentioned labor intensity numerical procedures.

Assumptions

The following assumptions were made to simplify the problem.

(*a*) The plate of thickness $t(t = 2h)$, extends infinitely in its plane, that is, the plate extends infinitely in both x- and y-directions in Fig. 1.
(*b*) The plate material is assumed to be isotropic, homogeneous, and linear elastic.
(*c*) It is assumed that the stress singularity at the intersection of the plate surface and the crack front is still $-\frac{1}{2}$ even though Sih [6], Benthem [7,8], Bazant and Estenssoro [9,10], and Shivakumar and Raju [11] have shown that, in the region of about 2% into the plate thickness from the surface, the stress singularity at the crack front is actually slightly weaker than $-\frac{1}{2}$ for materials with Poisson's ratio of 0.3.

Boundary Conditions

As shown in Figs. 1 and 2, boundary conditions for the three-dimensional crack problem are:

1. On $z = -t/2 = -h$

$$\sigma_{zz}(x,y,-h) = \sigma_{zx}(x,y,-h) = \sigma_{zy}(x,y,-h) = 0 \tag{1}$$

2. On $z = t/2 = h$

$$\sigma_{zz}(x,y,h) = \sigma_{zx}(x,y,h) = \sigma_{zy}(x,y,h) = 0 \tag{2}$$

where $t = 2h$ is the plate thickness.

3. On the crack surfaces

$$x_3 = 0,\ (x_1/a_1)^2 + (x_2/a_2)^2 \leq 1,\ (a_1 > a_2)$$

the traction can be expressed in the following form [1]

$$\sigma_{3\alpha}(x_1,x_2,0) = \sum_{i=0}^{1}\sum_{j=0}^{1}\sum_{m=0}^{M}\sum_{n=0}^{m} A^{(i,j)}_{\alpha,m-n,n} x_1^{2m-2n+i} x_2^{2n+j} \quad (\alpha = 1,2,3) \tag{3}$$

where $A^{(i,j)}_{\alpha,m-n,n}$ are known constants of the prescribed crack surface loading; $x_1-x_2-x_3$ is a Cartesian coordinate which, as illustrated in Figs. 1, 2, and 3, is related to the global $x-y-z$ coordinate system by three translations and three rotations in a coordinate transformation; and a_1 and a_2 are, respectively, lengths of the major and the minor axes of the bounding ellipse of the crack.

Analytical Solution I—An Elliptical Crack in an Infinite Space (the VNA Solution)

A brief summary of the VNA solution is given next in this paper. For an elliptical crack embedded in an infinite space, as shown in Fig. 3, subjected to arbitrary crack surface loads given by Eq 3, the solution to the problem can be written in terms of three stress functions in the Trefftz's formulation [12,13] as

$$f_\alpha = \sum_{i=0}^{1}\sum_{j=0}^{1}\sum_{m=0}^{M}\sum_{n=0}^{m} C^{(i,j)}_{\alpha,m-n,n} F_{2m-2n+i,2n+j}(x_1,x_2,x_3) \quad (\alpha = 1,2,3) \tag{4}$$

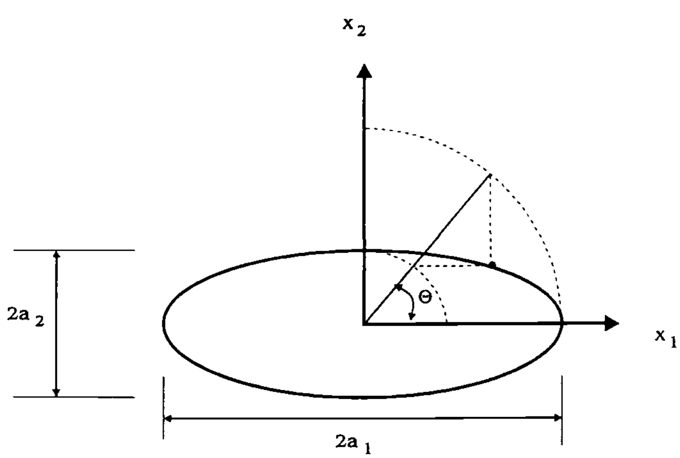

FIG. 3—*An elliptical crack embedded in an infinite space.*

where f_1, f_2, and f_3 are the three harmonic stress functions; $C^{(i,j)}_{\alpha,m-n,n}$ are constants that can be determined from the crack surface loading condition Eq 3; and $F_{m,n}(x_1,x_2,x_3)$ are functions defined as

$$F_{m,n} = \partial_1^m \partial_2^n \int_{s3}^{\infty} [\omega(s)]^{m+n+1} \frac{ds}{\sqrt{Q(s)}} \tag{5}$$

where

$$\partial_\alpha^m = \frac{\partial^m}{\partial x_\alpha^m} \quad (\alpha = 1,2) \tag{6}$$

$$\omega(s) = 1 - \frac{x_1^2}{a_1^2 + s} - \frac{x_2^2}{a_2^2 + s} - \frac{x_3^2}{s} \tag{7}$$

$$Q(s) = s(s + a_1^2)(s + a_2^2) \tag{8}$$

and s_1, s_2, and s_3 are the roots of the cubic equation

$$\omega(s) = 0 \tag{9}$$

The stress components, $\sigma_{\alpha\beta}$, and the stress functions, f_α, are related by Eqs 9*a* through *f* in Vijayakumar and Atluri's paper [*3*].

When calculating stresses from the stress functions, the following formulae given in Ref *1* will be used repeatedly

$$\int_{s_3}^{\infty} \partial_1^i \partial_2^j \partial_3^k [\omega(s)]^n \frac{ds}{\sqrt{Q(s)}} = n! \sum_{p=i/2}^{n} \sum_{q=j/2}^{p} \sum_{r=k/2}^{q} \left[J_{p-q,q-r,r}(s_3) \cdot \frac{(-1)^p (2p-2q)!(2q-2r)!(2r)! x_1^{2p-2q-i} x_2^{2q-2r-j} x_3^{2r-k}}{(n-p)!(p-q)!(q-r)!r!(2p-2q-i)!(2q-2r-j)!(2r-k)!} \right] \tag{10}$$

$$\begin{aligned} J_{p-q,q-r,r}(s_3) &= \int_{s_3}^{\infty} \frac{ds}{(s + a_1^2)^{p-q}(s + a_2^2)^{q-r} s^r \sqrt{Q(s)}} \\ &= \frac{2}{a_1^{2p+1}} \int_0^{u_1} (sn^{2p}u)(nd^{2q-2r}u)(nc^{2r}u)du \\ &= \frac{2}{a_1^{2p+1}} L_{p,q-r,r}(s_3) \end{aligned} \tag{11}$$

where *sn*, *nd*, and *nc* are Jacobian elliptic functions [*14*] defined as

$$sn^2 u_1 = \frac{a_1^2}{a_1^2 + s_3} \tag{12}$$

$$sn^2 u + cn^2 u = 1, \ \kappa^2 sn^2 u + dn^2 u = 1, \tag{13a}$$

$$dn^2u - \kappa^2 cn^2u = \kappa'^2,\ \kappa'^2 sn^2u + cn^2u = dn^2u, \tag{13b}$$

$$tnu = snu/cnu,\ dcu = dnu/cnu, \tag{13c}$$

$$cdu = cnu/dnu,\ ndu = 1/dnu, \tag{13d}$$

$$ncu = 1/cnu,\ sdu = snu/dnu \tag{13e}$$

$$\kappa^2 = 1 - (a_2/a_1)^2,\ \kappa'^2 = 1 - \kappa^2 \tag{13f}$$

and the L functions are defined as

$$L_{p,q-r,r} = \frac{1}{(2r-1)\kappa'^2}\{(sn^{2p+1}u)(nc^{2r-1}u)(nd^{2q-2r-1}u)|_0^{u_1}$$
$$+ [2(-p+r-1) + 2(p-q-r+2)\kappa^2]\cdot L_{p,q-r,r-1}$$
$$+ \kappa^2(-2p+2q-3)L_{p,q-r,r-2}\} \tag{14}$$

$$L_{p,q,-1} = \frac{1}{\kappa^{2p+2}}\sum_{j=0}^{p}\sum_{\gamma=0}^{1}\frac{(-1)^{j+\gamma+1}\kappa'^{2(1-\gamma)}p!}{(p-j)!j!(1-\gamma)!\gamma!}\cdot I_{2(q-j-\gamma)} \tag{15}$$

$$L_{p,q,-2} = \frac{1}{\kappa^{2p+4}}\sum_{j=0}^{p}\sum_{\gamma=0}^{2} 2\cdot\frac{(-1)^{j+\gamma+2}\kappa'^{2(2-\gamma)}p!}{(p-j)!j!(2-\gamma)!\gamma!}\cdot I_{2(q-j-\gamma)} \tag{16}$$

$$I_{2m+2} = \frac{2m(2-\kappa^2)I_{2m} + (1-2m)I_{2m-2} - \kappa^2 snu_1\cdot cnu_1\cdot nd^{2m+1}u_1}{(2m+1)\kappa'^2} \tag{17}$$

$$I_{-2m-2} = \frac{\kappa^2 dn^{2m-1}u_1\cdot snu_1\cdot cnu_1 + (1-2m)\kappa'^2 I_{-2m+2} + 2m(2-\kappa^2)I_{-2m}}{(2m+1)} \tag{18}$$

$$I_{-2} = E(\psi,\kappa), I_0 = F(\psi,\kappa) = u_1, I_2 = [E(\psi,\kappa) - \kappa^2 snu_1 cdu_1]/\kappa'^2, \psi = \tan^{-1}(a_1/s_3) \tag{19}$$

In Eq 19, $F(\psi,\kappa)$ and $E(\psi,\kappa)$ are incomplete elliptic integrals of the first and second kinds, respectively, and ψ is the amplitude of u_1.

By substituting Eq 4 into the equations for stresses then into Eq 3, a system of simultaneous linear algebra equations can be constructed for the unknown constants, $C^{(i,j)}_{\alpha,m-n,n}$, in Eq 4. Once the unknown constants, $C^{(i,j)}_{\alpha,m-n,n}$, in Eq 4 are solved, it has been shown that stress-intensity factors at the crack tip can be evaluated by the following equations [2,3]

$$K_I = 8\mu\sqrt{\pi/(a_1a_2)}\,B^{1/4}\left\{\sum_{i=0}^{1}\sum_{j=0}^{1}\sum_{m=0}^{M}\sum_{n=0}^{m}\left[(-2)^{2m+i+j}(2m+i+j+1)!\right.\right.$$
$$\left.\left.\frac{1}{a_1a_2}\left(\frac{\cos\theta}{a_1}\right)^{2m-2n+i}\left(\frac{\sin\theta}{a_2}\right)^{2n+j}C^{(i,j)}_{3,m-n,n}\right]\right. \tag{20}$$

$$K_{II} = 8\mu\left(\frac{\pi}{a_1a_2}\right)^{1/2}B^{-1/4}\frac{1}{a_1a_2}[H_1(\theta)a_2\cos\theta + H_2(\theta)a_1\sin\theta] \tag{21}$$

$$K_{III} = 8\mu\left(\frac{\pi}{a_1a_2}\right)^{1/2} B^{-1/4}\frac{(1-\nu)}{a_1a_2}\left[H_2(\theta)a_2\cos\theta - H_1(\theta)a_1\sin\theta\right] \tag{22}$$

where θ is defined in Fig. 3 and

$$H_1(\theta) = \sum_{i=0}^{1}\sum_{j=0}^{1}\sum_{m=0}^{M}\sum_{n=0}^{m}(-2)^{2m+i+j}(2m+i+j+1)! \left(\frac{\cos\theta}{a_1}\right)^{2m-2n+i}\left(\frac{\sin\theta}{a_2}\right)^{2n+j} C^{(i,j)}_{1,m-n,n} \tag{23}$$

$$H_2(\theta) = \sum_{i=0}^{1}\sum_{j=0}^{1}\sum_{m=0}^{M}\sum_{n=0}^{m}(-2)^{2m-i-j+2}(2m-i-j+3)! \left(\frac{\cos\theta}{a_1}\right)^{2m-2n-i+1}\left(\frac{\sin\theta}{a_2}\right)^{2n-j+1} C^{(1-i,1-j)}_{2,m-n,n} \tag{24}$$

$$B = a_1^2\sin^2\theta + a_2^2\cos^2\theta \tag{25}$$

However, the solutions given by Eq 4, in general, do not satisfy the stress-free boundary conditions, Eqs 1 and 2, on its bounding surfaces even though they satisfy the governing equations, $\nabla^2 f_\alpha = 0$, and the crack surface boundary conditions in Eq 3. That is, σ_{zz}, σ_{zx}, and σ_{zy} derived from the infinite space solution of Eq 4 are, in general, not zero on surfaces $z = \pm h$. It is worth noting a tensor transformation corresponding to a coordinate transformation is usually necessary in calculating the previously mentioned stresses because, in general, coordinate systems $x-y-z$ and $x_1-x_2-x_3$ are different. A typical distribution of the "residual" stresses on the bounding for an embedded crack in a plate is illustrated in Fig. 4.

To compensate for the nonzero stresses, $\sigma_{z\alpha}(\alpha = x,y,z)$, on the bounding surfaces of the plate, another analytical solution is required. In the analytical alternating procedure, the negatives of the stresses, σ_{zz}, σ_{zx}, and σ_{zy}, on the bounding surfaces of the plate, $z = \pm h$, due to the solution given by Eq 4 will be used as the surface loads in Analytical Solution II. The residual stresses on the plate bounding surfaces can be decomposed into a double Fourier series through the use of the fast Fourier transform (FFT) method (see, for example, Ref *15*).

Analytical Solution II—A Flat Plate Subjected to Arbitrary Surface Loads

For an infinite flat plate bounded by two surfaces at $z = h$ and $z = -h$, the governing equations are the classical Beltrami-Mitchell equations

$$\nabla^2\sigma_{zz} + \frac{1}{1+\nu}\frac{\partial^2 Q}{\partial z^2} = 0 \tag{26}$$

$$\nabla^2\sigma_{zx} + \frac{1}{1+\nu}\frac{\partial^2 Q}{\partial z\partial x} = 0 \tag{27}$$

$$\nabla^2\sigma_{zy} + \frac{1}{1+\nu}\frac{\partial^2 Q}{\partial z\partial y} = 0 \tag{28}$$

$$\nabla^2 Q = 0 \tag{29}$$

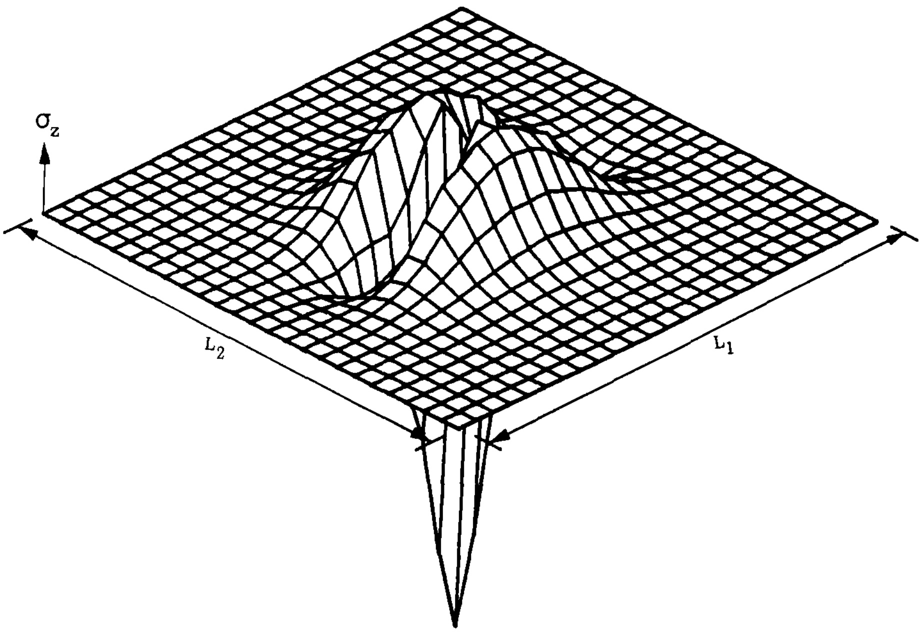

FIG. 4—*Residual normal stress on the plate bounding surface for an embedded elliptical crack under uniform tension.*

and the equilibrium equations

$$\nabla \cdot \sigma = 0 \tag{30}$$

where σ is the stress tensor, ∇ is the divergence operator, and

$$Q = \sigma_{xx} + \sigma_{yy} + \sigma_{zz} \tag{31}$$

is three times the volumetric pressure. The stress boundary conditions for the second analytical problem can be written as

$$\sigma_{zz}(x,y,h) = \sum_{m=-M}^{M} \sum_{n=-N}^{N} (f_{mn} + f'_{mn})\exp(im\pi x/L_1 + in\pi y/L_2) \tag{32a}$$

$$\sigma_{zx}(x,y,h) = \sum_{m=-M}^{M} \sum_{n=-N}^{N} (g_{mn} + g'_{mn})\exp(im\pi x/L_1 + in\pi y/L_2) \tag{32b}$$

$$\sigma_{zy}(x,y,h) = \sum_{m=-M}^{M} \sum_{n=-N}^{N} (h_{mn} + h'_{mn})\exp(im\pi x/L_1 + in\pi y/L_2) \tag{32c}$$

and

$$\sigma_{zz}(x,y,-h) = \sum_{m=-M}^{M} \sum_{n=-N}^{N} (f_{mn} - f'_{mn})\exp(im\pi x/L_1 + in\pi y/L_2) \tag{33a}$$

$$\sigma_{zx}(x,y,-h) = \sum_{m=-M}^{M} \sum_{n=-N}^{N} (-g_{mn} + g'_{mn})\exp(im\pi x/L_1 + in\pi y/L_2) \tag{33b}$$

$$\sigma_{zy}(x,y,-h) = \sum_{m=-M}^{M} \sum_{n=-N}^{N} (-h_{mn} + h'_{mn})\exp(im\pi x/L_1 + in\pi y/L_2) \tag{33c}$$

where f_{mn}, f'_{mn}, g_{mn}, g'_{mn}, h_{mn}, and h'_{mn} are known constants and L_1 and L_2 are characteristic lengths of the crack problem, which will be discussed in more detail in the remaining part of this paper. In this study, the constants $f_{mn}, f'_{mn}, \ldots$ etc. are obtained by decomposing the residual stresses calculated from the first analytical solution by the FFT method. Physically, the terms associated with f_{mn}, g_{mn}, and h_{mn} represent symmetric surface loads while the terms associated with f'_{mn}, g'_{mn}, and h'_{mn} represent antisymmetric surface loads. Since the surface tractions are stresses created by a system of self-equilibrium forces at the crack surfaces, according to the Saint-Venant's principle, we can find a set of L_1 and L_2 big enough that the surface tractions in the region $\{|x| > L_1, |y| > L_2\}$ of the bounding surfaces are negligible. For the same argument, we can also assume that the surface tractions are periodical functions of x and y with $2L_1$ and $2L_2$ as their periods, and that the fictitious tractions outside the region $\{|x| < L_1, |y| < L_2\}$ will not affect the resulting stresses in the crack region. In the preceding equations, Eqs 32 and 33 can be also interpreted as a Fourier series approximation of a Fourier integral. Physically, these fictitious periodic tractions are equivalent to tractions on the bounding surfaces of the plate caused by an infinite number of periodic cracks under the same crack surface loading conditions for each crack. It is worth noting that the plate is assumed to be uncracked in the second analytical problem.

Solutions to Eqs 26 through 30 with boundary conditions, Eqs 32 and 33, can be written as

$$\sigma_{\alpha\beta} = \sum_{-M}^{M} \sum_{-N}^{N} (C^s_{\alpha\beta mn} + C^a_{\alpha\beta mn})\exp(im\pi x/L_1 + in\pi y/L_2) \tag{34}$$

where α, $\beta = x$, y, or z; and $C^s_{\alpha\beta mn}$ and $C^a_{\alpha\beta mn}$ are functions of z to be determined by the governing equations and the boundary conditions. In the preceding equation, the $C^s_{\alpha\beta mn}$ terms are for the symmetric part of the solution and the $C^a_{\alpha\beta mn}$ terms are for the antisymmetric part of the solution. Substitution of Eq 34 into Eqs 26 through 30 leads to a system of ordinary differential equations for $C^s_{\alpha\beta mn}$ and $C^a_{\alpha\beta mn}$ with boundary conditions from Eqs 32 and 33. For each pair of harmonic numbers, m and n, their differential equations are decoupled from the differential equations associated with other pairs of harmonic numbers and can be solved explicitly. Stress solutions to these ordinary differential equations associated with harmonic numbers (m,n) are summarized next. Detailed derivation of these solutions can be seen in the Appendix of this paper.

(a) *Symmetric Parts*

$$C^s_{zzmn} = 2A_z\cosh(\gamma z) - \frac{A\gamma z}{1 + \nu}\sinh(\gamma z) \tag{35}$$

$$C^s_{xzmn} = -2A_x\sinh(\gamma z) - \frac{i\lambda_x zA}{1 + \nu}\cosh(\gamma z) \tag{36}$$

$$C^s_{yzmn} = -2A_y \sinh(\gamma z) - \frac{i\lambda_y z A}{1 + \nu} \cosh(\gamma z) \tag{37}$$

$$C^s_{xymn} = (i\lambda_y \Omega_1 + i\lambda_x \Omega_2 - \lambda_x \lambda_y \Omega_3)/\gamma^2 \tag{38}$$

$$C^s_{xxmn} = (-\Omega_1 - i\lambda_y C^s_{xymn})/(i\lambda_x) \tag{39}$$

$$C^s_{yymn} = (-\Omega_2 - i\lambda_x C^s_{xymn})/(i\lambda_y) \tag{40}$$

where

$$\lambda_x = \frac{m\pi}{L_1}, \qquad \lambda_y = \frac{n\pi}{L_2}, \qquad \gamma^2 = \lambda_x^2 + \lambda_y^2 \tag{41}$$

$$A = \frac{1 + \nu}{\Delta} [f_{mn} \sinh(\gamma h) + \frac{i}{\gamma} (\lambda_x g_{mn} + \lambda_y h_{mn}) \cosh(\gamma h)] \tag{42}$$

$$A_x = -\frac{1}{2 \sinh(\gamma h)} g_{mn} - \frac{i\lambda_x h A}{2(1 + \nu)} \coth(\gamma h) \tag{43}$$

$$A_y = -\frac{1}{2 \sinh(\gamma h)} h_{mn} - \frac{i\lambda_y h A}{2(1 + \nu)} \coth(\gamma h) \tag{44}$$

$$A_z = \frac{1}{2 \cosh(\gamma h)} f_{mn} + \frac{\gamma h A}{2(1 + \nu)} \tanh(\gamma h) \tag{45}$$

$$\Delta = [\sinh(2\gamma h) + 2\gamma h]/2 \tag{46}$$

$$\Omega_1 = -2A_x \gamma \cosh(\gamma z) - \frac{i\lambda_x A}{1 + \nu} \cosh(\gamma z) - \frac{i\lambda_x z A \gamma}{1 + \nu} \sinh(\gamma z) \tag{47}$$

$$\Omega_2 = -2A_y \gamma \cosh(\gamma z) - \frac{i\lambda_y A}{1 + \nu} \cosh(\gamma z) - \frac{i\lambda_y z A \gamma}{1 + \nu} \sinh(\gamma z) \tag{48}$$

$$\Omega_3 = 2A \cosh(\gamma z) - 2A_z \cosh(\gamma z) + \frac{A \gamma z}{1 + \nu} \sinh(\gamma z) \tag{49}$$

(b) *Antisymmetric Parts*

$$C^a_{zzmn} = 2A'_z \sinh(\gamma z) - \frac{A' \gamma z}{1 + \nu} \cosh(\gamma z) \tag{50}$$

$$C^a_{xzmn} = -2A'_x \cosh(\gamma z) - \frac{i\lambda_x z A'}{1 + \nu} \sinh(\gamma z) \tag{51}$$

$$C^a_{yzmn} = -2A'_y \cosh(\gamma z) - \frac{i\lambda_y z A'}{1 + \nu} \sinh(\gamma z) \tag{52}$$

$$C^a_{xymn} = (i\lambda_y\Omega'_1 + i\lambda_x\Omega'_2 - \lambda_x\lambda_y\Omega'_3)/\gamma^2 \tag{53}$$

$$C^a_{xxmn} = (-\Omega'_1 - i\lambda_y C^a_{xymn})/(i\lambda_x) \tag{54}$$

$$C^a_{yymn} = (-\Omega'_2 - i\lambda_x C^a_{xymn})/(i\lambda_y) \tag{55}$$

where

$$A' = \frac{1+\nu}{\Delta'}\left[f'_{mn}\cosh(\gamma h) + \frac{i}{\gamma}(\lambda_x g'_{mn} + \lambda_y h'_{mn})\sinh(\gamma h)\right] \tag{56}$$

$$A'_x = -\frac{1}{2\cosh(\gamma h)}g'_{mn} - \frac{i\lambda_x hA'}{2(1+\nu)}\tanh(\gamma h) \tag{57}$$

$$A'_y = -\frac{1}{2\cosh(\gamma h)}h'_{mn} - \frac{i\lambda_y hA'}{2(1+\nu)}\tanh(\gamma h) \tag{58}$$

$$A'_z = \frac{1}{2\sinh(\gamma h)}f'_{mn} + \frac{\gamma hA'}{2(1+\nu)}\coth(\gamma h) \tag{59}$$

$$\Delta' = [\sinh(2\gamma h) - 2\gamma h]/2 \tag{60}$$

$$\Omega'_1 = -2A_x\gamma\sinh(\gamma z) - \frac{i\lambda_x A'}{1+\nu}\sinh(\gamma z) - \frac{i\lambda_x zA\gamma}{1+\nu}\cosh(\gamma z) \tag{61}$$

$$\Omega'_2 = -2A_y\gamma\sinh(\gamma z) - \frac{i\lambda_y A}{1+\nu}\sinh(\gamma z) - \frac{i\lambda_y zA\gamma}{1+\nu}\cosh(\gamma z) \tag{62}$$

$$\Omega'_3 = 2A\sinh(\gamma z) - 2A_z\sinh(\gamma z) + \frac{A\gamma z}{1+\nu}\cosh(\gamma z) \tag{63}$$

Iteration Procedure

With the preceding two analytical solutions, the total solution to the problem of an elliptical or partial-elliptical crack in a flat plate under arbitrary crack surface loads can be then obtained by summing a series of the two analytical solutions until a convergence condition is met. The iteration procedure used in this study is shown in Fig. 5. In this study, the iteration of the alternating analytical procedure is terminated when the change of the maximum stress-intensity factor along the crack front is less than 1%. It is found that, for most of problems tested in this study, only three to four iterations are required.

Numerical Implementation

The alternating analytical procedure discussed in this paper has been implemented in a computer software, K-Solver [16], which can be executed in a mainframe computer or even an IBM or compatible personal computer. Users of this computer program need only to input material properties (E and ν), plate thickness ($t = 2h$), crack dimensions (a_1, a_2, and location of the center and orientation of the bounding ellipse of the crack), and crack surface loads ($A^{(i,j)}_{\alpha,m-n,n}$ values) and the software will calculate K_{I}, K_{II}, and K_{III} at the crack border automatically.

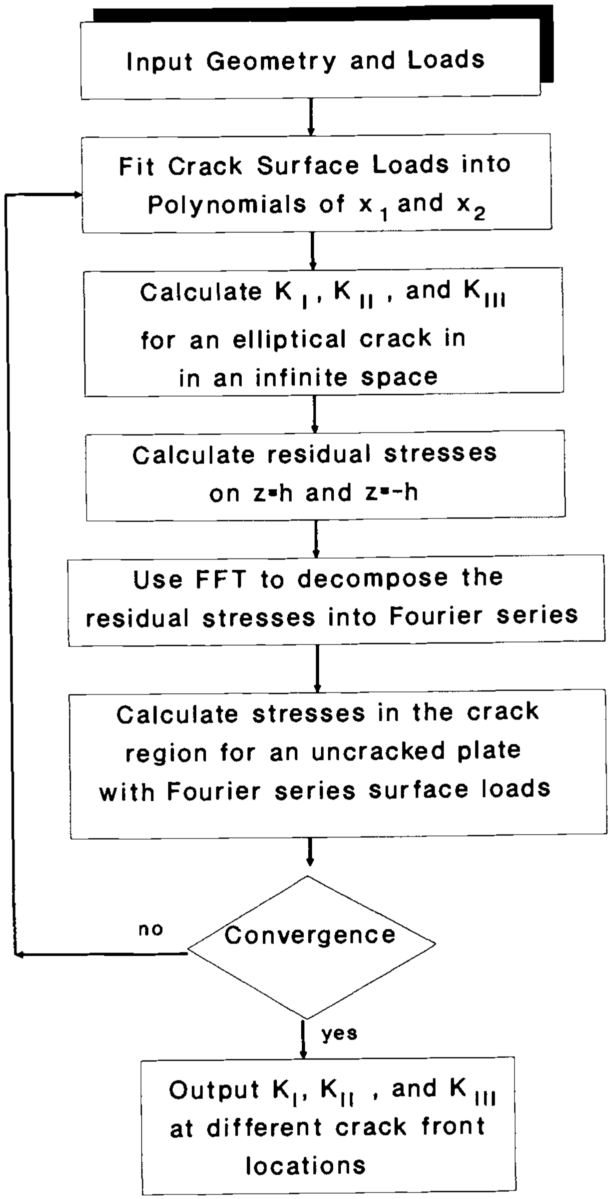

FIG. 5—*Flow chart for the alternating analytical technique.*

To verify the alternating analytical procedure as well as the resulting software, a number of crack problems have been tested and checked against reference solutions, which are available in the literature.

Embedded Crack—Mode I Fracture

The first test problem presented is an embedded elliptical crack at the middle of a finite thickness plate (thickness = $2h$ = t) subjected to a remote uniform tension, σ_0. Key dimensions in this problem are:

1. x_2 in the thickness (minus z) direction;
2. x_1 and x_3 parallel to x and y, respectively; and
3. a_2/a_1 = 0.4 and a_2/h = 0.75.

Solutions to this problem have been obtained by Shah and Kobayashi [17] with the conventional finite element method. Both present solutions and the reference finite element solution to this problem are plotted together in Fig. 6. In this figure, θ = 0° is at the

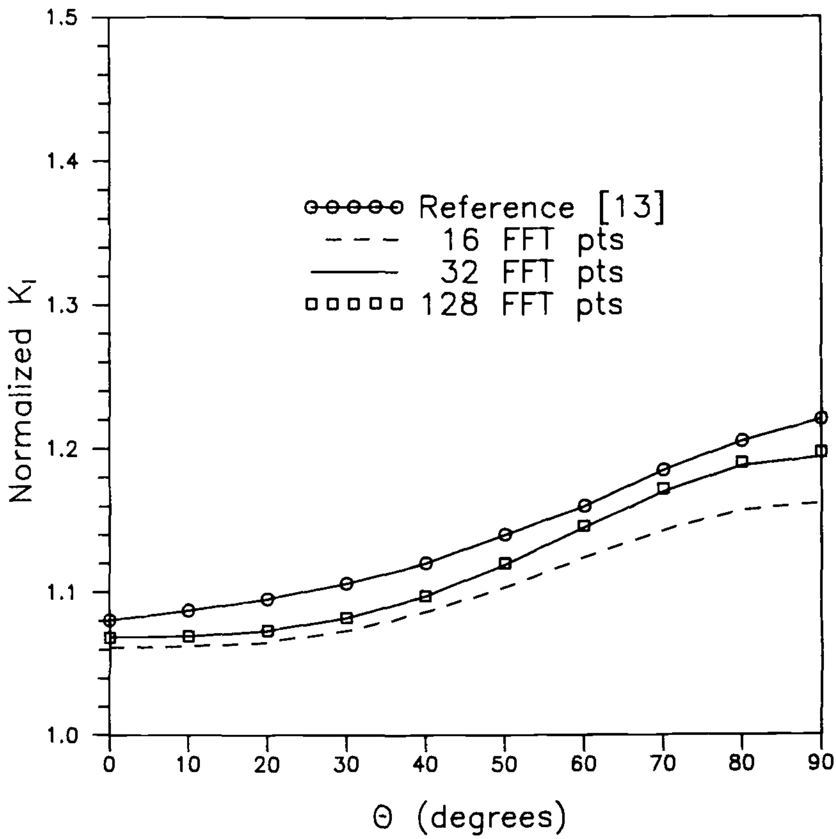

FIG. 6—*Normalized* K_I *for an embedded crack in a flat plate under uniform tension* (a_2/a_1 = *0.4*, a_2/h = *0.75*).

interception point of the crack surface and the plate surface and $\theta = 90°$ is at the deepest crack front into the plate thickness. The K_I solutions shown in this figure have been normalized by a factor of $\sigma_0/E(\psi,\kappa) \cdot (\pi a_2/a_1)^{1/2}B^{1/4}$ where $E(\psi,\kappa)$ and B are defined in Eqs 19 and 25, respectively. It is seen from this figure that current solutions are within 4% of the reference solution [*17*] even with only 32 FFT points in each direction of the plate. The alternating analytical solution converged after three iterations and took less than 45 min of computer time for the case of 32 FFT points in a 20-MHz, Intel-80386-based personal computer, which is also equipped with a 20-MHz, Intel-80387 math coprocessor. The standard setup for the K-Solver is 128 FFT points, which would require 15 times more computer time than the 32 FFT point case but, as illustrated in Fig. 6, would also provide a slightly better correlation with the reference solution.

Semielliptical Surface Crack—Mode I Fracture

In addition to the first test problem, the "benchmark problem" defined by Refs *18* and *19* and the surface crack problems analyzed by Newman and Raju [*5*] have been also checked. Because of the length constraint of this paper, only two cases are discussed here. One for the remote bending case in the "benchmark problem" and the other for the remote tension

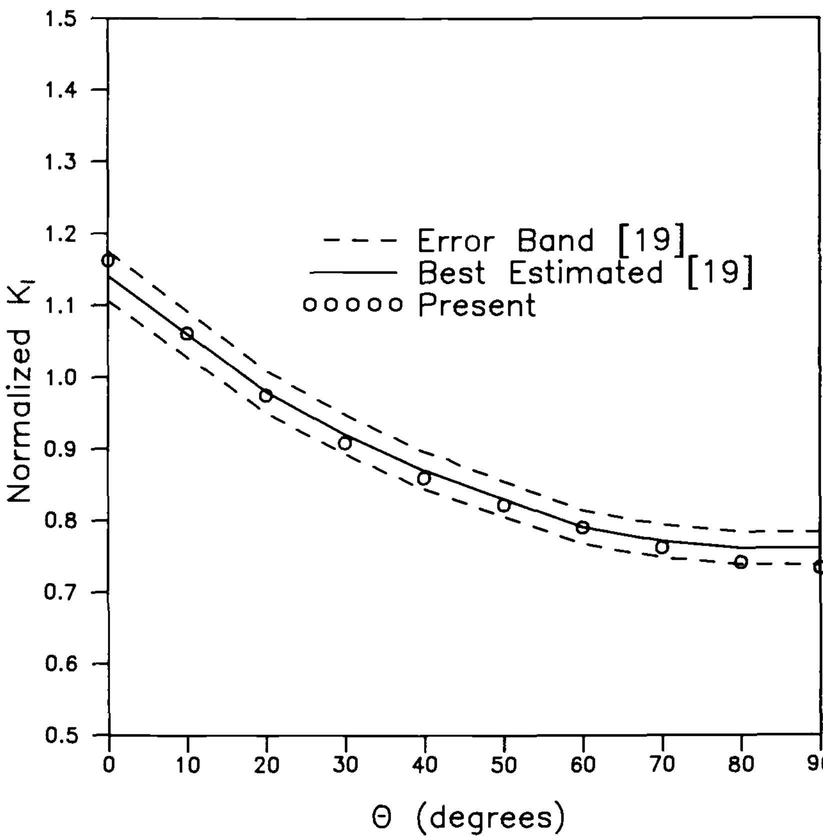

FIG. 7—*Normalized* K_I *for a semielliptical surface crack in a flat plate under remote bending* ($a_2/t = 0.25$, $a_2/a_1 = 0.5$).

tension case for one crack geometry in the Newman-Raju problems. Thickness of the plate in both check cases are $t(=2h)$. Dimensions for the benchmark problem are:

1. x_2 in the thickness (minus z) direction;
2. x_1 and x_3 parallel to x and y, respectively;
3. $a_2/t = 0.25$, $a_2/a_1 = 0.5$; and
4. maximum remote bending stress $= \sigma_0$.

The key dimensions for the Newman-Raju problem are:

1. x_1 in the thickness (minus z) direction;
2. x_2 in minus x direction, x_3 parallel to y;
3. $a_1/t = 0.80$, $a_2/a_1 = 0.5$; and
4. remote tension stress $= \sigma_0$.

These two check cases cover both shallow (25% plate thickness) and deep (80% plate thickness) surface crack problems and both remote tension and bending loads. Results for two check problems are depicted in Figs. 7 and 8. Definition of the angle, θ, in these two

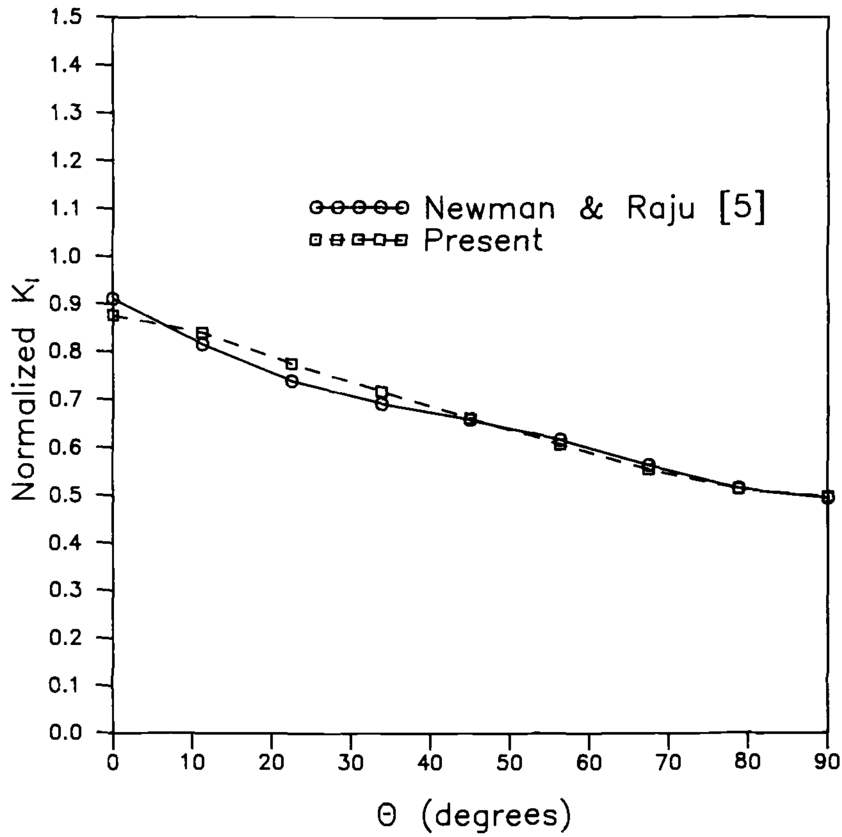

FIG. 8—*Normalized* K_I *for a semielliptical surface crack in a flat plate under uniform tension* ($a_1/t = 0.8$, $a_2/a_1 = 0.5$).

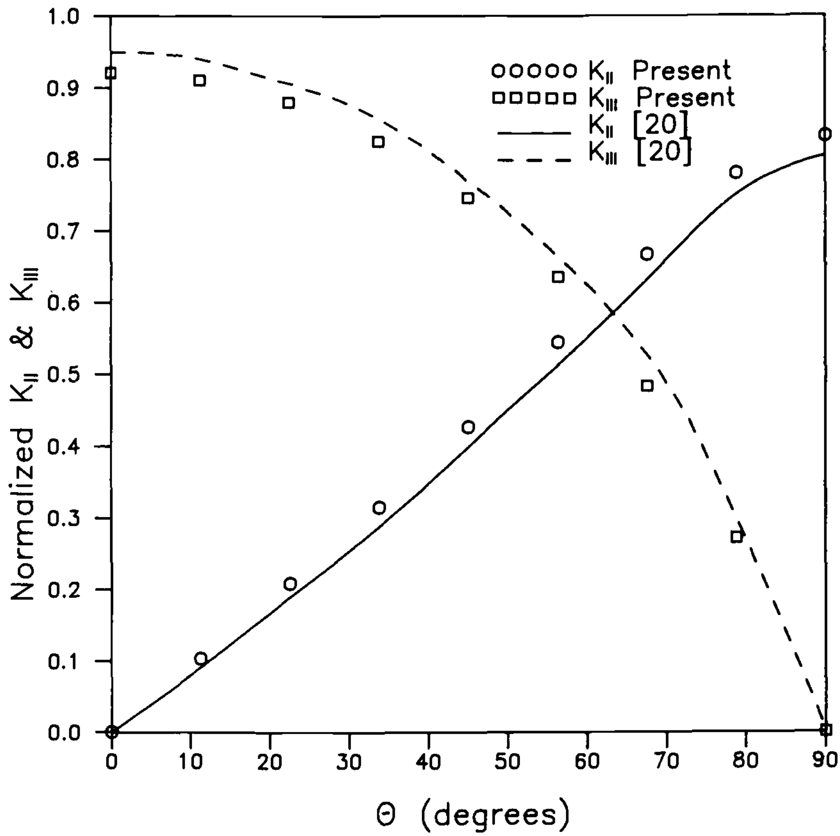

FIG. 9—*Normalized* K_I *for a semielliptical surface crack in a flat plate under remote shear,* τ_{31} *(*a_2/t *= 0.2,* a_2/a_1 *= 0.4).*

figures are the same as that for Fig. 6. The stress-intensity factor solutions shown in these figures have been also normalized by the same factor as that for Fig. 6. It is seen from Figs. 7 and 8 that current solutions with 128 FFT points in each direction correlate well with the reference solutions. Again, both cases converged in three to four iterations during the alternating analytical procedure.

Parametric studies on the effects of relative to L_1 and L_2 sizes, and number of FFT point in each direction of the plate have been also conducted. It is found after an extensive numerical exercise that the optimal settings, in light of computer time and solution accuracy, for the alternating analytical procedure are 128 FFT points and $L_1 = L_2 = 5$ maximum (a_1, a_2).

Semielliptical Surface Crack—Mode II and Mode III Fracture

The next check problem is a semielliptical surface crack subjected to shear loading. Key dimensions for this problem are:

1. x_2 in the thickness (minus z) direction;
2. x_1 and x_3 parallel to x and y, respectively;

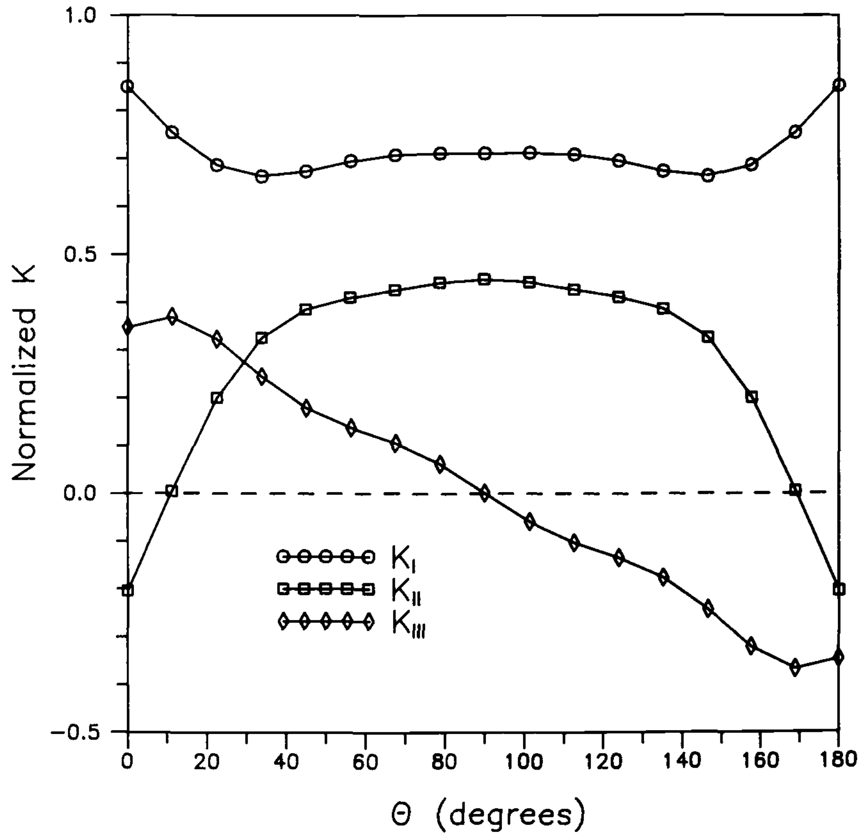

FIG. 10—*Normalized* K *for a semielliptical surface crack tilted 45° under remote tension* (a_2/t = *0.25*, a_2/a_1 = *0.5*).

3. $a_2/t = 0.2$, $a_2/a_1 = 0.4$; and
4. remote shear stress $\tau_{31} = \tau_{yx} = \sigma_0$.

Solution to this problem has been obtained by Smith and Sorensen [*20*] with an alternating technique different from the one used in this paper. Results for this check case are depicted in Fig. 9. Again, definition of this angle, θ, in this figure is the same as that in Fig. 6. Stress-intensity factors plotted in this figure have been also normalized by the same factor as Fig. 6. It is seen from this figure that present solutions are within 4% of the reference solution. The standard numerical setup with 128 FFT points and $L_1 = L_2 = 5a_1$ has been used in obtaining the solutions for this problem.

Tilted, Semielliptical Surface Crack—Mixed-Mode Fracture

To fully explore the mixed-mode nature of the three-dimensional crack problem, the last test case discussed here is a tilted semielliptical surface crack subjected to remote tension. Dimensions for this problem are the same as the benchmark problem just discussed, except that the surface crack is tilted 45° around its major axis a_1 (or 45° around the positive x_1-axis). That is, the surface crack is no longer perpendicular to the plate surface but has a

45° angle with the plate surface. The remote tension stress, σ_0, is applied in the y-direction, that is, $\sigma_{yy} = \sigma_0$ at the remote sections. Therefore, it is anticipated that the crack front will encounter all three fracture modes. Resulting stress-intensity factors for this problem are illustrated in Fig. 10. It is seen from this figure that K_I and K_{II} remain relatively constant along the crack front except at the regions of about 30° from the plate surface. All K values presented in this figure have been normalized against the same factor as Fig. 6. To the authors' knowledge, there are no reference solutions available in the literature for this problem. The normalized K_I and K_{II} solutions at the crack tip for the corresponding two-dimensional slant crack problem are found to be 0.99 and 0.51, respectively. As expected, the two-dimensional solutions are higher than the three-dimensional solutions at the deepest crack front ($\theta = 90°$).

Conclusions and Recommendations

An alternating analytical procedure has been developed in this study for the problem of an elliptical or partial-elliptical crack in a flat plate subjected to arbitrary crack surface loading. With such an approach, the three-dimensional crack problem can be solved with great ease in lieu of shorter computer time and more importantly no FEM mesh preparation. The alternating analytical procedure has been also implemented into a FORTRAN computer program, which is very easy to use and can be executed in a wide range of computers. Of course, its shortcoming with respect to the conventional FEM (for example, Ref *5*) or the alternating FEM (for example, Ref *4*) is that it can only handle the flat plate geometry.

An extension of the alternating analytical procedure to the problem of an elliptical or partial-elliptical crack in a cylindrical pipe subjected to arbitrary crack surface loading is also feasible and is worth exploring in the future.

Acknowledgment

This study is funded by an in-house research grant from Structural Integrity Associates, Inc. in San Jose, California. The authors wish to express their gratitude to Dr. Peter C. Riccardella of Structural Integrity Associates, Inc. for his encouragement during the course of the study.

APPENDIX

Derivation of Eqs 35 to 63

The methodology used in this paper for deriving Eqs 35 to 63 are very similar to the one discussed in Ref *21*. Since each harmonic pair (m,n) in the solution is decoupled from other harmonic pairs, we can consider solutions for each single harmonic pair separately. An obvious format for the solutions for the harmonic pair (m,n) to the problem defined by Eqs 26 to 33 is

$$Q = C_{mn}\exp(i\lambda_x x + i\lambda_y y) \tag{64}$$

$$\sigma_{zx} = C_{zxmn}\exp(i\lambda_x x + i\lambda_y y) \tag{65}$$

$$\sigma_{zy} = C_{zymn}\exp(i\lambda_x x + i\lambda_y y) \tag{66}$$

$$\sigma_{zz} = C_{zzmn}\exp(i\lambda_x x + i\lambda_y y) \tag{67}$$

$$\sigma_{xx} = C_{xxmn}\exp(i\lambda_x x + i\lambda_y y) \tag{68}$$

$$\sigma_{yy} = C_{yymn}\exp(i\lambda_x x + i\lambda_y y) \tag{69}$$

$$\sigma_{xy} = C_{xymn}\exp(i\lambda_x x + i\lambda_y y) \tag{70}$$

where λ_x and λ_y are defined in Eq 41, and C_{mn}, C_{zxmn}, . . . etc. are functions of z to be determined later from the governing equations and boundary conditions. Substitution of Eqs 64 to 67 into Eqs 26 to 29 yields the following four ordinary differential equations (ODEs) for C_{mn}, C_{zzmn}, C_{zymn}, and C_{zxmn}

$$C''_{zzmn} - \gamma^2 C_{zzmn} = -\frac{1}{1+\nu} C''_{mn} \tag{71}$$

$$C''_{xzmn} - \gamma^2 C_{xzmn} = -\frac{i\lambda_x}{1+\nu} C'_{mn} \tag{72}$$

$$C''_{yzmn} - \gamma^2 C_{yzmn} = -\frac{i\lambda_y}{1+\nu} C'_{mn} \tag{73}$$

$$C''_{mn} - \gamma^2 C_{mn} = 0 \tag{74}$$

where γ is defined in Eq 41, and functions with a prime or a double prime as superscript are for the first and second derivatives (with respect to z), respectively, of the function.

Symmetric Case

For symmetric loading, that is, for loading terms with coefficients f_{mn}, g_{mn}, and h_{mn} in Eqs 32 and 33, it can be easily deduced that general solutions to the four ODEs shown in Eqs 71 through 74 are

$$C_{mn} = 2A\cosh(\gamma z) \tag{75}$$

$$C_{zzmn} = 2A_z\cosh(\gamma z) - \frac{A\gamma z}{1+\nu}\sinh(\gamma z) \tag{76}$$

$$C_{xzmn} = -2A_x\sinh(\gamma z) - \frac{i\lambda_x zA}{1+\nu}\cosh(\gamma z) \tag{77}$$

$$C_{yzmn} = -2A_y\sinh(\gamma z) - \frac{i\lambda_y zA}{1+\nu}\cosh(\gamma z) \tag{78}$$

where A, A_x, A_y, and A_z are constants to be determined.

The next step is to find solutions for C_{xxmn}, C_{yymn}, and C_{xymn}. Substitution of the preceding solution for σ_{zz}, σ_{yz}, and σ_{xz} in to the first two equations of the equilibrium equations in Eq 30 and into Eq 31 yields three algebraic equations for C_{xxmn}, C_{yymn}, and C_{xymn} as follows

$$i\lambda_x C_{xxmn} + i\lambda_y C_{xymn} = \frac{i\lambda_x A\gamma z}{1+\nu}\sinh(\gamma z) + \frac{i\lambda_x A}{1+\nu}\cosh(\gamma z) + 2A_x\gamma\cosh(\gamma z) \tag{79}$$

$$i\lambda_x C_{xymn} + i\lambda_y C_{yymn} = \frac{i\lambda_y A\gamma z}{1+\nu}\sinh(\gamma z) + \frac{i\lambda_y A}{1+\nu}\cosh(\gamma z) + 2A_y\gamma\cosh(\gamma z) \tag{80}$$

$$C_{xxmn} + C_{yymn} = 2A\cosh(\gamma z) - 2A_z\cosh(\gamma z) + \frac{A\gamma z}{1+\nu}\sinh(\gamma z) \tag{81}$$

Solutions to the preceding three algebraic equations are

$$C_{xxmn} = (-\Omega_1 - i\lambda_y C_{xymn})/(i\lambda_x) \tag{82}$$

$$C_{yymn} = (-\Omega_2 - i\lambda_x C_{xymn})/(i\lambda_y) \tag{83}$$

$$C_{xymn} = (i\lambda_y\Omega_1 + i\lambda_x\Omega_2 - \lambda_x\lambda_y\Omega_3)/\gamma^2 \tag{84}$$

where Ω_1, Ω_2, and Ω_3 are defined in Eqs 47 through 49.

So far, there is a total of four unknown constants, A, A_x, A_y, and A_z, in the stress solutions. The number of unknown constants can be further reduced by one by substituting Eqs 76, 77, and 78 into the third equilibrium equation in Eq 30. After some algebraic manipulation, the unknown constant, A, can be expressed in terms of the other three unknown constants as

$$A = \frac{2(1+\nu)}{\gamma}(\gamma A_z - i\lambda_x A_x - i\lambda_y A_y) \tag{85}$$

By substituting the stress expressions into the first stress boundary condition, that is, Eq 32*a*, we obtain the following condition for the unknown constants, A and A_z

$$2A_z\cosh(\gamma h) - \frac{A\gamma h}{1+\nu}\sinh(\gamma h) = f_{mn} \tag{86}$$

Similarly, from boundary conditions in Eqs 32*b* and 32*c*, we come up with two more conditions

$$-2A_x\sinh(\gamma h) - \frac{i\lambda_x hA}{1+\nu}\cosh(\gamma h) = g_{mn} \tag{87}$$

$$-2A_y\sinh(\gamma h) - \frac{i\lambda_y hA}{1+\nu}\cosh(\gamma h) = h_{mn} \tag{88}$$

The four unknown constants, A, A_x, A_y, and A_z, can be then solved quite easily from Eqs 85 to 88. Expressions for the four unknown constants are depicted in Eqs 42 to 45, respectively.

Antisymmetric Case

Derivation of the solutions corresponding to antisymmetric loading terms, that is, terms with coefficients f'_{mn}, g'_{mn}, and h'_{mn} in Eqs 32 and 33, is very similar to the previously mentioned symmetric case except that all the hyperbolic sine functions and the hyperbolic cosine functions in the preceding equations should be interchanged. However, this interchange rule does not apply to Eq 60, which is the counterpart of Eq 46, because Eq 42, which contains the Δ term defined by Eq 46, is obtained by substitution of Eqs 43 to 45 into Eq 85. Similarly, Eq 56 is obtained by substitution of Eqs 57 to 59 into Eq 85. Equation 85 remains valid for both symmetric and antisymmetric cases.

References

[1] Atluri, S. N., *Computational Methods in Mechanics, Vol. 2—Computational Methods in the Mechanics of Fracture*, Elsevier Science Publishers, New York, 1986.
[2] Atluri, S. N. and Nishioka, T., "On Some Recent Advances in Computational Methods in the Mechanics of Fracture," *Advances in Fracture Research*, Vol. 3, 1989, pp. 1923–1969.
[3] Vijayakumar, K. and Atluri, S. N., "An Embedded Elliptical Crack, in an Infinite Solid, Subject to Arbitrary Crack-Face Tractions," *Journal of Applied Mechanics*, Vol. 48, 1981, pp. 88–96.
[4] Nishioka, T. and Atluri, S. N., "Analytical Solution for Embedded Elliptical Cracks, and Finite Element Alternating Method for Elliptical Surface Cracks, Subjected to Arbitrary Loadings," *Engineering Fracture Mechanics*, Vol. 17, 1983, pp. 247–268.
[5] Newman, J. C., Jr., and Raju, I. S., "Analysis of Surface Cracks in Finite Plates Under Tension or Bending Loads," NASA Technical Paper 1578, National Aeronautics and Space Administration, Hampton, VA, 1979.
[6] Sih, G. C., "A Review of the Three-Dimensional Stress Problem for a Cracked Plate," *International Journal of Fracture Mechanics*, Vol. 7, 1971, pp. 39–61.
[7] Benthem, J. P., "State of Stress at the Vertex of a Quarter-Infinite Crack in a Half-Space," *International Journal of Solids Structures*, 1977, pp. 479–492.
[8] Benthem, J. P., "The Quarter-Infinite Crack in a Half-Space; Alternative and Additional Solutions," *International Journal of Solids Structures*, 1980, pp. 119–130.
[9] Bazant, Z. P. and Estenssoro, L. F., "General Numerical Method for Three Dimensional Singularities in Cracked or Notched Elastic Solids," *Advances in Research on the Strength and Fracture of Materials*, D. M. R. Taplin, Ed., Vol. 3a, Pergamon Press, Oxford, 1977, pp. 371–385.
[10] Bazant, Z. P. and Estenssoro, L. F., "Surface Singularity and Crack Propagation," *International Journal of Solids Structures*, Vol. 15, 1979, pp. 405–426.
[11] Shivakumar, K. N. and Raju, I. S., "Treatment of Singularities in a Middle-Crack Tension Specimen," Fracture Mechanics: *Twenty-First Symposium, ASTM STP 1074*, J. P. Gudas, J. A. Joyce, and E. M. Hackett, Eds., American Society for Testing and Materials, Philadelphia, 1990, pp. 470–489.
[12] Trefftz, E., *Handbuck der Physik*, Vol. 6, Springer-Verlag, Berlin, 1928.
[13] Kassir, M. K. and Sih, G. C., "Embedded Elliptical Cracks," *Mechanics of Fracture, Vol. 2, Three-Dimensional Crack Problems*, Noordhoff International Publishing, Leyden, The Netherlands, 1975, pp. 74–117.
[14] Byrd, R. F. and Friedman, M. D., *Handbook of Elliptic Integrals for Engineers and Scientists*, Springer-Verlag, Berlin, 1971.
[15] Brigham, E. O., *The Fast Fourier Transformation and Its Applications*, Prentice-Hall, New York, 1988.
[16] Shvarts, S. and Kuo, A-Y., "K-Solver User's and Verification Manual," Structural Integrity Associates, Inc., San Jose, CA, 1990.
[17] Shah, R. C. and Kobayashi, A. S., "Elliptical Crack in a Finite-Thickness Plate Subjected to Tensile and Bending Loading," *Journal of Pressure Vessel Technology*, Vol. 96, 1974, pp. 47–54.
[18] Hulbert, L. E., "Benchmark Problems for Three-Dimensional Fracture Analysis," *International Journal of Fracture*, Vol. 13, 1977, pp. 87–91.
[19] McGowan, J. J., *A Critical Evaluation of Numerical Solutions to the "Benchmark" Surface Crack Problem*, SESA Monograph, Society for Experimental Stress Analysis, Westport, CT, 1980, pp. 253–264.
[20] Smith, F. W. and Sorensen, D. R., "Semielliptical Cracks Subjected to Shear Loading," *Pressure Vessel Technology—Part II*, Third International Conference, Tokyo, Japan, American Society of Mechanical Engineers, 1977.
[21] Parton, V. and Perlin, P., *Mathematical Methods of Elasticity*, Science Publishing Co., Moscow 1981, pp. 458–459 (in Russian).

Dong-Zhi Sun,[1] Reinhold Kienzler,[1] Bert Voss,[1] and Winfried Schmitt[1]

Application of Micromechanical Models to the Prediction of Ductile Fracture

REFERENCE: Sun, D.-Z., Kienzler, R., Voss, B., and Schmitt, W., "**Application of Micromechanical Models to the Prediction of Ductile Fracture,**" *Fracture Mechanics: Twenty-Second Symposium (Volume II), ASTM STP 1131*, S. N. Atluri, J. C. Newman, Jr., I. S. Raju, and J. S. Epstein, Eds., American Society for Testing and Materials, Philadelphia, 1992, pp. 368–378.

ABSTRACT: The ductile fracture behavior of different specimens is analyzed by continuum damage-mechanics techniques. A model introduced by Gurson and modified by Needleman and Tvergaard has been implemented in the finite element program package, ADINA. The damage parameters of the model are measured and calculated from smooth tension tests, and the characteristic material distance is estimated from compact tension experiments.

A steel, ASTM A710, and a weld metal for the steel, ASTM A508, are investigated. The damage parameters determined from the smooth bars are used to predict the deformation and fracture behavior of notched round bars and of sidegrooved compact specimens. For the weld metal, a side-grooved WOL-X-specimen is also simulated. In every case, a satisfactory agreement of prediction and experiment is observed.

In order to investigate the influence of the stress state (constraint) in cracked specimens, a series of numerical computations of different specimen geometries and loading situations is performed utilizing the same set of parameters of the ASTM A710 steel. The slopes of the predicted *J*-resistance curves increase with increasing ratio of tension versus bending load and with decreasing relative crack length.

KEY WORDS: damage mechanics, constitutive relationships, Gurson model, void growth, void coalescence, fracture mechanics, ductile fracture, numerical simulation, geometry effects, constraint

Global failure criteria, as the *J*-integral or the crack-tip opening displacement (CTOD), have been widely used to characterize ductile fracture processes. However, experimental results give evidence that these single-parameter criteria may not describe ductile crack growth completely, since the specimen size and the specimen geometry have a pronounced influence on the crack resistance curve [*1,2*]. One approach to improve fracture mechanics concepts is the combination of the *J*-integral with the local constraint [*3*]. Another approach is the concept of continuum damage mechanics. This is the attempt to simulate macroscopical failure numerically by using new constitutive relationships incorporating models of microscopical rupture processes. A major advantage of this type of micromechanical models is that initiation and propagation of the crack occur naturally, that is, without using additional numerical techniques, when the local softening due to the void growth results in the formation of a region transmitting only zero stresses.

The model adapted in this study is based on a flow function introduced by Gurson [*4*] and has further been developed by Needleman and Tvergaard [*5,6*]. The microscopical

[1]Senior scientists and head, Stress Analysis, respectively, Fraunhofer-Institut für Werkstoffmechanik, D-7800 Freiburg, Federal Republic of Germany. R. Kienzler is presently, Professor, University of Bremen.

rupture processes described by nucleation, growth, and coalescence of voids were incorporated in the constitutive relationships. This model has been used successfully to analyze fracture behavior in notched bars with different notch radii [5,7]. For the analysis of cracked specimens, however, two additional problems had to be solved because of the great gradient of the stress field at the crack tip. At first, according to the physical model for void coalescence [8] a characteristic microstructural distance, l_c, has to be introduced into the analysis of cracked structures to avoid underestimation of the fracture toughness. This critical distance, l_c, might be related to the average inclusion spacing. Secondly, due to the localization of the softening at the crack tip, the finite element solution exhibits strong mesh-size dependence [9]. Within the frame of this work, the problems were treated by utilizing a simple but practical method described in more detail in Ref *10*.

One purpose of this work is to check whether the damage parameters determined from simple tensile bars are applicable to complex cracked specimens; another is to explain the geometry dependence of the J_R-curve on the basis of the micromechanical model and to find the relationship between the stress multiaxiality and the slope of the J_R-curves.

Modified Gurson Model

The basis for the modified Gurson model is a plastic potential applicable to porous solids given by

$$\phi = \frac{3\sigma'_{ij}\,\sigma'_{ij}}{2\sigma_m^2} + 2q_1 f^* \cosh\left(\frac{\sigma_{kk}}{2\sigma_m}\right) - [1 + (q_1 f^*)^2] = 0 \tag{1}$$

with σ_m = flow stress of the material. The parameter, q_1, was introduced by Tvergaard [5] to improve the prediction of the Gurson model at small f values. f^* is a function of the void volume fraction, f. For $f^* = 0$, the plastic potential (1) is obviously identical with that of von Mises. If f^* reaches the limit, $1/q_1$, the material loses its load carrying capacity because all stress components have to vanish in order to satisfy Eq 1. Since for small f the von Mises equivalent stress, σ_e, is close to the flow stress, σ_m, it is evident that ϕ is strongly dependent on the ratio of the hydrostatic stress over the von Mises equivalent stress, $\sigma_{kk}/3\sigma_e$.

According to Needleman and Tvergaard, the nucleation of new voids and the growth of existing voids were introduced into the Gurson constitutive relationships by the following definition of the growth rate of f

$$\dot{f} = \dot{f}_{\text{nucleation}} + \dot{f}_{\text{growth}} \tag{2}$$

$$\dot{f}_{\text{nucleation}} = B(\dot{\sigma}_m + \dot{\sigma}_{kk}/3) + D\,\dot{\varepsilon}_m^p \tag{3}$$

$$\dot{f}_{\text{growth}} = (1 - f)\,\dot{\eta}_{kk}^p \tag{4}$$

where $\dot{\eta}_{ij}^p$ is the plastic part of the strain rate tensor and ε_m^p is the equivalent plastic strain. The parameters, B and D, were chosen under the assumption that void nucleation follows a normal distribution [*11*].

The effect of the void coalescence on the plastic deformation was modeled by replacing f of the original Gurson model by f^*

$$f^* = \begin{cases} f & f \le f_c \\ f_c + f_{uc}(f - f_c) & f \ge f_c, \quad (l \ge l_c) \end{cases} \tag{5}$$

In this work, the modeling of the void coalescence is active when the critical void volume fraction, f_c, is exceeded over a critical distance, l_c. The value of the constant, f_{uc}, can be derived by setting $(f^*(f_f) = 1/q_1)$ in Eq 5 with f_f, that is, the void volume fraction at final failure. A detailed description of the constitutive relationships is given in Refs *7* and *10*.

Numerical and Experimental Procedures

The modified Gurson model was implemented into the finite element program, ADINA. The inclusion volume determined by quantitative optical microscopy was used as the initial void volume in the numerical simulation. The void nucleation during the plastic deformation was assumed to be controlled by strain only, that is, $B = 0$. This assumption ensures that the stiffness matrix does not become asymmetric. The critical value, f_c, was obtained by fitting the sudden drop in the load versus diameter change curve for a smooth bar. The void volume fraction at rupture, f_f, was determined by quantitative metallography from specimens that were unloaded and sectioned close to the onset of macroscopical failure.

In order to simulate large amounts of crack extension, the meshes for the cracked specimens were generated with homogeneous element size in the crack-tip region. The element length was identified with the critical distance, l_c, and determined by matching the computed load versus displacement curve with the experimental one of a cracked specimen. Plane strain conditions were assumed for the numerical analysis. The J-integral was evaluated as a contour integral.

The experiments were performed with a sulfur shape-controlled steel, ASTM A710 Grade A, and a weld metal for a steel of Class ASTM A508. The yield points of the steels are 612 and 587 MPa, respectively. Fracture mechanics investigations were carried out using CT25-, CT23-, and WOL25-specimens with 20% side grooves and $a/W = 0.6$. The J_R-curves were determined by the partial unloading technique.

Results and Discussion

Critical Damage Parameters

In order to determine the critical void volume fraction at void coalescence, f_c, smooth and notched round bars were tested and analyzed. These specimen geometries were chosen for two reasons; first, axial symmetric problems can be exactly simulated by two-dimensional models, and, thus, the computation expense is significantly reduced. Second, the stress distributions at the cross section in these types of specimens are so homogeneous that the critical value, f_c, can be evaluated without accounting for a critical distance, l_c, and the corresponding damage variable, f, depends only little on the mesh size.

Since the standard smooth tensile bar is most widely used to characterize the material properties, special attention was paid to it in this work. An important step for the numerical description of the plastic deformation in the smooth bar is the simulation of the necking that occurs at maximum load during the displacement-controlled test. To consider the multiaxiality of the stress state in the necking region, the stress-strain curve for the computation was modified according to Bridgman [*12*]. In Fig. 1, the calculated specimen contour was compared with the contour measured experimentally at the same load close to rupture.

Obviously, an excellent agreement between the numerical and the experimental results was found. Figure 2 shows (for the smooth bar with a diameter of 8 mm and the notched bar with a notch radius of 4 mm and an inner diameter of 8 mm) the load versus diameter change curves from the numerical analysis and the experiments. An important phenomenon for the simulation is that due to void coalescence the load versus displacement curves of the tensile bars drop suddenly before final failure. By fitting the calculated load drop with

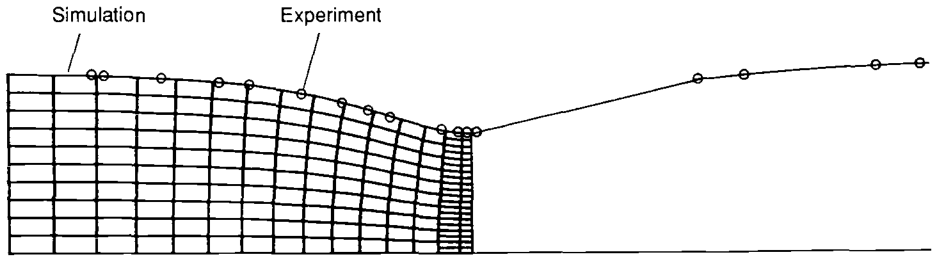

FIG. 1—*Comparison between simulated and measured necking of a smooth bar.*

the experimentally observed one, a critical value, $f_c = 0.045$, was determined from the smooth bar for the weld metal. Using the same f_c-value, the notched bar was also modeled. The good agreement between the predicted and the experimental onsets of the load drop for both specimen geometries implies that the effect of the strain constraint on the void growth is well covered by the modified Gurson model, and the critical value, f_c, seems to be independent of the stress state. For the ASTM A710 steel, $f_c = 0.03$ was obtained by simulating the smooth and notched bars. The predictions of both global and local behavior of the specimens were proved by accompanying experiments [7].

Simulation of Cracked Specimens

To relate the micromechanical model to macroscopic fracture-mechanics concepts, all parameters used for the simulations of the smooth tensile bars were also applied to the analyses of cracked specimens. The unknown parameter, l_c, was determined by matching

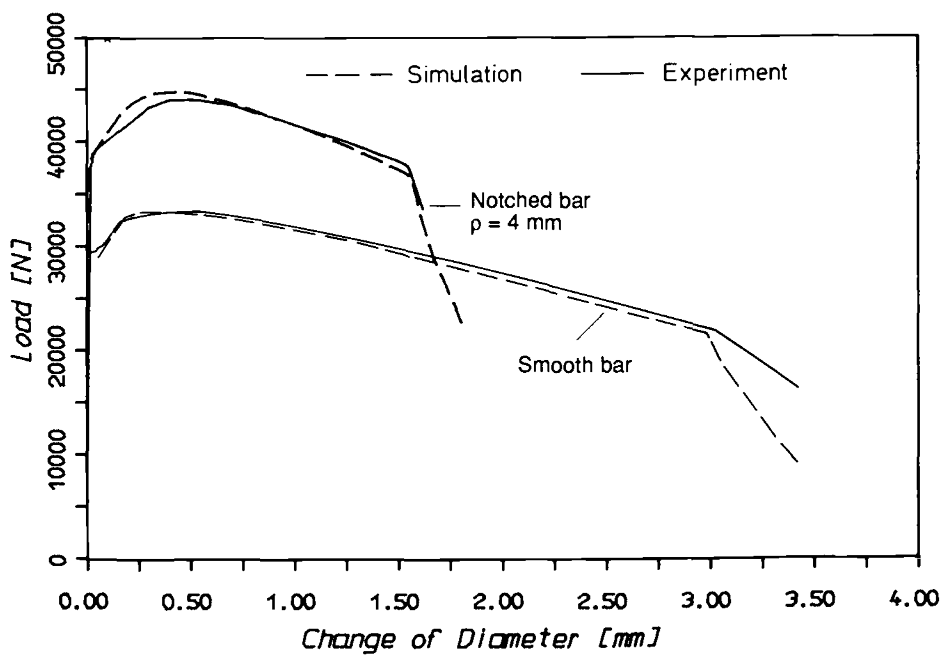

FIG. 2—*Comparison between numerical and experimental load versus diameter change curves for smooth bar and notched bar with notch radius of 4 mm.*

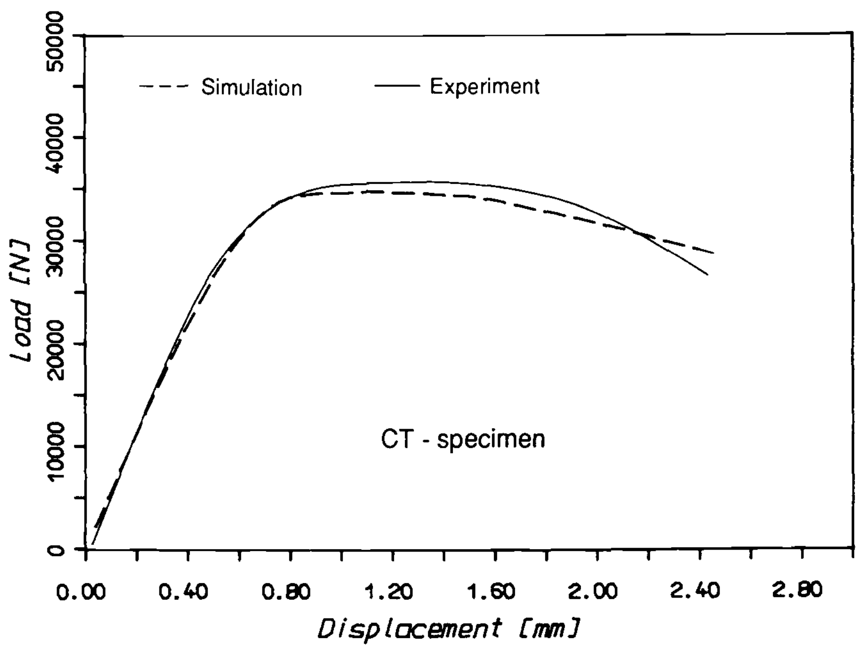

FIG. 3—*Measured and predicted load versus displacement curves of a CT specimen.*

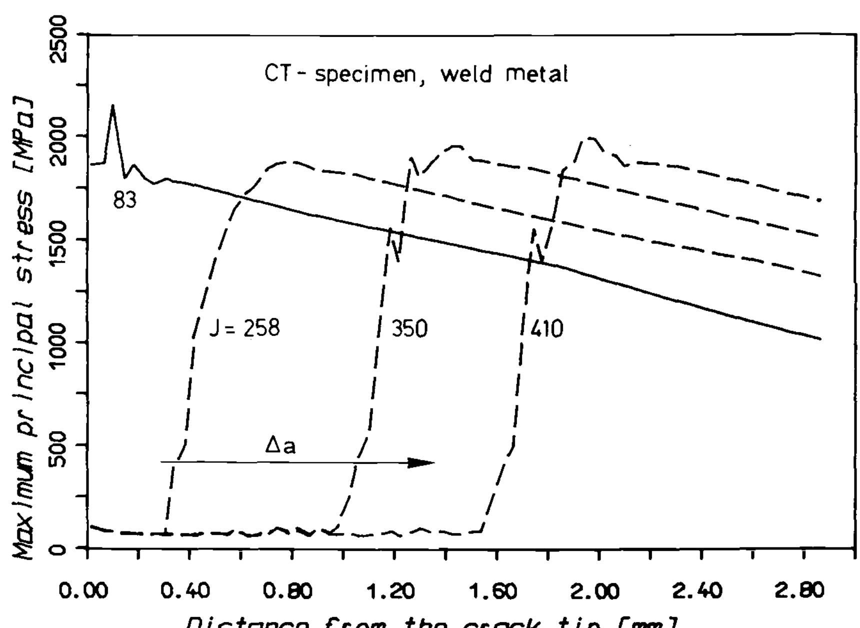

FIG. 4—*Distribution of the maximum principal stress, σ_1, ahead of the crack tip of a CT specimen.*

the calculated load versus displacement curve with the experimental curve of a compact tension (CT) specimen. Figure 3 shows for the weld metal a satisfactory agreement of the calculated and measured load versus displacement curves of the CT specimen with 20% side grooves. The applied l_c-value was 0.08 mm, which is identified with the length of the elements at the crack tip.

Figure 4 shows the calculated distribution of the maximum principal stress, σ_1, ahead of the crack tip for different load levels. The broken lines apply to load steps where the f_c-

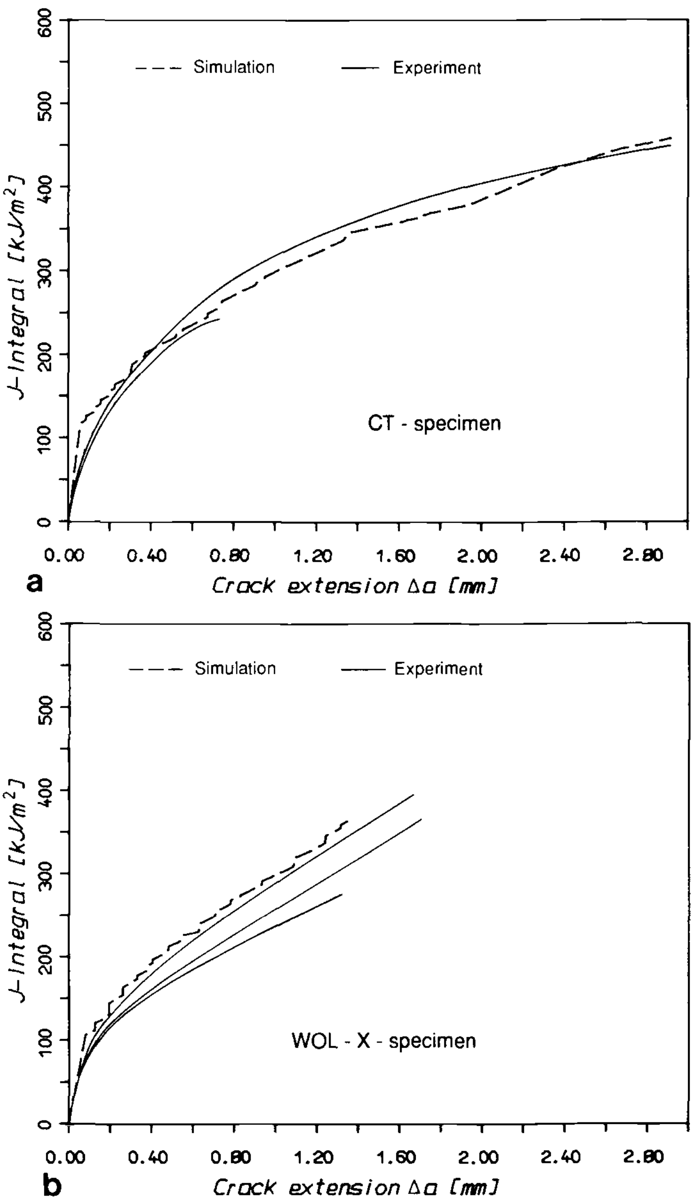

FIG. 5—*Measured and predicted* J_R*-curves for CT specimen* (a) *and WOL-X specimen* (b) *of a weld metal.*

value is exceeded locally. This figure explains that the numerical crack extension is a natural result of the creation of a layer that transmits only stresses close to zero. A good agreement between the calculated and experimental J-resistance curves of the CT specimen is shown in Fig. 5*a*.

For safety analyses of reactor pressure vessels, J-resistance curves are often determined using WOL-X specimens. Since the specimen geometries and loading conditions of WOL-X and CT specimens are different, a simulation of the WOL-X specimen can serve as a check of the universality of the micromechanical model. Figure 6 shows the deformed finite element mesh for the WOL-X specimen. Due to the unsymmetrical loading condition and specimen geometry, the whole specimen with a screw was modeled. The computation was performed using the same set of material parameters and the same mesh size in the crack tip region. The predicted J-resistance curve for the WOL-X specimen was compared with

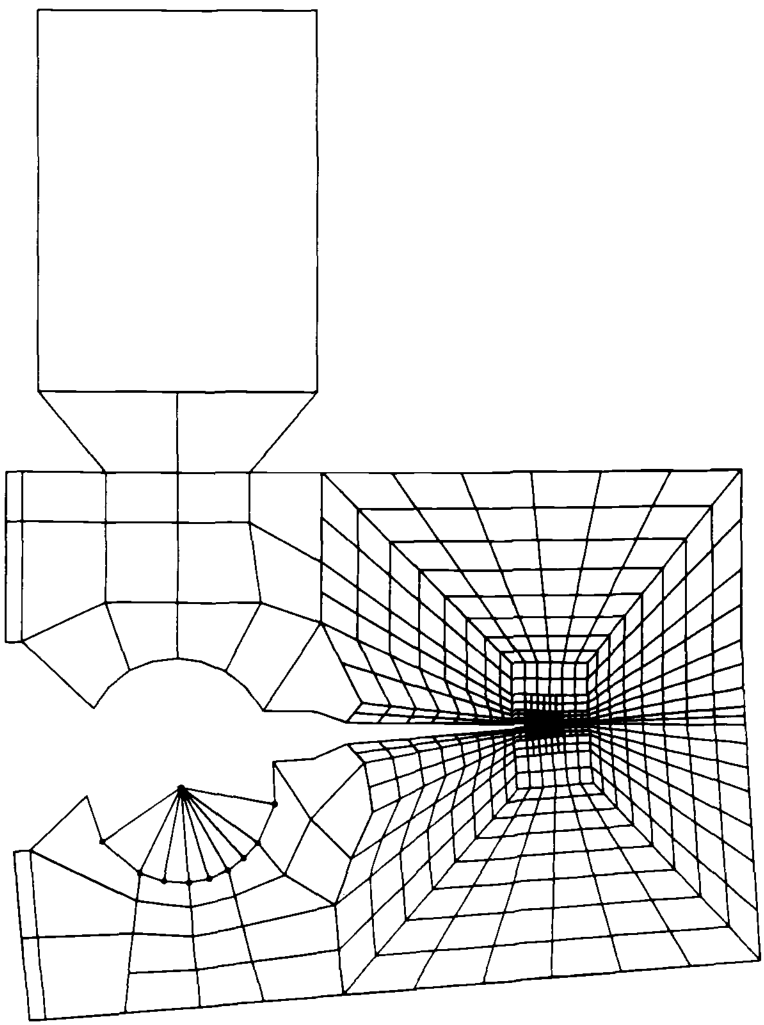

FIG. 6—*Deformed finite element mesh of a WOL-X specimen.*

the experimental curves determined from three specimens. Figure 5*b* shows that the calculated resistance curve lies within a scatter band of the experimental results.

Prediction of Geometry Effects on the J_R-*Curve*

Although up to now only two-dimensional simulations are feasible due to the very high computer time required, a number of different specimen types was analyzed in order to evaluate relative differences of the predicted *J*-resistance behavior that might be correlated to differences in the inplane constraint. In the simulations, the meshing of the crack-tip region and the damage parameters were kept constant. Only the remote part of the mesh was adjusted to match the actual specimen geometry and the loading.

Table 1 gives details of the investigated specimens of the ASTM A710 steel. For all computations, plane strain conditions were assumed.

Figure 7 compiles the *J*-resistance curves of all six specimens investigated. The differences between the CT specimen and the three-point bend specimen (SENB) are quite small, especially for small amounts of crack extension. This may be attributed to the fact that the compact specimen is essentially loaded in bending. The steepest curve comes from the center cracked panel (CCP). This specimen reflects the case of pure tension.

In Ref *13*, it has been found that the *J*-resistance curves of single-edge notched tension specimens (SENT) depend strongly on the loading situation. The model SENT-C "hydraulic clamps" reduces the bending reaction of the specimen due to the crack. As a consequence, the resistance curve is fairly steep and comes close to that for the CCP specimen. If, however, pin loading is modeled (SENT-P), the slope of the resulting resistance curve is much smaller and similar to those of the bending-type specimens. The explanation for this is that the pin load does not impede the transverse displacement of the specimen. This bending reaction of the specimen depends strongly on the crack length. Therefore, it is less pronounced in the model (SENT-S) with the short crack and the resulting resistance curve comes closer to the pure tension case.

These well-known variations of J_R-curves obtained for the same material with different specimen geometries can be attributed to differences in the state of stress at the crack front. The stress triaxiality is measured by the ratio, h, of the hydrostatic stress, $\sigma_{kk}/3$, and the von Mises equivalent stress, σ_e. Figure 8 shows the variation of h over the ligament shortly before initiation for all specimen configurations investigated. All curves have about the same shape with maximum constraint a short distance ahead of the crack tip. The constraint

TABLE 1—*Specimen geometries.*

Code	Width, W (mm)	Length, L (mm)	Crack Length a/W	Type of Loading
CT	50	37.5	0.624	mixed
SENB	50	225	0.624	pure bending three-point bend
CCP	100	225	0.624	pure tension
SENT-C	50	225	0.624	mixed, clamping grips
SENT-P	50	225	0.624	mixed, pin loaded
SENT-S	50	225	0.1	mixed, pin loaded

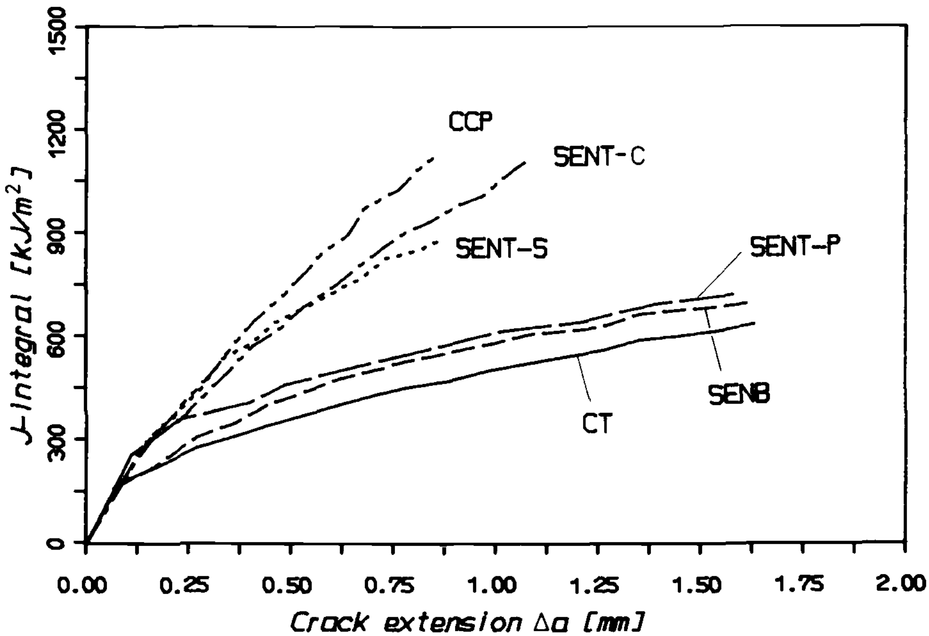

FIG. 7—*Predicted* J_R*-curves for different specimen configurations of ASTM A710 steel.*

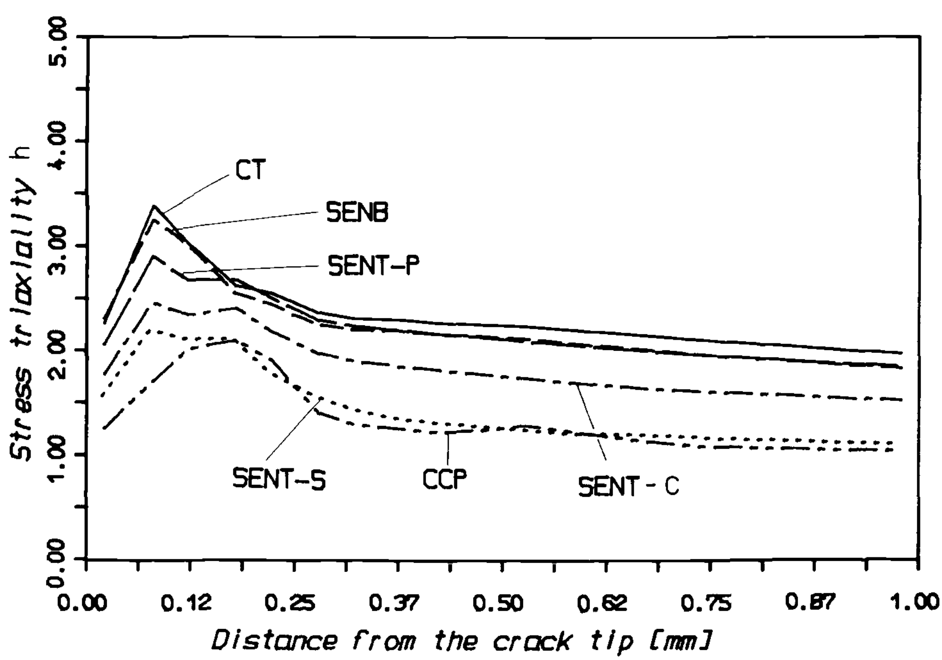

FIG. 8—*Distribution of stress triaxiality,* h, *for different specimen types at initiation load.*

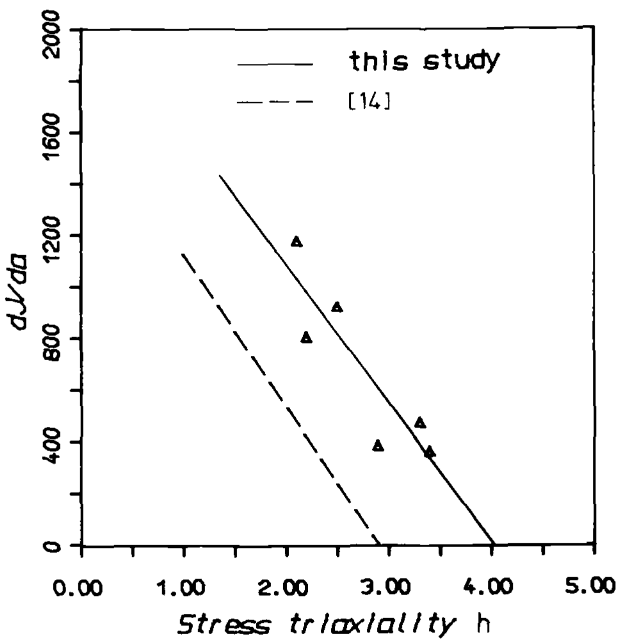

FIG. 9—*Slope of the* J_R*-curve,* dJ/da, *as a function of* h.

increases with increasing bending load, the CT and SENB specimens exhibit the highest constraint level throughout the curve.

In Fig. 9, the slopes of the calculated resistance curves, *dJ/da*, were plotted as a function of the maximum stress triaxiality, *h*, taken at the load at crack initiation. The *dJ/da*-values were in every case determined from the region between initiation and the crack extension of 0.85 mm. Obviously, a linear relation of *dJ/da* and *h* may be deduced. A similar function (dashed line) had been also postulated in Ref *14* for a similar material and applied successfully to surface flaws. It is surprising that the curve determined from numerical simulations in plane strain of different specimen and loading conditions is fairly parallel to that derived only from smooth and side-grooved compact specimens. The shift towards higher values of constraint is explained by the fact that plane strain provides an upper bound of stress triaxiality, although it must be kept in mind that the sizes of the (three-dimensional) crack-tip elements utilized in Ref *14* were about ten times larger than in this study.

Conclusions

The parameters for the application of the modified Gurson model can be determined by quantitative metallography and by comparing numerical and experimental load versus displacement curves of smooth tension bars. The fracture behavior of notched bars was simulated very accurately using the parameters obtained from the smooth bar.

For the analysis of cracked structures, the critical distance, l_c, becomes important. With the l_c-value determined from the CT specimen, the WOL-X specimen was simulated in a satisfactory way. The modified Gurson model was also applied successfully to predict differences in the slopes of J-resistance curves of different specimen geometries. In agreement with experimental observations, the slopes of the resistance curves increase with increasing ratio of tension versus bending load and decreasing crack length.

Acknowledgment

The authors are grateful to the Deutsche Forschungsgemeinschaft (German Science Foundation) and Preussen Elektra AG (Hannover) for their support.

References

[*1*] Sun, D-Z., Dormagen, D., and Dahl, W., "Influence of Specimen Geometry on Fracture Mechanics Values at the Onset of Stable Crack Extension," *Steel Research*, Vol. 56, 1985, pp. 445-449.

[*2*] Aurich, D. and Sommer, E., "The Effect of Constraint on Elastic-Plastic Fracture," *Steel Research*, Vol. 59, 1988, pp. 358-367.

[*3*] Kordisch, H. and Sommer, E., "3D-Effects Affecting the Precision of Lifetime Predictions," *Fracture Mechanics: Nineteenth Symposium, ASTM STP 969*, T. A. Cruse, Ed., American Society for Testing and Materials, Philadelphia, 1988, pp. 73-87.

[*4*] Gurson, A. L., "Continuum Theory of Ductile Rupture by Void Nucleation and Growth: Part I—Yield Criteria and Flow Rules for Porous Ductile Media," *Journal of Engineering Materials and Technology*, Vol. 99, 1977, pp. 2-15.

[*5*] Needleman, A. and Tvergaard, V., "An Analysis of Ductile Rupture in Notched Bars," *Journal of Mechanics and Physics of Solids*, Vol. 32, 1984, pp. 461-490.

[*6*] Needleman, A. and Tvergaard, V., "An Analysis of Ductile Rupture Modes at a Crack Tip," *Journal of Mechanics and Physics of Solids*, Vol. 35, 1987, pp. 151-183.

[*7*] Sun, D-Z., Siegele, D., Voss, B., and Schmitt, W., "Application of Local Damage Models to the Numerical Analysis of Ductile Rupture," *Fatigue & Fracture of Engineering for Materials & Structures*, Vol. 12, 1988, pp. 201-212.

[*8*] Rice, J. R. and Johnson, M. A., "The Role of Large Crack Tip Geometry Change in Plane Strain Fracture," *Inelastic Behavior of Solids*, M. F. Kanninen et al., Eds., McGraw-Hill, New York, 1970, pp. 641-672.

[*9*] Rousselier, G., "Ductile Fracture Models and Their Potential on Local Approach of Fracture," *Nuclear Engineering and Design*, Vol. 105, 1987, pp. 97-111.

[*10*] Sun, D-Z., Voss, B., and Schmitt, W., "Numerical Prediction of Ductile Fracture Resistance Behaviour Based on Micromechanical Models," *Defect Assessment in Components—Fundamentals and Applications*, ESIS/EGF9, J. G. Blauel and K.-H. Schwalbe, Eds., 1991, Mechanical Engineering Publications, London, pp. 447-458.

[*11*] Chu, C. C. and Needleman, A., "Void Nucleation Effects in Biaxially Stretched Sheets," *Journal of Engineering and Materials Technology*, Vol. 102, 1980, pp. 249-256.

[*12*] Bridgman, P. W., *Studies in Large Plastic Flow*, McGraw-Hill, New York, 1952.

[*13*] Hollstein, T., Schmitt, W., and Blauel, J. G., "Numerical Analysis of Ductile Fracture Experiments Using Single-Edge Notched Tension Specimens," *Journal of Testing and Evaluation*, Vol. 11, 1983, pp. 174-181.

[*14*] Kordisch, H., Sommer, E., and Schmitt, W., "The Influence of Triaxiality on Stable Crack Growth," *Nuclear Engineering and Design*, Vol. 112, 1989, pp. 27-35.

Composites Materials

H. Zhu[1] and J. D. Achenbach[1]

Matrix Cracks and Interphase Failure in Transversely Loaded Fiber Composites

REFERENCE: Zhu, H. and Achenbach, J. D., "**Matrix Cracks and Interphase Failure in Transversely Loaded Fiber Composites,**" *Fracture Mechanics: Twenty-Second Symposium (Volume II), ASTM STP 1131*, S. N. Atluri, J. C. Newman, Jr., I. S. Raju, and J. S. Epstein, Eds., American Society for Testing and Materials, Philadelphia, 1992, pp. 381–394.

ABSTRACT: Interphases in a unidirectionally fiber-reinforced composite with hexagonal packing are modeled by the spring-layer model. The composite is subjected to transverse tensile loading. A critical value of the circumferential stress (σ_θ) at the matrix side of the interphase is taken as a criterion for the initiation of radial matrix cracks, while interphase failure is assumed to occur when the interphase strain energy density (U) exceeds a critical value. All numerical calculations have been carried out by the use of the boundary-element method. For a perfect composite, the results show σ_θ and U for various values of the interphase stiffnesses. For a composite that develops radial matrix cracking, U has been computed and the proclivity towards subsequent interphase failure is discussed. Conversely, for a composite that first develops interphase failure, σ_θ has been calculated to determine the tendency towards subsequent radial matrix cracking.

KEY WORDS: fiber composites, interphase failure, matrix cracks, fracture mechanics, fatigue (materials)

The effect of fiber-matrix interphases on the mechanical behavior of fiber-composites has become of major interest. In analytical studies, two models have been employed. Broutman and Agarwal [*1*], Christensen and Lo [*2*], Theocaris et al. [*3*], Maurer et al. [*4*], Sideridis [*5*], and Benveniste et al. [*6*] have described the interphase as a layer between fiber (or inclusion) and matrix, of specified thickness and of elastic constants different from those of the matrix and the fiber. In an alternate model, a very thin interfacial zone of unspecified thickness has been considered. In this model, it is assumed that the radial and the tangential tractions are continuous across the interphase, but the displacements may be discontinuous from fiber to matrix, due to the presence of the interphase in-between. The tractions are assumed to be proportional to the corresponding displacement discontinuities. The proportionality constants then characterize the stiffness of the interphase. This so-called spring-layer model was employed by Lene and Leguillar [*7*], Benveniste [*8*], Aboudi [*9*], Steif and Hoysan [*10*], Achenbach and Zhu [*11–13*], and Hashin [*14,15*]. Both models just mentioned were studied by Jasiuk and Tong [*16*]. A corresponding linearly viscoelastic model of the interphase was employed by Moran et al. [*17*].

This paper is concerned with the study of the effect of an interfacial zone on the development of matrix cracks and interphase failure in fiber-reinforced composites that are subjected to uniform transverse loading applied in the far-field. A unidirectionally-reinforced

[1]Post-doctoral fellow and professor, respectively, Center for Quality Engineering and Failure Prevention, Northwestern University, Evanston, IL 60208. Mr. Zhu is now at the Department of Engineering Science and Mechanics, The University of Tennessee, Knoxville, TN 37996.

composite with hexagonal packing of the fibers is investigated. The boundary-element method (BEM) is used to obtain results within the framework of the two-dimensional theory of elasticity (plane strain). The interfacial zone is represented by the spring-layer model.

Formulation

Figure 1*a* shows a cross-sectional view of a fiber-reinforced composite with radial cracks in the matrix. The circular fibers, which are all of equal radius, *a*, are spaced periodically in a hexagonal packing sequence, and the matrix cracks, which are of equal length, *d*, are also located periodically in the composite. It is assumed that at some large distance the composite is subjected to uniform stresses, σ_0, applied in the transverse direction. The loading direction in Fig. 1*a* is called the midclosest packing direction (Mid-CPD). The basic cell chosen for analysis is a hexagon with sides, *b*, as shown in Fig. 1*a* (the region enclosed

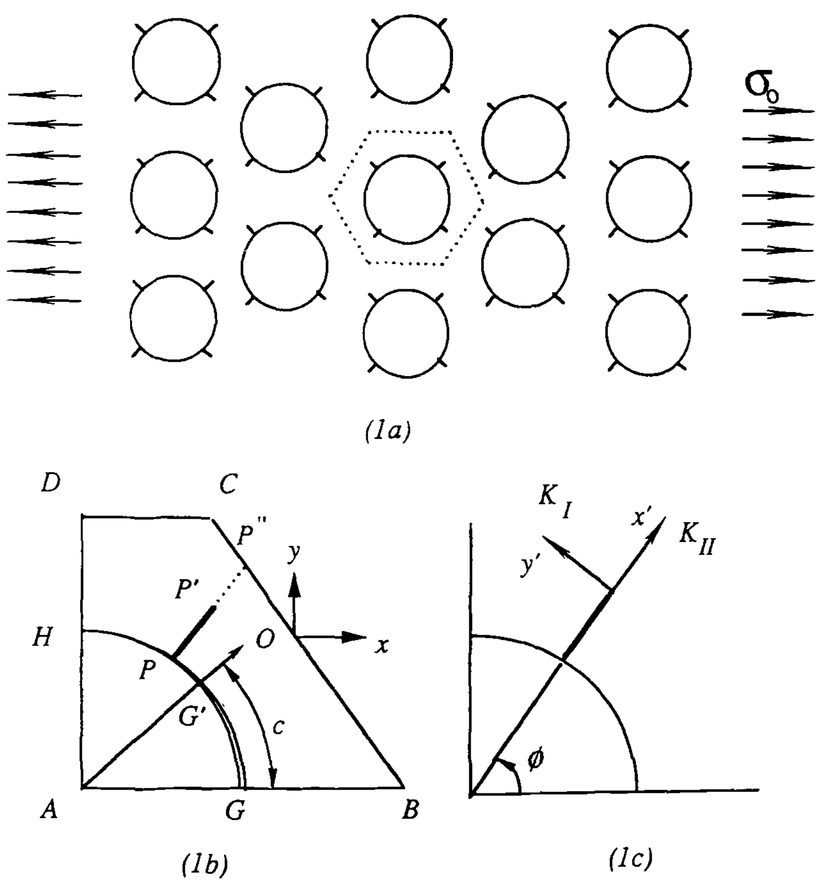

FIG. 1—(a) *Hexagonal array with matrix cracks and interphase failures subjected to Mid-CPD far-field uniform tensile stress* σ_0. (b) *Quarter region of basic cell,* a = *fiber radius, Length BC* = b, *matrix crack Length PP'* = d, *and half length of interphase failure GG'* = c. (c) *Coordinate system for stress-intensity factors.*

by the dashed lines). The periodicity of the composite then implies that the state of stress and deformation in the composite will be defined completely by the stresses and strains in a quarter region of a basic cell. This quarter region is shown in Fig. 1*b* with the crack being denoted by the bold Line $\overline{PP'}$

The boundary conditions on the external surfaces of the trapezoid in Fig. 1*b* can be expressed by

$$-\frac{3}{4}b \le x \le \frac{1}{4}b,\ y = -\frac{\sqrt{3}}{4}b : \sigma_{yx} = 0,\ v = -\frac{C_2}{2} \qquad (1a,b)$$

$$\underset{\sim}{x}\ \varepsilon\ \overline{CB}:\ u(-x,y) = -u(x-y),\ v(-x,y) = -v(x-y) \qquad (2a,b)$$

$$\underset{\sim}{x}\ \varepsilon\ \overline{CB}:\ t_x(-x,y) = t_x(x,-y),\ t_y(-x,y) = t_y(x,-y) \qquad (3a,b)$$

$$-\frac{3}{4}b \le x \le -\frac{1}{4}b,\ y = \frac{\sqrt{3}}{4}b:\ \sigma_{yx} = 0,\ v = \frac{C_2}{2} \qquad (4a,b)$$

$$x = -\frac{3}{4}b,\ -\frac{\sqrt{3}}{4}b \le y \le \frac{\sqrt{3}}{4}b:\ \sigma_{yx} = 0,\ u = C_1 \qquad (5a,b)$$

where (u, v) and (t_x, t_y) are the components of the displacement and traction fields, respectively; σ_{yx} is the shear stress; and C_1 and C_2 are unknown constants.

In addition, the condition that the crack faces are free of tractions yields the following relationships for (t_x, t_y) on Line $\overline{PP'}$

$$\underset{\sim}{x}+ \rightarrow \overline{PP'}:\ t_x(x+,y+) = t_y(x+,y+) = 0 \qquad (6a,b)$$

$$\underset{\sim}{x}- \rightarrow \overline{PP'}:\ t_x(x-,y-) = t_y(x-,y-) = 0 \qquad (7a,b)$$

Here, the $\underset{\sim}{x}+$ points are located on the upper face of the crack while $\underset{\sim}{x}^-$ points are on the lower crack face.

From equilibrium requirements in the x- and y-directions, two additional equations can be obtained as

$$\int_{CB} t_x(s)ds = \frac{\sqrt{3}}{2}b\,\sigma_0 \qquad (8)$$

$$\int_{DC} t_y(s)ds + \int_{CO} t_y(s)ds = 0 \qquad (9)$$

Following the authors' previous paper [*12*], the compliant interphase between fibers and matrix is modeled by a distribution of mechanical springs. With respect to polar coordinates centered at Point A (see Fig. 1*b*), the relationships between the relevant stress and displacement components may be then expressed as

$$\sigma_r^m = \sigma_r^f = k_r(u_r^m - u_r^f), \text{ if } u_r^m \geq u_r^f \tag{10}$$

$$\sigma_r^m = \sigma_r^f \text{ and } u_r^m - u_r^f, \text{ if } u_r^m \text{ not} \geq u_r^f \tag{11}$$

$$\sigma_{r\theta}^m = \sigma_{r\theta}^f = k_\theta(u_\theta^m - u_\theta^f) \tag{12}$$

where σ_r is the interfacial radial stress and $\sigma_{r\theta}$ is the interfacial shear stress. Quantities with upper index, m and f, are defined in the matrix and the fiber regions, respectively. The constants, k_r and k_θ, are the coefficients of the springs. The addition of Eq 11 ensures that the model will not allow an unrealistic radial overlap of the two materials in the interfacial zone.

It should be noted that the compliant conditions, Eqs 10–12, include the case of perfect contact ($k_r = \infty$, $k_\theta = \infty$), when the stresses and displacements are continuous, and the case of no contact, that is, interphase failure ($k_r = k_\theta \equiv 0$) when the stresses vanish. For an interphase that has failed over part of the circumference of a fiber, Eqs 10 and 12 imply that the stresses remain bounded by virtue of the boundedness of the displacements.

Boundary Integral Equations

The matrix region is further divided by adding a boundary, $\overline{\text{P}'\text{P}''}$, that is the straight elongation of Line $\overline{\text{PP}'}$. The new boundary consists of the crack surface and its extension from the crack tip, P′, to Point P″ at the intersection with Line $\overline{\text{BC}}$. Then, the trapezoid is divided into three separate regions, which may be denoted by PP″CDHP, GBP″PG, and AGHA, and the boundary integral equation method (BIE) is applied to these three regions. Again, using the same approach as in the authors' previous paper [12], the following boundary integral equations are obtained

$$\frac{1}{2} u_i^m(\underset{\sim}{x}) = \int_{\Gamma_1+\Gamma_2} U_{ij}^m(\underset{\sim}{x},\underset{\sim}{\xi})t_j^m(\underset{\sim}{\xi})d\Gamma(\underset{\sim}{\xi}) - \int_{\Gamma_1+\Gamma_2} T_{ij}^m(\underset{\sim}{x},\underset{\sim}{\xi})u_j^m(\underset{\sim}{\xi})d\Gamma(\underset{\sim}{\xi}), \qquad \underset{\sim}{x} \in \Gamma_1 + \Gamma_2 \tag{13}$$

where

$$\Gamma_1 = \overline{\text{PP}''} + \overline{\text{P}''\text{C}} + \overline{\text{CD}} + \overline{\text{DH}} \tag{14}$$

$$\Gamma_2 = \overline{\text{HP}} \tag{15}$$

and

$$\frac{1}{2} u_i^m(\underset{\sim}{x}) = \int_{\Gamma_3+\Gamma_4} U_{ij}^m(\underset{\sim}{x},\underset{\sim}{\xi})t_j^m(\underset{\sim}{\xi})d\Gamma(\underset{\sim}{\xi}) - \int_{\Gamma_3+\Gamma_4} T_{ij}^m(\underset{\sim}{x},\underset{\sim}{\xi})u_j^m(\underset{\sim}{\xi})d\Gamma(\underset{\sim}{\xi}), \qquad \underset{\sim}{x} \in \Gamma_3 + \Gamma_4 \tag{16}$$

where

$$\Gamma_3 = \overline{\text{GB}} + \overline{\text{BP}''} + \overline{\text{P}''\text{P}} \tag{17}$$

$$\Gamma_4 = \overline{\text{PG}} \tag{18}$$

Here, $t_j^m(\underset{\sim}{\xi})$ and $u_j^m(\underset{\sim}{\xi})$ are the traction and displacement components, and $U_{ij}^m(\underset{\sim}{x},\underset{\sim}{\xi})$ and $T_{ij}^m(\underset{\sim}{x},\underset{\sim}{\xi})$ are the fundamental solutions defined by

$$U_{ij}^m(\underset{\sim}{x},\underset{\sim}{\xi}) = \frac{1}{8\pi\mu^m(1 - \nu^m)}\left[(3 - 4\nu^m)\ell n\left(\frac{1}{R}\right)\delta_{ij} + \frac{\partial R}{\partial x_i}\frac{\partial R}{\partial x_j}\right] \tag{19a}$$

$$T_{ij}^m(\underset{\sim}{x},\underset{\sim}{\xi}) = -\left[\lambda^m \frac{\partial}{\partial x_\ell} U_{i\ell}^m\delta_{jk} + \mu^m \frac{\partial}{\partial x_k} U_{ij}^m + \mu^m \frac{\partial}{\partial x_j} U_{ik}^m\right] n_k(\underset{\sim}{\xi}) \tag{19b}$$

where, $R = |\underset{\sim}{x} - \underset{\sim}{\xi}|$, $n(\underset{\sim}{\xi})$ is the outward normal on the contour of interest. Also, λ^m and μ^m are the Lamé constants and the Poisson's ratio, ν^m, is related to λ^m and μ^m by

$$\lambda^m = 2\nu^m\mu^m/(1 - 2\nu^m) \tag{20}$$

The introduction of the $\overline{\mathrm{P'P''}}$ boundary allows us to use the displacement BIE representation to deal with the crack problem, thereby avoiding the use of the derivative of that BIE representation that would lead to higher order singularities and a more complicated algorithm. As discussed in some detail in the next section, a special crack tip element is used near the crack tip P′.

The third integral equation for the displacement components, the one in the fiber, may be written as

$$\frac{1}{2}u_i^f(\underset{\sim}{x}) = \int_{\Gamma_5+\Gamma_2+\Gamma_4} U_{ij}^f(\underset{\sim}{x},\underset{\sim}{\xi})t_j^f(\underset{\sim}{\xi})\,d\Gamma(\underset{\sim}{\xi})$$

$$- \int_{\Gamma_5+\Gamma_2+\Gamma_4} T_{ij}^f(\underset{\sim}{x},\underset{\sim}{\xi})u_j^f(\underset{\sim}{\xi})d\Gamma(\underset{\sim}{\xi}), \qquad \underset{\sim}{x} \in \Gamma_5 + \Gamma_2 + \Gamma_4 \tag{21}$$

where

$$\Gamma_5 = \overline{\mathrm{HA}} + \overline{\mathrm{AG}} \tag{22}$$

Here, the fundamental solutions, $u_{ij}^f(\underset{\sim}{x},\underset{\sim}{\xi})$ and $T_{ij}^f(\underset{\sim}{x},\underset{\sim}{\xi})$, are also defined by Eqs 19*a* and *b*, but with elastic constants, λ^f and μ^f, of the fiber, and the unit normal is now pointing out from the fiber material. For convenience, we employ indicial notation in this section; where $x_1 = x$ and $x_2 = y$, and the summation convention is implied for repeated indices.

The boundary integral equations in Eqs 13, 16, and 21 have been solved numerically by the boundary-element method (BEM). Details can be found in Ref *18*.

A complication in the calculation occurs because of the presence of the alternative interface conditions given by Eqs 10 and 11. In the initial phase of the calculations, the radial interface stress $\sigma_r^m(= \sigma_r^f)$ is computed under the assumption that Eq 10 applies. A positive value for the computed stress component indicates that the initial assumption was correct. If a negative value is obtained over one or more interface elements, Eq 10 is replaced by Eq 11 for those elements, and the calculation is redone. The radial interfacial stress should still be obtained as negative in this adjusted calculation.

The numerical calculations have been carried out for solids with the following material properties:

1. matrix = μ^m = 97.9 GPa, ν^m = 0.22, and
2. fibers = μ^f = 207 GPa, ν^f = 0.22.

The results will actually apply for any pair of solids, which have the stated Poisson's ratios, and whose ratio of the shear moduli is the same as for the preceding materials. The interphase constants, k_r and k_θ, were rendered dimensionless by dividing by μ^m/a, where a is the radius of the fibers

$$k_r/(\mu^m/a) = k_1, \qquad k_\theta/(\mu^m/a) = k_2 \tag{23a,b}$$

The variable parameters in the numerical algorithm are the half length of the interphase disbond, c, the length of the radial matrix crack, d, the fiber volume ratio, V_f, and the interphase stiffness constants, k_1 and k_2. The fiber volume ratio, V_f is defined by

$$V_f = \frac{\pi a^2}{4} \Big/ \frac{3/3b^2}{8} \tag{24}$$

The lengths of the boundary elements for all calculations were chosen as $0.04a$ or smaller, and the fields were assumed to be uniform over these elements (that is, "constant" elements are employed). It should be noted that the cracked configuration applies to a composite for which all fibers contain the same symmetrically oriented matrix cracks and interphase disbonds.

Crack Tip Element

It is to be expected that for bodies containing cracks, the use of conventional constant elements at the crack tips will not yield satisfactory numerical results. Blandford et al. [19] introduced the so-called traction singular quarter-point crack tip element with and without transition elements. The traction singular quarter-point element characterizes the behavior of the displacement and the traction at a crack tip by containing terms of the forms $r^{1/2}$ and $r^{-1/2}$, respectively. Martinez et al. [20,21] also considered the same quarter-point element, but they used a somewhat different procedure. These authors obtained quite accurate solutions for some simple crack problems. In the present paper, an alternative consideration is employed that avoids the lengthy programming that would be required if the quarter-point element method would be employed for the complicated geometrical configuration studied in this paper.

At the crack tip, the traction term, $t(\eta)$, is of the form of $K\eta^{-1/2}$. Here, K is a constant and η is the distance from the crack tip. If $t(\eta)$ is integrated with a known smooth kernal, $U(x,\eta)$, over a small interval, $(0,\ell)$, then the integration by parts yields

$$\int_0^\ell K\eta^{-1/2}U(x,\eta)d\eta = t(\eta^*)\int_0^\ell U(x,\eta)d\eta - \Delta, \qquad \eta^* = 0.25\ell \tag{25a,b}$$

$$\Delta = \ell^{3/2}\int_0^1 2K(\bar{\eta}^{1/2} - \bar{\eta})\, \partial U(x,\ell\bar{\eta})/\partial\eta \; d\bar{\eta} \tag{25c}$$

where, ℓ is the dimension of the crack tip element. The term, Δ, in Eq 25c is of the order $\ell^{3/2}$ and is omitted in our numerical program.

Equations 25*a* and *c* tell us that the conventional constant BEM can still be valid for the integral of the traction term over the crack-tip element, but the spatial variable of the traction term now is understood to be located at the quarterpoint, not the midpoint, of the element, and the trunction error is of the order $\ell^{3/2}$.

If $U(x,\eta)$ also has a logarithmic singularity in the interval $(0,\ell)$ (which is the case in the present crack problem when the field point is also located in the crack tip element), then the integral in Eq 25*c* can be evaluated analytically as

$$\int_0^\ell K\eta^{-1/2}\mathrm{Ln}|\eta - \ell/2|d\eta = t(\eta^* = 0.25\ell)\ell[\mathrm{Ln}(\ell/2) + \sqrt{2}\mathrm{Ln}(\sqrt{2} + 1) - 2 \tag{26}$$

Here, the field point, x, is taken the midpoint of the element.

Thus, the present approach follows the traditional constant element method, but the traction at the crack tip is understood as the traction at the quarterpoint of the element dimension away from the crack tip. The only modification needed is for the i^{th} diagonal terms of the displacement Green's function matrix

$$\bar{U}_{ij} = \int_0^\ell U_{ij}^m(\underset{\sim}{x},\underset{\sim}{\xi})d\Gamma(\underset{\sim}{\xi}) \tag{27a}$$

When the crack tip element is i^{th} numbered, only the following two matrix elements must be modified to

$$\bar{U}_{2i2i}^{\text{modified}} = \bar{U}_{2i2i}q_1 \tag{27b}$$

$$\bar{U}_{2(i+1)2(i+1)}^{\text{modified}} = \bar{U}_{2(i+1)2(i+1)}q_2 \tag{27c}$$

where

$$q_1 = \{(3\nu - 4)[0.753\,35 - \mathrm{Ln}(\ell/2)] + R_1^2\}/\{(3\nu - 4)[1 - \mathrm{Ln}(\ell/2)] + R_1^2\} \tag{28a}$$

$$q_2 = \{(3\nu - 4)[0.753\,35 - \mathrm{Ln}(\ell/2)] + R_2^2\}/\{(3\nu - 4)[1 - \mathrm{Ln}(\ell/2)] + R_2^2\} \tag{28b}$$

$$R_1 = (x_{i+1} - x_i)/\ell, \qquad R_2 = (y_{i+1} - y_i)/\ell, \qquad \ell = |\underset{\sim}{x}_{i+1} - \underset{\sim}{x}_i| \tag{29a,b,c}$$

Here, $\underset{\sim}{x}_i$ and $\underset{\sim}{x}_{i+1}$ are the coordinates of the two-end nodes of the i^{th} element; $\bar{U}_{2i2i}$ and $\bar{U}_{2(i+1)2(i+1)}$ are from the conventional BEM algorithm.

Even though the leading term of the traction at the crack tip plays the main role in the characterization of the stress behavior at the crack tip, the second term, which is a constant, should not be excluded. From our experience, it usually contributes about 3 to 12% of the traction at the quarterpoint node of the crack-tip element. In the present numerical program, the second term, which is assumed to be constant, has been also taken into account. The matrix elements corresponding to the second term are the same as those corresponding to the traction term at the crack-tip element for the conventional BEM. Now, we have, apparently, two more unknowns, namely, the second terms of the traction of the x- and y-directions at the crack tip element. Hence, two additional equations are required.

The displacements on the upper and lower crack faces can be decomposed as

$$\underset{\sim}{x}+ \rightarrow \overline{\mathrm{PP}'}: \underset{\sim}{u}(\underset{\sim}{x}+) = \bar{\underset{\sim}{u}}(\underset{\sim}{x}) + \Delta\underset{\sim}{u}(\underset{\sim}{x}) \tag{30a}$$

$$\underset{\sim}{x}- \rightarrow \overline{\mathrm{PP}'}: \underset{\sim}{u}(\underset{\sim}{x}-) = \bar{\underset{\sim}{u}}(\underset{\sim}{x}) - \Delta\underset{\sim}{u}(\underset{\sim}{x}) \tag{30b}$$

where, $\Delta \underline{u}(\underline{x})$ are the crack opening displacements. Analytical expressions near the crack tip are available for the crack opening displacements as well as for the stresses, for the plane strain case. In the (x',y') coordinates with their origin at Point P′ (see Fig. 1*c*), the crack opening displacements along Line $\overline{PP'}$ are

$$\Delta v_1(\underline{x}') = K_{II}\sqrt{|x'|}2(1 - \nu)/(\mu\sqrt{2\pi}), \qquad \underline{x}' \in \overline{PP'} \tag{31a}$$

$$\Delta v_2(\underline{x}') = K_{I}\sqrt{|x'|}2(1 - \nu)/(\mu\sqrt{2\pi}), \qquad \underline{x}' \in \overline{PP'} \tag{31b}$$

and the stresses along Line $\overline{P'P'}$ are

$$\sigma_{x'y'}(\underline{x}') = K_{II}/\sqrt{2\pi x'}, \qquad \sigma_{y'y'}(\underline{x}') = K_{I}/\sqrt{2\pi x'}, \qquad \underline{x}' \in \overline{P'P''} \tag{32a,b}$$

In our numerical program, the components of $\Delta \underline{v}(\underline{x}')$ at the crack-tip element on Line $\overline{PP'}$ are evaluated at the midpoint of the element while $\sigma_{x'y'}(\underline{x}')$ and $\sigma_{y'y'}(\underline{x}')$ at the crack-tip element on Line $\overline{P'P''}$ are evaluated at the quarterpoint. Therefore, we have the following relationships

$$\Delta v_1(x' = -0.5\ell, y' = 0) = \sigma_{x'y'}(x' = 0.25\ell, y' = 0)2\ell(1 - \nu)/(\mu\sqrt{8}) \tag{33a}$$

$$\Delta v_2(x' = -0.5\ell, y' = 0) = \sigma_{y'y'}(x' = 0.25\ell, y' = 0)\ell(1 - 2\nu)/(\mu\sqrt{8}) \tag{33b}$$

where, ℓ is the dimension of the crack-tip element.

The crack opening displacements in the (x,y) coordinates, $\Delta \underline{u}(\underline{x})$, can be related to $\Delta \underline{v}(\underline{x}')$ by

$$\Delta \underline{v}(\underline{x}') = \underline{T}(\phi) \cdot \Delta \underline{u}(\underline{x}) \tag{34a}$$

and the tractions, $\underline{t}(\underline{x})$, are related to $\underline{t}'(\underline{x}') = [\sigma_{x'y'}(\underline{x}') , \sigma_{y'y'}(\underline{x}')]$ by

$$\underline{t}'(\underline{x}') = -\underline{T}(\phi) \cdot \underline{t}(\underline{x}) \tag{34b}$$

where, $\underline{T}(\phi)$, which is called the 2×2 transform tensor, is defined by

$$\underline{T}(\phi) = \begin{bmatrix} \cos(\phi) & \sin(\phi) \\ -\sin(\phi) & \cos(\phi) \end{bmatrix} \tag{35}$$

where, ϕ is the crack orientation angle.

If $\Delta v_1(\underline{x}')$, $\Delta v_2(\underline{x}')$, $\sigma_{x'y'}(\underline{x}')$ and $\sigma_{y'y'}(\underline{x}')$ in Eqs 33*a* and *b* are replaced by $\underline{u}(\underline{x})$ and $\underline{t}(\underline{x})$ by the use of Eqs 34*a* and *b*, we obtain

$$\Delta u_1(\underline{x}^*) = -t_x(\underline{x}^{**})2\ell(1 - \nu)/(\mu\sqrt{8}) \tag{36a}$$

$$\Delta u_2(\underline{x}^*) = -t_y(\underline{x}^{**})2\ell(1 - \nu)/(\mu\sqrt{8}) \tag{36b}$$

where, $\underset{\sim}{x}^*$ is the point in the (x,y) coordinates corresponding to the point $(-0.5\ell,0)$ in the (x',y') coordinates, and $\underset{\sim}{x}^{**}$ is the point in the (x,y) coordinates corresponding to the point $(0.25\ell,0.)$ in the (x',y') coordinates. The quantities $\Delta u_1(\underset{\sim}{x}^*)$, $\Delta u_2(\underset{\sim}{x}^*)$, $t_x(\underset{\sim}{x}^{**})$, and $t_y(\underset{\sim}{x}^{**})$ are the unknowns in our calculations.

The preceding equations reduce the number of unknown by two. So the numerical system is now solvable.

In summary, the modified constant element method follows the conventional constant BEM, except that:

1. The traction term at the crack tip is located at the quarterpoint of the crack-tip element, and the corresponding diagonal matrix terms are multiplied by q_1 or q_2, which are defined by Eqs 28*a* and *b*.
2. The second term of the traction at the crack tip, which is assumed to be constant, is also included.
3. The crack opening displacements at the crack tip are related to the traction terms at the crack tip by Eqs 36*a* and *b*.
4. The number of unknowns of this modified constant element method is the same as that of the conventional constant element method.

This modified constant element method has been applied to the same cases as studied in Blandford's and Martinez's papers, and good results have been obtained, with less than 3% error when compared with analytical solutions. The numerical results in the following section have been also obtained by the use of this modified constant element method.

Numerical Results

Figure 2 displays circumferential stresses in the matrix at the fiber-matrix interphase. These results show that for low interphase stiffness, σ_θ has its largest value near $\theta = 45°$ (solid line). On the other hand for a higher value of k_1 and k_2 ($k_1 = k_2 = 1$, dashed line), the maximum is near $\theta = 80°$. If a maximum circumferential stress criterion for initiation of matrix cracking is assumed, Fig. 2 suggests that low interphase stiffness and higher fiber volume ratio give rise to radial matrix cracks at angles much smaller than $\theta = 90°$ (solid line) in accordance with the experimental observations of Daniel et al. [*22*] (see Ref *12* for more details).

The interphase strain energy density, $\bar{U}$, corresponding to the case of Fig. 2 is shown in Fig. 3. The definition of $\bar{U}$ is given by

$$\bar{U} = \frac{\bar{\sigma}_r^2}{2k_1} + \frac{\bar{\sigma}_{r\theta}^2}{2k_2} \tag{37}$$

where $\bar{\sigma}_r = \sigma_r/\sigma_0$ and $\bar{\sigma}_{r\theta} = \sigma_{r\theta}/\sigma_0$.

If a critical value of $\bar{U}$ is adopted as an interphase failure criterion, which has the advantage that it involves both σ_r and σ_θ, the results of Fig. 3 suggest that interphase failure, will start near $\theta = 0°$ because $\bar{U}$ has its largest value at that location. It should be noted here that σ_r is included in U only when σ_r is positive (tension). It is assumed that compressive values of σ_r do not affect the integrity of the interphase.

It is of interest to see the variation of the interphase strain energy density, $\bar{U}$, when matrix cracking has taken place. In Fig. 4, $\bar{U}$ is plotted for different lengths of a radial matrix crack. The crack is initiated at 50°, corresponding to the position of maximum σ_θ (solid line)

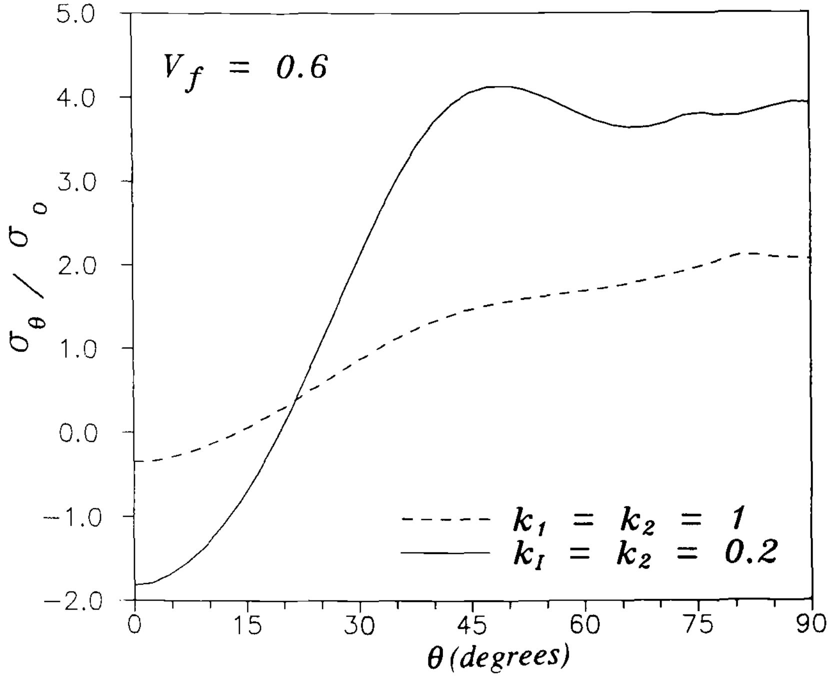

FIG. 2—*Circumferential stress σ_θ versus θ on the matrix side of the interphase for the case of no matrix cracking and no interphase failure.*

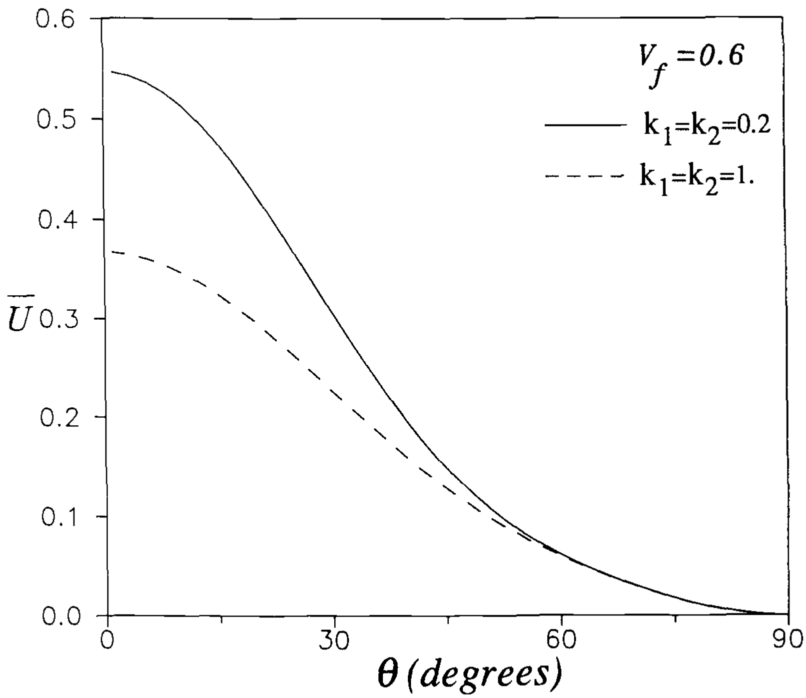

FIG. 3—*Dimensionless strain energy density $\overline{U}$ versus θ for the case of no matrix cracking and no interphase failure.*

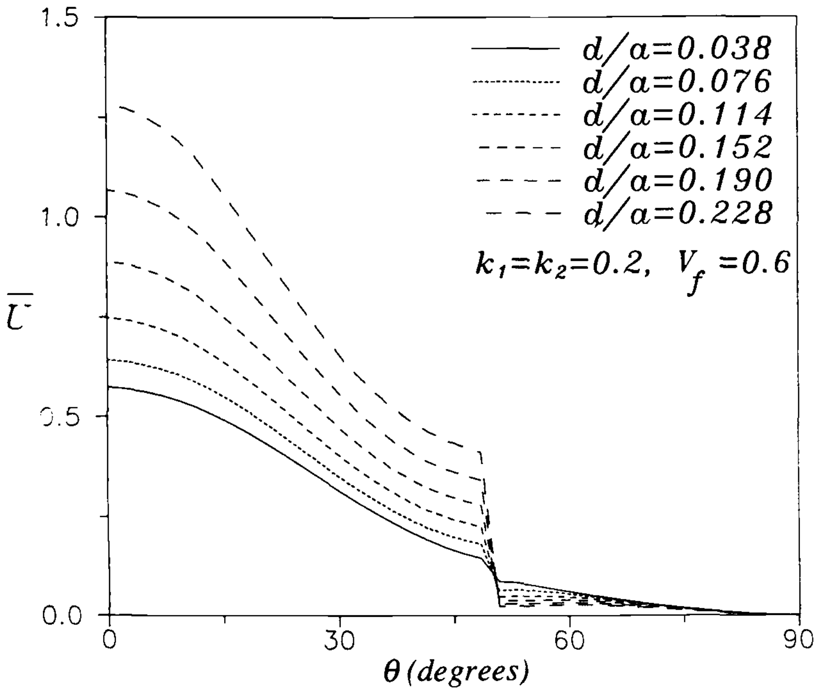

FIG. 4—*Strain energy density* $\bar{U}$ *versus* θ *for different matrix crack lengths;* d = *length of matrix crack and* a = *radius of circular fiber.*

shown in Fig. 2. In the interval $0 < \theta < 50°$, the magnitude of $\bar{U}$, which always has its maximum at $\theta = 0$, increases with increasing d/a. Hence, on the basis of a maximum strain energy density criterion for interphase disbond initiation, Fig. 4 suggests that failure of the fiber-matrix interphase may happen after the development of radial matrix cracks.

For the case that interphase failure has developed first, Fig. 5 shows the variation of σ_θ/σ_0 along the matrix side of the interphase versus the half interphase failure length, c. It is noted that the initiation and the subsequent development of interphase failure gives rise to a considerable increase of the magnitude of σ_θ/σ_0 at the interphase. This suggests that a radial matrix crack may be initiated after the development of the interphase failure.

The actual sequence of radial matrix cracking and interface failure depends on the critical values of σ_θ and U.

Figure 6 shows the effect of the interphase stiffness and the fiber volume ratio of the Mode I stress-intensity factor at the tips of the radial matrix cracks. The stress-intensity factor is defined in terms of the local crack tip coordinates shown in Fig. 1*c*. The value of K_I should be positive to be consistent with the existence of the matrix crack, and this is the case for all the numerical results presented here. Lower stiffness of the interphase in the circumferential direction, that is, lower k_2, leads to higher K_I values because there is less resistance to the crack opening displacement. For the same value of d/a, a greater part of the matrix is cracked for a higher value of V_f. Consequently, for fixed d/a, K_I increases with fiber volume ratio, as shown in Fig. 6.

Conclusions

A numerical technique has been developed to calculate microlevel stresses for transverse loading of a unidirectionally fiber-reinforced composite with hexagonal packing, for the case

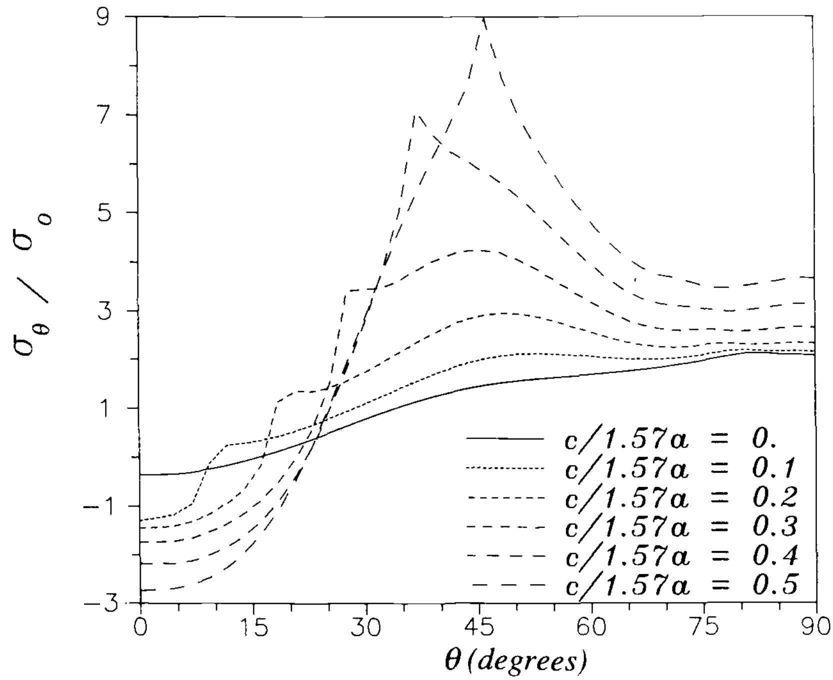

FIG. 5—*Circumferential stress* σ_θ *for different lengths of interphase failure;* c = *half length of interphase failure and* a = *radius of circular fiber.*

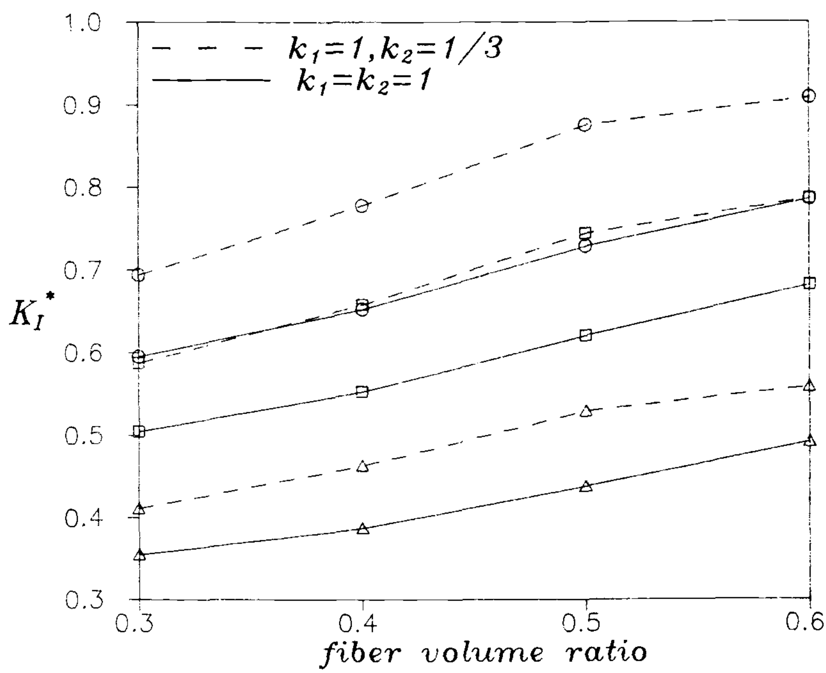

FIG. 6—*Normalized stress-intensity factors* $K_I^* = K_I/(\sqrt{a}\,\sigma_0)$ *at the matrix crack tip. The matrix crack orientation angle is 45°. Open triangles for* d/a = *0.04, open squares for* d/a = *0.08, and open circles for* d/a = *0.12.*

that the fiber-matrix interphases are modeled by the spring-layer model. Results are presented for the circumferential stress at the matrix side of the interphase, which is assumed to govern radial matrix cracking, and for the interphase strain energy density, whose critical value is assumed to govern interphase failure. The approach of this paper makes it possible to model failure scenarios of radial matrix cracking and interphase failure.

Acknowledgment

This work was carried out in the course of research sponsored by the Air Force Office of Scientific Research under Grant AFOSR-88-0124. The authors would like to acknowledge helpful discussions with I. M. Daniel and George Anastassopoulos.

References

[*1*] Broutman, L. J. and Agarwal, B. D., "A Theoretical Study of the Effect of an Interfacial Layer on the Properties of Composites," *Polymer Engineering Science*, Vol. 14, 1974, pp. 581–588.
[*2*] Christensen, R. M. and Lo, K. H., "Solutions for Effective Shear Properties in Three Phase Sphere and Cylinder Models," *Journal of Mechanics and Physics of Solids*, Vol. 27, 1979, pp. 315–330.
[*3*] Theocaris, P. S., Sideridis, E. P., and Papanicolaou, G. C., "The Elastic Longitudinal Modulus and Poisson's Ratio of Fiber Composites," *Journal of Reinforced Plastics and Composites*, Vol. 4, 1985, pp. 396–418.
[*4*] Maurer, F. H. J., Simha, R., and Jain, R. K., "On the Elastic Moduli of Particulate Composites: Interlayer versus Molecular Model," *Composites Interfaces*, H. Ishida et al. Eds., North-Holland, Amsterdam, 1986, pp. 367–374.
[*5*] Sideridis, E., "The In-Plane Shear Modulus of Fiber Reinforced Composites as Defined by the Concept of Interphase," *Composite Science and Technology*, Vol. 31, 1988, pp. 35–53.
[*6*] Benveniste, Y., Dvorak, G. J., and Chen, T., "Stress Fields in Composites with Coated Inclusion," *Mechanics of Materials*, Vol. 7, 1989, pp. 305–317.
[*7*] Lene, F. and Leguillon, D., "Homogenized Constitutive Law for a Partially Cohesive Composite Material," *International Journal of Solids and Structures*, Vol. 18, 1982, pp. 443–458.
[*8*] Benveniste, Y., "The Effective Mechanical Behavior of Composite Materials with Imperfect Contact between the Constituents," *Mechanics of Materials*, Vol. 4, 1985, pp. 197–208.
[*9*] Aboudi, J., "Damage in Composites Modeling of Imperfect Bonding," *Composite Science and Technology*, Vol. 28, 1987, pp. 103–128.
[*10*] Steif, P. and Hoysan, S. F., "An Energy Method for Calculating the Stiffness of Aligned Short-Fiber Composites," *Mechanics of Materials*, Vol. 6, 1987, pp. 197–210.
[*11*] Achenbach, J. D. and Zhu, H., "Effect of Interfacial Zone on Mechanical Behavior and Failure of Fiber-Reinforced Composites," *Journal of Mechanics and Physics of Solids*, Vol. 37, No. 3, 1989, pp. 381–393.
[*12*] Achenbach, J. D. and Zhu, H., "Effect of Interphases on Micro- and Macro-Mechanical Behavior of Hexagonal Array Fiber Composites," *Journal of Applied Mechanics*, Vol. 57, 1990, pp. 956–967.
[*13*] Zhu, H. and Achenbach, J. D., "Effect of Fiber-Matrix Interphase Defects on Microlevel Stress States at Neighboring Fibers," *Journal of Composite Materials*, Vol. 25, 1991, pp. 224–238.
[*14*] Hashin, Z., "Analysis of Properties of Fiber Composites with Anisotropic Constitutents," *Journal of Applied Mechanics*, American Society of Mechanical Engineers, Vol. 46, 1979, pp. 543–550.
[*15*] Hashin, Z., discussion at ONR-URI Program in Composite Materials Research Program Review, University of Maryland, College Park, MD, 12–13 June 1989.
[*16*] Jasiuk, I. and Tong, Y., "The Effect of Interface on the Elastic Stiffness of Composites," *Mechanics of Composite Materials and Structures, ASME AMD Vol. 100*, J. N. Reddy et al. Eds., 1989, American Society of Mechanical Engineers, New York, pp. 49–54.
[*17*] Moran, B., Gosz, M., and Achenbach, J. D., "Effect of a Viscoelastic Interface on the Transverse Behavior of Fiber-Reinforced Composites," *International Journal of Solids and Structures*, Vol. 27, 1991, pp. 1757–1771.
[*18*] Zhu, H., "Effect on Interfacial Zone on Mechanical Behavior and Failure of Fiber-Reinforced Composites," Ph.D. thesis, Northwestern University, Evanston, IL, 1989.

[19] Blandford, G. E., Ingraffea, A. R., and Liggett, J. A., "Two-Dimensional Stress Intensity Factor Computations Using the Boundary Element Method," *International Journal for Numerical Methods in Engineering*, Vol. 17, 1981.
[20] Martinez, J. and Dominguez, J., "Short Communication," *International Journal for Numerical Methods in Engineering*, Vol. 20, 1984.
[21] Martinez, J. and Dominguez, J., "Composites as Defined by the Concept of Interphase," *Composite Science and Technology*, Vol. 31, 1988, pp. 35–53.
[22] Daniel, I. M., Anastassopoulos, G., and Lee, J. W., "Failure Mechanics in Ceramic Matrix Composites," *Proceedings*, Spring Conference on Experimental Mechanics, Society for Experimental Mechanics, Cambridge, MA, 1989, pp. 832–838.

Mounir Bouden[1] *and Subhendu K. Datta*[2]

Dynamic Stress-Intensity Factors for Interface Cracks in Layered Media

REFERENCE: Bouden, M. and Datta, S. K., "**Dynamic Stress-Intensity Factors for Interface Cracks in Layered Media,**" *Fracture Mechanics: Twenty-Second Symposium (Volume II), ASTM STP 1131*, S. N. Atluri, J. C. Newman, Jr., I. S. Raju, and J. S. Epstein, Eds., American Society for Testing and Materials, Philadelphia, 1992, pp. 395–409.

ABSTRACT: The scattering of elastic waves by interfacial cracks in layered media has been investigated in this paper. A hybrid numerical method is employed for obtaining the solution. This method combines the finite element equations and the Green's function boundary integral representation. Numerical results are presented for the crack opening displacements (COD) and the Mode I and Mode II stress-intensity factors (SIF) as functions of nondimensional frequency when normal and tangential time harmonic line loads are applied on the free surface of the layered medium.

KEY WORDS: crack opening displacement, dynamic load, finite element method, Green's function, hybrid method, interface crack, layered medium, resonance, stress-intensity factors, fracture mechanics, fatigue (materials)

Nomenclature

a	Crack length
C_1	Longitudinal wave velocity
C_2	Shear wave velocity
C_R	Rayleigh wave velocity
$E^{(e)}$	Total elemental energy
G_{ki}	Green's function
H	Layer thickness
K_1	Mode I stress-intensity factor
K_2	Mode II stress-intensity factor
k_{21}	Shear wavenumber of the layer
$\mathrm{K}^{(e)}$	Elemental kinetic energy
L	Crack element length
N	Total number of nodal points
N_B	Number of nodal points on B
N_I	Number of nodal points interior to B
n_j	Normal to contour C
$p^{(e)}$	Elemental consistent nodal force vector
r	Radial distance from the crack tip
$\mathrm{R_E}$	Exterior region

[1]Research assistant, Department of Mechanical Engineering, University of Colorado, Boulder, CO 80309.

[2]Professor, Department of Mechanical Engineering and Cooperative Institute for Research in Environmental Science, University of Colorado, Boulder, CO 80309.

R_I Interior region
$S^{(e)}$ Elemental impedance matrix
$U^{(e)}$ Elemental strain energy
u_i Displacement field (i = 1,3)
$W^{(e)}$ Elemental work potential
x Horizontal coordinate
z Vertical coordinate

Greek

ε_{ij} Strain tensor
ε Nondimensional frequency
λ Lame's constant
μ Lame's constant
ξ Wavenumber in the y-direction
ρ Mass density
σ Poisson's ratio
τ_{ij} Stress tensor
ϕ_i Shape functions
ω Circular frequency
Σ_{kij} Stresses associated with the Green's functions

Subscripts

1 Properties related to the layer
2 Properties related to the half space

Superscripts

(f) Denotes a quantity relative to the free-field
(s) Denotes a quantity relative to the scattered field
t Denotes transpose
* Complex conjugate

In the past 20 years, corrosion-resistant coating technology has received a lot of attention from a multidisciplinary engineering and scientific community because of its wide applications. The selection of the coating material, its thickness, and the number of coats are based usually on the nature and the degree of aggressiveness of the environment to which the coated structure will be exposed. Also, coatings have to be compatible with the base material (substrate) in order to assure a good bonding. In the steel industry, the most commonly used processes for applying metal coatings are: hotdipping, electrodeposition, spraying, diffusion, and cladding. In all of these processes, it is not unusual to produce a coating with defects, such as cracks, debonding, or discontinuities. Moreover, these defects can also occur in situ due to fatigue or unusual stress levels applied to the material. The presence of these defects makes the structure vulnerable to failure due to propagation or growth of these defects. In this paper, we have examined the dynamic loading effects on the crack-opening displacements (COD) and the stress-intensity factors (SIF).

Among the works reported during the last decade that deal with scattering by interface cracks is that of Neerhoff [*1*], who investigated the diffraction of incident bulk horizontally polarized shear (SH) and Love waves by a crack of finite width at the interface of a layered medium. He solved the antiplane problem employing the integral equation method. Keer et al. [2] studied the resonance phenomena for a crack near the free surface of a homogeneous half space. The plane strain boundary value problem was reduced to that of finding solutions to a system of coupled singular integral equations. These integral equations were solved numerically for incident waves generated by uniform tension and shear applied at the free surface. The work done by Yang and Bogy [3] is the most relevant to our work. They considered a plane strain problem of a layered half space with a single interfacial crack. The solution method was similar to that developed by Neerhoff [1] for the antiplane problem. The transient response of an interface crack in a two-layered plate subject to an antiplane stress field was studied by Kundu [4]. He also employed the integral equation method proposed by Neerhoff. Kundu and Hassan [5] solved the same problem for a layered plate of finite length, by discretizing the whole domain with finite elements. First, the discretized equation of motion was solved in the frequency domain, then a fast Fourier transform (FFT) technique was used to obtain the time response. More recently, the interaction between two cracks at the interface of a layered isotropic and anisotropic medium under antiplane loading was studied by Kundu [6] and Karim and Kundu [7].

In this paper, we present a different method of studying the plane strain dynamic response of a layered half space with interfacial cracks due to surface line loads. It is assumed that a long interfacial crack lies at the interface between a layer and a substrate. The motivation for this particular choice comes from the need to understand the dynamic response of a fully open interfacial crack, along with the resonances. The solution method used here was suggested by Zienkiewicz [8], and has been applied by Shah et al. [9] for the diffraction of SH waves in a half-space. Franssens and Lagasse [10] used a similar technique to study the two-dimensional scattering of both SH and longitudinal and vertically polarized shear (P-SV) waves by a cylindrical obstacle in a layered medium. The most recent work by Khair et al. [11] is a generalization to three-dimensional amplification of seismic waves by arbitrarily shaped alluvial valleys embedded in a homogeneous half-space. The advantage of this method resides in the fact that once the Green's functions are obtained for a given frequency, the scattering due to any irregularity that fits inside the finite element region can be determined. In the next section, an outline of the method is given.

Formulation

The problem considered here is a single layer of thickness, H, bonded to a half-space, as illustrated in Fig. 1. The layer and half-space are made of linearly elastic, isotropic, and homogeneous materials. When necessary, a subscript or superscript (1,2) is used in describing properties related to the layer and substrate respectively, for example, ρ_1, μ_1, λ_1 represent the mass density and the Lamé's constants of the layer. The dynamic response due to time harmonic line loads is investigated. We consider a large crack of length 3.8 H located at the interface of the single-layered structure.

Let u_i be the displacement component in the ith direction in the Cartesian coordinate system shown, and τ_{ij} the stress tensor having time harmonic behavior of the form $e^{-i\omega t}$ The equation of motion in the frequency domain is written as

$$\tau_{ij,j} + \rho\omega^2 u_i = -f_i, \qquad (i,j = 1,2,3) \tag{1}$$

where ρ is the mass density, f_i is the body force per unit volume, and ω is the circular frequency.

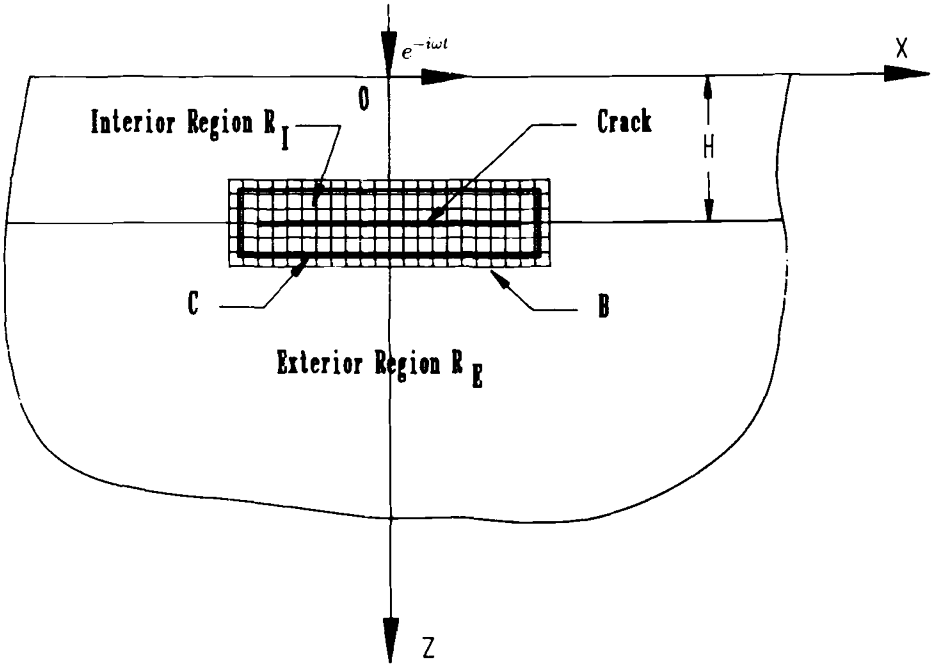

FIG. 1—*Layered half-space with interfacial crack. Geometry and Contours B and C are shown.*

The total fields generated by the interaction of the free field with the cracked medium can be expressed as

$$u_i = u_i^s + u_i^f \tag{2}$$

$$\tau_{ij} = \tau_{ij}^s + \tau_{ij}^f \tag{3}$$

where the symbols carrying the superscripts s and f are associated with the scattered and free fields, respectively.

It is assumed that the upper surface of the layered medium is traction free and that the bonding between the layer and the substrate is perfect except at the cracked region (crack or delamination). The crack surfaces are assumed to be traction free. The boundary and continuity conditions are

$$\tau_{xz}^{(1)} = \tau_{yz}^{(1)} = \tau_{zz}^{(1)} = 0;\ z = 0;\ -\infty < x < \infty. \tag{4}$$

$$u^{(1)} = u^{(2)}, v^{(1)} = v^{(2)}, w^{(1)} = w^{(2)};\ z = H;\ |x| > 1.9H \tag{5}$$

$$\tau_{xz}^{(1)} = \tau_{xz}^{(2)}, \tau_{yz}^{(1)} = \tau_{yz}^{(2)}, \tau_{zz}^{(1)} = \tau_{zz}^{(2)};\ z = H;\ |x| > 1.9H. \tag{6}$$

$$\tau_{xz}^{(1)} = \tau_{yz}^{(1)} = \tau_{zz}^{(1)} = 0;\ z = H;\ |x| < 1.9H \tag{7}$$

$$\tau_{xz}^{(2)} = \tau_{yz}^{(2)} = \tau_{zz}^{(2)} = 0;\ z = H;\ |x| < 1.9H \tag{8}$$

Moreover, the scattered field must satisfy the elastic radiation conditions at infinity. For the general three-dimensional formulation, we will consider the dependence of the displacement on the y-coordinate to be taken as

$$u_i(x,y,z) = u_i(x,z)e^{i\xi y} \tag{9}$$

This represents a propagating wave in the y-direction with wavelength $2\pi/\xi$ and amplitude varying with x and z. This allows us to consider incident waves that are propagating at an arbitrary angle to the axis of the crack. For the plane strain problem, $\xi = 0$. The solution method will be discussed in the following section.

Description of the Method

The solution method combines the Green's function boundary integral representation with the finite element equations. A simple fictitious contour, B, around the scatterer is introduced as shown in Fig. 1. We define the interior region, R_I, to be bounded by B. This region is then discretized with finite elements having $N = N_I + N_B$ number of nodes, N_I being the number of nodes interior to B and N_B the number of nodes on B.

Let the element domain and the boundary be denoted by $\Omega^{(e)}$ and $\Gamma^{(e)}$, respectively. The displacement field is written in the usual way in terms of the shape functions and the nodal displacements in matrix form:

$$\{\mathbf{u}\} = \begin{Bmatrix} u \\ v \\ w \end{Bmatrix} = \begin{bmatrix} \phi_1 & 0 & 0 & \dots & \phi_n & 0 & 0 \\ 0 & \phi_1 & 0 & \dots & 0 & \phi_n & 0 \\ 0 & 0 & \phi_1 & \dots & 0 & 0 & \phi_n \end{bmatrix} \begin{Bmatrix} u_1 \\ v_1 \\ w_1 \\ \vdots \\ u_n \\ v_n \\ w_n \end{Bmatrix}$$

$$= [\mathbf{\Phi}]\,\{\mathbf{u}^e\}, \tag{10}$$

in which n denotes the number of nodes per element and the superscript (e) is the element identifier. By using the strain-displacement relationship, we get

$$\{\boldsymbol{\varepsilon}\} = [\mathbf{D}][\mathbf{\Phi}]\{\mathbf{u}^e\} = [\mathbf{B}]\{\mathbf{u}^e\} \tag{11}$$

where $\boldsymbol{\varepsilon} = \{\varepsilon_{xx}, \varepsilon_{yy}, \varepsilon_{zz}, \varepsilon_{yz}, \varepsilon_{xz}, \varepsilon_{xy}\}^T$ and the derivative operator $\mathbf{D}$ is

$$\mathbf{D} = \begin{bmatrix} \frac{\partial}{\partial x} & 0 & 0 \\ 0 & \hat{i}\xi & 0 \\ 0 & 0 & \frac{\partial}{\partial z} \\ 0 & \frac{\partial}{\partial z} & \hat{i}\xi \\ \frac{\partial}{\partial z} & 0 & \frac{\partial}{\partial x} \\ \hat{i}\xi & \frac{\partial}{\partial x} & 0 \end{bmatrix} \tag{12}$$

The superscript, t, denotes transpose.

The stresses are related to the strains via the constitutive law that may be written in matrix form as

$$\{\boldsymbol{\tau}\} = [\mathbf{C}]\{\boldsymbol{\varepsilon}\} \tag{13}$$

where $\mathbf{C}$ is the (6×6) symmetric stiffness matrix. For an isotropic material, all the entries of $\mathbf{C}$ are in terms of the Lamé's constants, λ and μ.

The total energy associated with each element (e) is to be taken as

$$E^{(e)} = U^{(e)} + \mathrm{K}^{(e)} - W^{(e)} \tag{14}$$

where $U^{(e)}$ and $\mathrm{K}^{(e)}$ are the strain and kinetic energies, respectively, and $W^{(e)}$ is the surface traction work potential; these are defined as

$$U^{(e)} = \frac{1}{2}\int_{\Omega(e)} \{\boldsymbol{\tau}\}^t\{\boldsymbol{\varepsilon}\}^* dxdz \tag{15}$$

$$\mathrm{K}^{(e)} = -\frac{1}{2}\int_{\Omega(e)} \rho\omega^2\{\mathbf{u}\}^t\{\mathbf{u}\}^* dxdz \tag{16}$$

$$W^{(e)} = \frac{1}{2}\oint_{\Gamma(e)} (\{\mathbf{u}\}^t\{\mathbf{t}\}^* + \{\mathbf{t}\}^t\{\mathbf{u}\}^*)d\Gamma \tag{17}$$

Here $\{\mathbf{t}\}$ is the traction vector on the boundary and $\{\ \}^*$ represents the complex conjugate of the vector expressions. The integration in the y-direction is done over one wave length and the preceding expressions represent the energies per wave length in the same direction.

By setting the first variation of the total energy, δE, to zero, we obtain the elemental equations of motion written in the following form

$$S^{(e)}\,\mathbf{u}^{(e)} = p^{(e)} \tag{18}$$

where $S^{(e)}$ is the elemental impedance matrix and $p^{(e)}$ is the consistent nodal force vector. These are defined as

$$S^{(e)} = \int_{\Omega(e)} ([\mathbf{B}^*]^t[\mathbf{C}][\mathbf{B}] - \rho\omega^2[\boldsymbol{\Phi}]^t[\boldsymbol{\Phi}])dxdz \tag{19}$$

and

$$p^{(e)} = \oint_{\Gamma(e)} \{\mathbf{t}\}^t[\boldsymbol{\Phi}]\, d\Gamma \tag{20}$$

The elemental impedance matrices and load vectors are computed and assembled into a global impedance matrix and load vector. The global equations of motion are partitioned in such a way that the inside nodal displacements appear at the top and the boundary displacements at the bottom. Therefore the discretized equations of motion in Region R_I become

$$\begin{bmatrix} S_{II} & S_{IB} \\ S_{BI} & S_{BB} \end{bmatrix} \begin{Bmatrix} U_I \\ U_B \end{Bmatrix} = \begin{Bmatrix} 0 \\ P_B \end{Bmatrix} \tag{21}$$

For solution purposes, only a relationship between the inside nodal displacements and the boundary ones is needed, and this is given by

$$\{U_I\} = -[S_{II}]^{-1}[S_{IB}]\{U_B\} \tag{22}$$

The boundary integral representation is derived from the elastodynamic reciprocity theorem [12], written in the following form

$$\int_A (\{\mathbf{g}\}'\{\mathbf{u}\} - \{\mathbf{f}\}'\{\mathbf{v}\})\, dA = \oint_C (\{\mathbf{t}\}'\{\mathbf{v}\} - \{\mathbf{q}\}'\{\mathbf{u}\})\, dC \tag{23}$$

where **u** and **t** are the displacement and traction on the boundary, C, of Region A associated with the body force, **f**, and **v**, **q** are those associated with **g**. We shall denote the region exterior to C as R_E. Note that the region between Contour B and C is common to R_E and R_I. We will apply the preceding theorem to Region R_E, with the first field as the scattered field and the second field to be the line source Green's function solution. For this purpose, we define the Green's function and the scattered fields as solutions to the following equations

$$\Sigma_{kij,j} + \rho\omega^2 G_{ki} = -\delta_{ki}\delta(x - x')\delta(z - z')e^{i(-\omega t + \xi y)} \tag{24}$$

and

$$\tau^s_{ij,j} + \rho\omega^2 u^s_i = 0 \tag{25}$$

In Eqs 24 and 25, i denotes the displacement direction and k is the force direction. The Green's function solution for a layered medium has been discussed by Bouden [13].

After direct substitution of these two fields in Eq 23, we get

$$u^s_k(x',z') = \oint_C (\tau^s_{ij}G_{ki} - \Sigma_{kij}u^s_i)n_j\, dC \tag{26}$$

The contour integration is done in a clockwise manner.

Applying the elastodynamic reciprocity theorem (Eq 23) to the region interior to C with the two fields as the Green's solution and the free-field with no forcing terms, we get

$$\oint_C (\tau^f_{ij}G_{ki} - \Sigma_{kij}u^f_i)(-n_j)\, dC = 0 \tag{27}$$

This integral is evaluated in a counterclockwise manner. Combining Eqs 26 and 27, we obtain the integral representation of the total displacement at any point in Region R_E as

$$u_k(x',z') = u^f_k(x',z') + \oint_C (\tau_{ij}G_{ki} - \Sigma_{kij}u_i)n_j\, dC \tag{28}$$

Now, Eq 28 is evaluated for Points x' and z', coinciding with the nodes on Boundary B. This leads to an equation connecting the displacements at the nodes on B to those at the nodes on C in the form

$$\{U_B\} = \{U_B^i\} + \left[\oint_C ([G][C][B_C] - [\Phi_C]^t[\Sigma])\{n\}\, dC\right]\{U_C\}$$

$$+ \left[\oint_C ([G][C][B_B] - [\Phi_B]^t[\Sigma])\{n\}\, dC\right]\{U_B\} \tag{29}$$

where $[B_C] = [D][\Phi_C]$ and $[B_B] = [D][\Phi_B]$.

Using Eq 29 and completing U_C with the remaining inside nodal displacements yields

$$\{U_B\} = [A_{BI}]\{U_I\} + [A_{BB}]\{U_B\} + \{U_B^i\} \tag{30}$$

where $[A_{BI}]$ is $(3N_B \times 3N_I)$ and $[A_{BB}]$ is $(3N_B \times 3N_B)$ and both are complex matrices. Substituting Eq 22 into Eq 30 and solving for $\{U_B\}$, we get

$$\{U_B\} = \{[I] + [A_{BI}][S_{II}]^{-1}[S_{IB}] - [A_{BB}]\}^{-1}\{U_B^i\} \tag{31}$$

The inside nodal displacements can then be determined by using Eq 22. The displacement at any point in Region R_E can be found by applying Eq 28.

Numerical Results and Discussion

Numerical results were obtained for a nickel coating layer over an iron substrate. Single-layer coatings are usually of the order of microns topping base materials of several millimetres. This contrast in the thickness justifies the single-layered half-space model. In our analysis, all of the material and geometric parameters were nondimensionalized. Lengths were normalized with respect to the layer thickness, H. The material constants and densities were normalized with the layer rigidity and density, respectively. Then, the layer thickness, rigidity, and density were set equal to unity. Finally, all of the wavenumbers were normalized with respect to the layer shear wavenumber $k_{21}(= \omega/C_{21})$. Note that C_{1j} and C_{2j} $(j = 1,2)$ are the longitudinal and shear wave velocities, respectively, of the j^{th} medium.

The material properties of nickel and iron are listed in Table 1. Here σ is the Poisson's ratio and C_1, C_2, and C_R are the longitudinal, shear, and Rayleigh wave velocities, respectively. This case can be classified as a "loading" case according to Farnell and Adler [*14*], because the layer shear velocity is less than the half-space shear velocity (that is, $C_{21} < C_{22}$). For this case, multiple Rayleigh-like guided wave modes occur. The velocities of these modes, which are frequency-dependent, are higher than the layer Rayleigh velocity, C_{R1}. The numerical integration of the semi-infinite wavenumber-type of integrals that arise in the eval-

TABLE 1—*Material properties.*

Material, i	σ_i	ρ_i, kg/m^3	C_{1i}, m/s	C_{2i}, m/s	C_{Ri} m/s
Nickel	0.31	8800	5240	2750	2550
Iron	0.28	7700	5720	3160	2920

uation of the Green's displacements and their associated stresses is discussed by Xu and Mal [*15*] and Bouden [*13*]. We define the nondimensional frequency, ε, as $k_{21}H$. A single Griffith crack at the interface of this layered material is considered. The length of the crack is $a = 3.8H$.

The incident field is caused by a time-harmonic line load applied at the origin, O, of the coordinate system (Fig. 1). Both normal and tangential loads are considered.

The internal region, R_I, was discretized into finite elements. The mesh had 316 elements and 506 nodes. Regular isoparametric elements were used everywhere except at the crack tips, where eight six-node triangular quarter-point elements were used. Barsoum [*16*] showed that these singular elements could model crack tip singularity in a homogeneous medium. However, it has been shown that the stress singularity at the tip of an interfacial crack is oscillatory in general (see Williams [*17*] and Bogy [*18*]). However, for the material combination used, the singularity is square-root type and, thus, is identical to the case of a homogeneous material.

The finite element discretization and the numerical evaluation of the contour integral are the only sources of inaccuracy in this method. The size of the elements and number of Gauss points per element were varied in order to keep the relative error less than 5%. It was found that ten elements per wavelength was the minimum required in order to capture the physics of the problem, and that three Gauss points per element for the contour integration were sufficient for the desired accuracy. A comparison with published results can be found in Bouden [*13*].

Crack Opening Displacements

Crack opening and sliding displacements (COD) were computed at different nondimensional frequencies. Considering the geometric and loading symmetry, only the CODs on the right half are shown in Figs. 2 and 3 for $\varepsilon = 0.9$. The dotted line represents the inplane sliding of the crack surfaces, while the solid line represents the opening of the crack. The arrow on top of the layer is the force direction. It is interesting to note from Fig. 2 that the normal crack opening displacement for the tangential load is quite a bit larger than the tangential COD over most of the crack length. It was found that as the frequency was increased the CODs decreased. Also, the sliding displacement amplitude became larger than the normal displacements.

Figure 3 shows the results for normal line load. It is found that the normal COD is larger than the tangential one. At high frequencies, it was found that the shapes of the CODs became oscillatory.

Stress-Intensity Factors

The stress-intensity factors, K_1 and K_2, can be extracted from the finite element solution by identification of the coefficients of the singular terms in the analytical expressions of the displacement fields in the vicinity of the crack tip with the interpolated expressions from the six-noded triangular quarter-point elements.

The analytical expressions for the displacement fields in the vicinity of a crack tip along the bond line of two half-spaces of different materials shown in Fig. 4 can be derived in the same manner as for the homogeneous case. For details, the reader is referred to Bouden [*13*] and Sih and Rice [*19*].

For the finite element discretization, the collapsed quadrilateral quarterpoint element contains terms in the interpolated displacement fields proportional to the square root of the radial distance, r, emanating from the crack tip. For instance, the displacement field com-

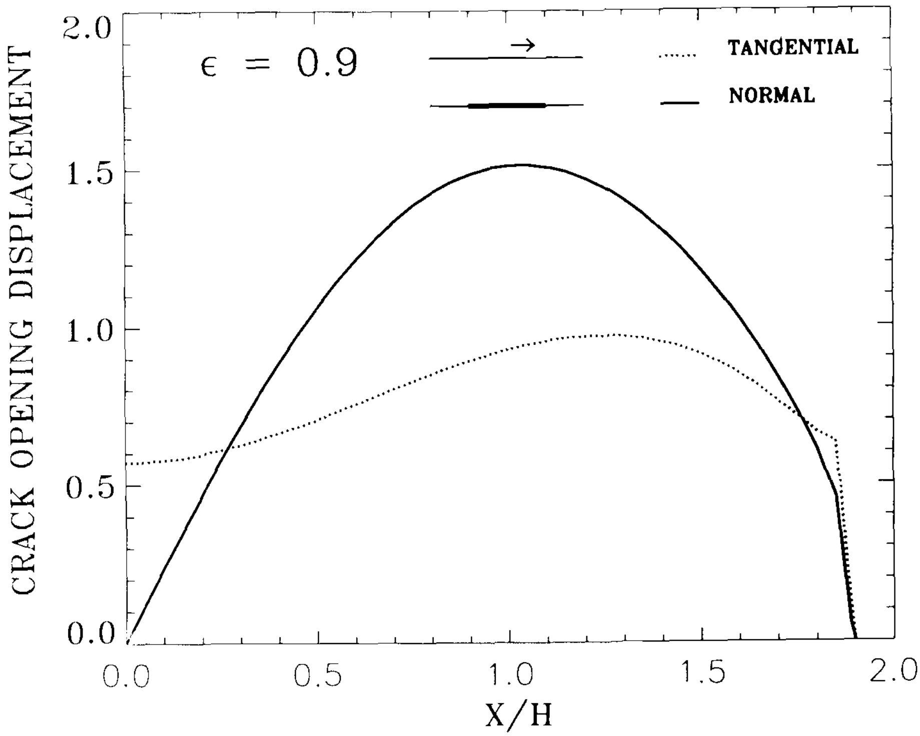

FIG. 2—*Crack opening and sliding for the right half of the single crack. This result is for a tangential time harmonic line load with a nondimensional frequency ε = 0.9.*

ponents along the edges containing Nodes A,B,C and A,D,E, shown in Fig. 4 are given by Owen and Fawkes [*20*], that is

$$u_1 = u_A + (4u_B - u_C - 3u_A)\sqrt{\frac{r}{L}} + (2u_C + 2u_A - 4u_B)\frac{r}{L} \tag{32}$$

$$v_1 = v_A + (4v_B - v_C - 3v_A)\sqrt{\frac{r}{L}} + (2v_C + 2v_A - 4v_B)\frac{r}{L} \tag{33}$$

$$u_2 = u_A + (4u_D - u_E - 3u_A)\sqrt{\frac{r}{L}} + (2u_E + 2u_A - 4u_D)\frac{r}{L} \tag{34}$$

$$v_2 = v_A + (4v_D - v_E - 3v_A)\sqrt{\frac{r}{L}} + (2v_E + 2v_A - 4v_D)\frac{r}{L} \tag{35}$$

The Mode I and Mode II stress-intensity factors presented in Figs. 5 and 6 are obtained by

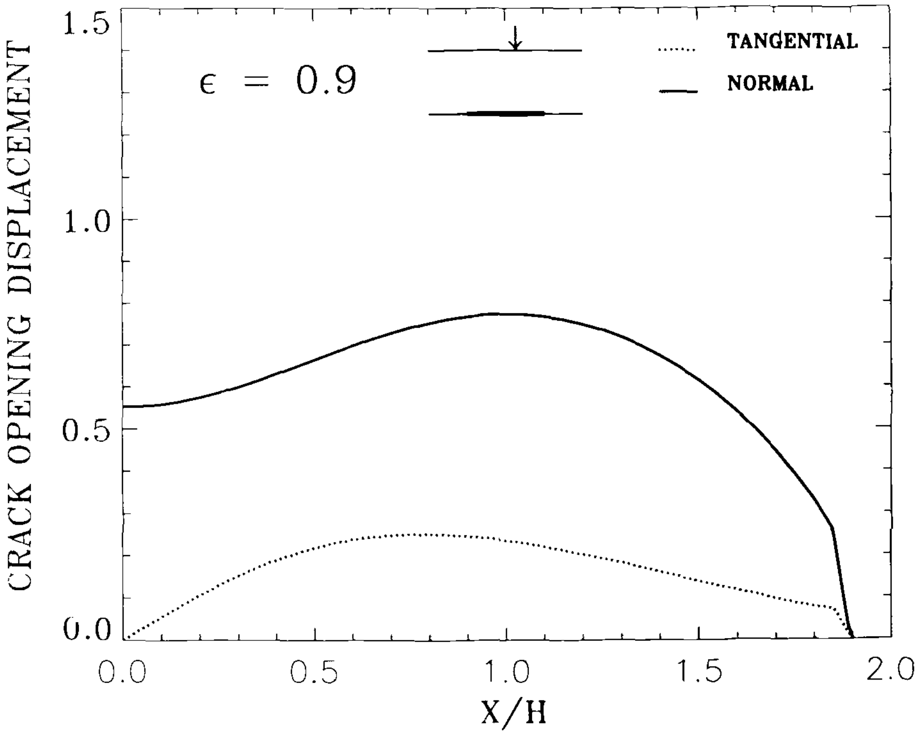

FIG. 3—*Crack opening and sliding for the right half of the single crack. This result is a normal time harmonic line load with a nondimensional frequency* $\varepsilon = 0.9$.

equating the coefficients of $\sqrt{r}$ in Eqs 32 through 35 with corresponding expressions arising in the analytical expressions. After nondimensionalization, we have

$$K_1 = |k_1| = \left| \frac{2}{\kappa_1 + 1} \sqrt{\frac{2}{L}} (4v_B - v_C - 3v_A) \right| \tag{36}$$

or

$$K_1 = |k_1| = \left| -\frac{2\mu_2}{\mu_1(\kappa_2 + 1)} \sqrt{\frac{2}{L}} (4v_D - v_E - 3v_A) \right| \tag{37}$$

and

$$K_2 = |k_2| = \left| \frac{2}{\kappa_1 + 1} \sqrt{\frac{2}{L}} (4u_B - u_C - 3u_A) \right| \tag{38}$$

or

$$K_2 = |k_2| = \left| -\frac{2\mu_2}{\mu_1(\kappa_2 + 1)} \sqrt{\frac{2}{L}} (4u_D - u_E - 3u_A) \right| \tag{39}$$

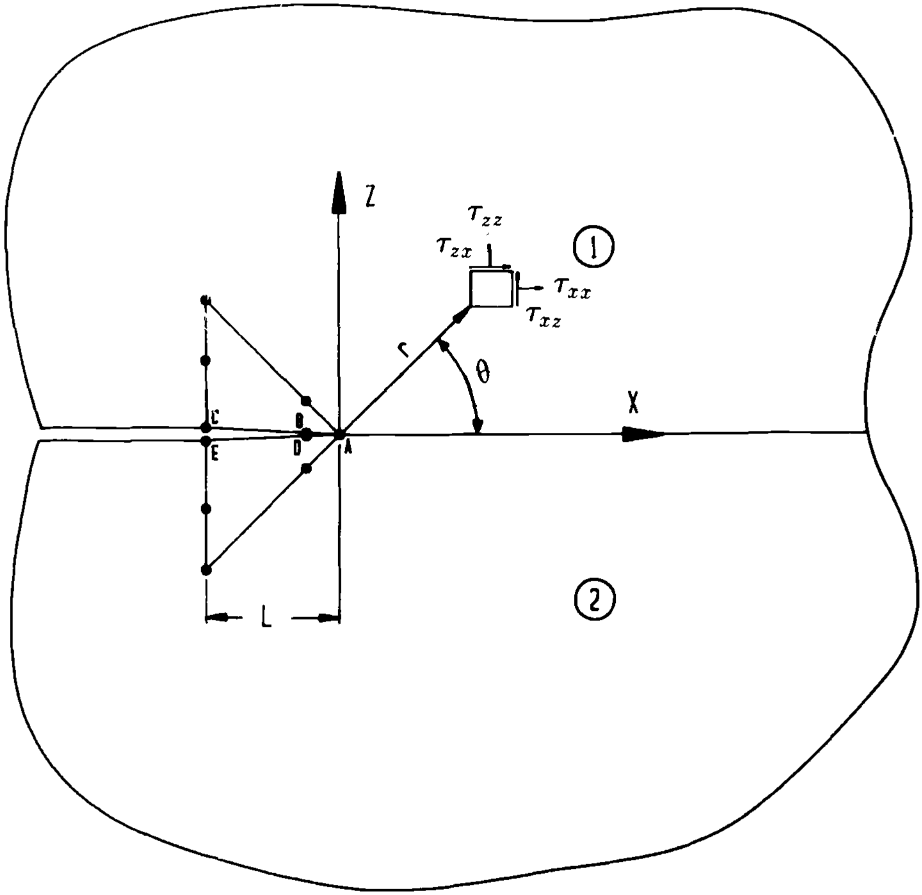

FIG. 4—*Geometry of an interface crack between bonded dissimilar half-spaces and crack-tip elements.*

Here, $\kappa_i = 3 - 4\sigma_i$ for the plane strain case. The numerical values of the stress-intensity factors presented here are the average of Eqs 36 and 37 for Mode I and Eqs 38 and 39 for Mode II.

Figure 5 shows K_1 and K_2 for the Crack Tip A versus the nondimensional frequency $\varepsilon = k_{21}H$ for a horizontal time harmonic line load, which is applied on the surface of the layer. It is observed that K_2 starts at a fairly high value for low frequencies, decreases, and then increases to a peak at about $\varepsilon \approx 0.9$. Beyond this frequency, it gradually decreases. K_1, on the other hand, starts at a low value, decreases slightly, and then increases to a fairly high value at the same frequency. Note that even though K_2 is dominant, as would be anticipated from the nature of the loading, dynamic K_1 is also quite high. Note that Mode I dynamic SIF is substantially higher than the static value in some range of frequency. Figure 6 shows K_1 and K_2 for a normal loading. In this case, the roles are reversed. The opening mode dominates. It is found now that K_1 and K_2 increase with frequency reaching sharp peak values at a lower frequency, that is, $\varepsilon \approx 0.3$. This lowering of the resonance frequency from the shear loading case to the normal one is in agreement with the results obtained by Keer et al. [2] for a horizontal crack buried near the surface of a half-space due to uniform shear

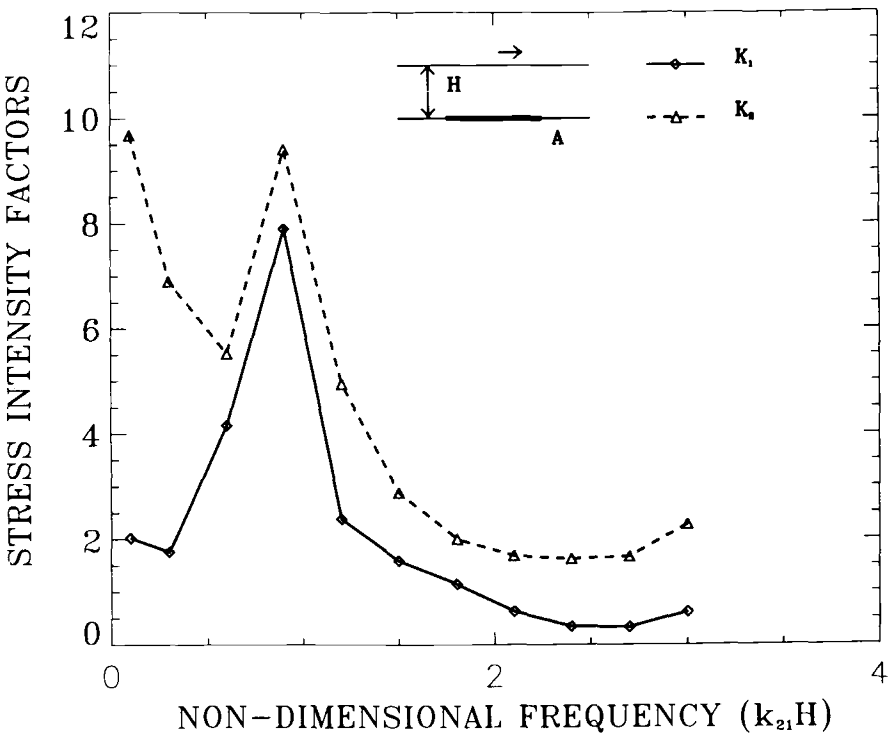

FIG. 5—*Mode I and Mode II stress-intensity factors as a function of nondimensional frequency at Crack Tip A of the single crack for tangential load.*

and tension loadings. It is seen that the dynamic SIFs (both K_1 and K_2) are much higher than the static values at low frequencies. It can be shown that the frequency values at which K_1 and K_2 have local maxima do not correspond to a cut-off frequency. However, when the frequencies at these peak values are compared to the natural frequencies of a Timoshenko plate of length 3.8 H (Table 2) with two different boundary conditions (simply supported or clamped), they show a good correlation. For the tangential loading, the peak occurs at $\varepsilon \simeq 0.9$. This value is bounded by the two natural frequencies of the second mode (ω_{21}). With the lower and upper bounds corresponding to the simply supported (SS) and clamped (C) case, respectively.

In the case of normal loading, the peak occurs at $\varepsilon \simeq 0.3$. This value is slightly lower than the natural frequency of the first mode (ω_{11}) for the simply supported case. However, since the frequency increment is 0.3, the accuracy of these peak frequency values is within this increment. It is concluded from these figures that the dynamic effects are quite substantial and, in general, give higher K_1 values for normal impact at low frequencies.

Conclusion

A combined finite element and integral representation technique to analyze scattering of waves by interfacial cracks in a layered half-space has been presented. The advantage of the technique is that it allows consideration of arbitrary crack geometry. This can be done by merely changing some of the interior elements. Numerical results showing CODs and

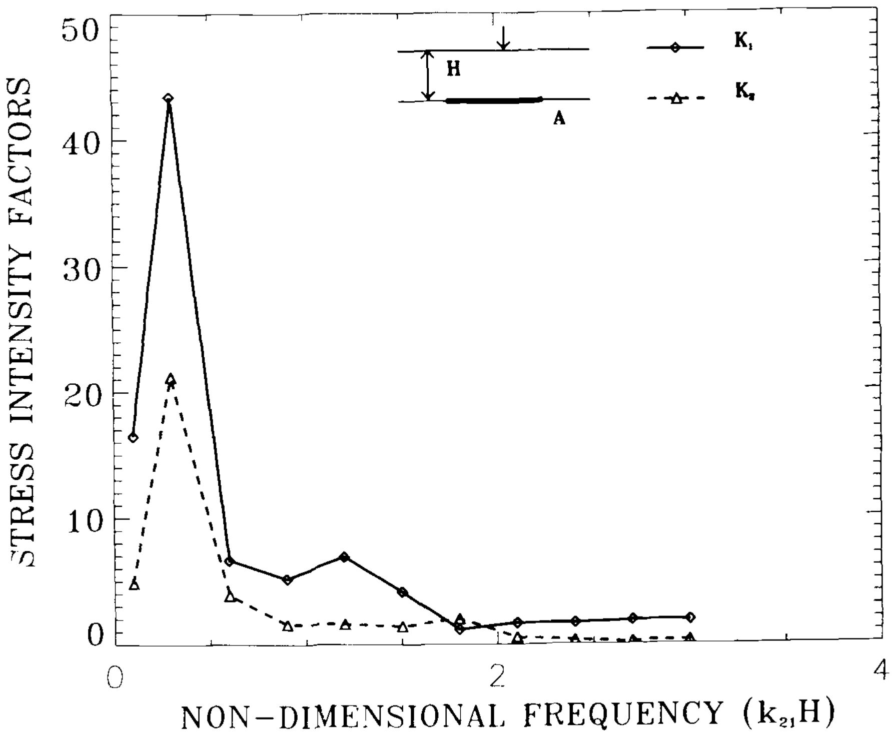

FIG. 6—*Mode I and Mode II stress-intensity factors as a function of nondimensional frequency at Crack Tip A of the single crack for normal load.*

TABLE 2—*Natural frequencies for simply supported (SS) and clamped (C) Timoshenko plate and frequency values at peaks of stress-intensity factors.*

	$\varepsilon = k_{21}H$	
Mode	1, ω_{11}	2, ω_{21}
SS	0.34	0.40
C	0.76	0.94
Peak	0.3	0.9

SIFs for a single interfacial crack due to normal and shear line loads have been presented. It is found that for both loading cases normal CODs are larger than the tangential one at low frequencies. Dynamic stress-intensity factors are found to attain high peak values at certain resonant frequencies, depending on the loading. Although results for a single crack have been presented here, multiple cracks can be considered with equal ease. This will be discussed in a later communication.

Acknowledgment

The work reported here was supported in part by a grant from the Office of Naval Research (No. N00014-86-K-0280). Mr. Bouden is grateful to the Tunisian government for granting a scholarship for his graduate studies. Numerical computations were carried out on a CRAY-XMP/48 at the National Center for Supercomputing Applications at the University of Illinois, Urbana, Illinois.

References

[1] Neerhoff, F. L., "Diffraction of Love Waves by a Stress-Free Crack of Finite Width in the Plane Interface of a Layered Composite," *Applied Scientific Research*, Vol. 35, 1979, pp. 265–315.

[2] Keer, L. M., Lin, W., and Achenbach, J. D., "Resonance Effects for a Crack Near a Free Surface," *Journal of Applied Mechanics*, American Society of Mechanical Engineers, Vol. 51, 1984, pp. 65–70.

[3] Yang, H. J. and Bogy, D. B., "Elastic Wave Scattering from an Interface Crack in a Layered Half Space," *Journal of Applied Mechanics*, American Society of Mechanical Engineers, Vol. 52, 1985, pp. 42–50.

[4] Kundu, T., "Transient Response of an Interface Crack in a Layered Plate," *Journal of Applied Mechanics*, American Society of Mechanical Engineers, Vol. 53, 1986, pp. 579–586.

[5] Kundu, T. and Hassan, T., "A Numerical Study of the Transient Behavior of an Interfacial Crack in a Bimaterial Plate," *International Journal of Fracture*, Vol. 35, 1987, pp. 55–69.

[6] Kundu, T., "The Transient Response of Two Cracks at the Interface of a Layered Half Space," *International Journal of Engineering Science*, Vol. 25, 1987, pp. 1427–1439.

[7] Karim, M. R. and Kundu, T., "Transient Surface Response of a Layered Isotropic and Anisotropic Half-Spaces with Interface Cracks: SH Case," *International Journal of Fracture*, Vol. 37, 1988, pp. 245–262.

[8] Zienkiewicz, O. C., *Finite Element Method*, McGraw-Hill, London, 1977.

[9] Shah, A. H., Wong, K. C., and Datta, S. K., "Diffraction of Plane SH Waves in a Half-Space," *International Journal of Earthquake Engineering and Structural Dynamics*, Vol. 10, 1982, pp. 519–528.

[10] Franssens, G. R. and Lagasse, P. E., "Scattering of Elastic Waves by a Cylindrical Obstacle Embedded in a Multilayered Medium," *Journal, Acoustical Society of America*, Vol. 76, 1984, pp. 1535–1542.

[11] Khair, K. R., Datta, S. K., and Shah, A. H., "Amplification of Obliquely Incident Seismic Waves by Cylindrical Alluvial Valleys of Arbitrary Cross Sectional Shape: Part I. Incident P and SV Waves," *Bulletin, Seismological Society of America*, Vol. 79, 1989, pp. 610–630.

[12] Achenbach, J. D., *Wave Propagation in Elastic Solids*, North-Holland, London, 1973.

[13] Bouden, M., "Wave Propagation and Scattering in Layered Media: Application to Earthquake Ground Motion and Ultrasonic Nondestructive Evaluation of Interfacial Cracks," Ph.D. thesis, University of Colorado, Boulder, CO, 1990.

[14] Farnell, G. W. and Adler, E. L., "Elastic Wave Propagation in Thin Layers," *Physical Acoustics*, Vol. 9, Academic Press, New York, 1972, pp. 85–127.

[15] Xu, P.-C. and Mal, A. K., "Calculation of the Inplane Green's Functions for a Layered Viscoelastic Solid," *Bulletin, Seismological Society of America*, Vol. 77, 1987, pp. 1823–1837.

[16] Barsoum, R. S., "On the Use of Isoparametric Finite Elements in Linear Fracture Mechanics," *International Journal of Numerical Methods in Engineering*, Vol. 10, 1976, pp. 25–37.

[17] Williams, M. L., "The Stresses Around a Fault or Crack in Dissimilar Media," *Bulletin, Seismological Society of America*, Vol. 49, 1959, pp. 199–204.

[18] Bogy, D. B., "Two Edge-Bonded Elastic Wedges of Different Materials and Wedge Angles under Surface Tractions," *Journal of Applied Mechanics*, American Society of Mechanical Engineers, Vol. 38, 1971, pp. 377–386.

[19] Sih, G. C. and Rice, J. R., "The Bending of Plates of Dissimilar Materials with Cracks," *Journal of Applied Mechanics*, American Society of Mechanical Engineers, Vol. 31, 1964, pp. 477–482.

[20] Owen, D. R. J. and Fawkes, A. J., *Engineering Fracture Mechanics: Numerical Methods and Applications*, Pineridge Press Ltd., Swansea, UK, 1983.

Ming-Chih Cheng[1] *and Kuen Y. Lin*[1]

Probabilistic Fracture Models for Predicting the Strength of Notched Composites

REFERENCE: Cheng, M.-C. and Lin, K. Y., "**Probabilistic Fracture Models for Predicting the Strength of Notched Composites,**" *Fracture Mechanics: Twenty-Second Symposium (Volume II), ASTM STP 1131*, S. N. Atluri, J. C. Newman, Jr., I. S. Raju, and J. S. Epstein, Eds., American Society for Testing and Materials, Philadelphia, 1992, pp. 410–420.

ABSTRACT: This paper presents two probabilistic fracture models for predicting the tensile strength of filamentary composites containing geometric discontinuities such as holes or cracks. The statistical fracture model considers the case of a constant load while the stochastic model deals with monotonically increasing loads. Both models use the Weibull distribution of fiber strength and elastic fiber/matrix properties to calculate the number of broken fibers near the crack tip in the 0-plies as a function of applied loads for different probability levels. Using the probabilistic models, the notched strength of $(\pm 45/0_2)_s$ boron/aluminum composites with various crack sizes have been predicted. These results agree well with existing experimental data. In addition, the relationship between fracture stress and notch size is found to be governed by a power law, as previously suggested by Mar and Lin using a deterministic approach.

KEY WORDS: filamentary composites, notch sensitivity, Markov process, Weibull distribution function, statistical fracture model, stochastic fracture model, boron/aluminum, fracture mechanics, fatigue (materials)

The notch sensitivity of fiber-reinforced composites has been a subject of extensive research during the past two decades. Numerous tests have been conducted to better understand the fracture behavior, and several fracture models have been proposed for predicting the notched composite strength. A pool of literature can be found in a review article by Awerbuch and Madhukar [*1*].

From the experimental study, it has been shown that the fracture stress is strongly dependent upon the notch size. To account for notch size effects, Waddoups, Eisenmann, and Kaminski [*2*] applied linear elastic fracture mechanics to composites with an assumed "intense energy region" ahead of the original notch. Whitney and Nuismer introduced stress fracture criteria along with the characteristic dimension for calculating the fracture stress [*3*]. Lin and Mar proposed a modified fracture mechanics formula for notched composites [*4*]. Although these methods are capable of predicting notched composite strength, the characteristic dimension of intense energy region in most laminates was found not to be a material constant. In addition, these fracture models cannot predict the large data scatter usually observed in strength tests nor the micromechanism that triggers the composite failure. Thus, a probabilistic approach to brittle fracture in composites seems more appropriate.

Recently, the present authors proposed two probabilistic models; a statistical fracture model [*5*] and a stochastic fracture model [*6*], for the analysis of composite laminates with geometric discontinuities. These models were developed based on the statistical fiber strength

[1]Graduate student and professor, respectively, Department of Aeronautics and Astronautics, University of Washington, Seattle, WA 98195.

distribution and elastic constituent material properties. In this paper, these two fracture models will be reviewed and their relationship will be discussed in detail. In addition, the validity of each model will be assessed by comparing the predicted results with the experimental data.

Model Assumptions

The analytical model considered is a composite laminate containing a geometric discontinuity, such as a central slit or a circular hole as shown in Fig. 1. The length of the laminate is $2b$, the width is w, and the initial crack size is $2a_0$. The laminate is subjected to a uniaxial tensile stress, σ^∞, at the remote boundary $y = \pm b$. In general, the microfracture process near the tip of a discontinuity is extremely complex due to the inhomogeneity of the damage zone [7]. It is necessary to make certain assumptions so that the problem can become mathematically tractable. The assumptions used in the present probabilistic models are summarized in the following paragraphs.

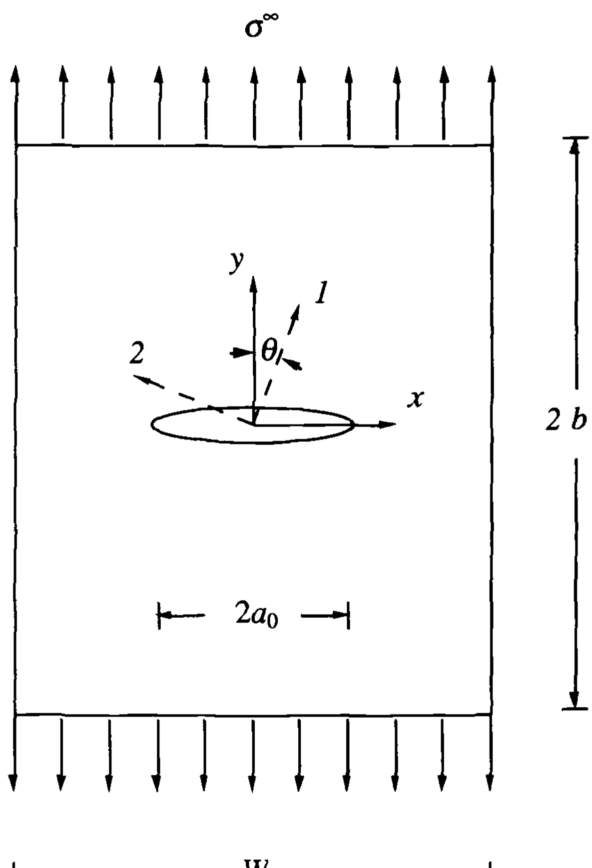

FIG. 1—*Geometry of a composite panel.*

The Fiber Dominated Failure Mode

It is assumed that the laminate shown in Fig. 1 comprises of a significant percentage of 0-plies with fibers aligned in the loading direction so that failure of the laminate is controlled predominantly by the fiber rather than the matrix. The 0-ply is considered as the primary load carrying agent while the other angle plies are present to restrain the composite failure from longitudinal splitting to fiber fracture. Thus, in our probabilistic models, we assume that the primary failure mechanism is due to fiber fracture in the 0-plies. Effects of other failure modes such as matrix cracking, fiber-matrix debonding, and ply delamination on the notched strength are neglected.

The Chain-of-Bundles-of-Links Assumption

The 0-plies in a laminate are modeled as a series of bundles, each bundle consisting of identical "fiber links" arranged parallel to each other [8]. The fiber link is defined to be a basic element comprising the filaments in composites (see Fig. 2). The dimension of each link is taken to be the ineffective length, δ, which can be determined from either the shear-

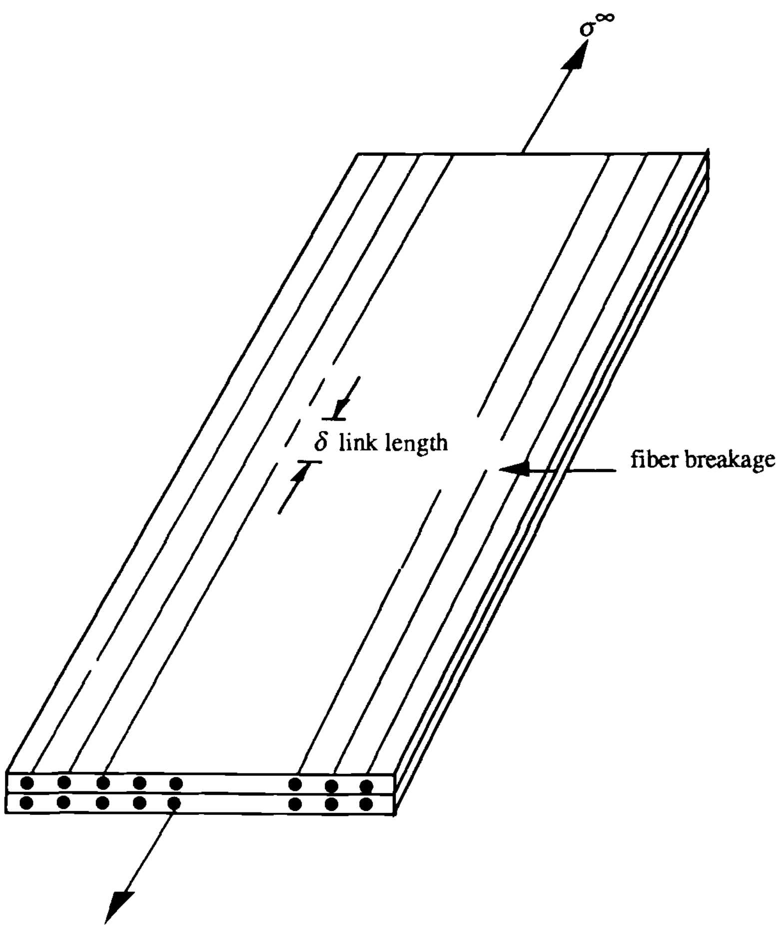

FIG. 2—*Fiber links in the chain-of-bundle-of-links model.*

lag analysis or the finite element method. For simplicity, the following shear-lag analysis result by Rosen [8] is used for estimating the ineffective length, δ

$$\frac{\delta}{d_f} = \frac{1}{2}\sqrt{\frac{1 - \sqrt{V_f}E_f}{\sqrt{V_f}G_m}} \cosh^{-1}\left(\frac{1 + (1 - \phi)^2}{2(1 - \phi)}\right) \tag{1}$$

where

d_f = fiber diameter,
V_f = fiber volume fraction,
E_f = Young's modulus of the fiber, and
G_m = shear modulus of the matrix.

The asymptotic value, ϕ, is taken as 0.90, meaning that the fiber stress has recovered 90% at a distance, δ, away from the broken end of a fiber. By the definition of δ, Tamuzs [9] experimentally measured the distribution function of fiber fragment length from the failed samples of several polymeric composites and drew a conclusion that the physical length of δ can be correlated practically with the analytical formula given in Eq 1. Consequently, δ can be taken as a material property and assumed to remain constant throughout the fracture process.

A Weibull Distribution for Fiber Strength

It is assumed that the strength of a fiber link of length δ can be described by a two-parameter Weibull distribution function, $f(\sigma)$ [10]

$$f(\sigma) = \frac{\beta}{\sigma_0^*}\left(\frac{\sigma}{\sigma_0^*}\right)^{\beta - 1} \exp\left\{-\left(\frac{\sigma}{\sigma_0^*}\right)^{\beta}\right\} \tag{2}$$

where β is the shape parameter, and σ_0^* is the scale parameter. Note that these Weibull parameters of fiber links are calculated from the distribution of single filaments by the weakest-link hypothesis. The hypothesis has been widely accepted, since it can explain successfully the well-known size effect in brittle fracture of fibers. The cumulative distribution function, $F(\sigma)$, associated with Eq 2 is

$$F(\sigma) = \int_0^{\sigma} f(s)ds = 1 - \exp\left\{-\left(\frac{\sigma}{\sigma_0^*}\right)^{\beta}\right\} \tag{3}$$

The mean strength of the filament, denoted by $\overline{\sigma}$, can be obtained by calculating the first moment

$$\overline{\sigma} = \int_0^{\infty} sf(s)\, ds = \sigma_0^*\Gamma\left(1 + \frac{1}{\beta}\right) \tag{4}$$

where Γ is the Gamma function.

Sequential Failure of Fibers from the Hole Edge

When loads are applied to a composite, the cross section on $y = 0$ has the highest probability to fail, since it is the minimum section on the plane of maximum longitudinal stress, σ_y. The bundle of fiber links on this plane is designated as the B_0 bundle, as depicted in Fig. 3. It is assumed that the fiber links in the B_0 bundle fail radially outward from the edge of the discontinuity along the axis, $y = 0$. This assumption of sequential failure is necessary in order to avoid a large number of permutations involved in calculating the failure probability of all possible failure paths. Although this assumption seems to be a limitation to the model, however, it has been justified from both the analysis of failure probability [5] and the experimental evidence [6].

Probabilistic Fracture Models

The Statistical Fracture Model

We define $x_i(\sigma)$ as a random variable to denote the state of fiber link, i, when the fiber link is under a stress, σ. The subscript, i, is the index of the fiber numbered from the edge of the discontinuity to the edge of the plate, thus, $i = 1, 2, 3, \ldots, N$, where N is the total number of fibers within the half uncut section. For each x_i, two outcomes; intact or broken, are possible, that is

$$x_i = 1 \quad \text{if the fiber link is broken}$$
$$x_i = 0 \quad \text{if the fiber link is intact}$$

The state of the specimen, $X(\sigma^\infty)$, at a given remote stress level, σ^∞, can be defined simply as the sum of all random variables, $x_i(\sigma)$. Note that σ is the axial stress induced in an individual fiber link when a remote stress, σ^∞, is applied along the boundaries of the panel, $y = \pm b$. That is,

$$X(\sigma^\infty) = \sum_{i=1}^{N} x_i(\sigma) \tag{5}$$

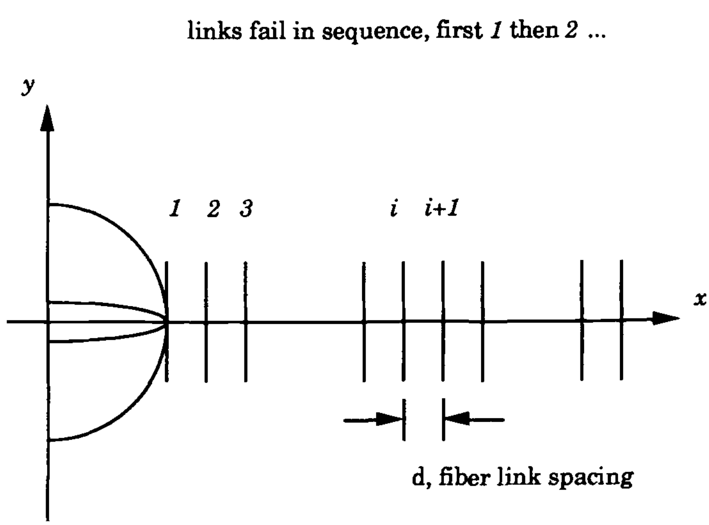

FIG. 3—*Failure sequence in* B_0 *bundle.*

where $\{X(\sigma^{\infty}), \sigma^{\infty} \geq 0\}$ is a stochastic process denoting the number of broken fibers or a pointer of the crack front. The total flaw size, $2a$, can be then calculated by $2(a_0 + X(\sigma^{\infty})d)$, in which d is the spacing distance between the centers of any two adjacent fibers. The state space of the random variable, $X(\sigma^{\infty})$, is $\{0, 1, 2, 3, \ldots, N\}$. The state, $X = 0$, represents the original undamaged state while $X = N$ means a complete failure of specimen.

Now, consider a composite panel subjected to a constant tensile stress, σ^{∞}, as shown in Fig. 4. When the panel is in the undamaged state, $X = 0$, damage initiation depends solely upon the failure or survival of the fiber link located immediately adjacent to the discontinuity.

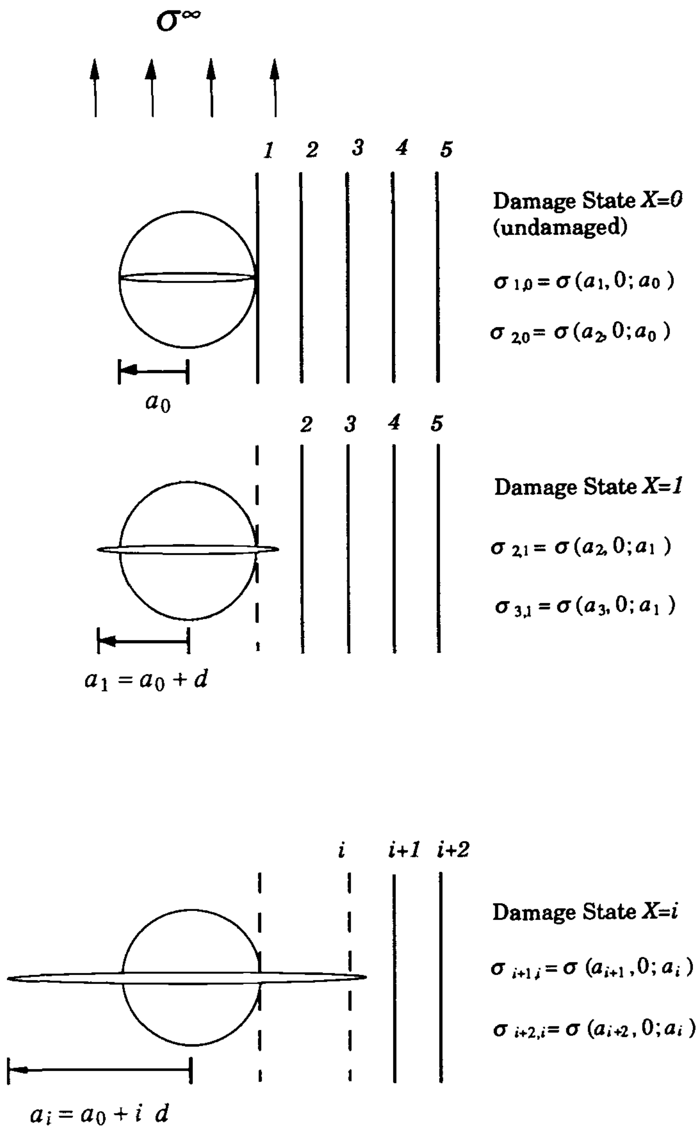

FIG. 4—*Schematic description of damage states in probabilistic fracture models.*

As the survival of all fiber links is governed by a Weibull distribution, the transitional probability, $P_{0,1}$, that is, the damage state increases from $X = 0$ to $X = 1$, can be obtained from the strength distribution of the first fiber link located next to the crack tip. Thus, when a constant load, σ^{∞}, is applied to the undamaged specimen, the first fiber link is stressed to $\sigma_{1,0}$ with a failure probability of $F(\sigma_{1,0})$.

$$P_{0,1} = F(\sigma_{1,0}) \tag{6}$$

In Eq 6, $\sigma_{1,0}$ denotes the axial (y-direction) stress in Fiber Link 1 under the 0th damage state. That is, $\sigma_{1,0} = \sigma_y(a_1,0;a_0)$, where the first two arguments in the σ_y expression are the x and y coordinates of each fiber, and the third argument indicates the instantaneous crack length. Because link failure is assumed to be sequential, the transitional probabilities, $P_{0,j}$, associated with damage states increasing from $X = 0$ to $X = j$, where $j = 2, 3, 4, \ldots,$ N, are all zero. The panel must fail to state $X = 1$ before it can fail further. Once in state $X = 1$, the further damage is governed solely by the failure of the second link. A general formula for the probability, $P_{i,i+1}$, of the transition from $X = i$ to $X = i + 1$ can be derived using the conditional probability

$$P_{i,i+1} = \frac{Pr(\text{link } i + 1 \text{ fails at a stress between } \sigma_{i+1,i-1} \text{ and } \sigma_{i+1,i})}{\Pr(\text{link } i + 1 \text{ survived the stress } \sigma_{i+1,i-1})}$$

$$= \frac{F(\sigma_{i+1,i}) - F(\sigma_{i+1,i-1})}{1 - F(\sigma_{i+1,i-1})}, \text{ for } i = 1, 2, 3, \ldots \tag{7}$$

In Eq 7, $\sigma_{i,j}$ represents the σ_y stress in Fiber Link i when the specimen is in the jth damage state. The σ_{ij} values can be calculated from either the shear-lag analysis or the finite element method. In this paper, the result obtained by Hedgepeth [*11*] using the shear-lag model is used. The model bears the assumptions that fibers carry only axial stress while the matrix takes only the shear stress. Goree [*12*] has shown that the shear-lag model can provide an accurate solution for fiber stresses.

Since the failure process occurs in sequence, the probability, P_n, that at least n fibers fail can be found by direct multiplication of the precedent transitions

$$P_n = \prod_{i=0}^{n-1} P_{i,i+1} \tag{8}$$

Thus, the statistical parameters of fibers and matrix properties can be used to establish interrelationships among the failure probability, P_n, the number of fibers fractured, n, and the applied stress level, σ^{∞}. Once this relationship is obtained, the failure stress in the 0-ply fibers can be calculated from one of the following two methods:

1. A two-dimensional contour plot of n versus σ^{∞} for a specified probability value, for example, $P_n = 0.99$, is first generated from the P_n-n-σ^{∞} relationship. The failure stress, σ_{ref}, for fibers in the 0-ply is then obtained from the n versus σ^{∞} plot at the stress level under which $dn/d\sigma^{\infty} = \infty$, representing unstable failure of the specimen.
2. The probability density function, f_n, associated with the cumulative distribution function, P_n, is first obtained for each fixed n value. The most probable stress level, σ^{∞}, for n number of fibers to fracture is found by setting $df_n/d\sigma^{\infty} = 0$. The failure stress, σ_{ref}, is then calculated from the n versus σ^{∞} plot at the point $dn/d\sigma^{\infty} = \infty$.

The failure stress of the 0-plies is determined from σ_{ref} by multiplying the volume fraction, V_f. The notched strength of a composite can be calculated from either the lamination theory or the stress-strain relationships of angle plies. Details of the computational procedures can be found in Ref *5*.

The Stochastic Fracture Model

For a monotonically increasing load, the applied remote stress, σ^{∞}, is proportional to the chronological time, that is, $\sigma^{\infty}(t) = L*t$, where the constant, L, is the loading rate. Hence the applied load in the stochastic fracture model can be interpreted as the index "time," which is used commonly in the Markov process formulation [*13,14*]. By the sequential failure assumption, the transition from one state to a future state depends only on the present stress state in the fiber ahead of the crack tip and is independent of how the present damage state was reached.

We recall that in the statistical fracture model, advancing of the crack front is caused by the fracture of fibers. Once a fiber has fractured, the local stress in other unbroken fibers near the crack front increases as a result of load redistribution. This fracture process continues under a constant applied load at remote boundaries. In contrast, in the stochastic fracture model, transition of a damage state is caused by an increasing applied load. If we assume that at most only one fiber can fail at an instant, it can be deduced that only $P_{i,i}$ and $P_{i,i+1}$ do not vanish. For $i = 0$, $P_{0,0}$ is the survival probability of the first fiber link and $P_{0,1}$ is the failure probability of the first fiber link. The transitional probabilities, $P_{i,i+1}$, can be obtained as follows

$$P_{i,i+1}(\sigma^{\infty},\sigma^{\infty} + d\sigma^{\infty}) = Pr\{\text{link } (i + 1) \text{ fails in } (\sigma^{\infty},\sigma^{\infty} + d\sigma^{\infty}] \text{ given that links } 1,2. \ . \ . \ ,i \text{ have sequentially failed in } (0,\sigma^{\infty}]\}$$

$$= \frac{f(K_{i+1,i}\,\sigma^{\infty})}{1 - F(K_{i+1,i}\,\sigma^{\infty})} K_{i+1,i}\, d\sigma^{\infty} = h(\sigma_{i+1,i})\, K_{i+1,i}\, d\sigma^{\infty} \equiv a_{i,i+1}\, d\sigma^{\infty} \tag{9}$$

In Eq 9, $d\sigma^{\infty}$ is an infinitesimal stress increment. $K_{i+1,i}$ is the stress enhancement factor and is defined as $K_{i+1,i} = \sigma_{i+1,i}/\sigma^{\infty}$. The function, $h(\sigma)$, is the hazard function or the failure rate function. For fibers with a Weibull distribution, the associated failure rate is geometrically increasing as the fiber stress increases.

A characterizing relationship among the unknown variables, $P_{ij}(\sigma^{\infty})$, can be established by analyzing the possibilities that arise at the end of the previous transition instant. Using the Markov process formulation, the following Markov-Kolmogorov equation can be derived [*6*]

$$\frac{d\mathbf{P}(\sigma^{\infty})}{d\sigma^{\infty}} = \mathbf{PA}(\sigma^{\infty}) \tag{10}$$

In which, $\mathbf{P} = [P_{i,j}]$, and the components of the coefficient matrix, $\mathbf{A}$, are

$$A_{i,i+1} = a_{i,i+1},$$

$$A_{i,i} = -A_{i,i+1},$$

$$\text{All other } A_{i,j} = 0 \tag{11}$$

The transitional probability, **P**, of the system is subjected to the initial condition $\mathbf{P}(0) = \mathbf{I}$, the identity matrix since the system remains unchanged in the "initial state" under zero loads. In Eq 10, the coefficient matrix, **A**, is a function of the fiber stress, and thus a function of the applied stress, σ^{∞}. The governing differential equation is a first order nonstationary system. It can be transformed into a stationary system by the change of variable [*6*] and a simple solution method can be applied to solve for the transitional probabilities, $p_{i,j}(\sigma^{\infty})$.

Among those transitional probabilities, $P_{0,N}(\sigma^{\infty})$ represents the probability of transition from the undamaged state, $X = 0$, to the totally damaged state, $X = N$, under an applied stress, σ^{∞}. After finding the probability function, $P_{0,N}(\sigma^{\infty})$, failure can be defined at a specific probability level, that is, we can choose $P_{0,N}(\sigma^{\infty}) = p$), where $0 \leq p \leq 1$. In this paper, the mean reference stress, that is, $p = 0.5$, is chosen in the following analysis.

Prediction of Notched Strength

The two probabilistic fracture models just described have been used to predict the strength of $(\pm 45/0_2)_s$ boron/aluminum (B/A1) composites containing central slits. The boron filaments are 0.14 mm (5.6 mil) in diameter, with an average strength of $\bar{\sigma} = 3474.8$ MPa (504 ksi) and the shape parameter $\beta = 8.0$ for a gage length of 25.4 mm (1.0 in.). The constituent properties of B/A1 composites are $E_f = 400$ GPa (58×10^6 psi), $E_m = 68.9$ GPa (10×10^6 psi), $V_f = 0.48$, $\upsilon_m = 0.33$, and $\delta = 0.432$ mm (0.017 in.).

To use the statistical strength model, we first construct a three-dimensional plot relating the applied stress, σ^{∞}, to the number of broken fibers, n, for each probability level, P_n. Taking a specific P_n value, for example, $P_n = 0.99$, the reference fiber stress, σ_{ref}, is found from the contour plot of n versus σ^{∞} at the stress level that makes $dn/d\sigma^{\infty}$ infinity [*5*]. The reference stress is then multiplied by the volume fraction of fiber, V_f, to yield the failure stress in the 0-plies. The stresses in the ± 45 plies are then obtained from the nonlinear stress-strain relationship of the $(45/\text{-}45)_s$ laminate [*4*], assuming the same strain through the laminate thickness. By adding the contributions from angle plies, the laminate failure stress, σ_f, can be estimated. Finally, the notched strength for an infinite panel, σ_f^{∞}, was obtained by taking into account the finite width correction factor that is a function of $2a_0/W$.

In using the stochastic model, the failure probability, $P_{0,j}$, which is a function of the applied stress, σ^{∞}, and the state number, j, is first constructed. The mean reference strength, σ_{ref}, of fibers in the 0-plies is determined from $P_{0,N}(\sigma^{\infty}) = 0.50$, although other $P_{0,N}(\sigma^{\infty})$ values can also be used. Once σ_{ref} is found, the remaining procedures are the same as those used in the statistical model. Results of the strength prediction for B/A1 composites both fracture models are shown in Fig. 5 on a log versus log plot. These predictions compare well with experimental data obtained in Ref *4*. Additionally, the relationship between composite fracture stress, σ_f^{∞}, and discontinuity size, $2a_0$, can be best described by the following power type equation as previously suggested by Mar and Lin [*4*]

$$\sigma_f^{\infty} = H_c\,(2a_0)^{-m} \tag{13}$$

where the parameter, H_c, is the material constant and m is the slope of the plot.

Conclusion

Two probabilistic fracture models: a statistical model and a stochastic model, for predicting the notched strength of laminated composites have been reviewed. The statistical fracture model treats the case of constant load while the stochastic fracture model deals with the effect of monotonically increasing loads.

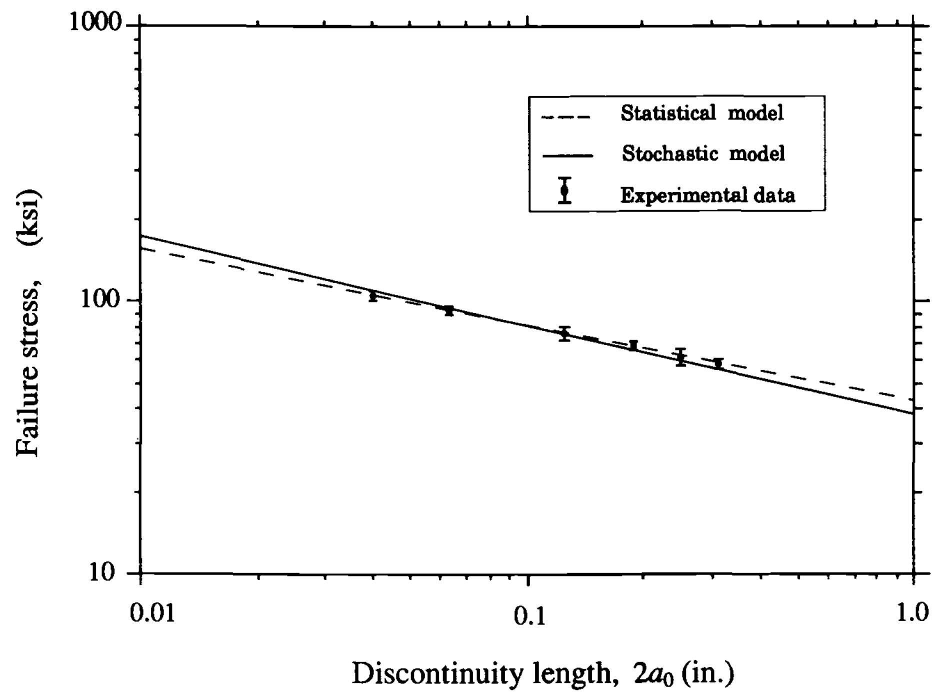

FIG. 5—*Comparison of probabilistic model predictions with experimental data (1 in. = 25.4 mm, 1 ksi = 6.89 MPa).*

The phenomenon of notch sensitivity in composites is studied. Employing the probabilistic approach, the notched strengths of boron/aluminum composites with various crack lengths have been predicted. The predicted results from both fracture models compare well with existing experimental data. The stochastic model is more accurate than the statistical model since it represents a more realistic loading situation. In addition, the present probabilistic approach predicts a power law type of relationship between fracture stress and notch size. This finding coincides with the previous results by Mar and Lin based on an entirely different approach.

Acknowledgment

The work reported in this paper is sponsored by The Boeing Company. The authors wish to thank Mr. Jerry R. Jaeb, Mr. Ronald W. Johnson, and Dr. Bjorn F. Backman of Boeing for their valuable discussions.

References

[1] Awerbuch, J. and Madhukar, M. S., "Notched Strength of Composite Laminates: Predictions and Experiments—A Review," *Journal of Reinforced Plastics and Composites*, Vol. 4, Jan. 1985, pp. 3–159.

[2] Waddoups, M. E., Eisenmann, J. R., and Kaminski, B. E., "Macroscopic Fracture Mechanics of Advanced Composite Materials," *Journal of Composite Materials*, Vol. 5, Oct. 1971, pp. 446–454.

[3] Whitney, J. M. and Nuismer, R. J., "Stress Fracture Criterion for Laminated Composites Containing Stress Concentrations," *Journal of Composite Materials*, Vol. 8, 1974, pp. 253–265.
[4] Mar, J. W. and Lin, K. Y., "Fracture of Boron/Aluminum Composites with Discontinuities," *Journal of Composite Materials*, Vol. 11, Oct. 1977, pp. 405–421.
[5] Lin, K. Y. and Cheng, M. C., "A Statistical Strength Model for Composites with Discontinuities," submitted for publication.
[6] Cheng, M. C., "Statistical Strength Models for Composites with Discontinuities," Ph.D. thesis, Department of Aeronautics and Astronautics, University of Washington, Seattle, WA, June 1991.
[7] Mandell, J. F., Wang, S. S., and McGarry, F. J., "The Extension of Crack Tip Damage Zones in Fiber Reinforced Plastic Laminates," *Journal of Composite Materials*, Vol. 9, 1975, pp. 266–287.
[8] Rosen, B. W., "Tensile Failure of Fibrous Composites," *Journal*, American Institute of Aeronautics and Astronautics, Vol. 2, Nov. 1964, pp. 1985–1991.
[9] Tamuzs, V., "Some Peculiarities of Fracture in Heterogeneous Materials, *Proceedings*, Second USA-USSR Symposium of Composite Fracture Mechanics, G. C. Sih and V. Tamuzs, Eds., Sythoff and Noordhoff International Publishers, The Netherlands.
[10] Weibull, W., "A Statistical Distribution Function of Wide Applicability," *Journal of Applied Mechanics*, Vol 18, 1951, pp. 293–297.
[11] Hedgepeth, J. M., "Stress Concentrations in Filamentary Structures," NASA Technical Note D-882, Langley Research Center, Langley, VA, 1961.
[12] Goree, J. G., "The Accuracy of Approximate Solutions in the Analysis of Fracture of Composites," *Composite Structures 3, Proceedings*, 3rd International Conference on Composite Structures, I. H. Marshall, Ed., Elsevier Applied Sciences, New York, 1985, pp. 589–595.
[13] Feller, W., *An Introduction to Probability Theory and Its Applications*, Vol. 1, 3rd ed., Wiley, New York, 1968.
[14] Karlin, S. and Taylor, H. M., *A First Course in Stochastic Processes*, Academic Press, New York, 1975.

Jian Li[1] *and Erian A. Armanios*[1]

Analysis of Unidirectional and Cross-Ply Laminates Under Torsion Loading

REFERENCE: Li, J. and Armanios, E. A., "**Analysis of Unidirectional and Cross-Ply Laminates Under Torsion Loading,**" *Fracture Mechanics: Twenty-Second Symposium (Volume II), ASTM STP 1131,* S. N. Atluri, J. C. Newman, Jr., I. S. Raju, and J. S. Epstein, Eds., American Society for Testing and Materials, Philadelphia, 1992, pp. 421–435.

ABSTRACT: A simple analytical method using a sublaminate approach is introduced to analyze unidirectional and cross-ply laminates under torsion loading. Interlaminar stresses and total energy release rate are evaluated based upon a displacement field that includes shear deformation. Closed-form expressions for the interlaminar stresses and total strain energy release rate in terms of the laminate stiffness coefficients are provided. Two sublaminate models are used for the interlaminar stress analysis and for the delamination analysis. The method is applied to the analysis of $[0]_{16}$ and $[0/90]_{4s}$ laminates made of IM6/3501-6 graphite/epoxy material. The interlaminar stress predictions are compared with a finite element simulation and an exact elasticity solution.

KEY WORDS: laminates, interlaminar stress, strain energy release rate, torsion, fracture (materials), fracture mechanics, fatigue (materials)

In rotorcraft structures, hingless and bearingless composite rotor hubs and flex beams currently used as a means of tailoring their response for specific performance requirements are subjected to axial, bending, and torsion loads. Delamination caused by interlaminar stresses can initiate at the free edges and ply terminations in these structures. An accurate knowledge of the interlaminar stresses and strain energy release rate is necessary in order to understand the behavior and design against such failures.

Interlaminar stress and delamination analysis of laminated composites under extension has been studied extensively [*1–8*]. However, there has been very limited work on bending and torsion loadings. Salamon [*9,10*] predicted the interlaminar stresses in a four-layer $[\pm 45]_s$ and $[\theta,0]_s$ laminate under uniform bending using a finite difference approach to solve the exact elasticity equations. He found that the interlaminar shear and normal stresses rise sharply near the free edges. Armanios and Rehfield [*11*] studied bending and combined bending and extension using a transverse shear deformation theory and a sublaminate approach for laminate layups where Mode III is negligible such as $[0_{2n}/90_n]_s$ and $[0_{4n}/(\pm 45)_n]_s$ laminates. Interlaminar stresses and energy release rates were obtained in closed form. They concluded that the energy release rate in a combined bending-extension loading may be more critical than extension loading only. Ye and Yang [*12*] developed a quasi-three-dimensional finite element procedure to investigate the free edge effects in symmetric composite laminates of finite width under bending. Results were presented for angle-ply $[\pm 45]_s$ and symmetric cross-ply laminates. Since the twisting effect induced by bending was not considered, their solution can be used only for those symmetric laminates where twisting

[1]Graduate research assistant and associate professor, respectively, School of Aerospace Engineering, Georgia Institute of Technology, Atlanta, GA 30332-0150.

and bending coupling effects are negligible. Chan and Ochoa [13] calculated the interlaminar stresses and energy release rates in symmetric laminates with various layups subjected to bending. They found that the total and Mode I strain energy release rate decrease as delamination size increases and reach a lower bound. They also obtained [14] the interlaminar stress distributions and energy release rates for laminates with a $[0]_{16}$, $[45_2,-45_2]_{2s}$ and $[45_2,-45_2,0_2,90_2]_s$ layups under torsion loading. Unlike the bending case, they found that the Mode III strain energy release rate increases steadily as a function of crack length and eventually reaches a plateau.

Kurtz and Whitney [15] developed an exact elasticity solution for simple torsion of cross-ply laminates. Comparison of this solution with the existing elasticity theory for the torsion of homogeneous orthotropic bars [16] showed that the homogeneous solution is sufficiently rigorous for most practical applications. Murthy and Chamis [17] used a three-dimensional finite element analysis to investigate the width- and loading-condition effects on the free-edge stress fields in composite laminates. The analysis included a special free-edge region refinement or superelement with progressive substructuring. Various loading conditions were considered including out-of-plane twisting moment and inplane bending. The three-dimensional free edge stresses were determined using a cantilever geometry. They found that axial extension produces the smallest magnitude of interlaminar free edge stress compared to other loading conditions. Daniel and Vizzini [18] calculated the interlaminar stresses in a $[0/90]_s$ and $[\pm 15]_s$ laminate under torsion using the MSC/NASTRAN anisotropic solid elements. In contrast to the results of Ref *15*, they reported nonzero interlaminar normal stress in $[0/90]_s$ laminate.

The objective of this work is to extend the sublaminate approach developed in Ref *8* to the analysis of laminates under torsion loading. This work is directed primarily towards providing a simple analytical model for predicting interlaminar stresses and strain energy release rate, and performing parametric design-related studies.

Mathematical Model

The generic laminate shown in Fig. 1 is subjected to torsion on two opposite sides. The laminate considered as made of sublaminates or groups of plies that are conveniently treated as single laminated units. The assumed displacement field within each sublaminate may be written as

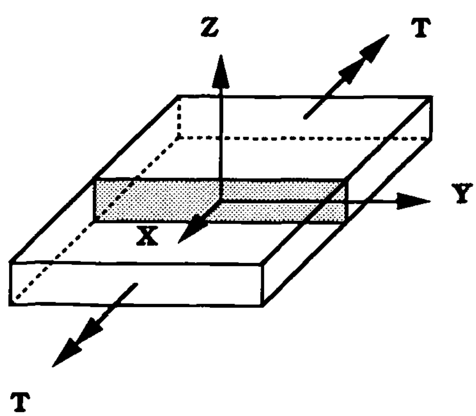

FIG. 1—*Laminate configuration and loading.*

$$u(x,y,z) = \varepsilon_0 \cdot x + \kappa \cdot x \cdot (z + \delta) + U(y) + z \cdot \beta_x(y)$$

$$v(x,y,z) = V(y) + z \cdot \beta_y(y) + C \cdot x \cdot (z + \delta)$$

$$w(x,y,z) = -\frac{1}{2}\kappa \cdot x^2 - C \cdot x \cdot (y + \rho) + W(y) \tag{1}$$

Where u, v, and w denote displacements relative to the x, y, and z axes, respectively. The relative angle of rotation about the x-axis is C. The arbitrary constants, δ and ρ, are to be determined by enforcing continuity of displacements at the interface between sublaminates. Axial extension and bending curvature are denoted by ε_0 and κ. These result from the coupling effects associated with unsymmetrical layups. Shear deformation is recognized through the rotations, β_x and β_y.

The corresponding strains are

$$\varepsilon_{xx} = \varepsilon_{xx}^0 + z\kappa_x \qquad \varepsilon_{yy} = \varepsilon_{yy}^0 + z\kappa_y \qquad \varepsilon_{zz} = 0$$

$$\gamma_{xy} = \gamma_{xy}^0 + z\kappa_{xy} \qquad \gamma_{yz} = \gamma_{yz}^0 \qquad \gamma_{xz} = \gamma_{xz}^0 \tag{2}$$

The strain components associated with the reference surface are denoted by superscript,^{0}. These are defined as

$$\varepsilon_{xx}^0 = \varepsilon_0 + \kappa \cdot \delta \qquad \varepsilon_{yy}^0 = V_{,y} \qquad \gamma_{xy}^0 = U_{,y} + C \cdot \delta$$

$$\kappa_x = \kappa \qquad \kappa_y = \beta_{y,y} \qquad \kappa_{xy} = \beta_{x,y} + C$$

$$\gamma_{yz}^0 = \beta_y + W_{,y} \qquad \gamma_{zx}^0 = \beta_x - C \cdot (y + \rho) \tag{3}$$

where partial differentiation is denoted by a comma. The constitutive relationship can be written using the force and moment resultants in terms of strains and curvatures as follows

$$\begin{Bmatrix} N_x \\ N_y \\ N_{xy} \\ M_x \\ M_y \\ M_{xy} \end{Bmatrix} = \begin{bmatrix} A_{11} & A_{12} & A_{16} & B_{11} & B_{12} & B_{16} \\ A_{12} & A_{22} & A_{26} & B_{12} & B_{22} & B_{26} \\ A_{16} & A_{26} & A_{66} & B_{16} & B_{26} & B_{66} \\ B_{11} & B_{12} & B_{16} & D_{11} & D_{12} & D_{16} \\ B_{12} & B_{22} & B_{26} & D_{12} & D_{22} & D_{26} \\ B_{16} & B_{26} & B_{66} & D_{16} & D_{26} & D_{66} \end{bmatrix} \begin{Bmatrix} \varepsilon_{xx}^0 \\ \varepsilon_{yy}^0 \\ \gamma_{xy}^0 \\ \kappa_x \\ \kappa_y \\ \kappa_{xy} \end{Bmatrix} \tag{4}$$

$$\begin{Bmatrix} Q_y \\ Q_x \end{Bmatrix} = \begin{bmatrix} A_{44} & A_{45} \\ A_{45} & A_{55} \end{bmatrix} \begin{Bmatrix} \gamma_{yz}^0 \\ \gamma_{xz}^0 \end{Bmatrix} \tag{5}$$

For a sublaminate of thickness h, the stiffness coefficients are defined as

$$(A_{ij},B_{ij},D_{ij}) = \int_{-(h/2)}^{h/2} \overline{Q}_{ij}(1,z,z^2) \cdot dz \tag{6}$$

Where $\overline{Q}_{ij}$ are the transformed reduced stiffnesses as defined in Ref *19*.

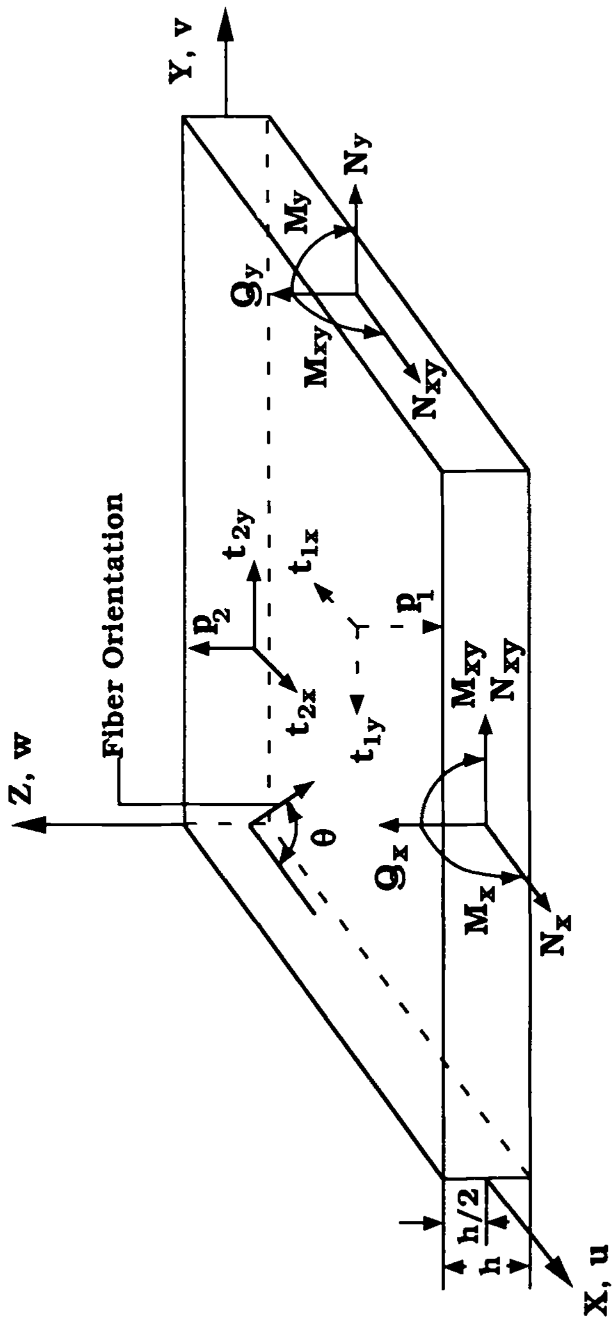

FIG. 2—*Sublaminate notation and sign convention.*

The equilibrium equations can be written as

$$
\begin{aligned}
N_{xy,y} + t_{2x} - t_{1x} &= 0 \\
N_{y,y} + t_{2y} - t_{1y} &= 0 \\
Q_{y,y} + p_2 - p_1 &= 0 \\
M_{xy,y} - Q_x + \frac{h}{2} \cdot (t_{2x} + t_{1x}) &= 0 \\
M_{y,y} - Q_y + \frac{h}{2} \cdot (t_{2y} + t_{1y}) &= 0
\end{aligned}
\tag{7}
$$

The interlaminar shear and peel stresses at the sublaminate upper and lower surfaces are denoted by t_{2x}, t_{2y}, p_2 and t_{1x}, t_{1y}, p_1, respectively, as shown in Fig. 2

Equations 1 through 7 will be applied to unidirectional and cross-ply laminates under torsion loading.

Interlaminar Stresses

Due to symmetry, a minimum of two sublaminates through the thickness for half the laminate is needed in order to determine the interlaminar stresses at a given interface. These are referred to as Sublaminate 0 and Sublaminate 1 as shown in Fig. 3*a*. The continuity of

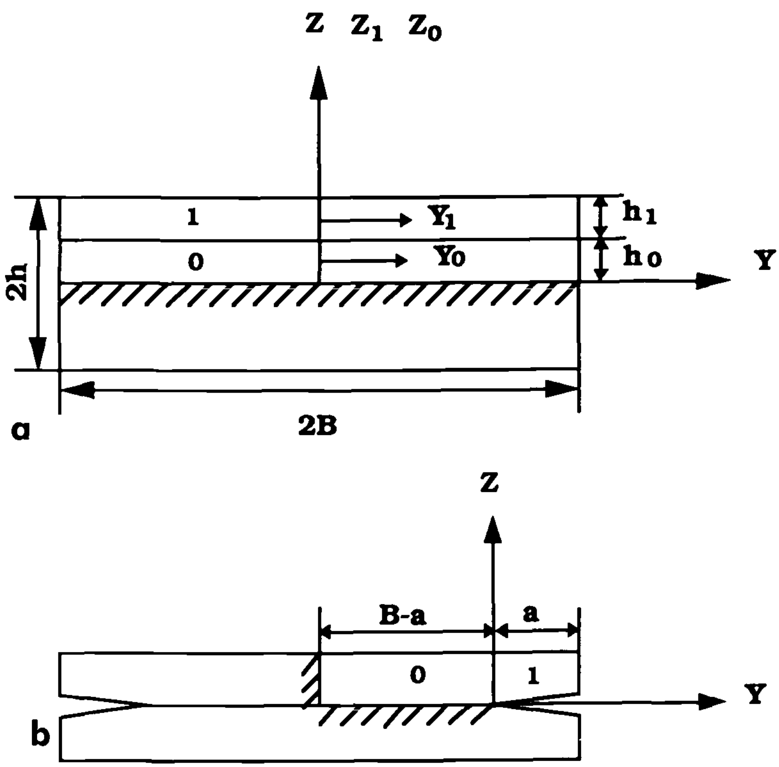

FIG. 3—*Sublaminate analysis models:* (a) *interlaminate stress analysis model, and* (b) *delamination analysis model.*

displacements at the interface between these sublaminates are

$$u_0\left(x,y,\frac{h_0}{2}\right) = u_1\left(x,y,-\frac{h_1}{2}\right)$$

$$v_0\left(x,y,\frac{h_0}{2}\right) = v_1\left(x,y,-\frac{h_1}{2}\right)$$

$$w_0\left(x,y,\frac{h_0}{2}\right) = w_1\left(x,y,-\frac{h_1}{2}\right) \tag{8}$$

At the laminate central plane

$$u_0\left(x,y,-\frac{h_0}{2}\right) = 0$$

$$v_0\left(x,y,-\frac{h_0}{2}\right) = 0 \tag{9}$$

The subscripts in Eqs 8 and 9 refer to the respective sublaminate. Substitute Eq 1 into Eqs 8 and 9 to obtain

$$U_0 = \frac{h_0}{2}\beta_{x0}$$

$$V_0 = \frac{h_0}{2}\beta_{y0}$$

$$U_1 = h_0\beta_{x0} + \frac{h_1}{2}\beta_{x1}$$

$$V_1 = h_0\beta_{y0} + \frac{h_1}{2}\beta_{y1} \tag{10}$$

The response associated with Sublaminates 0 and 1 is coupled through the interface continuity conditions. The upper surface of Sublaminate 1 is stress free. The shear and peel stresses at the bottom surface will be denoted by t_x, t_y, and p, respectively. From reciprocity of stresses at the interface between Sublaminates 1 and 0, the stresses at the upper surface of Sublaminate 0 are t_x, t_y, and p. From the antisymmetric condition at the sublaminate bottom surface, the peel stress is zero. The interlaminar shear stresses at the bottom surface are denoted by t_{1x} and t_{1y} for Sublaminate 0.

There are five boundary conditions at each sublaminate free edge, namely

$$N_{xyi}|_{y=\pm B} = 0,\ M_{xyi}|_{y=\pm B} = 0,\ N_{yi}|_{y=\pm B} = 0,$$

$$M_{yi}|_{y=\pm B} = 0,\ Q_{yi}|_{y=\pm B} = 0 \qquad i = 0,1 \tag{11}$$

where i refers to the respective sublaminate. By using the principle of virtual work, the boundary conditions that are consistent with the kinematic relationships provided in Eq 10, take the following form

$$\frac{h_1}{2} N_{xy1}\big|_{y=\pm B} + M_{xy1}\big|_{y=\pm B} = 0,\ h_0 N_{xy1}\big|_{y=\pm B} + \frac{h_0}{2} N_{xy0}\big|_{y=\pm B} + M_{xy0}\big|_{y=\pm B} = 0$$

$$\frac{h_1}{2} N_{y1}\big|_{y=\pm B} + M_{y1}\big|_{y=\pm B} = 0,\ h_0 N_{xy1}\big|_{y=\pm B} + \frac{h_0}{2} N_{y0}\big|_{y=\pm B} + M_{y0}\big|_{y=\pm B} = 0$$

$$Q_{y1}\big|_{y=\pm B} + Q_{y0}\big|_{y=\pm B} = 0 \tag{12}$$

For unidirectional and cross-ply layups, Eq 12 is equivalent to Eq 11 since the shear force vanishes, and N_{xyi} and N_{yi} are proportional to M_{xyi} and M_{yi}, respectively. Applying the equilibrium equation (Eq 7) to Sublaminates 1 and 0, and prescribing the boundary conditions (Eq 12) at the sublaminate free edges, the interlaminar stress, τ_{xz} (t_x), can be expressed as

$$t_x = N_{xy1,y} = h_0 A^1_{66}\beta_{x0,yy} + \overline{B}^1_{66}\beta_{x1,yy} \tag{13}$$

The interlaminar shear stress τ_{yz} (t_y) and peel stress σ_z (p) are zero for unidirectional and cross-ply constructions. The rotations, β_{x0} and β_{x1}, in Eq 13 are found to be

$$\beta_{x1} = Cy + 2C \cdot H_1 \sinh(s_1 y) + 2C \cdot H_3 \sinh(s_2 y)$$

$$\beta_{x0} = Cy + 2C \cdot \eta_1 H_1 \sinh(s_1 y) + 2C \cdot \eta_2 H_3 \sinh(s_2 y) \tag{14a}$$

Where s_1 and s_2 are the characteristic roots defined as

$$s_1 = \sqrt{\frac{F_2 + \sqrt{F_2^2 - 4 \cdot F_1 \cdot F_3}}{2 \cdot F_1}} \qquad s_2 = \sqrt{\frac{F_2 - \sqrt{F_2^2 - 4 \cdot F_1 \cdot F_3}}{2 \cdot F_1}} \tag{14b}$$

$$F_1 = \left(\overline{D}^1_{66} + \frac{h_1}{2}\overline{B}^1_{66}\right)\left(\overline{D}^0_{66} + \frac{h_0}{2}\overline{B}^0_{66} + h_0^2 A^1_{66}\right) - h_0^2(\overline{B}^1_{66})^2$$

$$F_2 = A^1_{55}\left(\overline{D}^0_{66} + \frac{h_0}{2}\overline{B}^0_{66} + h_0^2 A^1_{66}\right) + A^0_{55}\left(\overline{D}^1_{66} + \frac{h_1}{2}\overline{B}^1_{66}\right)$$

$$F_3 = A^1_{55} \cdot A^0_{55} \tag{14c}$$

$$\overline{D}^1_{66} = D^1_{66} + \frac{h_1}{2} B^1_{66} \qquad \overline{B}^1_{66} = B^1_{66} + \frac{h_1}{2} A^1_{66}$$

$$\overline{D}^0_{66} = D^0_{66} + \frac{h_0}{2} B^0_{66} \qquad \overline{B}^0_{66} = B^0_{66} + \frac{h_0}{2} A^0_{66} \tag{14d}$$

and H_1 and H_3 are integration constants given by

$$H_1 = -\frac{1 - \eta_2}{\eta_1 - \eta_2} \frac{1}{s_1 \cosh(s_1 B)}$$

$$H_3 = \frac{1 - \eta_1}{\eta_1 - \eta_2} \frac{1}{s_2 \cosh(s_2 B)}$$

$$\eta_j = \frac{\left(\overline{D}^1_{66} + \frac{h_1}{2} \overline{B}^1_{66}\right) s_j^2 - A^1_{55}}{h_0 \overline{B}^1_{66} \cdot s_j^2} \quad j = 1,2 \tag{14e}$$

The inplane stress, τ_{xy}, is calculated from the constitutive relationship and can be expressed as

$$\tau^k_{xy1} = \overline{Q}^k_{66} \left\{ h_0(\beta_{x0,y} + C) + \left(\frac{h_1}{2} + z^k\right)(\beta_{x1,y} + C) \right\} \tag{15}$$

Where τ^k_{xy1} and $\overline{Q}^k_{66}$ are the inplane shear stress and the reduced stiffness in Sublaminate 1 within the k^{th} ply, respectively, and z^k is measured from the midplane of Sublaminate 1. Superscripts 0 and 1 associated with the stiffness coefficients in Eq 14 refer to the respective sublaminate.

A comparison of the interlaminar shear stress, τ_{xz}, and inplane shear stress, τ_{xy}, predicted by the present approach, the finite element method (FEM) of Ref *14*, and the elasticity solution [*16*] is presented in Figs. 4 through 6. The laminate is $[0]_{16}$ unidirectional and the relative twisting angle is denoted by C. The material properties considered are those of

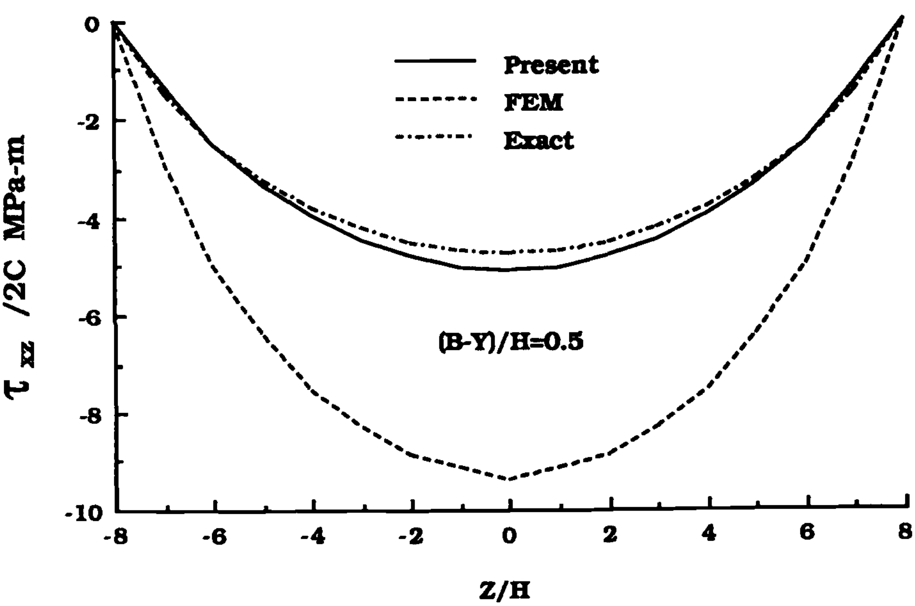

FIG. 4—*Interlaminar shear stress distribution across the thickness of a* $[0]_{16}$ *laminate.*

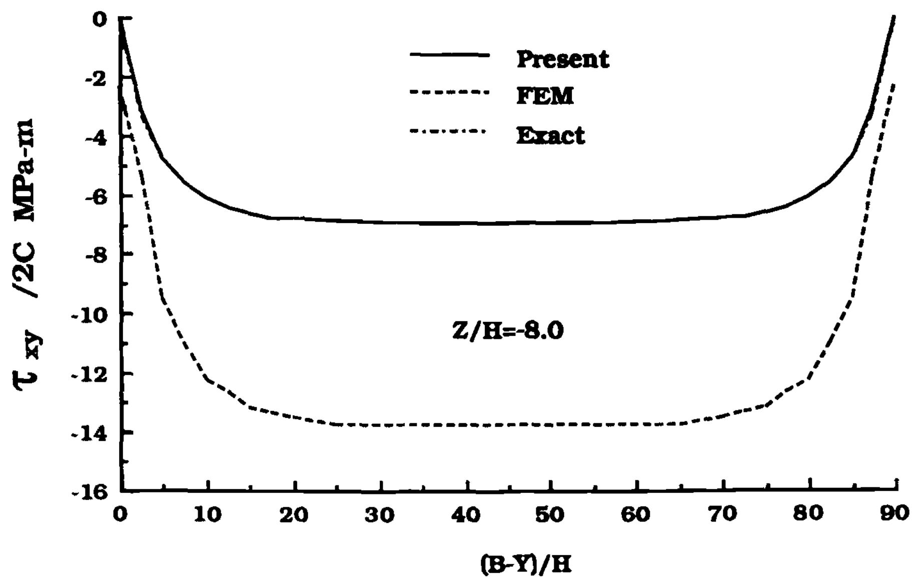

FIG. 5—*Inplane shear stress distribution across the width of a* $[0]_{16}$ *laminate.*

Hercules IM6/3501-6 graphite/epoxy [*14*]. They are given in Table 1. Subscripts 1, 2, and 3 in the table refer to the principal material directions. The laminate width, $2B$, is 90-ply thickness. The ply thickness is denoted by H, and the laminate thickness is denoted by $2h$.

Figure 4 shows the interlaminar shear stress, τ_{xz}, distribution through the thickness. The inplane shear stress, τ_{xy}, distribution through the width appears in Fig. 5, while its distribution through the thickness is shown in Fig. 6. The distributions in Figs. 4 and 6 are for a section

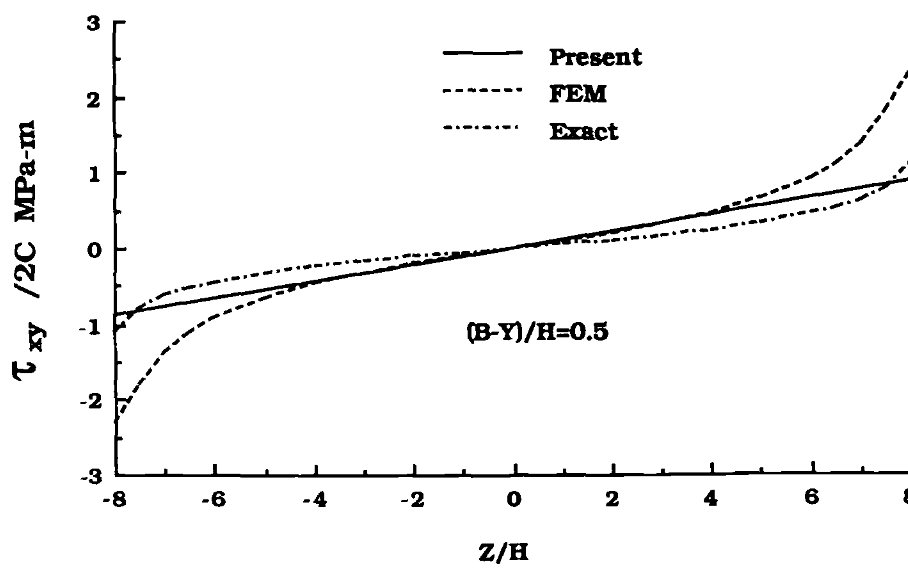

FIG. 6—*Inplane shear stress distribution across the thickness of a* $[0]_{16}$ *laminate.*

at a distance of 0.5 H from the free edges. The interlaminar shear stress, τ_{xz}, and inplane shear stress, τ_{xy}, predicted by the present approach are closer to the elasticity solution than the FEM results as shown in Figs. 4 and 6. The present approach predicts a linear shear stress, τ_{xy}, distribution through the thickness as depicted in Fig. 5. This is a result of the simple shear deformation theory used.

The effect of the thickness to width ratio on the accuracy of the interlaminar shear stress predictions is provided in Fig. 7. The error in τ_{xz} relative to the elasticity solution [*16*] at the midplane is denoted by e_1, while e_2 is associated with a plane located four plies above the midplane. Subscripts, *pre.* and *el.*, represent the present and elasticity predictions, respectively. The maximum error in the interlaminar stress is less than 1 and 8% for e_1 and e_2, respectively.

The stress distributions appearing in Figs. 4 through 6 show that the largest interlaminar shear stress at the free edges occurs at the midplane. Furthermore, the largest inplane shear stress occurs at the midpoints of the top and bottom surfaces. Moreover, the value of the maximum inplane shear stress is much higher than that of the maximum interlaminar shear stress. These observations indicate that the failure will be caused by inplane shear stress in the $[0]_{16}$ laminate, and by matrix cracking for $[90]_{16}$ laminate. This is in agreement with the test results of Ref *20*.

Similar comparisons between the present approach and the elasticity solution in a $[0/90]_{4s}$ laminate are given in Figs. 8 and 9. The elasticity solution in Figs. 8 and 9 is based on a smeared shear modulus expressed as

$$G_{xy} = G_{12}$$

$$\frac{1}{G_{xz}} = \frac{1}{2}\left(\frac{1}{G_{12}} + \frac{1}{G_{13}}\right) \tag{16}$$

This smeared approach was adopted in Ref *15*. The comparisons show good agreement between the present approach and the elasticity solution.

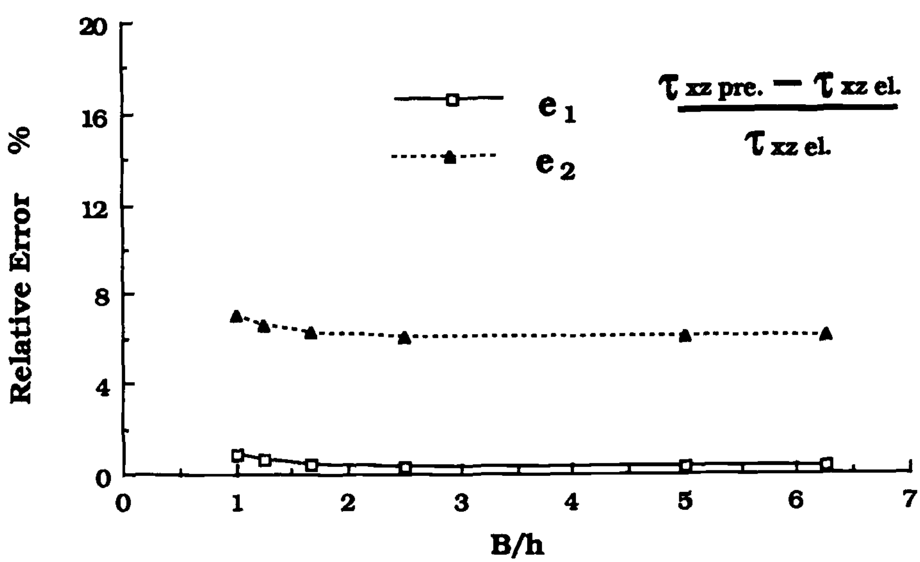

FIG. 7—*Geometric influence on the prediction of interlaminar shear stress* τ_{xz} *for a* $[0]_{16}$ *laminate.*

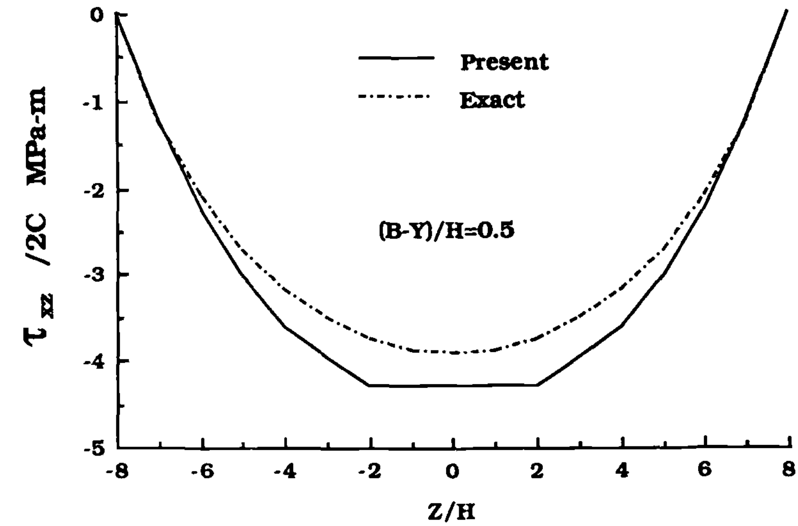

FIG. 8—*Interlaminar shear stress distribution across the thickness of a* $[0/90]_{4s}$ *laminate.*

Energy Release Rate

Cross-ply laminates may develop free edge delaminations. This possibility is investigated for a $[0/90]_{4s}$ laminate with two cracks initiating at the midplane free edges as shown in Fig. 3*b*. Also appearing in the figure is the sublaminate modeling of the cracked laminate.

The strain energy release rate is a global parameter and can be computed in terms of stress resultants. One sublaminate through the thickness is sufficient in order to determine the stress resultants in the cracked and uncracked regions. These are referred to as Sub-

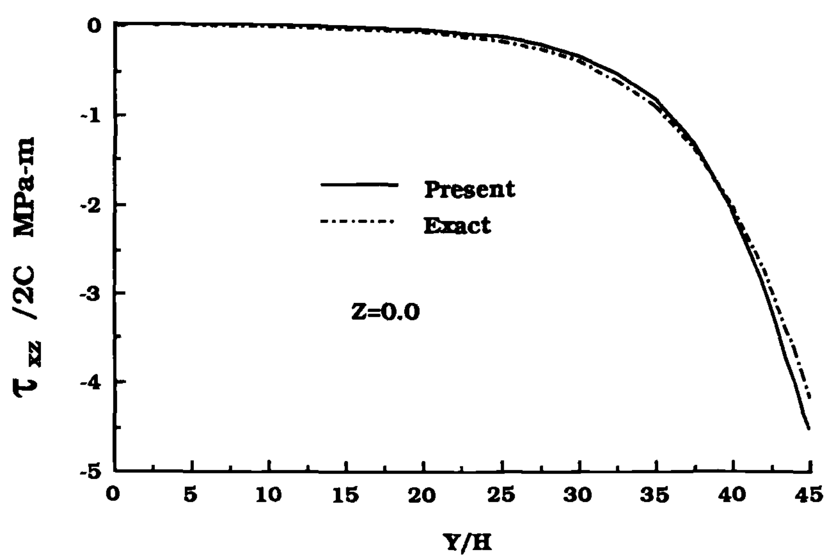

FIG. 9—*Interlaminar shear stress distribution across the width of a* $[0/90]_{4s}$ *laminate.*

laminates 1 and 0, respectively, in Fig. 3*b*. From symmetry, one quarter of the laminate is modeled. The crack length is denoted by a.

For Sublaminate 1, the upper and lower surfaces are stress free. While only the upper surface is stress free for sublaminate 0. Following the methodology outlined in the previous section, and prescribing the following boundary condition at the free edge of Sublaminate 1 and the continuity conditions between Sublaminates 0 and 1,

$$M_{xy1}\big|_{y=a} = 0 \tag{17a}$$

$$\frac{h_0}{2} N_{xy0}\big|_{y=0} + M_{xy0}\big|_{y=0} = M_{xy1}\big|_{y=0}, \qquad \beta_{x0}\big|_{y=0} = \beta_{x1}\big|_{y=0} \tag{17b}$$

the rotations, β_{x1} and β_{x0}, can be written as

$$\beta_{x0} = 2C \cdot I_0 e^{s_0 y} + C(y + B - a)$$

$$\beta_{x1} = 2C \cdot I_1 e^{s_1 y} + 2C \cdot I_2 e^{-s_1 y} + C(y + B - a) \tag{18a}$$

Where s_0 and s_1 are the characteristic roots for Sublaminates 0 and 1, respectively. These are given by

$$s_0 = \sqrt{\frac{A_{55}}{\lambda_0}} \qquad s_1 = \sqrt{\frac{A_{55}}{\lambda_1}} \tag{18b}$$

Parameters, λ_0 and λ_1, in Eq 18*b* are given as

$$\lambda_0 = D_{66} + hB_{66} + \frac{h^2}{4} A_{66}$$

$$\lambda_1 = D_{66} - \frac{B_{66}^2}{A_{66}} \tag{18c}$$

The integration constants I_0, I_1, and I_2 in Eq 18*a* are expressed in terms of the characteristic roots by

$$I_1 = -\frac{\frac{1}{s_1}(\lambda_0 s_0 + \lambda_1 s_1)e^{s_1 a} + \lambda_0 - \lambda_1}{\lambda_0 s_0 - \lambda_1 s_1 + (\lambda_0 s_0 + \lambda_1 s_1)e^{2s_1 a}}$$

$$I_2 = I_1 e^{2s_1 a} + \frac{1}{s_1} e^{s_1 a}$$

$$I_0 = I_1(1 + e^{2s_1 a}) + \frac{1}{s_1} e^{s_1 a} \tag{18d}$$

The strain energy release rate that is a pure Mode III is calculated as

$$G_{III} = -\frac{\partial U}{\partial a} \tag{19}$$

Where U is the strain energy associated with Sublaminate 1 and Sublaminate 0 and defined as

$$U = \frac{1}{2}\int (N_{xy}\gamma^0_{xy} + M_{xy}\kappa_{xy} + Q_x\gamma^0_{xz})dy$$

$$= \frac{1}{2}\int_{-(B-a)}^{0} \left\{ \left(\frac{h}{2}N_{xy0} + M_{xy0}\right)(\beta_{x0,y} + C) + Q_{x0}[\beta_{x0} - C(y + B - a)] \right\} \cdot dy \tag{20}$$

$$+ \frac{1}{2}\int_0^a \{M_{xy1}(\beta_{x1,y} + C) + Q_{x1}[\beta_{x1} - C(y + B - a)]\} \cdot dy$$

Since Sublaminates 0 and 1 have the same layup, Superscripts 0 and 1 associated with the stiffness coefficients are dropped for convenience. Substitute from Eq 20 into Eq 19 to get for the Mode III strain energy release rate the following expression

$$\frac{G_{III}}{4C^2} = \frac{1}{2}\left(\frac{h^2}{4}A_{66} + hB_{66} + \frac{B_{66}^2}{A_{66}}\right) - G(a) \tag{21}$$

The first term in Eq 21 is independent of the crack length and depends on the stiffness coefficients, A_{66} and B_{66}. The second term, $G(a)$, in Eq 21 is an exponential function of the crack length and the characteristic roots and is given by

$$G(a) = A_{55}\left[\frac{I_0}{s_0}(1 - e^{-2s0(B-a)})\frac{dI_0}{da} - I_0^2e^{-2s0(B-a)}\right]$$

$$+ \lambda_0\left[(1 - e^{-s0(B-a)})\frac{dI_0}{da} - s_0I_0e^{-s0(B-a)}\right) \tag{22}$$

$$+ A_{55}\left[\frac{I_1}{s_1}(e^{2s1a} - 1)\frac{dI_1}{da} + I_1^2e^{2s1a} + \frac{I_2}{s_1}(1 - e^{-2s1a})\frac{dI_1}{da} + I_2^2e^{-2s1a}\right)$$

$$+ \lambda_1\left[(e^{s1a} - 1)\frac{dI_1}{da} + s_1I_1e^{s1a} + (e^{-s1a} - 1)\frac{dI_2}{da} - s_1I_2e^{-s1a}\right)$$

For a crack length larger than a few ply thickness, the contribution of $G(a)$ is negligible. This is depicted in Fig. 10 where the strain energy release rate divided by $4C^2$ is plotted against the crack length per unit ply thickness for a graphite/epoxy laminate whose properties are given in Table 1. The strain energy release rate reaches the constant value (1.083 Nm) provided by the first term in Eq 21 for a crack length larger than 10-ply thickness.

Conclusion

A simple shear deformation model for the analysis of unidirectional and cross-ply laminates subjected to torsion loading has been developed. The interlaminar stresses and energy release rate are obtained in closed form, and the parameters controlling the behavior are identified. Comparisons between the interlaminar stresses predicted by the present approach, a FEM solution, and an exact elasticity solution for unidirectional and cross-ply laminates have been performed. The results predicted by the present approach are in good agreement with

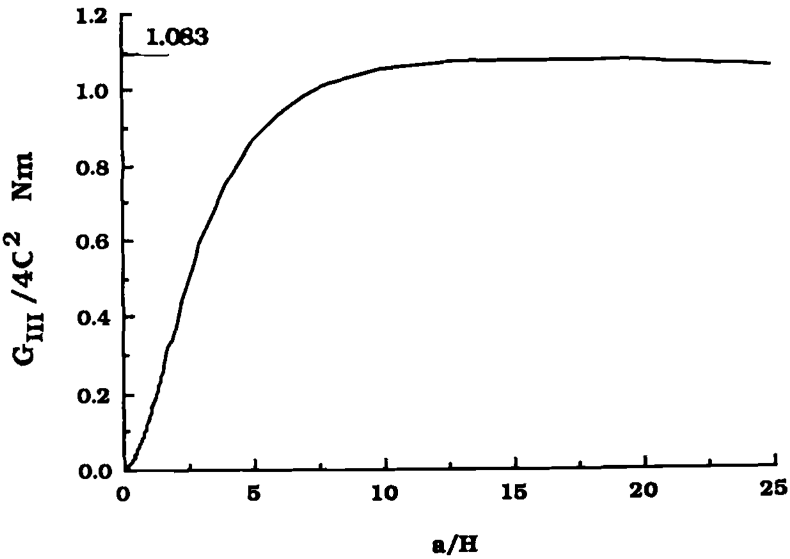

FIG. 10—*Energy release rate as a function of crack length for a* $[0/90]_{4s}$ *laminate.*

TABLE 1—*Material properties of IM6/3501-6 graphite epoxy.*

E_{11} = 24.8 Msi (170.97 GPa)
E_{22} = E_{33} = 1.41 Msi (9.72 GPa)
G_{12} = G_{13} = 0.90 Msi (6.20 GPa)
G_{23} = 0.54 Msi (3.72 GPa)
υ_{12} = υ_{13} = 0.329
υ_{23} = 0.41
Ply thickness H = 0.0055 in. (0.14 × 10^{-3} m)

the exact elasticity solution. The interlaminar stress distributions predicted by the present approach provide a plausible explanation of failure modes in previously tested laminates. The present approach is simple and useful in understanding the basic mechanics of the problem and predicting trend information.

Acknowledgments

This work was sponsored by the Army Research Office under Grant DAAL 03-88-C-0003. This support is gratefully acknowledged.

References

[1] Puppo, N. A. and Evensen, H. A., "Interlaminar Shear in Laminated Composites," *Journal of Composite Materials*, Vol. 4, 1970, p. 204.
[2] Pipes, R. B. and Pagano, N. J., "Interlaminar Stresses in Composites Under Axial Extension," *Journal of Composite Materials*, Vol. 4, 1970, pp. 538–548.
[3] Pagano, N. J., "Stress Field in Composite Laminates" *International Journal of Solids Structures*, 1978, Vol. 14. pp. 385–400.

[4] O'Brien, T. K., "Characterization of Delamination Onset and Growth in a Composite Laminate," *Damage in Composite Materials, ASTM STP 775*, K. L. Reifsnider, Ed., American Society for Testing and Materials, Philadelphia, 1982, pp. 140–167.
[5] O'Brien, T. K., "Mixed-Mode Strain-Energy-Release Rate Effects on Edge Delamination of Composites," *Effects of Defects in Materials, ASTM STP 836*, American Society for Testing and Materials, Philadelphia, 1984, pp. 125–142.
[6] Whitney, J. M. and Knight, M., "A Modified Free-Edge Delamination Specimen," *Delamination and Debonding of Materials, ASTM STP 876*. W. S. Johnson, Ed., American Society for Testing and Materials, Philadelphia, 1985, pp. 298–314.
[7] Whitney, J. M., "Stress Analysis of a Mode I Edge Delamination Specimen for Composite Materials," *AIAA Journal*, American Institute of Aeronautics and Astronautics, Vol. 24, No. 7, July 1986, pp. 1163–1168.
[8] Armanios, E. A. and Rehfield, L. W., "Sublaminate Analysis of Interlaminar Fracture in Composites: Part I—Analytical Model," *Journal of Composites Technology & Research*, Vol. 11, No. 4, Winter 1989, pp. 135–146.
[9] Salamon, N. J., "A Finite-difference Program for Stresses in Anisotropic, Layered Plates in Bending," NASA TN D-8059, National Aeronautics and Space Administration, Washington, DC, 1975.
[10] Salamon, N. J., "Interlaminar Stresses in a Layered Composite Laminate in Bending," *Fibre Science and Technology*, Vol. 11, 1978, pp. 305–317.
[11] Armanios, E. A. and Rehfield, L. W., "Interlaminar Fracture Analysis of Composite Laminates Under Bending and Combined Bending and Extension," *Composite Materials: Testing and Design (Eighth Conference], ASTM STP 972*, J. D. Whitcomb, Ed., American Society for Testing and Materials, Philadelphia, 1988, pp. 81–94.
[12] Ye, L. and Yang, B. X., "Interlaminar Stress Analysis in Symmetric Composite Laminates Under Bending," *Proceedings*, International Conference on Computational Mechanics, 25–29 May 1986, G. Yagawa and S. N. Atluri, Eds., Springer-Verlag, Berlin.
[13] Chan, W. S. and Ochoa, O. O., "An Integrated Finite Element Model of Edge-Delamination Analysis for Laminates due to Tension, Bending, and Torsion Loads," *Proceedings*, AIAA/ASME/AHS Twenty-Eighth Structures, Structural Dynamics, and Material (SDM) Conference, 1987, AIAA Paper No. 87-0704CP, Part 1, American Institute of Aeronautics and Astronautics, Washington, DC, pp. 27-35.
[14] Chan, W. S. and Ochoa, O. O., "Assessment of Free-Edge Delamination Due to Torsion," *Proceedings*, Second Technical Conference, American Society for Composites, Lancaster, PA, 1987, pp. 469–478.
[15] Kurtz, R. D. and Whitney, J. M., "Torsion of Laminates Containing Orthotropic Layers," *Proceedings*, Third Technical Conference, American Society for Composites, Lancaster, PA, 1988.
[16] Lekhnitskii, S. G., *Theory of Elasticity of an Anisotropic Body*, Holden-Day, Inc., San Francisco, CA, 1963.
[17] Murthy, P. L. N. and Chamis, C. C., "Free-Edge Delamination: Laminate Width and Loading Conditions Effects," *Journal of Composites Technology & Research*, Vol. 11, No. 1, Spring 1989, pp. 15–22.
[18] Daniel, W. K. and Vizzini, A. J., "Interlaminar Stresses in Composite Laminates Under Torsional Loading," *Proceedings*, Fourth Technical Conference, American Society for Composites, Blacksburg, VA, 1989, pp. 974–981.
[19] Vinson, J. R. and Sierakowski, R. L., *The Behavior of Structures Composed of Composite Materials*, Martinus Nijhoff Publishers, Dordrecht, The Netherlands, 1986.
[20] Kurtz, R. D. and Sun, C. T., "Composite Shear Moduli and Strengths from Torsion of Thick Laminates," *Composite Materials: Testing and Design (Ninth Volume), ASTM STP 1059*, S. P. Garbo, Ed., American Society for Testing and Materials, Philadelphia, 1990, pp. 508–520.

Summary

Summary

The Twenty-Second National Symposium on Fracture Mechanics was divided into two dual sessions. Session I concentrated on experimental and theoretical aspects of fracture mechanics, while Session II concentrated on numerical and computational aspects of fracture. In Session II, there were 44 presentations made at the Symposium. For a variety of reasons, related to technical and time constraints in preparing a submission for publication, 26 papers appear in this volume. At the Symposium and in this volume, the presentations and papers were divided into four categories: Elastic Fracture Mechanics and Applications, Nonlinear Fracture Mechanics and Applications, Novel Mathematical and Computational Methods, and Composite Materials.

Elastic Fracture Mechanics and Applications

The papers in this section are concerned with the application of linear elastic fracture mechanics concepts to the analysis of three-dimensional crack configurations, fatigue-crack growth and fracture, and to the development of efficient methods of analysis.

Smith presented a review of two established optical methods to accurately measure the stress states for three-dimensional cracked bodies. In particular, he presented the results on several example problems: (1) stress-intensity factor distribution for a nozzle corner crack in a pressure vessel model, (2) a surface crack in a rocket motor propellant model, and (3) determination of the order of the singularity for a crack intersecting a free surface. Photoelastic results presented agreed well with numerical and analytical analyses from the literature.

Raju, Newman, and Atluri presented closed-form equations for the crack-mouth-opening displacements for a surface crack in a flat plate subjected to remote tension and bending loads. They used both the finite element and finite element alternating methods to analyze a wide range in crack shapes and sizes. Their results agreed well with experiments conducted by McCabe for remote tension. Their results agreed well with equations developed by Fett for nearly semicircular surface cracks but gave substantially higher displacements for low aspects ratio (low a/c) and deep (large a/t) cracks.

The finite element alternating method (FEAM) was also used by *Stonesifer, Brust, and Leis* to analyze a surface crack located on the inside of a large pipe. The FEAM included the Vijayakumar-Nishioka-Atluri (VNA) analytical solution which allows for high-order traction variations on the crack surfaces, a deficiency found in earlier alternating solutions. Their results compared well with the results for Raju and Newman except where the crack intersected the wall of the pipe. Here the boundary-layer effect causes difficulties in obtaining accurate solutions.

Dawicke, Shivakumar, Newman, and Grandt presented a hybrid experimental numerical method to determine fatigue crack-opening stresses along a crack front in middle-crack and compact specimens. The method combines experimental measurements of crack-growth rates and crack-front curvature with three-dimensional elastic finite element analyses to determine stress-intensity factor variations and, subsequently, crack-opening stresses. These calculations agreed fairly well with measured results from Sunder's fatigue striation technique and measurements from a remote displacement and near tip strain gages. The proposed method appears to offer a reliable method to study crack-closure effects for three-dimensional crack configurations.

The ASTM Standard Test Method for Plane-Strain Fracture Toughness of Metals Using Chevron-Notched Specimens has been in existence for two years. The paper by *Barker* discusses the origins, significance, and usage of the toughness values that are measured by ASTM E 1304-89.

Bittencourt, Barry, and Ingraffea presented results on the calculation of mixed-mode stress-intensity factors using three different methods (displacement, J-integral and modified crack-closure integral). The modified crack-closure integral showed very good performance for all the applied mixed-mode conditions analyzed.

The last two papers in this section were concerned with the application of efficient methods to analyze three-dimensional crack configurations under complex loading and structures. *Malik* using a weight-function method based on crack-surface-opening displacements and the Newman-Raju stress-intensity factor solutions. He made an extensive comparisons between the stress-intensity factor solutions of Raju and Newman for various crack configurations under remote bending to verify the method for application to general stress gradients. *Rithie, Voermans, Bell, and deLange* used the line-spring model to analyze surface cracks in complex welded structure. Comparisons made between predicted and measured fatigue crack growth patterns and lives agreed well.

Nonlinear Fracture Mechanics and Applications

The section on nonlinear fracture consisted of nine contributed papers on the subjects of experimental Hutchinson, Rice, and Rosengren (HRR) field analysis in homogeneous specimens, hybrid finite element studies of structures and fracture parameters, coupled problems of thermoelastic fracture, three dimensional fracture analysis of crack growth, fatigue crack growth with elastic and viscoelastic dynamic fracture. Specifically, two papers by *Dadkhan, Kobayashi, and Morris*, and *Chiang, Li, and Wang* utilized near tip optical methods to examine the extent and validity of HRR fields during crack initiation and growth. The paper by *Tong, Greif, and Chen* concerned the utilization of hybrid finite element techniques to study complex aircraft structures. The paper by *Nishioka, Fujimoto, and Sakakura* used a hybrid numerical and experimental scheme to combine the caustic experimental technique with the T^* fracture parameter. The paper by *Franco and Gilles* employed three-dimensional finite element methods to study the changes in validity of various fracture parameters from linear elastic, to HRR under contained yield, and finally the Central Electricity Generating Board's (CEGB) two-criteria approaches. The paper by *Brust, Ahmad, and Naboulsi* studied the effects of cyclic fatigue damage and plasticity on crack-growth behavior in terms of the J and T^* fracture parameters. The paper by *Gu* concerned the development of K-R curves for 2024-T531 aluminum alloy that are independent of specimen configuration. The work by *Chen and Huang* implemented a three-dimensional finite element method with path-independent integrals to study an embedded elliptical crack under thermal gradients. The final paper in this section by *O'Donoghue, Kanninen, Popelar, and Popelar* studied rate dependent fracture in polyethylene piping systems showing most notably a validity of linear elastic fracture mechanics (LEFM) provided the craze zone is small and contained. As a whole, this collection of papers represents an excellent cross section of the state of the art in nonlinear fracture research.

Novel Mathematical and Computational Methods

This section describes computational and mathematical methods that are new, novel, and efficient to analyze two- and three-dimensional crack configurations made of brittle and ductile materials.

Yagawa, Yoshimura, Yoshioka, and Pyo presented a study of a crack growing in a ductile material using hybrid experimental and numerical methods. A computer image process was used to measure the displacement field near a growing crack. The stress, strain, and near crack-tip (local) J-integral were evaluated from the measured displacement field. Their study on Type 304 stainless steel showed that the HRR field seems to exist outside a small nonlinear region where the crack tip is largely blunted and for a small amount of crack growth. The local J-integral showed good path independence outside the small nonlinear region and they agreed well with conventional J-integral evaluations for small amounts of crack extension. For large values of crack extension, the local J tended to approach a constant value while the conventional J estimates continued to rise.

Cruse and Novati formulated a traction boundary integral equation (BIE) for application to nonplanar curved cracks and multiple cracks. The nonplanar curved cracks were modeled as piecewise flat regions. These regions were modeled as triangular boundary elements. The implementation of the integral equations for these elements was presented. The new formulation was applied to several problems that are three-dimensional approximations to plane strain fracture problems. In all cases the piecewise flat traction BIE implementation agreed well with limited results from the literature.

Barsoum and Chen studied three-dimensional singularity fields for interfacial surface and corner cracks by a finite element iterative method. Their results on the bimaterial free surface singularity suggests that the two-dimensional analyses at the interfaces are nonconservative and three-dimensional analysis must be used.

Kuo, Shvarts, and Stonesifer presented an alternating analytical procedure for the analysis of an elliptical or part elliptical crack in an infinite flat plate of finite thickness subjected to arbitrary crack surface loading. In this method, in contrast to the other alternating methods, the uncracked infinite flat plate was analyzed by decomposing the residual stresses on the plate bounding surfaces into double Fourier series and by using Fast Fourier Transform methods. With this approach, three-dimensional crack problems are solved with great ease because no finite element model needs to be prepared as in the finite element alternating method (FEAM). However, this method appears to have limited applicability compared to the FEAM because it can only handle flat plate configurations.

Sun, Kienzler, Voss, and Schmitt studied the ductile fracture behavior of different specimens by continuum damage mechanics techniques. They used a modified Gurson model. The damage parameters used in the model were obtained from the tests on smooth bars. The critical distance over which void coalescence is active was determined by matching load against displacement from a cracked specimen. The model was then used to predict the deformation and fracture behavior of notched round bars and side-grooved compact specimens. In all cases, satisfactory agreement was obtained between the predictions and the test results.

Composite Materials

In the composite materials section, four papers were published. They are concerned with the analysis and prediction of strength and failure of laminated composite materials.

Zhu and Achenbach presented a numerical technique to calculate microlevel stresses for transverse loading of a unidirectional fiber-reinforced composite with hexagonal packing.

The composite fiber-matrix interphases were modeled by the spring-layer model. The numerical technique presented should be useful in modeling failure scenarios of radial matrix cracking and interphase failure.

Bouden and Datta used the finite element and integral representation technique to analyze scattering of waves by interfacial cracks in a layered half-space. With this technique, arbitrary crack configurations can be analyzed. An analysis of a interfacial crack subjected to both normal and shear loadings was demonstrated. For both loading cases, the normal crack-opening displacements (COD) are larger than the tangential COD's at low frequencies. Dynamic stress-intensity factors were found to attain high peak values at certain resonant frequencies.

Cheng and Lin presented two probabilistic fracture models—statistical and stochastic—for predicting the notched strength of laminated composites. The statistical model considered the case of constant load while the stochastic model dealt with the effect of monotonically increasing loads. The notched strength of boron/aluminum composites with various crack lengths was predicted using the statistical model. The predicted results agreed well with the experimental data. However, the stochastic model appears to be more accurate since it represents a more realistic loading situation and also this model provides upper and lower bound predictions. The probabilistic approach proposed appears to predict a power-law type relationship between fracture stress and notch size.

Li and Armanios introduced a simple analytical method using a sublaminate approach to analyze unidirectional and cross-ply laminates under torsion loading. Interlaminar stresses and total strain energy release rates were evaluated based on a displacement field that included shear deformation. Closed form expressions for the interlaminar stresses and total strain energy release rates were obtained for unidirectional and cross-ply laminates in terms of the laminate stiffness coefficients. The interlaminar stresses for these laminates, predicted by this simple method agreed well with a finite element solution and an exact elasticity solution.

Satya N. Atluri
Georgia Institute of Technology,
Atlanta, GA 30332; editor.

James C. Newman, Jr.
NASA Langley Research Center,
Hampton, VA 23665; editor.

Ivatury S. Raju
North Carolina State University,
Greensboro, NC 27411; editor.

Jonathan S. Epstein
Idaho National Engineering
Laboratory, Idaho Falls,
ID 83415, editor.

Author Index

S

T

V

W

Y

Z

Subject Index

ISBN 0-8031-1440-0